SEISMIC PERFORMANCE ASSESSMENT OF REINFORCED CONCRETE BUILDINGS WITH PRECAST CONCRETE FLOOR SYSTEMS

A THESIS
SUBMITTED IN PARTIAL FULFILMENT
OF THE REQUIREMENTS FOR THE DEGREE
OF
DOCTOR OF PHILOSOPHY
AT THE
UNIVERSITY OF CANTREBURY

By

Brian Hsuan-Hsien PENG

July 2009

Department of Civil and Natural Resources Engineering
University of Canterbury
Christchurch
New Zealand

To My Parents

ABSTRACT

In the seismic design of reinforced concrete frames, plastic hinges are allocated to beams such that a ductile beam-sway mechanism will form in preference to other less ductile mechanisms in the event of a major earthquake. This is achieved by ensuring that the flexural strength of columns is greater than that corresponding to the maximum likely flexural strength of beam plastic hinges.

Recent experimental studies in New Zealand have shown that elongation of ductile beam plastic hinges, and its interaction with nearby floor slab containing precast-prestressed floor units, increases the strength of beams much more than that specified in New Zealand and American Concrete standards. This level of strength enhancement has raised concern on the adequacy of the current design provisions. To further investigate this problem, a research project was initiated to examine the strength of beam plastic hinges in reinforced concrete frames containing precast-prestressed floor units.

In this research, the strength of beam plastic hinges was assessed through experimental and analytical studies. A three-dimensional, one-storey, two-bay reinforced concrete moment resisting frame with prestressed floor units and cast-in-situ concrete topping was tested under quasi-static displacement-controlled cyclic loading. The experimental results provided insight into the mechanics associated with frame-floor interaction. Subsequently, improved design specifications were proposed based on the observed behaviour.

To analytically predict the beam-floor interaction, a ductile reinforced concrete plastic hinge multi-spring element was developed and validated with experimental results from cantilever beam and frame sub-assembly tests reported in the literature. The comparisons have demonstrated the ability of the proposed plastic hinge element to predict the flexural, shear, axial, and most importantly, elongation response of ductile plastic hinges.

The proposed plastic hinge element was implemented into an analytical model to simulate the behaviour of the frame-floor sub-assembly tested in this research. Specially arranged truss-like elements were used to model the linking slab (the region connecting the main beam to the first prestressed floor unit), where significant inelastic behaviour was expected to occur. The analytical model was found to be capable of predicting the non-linear hysteretic response and the main deformation mechanisms in the frame-floor sub-assembly test.

The analytical frame-floor model developed in this study was used to examine the effect of different structural arrangements on the cyclic behaviour of frames containing prestressed floor units. These analyses indicated that slab reinforcement content, the number of bays in a frame and the position of frame in a building (i.e., perimeter or internal frame) can have a significant influence on the strength and elongation response of plastic hinges.

ACKNOWLEDGEMENTS

The research presented in this thesis was carried out under the supervision of Associate Professor Rajesh Dhakal, Associate Professor Richard Fenwick, Professor Athol Carr and Professor Des Bull. I wish to sincerely thank all of you for the support and encouragement throughout this project. Your guidance in all aspects of this research has helped my professional and personal development towards being an independent and critically minded researcher for which I am grateful to you all.

This project would not have been possible without the financial support provided by: the Tertiary Education Commission through Top Achieve Doctoral Scholarships; the New Zealand Society for Earthquake Engineering; The Todd Foundation; University of Canterbury; Stahlton Ltd; and Firth Ltd. Their contributions are greatly acknowledged.

I would like to thank the technicians who have helped on this project. In particular, Russell McConchie, Gavin Keats, Richard Newton and Michael Weavers for their assistance in making the experimental research a smooth and pleasant experience.

I am grateful to the assistance of Brendon Bradley, Adam Walker, Euving Au, Michael Newcombe, and Perry Jackson for editing the draft of my thesis. I would also like to thank my fellow postgraduate students Weng Yuen Kam, Dion Marriott, Vinod Sadashiva, Gregory Cole and numerous others for their friendships and social activities during my study. You have made this an enjoyable and memorable experience.

Finally, I wish to express my deepest gratitude to my family. To my parents, Betty and Ting-Yung, my partner, Christy, and my brother, Steven, thank you for all your love, support, understanding and encouragement during these past years.

TABLE OF CONTENTS

LIST OF FIGURES

LIST OF TABLES

1 INTRODUCTION

1.1 BACKGROUND AND RESEARCH MOTIVATION

The concept of seismic design of structures has evolved over the last century. The initial approach was to design structures on the basis of elastic response. The present approach, which incorporates the capacity design concept (Hollings 1969; Park and Paulay 1975), ensures that inelastic deformation is confined to predetermined potential plastic hinge regions such that a ductile mechanism forms in an event of a major earthquake. This shift in design approach has improved building performance under seismic actions.

In the capacity design philosophy, plastic hinges in reinforced concrete (RC) moment-resisting frames are generally allocated to beams and to the base of columns, as shown in Figure 1-1(a). This is to ensure that in the event of a major earthquake, a desirable ductile beam sway-mechanism will develop in preference to other less ductile modes, such as a column-sway mechanism as shown in Figure 1-1(b). This is because for the same applied displacement, Δ, the effect of P-Δ is more detrimental to the plastic hinges in the column-sway mechanism. In addition, the rotational demands in plastic hinges of a column-sway mechanism are much greater than that in plastic hinges of a beam-sway mechanism. The level of rotational demand, associated with the column-sway mechanism, is generally difficult to achieve.

The capacity design approach requires potential beam plastic hinges to be detailed for ductility. More importantly, it requires the columns and the rest of members being able to resist the maximum likely actions (i.e., over-strength actions) associated with the beam plastic hinges, without sustaining appreciable inelastic deformation. This is also known as “strong column-weak beam” design. Therefore, the determination of the over-strength of beam plastic hinges is a critical issue for the design of RC moment-resisting frames.

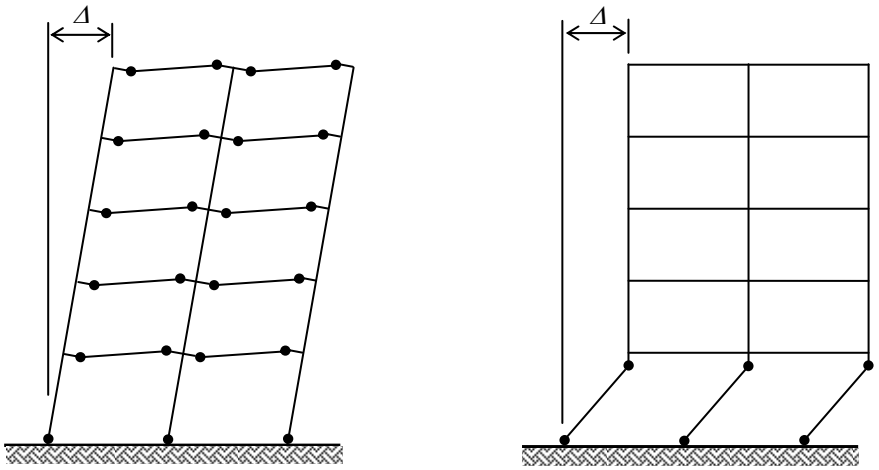

(a) Beam-sway mechanism (b) Column-sway mechanism

Figure 1-1. Deformation mechanisms in a multi-storey frame building

For beams, where there is no composite action with floor slabs, the over-strength of plastic hinges can be calculated using standard flexural theory with appropriate over-strength factors to account for strain hardening effects and statistical variation in the strength of reinforcing steel and concrete. For beams coupled with cast-in-situ floor slabs, the negative flexural strength of beam plastic hinges can increase significantly due to elongation of plastic hinges and its interaction with the floor slab (French and Boroojerdi 1989; Jirsa 1991). To accommodate this, an effective flange width of floor slabs is assigned to calculate the flexural over-strength of beam plastic hinges. This is commonly referred to as “flange effect.” Based on experimental results, empirical equations were developed by Cheung (1991) to account for this strength enhancement. These equations were later adopted by the New Zealand Concrete Structures Standard, NZS 3101:1995 (Standards New Zealand 1995).

Recent large scale experimental studies of RC moment resisting frames coupled with precast-prestressed flooring systems, such as hollow-core and rib-and-infill units (Lindsay 2004; Matthews 2004; MacPherson 2005; Lau 2007), have shown that the presence of prestressed floor units increases the strength of beams much more than that specified in the New Zealand code, which were based on the experimental results with cast-in-situ floor slabs. The strength enhancement was found to arise due to elongation of plastic hinges and its interaction with the surrounding floor slabs

containing prestressed floor units. In addition, the level of strength enhancement was shown to vary with different structural arrangements (Fenwick et al. 2005).

While experimental results have provided some insight into the level of strength enhancement that may occur and the mechanisms associated with the interaction between beams and floor slabs, they cannot by themselves be used to develop satisfactory design guidelines due to the wide range of structural arrangements and prestressed flooring systems used in practice. Repetitive experimental studies on this topic would be complex, time and resource consuming; therefore, numerical simulation provides a more feasible alternative.

To simulate the strength enhancement of beams coupled with floor slabs containing prestressed units and in-situ concrete topping, analytical models must be able to predict elongation response of plastic hinges as well as the interaction between beams and floor slabs. However, the conventional analysis techniques, using lumped plasticity approach to model beams, cannot capture elongation of plastic hinges. On the other hand, complex finite element programs are computationally demanding and are not appropriate for running multiple time-history analyses. To overcome this difficulty, an analytical model that can predict the elongation of plastic hinges is required.

1.2 RESEARCH OBJECTIVES

The main aim of this project is to develop an analytical tool that incorporates the effect of beam elongation and models the interaction of beams with precast-prestressed floor diaphragms. This is required to enable the seismic behaviour of RC frame buildings containing prestressed floor units to be assessed.

More specific objectives are:

1. To develop and verify a plastic hinge element that can capture flexural, shear, axial load, and most importantly, elongation responses of plastic hinges.
2. To gather experimental data on elongation of RC members.
3. To investigate the seismic response of a 3D frame-floor sub-assembly test; with special attention on the frame-floor interaction.

4. To develop a three-dimensional frame-floor analytical model that incorporates the elongating plastic hinge element so that the response of beams and floor slabs containing precast prestressed units can be predicted.
5. To examine the validity of the current specifications in the New Zealand Concrete Structures Standard, NZS 3101:2006 (Standards New Zealand 2006), on floor contribution to the negative flexural over-strength of beam plastic hinges.

1.3 ORGANISATION OF THESIS

The dissertation is divided into four main parts: development, verification and application of the elongating plastic hinge element; experimental study of a three dimensional, one-storey RC frame sub-assembly with floor slabs containing precast-prestressed floor units; development and validation of an analytical model for the sub-assembly test; and parametric studies identifying the key parameters that influence the interaction between a floor and surrounding frame. For simplicity, all investigations were carried out under quasi-static conditions.

Chapter 2 describes the development of a plastic hinge element which takes into account flexural, shear, axial load and elongation responses of ductile RC plastic hinges. Experimental results available from the literature were used to validate the plastic hinge element. The model was validated using experimental results of cantilever beams tested under different levels of axial force, with different transverse reinforcement contents, top and bottom reinforcement ratios and loading histories.

Chapter 3 extends the work reported in Chapter 2 by improving the shear deformation modelling of the plastic hinge element. The shear deformation mechanisms in plastic hinges were investigated and a simple relationship relating the total shear deformation to elongation of plastic hinges was proposed. The refined plastic hinge element was validated with experimental results obtained from the literature.

Chapter 4 focuses on the application of the plastic hinge element in analyses of two dimensional RC frames. Experimental results of three different RC frames with different boundary conditions were obtained from the literature. Analytical models

containing the refined plastic hinge element were developed to enable predictions to be made and compared to the experimental results. The effects of elongation on the seismic response of RC frames were also investigated.

Chapter 5 documents the design of a three dimensional frame-floor sub-assembly test, which contained precast-prestressed flooring units. The specimen layout, test set up and the loading protocol were designed to simulate building behaviour under inelastic cyclic loading. A detailed instrumentation plan and procedures for interpreting the test results are discussed in this chapter.

Chapter 6 presents the experimental results from the 3D sub-assembly test described in Chapter 5. The results focus on the interaction between elongation of plastic hinges and the surrounding floor slabs; in particular, the flexural over-strength of plastic hinges due to slab contribution. The experimental results on slab contribution were compared to the recommendations of the New Zealand standard, NZS 3101:2006, and ACI concrete code, ACI 318-05, (American Concrete Institute 2005). A list of general observations made during the test and the interpreted experimental results are provided in this chapter. A method of estimating the slab participation to the negative flexural over-strength of plastic hinges next to external columns is described in the chapter.

Chapter 7 describes the analytical model developed to simulate the 3D frame-floor sub-assembly test described in Chapter 5. Unlike the conventional analysis technique, where the plastic hinges are modelled using the lumped plasticity approach, the analytical model used in the analyses contains the refined plastic hinge element, described in Chapter 3, which allows elongation of plastic hinges to be predicted. Interaction between elongating plastic hinges and floor slabs are modelled using the strut-and-tie method. These struts-and-ties are placed over the linking slab region, denoted as the region between the first prestressed floor unit and the main beam, where appreciable non-linearity is expected to occur. The analytical model was validated using experimental results. Sensitivity studies were carried out to examine the effects of a number of different parameters.

Chapter 8 describes the effects of different parameters, such as slab reinforcement ratios and number of bays in the moment resisting frame, on the slab contribution to the negative flexural strength of plastic hinges. The validity of defining a constant effective flange width for slab participation is also examined.

Chapter 9 presents a summary of the research outcomes, the main conclusions and the recommendations for future research.

1.4 REFERENCES

American Concrete Institute. (2005). *Building code requirements for structural concrete and commentary (ACI 318M-05)*, American Concrete Institute, Farmington Hills, Michigan.

Cheung, P. C. (1991). "Seismic design of reinforced concrete beam-column joints with floor slab," PhD. Thesis, Department of Civil Engineering, University of Canterbury, Christchurch, New Zealand.

Fenwick, R. C., Davidson, B. J., and Lau, D. B. N. "Interaction between ductile RC perimeter frames and floor slabs containing precast units." *New Zealand Society for Earthquake Engineering Conference 2005*, 23-35.

French, C. W., and Boroojerdi, A. (1989). "Contribution of R/C floor slabs in resisting lateral loads." *Journal of Structural Engineering*, 115(1), 1-18.

Hollings, J. P. (1969). "Reinforced concrete seismic design." *Bulletin of the New Zealand National Society for Earthquake Engineering*, 2(3), 217-250.

Jirsa, J. O. (1991). *Design of beam-column joints for seismic resistance, ACI SP-123*, American Concrete Institute, Detroit, Michigan.

Lau, D. B. N. (2007). "Influence of precast prestressed flooring on the seismic performance of reinforced concrete perimeter frame buildings." *Report Number 653*, Dept. of Civil and Environmental Engineering, University of Auckland, Auckland, New Zealand.

Lindsay, R. (2004). "Experiments on the seismic performance of hollow-core floor systems in precast concrete buildings," Master Thesis, University of Canterbury, Christchurch, New Zealand.

MacPherson, C. (2005). "Seismic performance and forensic analysis of a precast concrete hollow-core floor super-assemblage," Master Thesis, University of Canterbury, Christchurch, New Zealand.

Matthews, J. (2004). "Hollow-core floor slab performance following a severe earthquake," PhD. Thesis, University of Canterbury, Christchurch, New Zealand.

Park, R., and Paulay, T. (1975). *Reinforced concrete structures*, Wiley, New York.

Standards New Zealand. (1995). *Concrete structures standard: NZS 3101:1995*, Standards New Zealand, Wellington.

Standards New Zealand. (2006). *Concrete structures standard: NZS 3101:2006*, Standards New Zealand, Wellington.

2 DEVELOPMENT OF PLASTIC HINGE MODEL

Extensive experimental studies on the seismic behaviour of reinforced concrete (RC) beams have shown that ductile RC beam plastic hinges designed in accordance with New Zealand Concrete Structures Standard typically elongate between two and five percent of the beam depth before strength degradation occurs (Fenwick et al. 1981; Issa 1997; Matti 1998; Liddell et al. 2000; Walker 2007). This level of elongation can have significant effects on the seismic performance of RC buildings as illustrated in Figure 2-1. The figure plots the schematic displacement pattern at the bottom storey of a RC frame arising from different deformation mechanisms. It can be seen that elongation of the beam plastic hinges affects the deflected shape of the frame, which will lead to changes in the moment and shear force distribution within the frame. It also increases the maximum column deformation, shear force and moment demand. This has been highlighted in the experimental and analytical studies on 2D frames by various researchers (Fenwick and Davidson 1995; McBride et al. 1996; Wuu 1996; Kim et al. 2004).

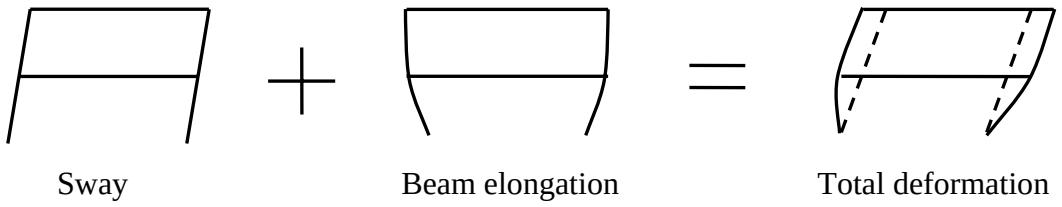

Figure 2-1. Frame deformation considering beam elongation

Experimental tests on moment resisting frames coupled with floor slab containing precast-prestressed floor units (Lindsay 2004; Matthews 2004; MacPherson 2005; Lau 2007) have also shown that elongation of beam plastic hinges and its interaction with prestressed floor units can affect the seismic performance of RC frames. Undesirable failure mechanisms, such as: unseating of precast floor units from the supporting beams in cases where insufficient seating length is specified; or the formation of a column side-sway mechanism due to an increase in beam strength from slab-participation, may occur in the event of a major earthquake.

Although the aforementioned research has found that elongation of plastic hinges can have a significant influence on the seismic performance of RC frames, it is generally not considered in seismic design and analysis due to a lack of satisfactory analytical models capable of predicting plastic hinge elongation. Several methods for predicting elongation within plastic hinges have been proposed in the past, most of these were developed empirically from experimental results. The first empirical equations for predicting elongation of uni-directional and reversing plastic hinges were proposed by Megget and Fenwick (1989) and Fenwick and Megget (1993). More advanced micro-mechanics theory correlating elongation with reinforcement strain and beam rotation was later proposed by Lee and Watanabe (2003). The Rainflow method, where elongation of a beam coupled to a floor slab, was introduced by Mathews et al. (2004). While some of these theories predict the elongation behaviour satisfactorily, they cannot be readily incorporated into time-history analysis programs.

An analytical elongation model for RC beams was proposed by Douglas (1996) and later refined by Lau (2003). Both of these models employ a filament type element to represent the plastic hinge region. Although both models have shown promising elongation prediction, they require calibration with experimental results prior to the analysis. An elongation model for precast RC beams containing prestressed tendons was proposed by Kim et al. (2004). However, this model is not directly applicable for predicting plastic hinge elongation in monolithic moment resisting frames where the behaviour is more complex. The details of these models are elaborated in Section 2.1.4.

While detailed finite element analysis, using a fibre model implementing fully path-dependent cyclic material models for reinforcing bars and concrete, may be able to predict the elongation response, such models are seldom used to analyze large-scale structures, presumably due to excessive computational demands. Therefore, it is desirable to have a fibre-model-based plastic hinge element that can be used together with the traditional one-dimensional frame elements to predict seismic performance of RC frames, adequately accounting for plastic hinge elongation phenomena.

This chapter describes the development of a generic plastic hinge element that can account for elongation of plastic hinges in ductile RC members. Background on the

types of plastic hinges formed in beams and their corresponding elongation mechanisms are described. Previous studies on elongation predictions are summarised. Finally, the development and verification of a plastic hinge element is presented.

2.1 LITERATURE REVIEW

2.1.1 Plastic Hinge Background

In seismic design of RC structures, plastic hinges in frames are carefully positioned and detailed to ensure that structures behave in a ductile manner. These plastic hinges are designed to sustain large inelastic rotations while maintaining their strength. This action induces large plastic strains in flexural reinforcement and consequently plastic hinges "grow" in length under cyclic loading. Even in the presence of an axial compression, plastic hinges are found to elongate, albeit to a lesser extent (Matti 1998).

There are two different types of plastic hinge, namely uni-directional and reversing plastic hinges. The type of plastic hinge that can potentially form in a beam depends on the relative moment contributions from gravity and seismic actions, and the distribution of the top and bottom flexural reinforcement in the beam. Uni-directional plastic hinges, as illustrated in Figure 2-2, typically form in gravity dominated frames where the gravity-induced moments are relatively large compared to the seismic moments. In this case, the maximum positive (tension on the bottom) and negative (tension on the top) moments occur at different locations in the beam as the frame sways backwards and forwards. Consequently, the rotation in each plastic hinge accumulates under repetitive cyclic loadings.

In such uni-directional plastic hinges, the length of the positive moment plastic hinge is generally longer than the negative moment plastic hinge. This is because the positive plastic hinge (formed within the beam span), develops in region of low shear, and hence the reinforcement can yield towards both directions from the critical section. In comparison, the negative plastic hinge (formed at the column face), develops in region of relatively high shear and the reinforcement tends to yield predominantly on one side.

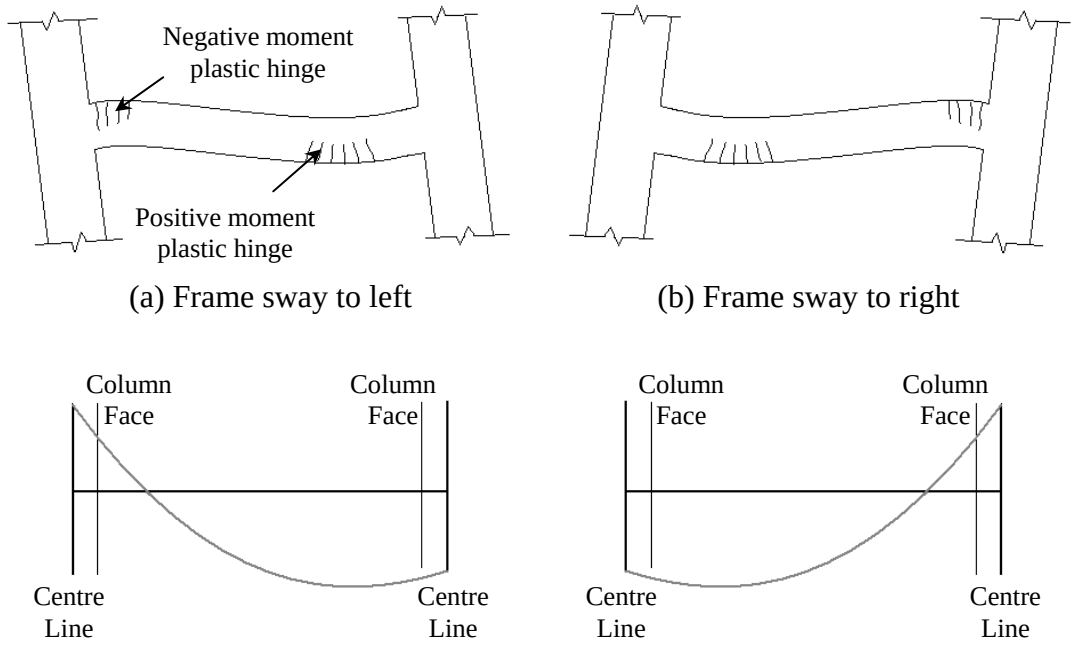

(a) Frame sway to left (b) Frame sway to right

(c) Associated bending moment diagram

Figure 2-2. Illustrative diagrams for uni-directional plastic hinges

In seismic dominated frames, where the potential seismic moments are relatively large compared to the gravity moments, both the maximum positive and maximum negative moments occur next to the column faces, as illustrated in Figure 2-3. In such cases, the maximum hinge rotation is proportional to the column drift and the rotational demand in the plastic hinges is much smaller than that incurred in the uni-directional plastic hinges.

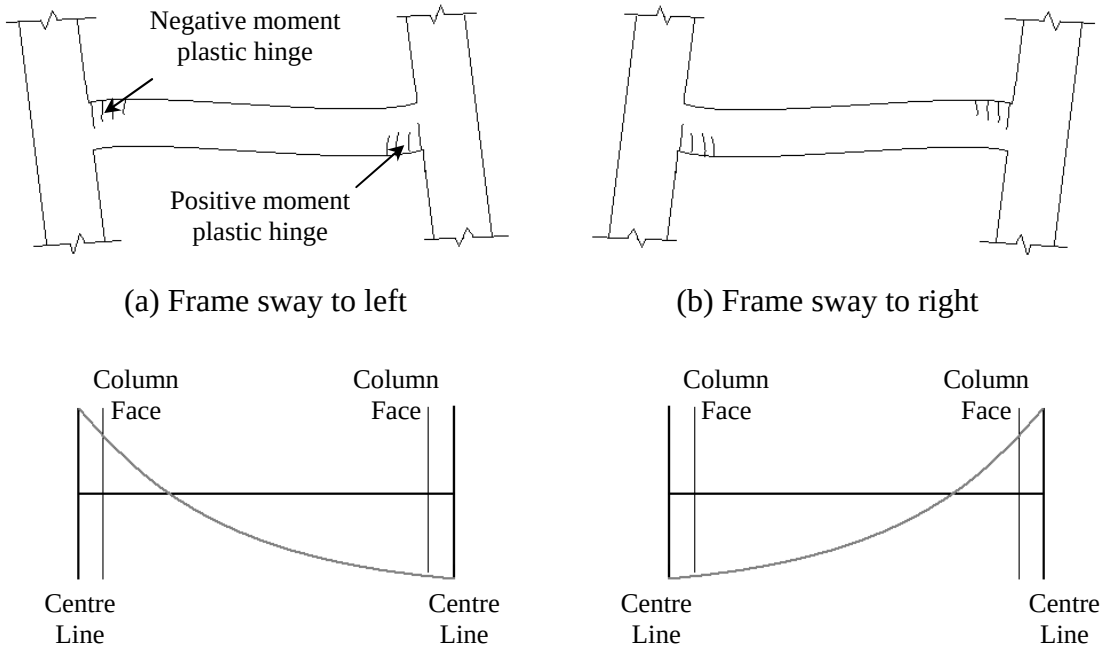

(a) Frame sway to left (b) Frame sway to right

(c) Associated bending moment diagram

Figure 2-3. Illustrative diagrams for reversing plastic hinges

2.1.2 Mechanisms of Beam Elongation

The elongation behaviour in plastic hinges differs significantly in uni-directional and reversing plastic hinges. Elongation in reversing plastic hinges arises due to two main factors (Fenwick and Megget 1993): (i) inelastic extension of the tension reinforcement to accommodate the inelastic rotation of plastic hinges; and (ii) irrecoverable extension of the compression reinforcement. These are illustrated in Figure 2-4 where the extension of top and bottom reinforcement over the plastic hinge region in a beam test is plotted. In this figure, L_T represents the extension of tension reinforcement associated with inelastic rotation and L_C represents the irrecoverable extension of the compression reinforcement upon load reversal.

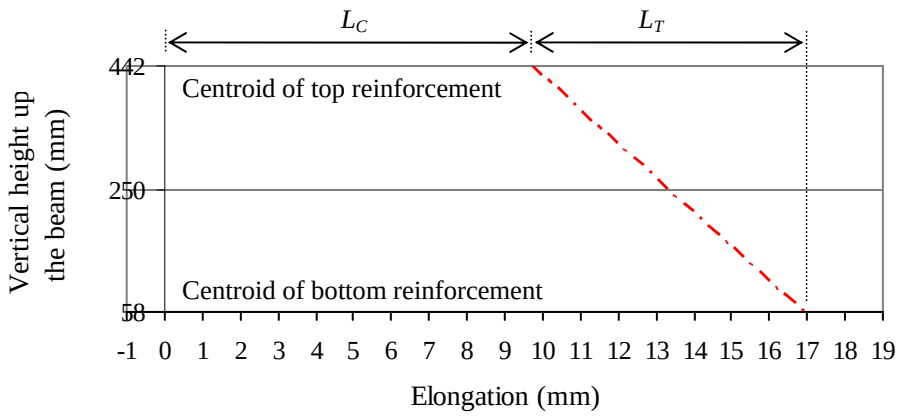

Figure 2-4. Schematic diagram showing the reinforcement extension over a plastic hinge region at a peak displacement cycle

The irrecoverable extension of the compression reinforcement observed in Figure 2-4 arises due to two main actions:

1. Intersecting diagonal cracks in the plastic hinge region greatly reduce the shear resistance of member from aggregate interlock and dowel action of reinforcement. Consequently, “truss-like” actions, as illustrated in Figure 2-5, develop in plastic hinges where the shear force is resisted by the shear reinforcement and the diagonal compression struts in the webs. In this figure, T and C are the flexural tension and compression forces in the reinforcement; V is the shear force acting in the beam; and θ is the angle of the diagonal struts to the axis of the beam. To satisfy force equilibrium at a given section, the flexural tension force in the reinforcement must be larger than the flexural compression force as the horizontal component of the diagonal compression forces in the web also contributes to the total compression force in the section. Consequently, reinforcement which yielded in tension in the previous half cycle does not fully recover when subjected to compression in the following half cycle. As a result, inelastic extension in the reinforcement tends to accumulate as the cyclic loading continues.

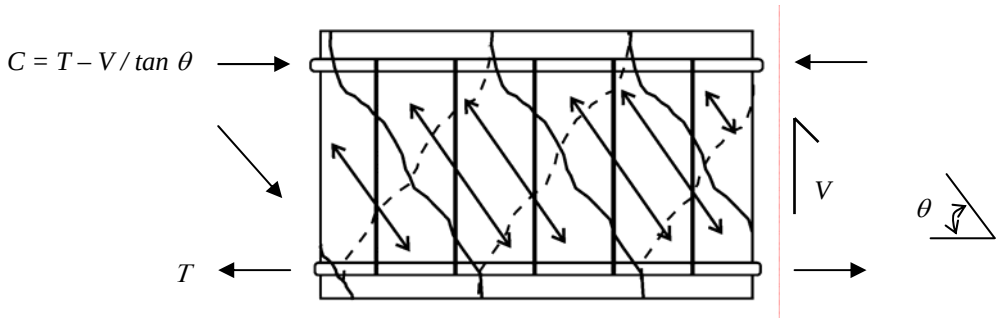

Figure 2-5. Truss-like action in a plastic hinge region

2. Aggregate particles become dislodged from crack surfaces and these prevent the cracks from closing fully when the load is reversed, particularly when large shear displacement develops across the cracks. This phenomenon is also known as “contact stress effect” where the concrete member experiences compressive stress before the strain reverses into compression.

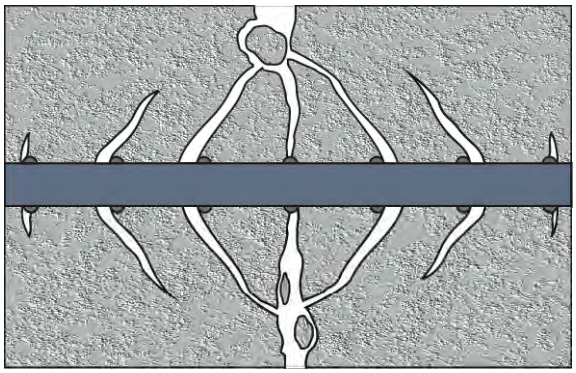

Figure 2-6. Wedging action of cracked concrete

In uni-directional plastic hinges, as reinforcement on one side never yields in tension, elongation arises only due to extension in the tension reinforcement from cumulative inelastic rotation, as described by Fenwick and Davidson (1995) and Fenwick and Megget (1993).

2.1.3 Empirical Elongation Formulae Available in Literature

2.1.3.1 Fenwick and Megget

As previously mentioned, Fenwick and Megget were the first to measure elongation in plastic hinges, as illustrated in Figure 2-7. Based on a series of experimental tests

on RC beams and RC portal frames (Fenwick and Fong 1979; Fenwick et al. 1981; Megget and Fenwick 1989; Fenwick and Megget 1993), they proposed two empirical formulae to estimate elongation in uni-directional and reversing plastic hinges.

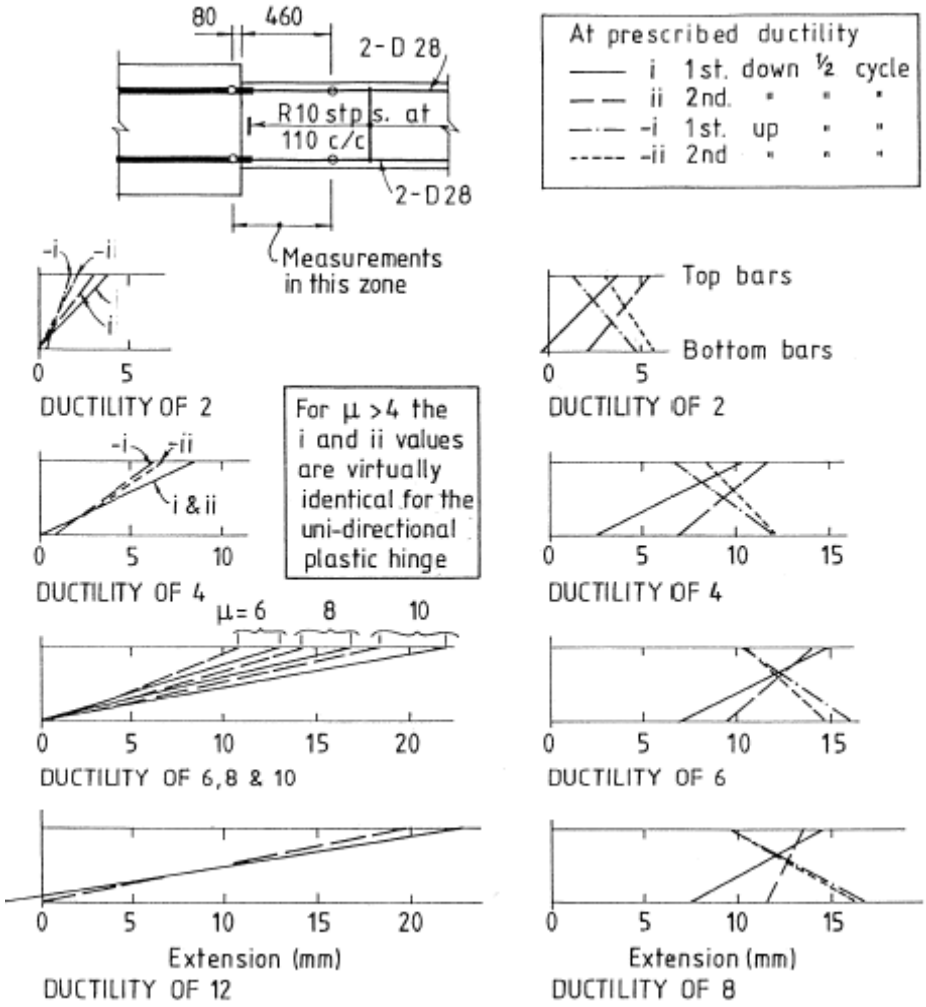

(a) Uni-directional plastic hinge (b) Reversing plastic hinge

Figure 2-7. Extension of flexural reinforcement in uni-directional and reversing plastic hinges (Fenwick and Megget 1993)

For uni-directional plastic hinges, elongation can be estimated using Equation 2-1, where *d-d'* is the distance between the centroids of the flexural reinforcement and $\Sigma\theta$ is the sum of the inelastic rotations applied to the plastic hinge. Equation 2-1 assumes that the compression reinforcement has never yielded in tension so that the strain in the reinforcement is negligible.

$$Elongation = \Sigma\theta \frac{d - d'}{2} \quad (2\text{-}1)$$

For reversing plastic hinges, elongation can be estimated by Equation 2-2, where *e* is the permanent extension in the compression reinforcement, which varies significantly with applied displacement histories, section and material properties, applied axial force and amount of shear reinforcement. Based on the experimental results for beams with no axial load, *e* was found to be generally more than twice the extension arising from the plastic hinge rotation at the end of displacement ductility of 6 cycles (Fenwick and Megget 1993). Despite these general observations, no specific guidelines were given for calculating *e*.

$$Elongation = e + \Sigma\theta \frac{d - d'}{2} \quad (2\text{-}2)$$

2.1.3.2 Lee and Watanabe

Lee and Watanabe (2003) developed a micro-mechanics theory by correlating reinforcement strain to the displacement history and beam rotation. They identified four main paths to describe axial strain in plastic hinges. The total axial strain in the plastic hinge is the sum of the four cumulative strains from each path as shown in Equation 2-3. These paths are illustrated in Figure 2-8 and are described below:

1) Elastic and unloading regions; the decreasing axial strain rate in the unloading zone is the same as the increasing strain rate in the elastic zone.
2) Post-flexural yielding region where the axial strain increases significantly.
3) Slip region where the change in axial strain is assumed to be negligible.
4) Repeated loading region where the increase in the axial strain is assumed to be inversely proportional to the number of reloading cycles.

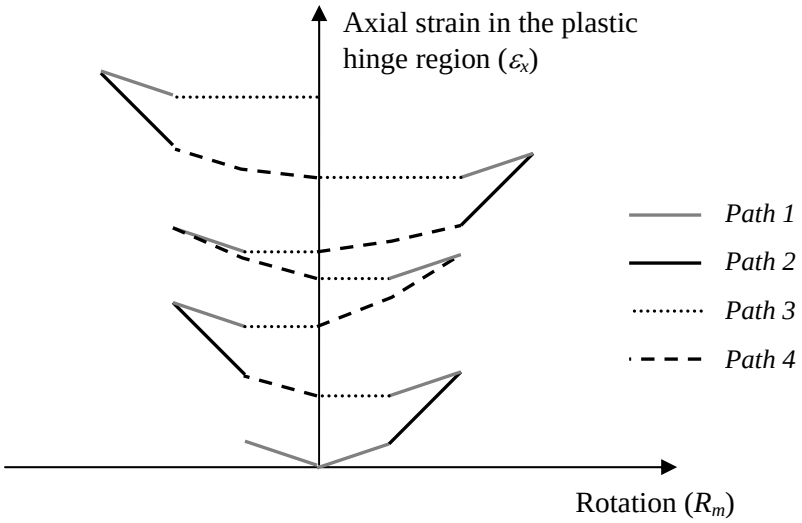

Figure 2-8. Elongation model proposed by Lee and Watanabe

$$\varepsilon_x = (1-F)\varepsilon_{xf} + \frac{(R_{pmp} + R_{pmn})jd}{2l_h} + \sum_{i=1}^{m}\sum_{j=1}^{n}\left(\frac{R_{mi}\,jd}{2l_h}\right)^{0.85}\frac{1}{4N_j} \qquad (2\text{-}3)$$

where

ε_x = axial strain in the plastic hinge,

F = number of unloading cycles beyond flexural yielding,

ε_{xf} = axial strain at flexural yield point,

R_{pmp} = positive plastic rotation,

R_{pmn} = negative plastic rotation,

jd = distance between the centroids of flexural reinforcement,

l_h = length of the plastic hinge (defined by Equation 2-5),

R_{mi} = i^{th} rotation component, and

N_j = number of j^{th} reload for the rotation component R_{mi}, ($1 \le N_j \le 5$).

It should be noted that despite this equation giving accurate predictions for beams with no axial load (Lee and Watanabe 2003); its applicability for beams with different levels of axial loads is yet to be verified.

To reduce the computational complexity associated with Equation 2-3, they assumed that the decreasing rate of the axial strain in *Path 1* was similar to the increasing rate in *Path 4*. Consequently, the simplified equation below was developed where R_{mp} and R_{mn} are the positive and negative rotations of the beam, respectively.

$$\varepsilon_x = \frac{\left(R_{mp} + R_{mn}\right) jd}{2l_h} \tag{2-4}$$

$$l_h = 0.5\left(\frac{M}{Vh}\right)d \qquad \text{with } (0.75d \le l_h \le d) \tag{2-5}$$

where

M = applied moment,

V = applied shear force,

h = overall beam depth, and

d = effective beam depth.

2.1.3.3 Matthews

The Rainflow counting method was proposed by Matthews (2004) to predict elongation of beams coupled with floor slabs. Similar to the simplified equation proposed by Lee and Watanabe (2003), elongation was defined as a function of the rotation in the plastic hinges as shown in Equation 2-6 and Figure 2-9. The only difference between these two methods is that the centroid of the compression region is evaluated at each step by Matthews (2004), rather than assumed at the centroid of the compression steel. This continual computation of the centroid allows for composite beam actions to be considered. Despite this improvement, it should be noted that this method does not capture beam growth under repeated cycles at the same displacement magnitude that was observed in the experiments of Mathews (2004) and it also does not take into account the influence of axial loads on beam elongation.

$$\delta_{max} = \left(\left|\theta_p{}^{+}\right| + \left|\theta_p{}^{-}\right| + \left|\theta_y\right|\right)\sum_{i=1}^{n} e_{cri} \tag{2-6}$$

where

δ_{max} = total elongation in the frame,

θ_p^{+} = maximum positive plastic rotation imposed on the frame,

θ_p^{-} = maximum negative plastic rotation imposed on the frame,

θ_y = yield rotation of the frame,

e_{cri} = eccentricity between the centre of gravity of the beam and the centroid of the compression force for the i^{th} hinge.

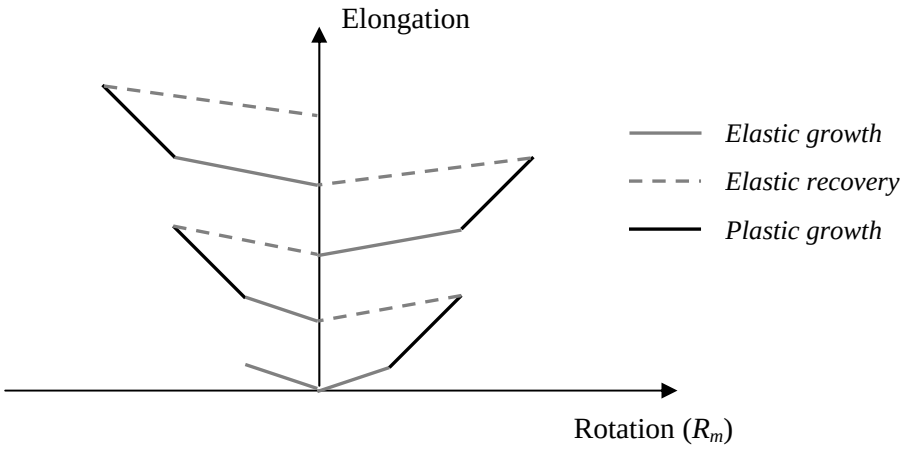

Figure 2-9. Rainflow method for predicting elongation of RC plastic hinges

2.1.4 Analytical Elongation Model Available in Literature

2.1.4.1 Douglas

The first analytical model developed to predict elongation in plastic hinges, of which the author is aware, was proposed by Douglas (1996). The set up of the model is illustrated in Figure 2-10. The proposed plastic hinge element consists of four truss elements and a shear element connected between two rigid arms. The rigid arms are 2mm apart and are attached to the ends of two semi-rigid elements. As all of the inelastic deformations are confined within the rigid arms, the length of the semi-rigid elements is calibrated to give the correct total deformation prediction. The properties of the semi-rigid elements are also calibrated to give the correct initial elastic stiffness.

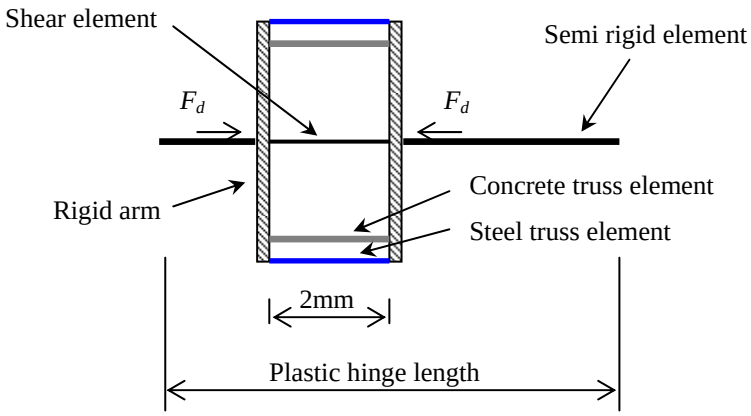

Figure 2-10. Analytical plastic hinge element developed by Douglas

Figure 2-10 illustrates that the steel and concrete truss elements are located at the centroids of the flexural reinforcement to represent the flexural actions. The stiffness of the truss elements are calculated based on the length over which the reinforcement yields, while the shear element provides the shear resistance. Additional self equilibrating horizontal forces, F_d, are applied between the rigid links to represent the horizontal component of the diagonal compression force.

As the model requires calibration of several parameters to match the experiments, it cannot be used to predict elongation of RC plastic hinges, where such experimental data is unavailable (the common case in practice).

2.1.4.2 Lau

The model developed by Douglas was simplified by Lau (2007) and incorporated into the finite-element program, SAP2000 Nonlinear 8.1 (CSI 2003). As shown in Figure 2-11, the model of Lau (2007) consists of 10 axial truss elements with five different member types connected between two rigid arms. *Member A* and *member B* are used to model the longitudinal steel and concrete materials, respectively. *Member C* is used to simulate the diagonal compression struts in RC plastic hinges. *Member D* provides shear resistance to ensure the model is stable at low levels of applied force and *Member E* is used to calibrate the analytical elongation with experimental results. The length of the plastic hinge element was taken as (*d - d'*).

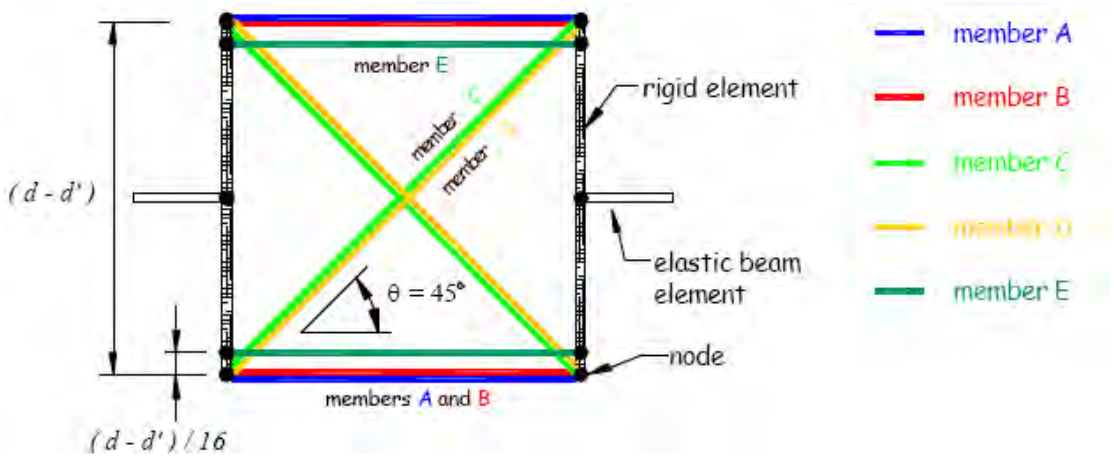

Figure 2-11. Analytical plastic hinge element proposed by Lau (2003)

Again, as this model requires manipulation of the properties in *Member E* to match experiments results, it cannot be used by itself to predict the elongation of RC plastic hinges.

2.1.4.3 Kim

The model proposed by Kim (2002) was originally developed for precast hybrid frames where most of the non-linearity occurs at the column face. This model was then modified to simulate monolithic connections (Kim 2002). The set up of the model is shown in Figure 2-12, where the length of the interface is calculated based on the empirical equation for plastic hinge length proposed by Priestley et al. (1996). Truss elements are used to represent the flexural behaviour in the plastic hinges, and the shear force is transferred between nodes b5 and c5 via a stiff vertical spring.

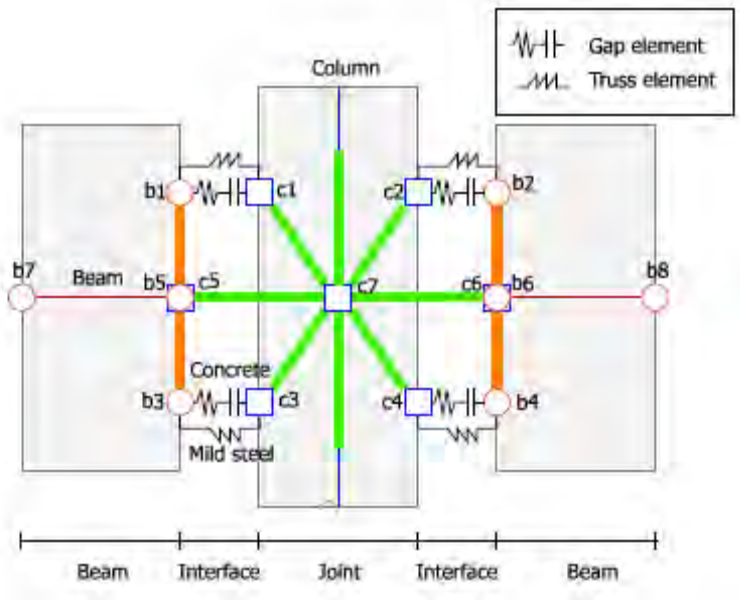

Figure 2-12. Analytical model allowing for beam growth (Kim et al. 2004)

One shortcoming of the model is that it does not take into account the diagonal compression struts developed in the plastic hinges, and therefore the permanent extension in the compression reinforcement cannot be captured. Consequently, the predicted elongation is expected to be smaller than that observed in the experiments. Furthermore, as the shear spring across the hinge is infinitely stiff, shear deformation in the plastic hinges is also not captured.

2.2 PROPOSED ANALYTICAL MODEL

In the proposed analytical approach, individual RC members are modelled using a combination of an elastic beam element and the newly developed plastic hinge element discussed herein. The analytical cantilever beam model is implemented in RUAUMOKO2D (Carr 2008), an inelastic time history analysis program, as shown in Figure 2-13, where Δ and P are the applied displacement and applied axial force respectively, L is the length of the beam and L_P is the length of the plastic hinge element, chosen to represent the inclination of the diagonal compression struts in the plastic hinge, as described in Section 2.2.1.

The shear modulus of the elastic beam element is taken as $0.4E_c$ according to Clause 6.9.1 in NZS 3101:2006 (Standards New Zealand 2006) where E_c is the Young's modulus of concrete. The shear area of the elastic beam is taken as bd, where b and d are the width and effective depth of the section, respectively. The effective moment of inertia of the elastic beam is taken as $0.4I_g$ given by Table C6.6 in NZS 3101 where I_g is the gross section moment of inertia. The 0.4 factor is used to represent the loss of stiffness due to flexural cracking and to represent the effective stiffness associated with first yield.

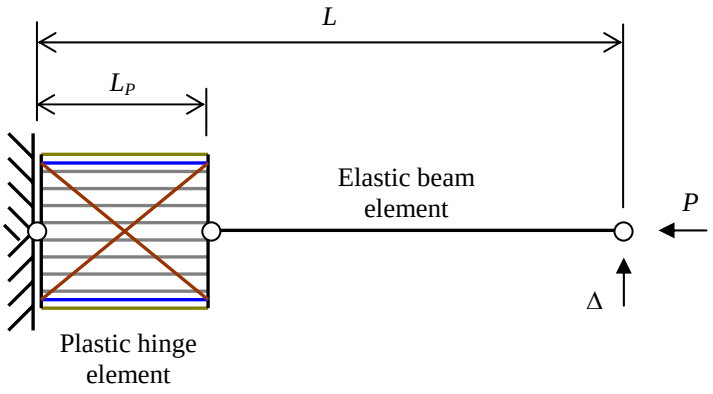

Figure 2-13. Analytical model for a cantilever beam

2.2.1 Development of Plastic Hinge Element

The plastic hinge element is developed with the aim of capturing the elongation mechanisms described in Section 2.1.1 based on fundamental mechanics, i.e., not requiring the calibration of empirical parameters with experimental results on a case-

by-case basis. A schematic representation of the proposed plastic hinge element is shown in Figure 2-14. It can be seen that the plastic hinge element consists of a series of longitudinal and diagonal axial springs connected between the rigid links at the two ends. The longitudinal springs are used to represent flexural and axial response of the plastic hinge, and the diagonal springs are used to represent the diagonal compression struts in the web, which provide shear resistance. With this arrangement, the moment and shear are evaluated at the centre of the plastic hinge element and are extrapolated to obtain the nodal moments and forces at the two ends of the plastic hinge element.

In the element, two steel springs are located at the centroids of the top and bottom reinforcement to represent the reinforcing bars, two concrete springs are located at the centre of the top and bottom covers to represent unconfined concrete, eight concrete springs are distributed evenly between the centroids of the tensile and compressive reinforcing bars to represent the confined core concrete and two diagonal concrete springs are connected between the ends of top and bottom steel springs to represent the diagonal compression struts. The material models adopted for the concrete and steel springs are based on uni-axial averaged (over the spring length) stress-strain relationships of concrete and reinforcing steel obtained from literature. Important characteristics of the material models such as spalling and contact effect of concrete and Bauschinger and cyclic behaviour of steel are included in these models and are elaborated in Section 2.2.1.4.

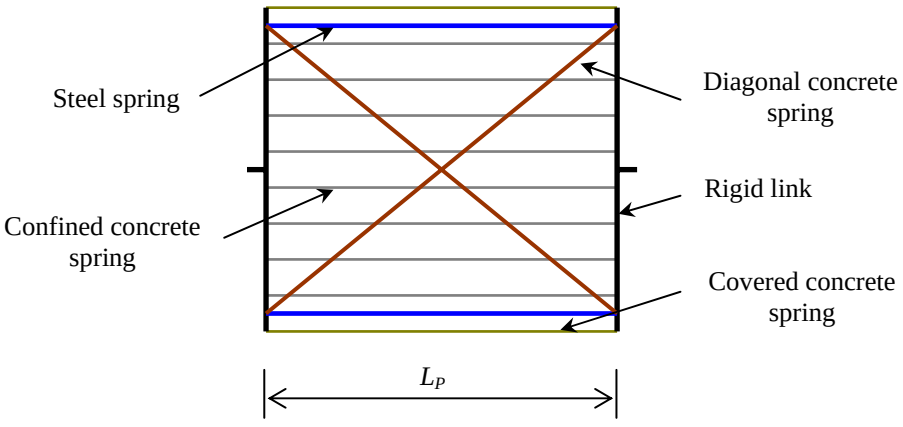

Figure 2-14. Schematic illustration of the plastic hinge element

The element is developed to predict the behaviour of RC plastic hinges up to the peak response (before strength degradation occurs). Therefore, significant buckling of

longitudinal reinforcement, which mainly affects the post-peak response of plastic hinges, is not considered in this model. In addition, it was not possible to quantify the variation of bond slip of beam reinforcement in the beam column joint within the scope of this project. Consequently, the variation in bond slip (strain penetration) with applied displacement cycles was not considered in developing the plastic hinge element.

2.2.1.1 Length of Plastic Hinge Element

The length of the plastic hinge element, L_P, as shown in Figure 2-14, is chosen to represent the inclination of the diagonal compression struts, θ, in the plastic hinge region as illustrated in Figure 2-15. This length does not represent the length of the effective plastic hinge region that is used for calculating the curvature from plastic hinge rotation as specified in NZS 3101:2006. Nor does it represent the ductile detailing length as specified in NZS 3101:2006 where inelastic deformation may develop in the reinforcement. It should not be misunderstood with the equivalent plastic hinge length proposed by other researchers (Priestley and Park 1987; Mendis 2001; Panagiotakos and Fardis 2001; Bae and Bayrak 2008), which was proposed to give a reasonable estimate of the tip displacement based on lumped plasticity approach.

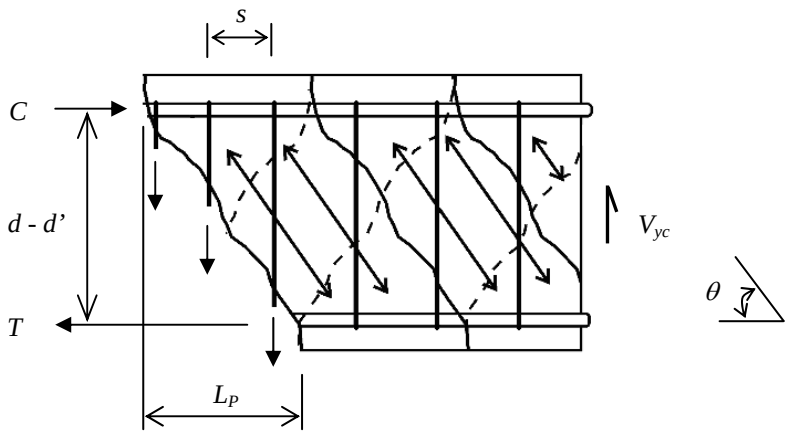

Figure 2-15. Schematic diagram showing the diagonal crack pattern in a RC plastic hinge

Based on the truss analogy, it is hypothesized that the diagonal cracks will form at an angle such that the crack crosses just enough stirrups to resist the shear force in the web corresponding to the theoretical flexural capacity. Consequently, L_P is equal to

the number of stirrups required to resist the shear force multiplied by the spacing of the stirrups, *s*. This can be expressed as Equation 2-7.

$$L_P = \frac{d - d'}{\tan\theta} = \frac{(V_{yc} - V_c)s}{A_v f_{vy}} \tag{2-7}$$

where

d - d’ = distance between the centroids of top and bottom reinforcing bars,

θ = angle of the diagonal struts to the horizontal plane,

V_{yc} = shear force corresponding to the theoretical flexural strength of the beam, M_{yc}, given by Equation 2-8,

V_c = shear resistance of concrete,

A_v = area of the shear reinforcement, and

f_{vy} = yield stress of the shear reinforcement.

$$M_{yc} = A_s f_y (d - d') + P\frac{(d - d')}{2} \tag{2-8}$$

where

A_s = area of the longitudinal reinforcement,

f_y = yield stress of the longitudinal reinforcement, and

P = applied axial force (taken here as a positive value for axial compression force).

The theoretical flexural strength, M_{yc}, where the top and bottom reinforcement has yielded in tension in the previous cycles, is used for calculating L_p instead of the nominal flexural strength, M_n. This is because under cyclic loading, during which the compression reinforcement has been yielded in tension in the previous cycles, the majority of the compression force is resisted by the compression reinforcement unless the compression reinforcement yields back to enable the cracks to close (in which case the concrete contribution may be significant). It should be noted that V_{yc} is generally smaller than the maximum shear force sustained in the beam due to strain hardening of the longitudinal reinforcement. For simplicity, it is assumed that the longitudinal and transverse reinforcement strain-hardens at the same rate. The adoption of V_{yc} in Equation 2-7 can hence be justified.

In the concrete codes, such as ACI 318-05 (American Concrete Institute 2005) and NZS 3101:2006 (Standards New Zealand 2006), it is commonly assumed that the shear resistance of concrete in beam plastic hinges is negligible as wide intersecting diagonal cracks in the plastic hinges destroy the shear resistance of concrete. However, as the axial compression force increases the shear resistance of concrete may also increase. Unfortunately, there is no guidance available in the literature specifying the shear resistance of concrete in plastic hinges with different levels of axial force. Therefore, despite acknowledging that the concrete contribution to shear resistance may not be insignificant in the presence of axial compression force, the concrete shear resistance is taken as zero and Equation 2-7 can be simplified to Equation 2-9. Further research is required to quantify the shear resistance of concrete in plastic hinges with different levels of axial loads.

$$L_P = \frac{V_{yc}\, s}{A_v\, f_{vy}} \tag{2-9}$$

2.2.1.2 Stiffness of Steel Springs

As the flexural stiffness of the plastic hinge element is governed by the axial stiffness of the longitudinal springs, it is imperative to have accurate axial stiffness values for these springs, in order to correctly model the flexural response of the plastic hinges using the proposed model. The axial stiffness of these springs is calculated as the product of the tangent modulus and cross-sectional area divided by the length of the spring. As concrete cracks at an early stage, and the post-cracking tangent modulus of concrete (i.e. concrete springs) is insignificant, the overall flexural behaviour of the plastic hinge element is largely governed by the axial behaviour of the steel springs.

Here the axial behaviour of the steel springs represents the average behaviour of the reinforcing bars over the yielded length. Therefore, the length of steel spring for evaluating the stiffness of the steel spring in the plastic hinge element is taken as the actual length over which the reinforcement yields, L_{yield}, as illustrated in Figure 2-16 and given by Equation 2-10. The equation takes into account the length of tension shift effect, L_{ts}. It also makes a nominal allowance for the length of strain penetration into the support, L_e, which is different to the equation proposed by Priestley et al.

(1996) for RC columns. In the proposed model, the strain in the steel spring is constant throughout the plastic hinge element length.

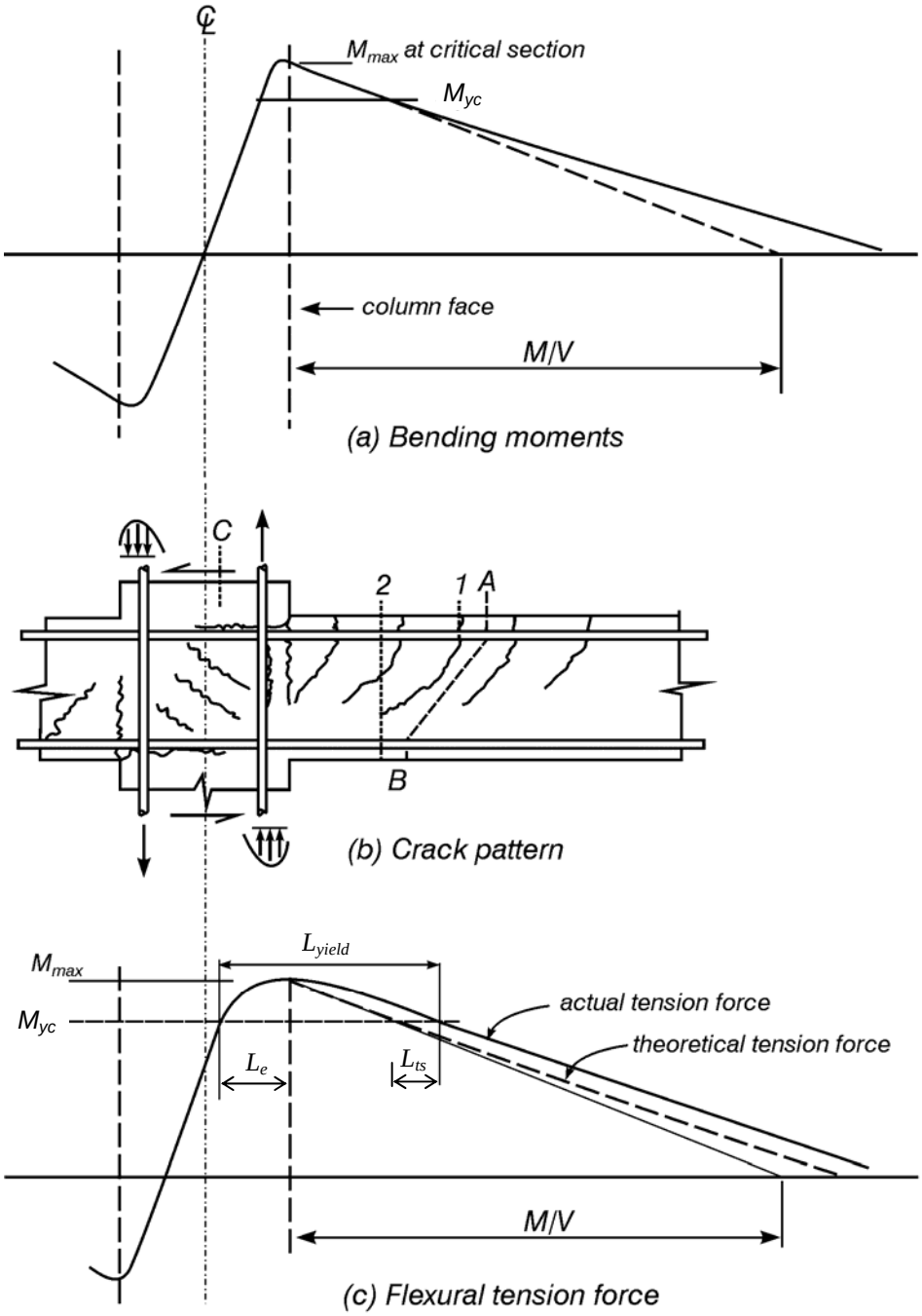

Figure 2-16. Moment, crack pattern and internal tension force in a beam

$$L_{yield} = \frac{M}{V}\frac{M_{max} - M_{yc}}{M_{max}} + L_{ts} + L_e \qquad (2\text{-}10)$$

where

M / V = moment to shear ratio,

M_{max} = maximum moment sustained in the beam,

L_{ts} = length of tension shift effect and,

L_e = length of yield penetration of longitudinal reinforcement into the support which in this project has been taken as a portion of the development length specified in the code.

For a beam with no axial force, the length of tension shift, L_{ts}, can be approximated using Equation 2-11 (Paulay and Priestley 1992).

$$L_{ts} = \frac{d - d'}{2} \tag{2-11}$$

This is based on the assumption that the diagonal crack extends over a distance *(d – d')* along the member at the low moment end of plastic hinges, as illustrated in Figure 2-17, where C_1 is the flexural compression force at section 1, T_2 is the flexural tension force at section 2 and V_s is the shear force resisted by shear reinforcement. As the shear force in the plastic hinge region is assumed to be carried solely by the stirrups crossing the crack, $V_s = V$. The moment at section 1 in Figure 2-17 can therefore be expressed as:

$$M_1 = T_2(d - d') + 0.5(d - d')V_s \tag{2-12}$$

$$M_1 = M_2 + V(d - d') \tag{2-13}$$

Rearranging the above equations; a relationship between the tension force and moment at section 2 can be derived as:

$$T_2 = \frac{M_2}{d - d'} + 0.5V \tag{2-14}$$

In Equation 2-14, the term $0.5V$ implies that the flexural tension force at section 2 is proportional to moment at a distance $0.5(d - d')$ to the left of the section. For beams with axial compression force, the diagonal crack angle would decrease and the length of tension shift would increase. Unfortunately, the relationship between the crack angle and the applied axial force in the low moment end of plastic hinges under

reversing cyclic actions is not readily available in literature. Therefore, the length of tension shift is assumed to be 0.5($d - d'$) for all axial load cases.

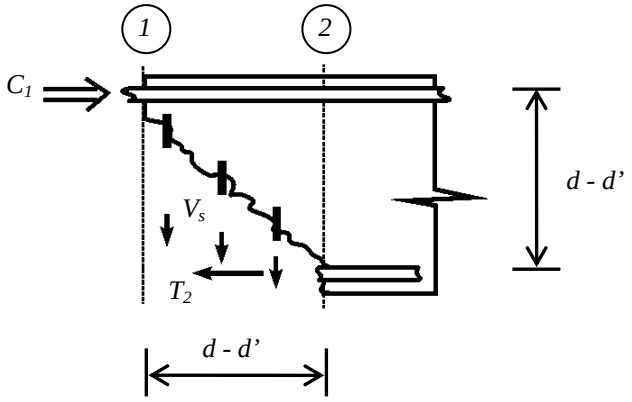

Figure 2-17. Internal forces in a reinforced concrete member

Intuitively, the yielding length of the reinforcing bars changes with the level of loading. However, as it is not possible to qualify the length of the plastic hinge element under cyclic loading, a constant yield length corresponding to the maximum flexural capacity of the member is used for the plastic hinge element. As a result, the length of the steel springs at small displacement cycles is over-estimated. This resulted in a smaller predicted initial stiffness and slightly greater predicted elongation. With this assumption in mind, Equation 2-10 requires the maximum moment, M_{max}, to be predetermined. This can be assessed from the experimental results or calculated giving due consideration to the strain hardening of reinforcing bars.

2.2.1.3 Stiffness and Strength of Diagonal Struts

The initial stiffness of the diagonal strut is calculated as the product of its cross-sectional area and the elastic modulus of concrete divided by its length. The area of the diagonal concrete spring is equal to the width of the beam, b, multiplied by the effective depth of the compression strut, D. The effective depth is taken as the perpendicular distance from the diagonal strut to the end-point of the reinforcement spring as illustrated in Figure 2-18, and can be calculated using Equation 2-15.

$$D = L_p \sin\theta \tag{2-15}$$

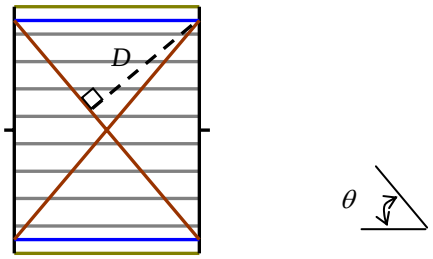

Figure 2-18. Area of diagonal concrete strut in the plastic hinge element

It has been found that transverse tensile strains in concrete members reduce their longitudinal concrete compressive strength (Vecchio and Collins 1986; Pang and Hsu 1996). Experimental results from Schlaich et al. (1987) showed a 15% reduction of concrete compressive strength, in which the nearby steel was previously subjected to high inelastic strain. For regions where significant inelastic strain occurs in the neighbouring reinforcement, To et al. (2001) found that the effective concrete compressive strength of the diagonal struts can be taken as $0.34f_c'$. Hence, herein the effective compressive strength of the diagonal springs used is set to $0.34f_c'$.

2.2.1.4 Material models

The ability of the proposed plastic hinge element to reliably capture the cyclic response and to predict the elongation depends heavily on how accurately the path-dependent cyclic behaviour of the axial springs is modelled. The material models adopted for the concrete and steel springs are based on uni-axial averaged (over the spring length) stress-strain relationships of concrete and reinforcing steel.

The concrete hysteretic model used in this research was developed by Maekawa et al. (2003). The envelope of the constitutive relationship used for the concrete springs consists of a tension stiffening model in the tension region (Shima et al. 1987) and an elasto-plastic fracture model in the compression region (Maekawa and Okamura 1983). Detailed information on these models is summarised in Appendix A. The response of the concrete spring during an arbitrary loading regime is shown in Figure 2-19. As shown in the figure, the loss of stiffness due to fracture of concrete is taken into account in the cyclic model. Also, the unloading loop from tension into

compression includes an allowance for the contact stress effect, where axial compression stress develops before the strain reverses into compression. As previously mentioned in Section 2.1.2, the contact stress effect arises due to wedging action of dislocated aggregate particles in the cracks.

The level of contact stress effect in the concrete model (Maekawa et al. 2003) was based on the results of uni-axial cyclic tests. However, for RC members under combined axial and shear actions, contact stress effects would intuitively be much larger than those observed in the uni-axial tests. The level of contact stresses would depend on the level of axial force and shear displacement sustained across the cracks, aggregate size, concrete compressive strength, and displacement histories applied to the member. As there is currently no literature available to quantify these effects, a constant amplification factor, *TFACTOR*, of 1.5 is incorporated into the constitutive model used for concrete springs in the proposed plastic hinge element to allow for a larger contact stress effect. Detailed discussion on the contact stress parameters is given in Appendix A.

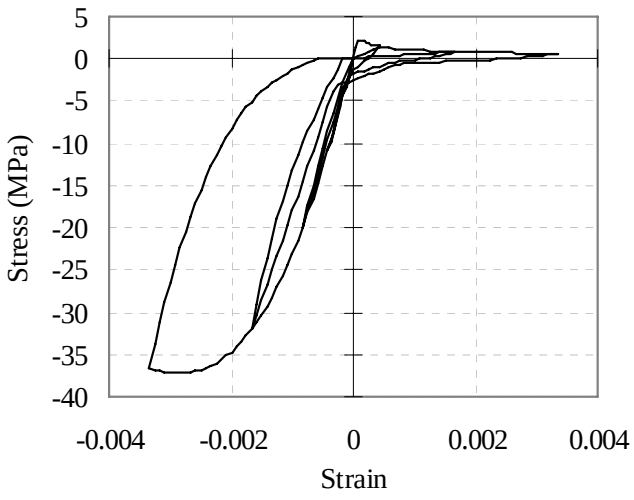

Figure 2-19. Concrete hysteresis

The steel hysteric model implemented for the steel axial springs was developed by Dhakal and Maekawa (2002a; 2002b). Although the original model accounted for buckling of reinforcing bars inside RC members, it has been neglected in the constitutive model used for steel springs in the proposed plastic hinge element. This is because the original model was developed based on RC prisms under uni-axial

loading which would not be representative of the behaviour of RC plastic hinges under combined shear and axial deformation. It was observed in previous experiments that inelastic extension of shear reinforcement in the plastic hinges increases with the applied displacements (Issa 1997; Matti 1998; Walker 2007). This would accelerate the onset of bar buckling which is generally neglected in most of the buckling models.

The path-dependent cyclic steel model consists of compression/tension envelopes with Mander's strain hardening model (Mander 1983) and the unloading/reloading loops represented by Giuffre-Menegotto-Pinto model (CEB-FIP 1996), which takes into account the Bauschinger effect. The response of the steel spring under monotonic and cyclic loading is shown in Figure 2-20.

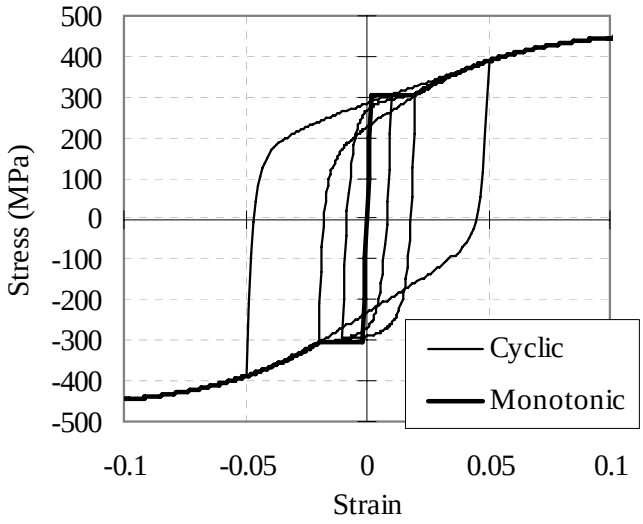

Figure 2-20. Steel hysteresis

2.3 HAND ANALYSIS TECHNIQUE

For the purpose of understanding the key features of the proposed plastic hinge element, a simple hand analysis method was developed. For simplicity, the plastic hinge element was reduced to two longitudinal and two diagonal axial springs as illustrated in Figure 2-21. The longitudinal springs were used to represent the reinforcing bars. A bilinear hysteresis rule with a bilinear factor of 0.4% was used for the longitudinal springs. The diagonal springs were used to represent the concrete struts, which only act in compression and were assumed to behave elastically.

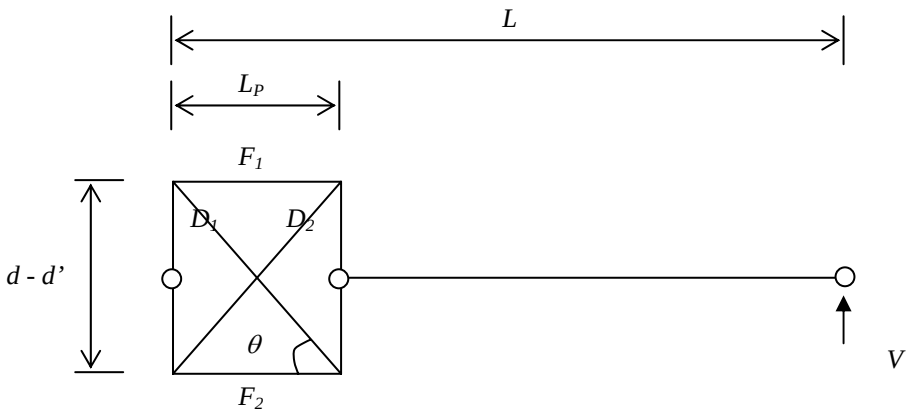

Figure 2-21. Hand analysis technique for modelling a RC beam

For a given upward elastic force, *V*, the force in each spring can be calculated from the relationship given in Equation 2-16. These relationships are derived from truss geometry where a negative value implies compression force. The corresponding deformation in each spring, ΔF_1, ΔF_2, ΔD_1 as shown in Figure 2-22, can also be calculated from the constitutive stress-strain relationship of each individual spring, where a negative value implies axial shortening. Deformation ΔD_2, as illustrated in Figure 2-22, can then be evaluated using Equation 2-17. From the deformation of each spring, the deflection at the point of the applied force, Δ, can be calculated using Equation 2-18. When the load is released, the force in each spring is zero (i.e., $F_1 = F_2 = D_1 = D_2 = 0$) and the deformation in each member returns back to zero.

$$F_1 = \frac{-V \times (L - L_P)}{d - d'}$$

$$F_2 = \frac{V \times L}{d - d'} \qquad (2\text{-}16)$$

$$D_1 = -V / \sin\theta$$

$$D_2 = 0$$

$$\Delta D_2 = \left(\frac{-\Delta D_1}{\sin\theta} + \frac{\Delta F_2}{\tan\theta} \right) \sin\theta + \Delta F_1 \cos\theta \qquad (2\text{-}17)$$

$$\Delta = \frac{\Delta D_1}{\sin\theta} + \frac{\Delta F_2}{\tan\theta} + \frac{(\Delta F_2 - \Delta F_1) \times (L - L_P)}{d - d'} \qquad (2\text{-}18)$$

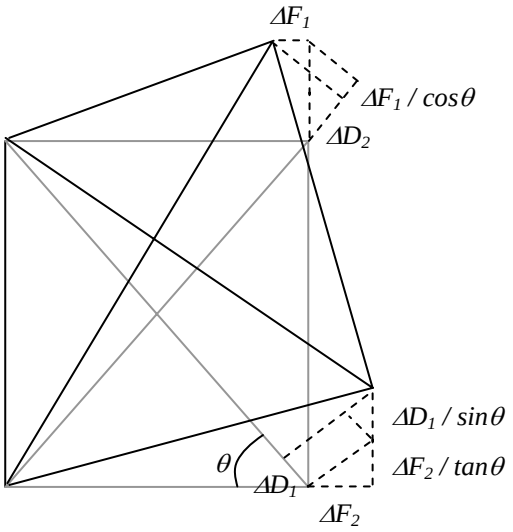

Figure 2-22. Deformation of the plastic hinge

A cantilever beam test was selected for modelling purposes. The beam is labelled Beam 2A, and is described in detail in Section 2.7.1. The displacement history applied to Beam 2A was used in the analysis. The analytical and experimental force-displacement and elongation responses of Beam 2A are shown in Figure 2-23. Points 1 to 5 in these plots correspond to each other and indicate different stages of cyclic loading. As a simple bilinear model was used to represent the behaviour of steel bars in the hand analysis, it does not capture the Bauschinger effect as shown in Figure 2-24. Consequently, the longitudinal reinforcement would not yield back as much into compressive strain upon load reversal in the analysis and hence elongation is over-estimated.

Between points 1 and 2 in Figure 2-23, the beam elongates during the elastic loading phase due to the neutral axis not coinciding with the nodal line; however there is no permanent elongation when the load is reversed to zero. As the beam starts to undergo inelastic response, elongation starts to accumulate. During the loading phase of a cycle, elongation increases rapidly. However, only a small portion of this is recovered during the unloading phase (points 3 to 5). At point 4, the deformation of the diagonal, ΔD_1, reverses to zero. As the top/bottom bars have yielded, ΔF_1 and ΔF_2 do not reverse back to zero and the gap ΔD_2 will not close fully. This gap, ΔD_2, and the total deflection, Δ, can be determined using Equations 2-17 and 2-18. Before the force can take up in the opposite direction, the deformation ΔD_2 must decrease to zero. This results in the

plastic hinge deforming vertically without any change in the shear force between points 4 and 5. As the gap in ΔD_2 closes, ΔD_1 starts to increase. The change in the deformation in these two members is equal and opposite.

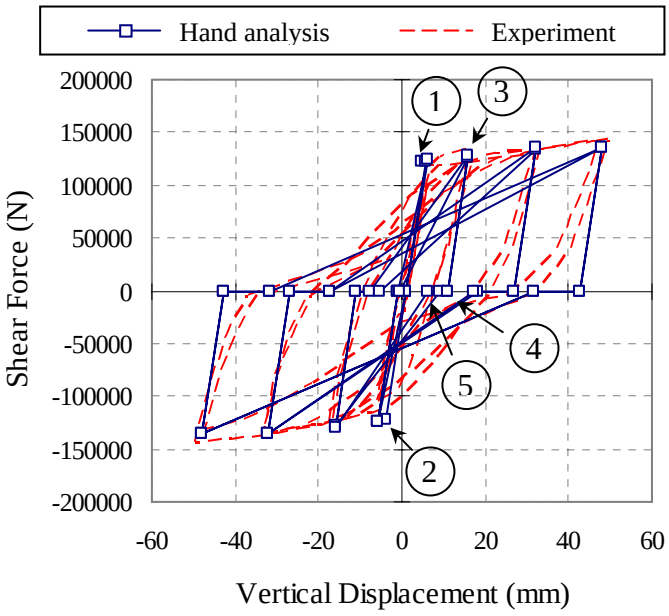

(a) Force-displacement relationship

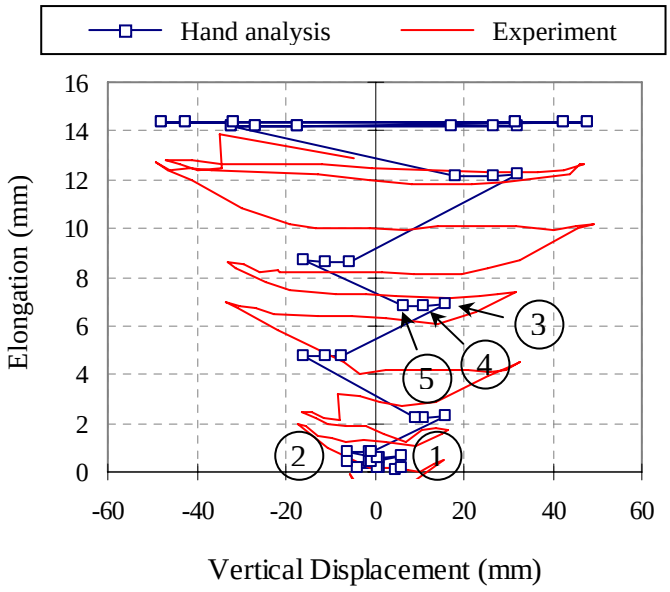

(b) Elongation history

Figure 2-23. Comparison of the analytical predictions and experimental results

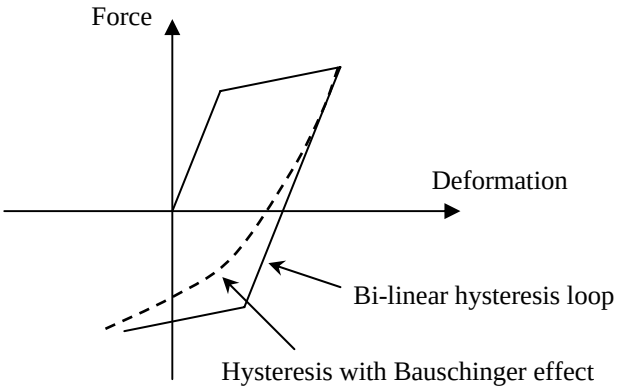

Figure 2-24. Schematic diagram showing the hysteretic response of steel spring

2.4 SENSITIVITY STUDY

A sensitivity study for the analytical model described in Section 2.2 was carried out to investigate the effects of the key modelling parameters such as incremental displacement step size, mesh size, plastic hinge element length, effective steel yield length, area of diagonal compression strut, and the concrete contact stress effect on the overall behaviour of the plastic hinge element. The experimental beam 2A, as described in Section 2.7.1, was selected for modelling purpose.

2.4.1 Incremental Displacement Step Size

Three different displacement step sizes from 0.0005mm (the control case) to 0.05mm were examined. The force-displacement, moment-rotation and elongation histories at the load point are plotted in Figure 2-25. The comparisons show that the step size can change the force-displacement and elongation predictions; especially in regions where a sudden change in stiffness occurs. This is because a larger step size causes the force to “over-shoot” the desired target. Therefore, analyses with a larger step size do not predict the pinching and yield behaviour accurately. It was found that the response converges when the incremental step size is 0.0005mm, which is equivalent to an average beam rotation of 3.3E-7 radians in this case.

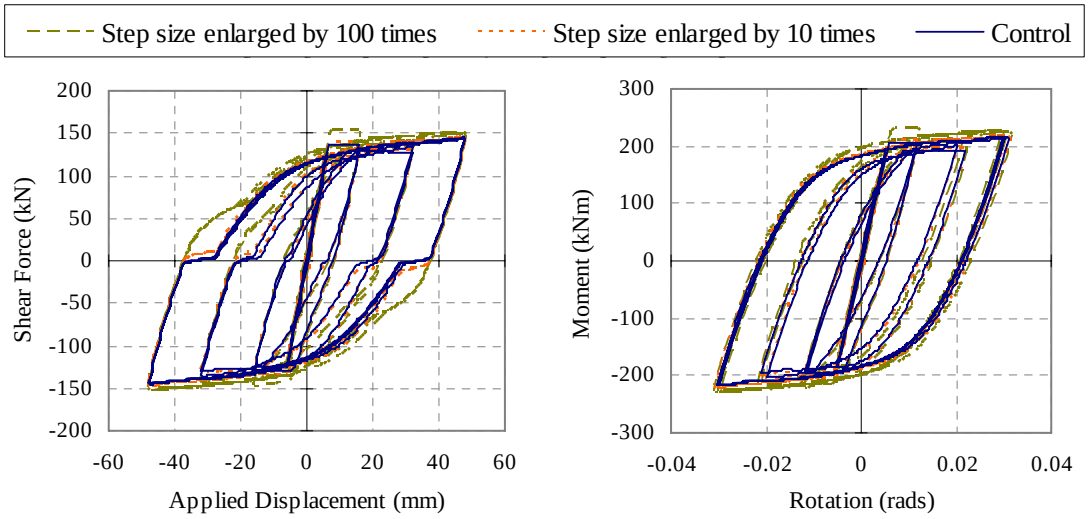

(a) Force displacement (b) Moment rotation

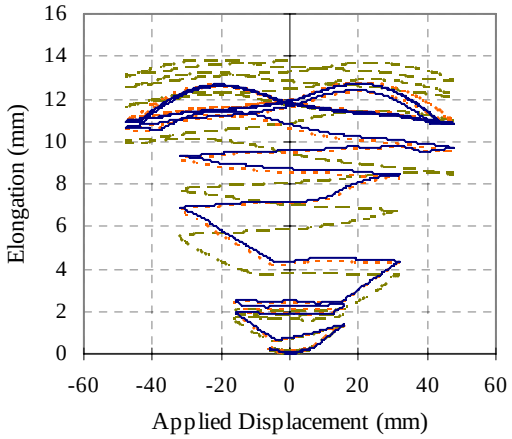

(c) Elongation

Figure 2-25. Effect of incremental displacement step size

2.4.2 Concrete Mesh Size

To investigate the effect of the concrete mesh sensitivity, the plastic hinge element was divided into 10 layers (the control case), 5 layers, and 2 layers, respectively.

The force-displacement, moment-rotation and elongation comparisons are illustrated in Figure 2-26. It can be seen that the mesh size has little influence on the force-displacement and moment-rotation response. Elongation converges as the number of concrete layers increases to 5. This observation coincides with findings from previous research (Peng 2005). Despite the plastic hinge response converging when 5 concrete

springs were used, it is felt that dividing the element into 10 layers gives a better representation of the overall section.

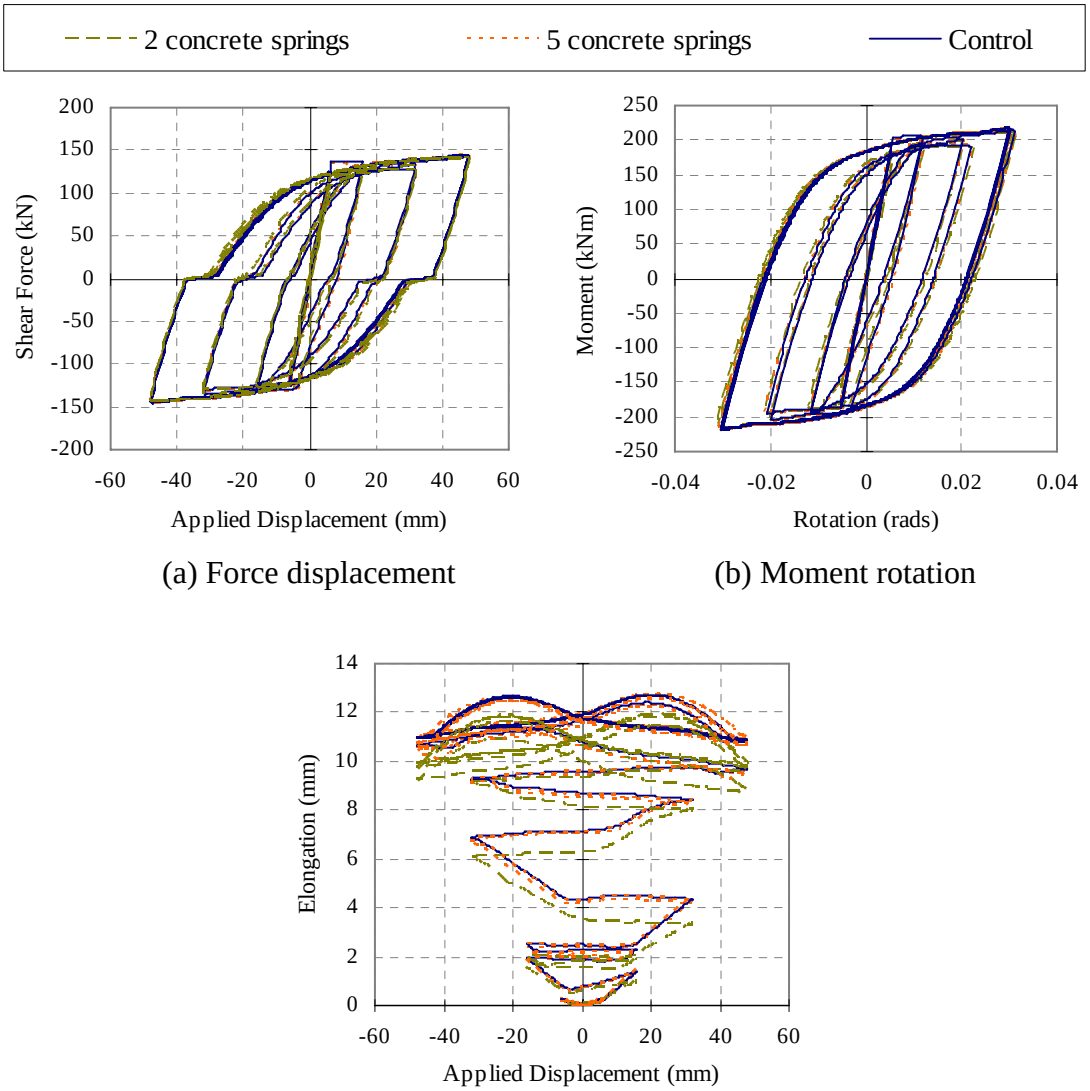

(a) Force displacement

(b) Moment rotation

(c) Elongation

Figure 2-26. Effect of mesh discretization in the plastic hinge element

2.4.3 Effect of Plastic Hinge Element Length

As the proposed equation for L_P (Equation 2-7) assumes that the diagonal struts form at an angle such that the diagonal cracks cross enough stirrups to resist the shear force in the beam, it is uncertain how significant rounding in the number of stirrups (to an integer number) has on the response of plastic hinges. To examine its effect, four different lengths were chosen, these were 300mm, 250mm, 220mm and 200mm. Note

that in this beam, the number of stirrups required was 2.2 sets, equivalent to a plastic hinge element length of 220mm.

From the hysteresis and elongation comparisons shown in Figure 2-27, the following observations can be drawn:

1. Yield force is independent of L_P. It only depends on the amount of flexural reinforcement.
2. Increasing L_P increases the overall elongation. This is because the force in the diagonal strut increases as L_P increases. Consequently, a smaller flexural compression force is resisted by the longitudinal steel; thereby increasing the permanent tensile strain in the longitudinal reinforcement. It should be noted that shear deformation increases as elongation increases, thus rotation decreases as elongation increases. An important point to note here is that an increase in rotation in the analysis does not lead to an increase in elongation.

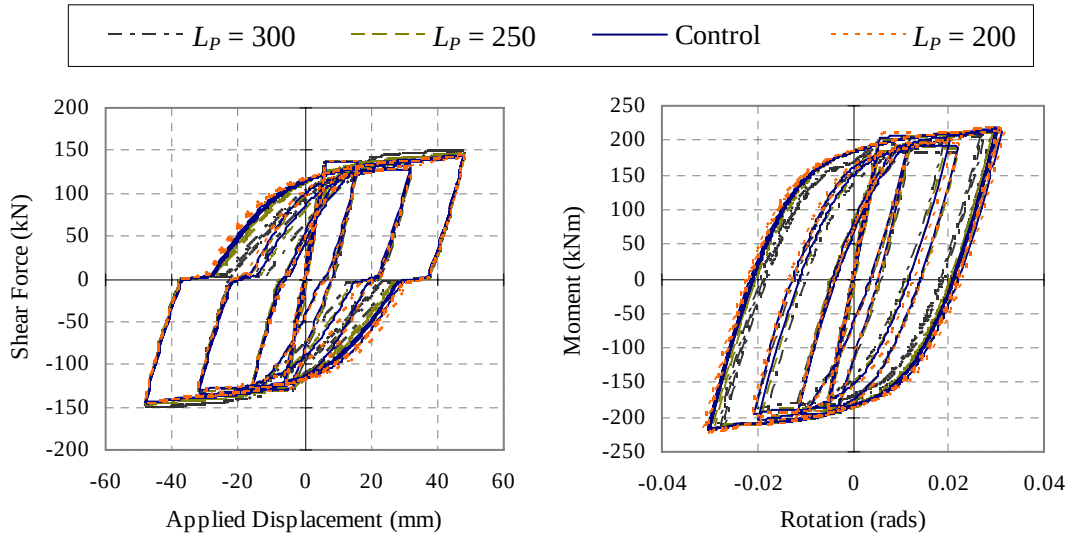

(a) Force displacement (b) Moment rotation

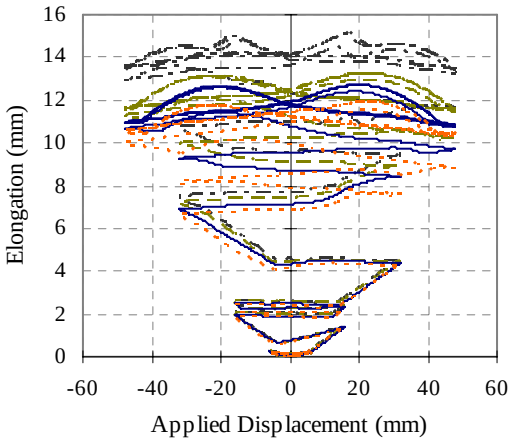

(c) Elongation

Figure 2-27. Effect of the length of plastic hinge element

As L_P is shown to affect the analytical predictions, rounding of plastic hinge element length may be significant. The author feels that it is better to take the actual un-rounded value as it represents the average diagonal strut angle. This is justifiable because in the actual member behaviour some diagonal cracks may cross more stirrups than others.

2.4.4 Effect of Steel Length

Three different values of L_{yield}, 463mm, 368mm and 220mm, were chosen to examine the sensitivity of the steel spring stiffness in the proposed plastic hinge element. The

first and second values were calculated based on Equation 2-10, with M_{max} taken as M_{max} and M_n respectively and the third value was taken equal to L_P.

The hysteresis and elongation comparisons in Figure 2-28 show that L_{yield} has a significant influence on the analytical predictions. As expected, a reduction in the steel length increases the loading, unloading and strain hardening stiffness of the plastic hinge. As the steel length decreases, elongation increases during the initial inelastic cycles. This is because the longitudinal steel springs strain-harden at a smaller cycle. This in turn increases the force in the diagonal strut and reduces the compression force in the longitudinal springs. Consequently, elongation is greater in the initial cycles. However, during larger cycles, elongation decreases as the steel length decreases. This is because the compressive force is large enough to force the longitudinal steel spring to yield back further into compression strain.

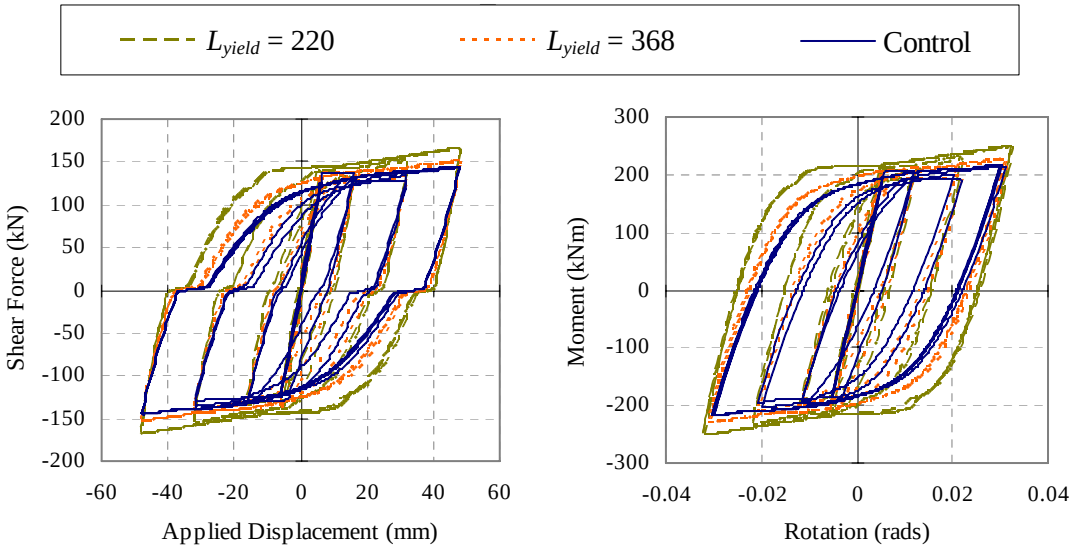

(a) Force displacement (b) Moment rotation

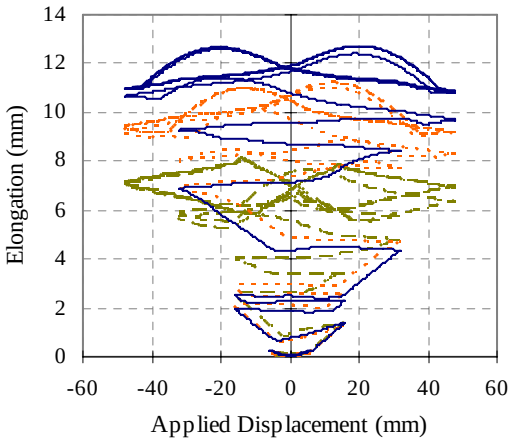

(c) Elongation

Figure 2-28. Effect of steel length in the plastic hinge element

2.4.5 Effect of Diagonal Spring Area

The diagonal spring area controls the stiffness and strength of the diagonal spring. To investigate the plastic hinge model sensitivity to this parameter, four different areas were examined. The force-displacement, moment-rotation and elongation comparisons are shown in Figure 2-29.

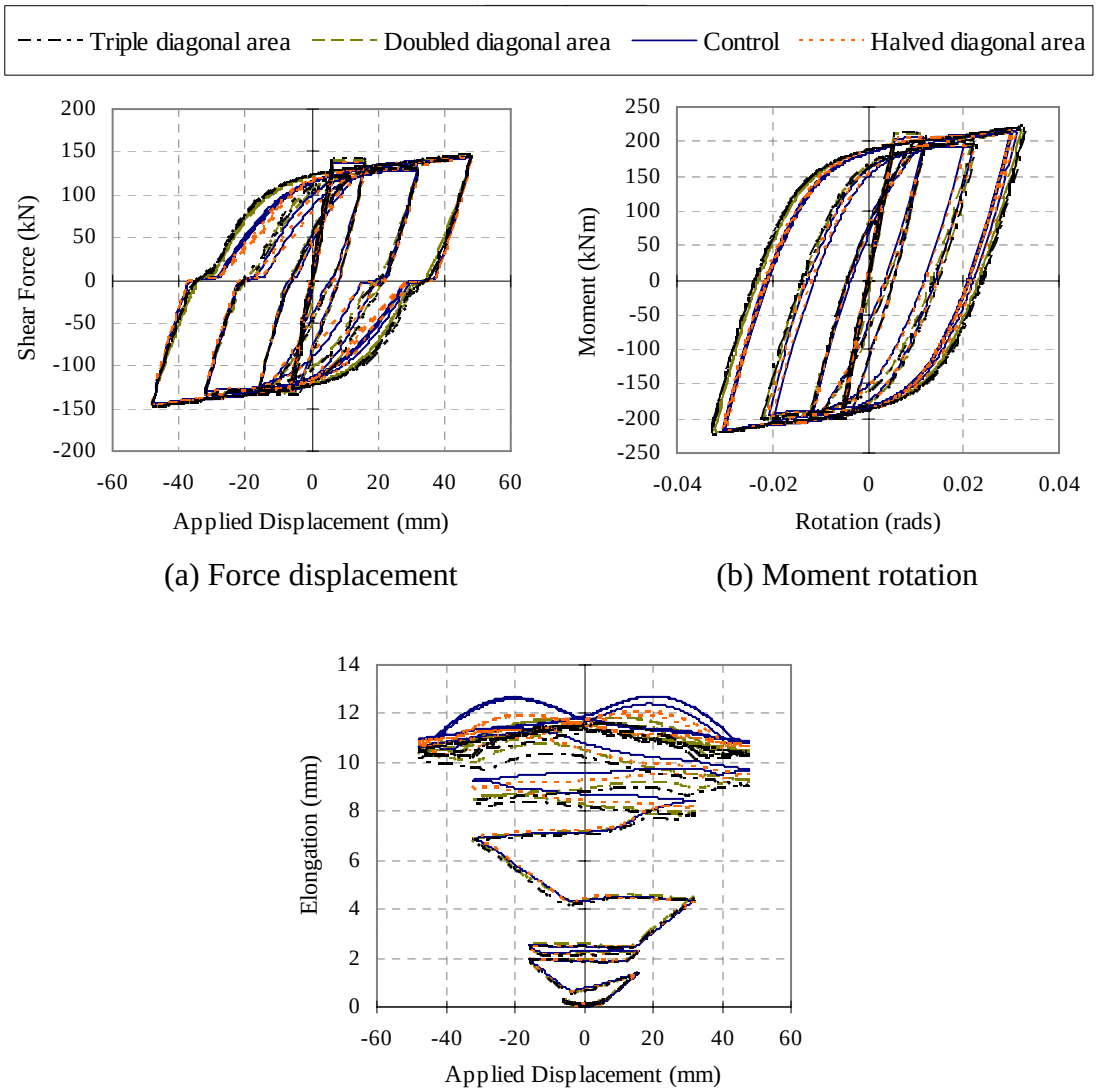

(a) Force displacement

(b) Moment rotation

(c) Elongation

Figure 2-29. Effect of diagonal spring area on the analytical results

The following observations can be drawn from the comparisons above:

1) The area of diagonal springs has little influence on the hysteretic response. This is expected as the overall displacement arising from shortening of the diagonals is small compared to the plastic hinge rotation. It is important to note that the diagonal springs remain elastic in all four analyses.
2) Increasing the diagonal spring area slightly increases the rotation. This is because an increase in the diagonal area increases the diagonal stiffness and reduces the shear deformation in the plastic hinge element.

3) In general, as the diagonal spring increases, elongation decreases. This is because elongation is directly related to shear deformation; hence as shear deformation decreases, elongation decreases.

2.4.6 Effect of Longitudinal and Diagonal Concrete Compressive Strength

The effect of concrete strength on the analytical behaviour was examined. In the controlled analysis, the effective compressive strength of the longitudinal and diagonal concrete springs was taken as f_c'. In the other case, the compressive stress of the longitudinal concrete springs was taken as $0.85f_c'$ as recommended by (Schlaich et al. 1987) and the compressive stress of diagonal springs was taken as $0.34f_c'$, as recommended by (To et al. 2001).

The hysteresis and elongation comparisons in Figure 2-30 show that the concrete compressive strength has very little effect on the analytical results. It should be noted that the compression force in the diagonal struts in both analyses is much smaller than the concrete crushing strength.

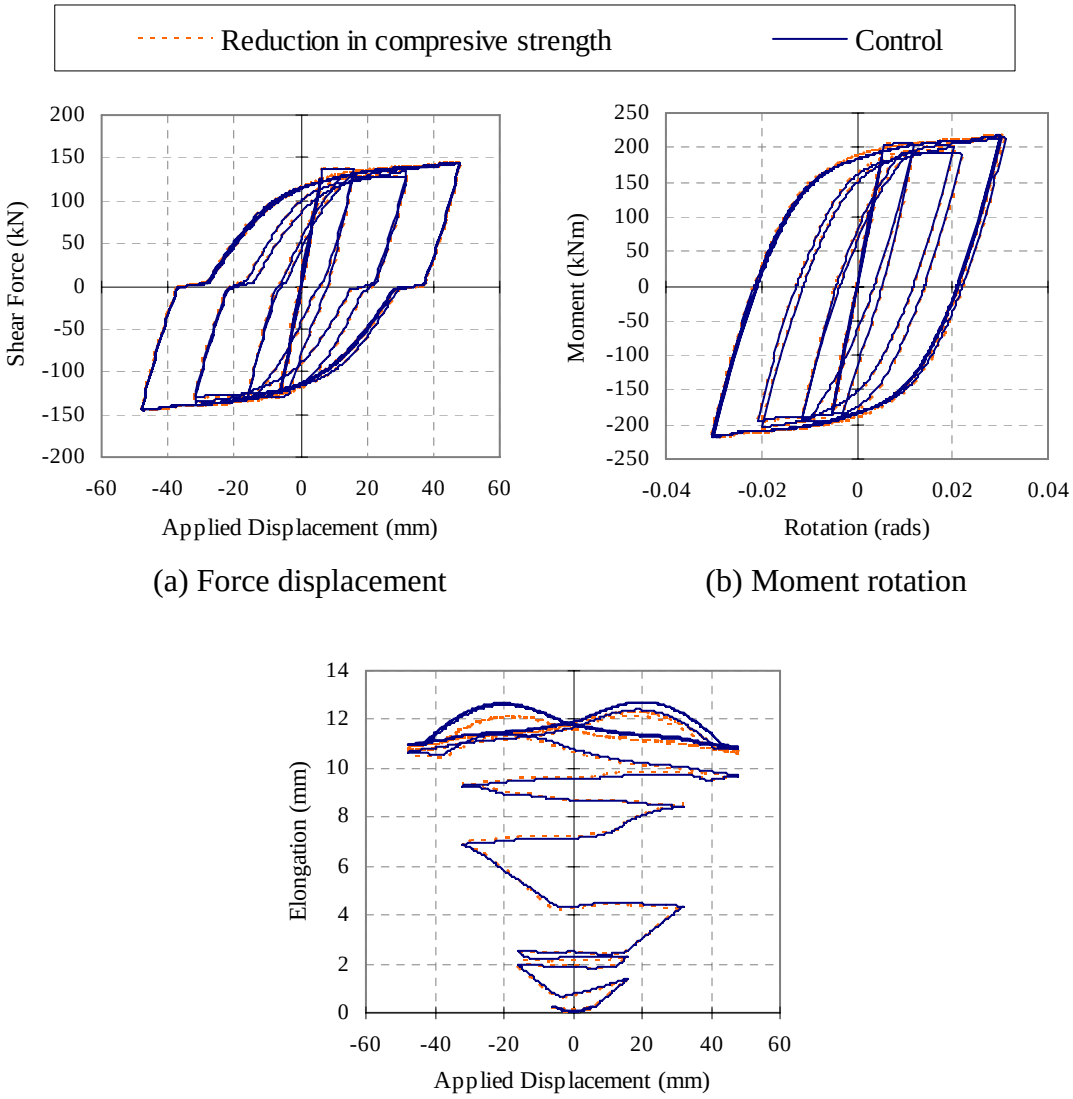

(a) Force displacement (b) Moment rotation

(c) Elongation history

Figure 2-30. Effect of concrete compressive strength

2.4.7 Contact Stress Parameters in the Concrete Springs

As mentioned earlier in Section 2.2.1.4, amplification factors were implemented into the concrete model to allow for a larger contact stress effect. These factors, denoted as *TFACTOR* and *CFACTOR*, magnify the strain at which the contact stress starts and finishes. There are two other limiting factors, *TLIMIT* and *CLIMIT*, that control the maximum allowable strains at which the contact stress starts and finishes. Values of *TLIMIT* = 0.0025 and *CLIMIT* = 0.005, as suggested by Maekawa et al. (2003), were set as the default values in RUAUMOKO. Details regarding to the effect of these parameters on the concrete hysteresis behaviour are described in Appendix A.

2.4.7.1 Longitudinal Concrete Springs

The hysteretic and elongation responses are compared in Figure 2-31 where in the control case, *TLIMIT* was increased so that it does not limit the strain at which the contact stress initiates. It can be seen that contact stress parameters of the longitudinal concrete springs can change the behaviour of plastic hinges. The effect of *CFACTOR* is smaller than the effect of *TFACTOR*. This is expected as the longitudinal concrete springs remain predominantly in tension. Increasing the *CFACTOR* increases the slope of the contact stress path, and therefore elongation increases slightly.

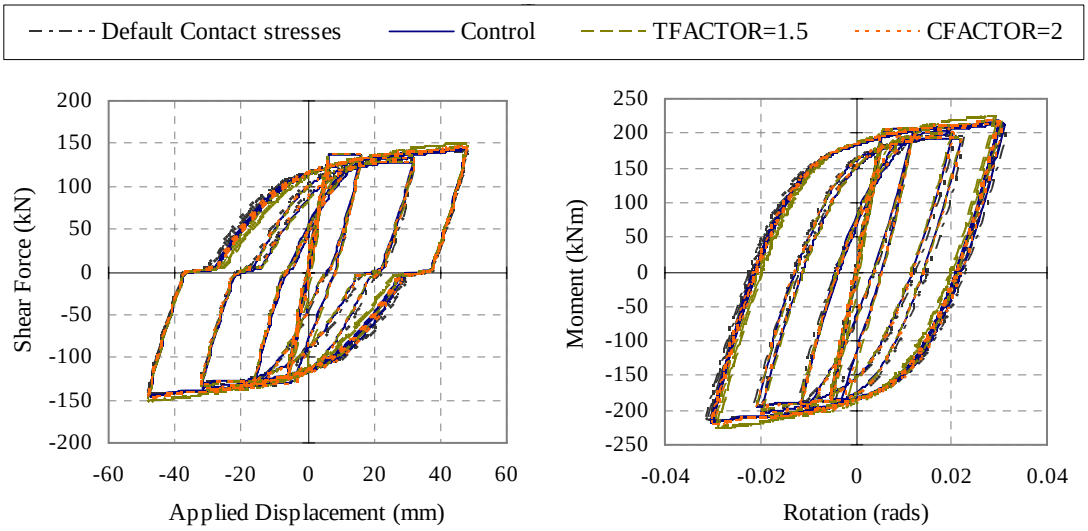

(a) Force displacement (b) Moment rotation

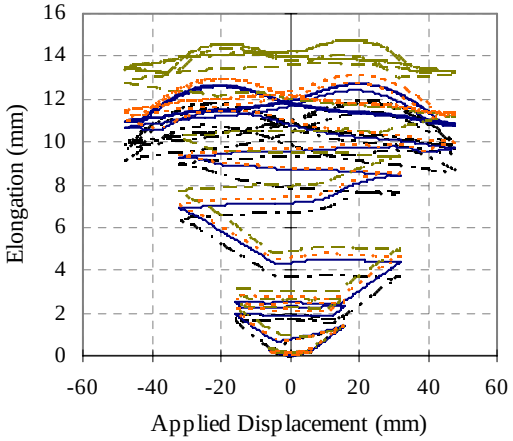

(c) Elongation

Figure 2-31. Effect of contact stresses in the longitudinal concrete springs

An increase in the *TFACTOR* causes the longitudinal concrete spring to take up compression force at larger tensile strain as illustrated in Figure 2-32. Consequently, the steel strain reduces less when subjected to compression and the elongation increases. As elongation increases, shear deformation in the plastic hinge increases, and hence the rotation decreases. An important point to note here is that an increase in rotation in the analysis does not lead to an increase in elongation.

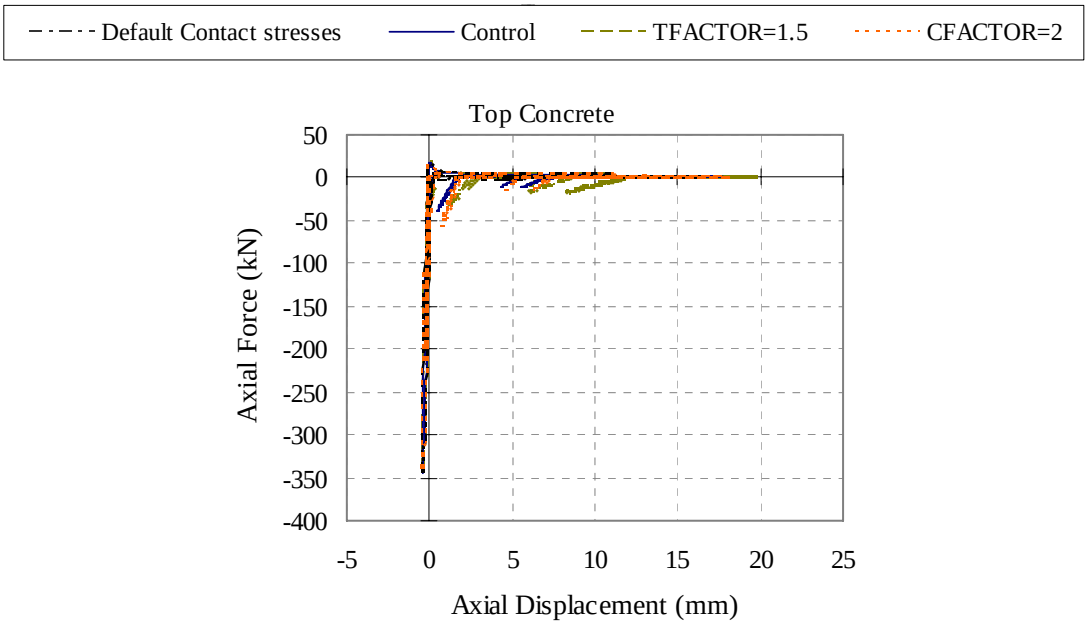

Figure 2-32. Deformation of top cover concrete for different contact stress parameters

When *TFACTOR* is larger than 2, the analysis becomes unstable. However, this instability was not apparent when the 'large displacement' (i.e., second order analysis) option is turned off in RUAUMOKO.

2.4.7.2 Diagonal Concrete Springs

The effects of contact stress parameters in the diagonal concrete springs are plotted in Figure 2-33. As mentioned earlier, *TLIMIT* was increased so that it does not limit the strain at which the contact stress starts. The key observations are summarised below:

1. *TFACTOR* has little influence on the elongation response. However, it changes the amount of "pinching" in the force-displacement relationship. If *TFACTOR* is small, the diagonal strut resists compressive force when the diagonal crack

is fully closed. This leads to a larger shear deformation and therefore a more pinched hysteresis loop as shown in Figure 2-33.

2. Increasing the *CFACTOR* indirectly increases the slope of the contact stress path. This implies that the shear deformation reduces and the rotation increases.

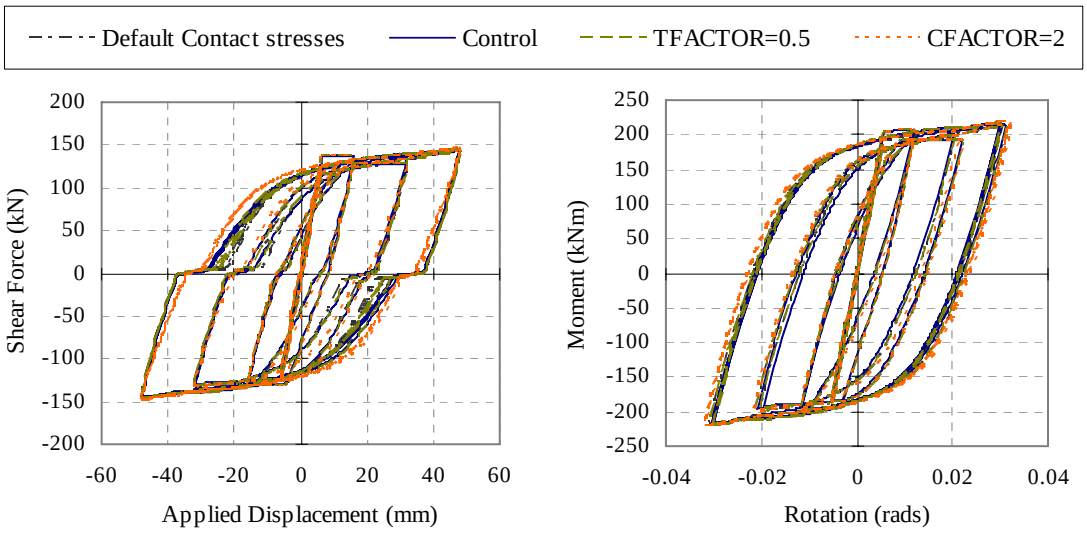

(a) Force displacement (b) Moment rotation

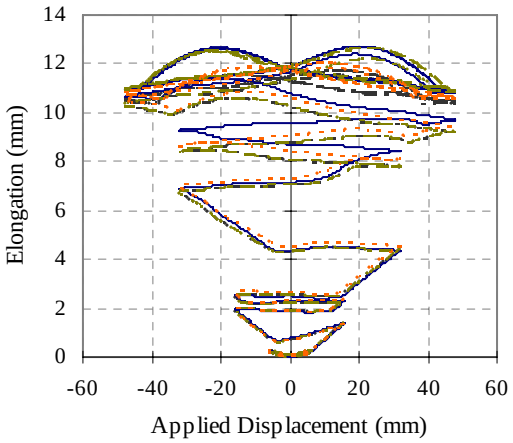

(c) Elongation

Figure 2-33. Effect of contact stresses in the diagonal concrete springs

2.4.8 Large Displacement Analysis

There is an option in RUAUMOKO to consider large displacement analysis where the nodal coordinates are updated and the stiffnesses, allowing for changes in the axial

forces and geometry in the members, are recomputed at every time-step. Two analyses were carried out to examine its effect.

The comparisons in Figure 2-34 show that the large displacement option has little influence on the hysteretic behaviour. However, it does influence the elongation predictions. It was also found that this causes the analyses to become unstable in some cases.

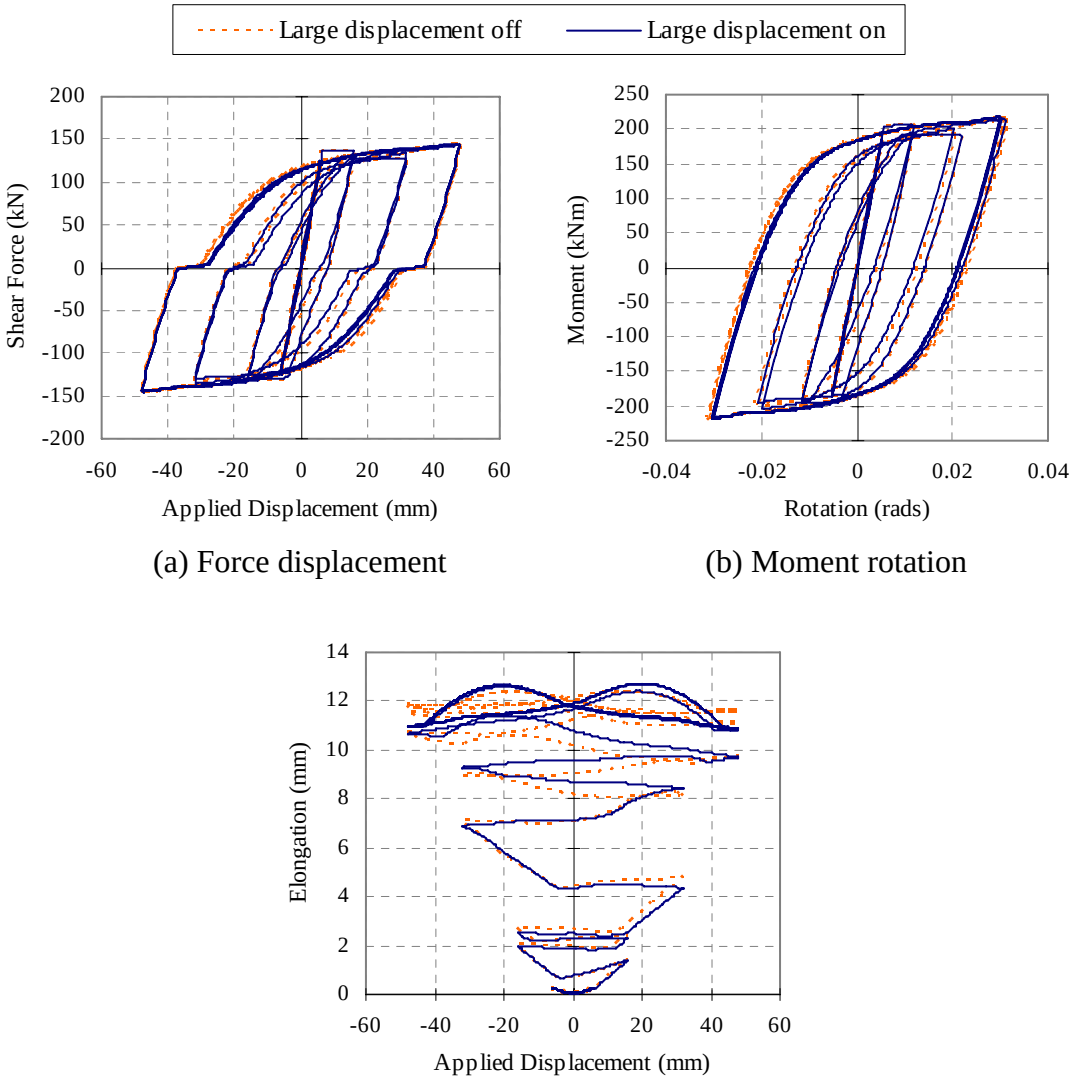

(a) Force displacement

(b) Moment rotation

(c) Elongation

Figure 2-34. Effect of large displacement modelling parameter

2.4.9 Analysis without Diagonal Springs

To examine the sensitivity of the diagonal spring in the proposed plastic hinge element, analyses were performed with the diagonal springs in the plastic hinge element replaced with a very stiff elastic shear spring as shown in Figure 2-35. The analytical predictions of these two different models are compared in Figure 2-36. It can be seen that analysis without the diagonal springs does not capture shear pinching behaviour. Consequently, the predicted rotation is larger in the analysis. It should be noted that despite the rotation being larger in the analysis without the diagonal springs, the observed elongation is smaller. This is because the flexural compression force of the longitudinal steel spring is larger in the plastic hinge element without the diagonal springs. As a result, the steel springs yield back further into compression and hence elongation is smaller. This emphasises that elongation is not directly proportional to the plastic hinge rotation as suggested by other researchers (Matthews 2004). It should be noted that, the amount of elongation predicted in the analysis without the diagonal springs is still quite large; because the contact stresses in the concrete springs prevent the steel from re-yielding fully in compression.

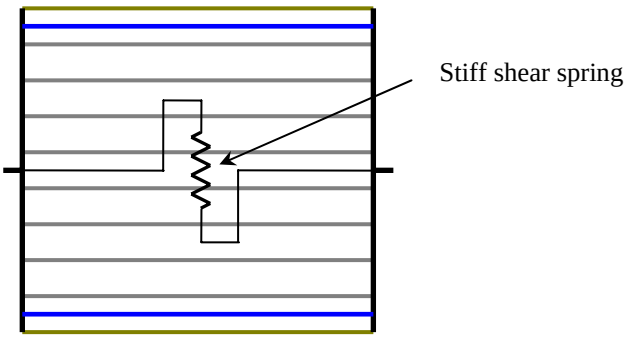

Figure 2-35. Plastic hinge element without the diagonal springs

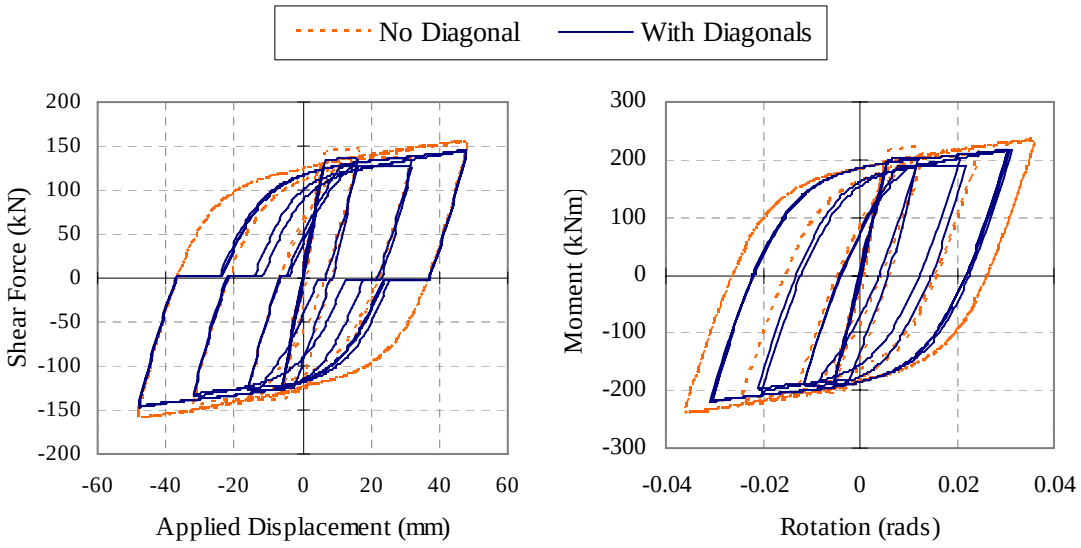

(a) Force-displacement (b) Moment-rotation

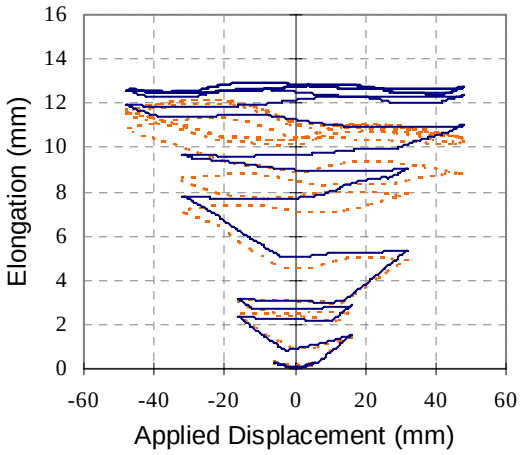

(c) Elongation history

Figure 2-36. Analytical results for plastic hinge element without the diagonal springs

2.4.10 Summary

Based on the findings of the sensitivity studies, the recommended values for the key modelling parameters are suggested below:

- Incremental step size is important especially at the location where there is a sudden change in stiffness. The recommended displacement size is 0.0005mm i.e., an average rotation of 3.3E-7 radians.
- The analysis is not sensitive to the concrete mesh discretization. It is recommended that the beam section be divided into 10 layers.

- The length of the plastic hinge element has a significant influence on elongation; however its effect on the hysteretic response of the plastic hinges is relatively minor. It is recommended in this study that the length be calculated based on Equation 2-7.
- The effective length of the steel spring controls the stiffness of the plastic hinge element. It can significantly affect the hysteretic and elongation responses of the plastic hinges. It is recommended to calculate the steel length using Equation 2-10 with an estimate of the maximum moment allowing for strain hardening if it is not available from experimental results.
- The diagonal compression strut area was found to have little influence on the overall response. Equation 2-15 is recommended for calculating the effective area of the diagonal strut.
- For the cases considered, the effective compressive strength of the strut had little influence on the overall response. This is because the strength of the diagonal struts was much higher than the applied shear force in the beam. The effective compressive strength of the diagonal springs is recommended to be taken as $0.34f_c'$, as suggested by To et al. (2001).
- Contact stress parameters of the longitudinal concrete springs affect the elongation response. On the other hand, contact stress parameters of the diagonal concrete springs affect the pinching in the hysteretic behaviour. The recommended values for the longitudinal concrete spring parameters are *TLIMIT* = 1, *CLIMIT* = default, *TFACTOR* = 1.5, and *CFACTOR* = default. The recommended values for the diagonal spring are *TLIMIT* = default, *CLIMIT* = default, *TFACTOR* = default, and *CFACTOR* = default. The value for *TFACTOR* cannot be verified in this research as explained in Section 2.2.1.4 and should be examined in the future.
- The tensile strength of the diagonal concrete springs was set to a very small value. It was thought that once the concrete cracked in flexure, the diagonal spring would not be able to sustain any tensile stress.
- The large displacement option in RUAUMOKO can inherently lead to an unstable behaviour. This may be a problem with the solution algorithms used in RUAUMOKO and not generic to the element. Nevertheless, this option should be turned off.

2.5 MULTI-SPRINGS VERSUS SINGLE PLASTIC HINGE ELEMENT

The initial plastic hinge element was set up such that there were 14 individual axial spring elements connected between two rigid arms with 26 external nodes. As a result, the computational effort required for this element was significantly greater than a standard beam/frame member. A refined two-node plastic hinge element was therefore developed in RUAUMOKO by Professor Athol Carr, which combined all these axial spring elements into one element with two external nodes only (Carr 2008). The two nodes element is more efficient than the original multi-springs element because it requires only one input/output operation per incremental step instead of 14 input/output operations (one for each spring element).

The force-displacement, moment-rotation and elongation predictions from the refined plastic hinge element and the original multi-spring element are shown in Figure 2-37. The comparisons show that the two models behave similarly. Therefore, the refined two-node plastic hinge element was used for further analyses to reduce the computational time.

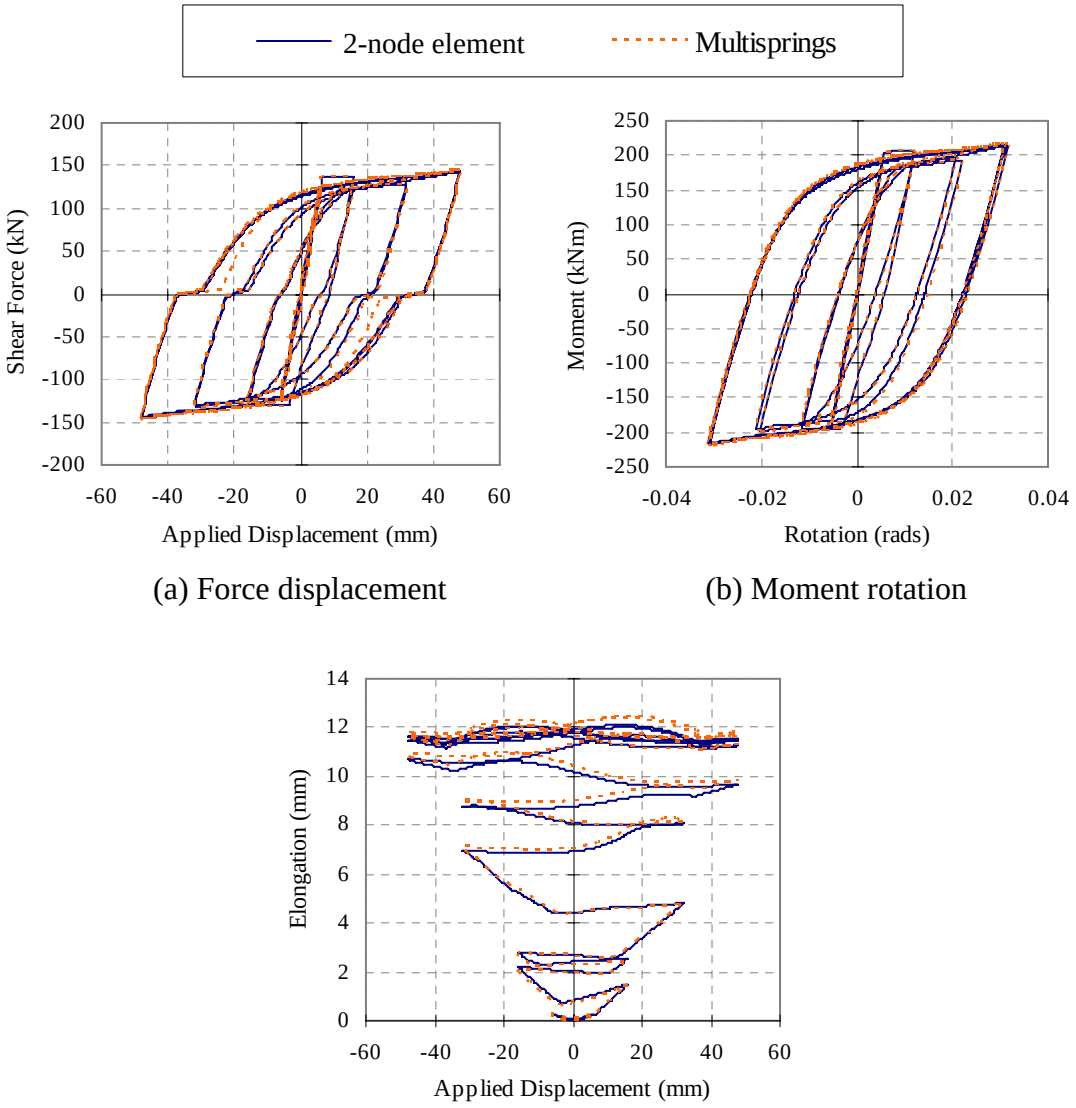

(a) Force displacement (b) Moment rotation

(c) Elongation

Figure 2-37. Comparison between multi-springs and refined 2-node plastic hinge elements

2.6 EXPERIMENTAL DATA USED FOR MODEL VALIDATION

To validate the plastic hinge element developed in this research, experimental data was obtained from cantilever beam tests carried out at the University of Auckland (Fenwick et al. 1981; Issa 1997; Matti 1998; Liddell et al. 2000) and University of Canterbury (Walker 2007). These tests were conducted to examine the effect of axial load, shear span, area of top and bottom reinforcement, concrete and steel strength, stirrup spacing, and loading history on the cyclic performance of RC members.

The typical set up of the cantilever beam test is illustrated in Figure 2-38 where P is the applied axial force and Δ is the applied displacement. The central block was bolted to the strong floor with two cantilever beams extending on both sides. Each of the two cantilever beams was tested separately. Additional steel bars were welded to the longitudinal reinforcement passing through the central block to prevent yield penetrating into the support and to confine the inelastic deformation within the beam plastic hinge. The typical beam sections employed in these experiments are illustrated in Figure 2-39 where R and D stand for Grade 300 round and deformed bars, respectively and H stands for Grade 500 reinforcement. The number following the letters represents the diameter of the reinforcing bars in millimetres.

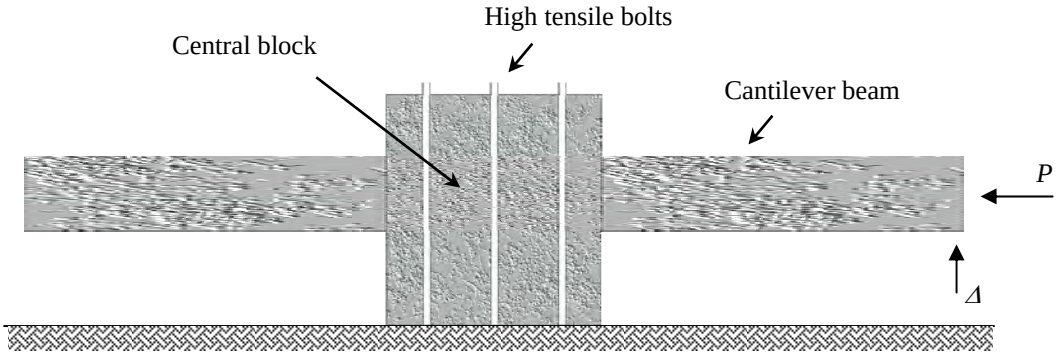

Figure 2-38. Typical test arrangement

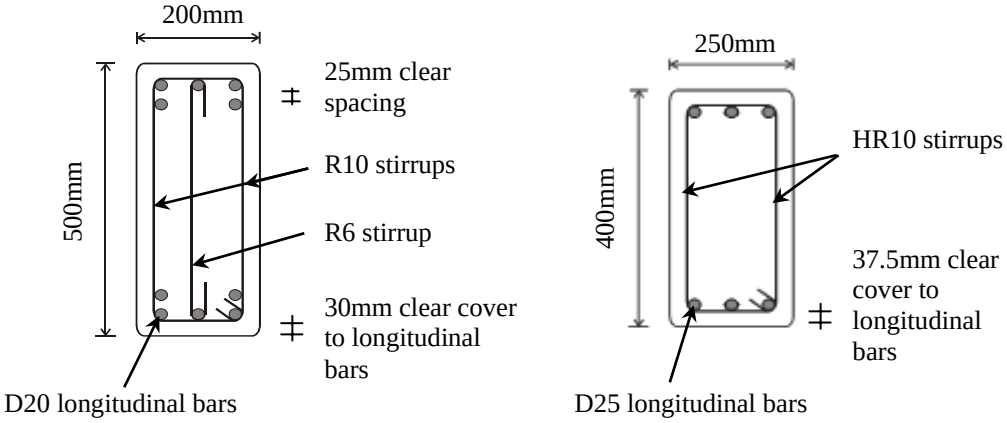

(a) University of Auckland (b) University of Canterbury

Figure 2-39. Typical beam configuration

The displacement loading history adopted by Fenwick, Issa and Matti (Fenwick et al. 1981; Issa 1997; Matti 1998) is illustrated in Figure 2-40. The loading started with a

minimum of two elastic cycles where the loading was force-controlled. A maximum force corresponding to 75% of the calculated theoretical nominal flexural strength of the beam, M_n, was applied in each direction. From these elastic cycles, the force-displacement curve was plotted, and a straight line extrapolation was made to assess the displacement corresponding to the nominal flexural strength of the beam. This displacement was taken as the ductility one displacement, *D1*. The loading history after these elastic cycles was displacement controlled. In general, two cycles at displacement ductility of two, *D2*, followed by two cycles at displacement ductility of four, *D4*, and two to four cycles at displacement ductility of six, *D6*, were applied to the beams. The loading history adopted by Walker (2007) was drift-controlled. Two cycles were applied at each drift level with the peak drift amplitude increased in increments of 0.5% drift after the initial elastic cycles. The drift was defined as the applied vertical beam displacement divided by the length of the shear span. The tests were terminated when the peak force in a displacement cycle was less than 80% of the maximum force sustained.

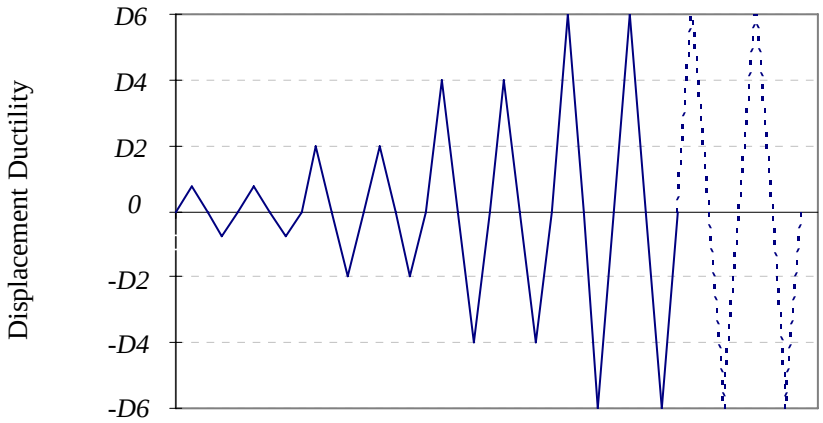

Figure 2-40. Typical loading history applied in the beam tests

A grid of linear potentiometers was mounted on each beam as illustrated in Figure 2-41. These potentiometers were fixed to studs that were welded on the beam bars. Measurements from these linear potentiometers were used to determine the deformation along the beam. The deformation of the beam can be divided into four categories; deflection due to flexural rotation of the beam, Δ_f, deflection due to shear deformation of the beam, Δ_s, elongation of the beam, and deflection due to rotation of the supporting block. Equations for calculating the first three deformation components

are given below, where δ_{bi} and δ_{ti} are the deformation of the top and bottom linear potentiometers at the i^{th} grid, l_i is the distance between the centre of the i^{th} grid to the load point on the beam, δ_{Dbi} and δ_{Dti} are the deformations of the diagonal potentiometers at the i^{th} grid, ϕ_i is the angle of the diagonal potentiometer to the horizontal plane at the i^{th} grid, and h is the distance between the top and bottom reinforcement. These symbols are also illustrated in Figure 2-41 where a positive value indicates that the linear potentiometer is extending.

$$\Delta_f = \sum_{i=1}^{n} l_i \times \frac{\delta_{bi} - \delta_{ti}}{h} \tag{2-19}$$

$$\Delta_s = \sum_{i=1}^{n} \frac{\delta_{Dbi} - \delta_{Dti}}{2 \sin \phi_i} \tag{2-20}$$

$$Beam\ elongaiton = \sum_{i=1}^{n} \frac{\delta_{bi} + \delta_{ti}}{2} \tag{2-21}$$

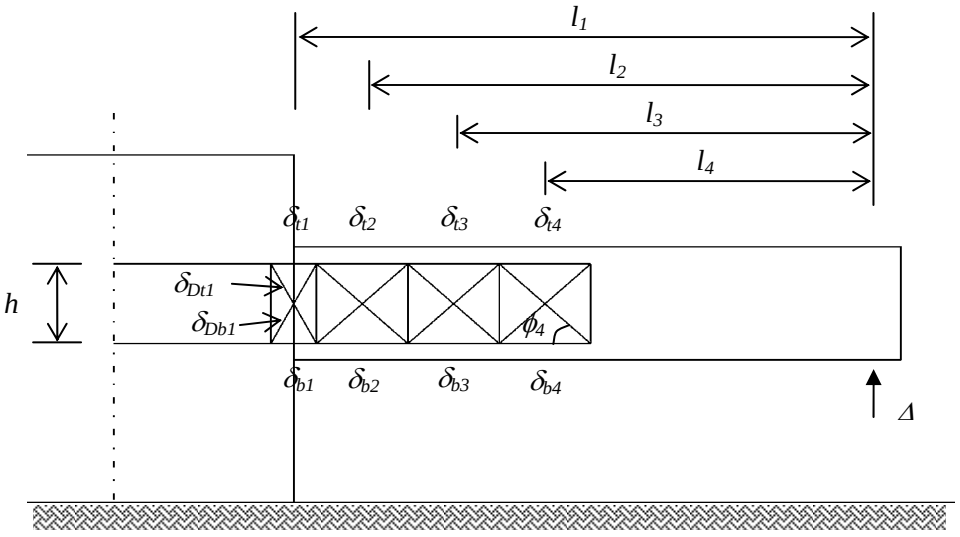

Figure 2-41. Instrumentation attached on the beam

2.7 COMPARISON OF ANALYTICAL AND EXPERIMETNAL RESULTS

The comparisons between analytical and experimental results are divided into 4 categories: (i) beams with no axial force; (ii) beams with different amounts of top and

bottom reinforcement; (iii) beams with different levels of axial load; and (iv) beams with different applied displacement histories. These are described separately in each of the following sections.

2.7.1 Beams with No Axial Force

The measured material properties of the selected tests are summarised in Table 2-1, where f_{vy} is the yield stress of shear reinforcement, f_y and f_u are the yield and ultimate stress of the longitudinal bars respectively, and f_c' is the concrete compressive strength. Beams 2A, 1A and 1B were tested by Fenwick et al. (1981), beams AA1 and AA2 were tested by Walker (2007) and beam S1A was reported by Issa (1997).

Table 2-1. Stirrup arrangement and measured material properties for beams with no axial force

Test	Stirrups arrangement	f_{vy} (MPa)	f_y (MPa)	f_u (MPa)	f_c' (MPa)
2A	2R10 + R6 @ 100c/c	298[(1)] 357[(2)]	306	459	37.6
S1A	2R10 + R6 @ 100c/c	344[(1)] 391[(2)]	331.6	476	37
1A	2R10 + R6 @ 100c/c	298[(1)] 357[(2)]	311	460	33.2
1B	2R10 + R6 @ 100c/c	298[(1)] 357[(2)]	311	460	42.1
AA1	HR10 @ 175c/c	445	350	525	41.5
AA2	HR10 @ 100c/c	445	350	525	42.2

[(1)] Yield stress for R10 stirrup [(2)] Yield stress for R6 stirrup

The calculated material properties of the test specimens are summarised in Table 2-2, where f_t is the direct tensile strength of concrete; E_c is the Young's modulus of concrete; $f_{c\,(D)}'$ is the effective compressive strength of the diagonal struts taken as $0.34f_c'$; M_{yc} is the theoretical flexural strength of the beam given by Equation 2-8; L is the span length of the cantilever beam; V_{yc} is the shear force corresponding to the theoretical flexural strength of the beam; and ε_y, ε_{sh} and ε_u are the yield, strain hardening and ultimate strains, respectively. The values for f_t and E_c are calculated based on Clause 5.2.6 and Clause 5.2.3 in NZS 3101:2006 and are given in the equations below. The units in these equations are MPa.

$$f_t = 0.36\sqrt{f_c'} \tag{2-22}$$

$$E_c = 3320\sqrt{f_c'} + 6900 \quad (2\text{-}23)$$

Table 2-2. Calculated material and section properties for beams with no axial force

Test	f_t (MPa)	E_c (GPa)	$f_{c\,(D)}'$ (MPa)	M_{yc} (kNm)	L (mm)	V_{yc} (kN)	ε_{sh} / ε_y	ε_u / ε_y
2A	2.2	27.3	12.8	185	1500	123	13	130
S1A	2.2	27.1	12.6	200	1500	133	14	62
1A	2.1	26.0	11.3	188	1500	125	14	130
1B	2.3	28.4	14.3	188	1500	125	14	130
AA1	2.3	28.3	14.1	155	1420	109	10	80
AA2	2.3	28.5	14.3	155	1420	109	10	80

Table 2-3 summarises the calculated plastic hinge parameters, where L_p is the length of the plastic hinge element calculated from Equation 2-7; θ is the angle of the diagonal strut to the horizontal plane; D is the effective diagonal depth given by Equation 2-15; M_{max} is the maximum moment sustained in the beam; M_{y1} is the theoretical first yield moment (this is only used to compared with M_{yc}); L_{ts} is the length of tension shift; and L_{yield} is the steel yield length given by Equation 2-10. Here the yield penetration into the support is taken as the distance to where the additional bars are welded to the longitudinal reinforcement in the central block, which was equal to 50mm.

Table 2-3. Calculated plastic hinge properties for beams with no axial force

Test	L_p (mm)	θ (degree)	D (mm)	M_{max} (kNm)	M_{y1} (kNm)	L_{ts} (mm)	L_{yield} (mm)
2A	220	60	190.5	217	187	192	463
S1A	210	61.3	192.9	233	203	192	452
1A	220	60	190.5	233	190	192	532
1B	220	60	190.5	227	190	192	498
AA1	280	47	205	170	159	150	328
AA2	160	61.9	141	179	159	150	390

2.7.1.1 Beam 2A

The RUAUMOKO input file for beam 2A is attached in Appendix B. The hysteretic and elongation responses of the beam predicted from the analytical model, up to displacement ductility of 4, are plotted in Figure 2-42. The letters *A* to *O* in the different plots correspond to each other and indicate different stages of the beam's

cyclic response. Figure 2-42(a) shows the force-displacement relationship at the beam load point, Figure 2-42(b) plots the moment-rotation response of the beam, Figure 2-42(c) shows the elongation prediction and Figure 2-42(d) plots the shear force versus shear displacement of the plastic hinge element.

It can be seen that the force-displacement loops show some pinching, which arises from shear response of plastic hinges. For example, points *L* and *M* almost coincide in the moment-rotation curve (Figure 2-42(b)), but in Figure 2-42(d) they refer to the start and end of the shear pinching in that cycle which arises due to opening and closing of the diagonal cracks. Comparison between Figures 2-42(a) and (d) reveals that shear deformation accounts for about 16% of the total deformation at the *D4* cycle. Figure 2-42(d) also shows that the shear deformation is noticeably larger during the second cycle than in the first cycle of the same displacement amplitude (see points *E* and *J*). As a result, the rotation in the second cycle has to decrease slightly to accommodate this increase in shear deformation, which can be observed in Figure 2-42(b).

During the elastic loading, between points *B* and *C*, the beam elongates during the loading phase due to the neutral axis not coinciding with the nodal line at the mid-height; however there is no residual/permanent elongation in this elastic loading range. As the beam starts to undergo inelastic response, after point *D*, elongation starts to accumulate. During the loading phase of a cycle, the elongation increases rapidly, but only a small portion of this is recovered during the unloading phase. Another noteworthy point in this figure is the significant increase in the elongation in the second cycle of the same displacement amplitude compared to the first cycle. However, this increase in elongation between the second and the third cycles is significantly less than that between the first and the second cycles. For example, compare points *E* and *J* with points *J* and a point at the same applied displacement in the line immediately above it in Figure 2-42(c).

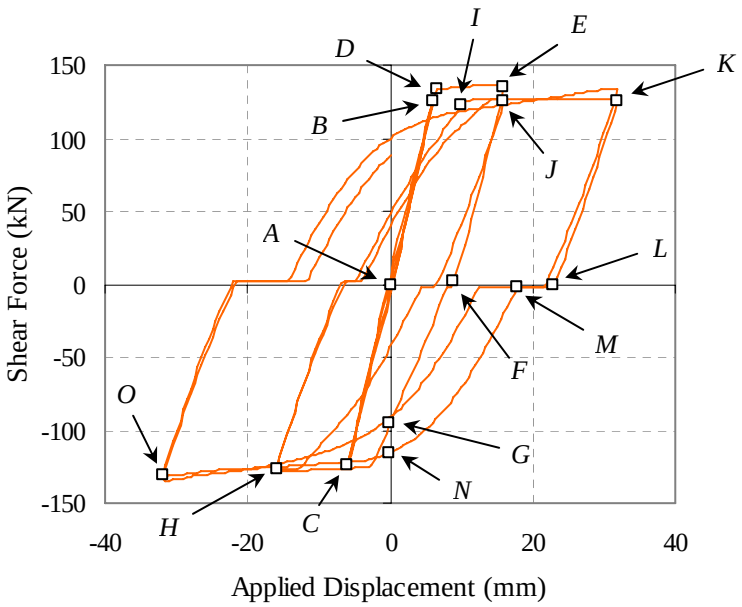

(a) Force-displacement

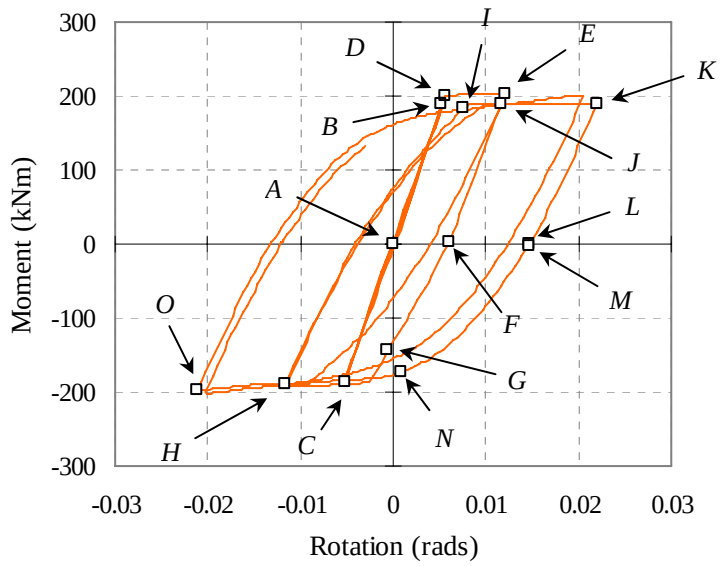

(b) Moment-rotation

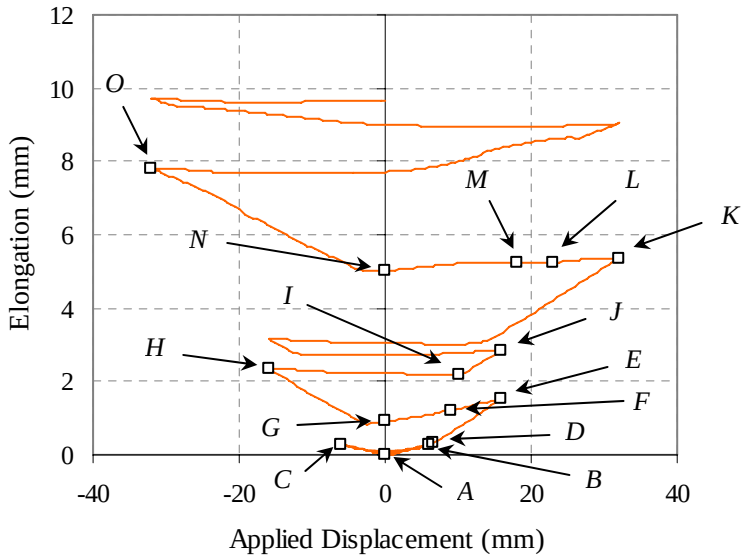

(c) Elongation

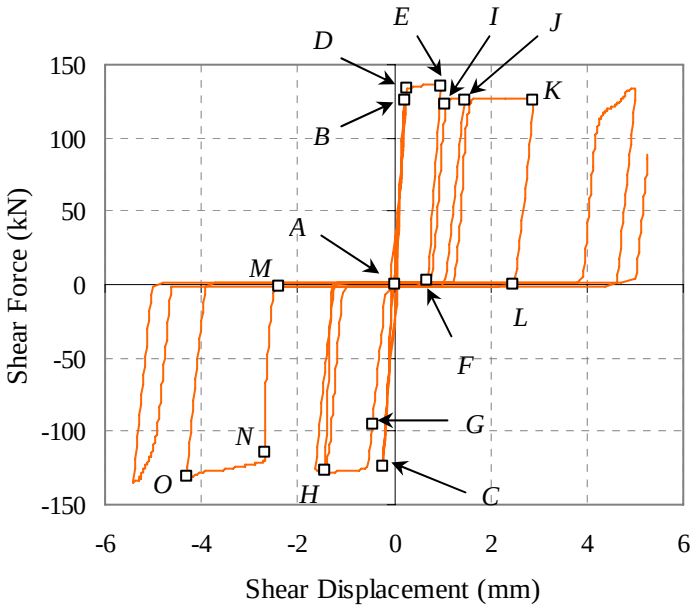

(d) Force-shear displacement

Figure 2-42. Analytical global response of beam 2A

The above mentioned predictions are direct results of the plastic hinge element, based on the mechanics of the model, and not requiring any calibration with experimental results. The hysteretic response could also have been predicted reasonably well with conventional analysis methods using nonlinear frame elements with moment-rotation or force-displacement models, but several parameters of the nonlinear relationships

would need to be calibrated for this purpose. In the absence of experimental data for calibration, the values of these parameters, and consequently the predicted performance, would be open to significant scrutiny. More importantly, the conventional analysis does not have the capability to predict elongation nor take into account the inelastic shear deformation as shown in Figure 2-42(d). Hence, the proposed plastic hinge element provides an objective and more rational approach to assess the performance of ductile RC beams.

To facilitate discussion on qualitative and quantitative contributions of the newly developed plastic hinge element on the predicted hysteretic and elongation responses of beam 2A, hysteretic behaviour of four longitudinal springs (two from reinforcing bars and two from cover concrete at the top and bottom) and two diagonal springs are plotted in Figures 2-43 to 2-45. In these figures, the letters *A* to *O* correspond to each other and also with the plots in Figure 2-42.

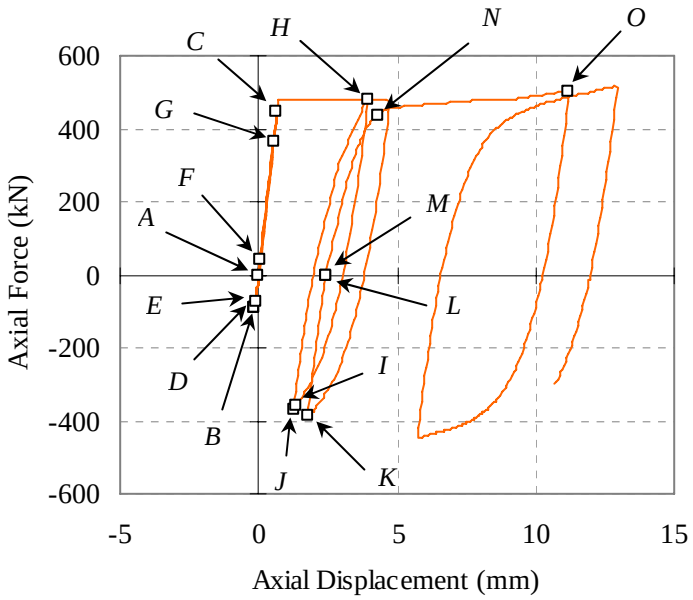

(a) Top reinforcement

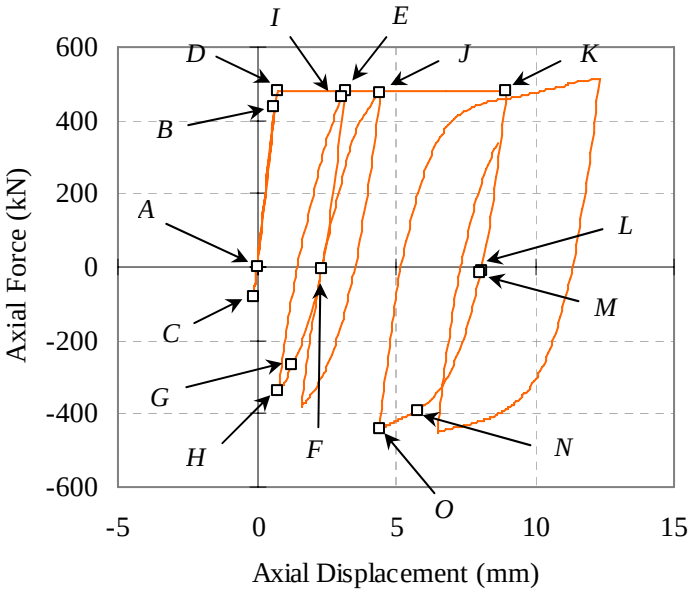

(b) Bottom reinforcement

Figure 2-43. Predicted deformation history of reinforcing bars in beam 2A

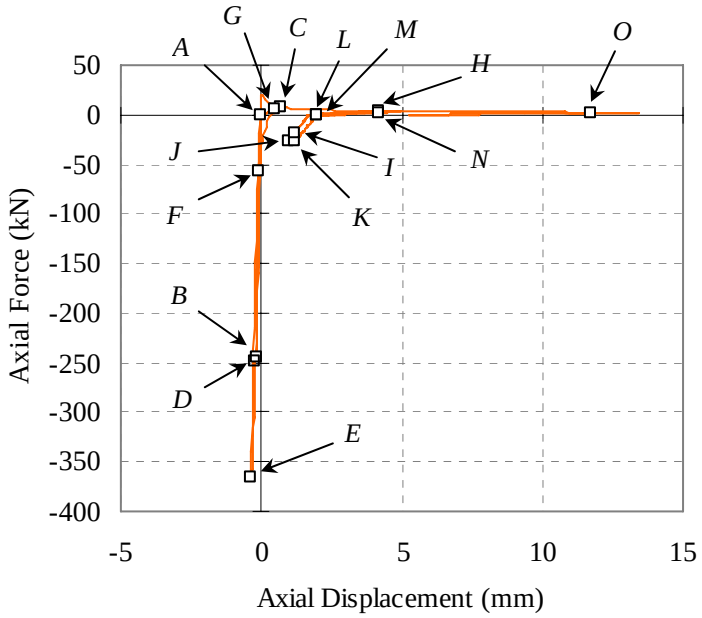

(a) Top cover concrete

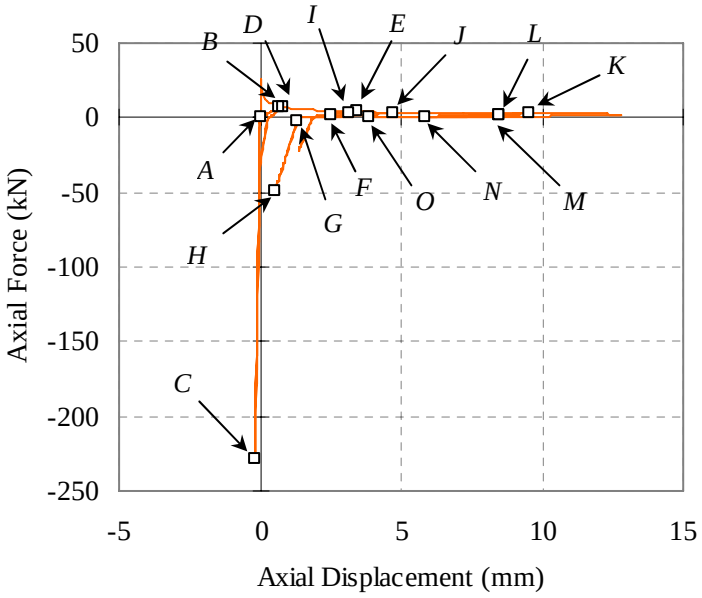

(b) Bottom cover concrete

Figure 2-44. Predicted deformation history of cover concrete in beam 2A

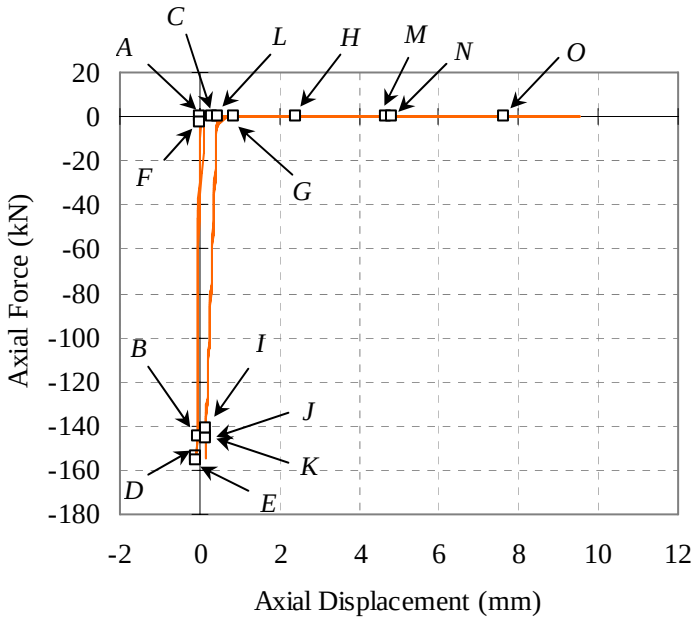

(a) Top Diagonal

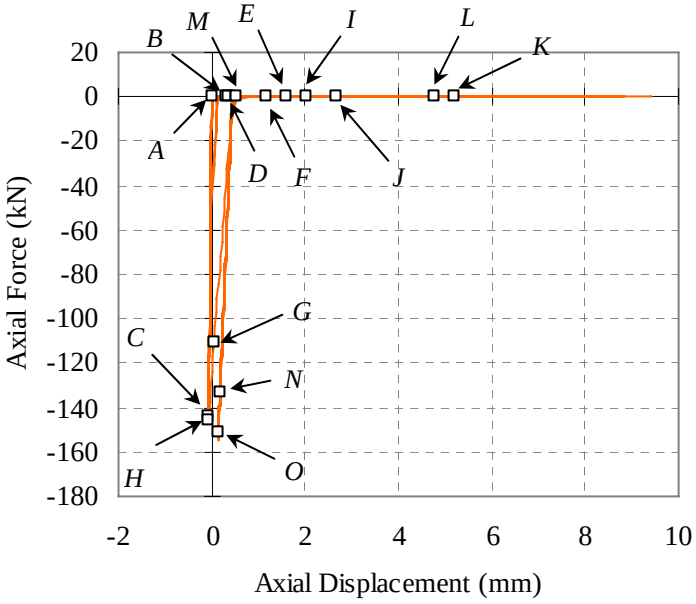

(b) Bottom Diagonal

Figure 2-45. Predicted deformation history of diagonal struts in beam 2A

In Figures 2-43 to 2-45, points *B* and *C* represent the two extremes of elastic response, while point *D* represents the onset of yielding. During the inelastic response phase (e.g. from *D* to *E*), the compression force sustained in the top cover concrete increases elastically (Figure 2-44(a)) and the reinforcing bars in tension (i.e. the bottom side)

experience large inelastic extension while maintaining the yield force (Figure 2-43(b)). To accommodate the aforementioned behaviour of cover concrete and tensile steel, the neutral axis moved upward during this inelastic loading phase, and the beam underwent extension at the mid-depth due to the additional rotation. This indicates that the elongation from inelastic rotation (i.e. inelastic extension of tension reinforcement) is captured in the analysis.

When the load returns back to zero after inelastic loading (i.e. point *F*), the tensile stresses in the bottom bars returns to zero; but this elastic recovery leaves plastic extension unrecovered (Figure 2-43(b)). From point F, the beam sustains permanent elongation when the applied displacement reverses back to zero at point *G*. Consequently, the crack in the bottom cover concrete does not close fully, as shown in Figure 2-44(b). As the displacement reverses to 16 mm downwards, at point *H*, the top bars undergo a significant inelastic extension (see Figure 2-43(a)) but the absolute strain in the bottom steel is still positive (i.e., tensile, see Figure 2-43(b)). Similarly, the cracks at the bottom from the previous loading are still open, and only minor compression force is sustained by the bottom cover concrete due to contact stress effect (see Figure 2-44(b)). As a result, the bottom bars sustain much higher compressive force compared to that in point *C* (see Figure 2-43(b)). The compression force in the bottom reinforcement is smaller than the tension force in the top tension reinforcement at point *H* mainly due to the diagonal strut contribution. This highlights the importance of diagonal struts in modelling elongation of plastic hinges.

From point *I* to *J*, during inelastic loading in the upward direction, the response of top bars does not change noticeably (see Figure 2-43(a)) whereas the bottom bars sustain further inelastic extension (see Figure 2-43(b)), which results in additional elongation. From Figure 2-42(b), it can be seen that despite the inelastic rotation at point *J* being similar to that at point *E* (i.e. the same displacement in the previous cycle), elongation continues to increase. This is a clear indication that the analysis is capturing the elongation mechanism associated with the irrecoverable extension of the compression reinforcement, as described in Section 2.1.2.

During the next unloading phase from point *K* to *L*, the top and bottom bars deform elastically as the Bauschinger effect is not significant in this range. The pinching

behaviour from point *L* to *M* arises as a result of the diagonal cracks in both directions remaining open, which facilitates the shear displacement associated with closing and opening of diagonal cracks. In this case, one diagonal spring extends by 4mm (see Figure 2-45(a)) and the other contracts by 4mm (see Figure 2-45(b)). Consequently, the beam deflects vertically by about 5mm without a significant change in the shear force (Figure 2-42(a)). It can be seen from the force-displacement relationship of the diagonal struts in Figure 2-45 that the diagonal struts remain elastic in the compression region through out the loading history. The amount of shear pinching in the analysis is governed by the amount of predicted elongation in the plastic hinges.

It is also interesting to note that as the applied displacement is reversed back to zero at point *N*, the rotation in the plastic hinge calculated based on the extensions of the top and bottom reinforcement in Figure 2-43 is still positive. Nevertheless, the total rotation at point *N* is close to zero in Figure 2-42(b) because it is the combination of elastic beam rotation and plastic hinge rotation. In this case, the elastic beam rotation at point *N* is negative, thereby reducing the total rotation in the system.

The closure error at the peak positive and negative displacements from the experimental results is 2mm and 6mm, respectively. The closure error is denoted as the difference between the interpolated displacement using linear potentiometers mounted on the beam and the direct measured displacement from the hydraulic ram. It gives an indication of the accuracy of the measurement from the linear potentiometers. A positive value implies that the sum of the interpolated displacement from the potentiometers is greater than the actual applied displacement. It should be noted that most of the cantilever beam tests reported herein provide insight into the likely accuracy of the measurements which often cannot be obtained from other experiments. The closure error often escalates at the end of the test due to buckling of longitudinal reinforcement. However, large closure error reported at the end of test may not be directly proportional to the accuracy of the measurements.

Comparisons between the analytical and experimental force-displacement, moment-rotation and elongation responses of beam 2A are shown in Figures 2-46 to 2-50. It can be seen from the force-displacement comparisons that the analysis predicts the elastic stiffness, yield displacement and the ultimate force accurately. The elastic

stiffness in the experiment is 17kN/mm and in the analysis is 20.9kN/mm. The over-estimation of the stiffness is partially due to rotation of central block not being considered in the analysis. The over-prediction of the yield force in the analysis may be due to a reduction in concrete compressive strength from tensile strain in the transverse direction not being considered in the plastic hinge element.

Strength degradation observed in the experiment in the large displacement cycles is not captured in the analysis. This is partially due to the steel model not taking into account buckling of reinforcing bars during unloading from a large tensile strain. Under-estimation of the shear deformation in the analysis, as mentioned later, could also lead to this discrepancy. In addition, crushing and degradation of concrete under large cyclic loading may not be modelled accurately.

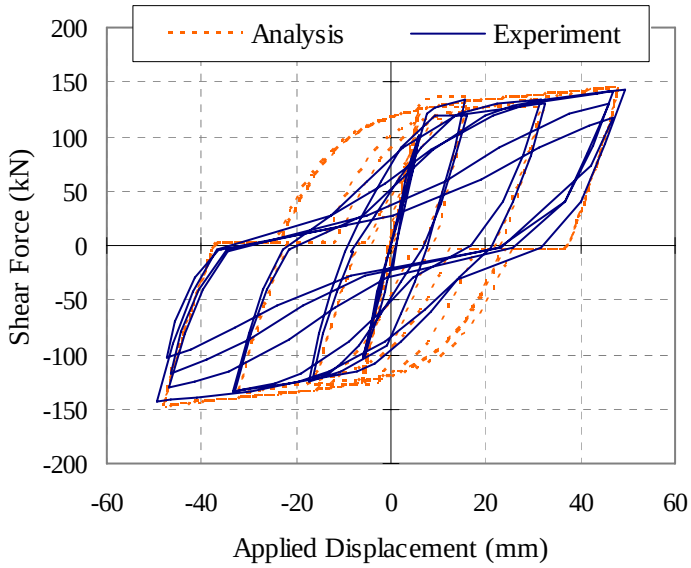

Figure 2-46. Total force versus total applied displacement for beam 2A

Pinching in the force-displacement relationship is under-estimated in the analysis after *D4* cycles as shear deformation in the plastic hinges is captured only partially by the analysis. The pinching behaviour predicted in the analysis is a natural outcome the analytical model which does not require any calibration with experimental results.

Shear deformation in the plastic hinges is contributed from two main mechanisms as described by Fenwick and Thom (1982): (i) elongation of plastic hinges, and (ii)

yielding/inelastic extension of stirrups. These mechanisms are described in detail in Section 3.1.

The proposed plastic hinge element automatically takes into account shear deformation from beam elongation, but it does not model shear deformation from the extension of stirrups. It can be seen from Figure 2-47 that the elongation component contributes to about half of the total shear deformation before strength degradation occurs. An attempt has been made to develop a simple analysis method to predict shear deformation in the plastic hinges. The refinement in shear deformation modelling is described in Section 3.2.

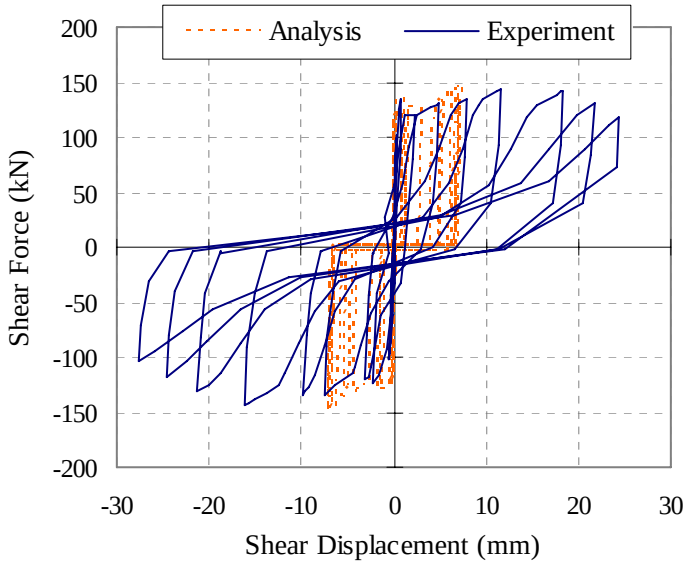

Figure 2-47. Shear force versus shear displacement for beam 2A

Figure 2-48 shows the experimental and analytical moment-rotation relationship of the beam. The comparison shows that the model predicts the loading/unloading stiffness, yield/ultimate moment, and yield rotation satisfactorily. As the model does not capture shear deformation from stirrup extension, the rotation is understandably over-predicted in the analysis. In the experiment, the rotation decreased during the repeated cycles of the same displacement ductility due to an increase in shear deformation. In the analytical prediction, this phenomenon is not profound because of the inability of the model to capture the total shear deformation accurately.

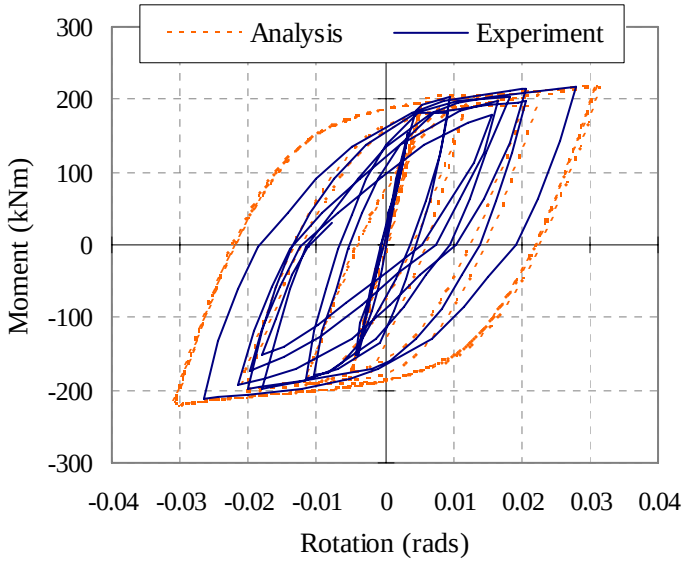

Figure 2-48. Moment rotation comparison for beam 2A

Figure 2-49 shows the analytical and experimental elongation history. It can be seen that the analytical elongation matches satisfactorily with the experimental results, and the following trends can be observed: (i) in the elastic cycles, the beam elongates by a small amount but the elongation is fully recovered when the displacement is reversed to zero; (ii) elongation increases when more than one displacement cycle of the same amplitude is applied, but the magnitude of increase in elongation reduces as the number of displacement cycles at the same amplitude increases; and (iii) during unloading from a peak displacement, elongation remains more or less constant until the displacement is reversed back into the opposite direction, after which the elongation starts to increase. This observation, however, is not true for beams with substantial axial compression force as examined later on.

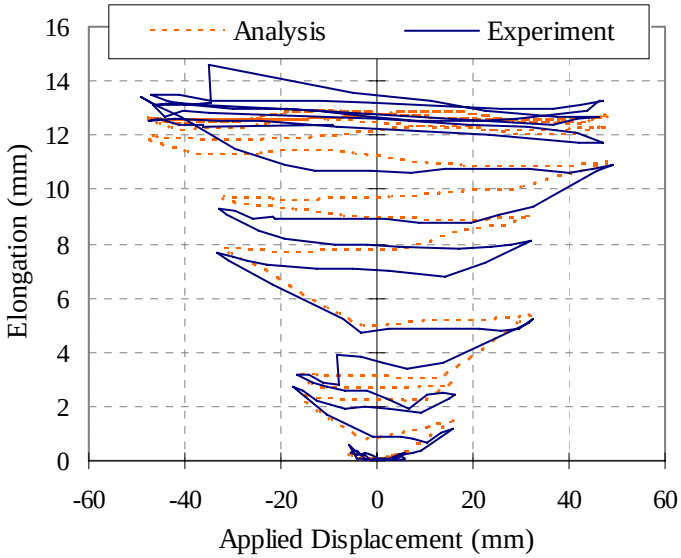

Figure 2-49. Elongation history for beam 2A

The deformation of the top and bottom longitudinal reinforcement within the plastic hinge region at the peak displacement ductility cycles is plotted in Figure 2-50. In this figure, 'D' stands for displacement ductility, the number following 'D' represents the magnitude and 'i' stands for the number of cycles; for example, -D2ii stands for the peak of the second negative displacement cycle of ductility 2. It can be seen that the analytical reinforcement extension compares satisfactorily with the experimental results up to the first cycle of displacement ductility 6. The analytical rotation after this displacement cycle is larger than the experimental rotation. The rotation can be evaluated by taking the difference in the top and bottom reinforcement extensions and divided it by the distance between the reinforcement.

It should be noted that a larger rotation in the analysis does not necessarily lead to a larger elongation. In this case, the rotation increases the strain of tensile reinforcement and reduces the strain of the compression reinforcement by a similar amount. This is shown in the deformation history of the top reinforcing steel, plotted in Figure 2-51.

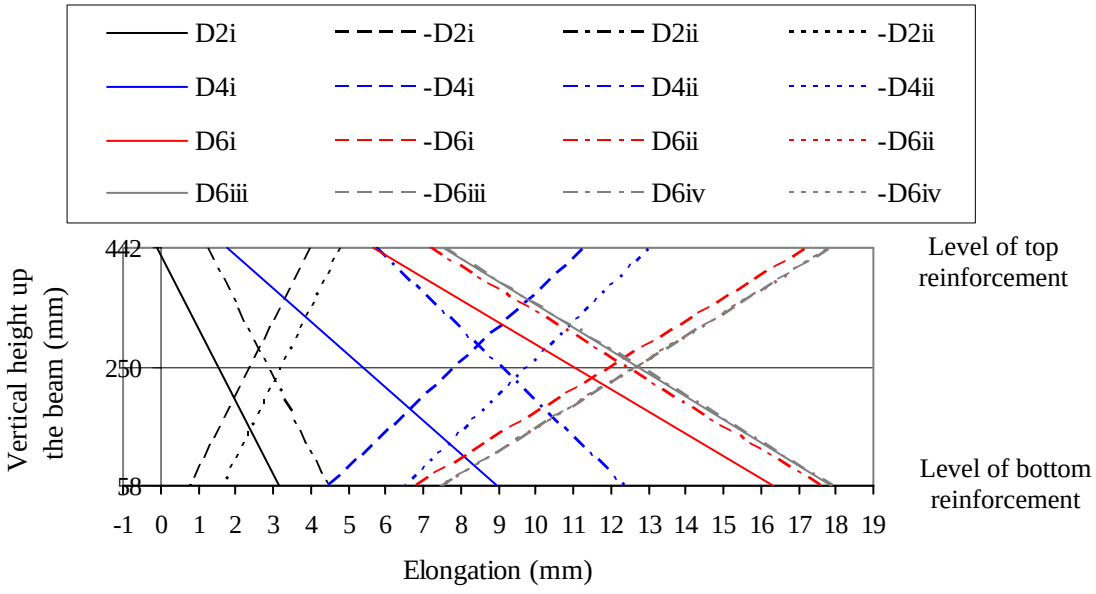

(a) Analysis

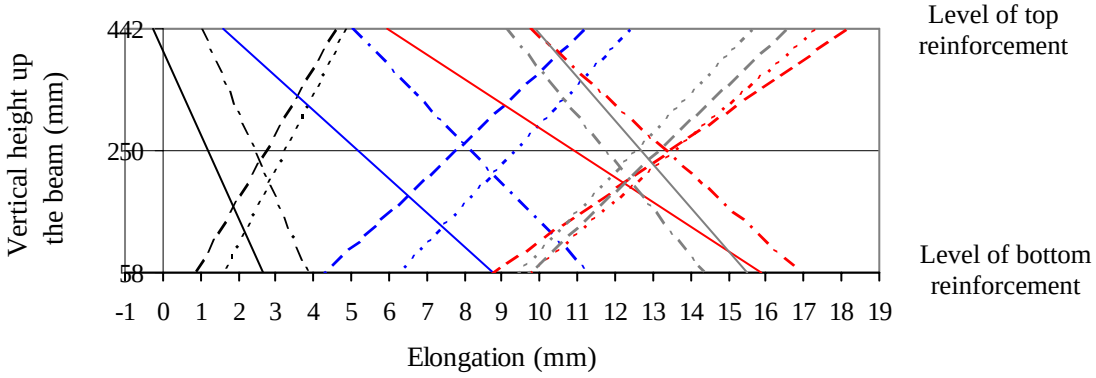

(b) Experiment

Figure 2-50. Reinforcement extension in plastic hinge region of beam 2A

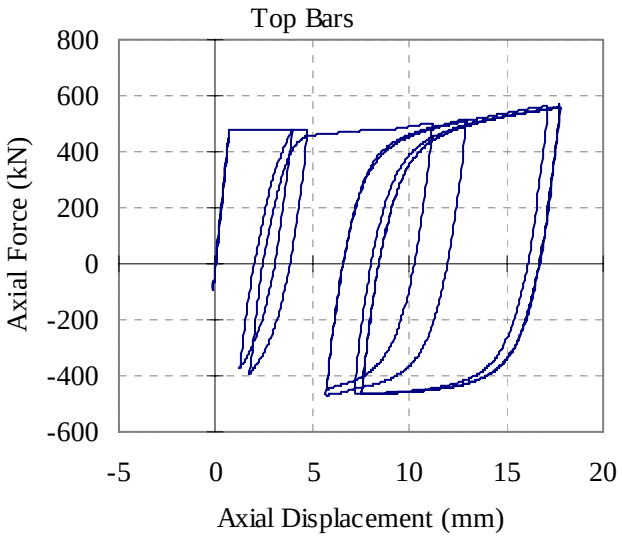

Figure 2-51. Deformation of reinforcing bar in the plastic hinge element

2.7.1.2 Beam S1A

Figure 2-53 shows the comparisons between the experimental and analytical shear force versus total displacement and shear displacement, moment-rotation and elongation responses of beam S1A. The comparisons show similar trends to those observed in beam 2A. While the analysis is able to capture the major features of the hysteresis and elongation responses, shear deformation is under-predicted. As a result, pinching is not fully captured, elongation is under-predicted, and rotation is over-predicted. The closure error in the experiment is 8mm and 5mm, respectively at the peak positive and negative *D6* cycles. The ductility 1 displacement reported in the test was 9mm.

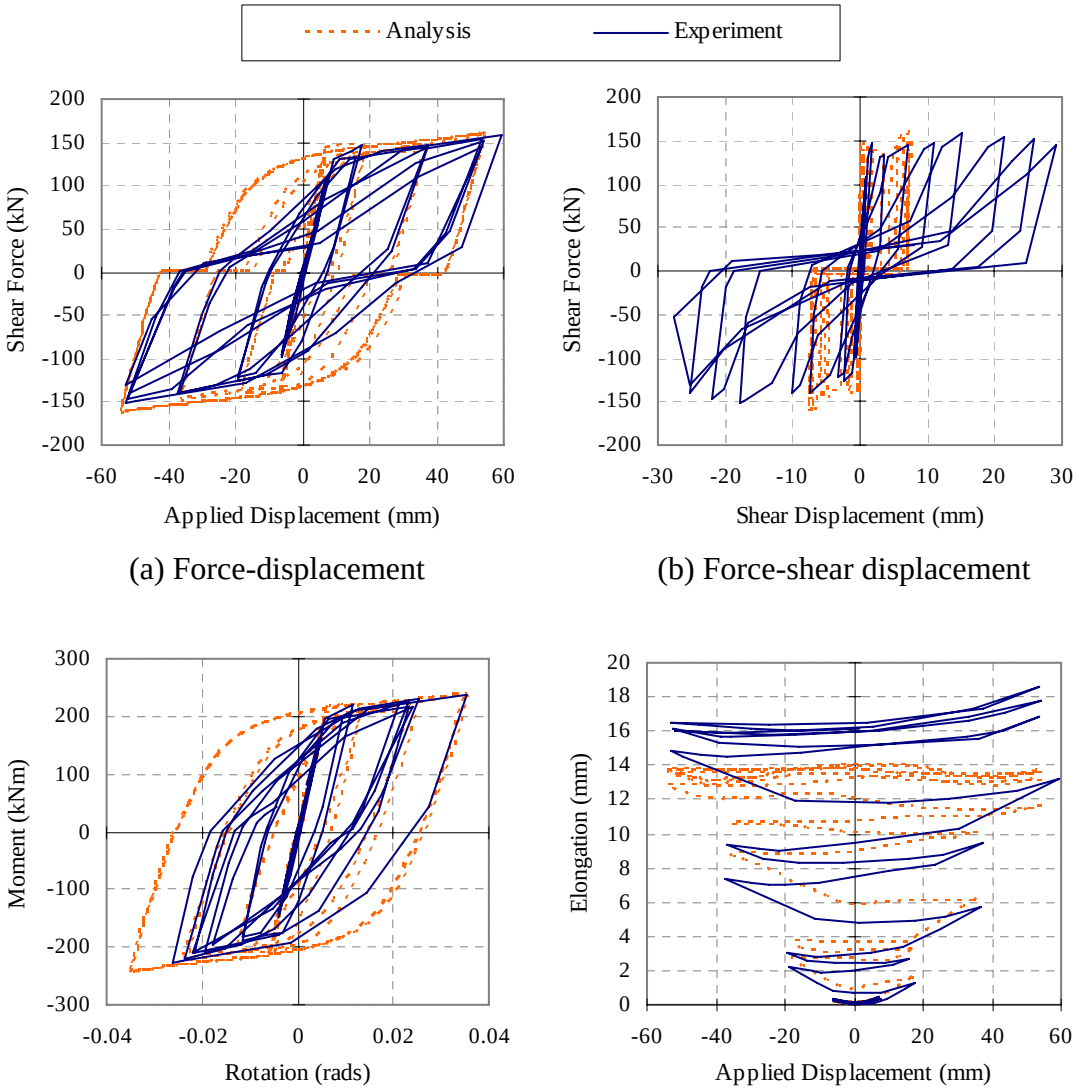

(a) Force-displacement (b) Force-shear displacement

(c) Moment-rotation (d) Elongation

Figure 2-52. Analytical and experimental comparisons for beam S1A

The top and bottom reinforcement extension over the plastic hinge region at peak displacement cycles is plotted in Figure 2-53. It can be seen that the predicted elongation has two components; inelastic extension of the tension reinforcement from inelastic rotation, and permanent extension in the compression reinforcement (see Figure 2-4 for the definition of these components). It can be observed that during the repeated displacement cycles, the increase in elongation is due to the additional extension of the compression (and tension) reinforcement without any noticeable change in the inelastic rotation. On the other hand, the increase in elongation during larger inelastic displacement in the same direction is due to the additional inelastic rotation.

The comparison in Figure 2-53 shows that the predicted reinforcement extension matches well with the experimental results until the first *D6* cycle. After this cycle, inelastic rotation decreases in the experiment as a result of an increase in shear deformation, which is not captured in the analysis. However, it should be noted that this reduction in the experimental rotation leads to a larger elongation as shown in Figure 2-53, where the compression reinforcement does not yield back as much as that observed in the analysis.

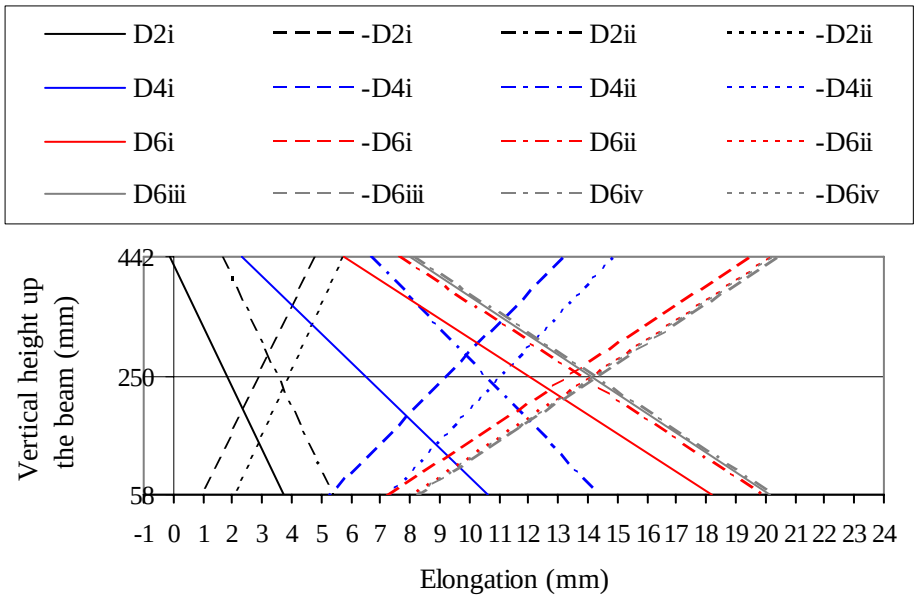

(a) Analysis

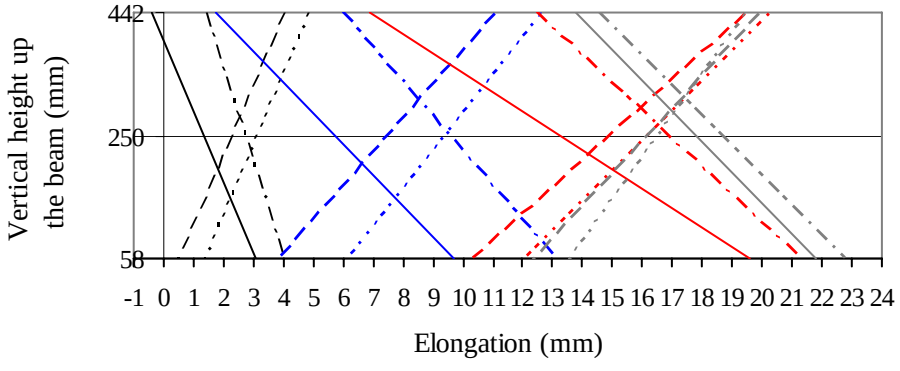

(b) Experiment

Figure 2-53. Reinforcement extension in the plastic hinge region for beam S1A

2.7.1.3 Beam 1A and Beam 1B

The comparisons between experimental and analytical results for these two beams are presented in Figures 2-54 to 2-57. The comparisons show similar trends to those observed in the previous cases. The closure error at the peak positive and negative *D6* cycles for beam 1A is -7mm and 9mm and for beam 1B is 10mm and 4mm, respectively. These errors are quite large and could affect the accuracy of the experimental results. The ductility 1 displacement reported in the test was 9.5mm and 8.5mm, respectively.

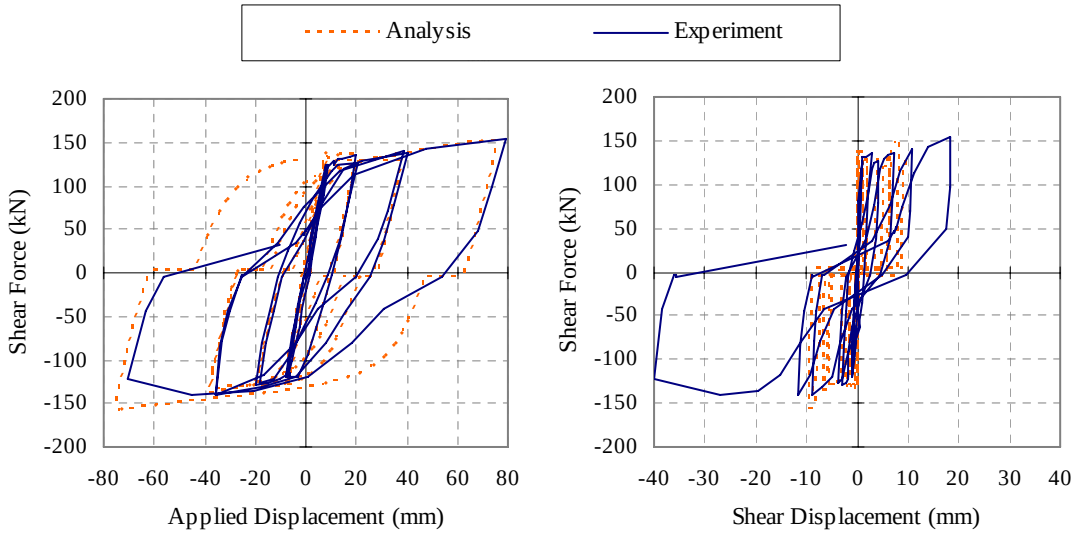

(a) Force-displacement (b) Force-shear displacement

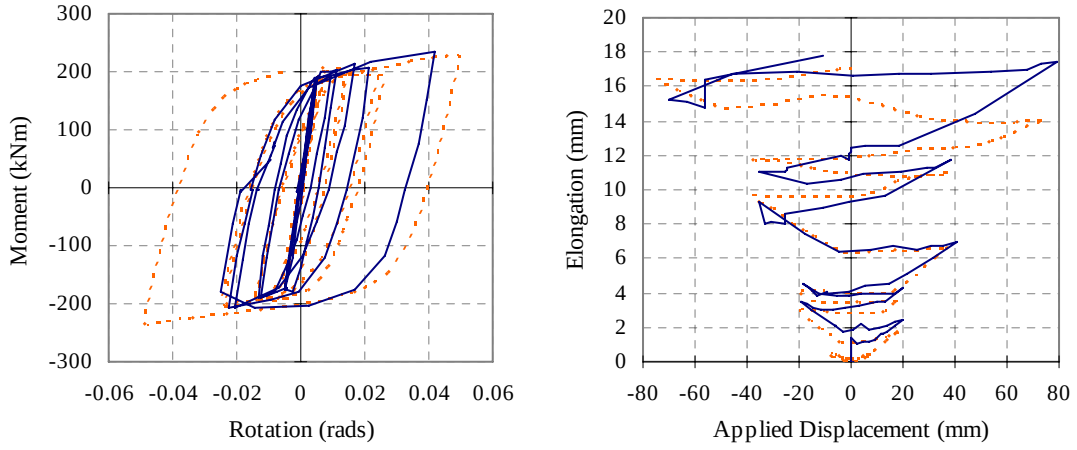

(c) Moment-rotation (d) Elongation

Figure 2-54. Analytical and experimental comparisons for beam 1A

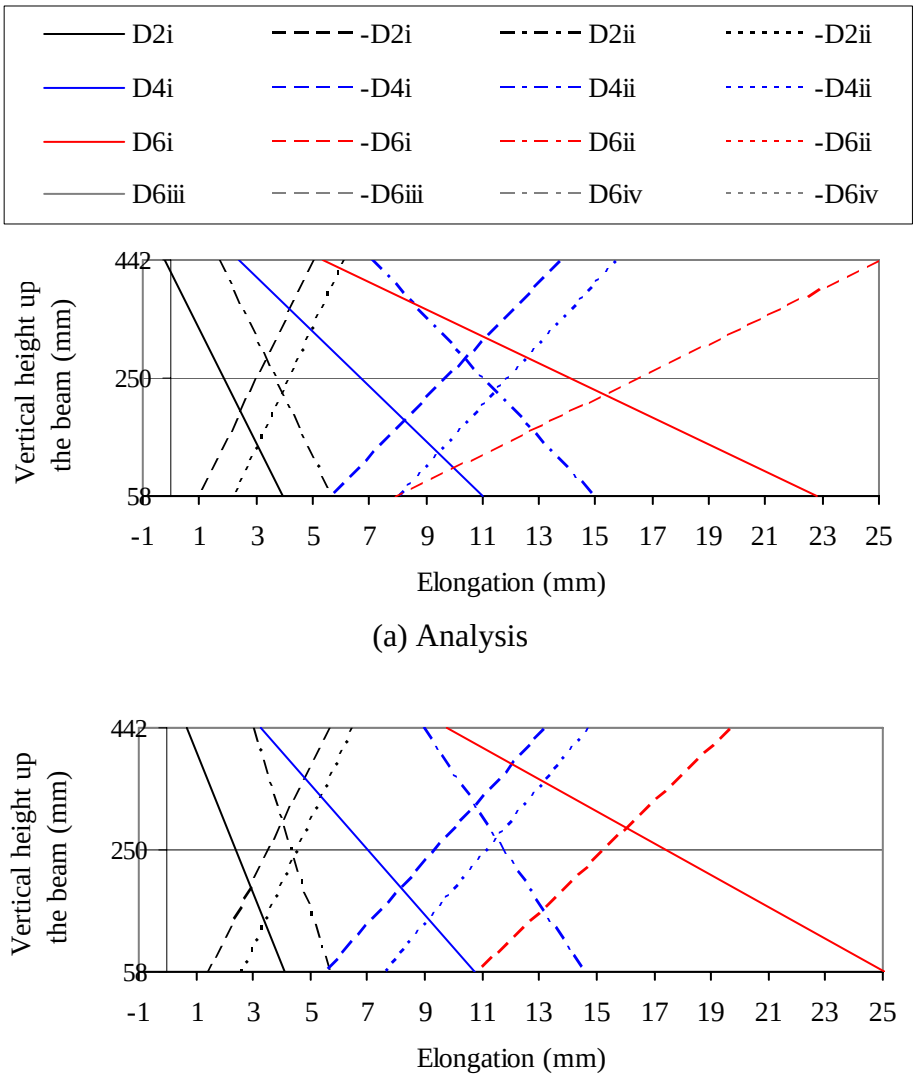

(a) Analysis

(b) Experiment

Figure 2-55. Reinforcement extension in the plastic hinge region for beam 1A

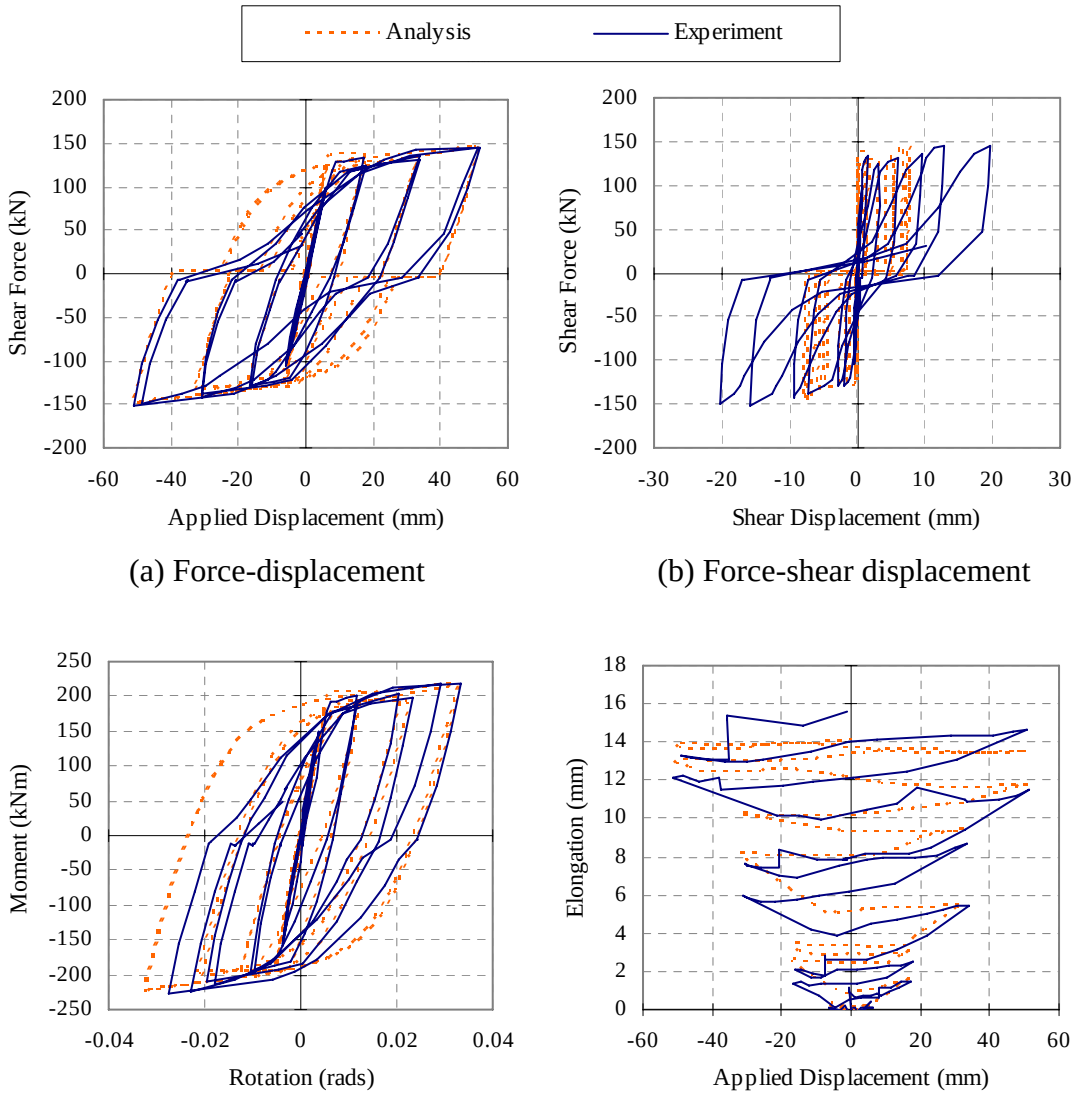

(a) Force-displacement

(b) Force-shear displacement

(c) Moment-rotation

(d) Elongation

Figure 2-56. Analytical and experimental comparisons for beam 1B

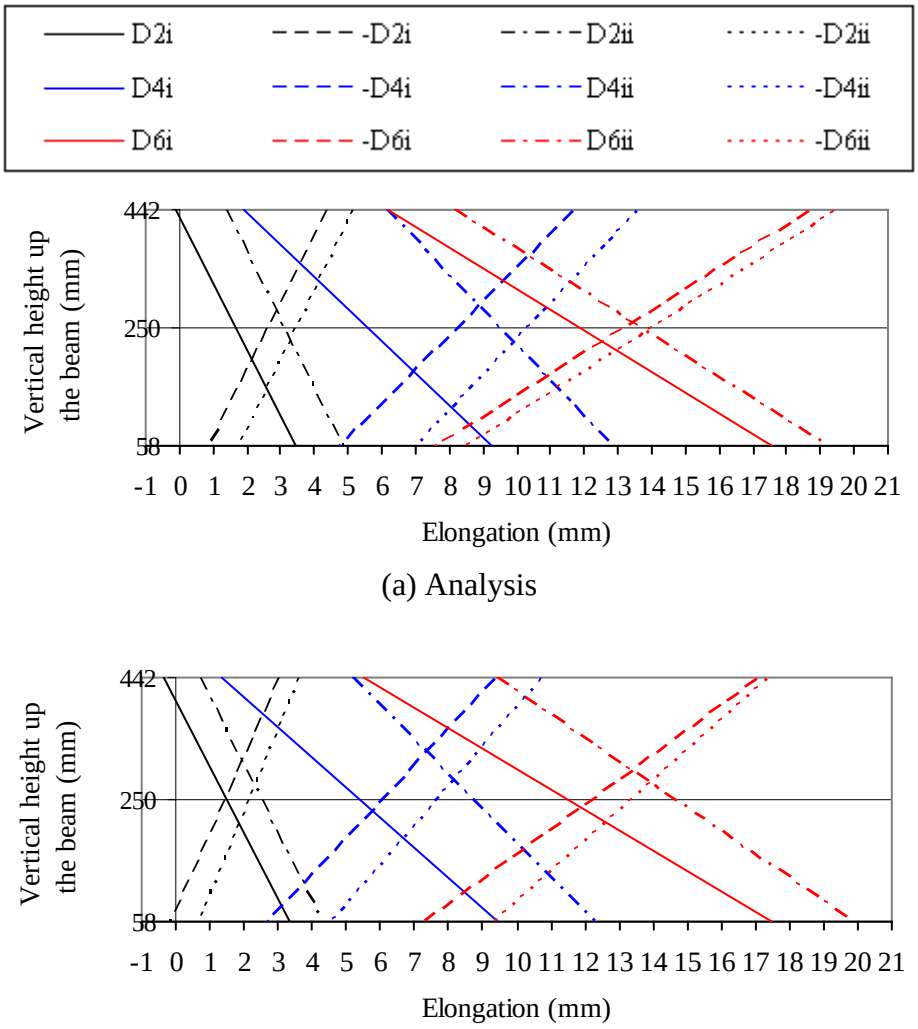

Figure 2-57. Reinforcement extension in the plastic hinge region for beam 1B

2.7.1.4 Beam AA1

This beam was built to simulate the nominally ductile beam specified in NZS 3101:2006 (Standards New Zealand 2006) where the stirrups are widely spaced. The observed horizontal projection of the diagonal strut was approximately 300mm (compared to 280mm calculated using Equation 2-7). The closure error at the peak positive and negative displacements is 5mm and 10mm, respectively.

It can be seen from the hysteresis and elongation comparisons in Figure 2-58 that the loading/unloading stiffness is predicted accurately in the analysis. However, the analysis over-estimates the peak positive strength of the beam. It should be noted that

the force of the symmetrical beam measured in the experiment is smaller in the positive drift than the negative drift. The measured moment-rotation in the experiment is slightly pinched. This may have arisen due to experimental errors.

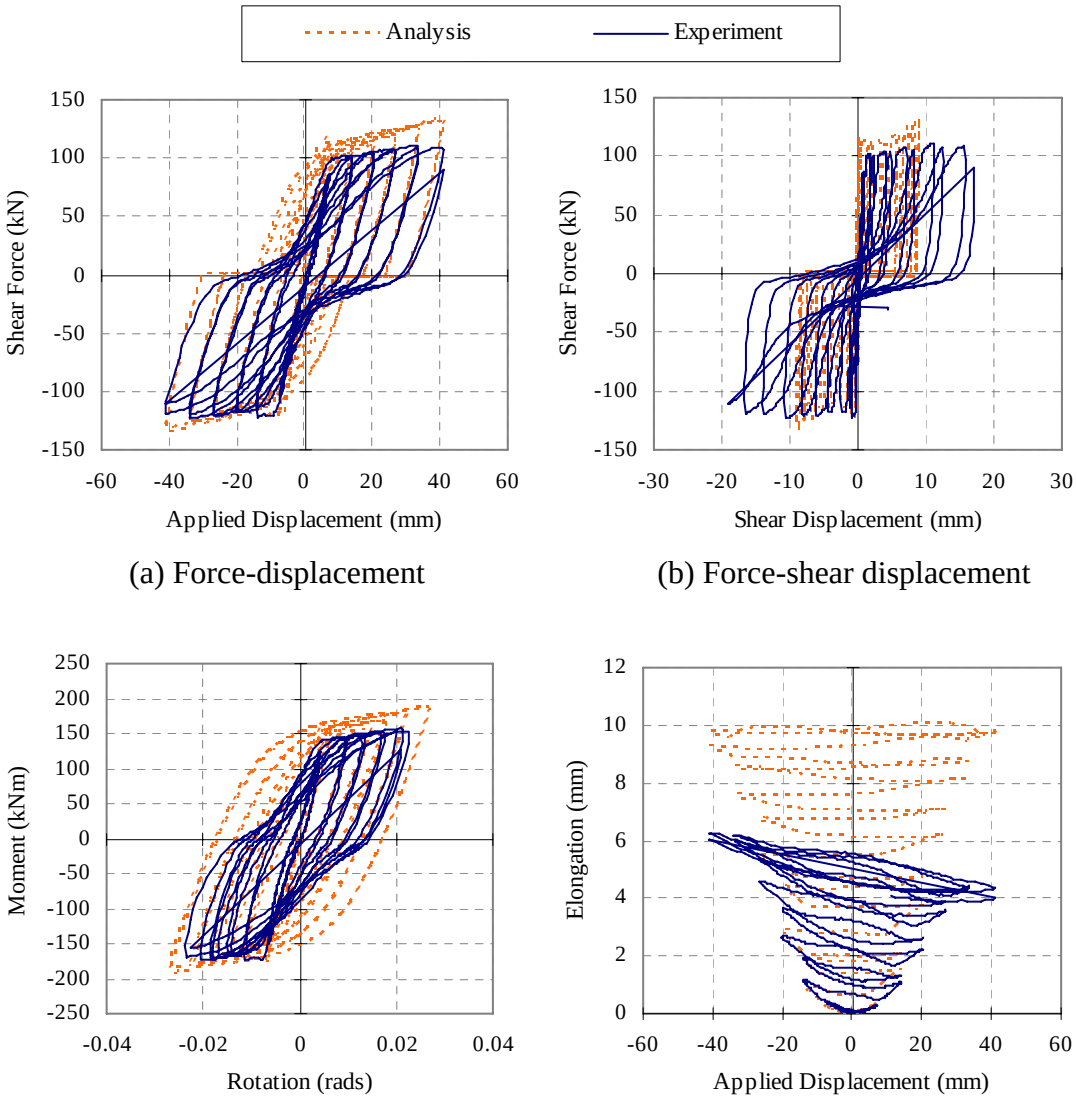

(a) Force-displacement (b) Force-shear displacement

(c) Moment-rotation (d) Elongation

Figure 2-58. Analytical and experimental comparisons for beam AA1

The extension of the top and bottom reinforcement is shown in Figure 2-59. It can be seen the extension of the compression reinforcement is much smaller in the experiment than that in the analysis. A separate analysis was carried out with concrete contact stress parameters changed to default values in an attempt to reduce elongation. The predicted elongation at the end of the test is 9.5mm, which is still significantly higher than the experimentally measured value. As these experiments indicate the

behaviour of nominally ductile and ductile beams may be quite different at large inelastic cycles, more experimental results are required to verify the applicability of the plastic hinge element in predicting elongation response of nominally ductile and non-ductile beams.

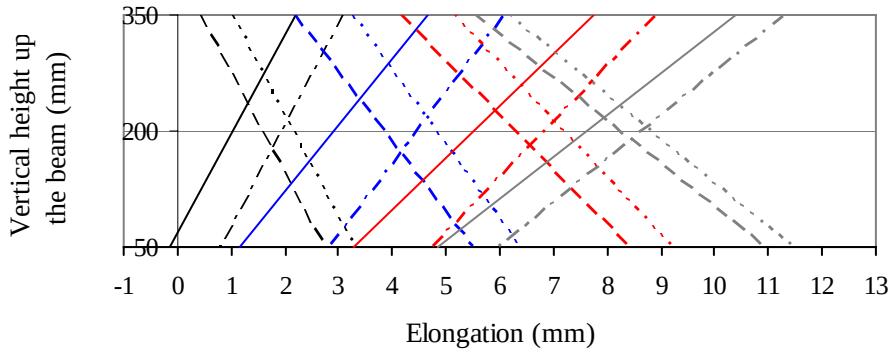

(a) Analysis

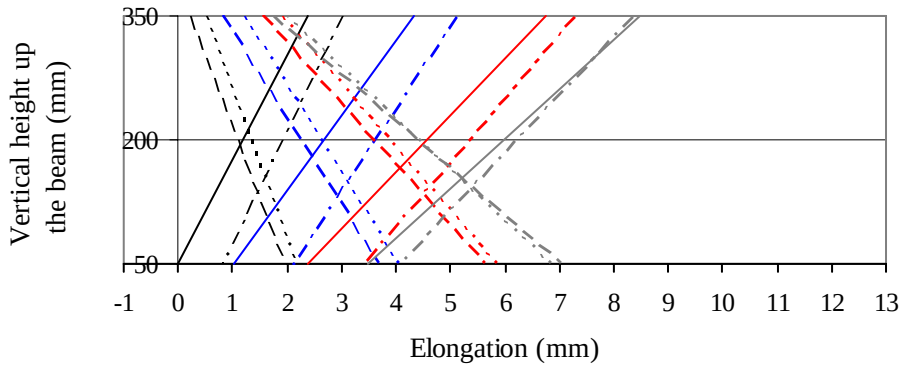

(b) Experiment

Figure 2-59. Reinforcement extension in the plastic hinge region for beam AA1

2.7.1.5 Beam AA2

This beam has the same material and section properties as beam AA1, with the only difference being that the stirrup spacing in this beam is much narrower, at 100mm centres. This beam was built to represent the ductile beam specified in NZS 3101:2006. The closure error at the end of experiment is -10mm and 9mm, respectively. This is about 25% of the total displacement; and hence the experimental results may not be reliable. The observed horizontal projection of the diagonal strut was approximately 200mm (compared to 160mm calculated using Equation 2-7).

Figure 2-60 shows the comparisons between the force-displacement, moment-rotation and elongation responses of the beam. It can be seen that the peak force measured in this beam is higher than that in beam AA1. This is because the tension reinforcement sustained higher tensile strain and strain hardened towards the end of the test.

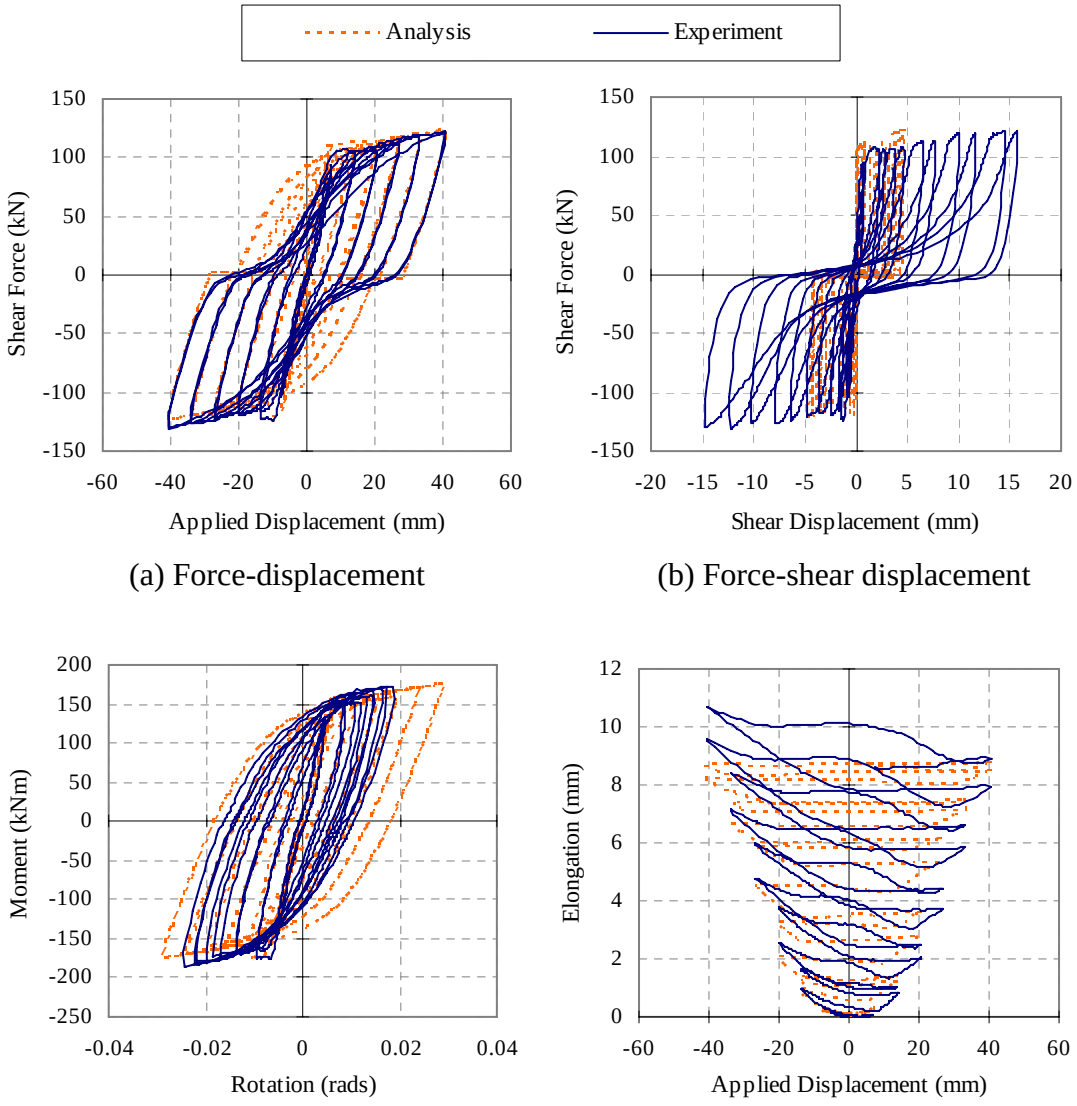

(a) Force-displacement

(b) Force-shear displacement

(c) Moment-rotation

(d) Elongation

Figure 2-60. Analytical and experimental comparisons for beam AA2

The comparison of the analytical and experimental reinforcement extension is shown in Figure 2-61. It can be seen that the analysis predicts the elongation behaviour satisfactorily.

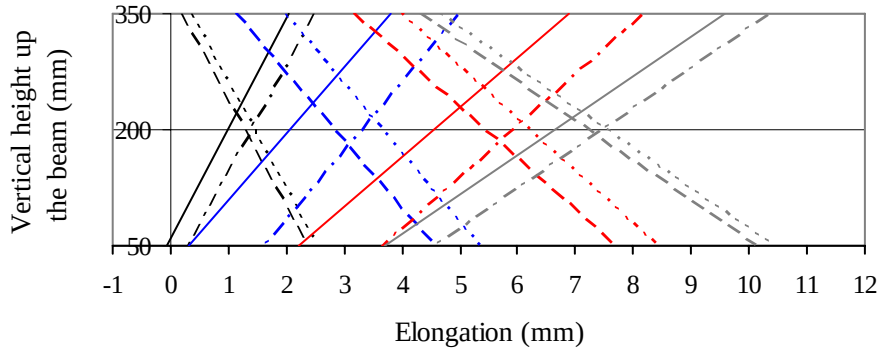

(a) Analysis

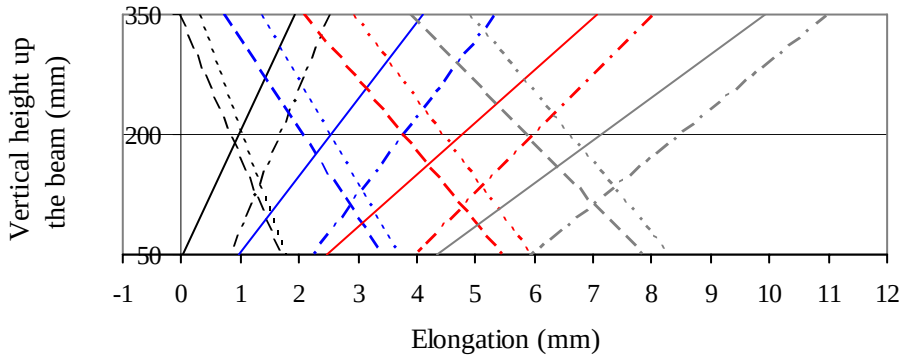

(b) Experiment

Figure 2-61. Reinforcement extension in the plastic hinge region for beam AA2

2.7.1.6 Summary

The analytical and experimental elongation, for the beams described in the previous sections, are summarised in Figure 2-62. For a perfect match, the points will lie on top of the solid line. Given the inherent scatter in elongation measurements in beam tests with similar section properties and the closure errors associated with the experimental results, the analytical elongation predictions for ductile beams matched satisfactorily with the experiments. Elongation at the end of most tests is under-estimated in the analysis. This is due to the rotation being over-predicted in the analysis as mentioned in the earlier sections.

Elongation in the nominally ductile beam, beam AA1, was over-estimated in the analysis. The applicability of the plastic hinge element in predicting elongation response of nominally ductile and non-ductile beams needs to be examined in further detail.

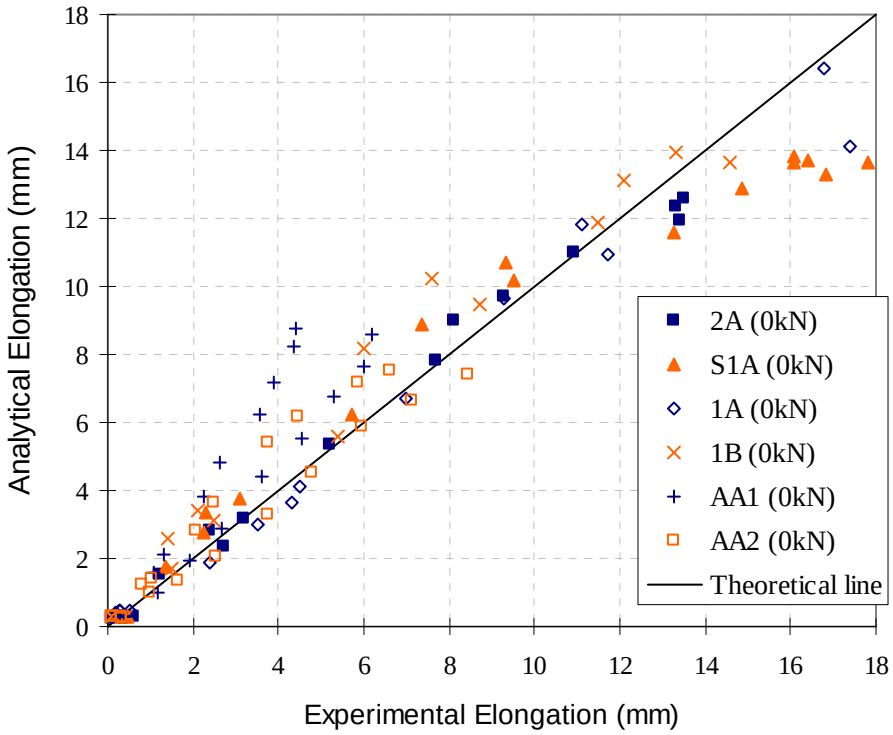

Figure 2-62. Elongation comparisons for beams with no axial force

2.7.2 Beams with Unequal Shear

Two beams with unequal top and bottom longitudinal reinforcement are examined here. The cross-section of the beams is illustrated in Figure 2-63. The material properties of the selected tests are summarised in Table 2-4. Beam 2B was tested by Fenwick et al. (1981), and beam AC1 was tested by Walker (2007). Tables 2-5 and 2-6 summarise the calculated material and plastic hinge properties.

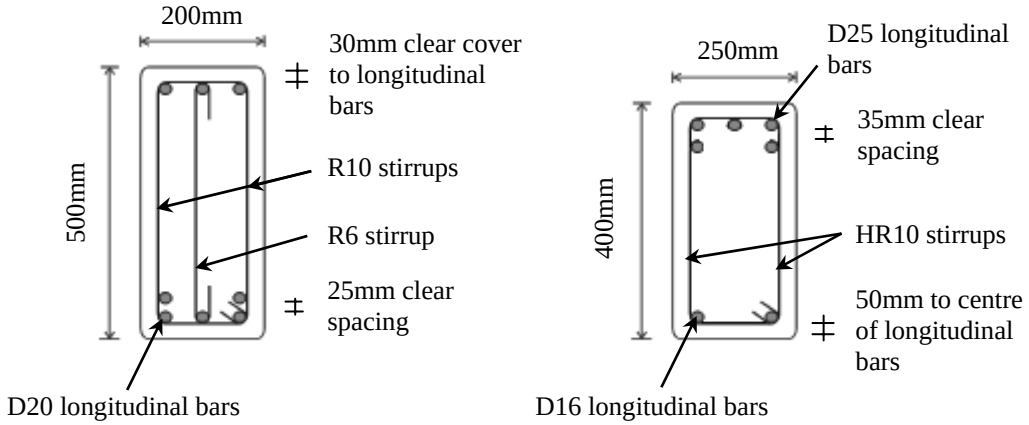

(a) Beam 2B (b) Beam AC1

Figure 2-63. Cross section of beams

Table 2-4. Stirrup arrangement and measured material properties for beams with unequal shear

Test	Stirrups arrangement	f_{vy} (MPa)	f_y (MPa)	f_u (MPa)	f_c' (MPa)
2B	2R10 + R6 @ 100c/c	298[(1)] 357[(2)]	306	459	37.6
AC1	2HR10 @ 130c/c	570	350	520	27.4

[(1)] Yield stress for R10 stirrup [(2)] Yield stress for R6 stirrup

Table 2-5. Calculated material and section properties for beams with unequal shear

Test	f_t (MPa)	E_c (GPa)	$f_{c\ (D)}'$ (MPa)	M_{y1} (kNm)	L (mm)	V_{y1} (kN)	ε_{sh} / ε_y	ε_u / ε_y
2B	2.2	27.3	12.8	188	1500	125	13	130
AC1	1.9	24.3	9.3	235	1420	166	11	104

Table 2-6. Calculated plastic hinge properties for beams with unequal shear

Test	L_p (mm)	θ (degree)	D (mm)	M_{max} (kNm)	L_{ts} (mm)	L_{yield} (mm)
2B	220	61.3	193	211	201	422
AC1	241	48.9	182	210	138	250

The first yield moment, M_{y1}, is used instead of M_{yc} for calculating L_p and L_{yield} in these analyses. This is because the assumption that concrete does not contribute to the flexural strength of the beam does not hold true. However, it should be noted that the difference between M_{yc} and M_{y1} is small. The first yield moment was calculated based

on lumped tension reinforcement, which would slightly over-estimate the actual yield moment.

The plastic hinge element, as implemented in RUAUMOKO for this study, does not have the option of having unequal top and bottom concrete cover. Therefore, the analytical beam section does not match completely with the experiment. Also, based on the plastic hinge mechanisms adopted in this study, the diagonal angles in the two directions should be different. Currently, the plastic hinge element does not allow for different diagonal angles. Therefore the analysis was carried out based on the larger shear force which gives a shallower strut angle.

2.7.2.1 Beam 2B

The closure error at the peak positive and negative *D6* cycles is 3mm and -4mm, respectively. The force-displacement, moment-rotation and elongation comparisons are shown in Figure 2-64. It can be seen that the analysis predicts the loading/unloading stiffness, yield displacement and yield/ ultimate force accurately. Shear deformation is under-estimated in the analysis because only part of the shear deformation mechanisms is taken into account.

Intuitively, as the flexural reinforcement is greater on one side, the reinforcement on the opposite side should yield back more under cyclic loading. This behaviour is observed qualitatively in both the analytical and experimental elongation response as shown in Figure 2-64(d). However, at larger displacement cycles, the top reinforcement in the analysis yields back much further than that observed in the experiment, see Figure 2-65. This may be partially due to the negative rotation being over-predicted in the analysis. Consequently, compression reinforcement is forced to yield back further so that enough compression force can be developed in the longitudinal concrete springs to balance the tension force in the tension reinforcement. In addition, buckling of the top reinforcement observed in the experiment is not captured in the analysis. When the reinforcement buckled, it causes further dislocation of aggregate particles in the compression region and hence, restraining the bars to yield back in the compression region.

In the experiment, the gap in the concrete at the compression region remained open. It is unclear what provided the large compression force that was required to resist the large tension force to satisfy force equilibrium in the experiment.

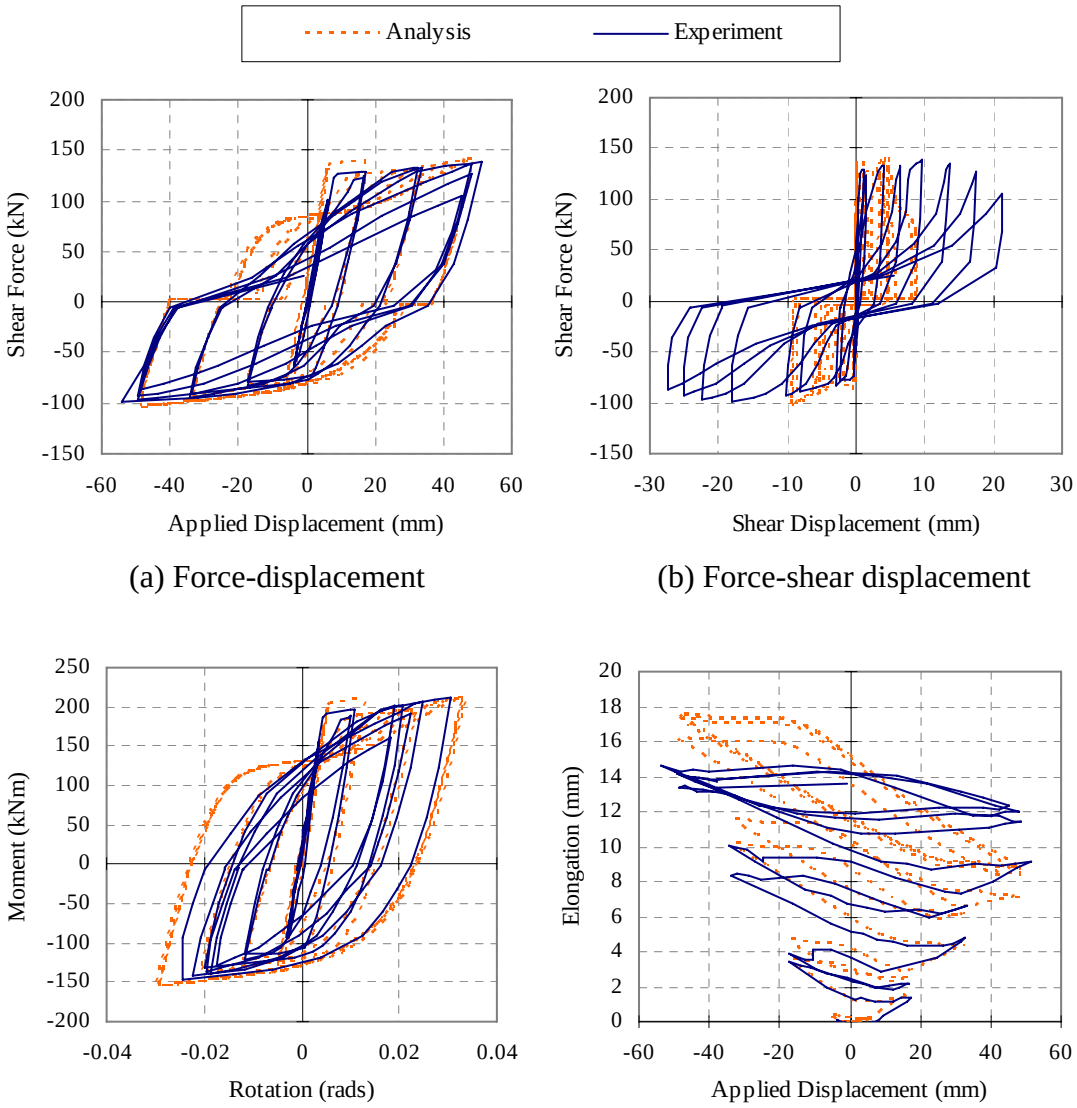

(a) Force-displacement

(b) Force-shear displacement

(c) Moment-rotation

(d) Elongation

Figure 2-64. Analytical and experimental comparisons for beam 2B

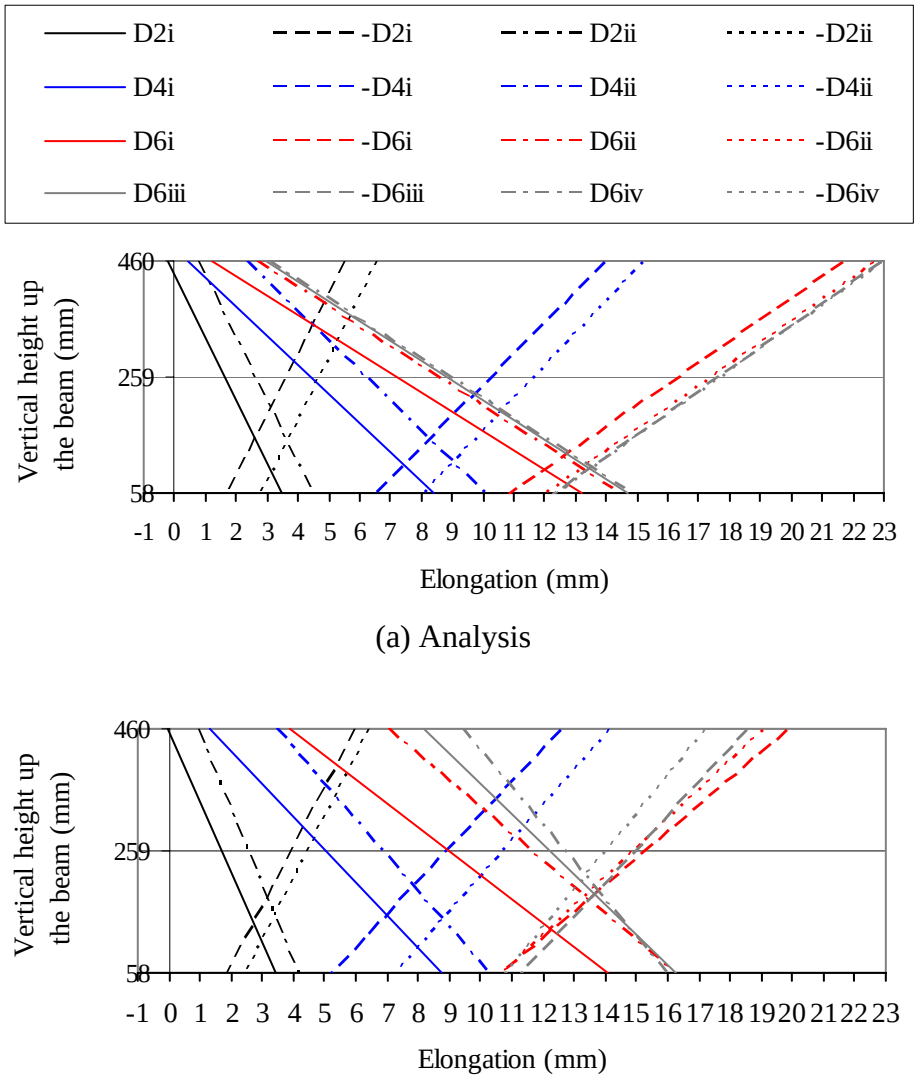

Figure 2-65. Reinforcement extension in the plastic hinge region for beam 2B

2.7.2.2 Beam AC1

The amount of reinforcement on one side is much greater than that on the other side in this beam as shown previously in Figure 2-63(b). The closure error at the peak positive and negative displacements is -1mm and -3mm, respectively. The observed horizontal projection of the diagonal strut was approximately 150mm (compared to 240mm calculated using Equation 2-7).

Comparing the analytical and experimental force-displacement, moment-rotation and elongation responses in Figure 2-66, the yield moment in the analysis on one side is

higher than that measured in the experiment and lower on the other side. It appears that the negative moment obtained in the experiment is smaller than the calculated theoretical strength of 230kNm, whereas the positive moment is larger than the calculated theoretical strength of 64kNm. The stiffness in the analysis is higher than that in the experiment. This is because the length of steel spring calculated using the Equation 2-10 is very small as M_{max} is equal to M_{y1}.

As the amount of top longitudinal reinforcement is much higher than the bottom reinforcement, elongation is much higher in the positive drift than in the negative drift. This is because the gap in the bottom reinforcement needs to close for the concrete to resist the large flexural tension force arising from the top reinforcement. This behaviour is captured in the analysis as shown in Figures 2-66(d) and 2-67.

It can be observed in Figures 2-66(b) that there are odd loops associated with the predicted shear deformation at small negative shear force. This arises mainly due to a sharp decrease in elongation from positive to negative displacements in combination with the angle of one of the diagonal struts being under-estimated in the analysis. For the same amount of elongation, if the angle of the diagonal strut is being under-estimated, the level of shear deformation would be over-predicted.

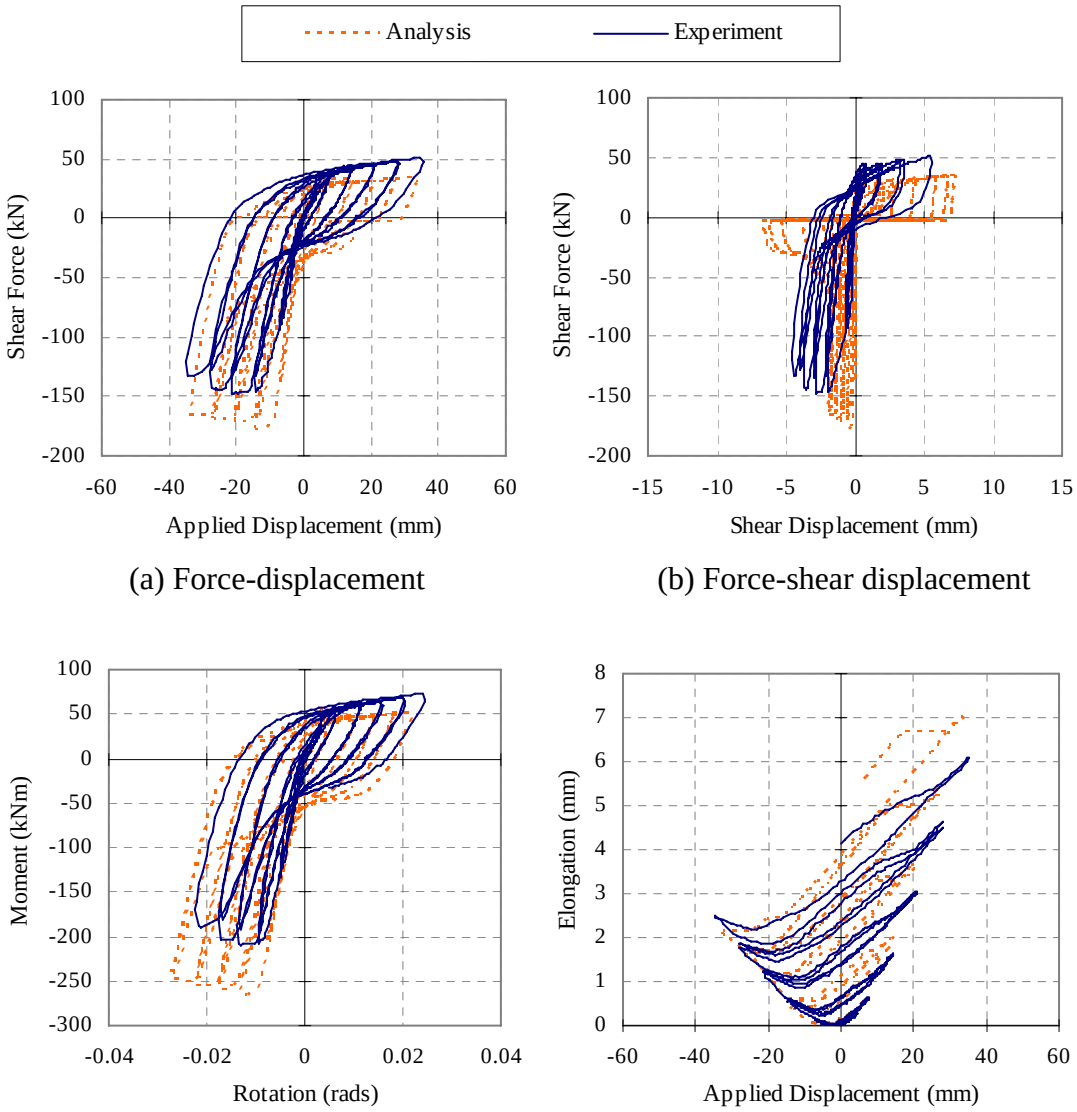

(a) Force-displacement (b) Force-shear displacement

(c) Moment-rotation (d) Elongation

Figure 2-66. Analytical and experimental comparisons for beam AC1

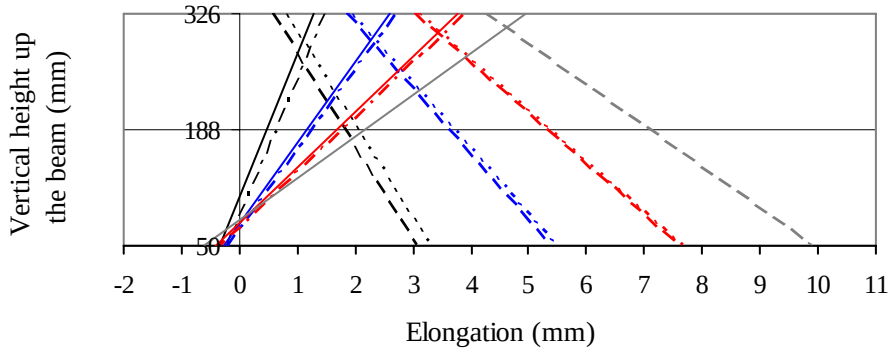

(a) Analysis

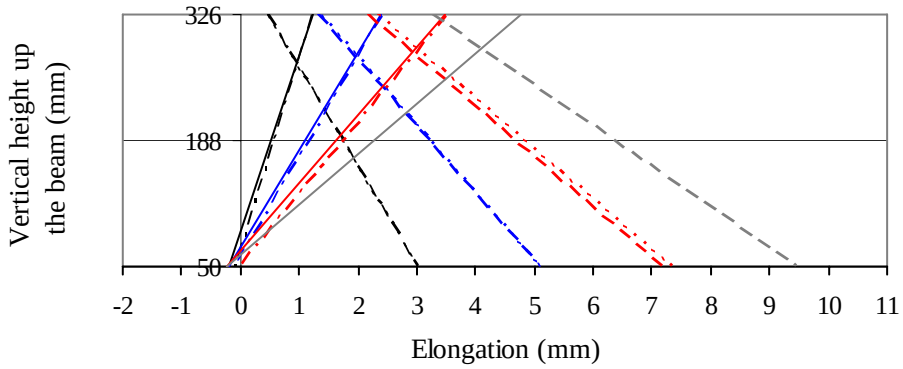

(b) Experiment

Figure 2-67. Reinforcement extension in the plastic hinge region for beam AC1

2.7.2.3 Summary

The analytical and experimental elongation histories, for beams with unequal top and bottom reinforcement are summarised in Figure 2-68. The analytical model, despite not allowing for different diagonal angles associated with the different upward and downward shear forces, still provides reasonable elongation predictions. More experimental results are required to validate the accuracy of the plastic hinge element for beams with different top and bottom reinforcement ratios.

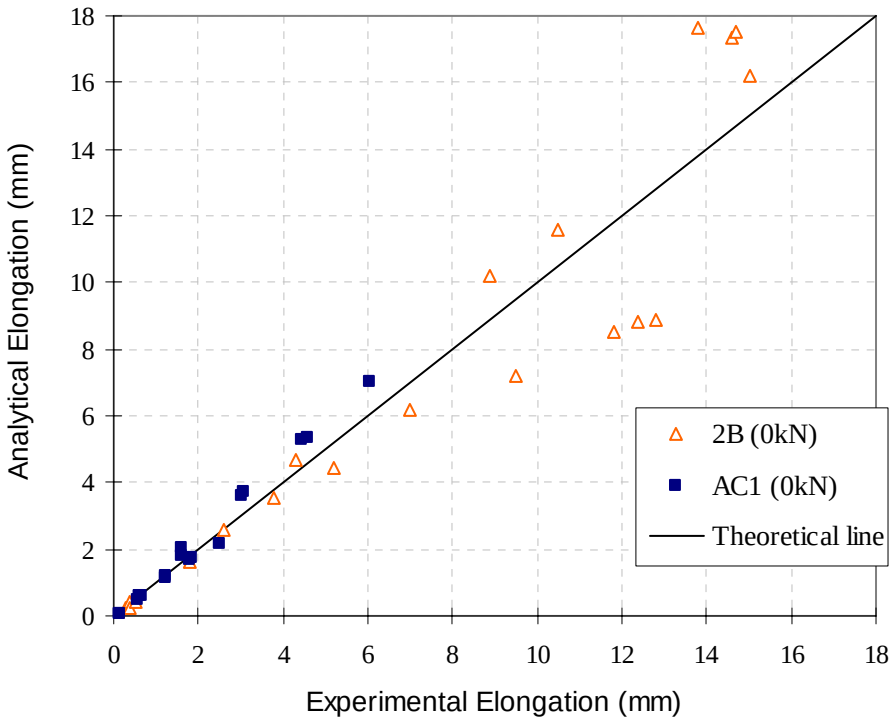

Figure 2-68. Elongation comparisons for beams with unequal top and bottom reinforcement

2.7.3 Beams with Different Levels of Axial Force

To cover the effect of a wide range of axial force on the behaviour of plastic hinges, experimental beam tests with different levels of axial force were obtained from the literature (Issa 1997; Matti 1998). The material properties of the selected tests are summarised in Table 2-7. Tables 2-8 and 2-9 summarise the calculated material and plastic hinge properties.

Table 2-7. Stirrup arrangement and measured material properties for beams with axial force

Test	N (kN)	Stirrups arrangement	f_{vy} (MPa)	f_y (MPa)	f_u (MPa)	f_c' (MPa)
S1B	-500*	2R10 + R6 @ 100c/c	344(1) 391(2)	331.6	478	37
M1	-200*	3R6 @ 55c/c	377	318	577	29.4
S2A	-100*	2R10 + R6 @ 100c/c	344(1) 391(2)	331.6	478	37.8
M2	75	3R6 @ 55c/c	377(2)	318	577	29.4
I1B	125	3R6 @ 55c/c	331	320.7	474	40

(1) Yield stress for R10 stirrup (2) Yield stress for R6 stirrup

* Negative value implies axial compression force

Table 2-8. Calculated material and section properties for beams with axial force

Test	f_t (MPa)	E_c (GPa)	$f_{c\ (D)}^{'}$ (MPa)	M_{yc} (kNm)	L (mm)	V_{yc} (kN)	ε_{sh} / ε_y	ε_u / ε_y
S1B	2.2	27.1	12.6	296	1500	197	14	62
M1	2.0	24.9	10	230	1500	153	14	116
S2A	2.2	27.3	12.9	219	1500	146	14	62
M2	2.0	24.9	10	177	1500	118	14	116
I1B	2.3	27.9	13.6	170	1500	113	20	154

Table 2-9. Calculated plastic hinge properties for beams with axial force

Test	L_p (mm)	θ (degree)	D (mm)	M_{max} (kNm)	M_{y1} (kNm)	L_{ts} (mm)	L_{yield} (mm)
S1B	300	52	236	326	290	192	380
M1	264	55.5	218	286	230	192	535
S2A	224	59.7	193	265	221	192	502
M2	204	62	180	228	180	192	578
I1B	221	60.1	192	243	173	192	696

2.7.3.1 Beam S1B (-500kN)

A constant axial compression force of 500kN, equal to $0.14A_g f_c^{'}$, was applied to this beam. This is the highest compressive force examined in this study. The closure error at the peak positive and negative *D6* cycles is 2mm and 4mm, respectively. Comparisons of the force-displacement, moment-rotation and elongation responses in Figure 2-69 show that pinching behaviour reduces dramatically where there is moderate axial compression force. In this case, the measured shear deformation contributes to approximately 15% of the total deflection at the end of the *D6* cycles. Most of the shear deformation arises due to elongation of plastic hinges, which is captured by the analysis. Therefore the predicted force-displacement relationship matches satisfactorily with the experiment.

The elastic stiffness is over-estimated in the analysis; this is because the length of tension shift effect calculated based on Equation 2-11 does not allow for an increase in length under axial compression load. Therefore, the length of the steel spring is under-estimated and the stiffness is over-estimated.

The elongation in this beam is significantly less than that of the beams with no axial force examined earlier. The trend of elongation is also distinctly different to beams

with no axial force. In the presence of axial compression force, the beam elongates during the loading in either direction, but a major portion of the elongation is recovered during unloading; thereby resulting in a very small residual elongation at zero displacement. The top and bottom reinforcement extension observed in the experiment and analysis is plotted in Figure 2-70.

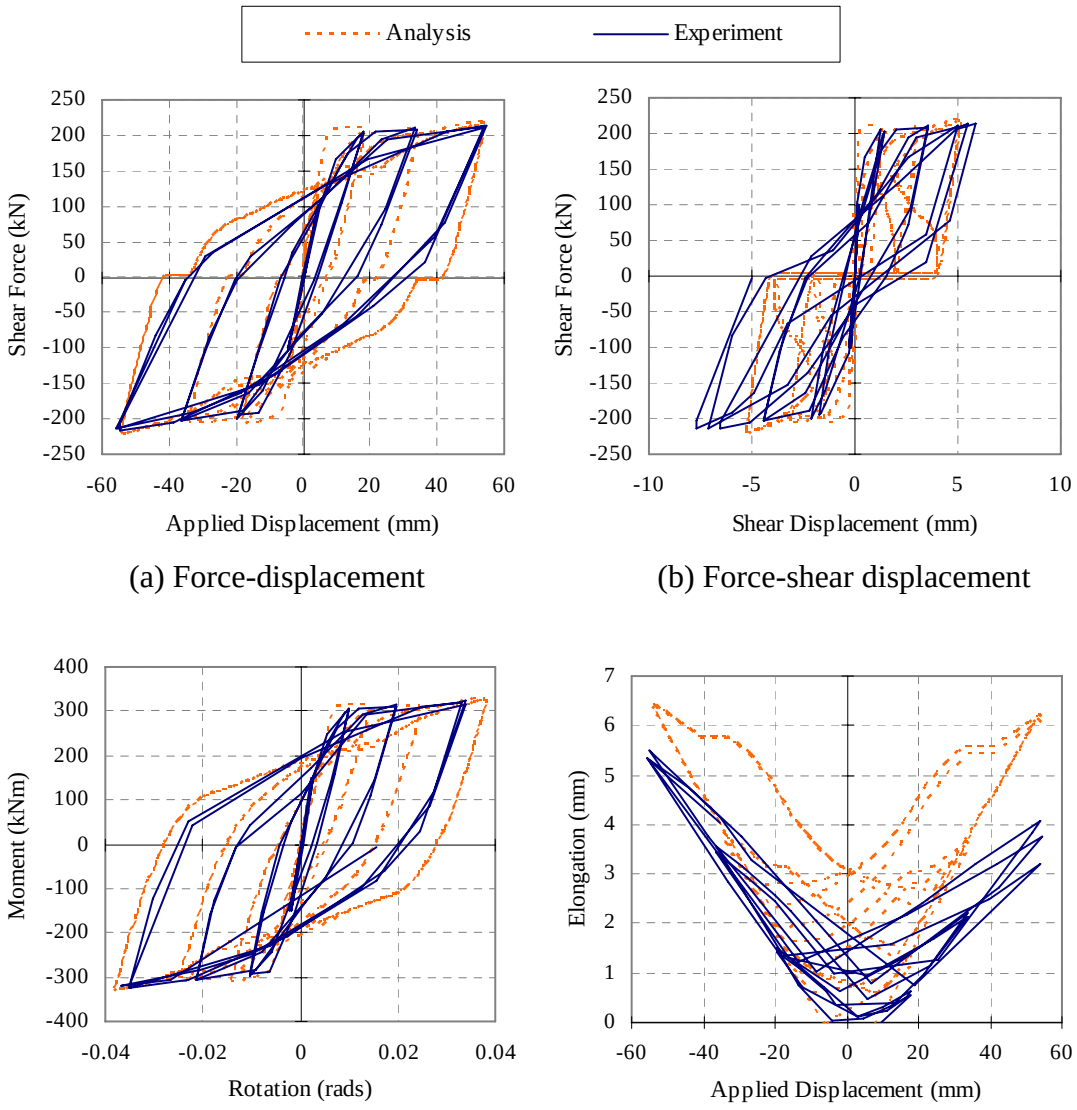

(a) Force-displacement

(b) Force-shear displacement

(c) Moment-rotation

(d) Elongation

Figure 2-69. Analytical and experimental comparisons for beam S1B

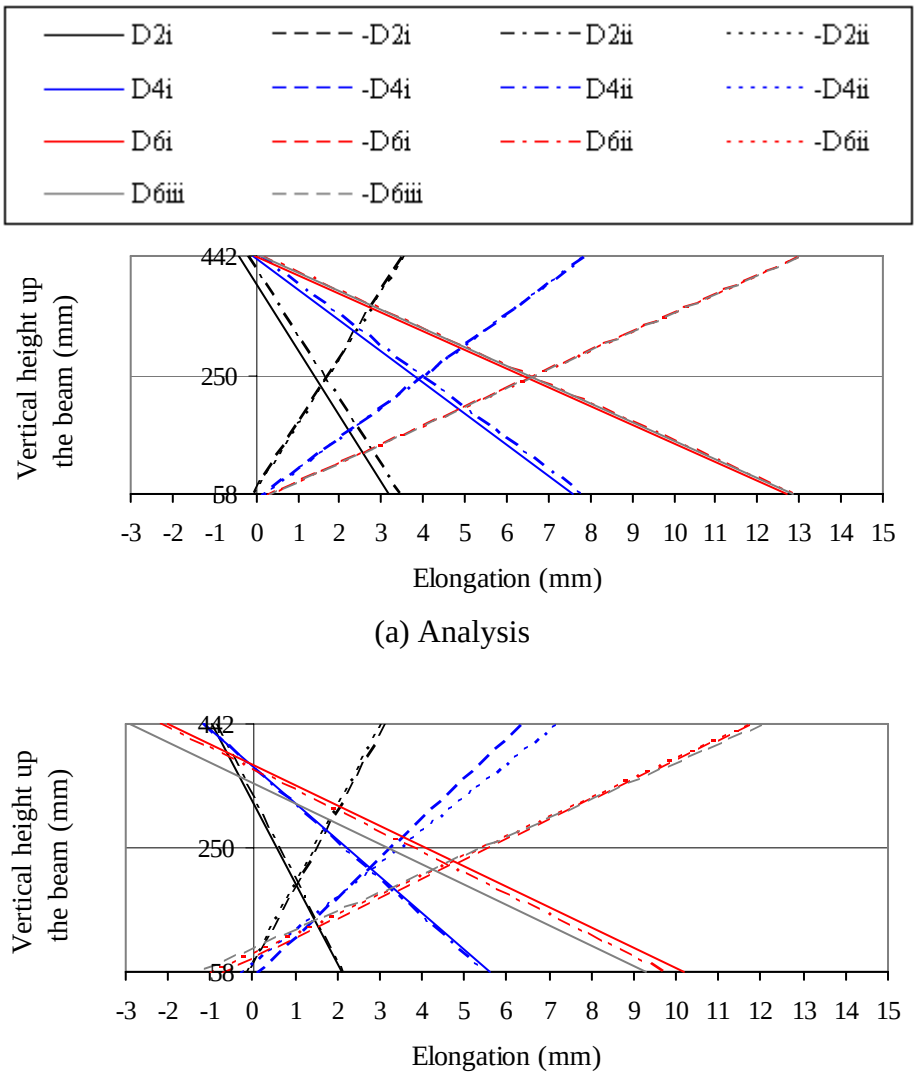

(a) Analysis

(b) Experiment

Figure 2-70. Reinforcement extension in the plastic hinge region for beam S1B

2.7.3.2 Beam M1 (-200kN)

The closure error at the peak positive and negative displacements is -2mm and -3mm, respectively. The observed horizontal projection of the diagonal strut was approximately 275mm (compared to 264mm calculated using Equation 2-7). The force-displacement, moment rotation and elongation comparisons in Figure 2-71 show similar trends to those observed in beam S1B. The moment measured in the experiment is much higher than the calculated theoretical strength. This may be the reason why the analysis under-predicts the peak force and moment. The rotation is over-predicted in the analysis. It should be noted that the rotation measured in this

experiment is much smaller than that measured in other experiments with similar axial compression load.

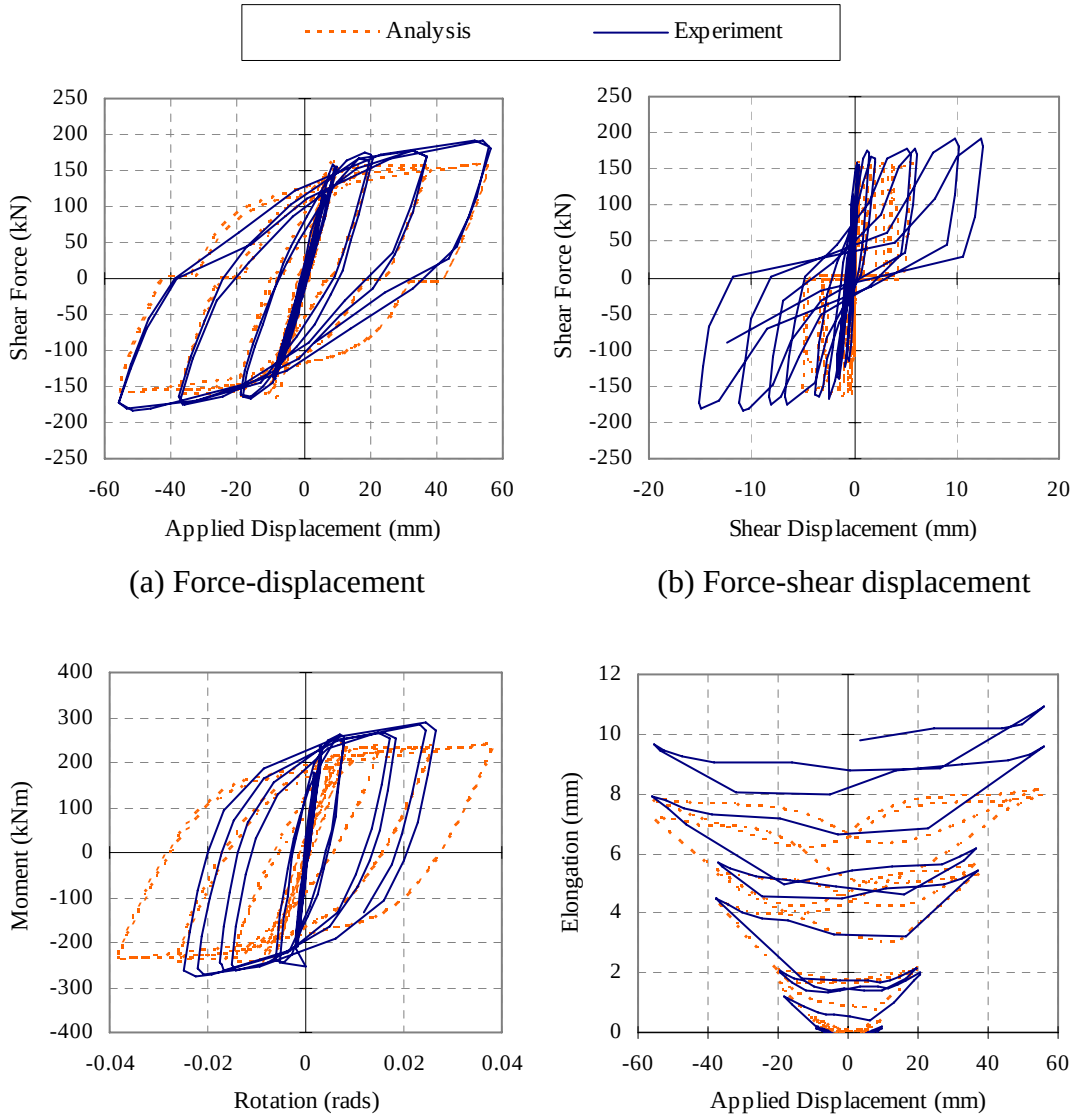

(a) Force-displacement (b) Force-shear displacement

(c) Moment-rotation (d) Elongation

Figure 2-71. Analytical and experimental comparisons for beam M1

2.7.3.3 Beam S2A (-100kN)

Satisfactory force-displacement, moment-rotation, and elongation comparisons can be observed in Figure 2-72. It should be noted that as the level of axial compression force decreases in the beam, the behaviour of plastic hinges is similar to beams with no axial force (i.e., shear deformation and elongation increases, and rotation decreases).

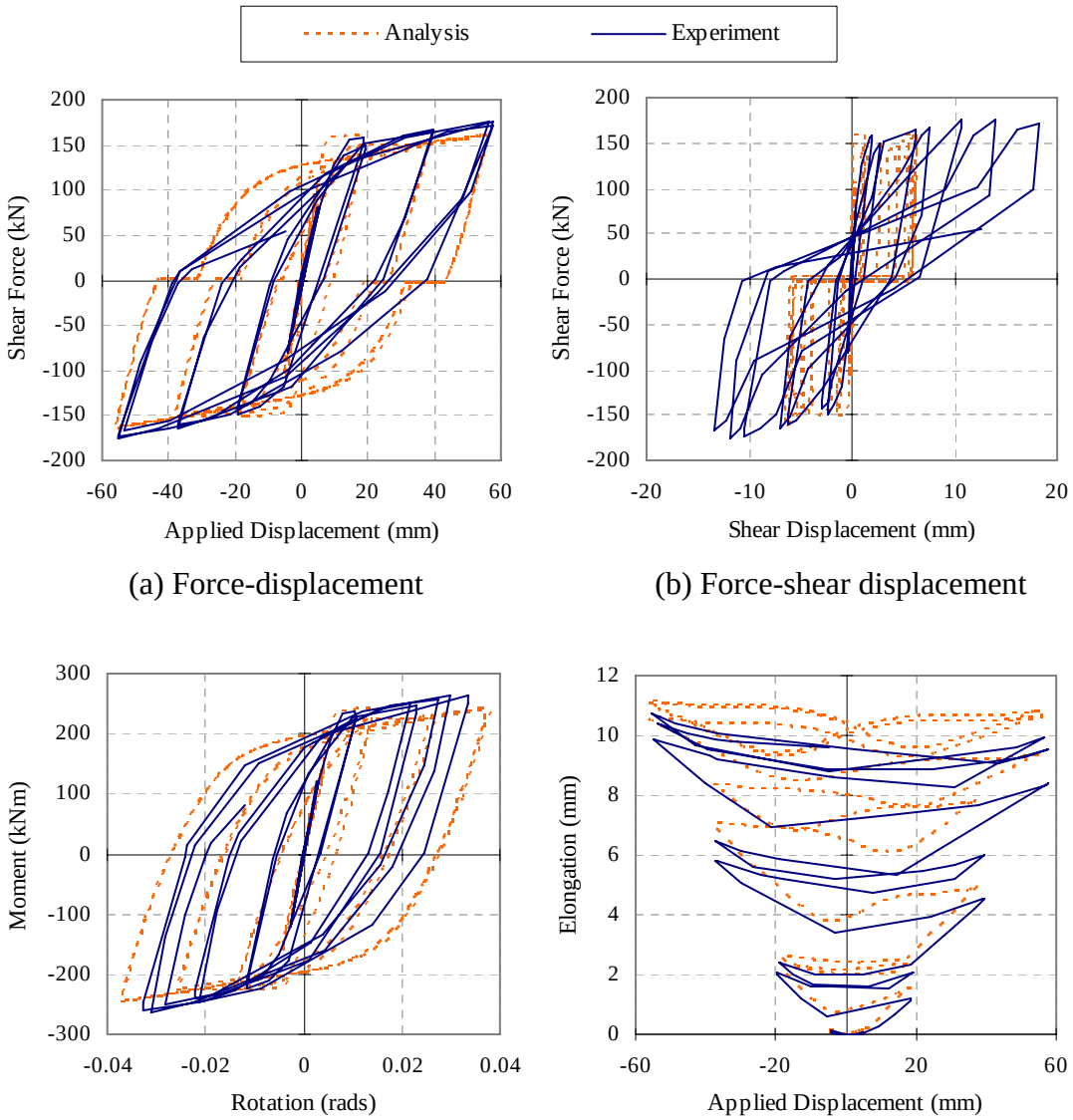

(a) Force-displacement (b) Force-shear displacement

(c) Moment-rotation (d) Elongation

Figure 2-72. Analytical and experimental comparisons for beam S2A

2.7.3.4 Beam M2 (75kN)

The closure error at the peak positive and negative displacements is -7mm and 6mm, respectively. The observed horizontal projection of the diagonal strut was approximately 220mm (compared to 204mm calculated using Equation 2-7). It can be seen from Figure 2-73(b) that the shear deformation contributes to more than half of the total applied displacement at the end of the test. Consequently, the rotation is over-predicted in the analysis (Figure 2-73(c)). Elongation is over-predicted in the analysis at large displacement cycles. This is partially due to shear deformation being

under-estimated in the analysis. Consequently, rotation and elongation are being over-estimated. In addition, it was observed in the experiment that the longitudinal reinforcement buckled at an earlier loading stage (signalling by the onset of strength degradation as shown in Figure 2-73). Consequently, elongation in the experiment ceased to increase. It should also be noted that elongation measured in this test (13mm), with 75kN applied axial tension force, is smaller than the averaged elongation measured in beams with no axial force (16mm).

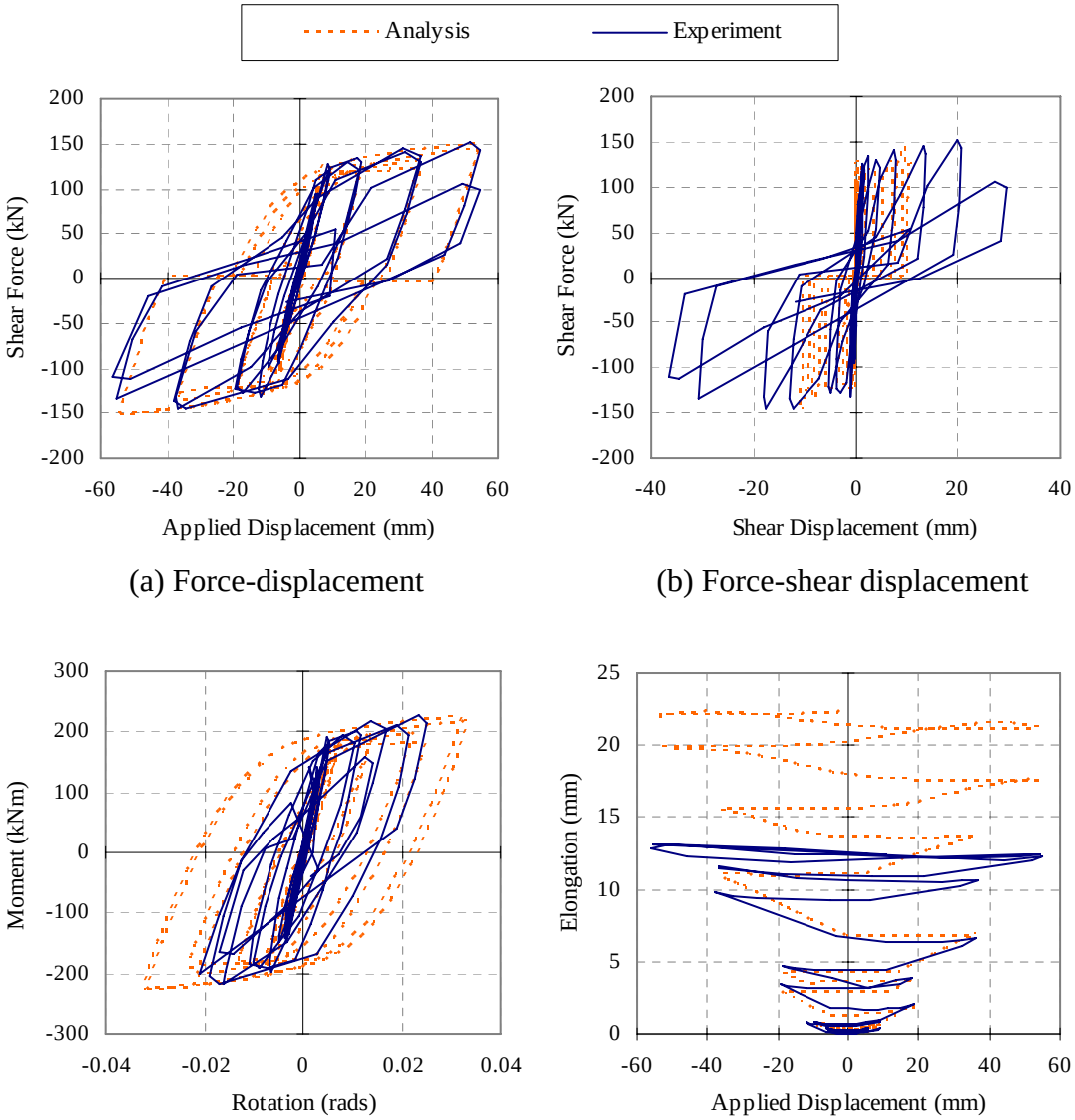

(a) Force-displacement

(b) Force-shear displacement

(c) Moment-rotation

(d) Elongation

Figure 2-73. Analytical and experimental comparisons for beam M2

Figure 2-74 shows the reinforcement extension obtained from the analysis and experiment. It can be seen that the reinforcement extension matches satisfactorily until second displacement ductility four cycles.

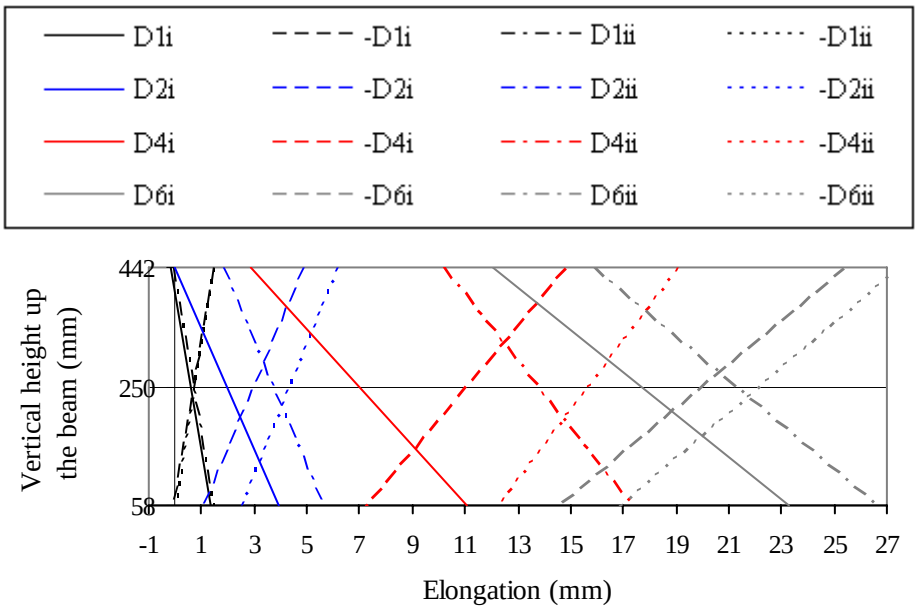

(a) Analysis

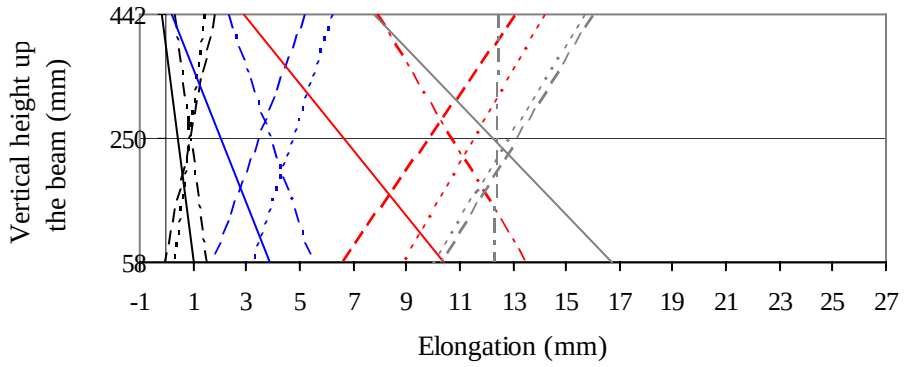

(b) Experiment

Figure 2-74. Reinforcement extension in the plastic hinge region for beam M2

2.7.3.5 Beam I1B (125kN)

This beam sustained a constant axial tension force of 125kN, equivalent to $0.13A_sf_y$. This is the highest tensile force examined in this research. The observed horizontal projection of the diagonal strut was approximately 200mm (compared to 221mm in the analysis). The hysteresis and elongation comparisons are shown in Figure 2-75. It can be seen from Figure 2-75(b) that the shear deformation at the end of *D6* cycles is

more than 60% of the total deflection. In this case, the majority of the shear deformation arises due to extension of the stirrups. Hence pinching is under-estimated in the analysis. The analysis is still able to predict the loading/unloading stiffness, yield/ultimate force and yield displacement accurately as they are not affected by the shear pinching mechanism.

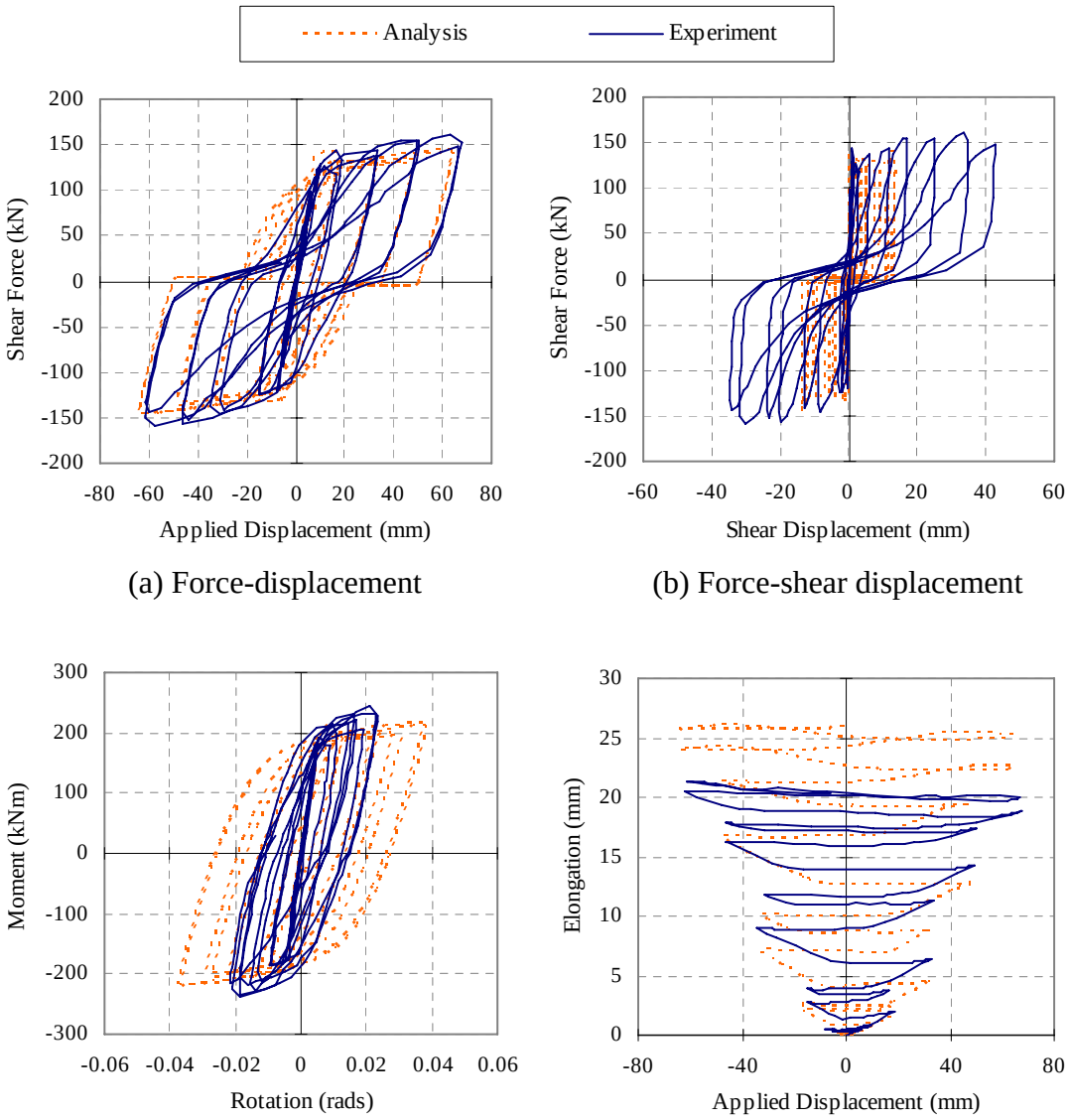

(a) Force-displacement (b) Force-shear displacement

(c) Moment-rotation (d) Elongation

Figure 2-75. Analytical and experimental comparisons for beam I1B

The elongation trend observed in Figure 2-75(d) is similar to beam with no axial force. Elongation is over-predicted in the analysis at large displacement cycles because shear deformation is being under-estimated and rotation is being over-estimated. It should also be noted that in the analysis, the axial tension force in the beam forces the

tension reinforcement to extend and prevent the compression reinforcement to yield back fully in the analysis as illustrated in Figure 2-76. Comparing this with the deformation of top bars in beam 2A (see Figure 2-51), the behaviour is quite different.

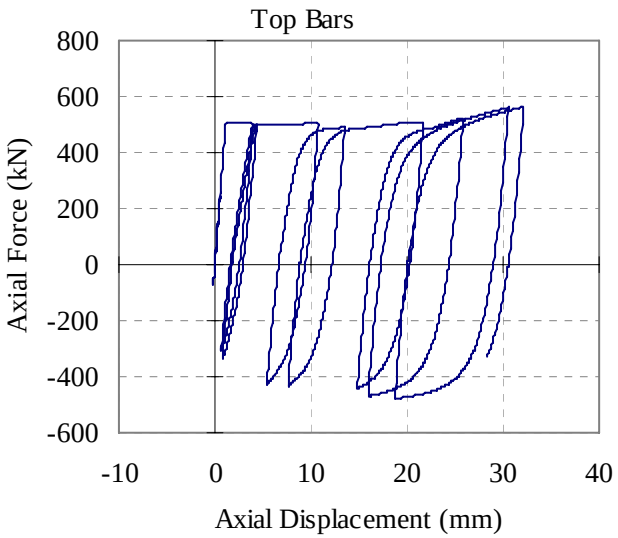

Figure 2-76. Predicted deformation in the top reinforcement of beam I1B

Extension of the top and bottom reinforcement is shown in Figure 2-77. It can be seen that the predicted reinforcement deformation matches satisfactorily with the experiment till second displacement ductility six cycles.

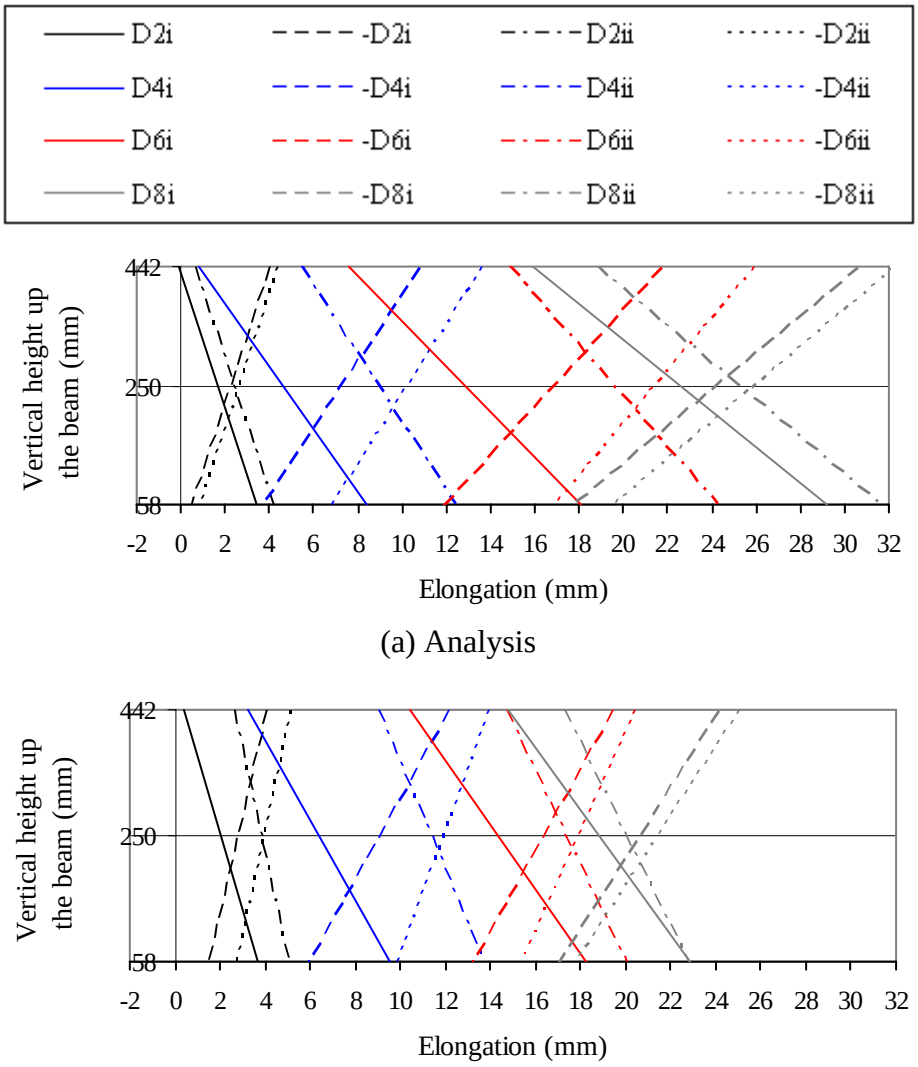

Figure 2-77. Reinforcement extension in the plastic hinge region for beam I1B

2.7.3.6 Summary

The analytical and experimental elongation histories for beams with different levels of axial force are summarised in Figure 2-78. It can be seen that the elongation results vary appreciably between the tests. However, there is a trend between the amount of measured elongation and the applied axial force. In general, elongation increases with increasing axial tension force and decreases with increasing axial compression force. This is because the applied axial compression force increases the magnitude of the flexural compression force relative to the flexural tension force in the reinforcement. Hence the compression reinforcement has to yield back further and the extension of

tensile reinforcement is restrained during load reversals. This consequently reduces the overall beam elongation.

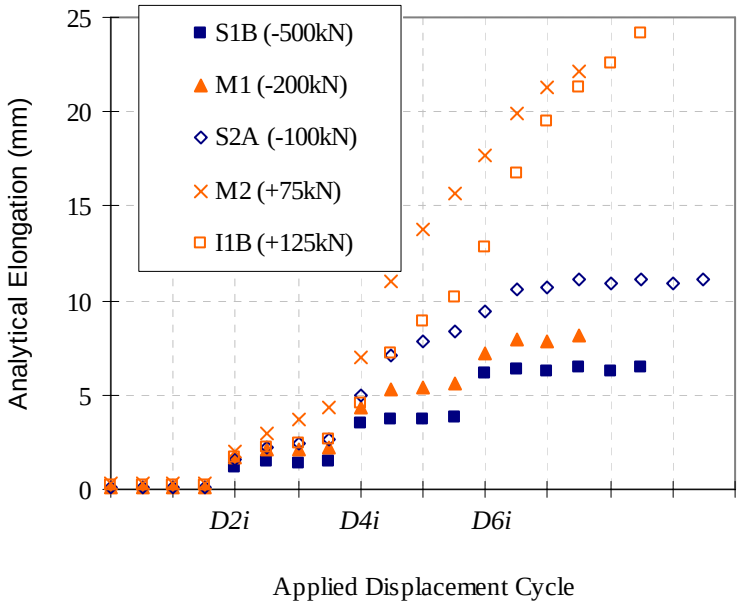

(a) Analytical predictions

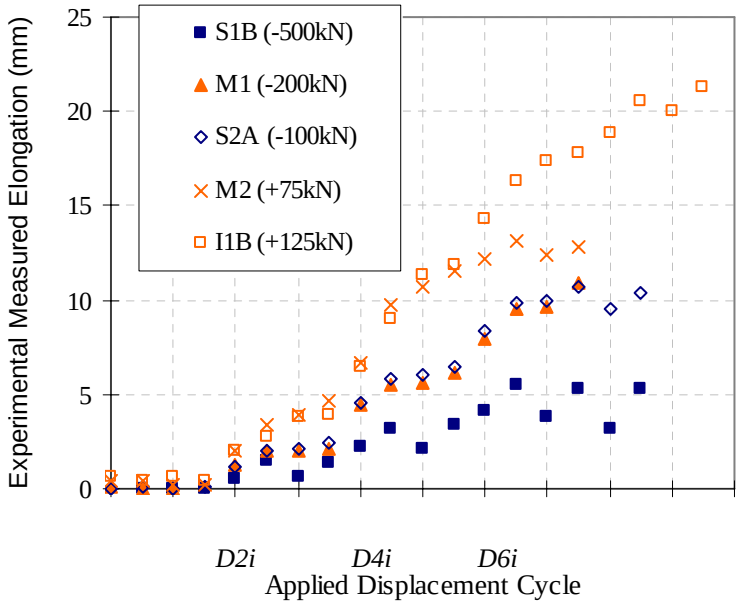

(b) Experimental results

Figure 2-78. Elongation histories for beams with axial force

The analytical and experimental elongation comparisons for beams with different levels of axial force are illustrated in Figure 2-79. The figure shows that the analytical elongation matches reasonably well with the experimental results for beams with axial

compression force. For beams with axial tension force, the predicted elongation in is generally over-estimated at large displacement cycles. This is partly due to rotation being over-predicted in the analysis and bar buckling not being captured accurately in the analysis as indicated previously.

It should be noted that beams examined herein were under constant axial force throughout the test. It is uncertain if the results would match as good in beams with varying axial loads. More studies are required to validate the plastic hinge element with varying axial force levels.

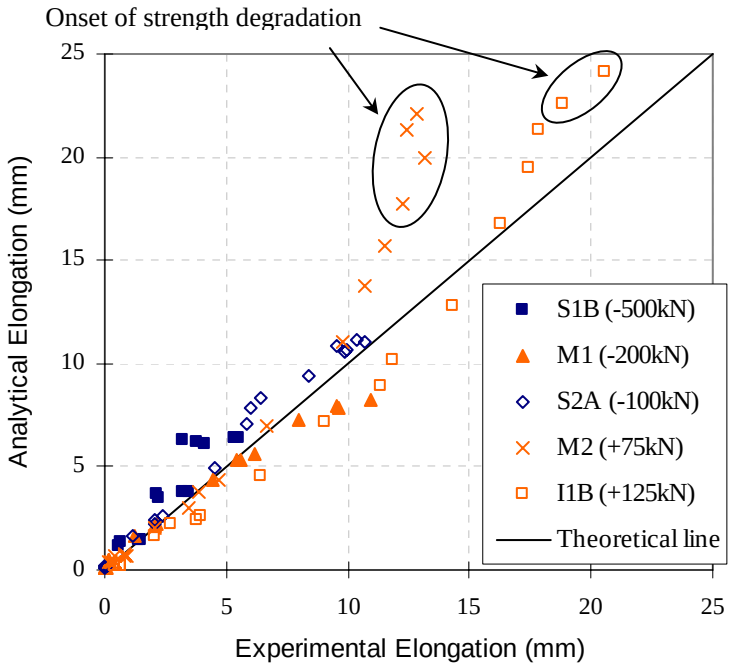

Figure 2-79. Elongation comparisons for beams with axial force

2.7.4 Beams with Different Loading Histories

The effect of different loading histories on the seismic response of reinforced concrete beams were examined by Liddell (2000). Results from 6 tests with different loading histories were extracted for comparison. The displacement histories are summarised in Table 2-10. The yield displacement, *D1*, was reported as 8.8mm.

For the PRESSS test, small cycles equal to approximately 30% of the peak load in between the peak cycles were omitted in the analysis. A few cycles between 0.1% and 0.25% were also omitted to simplify the analysis.

Table 2-10. Loading histories applied in the experiments

Test	Displacement Histories
Push Over	+*D8*
Repetitive *D8* cycles	5±*D8*
Uni-directional loading	2+*D2*, 2+*D4*, 2+*D6*, 2+*D8*
New Zealand	2±*D2*, 2±*D4*, 2±*D6*, 2±*D8*
University of California Berkeley	3±*D1*, 3±*D2*, 3±*D3*, 3±*D4*, 3±*D5*, 3±*D6*, 3±*D7*, 3±*D8*
PRESSS	3±0.1%, 3±0.25%, 3±0.35%, 3±0.5%, 3±0.75%, 3±1.0%, 3±1.5%, 3±2.0%, 3±2.5%, 3±3.0%

The experimental set up is similar to that described in Section 2.6. The cross section of the beam is illustrated in Figure 2-80 and the material properties are summarised in Table 2-11. The observed horizontal projection of the diagonal strut was approximately 130mm.

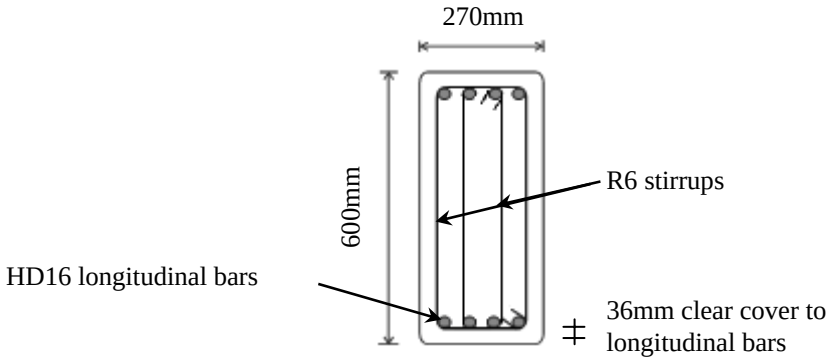

Figure 2-80. Beam section

Table 2-11. Stirrup arrangement and measured material properties for beams with different loading histories

Test	Stirrups arrangement	f_{vy} (MPa)	f_y (MPa)	f_u (MPa)	f_c' (MPa)
Liddell	4R6 @ 100c/c	350	467	630	37.5

Table 2-12. Calculated material and section properties for beams with different loading histories

Test	f_t (MPa)	E_c (GPa)	$f_c'^{(D)}$ (MPa)	M_{yc} (kNm)	L (mm)	V_{yc} (kN)	ε_{sh} / ε_y	ε_u / ε_y
Liddell	2.2	27.2	12.8	192	2150	89.3	7	61

Table 2-13. Calculated plastic hinge properties for beams with different loading histories

Test	L_p (mm)	θ (degree)	D (mm)	M_{max} (kNm)	M_{y1} (kNm)	L_{ts} (mm)	L_{yield} (mm)
Liddell	115	77.3	112	265	193	278	840

It was found that the total elongation reported in the experiments does not match with the elongation interpolated from the top and bottom reinforcement extension measured in the tests. For example, the elongation reported in the push over test is 15mm at the end of the test. However, elongation interpolated from the extension of the top and bottom reinforcement in the experiment is only 8.9mm, which raises some doubt about which value should be used. In this case, elongations calculated from the top and bottom reinforcement extensions were used as the basis for comparisons.

The comparisons between the analytical and experimental elongation for tests with different loading histories are shown in Figure 2-81. The following observations can be made:

- The predicted elongations match satisfactorily with the experimental results for beams with different loading histories.
- The amount of elongation in the push over test is similar to that in the uni-directional test at displacement ductility of 8. This is expected as the amount of inelastic rotation in these plastic hinges is similar and the amount of compression reinforcement extension is negligible.

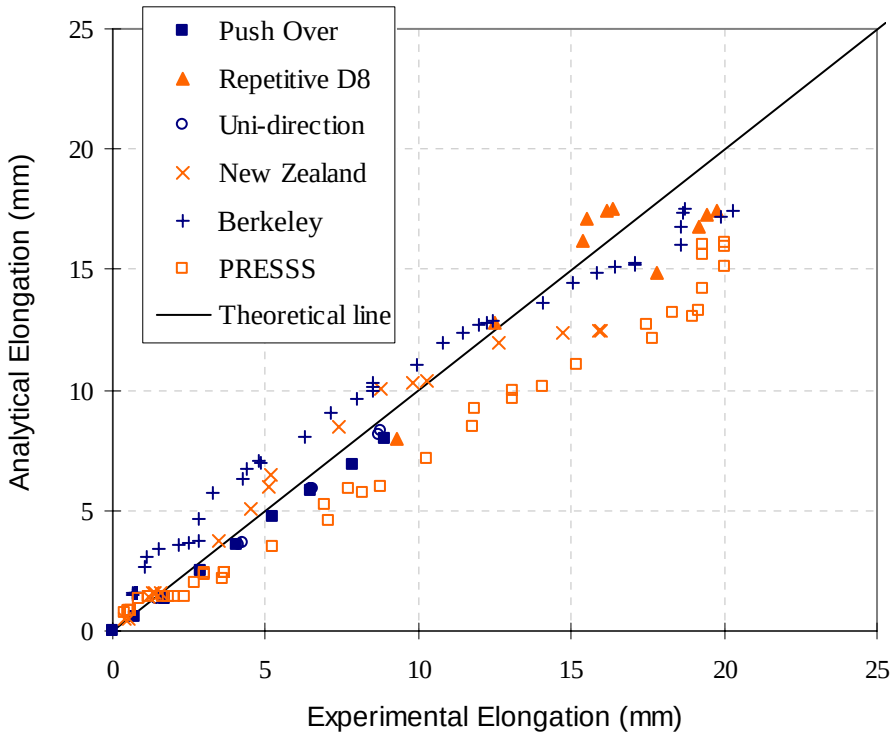

Figure 2-81. Elongation comparisons for beams with different loading histories

2.8 LIMITATIONS OF PLASTIC HINGE ELEMENT

Although the analytical and experimental comparisons for beams with different level of axial force, different top and bottom reinforcement ratio and different loading histories have shown promising results, there are limitations in the current plastic hinge element where further research and refinement may be required. These limitations include:

- The length of plastic hinge element is calculated assuming the shear resistance of concrete in plastic hinges is negligible. This may not be the case when large axial compression force is applied to the beam. No results were found in the literature that would enable the shear resistance of concrete in plastic hinge zones to be predicted when axial compression is present. The significance of axial compression on the hysteretic and elongation response is an area which requires further research.
- The yielding length of the reinforcing bars changes with the level of loading in the experiment. However, as it is difficult to quantify the reinforcement yield length during different stages of an analysis, a constant yield length corresponding to the maximum flexural capacity of the member is used.

- The length of tension shift, L_{ts}, depends on the level of axial force sustained in the plastic hinges. It contributes to part of L_{steel} which can have a significant effect on the stiffness, strain hardening and elongation response of plastic hinges. As there are currently no experimental results available in literature that quantify the relationship between L_{ts} and axial load level, more research is required.
- A constant value is set for the contact stress parameters in the concrete springs. This can have a large effect on the elongation and shear pinching behaviour. The value applied here has not been verified with experimental results as there are currently no data available in literature where the effects of shear have been included. More research is required to examine the assumption used in this study.
- Bond slip is not modelled in the analysis. Consequently, shear pinching in the force-displacement behaviour could be under-estimated.
- Buckling of longitudinal reinforcement is not considered in the analysis. This would have a significant impact on the predicted post peak behaviour. An analytical model that can accurately predict buckling response of reinforcing bars in RC plastic hinges under combined shear and axial deformations is required.
- Shear deformation from stirrup extension is not modelled in the analysis. Consequently shear pinching in the force-displacement response is under-estimated and the rotation is over-predicted by the analysis at large inelastic displacement cycles. Mechanisms associated with shear deformation from stirrup extension are complex and difficult to model. A simplified model is developed in Chapter 3 to improve the shear deformation modelling. It was shown in some cases that a bigger predicted rotation at large displacement cycles may not directly increase elongation. In the case where no axial force or axial compression force is applied to the beam, a larger rotation often leads to a reduction in elongation prediction. Whereas when axial tension force is applied, a larger rotation increases the elongation prediction.
- Behaviour of nominally ductile and ductile RC beams appears to be different at large inelastic cycles. Currently, the plastic hinge element is developed based on the mechanisms observed in ductile RC beams. More study is

required to verify the applicability of the model in predicting elongation response of nominally ductile and non-ductile beams.

2.9 CONCLUSIONS

As conventional analysis techniques using frame elements based on moment-rotation or force-displacement relationships are incapable of capturing elongation response under reversed cyclic actions, a new plastic hinge element has been proposed in this chapter. The proposed plastic hinge model is a two-node element comprising two rigid plates, which hold the opposite ends of two diagonal springs representing the diagonal compression struts and several longitudinal springs representing reinforcing bars and concrete. The axial behaviour of these springs is modelled using path-dependent uni-axial cyclic stress-strain relationships for reinforcing steel and concrete obtained from literature. Important mechanisms such as Bauschinger effect of reinforcing bars and contact stress effect and spalling of concrete are taking into account in the material models. These mechanisms were shown to have significant effects on the elongation response.

Validation of the proposed plastic hinge element with cantilever beam tests, under different axial force, loading histories and top and bottom reinforcement ratios, reported in literature show that elongation can be predicted satisfactorily by the proposed model and the predicted mechanisms can be explained using the path-dependent cyclic behaviours of the springs in the plastic hinge element. Although the analyses have shown promising results, the effects of bar buckling, bond slip and strain penetration were not captured accurately in the model. Further research and investigation is required to improve its accuracy. Analytical and experimental comparisons also show that shear deformation is under-estimated in the analysis. Improvement in shear deformation modelling would enhance the elongation predictions, particularly at large displacement cycles for beams sustaining axial tension force.

A number of advantages have been presented for the proposed analytical plastic hinge element over the traditional frame element:

1) The proposed element does not require calibration of any modelling parameters; instead generic path-dependent material models, with known material properties, together with the proposed analytical framework automatically give a satisfactory cyclic response prediction,
2) The inelastic shear deformation due to elongation can be accounted for and can be easily separated from the flexural deformation in the analysis; and most importantly,
3) Elongation of plastic hinges during reversed cyclic actions can be predicted.

2.10 REFERENCES

American Concrete Institute. (2005). *Building code requirements for structural concrete and commentary (ACI 318M-05)*, American Concrete Institute, Farmington Hills, Michigan.

Bae, S., and Bayrak, O. (2008). "Plastic hinge length of reinforced concrete columns." *ACI Structural Journal*, 105(3), 290-300.

Carr, A. J. (2008). "RUAUMOKO2D - Inelastic dynamic analysis." Department of Civil Engineering, University of Canterbury, Christchurch, New Zealand.

CEB-FIP. (1996). *RC elements under cyclic loading - state of the art report*, Thomas Telford, London.

CSI. (2003). "SAP2000 Nonlinear 8.1 ", Computers and Structures, Inc., Berkeley, USA.

Dhakal, R. P., and Maekawa, K. (2002a). "Modeling for postyield buckling of reinforcement." *Journal of Structural Engineering*, 128(9), 1139-1147.

Dhakal, R. P., and Maekawa, K. (2002b). "Reinforcement stability and fracture of cover concrete in reinforced concrete members." *Journal of Structural Engineering*, 128(10), 1253-1262.

Douglas, K. T., Davidson, B. J., and Fenwick, R. C. "Modelling reinforced concrete plastic hinges." *Eleventh World Conference on Earthquake Engineering*, Acapulco, Mexico.

Fenwick, R., and Fong, A. (1979). "The behaviour of reinforced concrete beams under cyclic loading." *Report No. 176*, University of Auckland, Auckland, New Zealand.

Fenwick, R. C., and Davidson, B. J. (1995). "Elongation in ductile seismic-resistant reinforced concrete frames." *ACI SP-157, Recent developments in lateral force transfer in buildings*, 143 -170.

Fenwick, R. C., and Megget, L. M. (1993). "Elongation and load deflection characteristics of reinforced concrete members containing plastic hinges." *Bulletin of the New Zealand National Society for Earthquake Engineering*, 26(1), 28-41.

Fenwick, R. C., Tankut, A. T., and Thom, C. W. (1981). "The deformation of reinforced concrete beams subjected to inelastic cyclic loading: experimental results." *School of Engineering Report No. 268*, University of Auckland, Auckland, New Zealand.

Fenwick, R. C., and Thom, C. W. (1982). "Shear deformation in reinforced concrete beams subjected to inelastic cyclic loading." *School of Engineering Report No. 279*, University of Auckland, Auckland, New Zealand.

Issa, M. S. (1997). "The deformations of reinforced concrete beams containing plastic hinges in the presence of axial compression or tension load," Master Thesis, University of Auckland, Auckland, New Zealand.

Kim, J. (2002). "Behaviour of hybrid frames under seismic loading," PhD. Thesis, University of Washington, Washington, USA.

Kim, J., Stanton, J., and MacRae, G. (2004). "Effect of beam growth on reinforced concrete frames." *Journal of Structural Engineering*, 130(9), 1333-1342.

Lau, D. B. N. (2007). "Influence of precast prestressed flooring on the seismic performance of reinforced concrete perimeter frame buildings." *Report Number 653*, Dept. of Civil and Environmental Engineering, University of Auckland, Auckland, New Zealand.

Lau, D. B. N., Davidson, B. J., and Fenwick, R. C. "Seismic performance of RC perimeter frames with slabs containing prestressed units." *Pacific Conference on Earthquake Engineering 2003*, Christchurch, New Zealand.

Lee, J.-Y., and Watanabe, F. (2003). "Predicting the longitudinal axial strain in the plastic hinge regions of reinforced concrete beams subjected to reversed cyclic loading." *Engineering Structures*, 25(7), 927-939.

Liddell, D., Ingham, J. M., and Davidson, B. J. (2000). "Influence of loading history on ultimate displacement of concrete structures." *Report No. 597*, University of Auckland, Auckland, New Zealand.

Lindsay, R. (2004). "Experiments on the seismic performance of hollow-core floor systems in precast concrete buildings," Master Thesis, University of Canterbury, Christchurch, New Zealand.

MacPherson, C. (2005). "Seismic performance and forensic analysis of a precast concrete hollow-core floor super-assemblage," Master Thesis, University of Canterbury, Christchurch, New Zealand.

Maekawa, K., and Okamura, H. (1983). "The deformation behaviour and constitutive equation of concrete using elasto-plastic and fracture model." *Journal of Faculty of Engineering, University of Tokyo*, 37(2), 253-328.

Maekawa, K., Pimanmas, A., and Okamura, H. (2003). *Nonlinear mechanics of reinforced concrete*, Spon Press, London.

Mander, J. B. (1983). "Seismic design of bridge piers," PhD. Thesis, University of Canterbury, Christchurch, New Zealand.

Matthews, J. (2004). "Hollow-core floor slab performance following a severe earthquake," PhD. Thesis, University of Canterbury, Christchurch, New Zealand.

Matthews, J. G., Mander, J. B., and Bull, D. K. "Prediction of beam elongation in structural concrete members using a rainflow method." *New Zealand Society of Earthquake Engineering Conference 2004*, Rotorua.

Matti, N. A. (1998). "Effect of axial loads on the behaviour of reversing plastic hinges in reinforced concrete beams," Master Thesis, University of Auckland, Auckland, New Zealand.

McBride, A., Fenwick, R. C., and Davidson, B. J. (1996). "The influence of slabs on the lateral cyclic behaviour of ductile concrete frames." *Report No. 566*, Department of Civil and Resource Engineering, University of Auckland, Auckland, New Zealand.

Megget, L. M., and Fenwick, R. C. (1989). "Seismic behaviour of a reinforced concrete portal frame sustaining gravity loads." *Bulletin of the New Zealand National Society for Earthquake Engineering*, 22(1), 39-49.

Mendis, P. (2001). "Plastic hinge lengths of normal and high-strength concrete in flexure." *Advances in Structural Engineering*, 4(4), 189-195.

Panagiotakos, T. B., and Fardis, M. N. (2001). "Deformations of reinforced concrete members at yielding and ultimate." *ACI Structural Journal*, 98(2), 135-148.

Pang, X. B., and Hsu, T. T. C. (1996). "Fixed angle softened truss model for reinforced concrete." *ACI Structural Journal*, 93(2), 197-207.

Paulay, T., and Priestley, M. J. N. (1992). *Seismic design of reinforced concrete and masonry buildings*, Wiley, New York,.

Peng, B. H. H. (2005). "Finite element modelling on beam elongation within the plastic hinge zone." *Final Year Honours Project Report*, University of Canterbury, Christchurch, New Zealand.

Priestley, M. J. N., and Park, R. (1987). "Strength and ductility of concrete bridge columns under seismic loading." *ACI Structural Journal*, 84(1), 61-76.

Priestley, M. J. N., Seible, F., and Calvi, G. M. (1996). *Seismic design and retrofit of bridges*, Wiley, New York.

Schlaich, J., Schaefer, K., and Jennewein, M. (1987). "Toward a consistent design of structural concrete." *PCI Journal*, 32(3), 74-150.

Shima, H., Chou, L., and Okamura, H. (1987). "Micro and macro models for bond behaviour in reinforced concrete." *Journal of Faculty of Engineering, University of Tokyo*, 39(2), 94-133.

Standards New Zealand. (2006). *Concrete structures standard: NZS 3101:2006*, Standards New Zealand, Wellington.

To, N. H. T., Ingham, J. M., and Sritharan, S. (2001). "Monotonic non-linear analysis of reinforced concrete knee joints using strut-and-tie computer models." *Bulletin of the New Zealand Society for Earthquake Engineering*, 34(3), 169-190.

Vecchio, F. J., and Collins, M. P. (1986). "Modified compression field theory for reinforced concrete elements subjected to shear." *Journal of the American Concrete Institute*, 83(2), 219-231.

Walker, A. (2007). "Assessment of material strain limits for defining different forms of plastic hinge region in concrete structures," Master Thesis, University of Canterbury, Christchurch, New Zealand.

Wuu, P. J. Y. (1996). "Deformations in plastic hinge zone of RC beam in ductile frame structures subjected to inelastic cyclic loading," Master Thesis, University of Auckland, Auckland, New Zealand.

3 PLASTIC HINGE ELEMENT WITH ADDITIONAL SHEAR FLEXIBILITY

In Chapter 2, an elongating plastic hinge element was developed and incorporated into RUAUMOKO (Carr 2008), an inelastic dynamic analysis program. Validation of the plastic hinge element with cantilever beam tests available in literature has demonstrated that, in its current form, the model under-estimates shear deformation. Shear deformation in the plastic hinges arises due to two main mechanisms (Fenwick and Thom 1982); (i) elongation of plastic hinges, and (ii) inelastic extension of transverse reinforcement. As the proposed plastic hinge element does not take into account the shear deformation from stirrup extension, improvement and refinement of the plastic hinge element is required.

This chapter describes methods used to improve the shear deformation modelling in the proposed plastic hinge element. Firstly, the contribution of different mechanisms to the overall shear deformation is evaluated. Secondly, a simple relationship relating elongation to the total shear deformation within plastic hinges is proposed. Thirdly, the previously developed plastic hinge element is modified to improve the shear deformation response. Finally, the refined plastic hinge element is validated against cantilever beam tests obtained from literature.

3.1 SHEAR DEFORMATION MECHANISMS

3.1.1 Shear Deformation from Elongation of Plastic Hinges

Shear deformation from elongation of plastic hinges is shown in Figure 3-1. The solid line shows the shear deformation corresponding to elongation at a peak applied displacement. When the applied displacement reverses, the diagonal, *D1*, gets stretched. As concrete does not carry any stress in tension due to opening of the diagonal cracks, the elongation of diagonal *D1* does not resist any shear force. On the other hand the diagonal, *D2*, which had been stretched substantially in tension, has to shorten until the diagonal cracks close so that it can resist compression and contribute to shear resistance. The closure of the diagonal cracks resulted in a shear displacement

with little change in force; thereby inducing a pinched hysteresis loop in the force-displacement response.

Relationship between elongation, E, and the corresponding shear deformation, S_E, can be expressed in Equation 3-1, where θ is the angle between the diagonal and the horizontal plane as illustrated in Figure 3-1.

$$S_E = \frac{E}{\tan\theta} \tag{3-1}$$

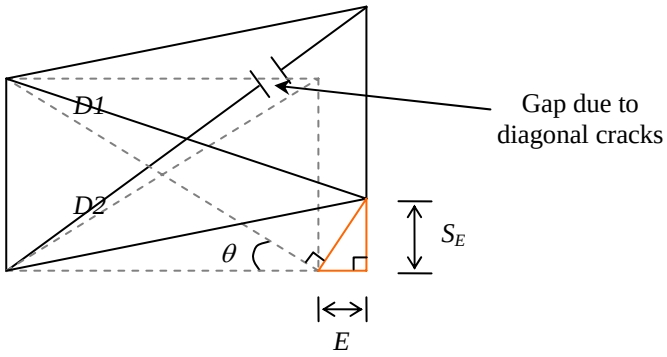

Figure 3-1. Shear deformation arising from beam elongation

3.1.2 Shear Deformation from Extension of Shear Reinforcement

Previous experimental studies have illustrated the tendency of plastic hinges to increase in depth under inelastic cyclic loading due to inelastic extension of the shear reinforcement (Fenwick and Fong 1979; Booth 1994; McBride et al. 1996; Wuu 1996; Issa 1997; Matti 1998). Shear deformation from stirrup extension is illustrated in Figure 3-2. With the shear force acting in an anti-clockwise direction, the diagonals (*D2* and *D4*) elongate due to the extension of the stirrups. When the shear force reverses, cracks open up in the diagonals (*D1* and *D3*) and the cracks in *D2* and *D4* have to close before significant shear can be resisted. The vertical movement of the beam associated with closing of the cracks in *D2* and *D4* contribute to the pinched force-displacement response of the beam.

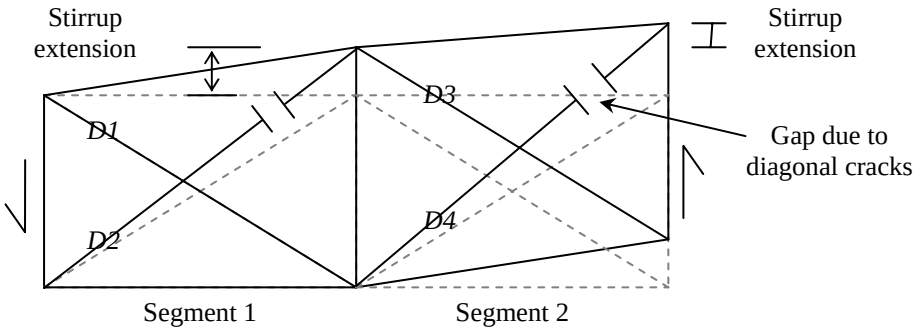

Figure 3-2. Shear deformation from extension of transverse reinforcement

A method of calculating shear deformation from stirrup extension for beams with equal top and bottom reinforcement and with no axial force was proposed by Fenwick and Thom (1982). This method was developed based on equilibrium and compatibility requirements and is summarised here. In this approach, the stirrup extension is postulated to be a function of plastic hinge rotation.

After diagonal cracks develop in a plastic hinge, a rotation, θ, between point *B* to point *A* about point *A* induces an upward movement at point *B* as illustrated in Figure 3-3(b). This upward movement at point *B* causes extension in the shear reinforcement on line *BC*. Fenwick and Thom (1982) expressed this extension by Equation 3-2, where S_S is the shear deformation due to stirrup extension and L_P is the horizontal projection of the diagonal strut, given by Equation 2-9.

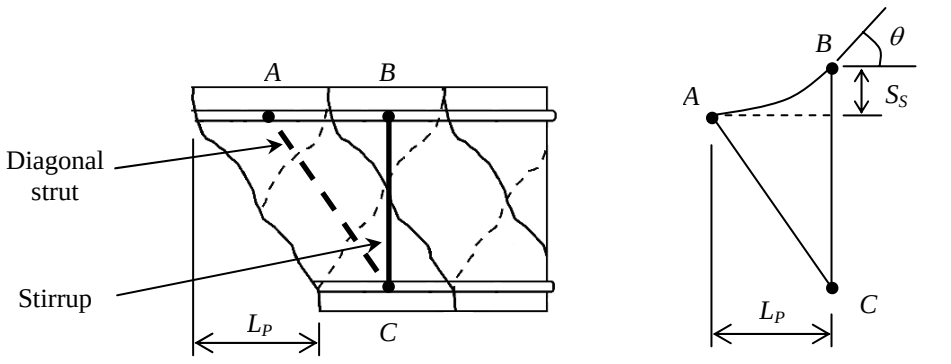

(a) Original shape (b) Deformed shape

Figure 3-3. Extension of stirrup due to rotation of the plastic hinge

$$S_S = \frac{L_P \theta}{2} \tag{3-2}$$

3.1.2.1 Inelastic Stirrup Extension

For a stirrup to yield, its extension must exceed the elastic extension of stirrup as shown in Equation 3-3, where f_{vy} is the yield stress of stirrup, l_s is the effective length of the stirrup leg taken between the outer edges and E_s is the Young's modulus of steel.

$$S_S \geq \frac{f_{vy} l_s}{E_s} \tag{3-3}$$

Combining Equations 3-2 and 3-3, the critical rotation, θ_{crit}, that leads to inelastic extension of stirrup can be expressed as

$$\theta_{crit} = \frac{f_{vy} l_s}{E_s} \frac{2}{L_P} \tag{3-4}$$

Assuming that the curvature is constant over the diagonal strut length, the corresponding curvature, ψ_{crit}, can be expressed as

$$\psi_{crit} = \frac{f_{vy} l_s}{E_s} \frac{2}{L_P{}^2} \tag{3-5}$$

When the beam undergoes inelastic cyclic actions, high strains may be induced in the flexural and shear reinforcement. Therefore, it is important to assess the stress level at which the stirrup undergoes inelastic extension. For simplicity, it was assumed that the transverse and flexural reinforcement strain-harden at the same rate. Hence, if the moment to shear ratio and the internal lever arm of the beam section remains constant, the strain hardened stress of the stirrup, f_{vy}', can be given by Equation 3-6, where V_{max} is the maximum shear which has been sustained in the beam and V_{yc} is the shear force corresponding to the flexural strength of the beam specified in Chapter 2.

$$f_{vy}' = f_{vy}\frac{V_{max}}{V_{yc}} \tag{3-6}$$

Therefore, the critical curvature which will lead to additional inelastic extensions of stirrup can be calculated combining Equations 3-5 and 3-6 and is expressed in Equation 3-7.

$$\psi_{crit} = \frac{f_{vy}' l_s}{E_s}\frac{2}{L_P{}^2} = \frac{f_{vy} l_s}{E_s}\frac{2}{L_P{}^2}\frac{V_{max}}{V_{yc}} \tag{3-7}$$

From experimental measurements, Fenwick and Thom (1982) observed that the curvature distribution decreases approximately linearly from the column face to the end of plastic hinge region as shown in Figure 3-4(b). Therefore, the maximum curvature, ψ_{max}, that causes the stirrup to extend can be calculated using Equation 3-8, where θ_T is the total rotation in the plastic hinge from when the shear force changed sign to the peak applied displacement (see Figure 3-4(a)) and L_H is the length of the plastic hinge region. This length is taken as the length over which the reinforcement yields, L_{yield}, and is described in detailed in Section 2.2.1.2.

$$\psi_{max} = \frac{2\theta_T}{L_H} \tag{3-8}$$

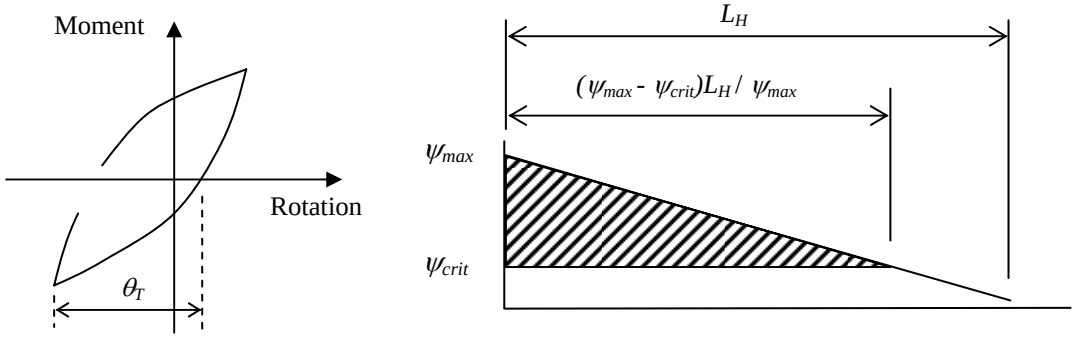

(a) Beam rotation (b) Curvature distribution in the beam plastic hinge

Figure 3-4. Schematic diagram showing beam rotation and its corresponding curvature distribution

In Figure 3-4(b), the curvatures which lie below ψ_{crit} generate elastic stirrup extension; whereas the curvatures in excess of ψ_{crit} induce inelastic and permanent stirrup extension. Therefore, the shaded area in Figure 3-4(b) represents the rotation that causes inelastic extension of the stirrup, θ_{in}, and is equal to

$$\theta_{in} = \frac{(\psi_{max} - \psi_{crit})}{2} \frac{(\psi_{max} - \psi_{crit})}{\psi_{max}} L_H \tag{3-9}$$

Equation 3-9 can be substituted into Equation 3-2 to calculate the inelastic permanent extension of the stirrups as shown in Equation 3-10. It should be noted that the inelastic extension of the stirrup accumulates each time the critical curvature is exceeded.

$$S_{S\_inelastic} = \frac{L_P}{2} \frac{(\psi_{max} - \psi_{crit})^2}{2\psi_{max}} L_H \tag{3-10}$$

As there may be several sets of diagonal trusses in the plastic hinge region, as shown in Figure 3-5, the inelastic shear deformation may be found from any one of these trusses.

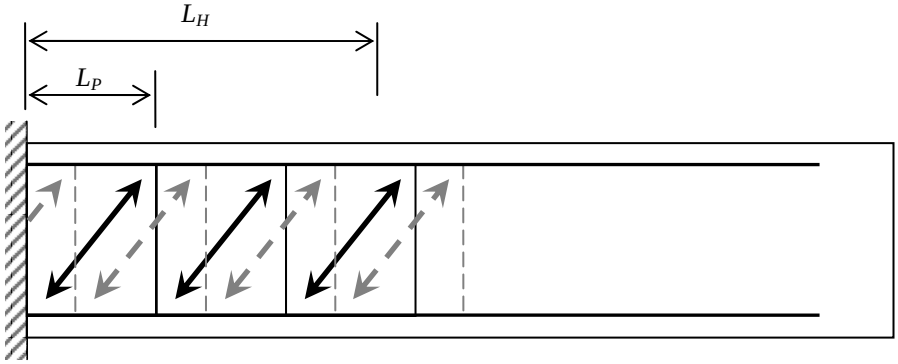

Figure 3-5. Schematic diagram showing diagonal trusses in the beam

3.1.2.2 Elastic Stirrup Extension

The sum of elastic extension of stirrups over the plastic hinge region, L_H, can be expressed by

$$S_{S\_elastic} = \frac{f_{vy} l_s}{E_s} \frac{L_H}{L_P} \quad (3\text{-}11)$$

3.1.3 Total Shear Deformation

An equation for calculating the total shear deformation in the plastic hinges, S_T, from different mechanisms as described above, is given by Equation 3-12. In this equation, S_E is the shear deformation from elongation as expressed in Equation 3-1 and $S_{S\_inelastic}$ and $S_{S\_elastic}$ are the shear deformation from inelastic and elastic stirrup extensions described by Equations 3-10 and 3-11.

$$S_T = S_E + S_{S\_inelastic} + S_{S\_elastic} \quad (3\text{-}12)$$

3.1.4 Comparison of Analytical Predictions and Experimental Results

Figure 3-6 shows the comparison between the total shear deformation predicted using Equation 3-12 and the total shear deformation measured in the beams obtained from literature (Fenwick et al. 1981; Issa 1997). The comparison shows that the method proposed by Fenwick and Thom predicts shear deformation of beams satisfactorily (within ±20%).

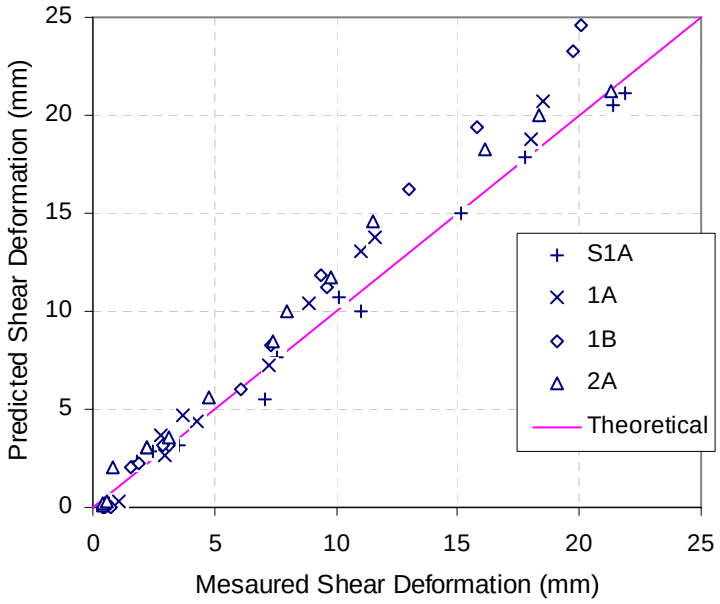

Figure 3-6. Analytical and experimental shear deformation comparisons for beams with no axial load

Despite the method proposed by Fenwick and Thom showing good shear deformation predictions for beams with no axial force, it was found that this method did not give accurate predictions for beams with different levels of axial force. More research is required to improve the proposed approach so that it can be applied to beams with different levels of axial force. The development, refinement, and validation of such a model for shear deformation is beyond the scope of this project, and therefore a simple analytical method is desired.

3.1.5 Contribution of Shear Deformation from Different Mechanisms

Shear deformation calculated from the measured elongation in the ductile beam tests, which were examined in Chapter 2, and the associated measured shear deformation, before strength degradation occurred, is plotted in Figure 3-7. Here, a negative force implies axial compression. A line with a slope of 1 to 2 is also plotted in these figures. It can be seen that the points lie close to this line, with the exception of beam M2. This indicates that shear deformation from elongation contributes approximately half of the total shear deformation before strength degradation occurs. It should be noted that in beam M2, the measured elongation is smaller than the average elongation measured for beams with no axial force.

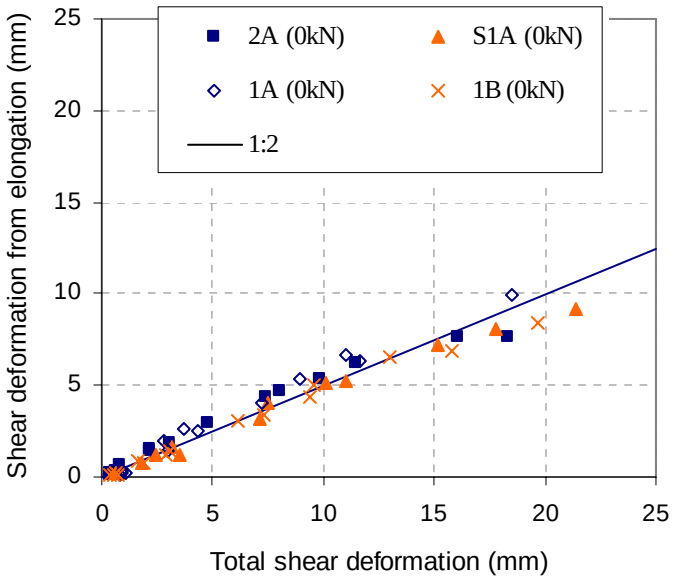

(a) Beams with no axial force

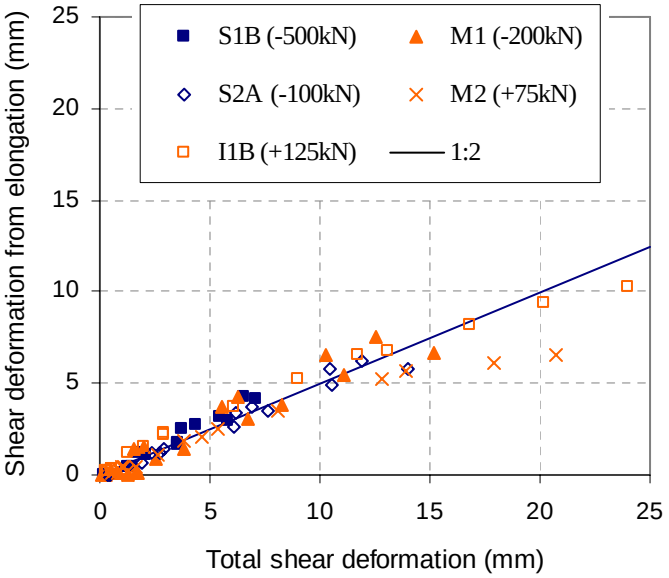

(b) Beams with different levels of axial force

Figure 3-7. Shear deformation relationship for ductile beams

3.2 MODIFIED PLASTIC HINGE ELEMENT

An approximate method was proposed in which shear flexibility factor was incorporated into the plastic hinge element. The shear flexibility factor can be visualised as an additional shear spring with zero length connected in series with the plastic hinge element as shown in Figure 3-8. The shear flexibility factor induces

additional shear deformation in the plastic hinge element based on the calculated magnitude of the shear deformation arising from elongation.

It was shown in Section 3.1.5 that the total shear deformation measured in beam test was approximately twice the calculated shear deformation due to beam elongation. Therefore, provided that elongation can be captured accurately in the analytical plastic hinge element, the predicted shear deformation can be taken as twice the value predicted from elongation. As a result, the shear flexibility factor in the plastic hinge element is set to 2.0 so that the shear deformation is doubled to account for shear deformation from other mechanisms.

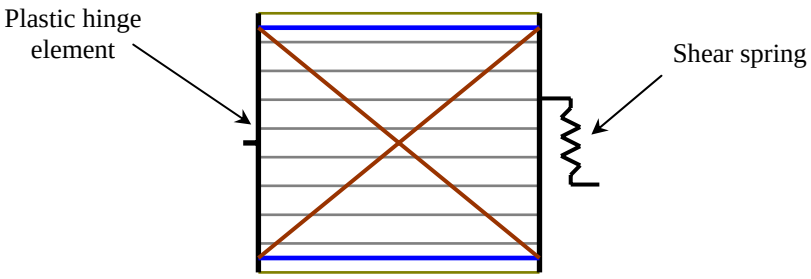

Figure 3-8. Plastic hinge element with additional shear spring

3.2.1 Analytical and Experimental Comparisons for Beams with No Axial Load

Analysis with improved shear deformation modelling was carried out for beams with no axial force. The analytical force-displacement and moment-rotation relationships for these beams are compared with the experimental results in Figures 3-9 to 3-12. It can be seen that the modified plastic hinge element predicts the force-displacement and moment-rotation response accurately with the exception of beam 1A. In beam 1A, rotation is over-estimated in the analysis in the last half cycle. This difference could be due to buckling of bars causing errors in the rotation measurement Pinching predicted in the force-displacement response with improved shear modelling is much closer to the experimental results than those observed in Chapter 2. As a result, rotation is predicted more accurately prior to strength degradation.

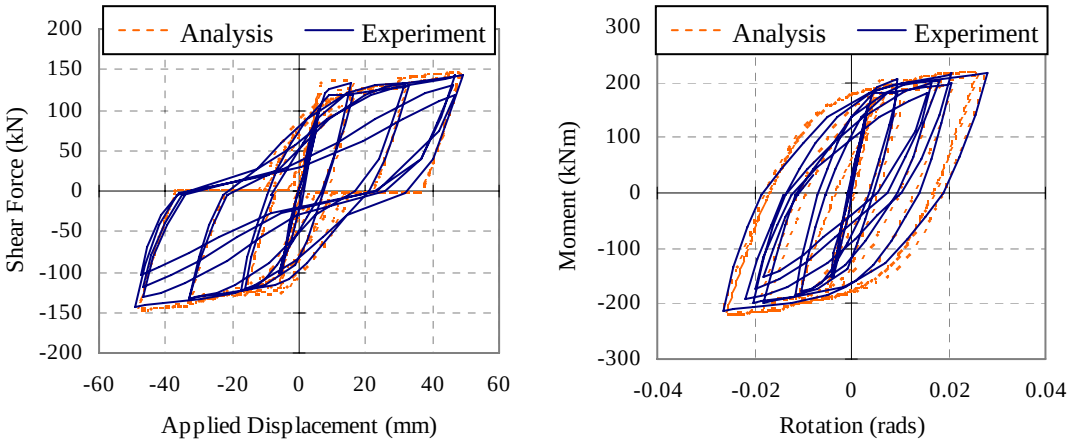

(a) Force-displacement relationship (b) Moment-rotation relationship

Figure 3-9. Analytical and experimental comparisons for Beam 2A

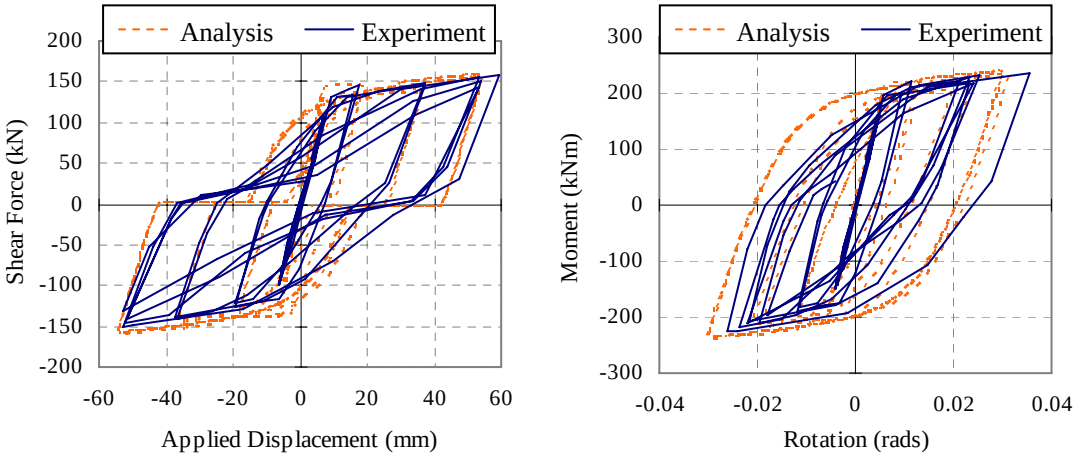

(a) Force-displacement relationship (b) Moment-rotation relationship

Figure 3-10. Analytical and experimental comparisons for Beam S1A

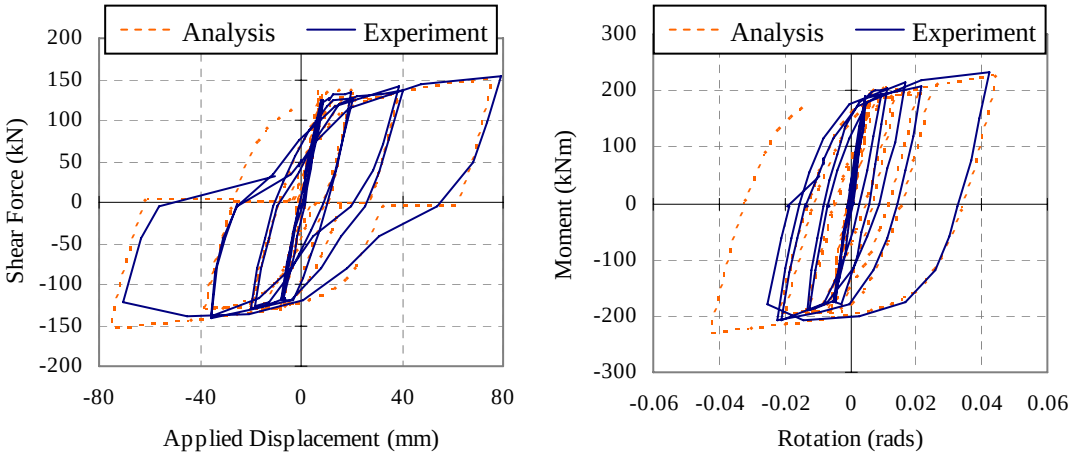

(a) Force-displacement relationship (b) Moment-rotation relationship

Figure 3-11. Analytical and experimental comparisons for Beam 1A

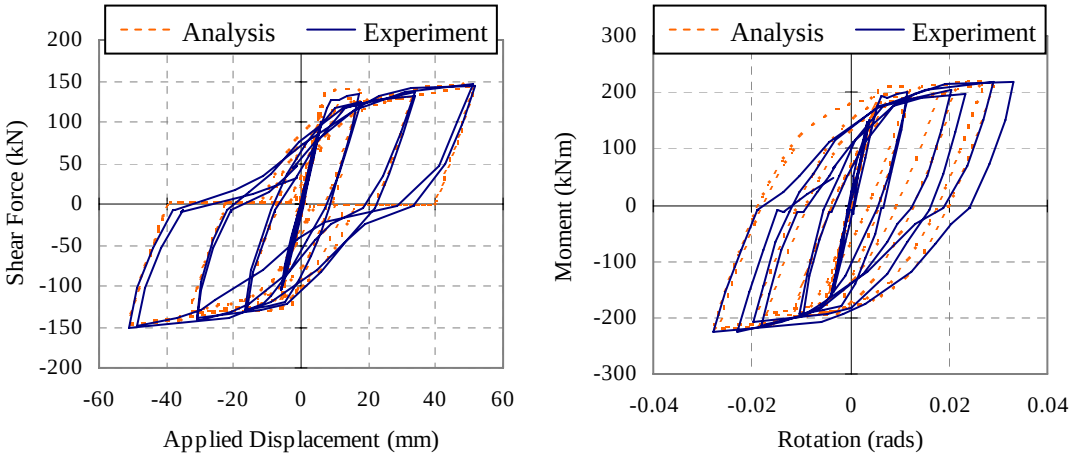

(a) Force-displacement relationship (b) Moment-rotation relationship

Figure 3-12. Analytical and experimental comparisons for Beam 1B

3.2.1.1 Elongation Summary

The comparison of analytical and measured elongation for beams with no axial force in Figure 3-13 shows that the predicted elongation matches well with the experimental results. Elongation is generally under-estimated at large displacement ductility cycles. This is due to rotation being over-predicted in the analysis as mentioned earlier in Section 2.7.1.6. It should be noted that elongation predicted with the original model, as shown in Section 2.7.1.6, also matches well with the experimental results. Therefore, improving shear deformation modelling does not make a significant difference on the elongation prediction.

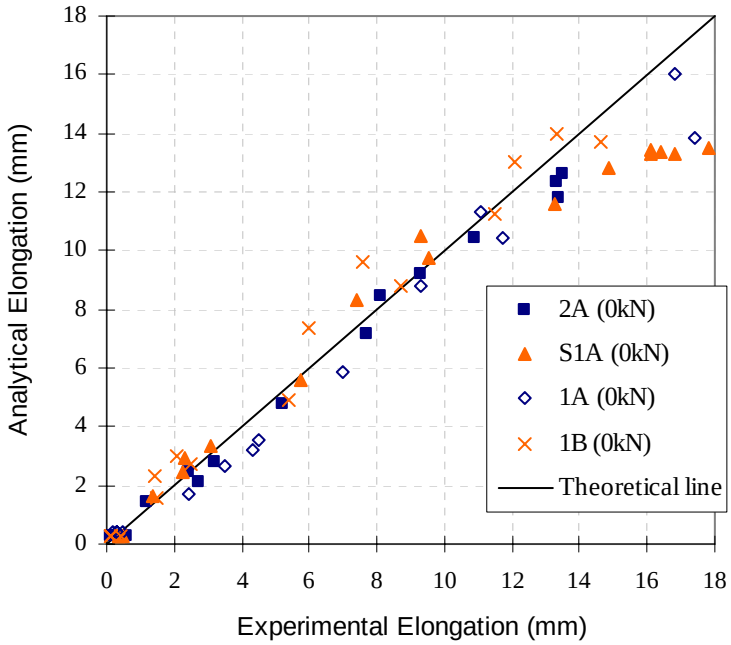

Figure 3-13. Elongation comparisons for beam with no axial force

3.2.2 Analytical and Experimental Comparisons for Beams with Different Levels of Axial Force

Analyses with improved shear deformation modelling were carried out for beams with different levels of axial force. Comparisons of the analytical and experimental force-displacement and moment-rotation relationships are shown in Figures 3-14 to 3-18. The comparisons show that the modified plastic hinge element predicts the force-displacement and moment-rotation response accurately with the exception of beams M1 and I1B, where the rotation is over-estimated and the moment is under-estimated in the analysis. It should be noted that the peak moment measured in the experiment is much higher than the theoretical strength.

Pinching in the force-displacement response is predicted more accurately with the modified plastic hinge element than that in the original model. As a result, rotation is predicted more accurately prior to strength degradation.

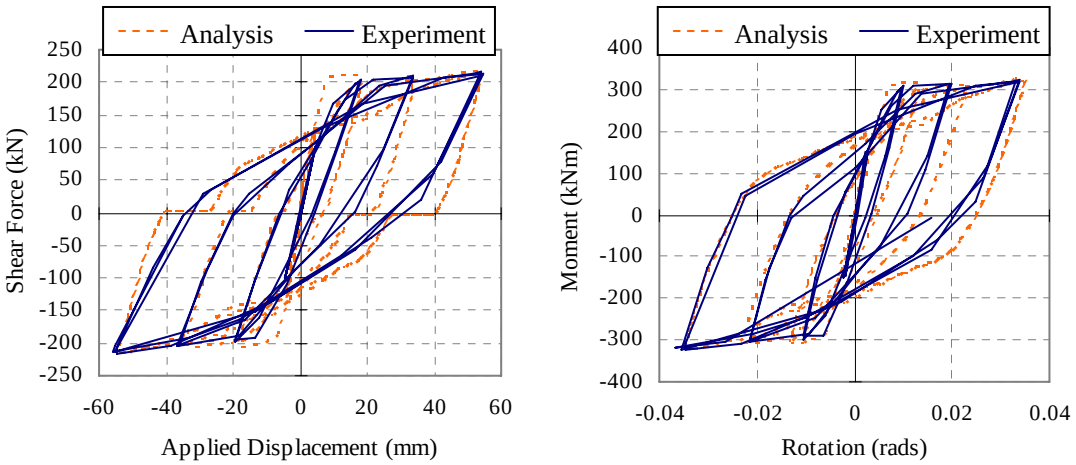

(a) Force-displacement relationship (b) Moment-rotation relationship

Figure 3-14. Analytical and experimental comparisons for Beam S1B with -500kN axial force

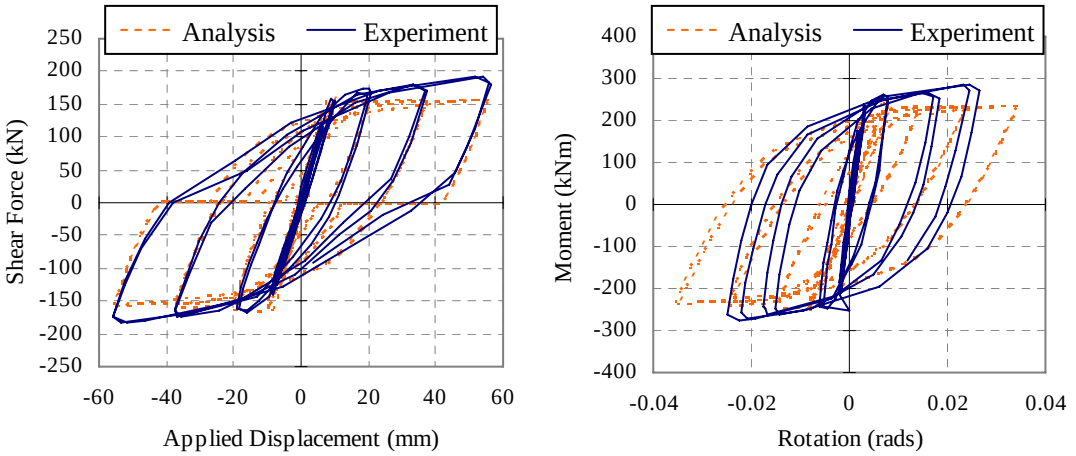

(a) Force-displacement relationship (b) Moment-rotation relationship

Figure 3-15. Analytical and experimental comparisons for Beam M1 with -200kN axial force

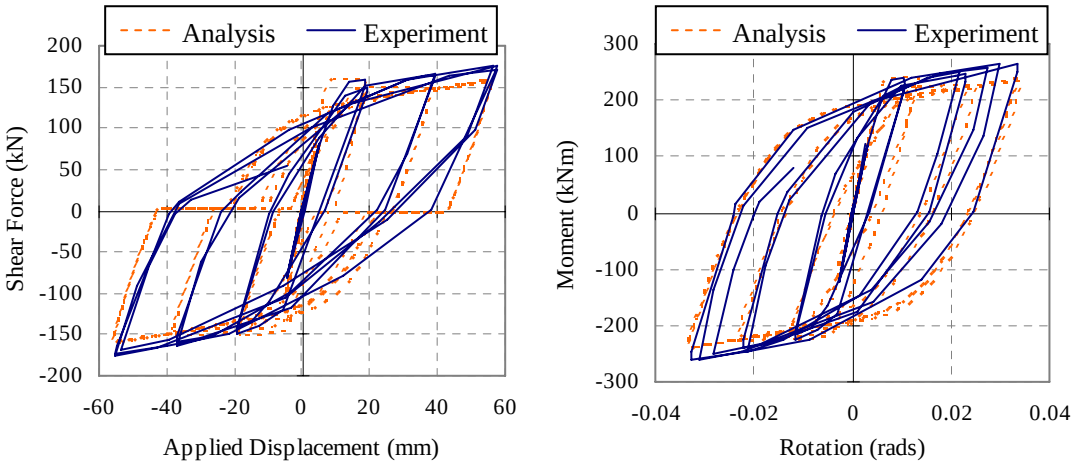

(a) Force-displacement relationship (b) Moment-rotation relationship

Figure 3-16. Analytical and experimental comparisons for Beam S2A with -100kN axial force

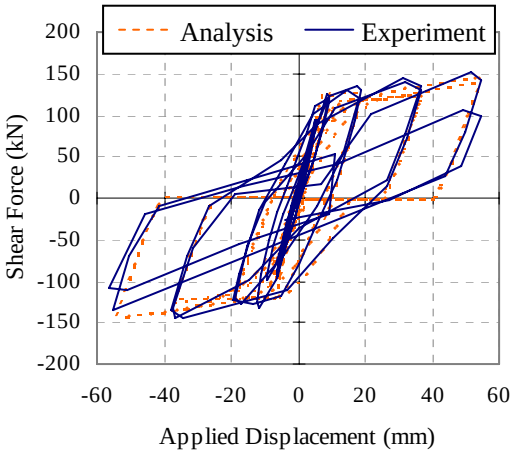

(a) Force-displacement relationship

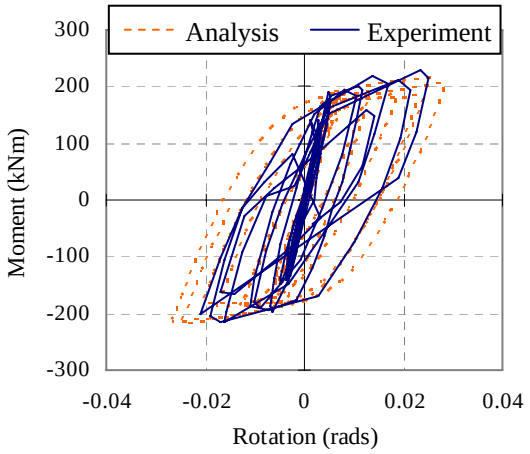

(b) Moment-rotation relationship

Figure 3-17. Analytical and experimental comparisons for Beam M2 with 75kN axial force

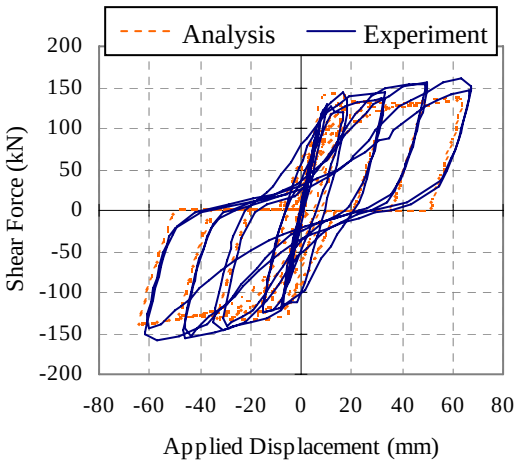

(a) Force-displacement relationship

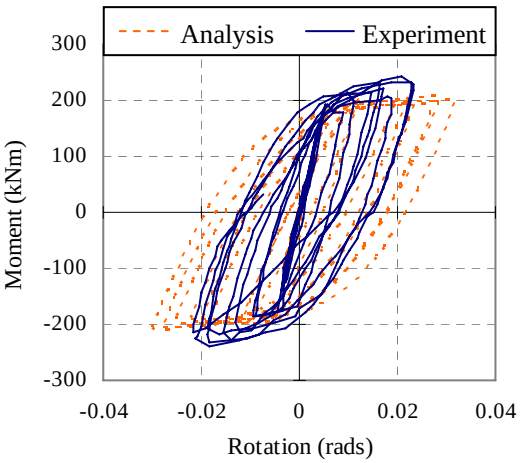

(b) Moment-rotation relationship

Figure 3-18. Analytical and experimental comparisons for Beam I1B with 125kN axial force

3.2.2.1 Elongation Summary

Comparison of the analytical and experimental elongation for beams with different levels of axial force in Figure 3-19 shows that the predicted elongation matches satisfactorily with the experimental results with the exception of beam M2. It should be noted that the elongation measured in beam M2, which sustained an axial tension force, is smaller than the average elongation measured for beams with no axial force, which defies the general trend. The predicted elongation in beams with applied axial tension force is over-estimated in the large displacement cycles. This is due to shear

deformation and bar buckling not being captured accurately in the analysis as indicated in Sections 2.7.3.4 and 2.7.3.5.

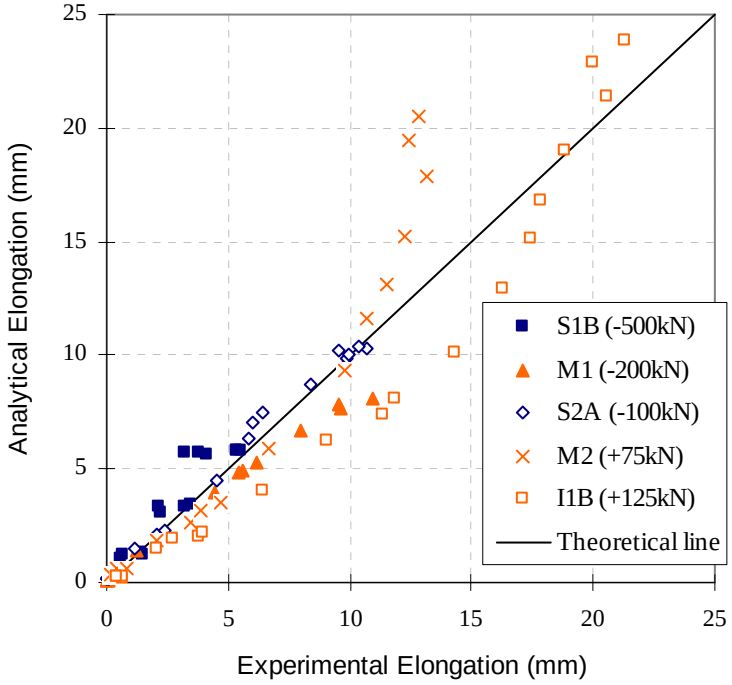

Figure 3-19. Elongation comparisons for beam with different level of axial force

3.3 CONCLUSIONS

The method of Fenwick and Thom (1982), proposed to quantify shear deformation from elongation and extension of stirrups, was examined against various experimental results. It was shown that the method provides good shear deformation prediction for beams with no axial force. However, refinement is required for beams with different levels of axial force.

Investigation on cantilever beam tests obtained from literature has shown that the total shear deformation in beams before strength degradation occurs is approximately twice the shear deformation arising from elongation of plastic hinges. Based on this relationship, a shear flexibility factor, which can be visualised as an additional shear spring connected in series with the plastic hinge element, was incorporated into the plastic hinge element to improve the shear deformation prediction. The shear

flexibility factor was set as 2.0 so that the total predicted shear deformation is twice the shear deformation arising from elongation of plastic hinges.

Comparisons of the analytical predictions with the experimental results have shown that pinching in the force-displacement relationship and plastic hinge rotation can be predicted more accurately using the improved plastic hinge element. It was also found that elongation is not significantly affected when the shear deformation of the plastic hinge is increased. The improved plastic hinge element can hence be used to investigate the effect of elongation on the seismic performance of reinforced concrete frame structures.

3.4 REFERENCES

Booth, E. (1994). *Concrete Structure in Earthquake Regions*, Addison Wesley Longman.

Carr, A. J. (2008). "RUAUMOKO2D - Inelastic dynamic analysis." Department of Civil Engineering, University of Canterbury, Christchurch, New Zealand.

Fenwick, R., and Fong, A. (1979). "The behaviour of reinforced concrete beams under cyclic loading." *Report No. 176*, University of Auckland, Auckland, New Zealand.

Fenwick, R. C., Tankut, A. T., and Thom, C. W. (1981). "The deformation of reinforced concrete beams subjected to inelastic cyclic loading: experimental results." *School of Engineering Report No. 268*, University of Auckland, Auckland, New Zealand.

Fenwick, R. C., and Thom, C. W. (1982). "Shear deformation in reinforced concrete beams subjected to inelastic cyclic loading." *School of Engineering Report No. 279*, University of Auckland, Auckland, New Zealand.

Issa, M. S. (1997). "The deformations of reinforced concrete beams containing plastic hinges in the presence of axial compression or tension load," Master Thesis, University of Auckland, Auckland, New Zealand.

Matti, N. A. (1998). "Effect of axial loads on the behaviour of reversing plastic hinges in reinforced concrete beams," Master Thesis, University of Auckland, Auckland, New Zealand.

McBride, A., Fenwick, R. C., and Davidson, B. J. (1996). "The influence of slabs on the lateral cyclic behaviour of ductile concrete frames." *Report No. 566*, Department of Civil and Resource Engineering, University of Auckland, Auckland, New Zealand.

Wuu, P. J. Y. (1996). "Deformations in plastic hinge zone of RC beam in ductile frame structures subjected to inelastic cyclic loading," Master Thesis, University of Auckland, Auckland, New Zealand.

4 ANALYSES OF 2D FRAMES

In Chapters 2 and 3, a reinforced concrete (RC) plastic hinge element was developed and validated with cantilever beam tests obtained from literature. In this chapter, the developed plastic hinge element is implemented into different analytical models to predict the cyclic response of: (i) a beam-column joint sub-assembly; (ii) a two-bay and a three-bay one-storey frame; and (iii) a three-bay two-and-a-half storey frame, reported in the literature. Modelling of these sub-assembly tests and comparisons between the predicted and experimental results are described. These comparisons are useful in identifying the applicability of the plastic hinge element in assessing the seismic performance of RC frame buildings. The analytical and experimental results are used to highlight the effect of elongation on the cyclic response of RC frames.

4.1 INTERIOR BEAM-COLUMN JOINT SUB-ASSEMBLY

4.1.1 Experimental Program

An interior beam-column joint sub-assembly was tested by Fenwick and Nguyen (1981). The experimental arrangement and section details are shown in Figures 4-1 and 4-2 where the letters R and D stand for Grade 300 round and deformed bars and the number following the letters represents the diameter of the reinforcing bars.

Additional 12mm bars were welded to each longitudinal beam bars within the beam-column joint to prevent yield penetration into the joint. These additional bars were extended 170mm out from the column face. The column was designed to remain elastic. An axial load of 125kN was applied at the bottom of the column by a hydraulic jack as shown in Figure 4-1. The oil pressure in the jack was adjusted at regular intervals to maintain the axial load in the column close to the required level. However, the axial force did fluctuate between 118kN and 131kN during the test.

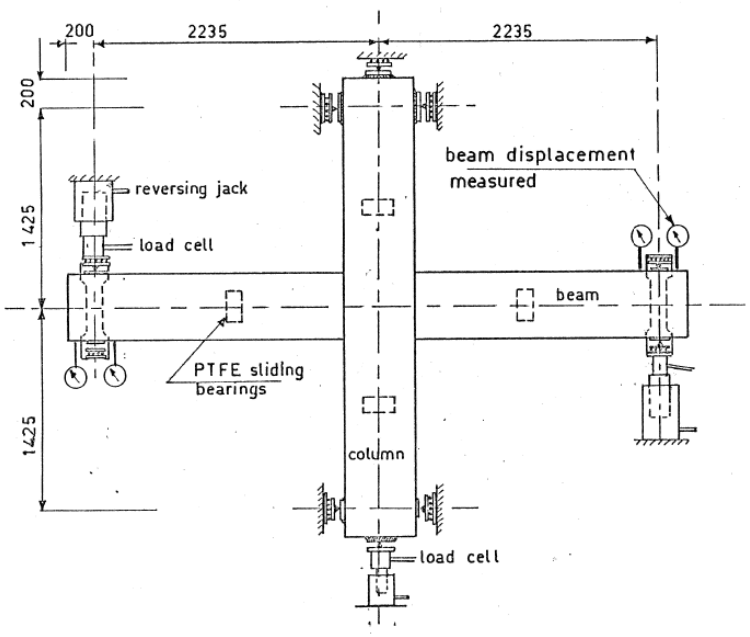

Figure 4-1. Beam-column joint test arrangement (units in mm) (Fenwick and Nguyen 1981)

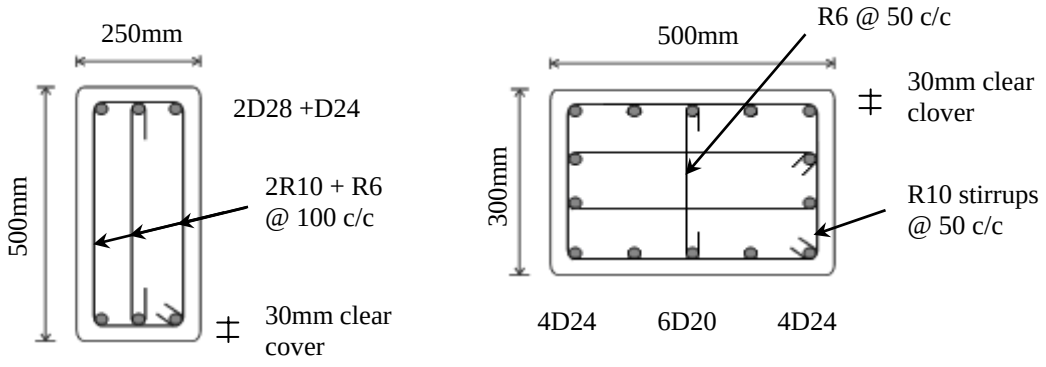

(a) Beam section (b) Column section

Figure 4-2. Member details in the beam-column joint sub-assembly

The loading history applied in the test is shown in Figure 4-3. The loading history started with two elastic cycles where the loading was force controlled. A maximum force corresponding to 75% of the calculated theoretical nominal flexural strength of beam was applied in each direction. From these elastic cycles, the force-displacement curve was plotted and a straight line extrapolation was made to assess the displacement corresponding to the theoretical nominal flexural strength. This displacement was taken as the displacement ductility of 1, *D1*.

The loading history after these elastic cycles was displacement controlled; the displacement was applied at the ends of the beams through two hydraulic actuators, as

illustrated in Figure 4-1. Two cycles at displacement ductility of two, *D2*, followed by two cycles at displacement ductility of four, *D4*, and four cycles at displacement ductility of six, *D6*, were applied.

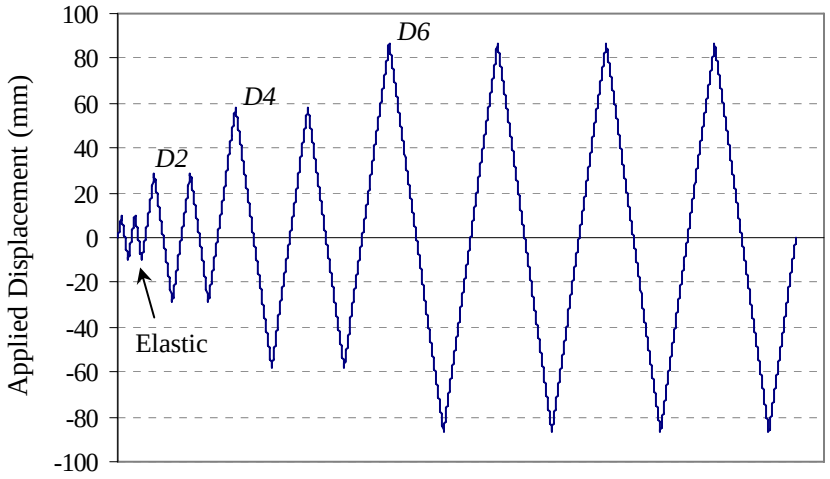

Figure 4-3. Applied displacement history in the beam-column joint test

The measured material properties of the beam-column joint sub-assembly are summarised in Table 4-1, where f_{vy} is the yield stress of the shear reinforcement, f_y and f_u are the yield and ultimate stress of the longitudinal bars, respectively, and f_c' is the concrete compressive strength. It should be noted that the yield stress of shear reinforcement was not provided in the report and hence, the value was assumed here.

Table 4-1. Stirrup arrangement and measured material properties in the beam-column joint sub-assembly

Member	**Stirrups arrangement**	f_{vy} **(MPa)**	f_y **(MPa)**	f_u **(MPa)**	f_c' **(MPa)**
Beam	2R10 + R6 @ 100 c/c	300[(1)] 350[(2)]	279	450	36.2

Table 4-2 summarises the calculated material properties where f_t and E_c are the tensile stress and Young's modulus of concrete calculated based on the New Zealand Concrete Structures Standard, NZS 3101:2006 (Standards New Zealand 2006), $f_{c\,(D)}'$ is the effective compressive stress of the diagonal strut taken as $0.34f_c'$ (as recommended by To et al. (2001)), M_{yc} is the theoretical flexural strength of the beam specified in Section 2.2.1.1, L is the span length of the beam, V_{yc} is the shear force corresponding to M_{yc} and ε_y, ε_{sh} and ε_u are the yield, strain hardening and ultimate strain respectively.

Table 4-2. Calculated material and section properties for the beam-column joint sub-assembly

Member	f_t **(MPa)**	E_c **(GPa)**	$f'_{c\,(D)}$ **(MPa)**	M_{yc} **(kNm)**	L **(mm)**	V_{yc} **(kN)**	ε_{sh} / ε_y	ε_u / ε_y
Beam	2.2	26.9	12.3	193	1815	106	15	69

4.1.2 Analytical Model

The analytical model of the interior beam-column joint sub-assembly was setup in RUAUMOKO2D (Carr 2008a) as shown in Figure 4-4. It can be seen that the top and bottom of the columns are free to rotate, but are fixed against all translational movement. The beam was divided into two parts, namely the elastic and the plastic hinge regions. The elastic region was modelled using an elastic beam element and the plastic hinge region was modelled using the modified plastic hinge element described in Chapter 3. The column and beam-column joint were modelled using elastic elements.

Shear deformation in the elastic members was included in the analysis, although it was not expected that this would affect the analytical results significantly. The shear modulus of these members was calculated based on NZS 3101:2006 and the shear area was taken as bd, where b is the width of the section and d is the effective depth. The effective moment of inertia of the elastic beam and column was taken as $0.4I_g$ recommended in NZS 3101:2006 where I_g is the gross section moment of inertia. To account for a stiffer beam-column joint, the effective moment of inertia of the beam-column joint is taken as twice the effective moment inertia of beam and column as illustrated in Figure 4-4.

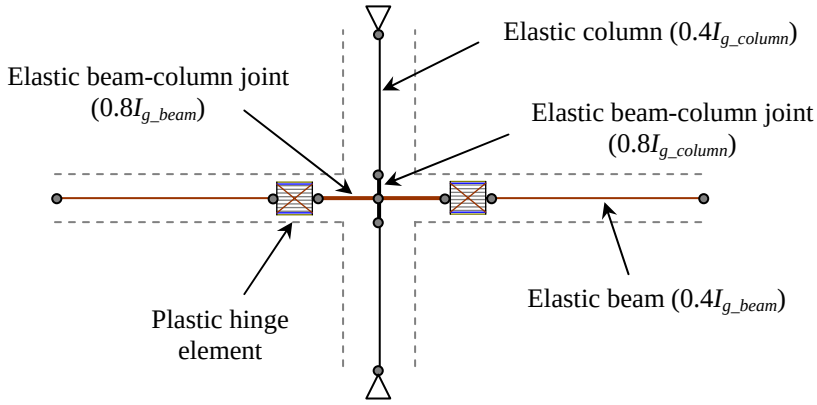

Figure 4-4. Analytical beam-column joint sub-assembly

The calculated plastic hinge parameters are summarised in Table 4-3, where: L_p is the length of the plastic hinge element specified in Section 2.2.1.1; θ is the angle of the diagonal strut to the horizontal plane; D is the effective diagonal depth specified in Section 2.2.1.3; M_{max} is the maximum moment sustained in the beam; M_{y1} is the theoretical first yield moment (this is only used to compare with M_{yc}); L_t is the length of tension shift; and L_{yield} is the steel yield length described in Section 2.2.1.1. Here the length of yield penetration into the support is zero as additional bars were welded to prevent yield penetration.

Table 4-3. Calculated plastic hinge properties for the beam-column joint sub-assembly

L_p (mm)	θ (degree)	D (mm)	M_{max} (kNm)	M_{y1} (kNm)	L_t (mm)	L_{yield} (mm)
186	65.7	170	252	192	206	631

4.1.3 Analytical and Experimental Comparisons

Figures 4-5 and 4-6 compare the analytical and experimental force-displacement and elongation responses of the sub-assembly test. It can be seen from the force-displacement comparison that the analytical results match closely with the experimental measurements. The analysis predicts the elastic stiffness, yield displacement and the ultimate force satisfactorily. The pinched hysteresis in the unloading force-displacement experimental results is also predicted accurately up to the second *D6* cycle. It should be noted that the hysteretic behaviour predicted in the analysis is a natural outcome of the generic material models, which do not require any

prior calibration with the experimental results. Strength degradation observed in the experiment at large displacement cycles is not captured in the analysis. This may due to the steel model in the plastic hinge element not considering buckling of reinforcing bars at large tensile stain levels. It may also due to shear deformation being under-estimated in the analysis at the latter cycles.

The analysis predicts the plastic hinge elongation accurately up to the first *D6* cycle. After this cycle, elongation predicted in the analysis is smaller than that in the experiment. However, it should be noted that beams with similar section properties and axial load condition examined in the earlier chapter only elongated between 14 to 18mm where as elongation in this experiment was 22mm. This indicates that elongation is highly variable in nature and the analysis still provides reasonable prediction.

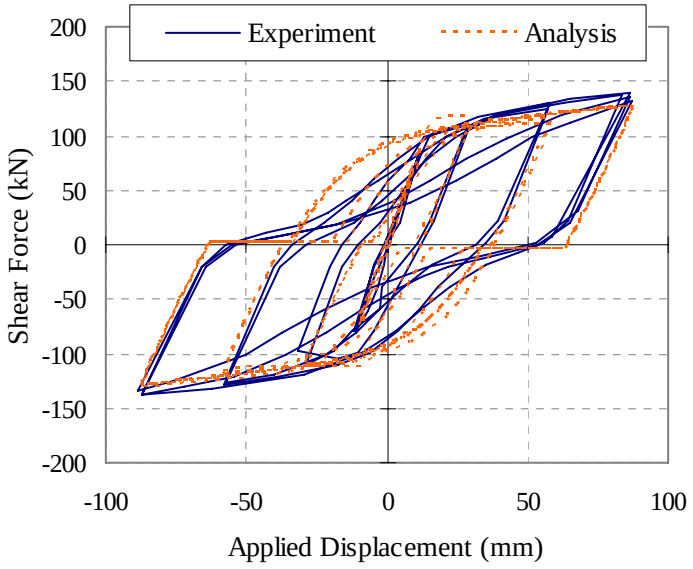

Figure 4-5. Force-displacement response of the beam-column joint sub-assembly

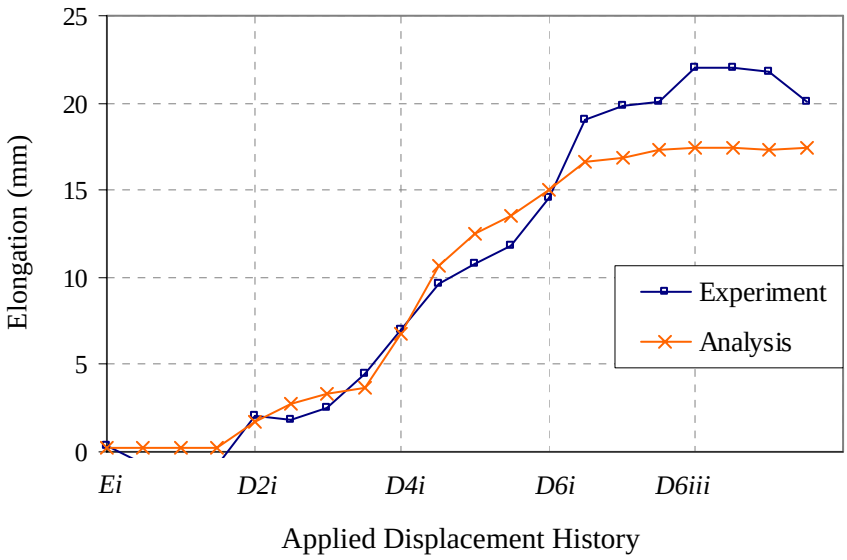

Figure 4-6. Elongation response of the beam-column joint sub-assembly

4.2 TWO-BAY ONE-STOREY MOMENT RESISTING FRAME

4.2.1 Experimental Program

The test results of a two-bay one-storey approximately one-third scale model of a RC moment resisting frame were extracted from LAU (2007). The test arrangement and the section details of the beams and columns are shown in Figures 4-7 and 4-8. The columns were designed to remain elastic throughout the test. The loading was displacement controlled; the displacements were applied at the top and bottom of each column through six hydraulic actuators as shown in Figure 4-7. The displacement histories applied in the test is summarised in Figure 4-9.

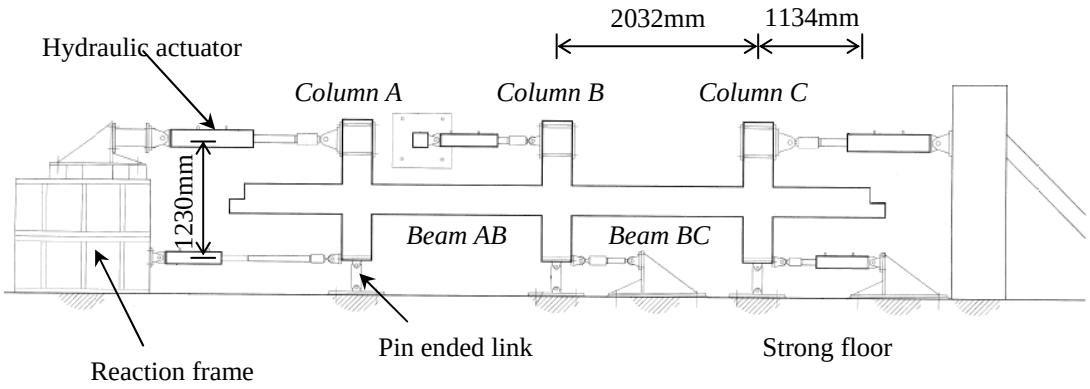

Figure 4-7. Two-bay one-storey sub-assembly test arrangement (Lau 2007)

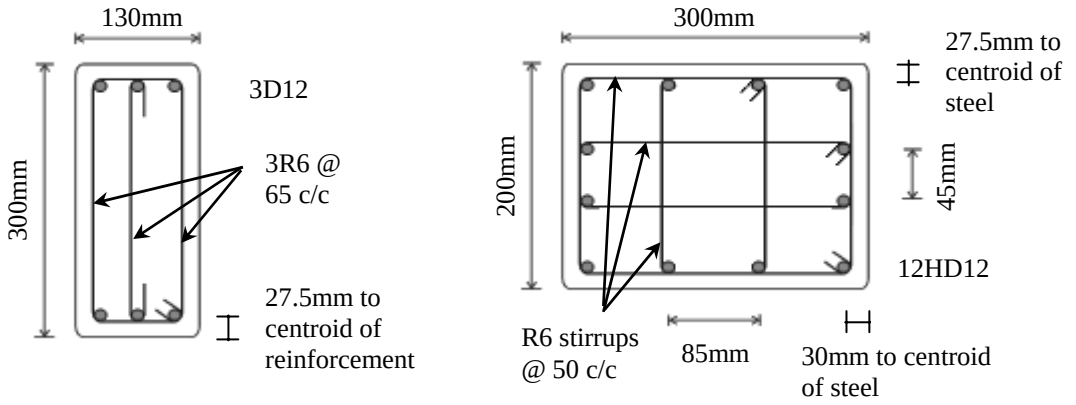

(a) Beam section (b) Column section

Figure 4-8. Member details in the two-bay one-storey frame

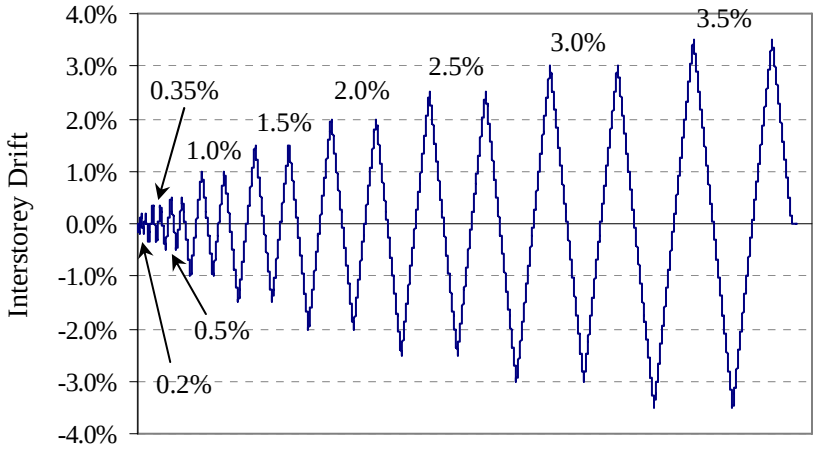

Figure 4-9. Displacement sequence applied in the two-bay one-storey frame test

Within a loading increment, the top and bottom of each column was first displaced to a target incremental displacement, *t*, prescribed in Equation 4-1 where t_A and b_A are the displacements at the top and bottom of *Column A* and t_B, b_B, t_C, and b_C are the displacements at the top and bottom of *Column B* and *Column C* respectively as shown in Figure 4-10.

$$t = t_A + b_A = t_B + b_B = t_C + b_C \tag{4-1}$$

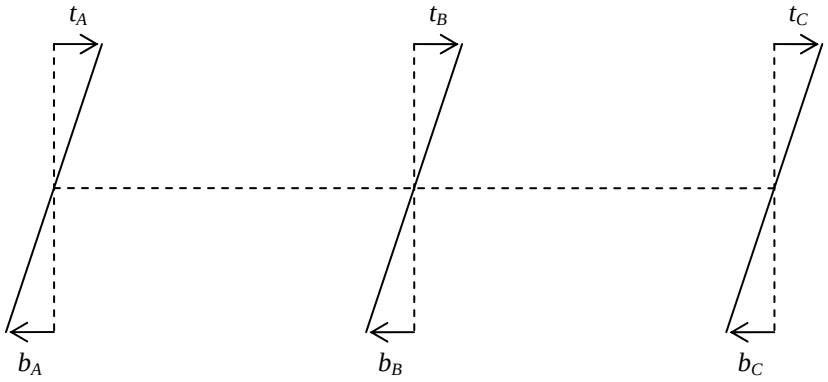

Figure 4-10. Schematic diagram showing the applied displacement in the two-bay frame

To allow for elongation of plastic hinges, the bottom actuators in the external columns were adjusted such that the distance between the bottoms of each column was equal to the elongation of the beam in the respective bay. This can be expressed in Equations 4-2 and 4-3, where E_{AB} and E_{BC} are the beam elongation in *Beam AB* and *Beam BC*.

$$b_A = b_B + E_{AB} \tag{4-2}$$

$$b_C = b_B + E_{BC} \tag{4-3}$$

To maintain the same drift in each column, the top of each column was then adjusted to match the incremental target displacement specified in Equation 4-1. This loading scheme ensures that the columns remained parallel throughout the test. However, it does not guarantee that the axial force in the beams is zero and it has no ability to change the level of axial force induced in the beams. It should be noted that a positive drift here implies a clockwise rotation.

The measured and calculated material properties of the frame are summarised in Tables 4-4 and 4-5.

Table 4-4. Stirrup arrangement and measured material properties in the two-bay frame

Member	**Stirrups arrangement**	f_{vy} **(MPa)**	f_y **(MPa)**	f_u **(MPa)**	f_c' **(MPa)**
Beam	3R6 @ 65c/c	364	315	442	26.1

Table 4-5. Calculated material and section properties for the two-bay frame

Member	f_t **(MPa)**	E_c **(GPa)**	$f_{c\,(D)}^{'}$ **(MPa)**	M_{yc} **(kNm)**	L **(mm)**	V_{yc} **(kN)**	ε_{sh} / ε_y	ε_u / ε_y
Beam	1.8	23.8	8.9	26.2	866	30.3	18	159

There were several issues encountered during the test that could affect the experimental results. These are summarised below:

1/ During first cycle at 2.5% drift, the base of *Column B* was observed to slide around 8mm in both directions due to de-lamination of the concrete mortar bed at the base of column. The test was stopped and the loads were released at the end of the first cycle. The mortar bed was replaced and the frame was re-stressed down to the strong floor. It is uncertain how the mortar was replaced and how the sub-assembly was maintained during the reconstruction. In any case, it may have been extremely difficult to ensure that the alteration would not affect the subsequent results.

2/ *Column A* was observed to rotate out of plane to the frame at displacement cycles beyond 3% drift. As a result, the measured elongation between *Columns A* and *B* had been less than the actual elongation as illustrated in Figure 4-11. Consequently, the hydraulic actuators moved *Column A* away from *Column B* less than what it should have been. Consequently, a large axial compression force was induced in *Beam AB.*

3/ The axial force measured in the beams was not zero. *Beam AB* was sustaining a large compression force (up to $0.15A_g f_c^{'}$), whereas *Beam BC* was sustaining an axial tension force (up to $0.19A_s f_y$).

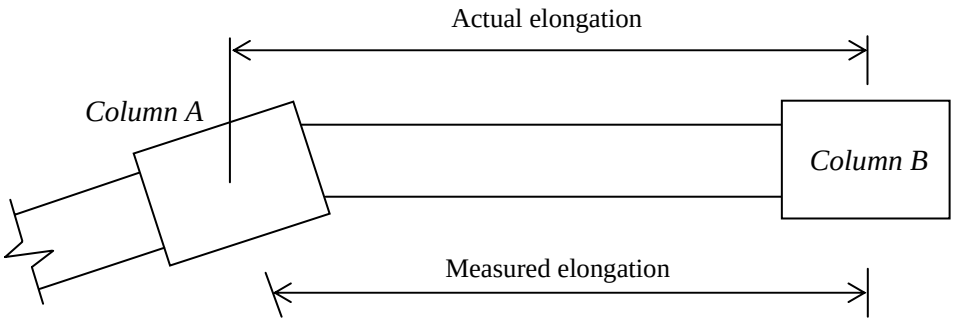

Figure 4-11. Out-of-plane rotation of *Column A* in the two-bay frame reducing elongation measurement

4.2.2 Analytical Model

The analysis was carried out in RUAUMOKO3D (Carr 2008b). The set-up of the analytical model is illustrated in Figure 4-12. The base of each of the columns was free to translate in the x-direction and rotate about z-axis. The beam was divided into two sections; (i) an elastic region, modelled using elastic beam element; and (ii) a plastic hinge region, modelled using the modified plastic hinge element described in Chapter 3. The beam-column joints and the columns were modelled using elastic elements.

Shear deformation in all of the elastic members was suppressed. The effective moment of inertia of the elastic beams and columns was taken as $0.4I_g$, as recommended in NZS 3101:2006. The effective moment of inertia of the beam-column joint was set as twice of the effective moment of inertia of the elastic beam.

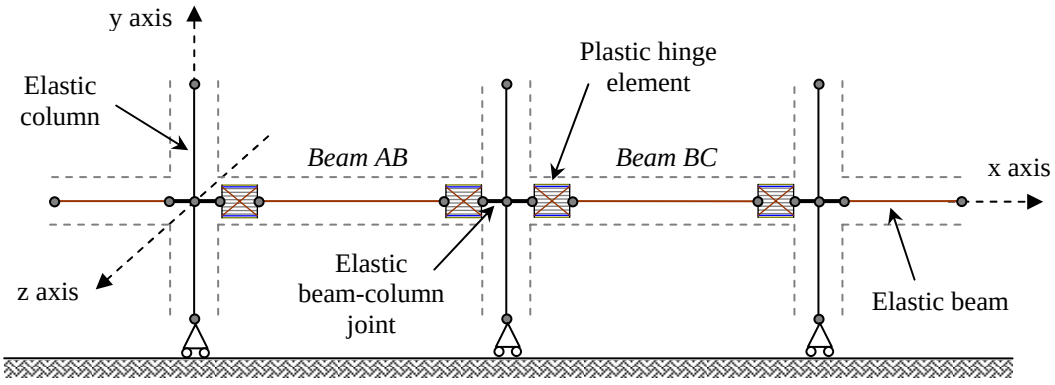

Figure 4-12. Schematic diagram of the analytical two-bay frame model

As the displacement applied in the experiment was iterative to allow elongation of the plastic hinges to develop freely, the same displacement could not be directly fed into the analysis because it would artificially generate the same elongation as in the experiment. To resolve this problem, it was assumed that the flexural and shear deformation of the columns was negligible and hence equivalent column rotation was imposed at the centre of each beam-column joint. Thus, it should be noted that despite the column drifts applied in the analysis being the same as that employed in the experiment, no axial force can be induced in the beams in the analysis.

To evaluate the shear force in each column from the predicted plastic hinge moment in the analysis, it was assumed that the column shear force is constant throughout the height. Therefore, the shear force in each column is simply the total moment accumulated at each beam-column joint divided by the inter-storey height.

The input parameters for the plastic hinge element are summarised in Table 4-6. Unlike the sub-assembly test examined previously, no reinforcing bars were welded to the longitudinal beam bars in the beam-column joint to prevent yield penetration. Therefore, the length of yield penetration into the beam-column joint, L_e, needs to be assessed. Here, L_e is taken nominally as a portion of the development length, L_{db}, as shown in Equation 4-4, where the development length is based on the provision given in NZS 3101:2006. It should be noted that this is a crude method to estimate L_e. In reality, it is difficult to determine accurately the stress distribution of the longitudinal reinforcement in the beam-column joint and future research is required.

$$L_e = L_{db}\left(1 - \frac{M_{yc}}{M_{max}}\right) \tag{4-4}$$

Table 4-6. Calculated plastic hinge properties for the two-bay frame

L_p (mm)	θ (degree)	D (mm)	M_{max} (kNm)	M_{y1} (kNm)	L_t (mm)	L_{yield} (mm)
64	75.4	62	32.9	26.2	123	374

4.2.3 Analytical and Experimental Comparisons

The analytical and experimental force-displacement relationships of the frame and each individual column are shown in Figures 4-13 and 4-14. The analysis predicts both the loading and unloading stiffness together with the yield force and the peak force accurately. However, shear pinching behaviour was under-estimated in the analysis. It is believed that this was due to strain penetration and bond slip of reinforcing bars in the beam-column joints as well as the joint shear deformation, both of which were not modelled in the analysis. It can be seen that pinching is predicted more accurately in the external columns as compared to the internal column. This is because the bars were anchored more effectively in the exterior plastic hinges and hence the amount of slip and hence pinching is less profound.

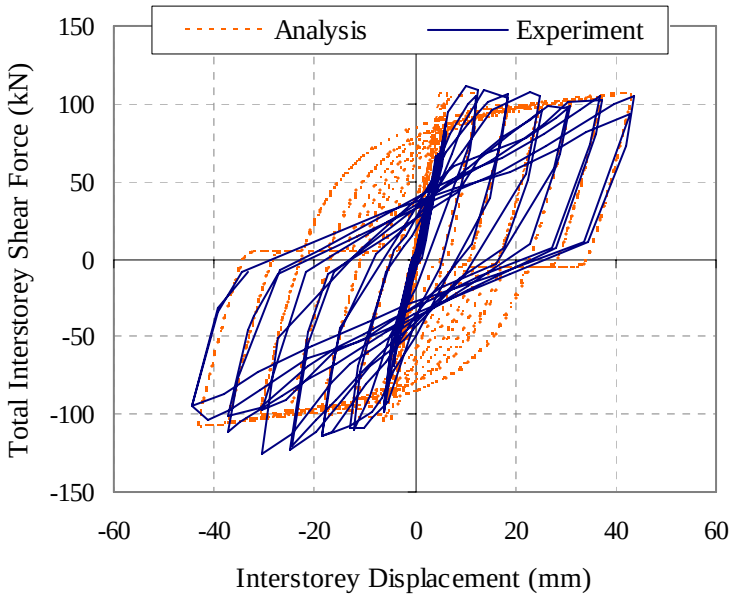

Figure 4-13. Total force-displacement response of the two-bay one-storey frame

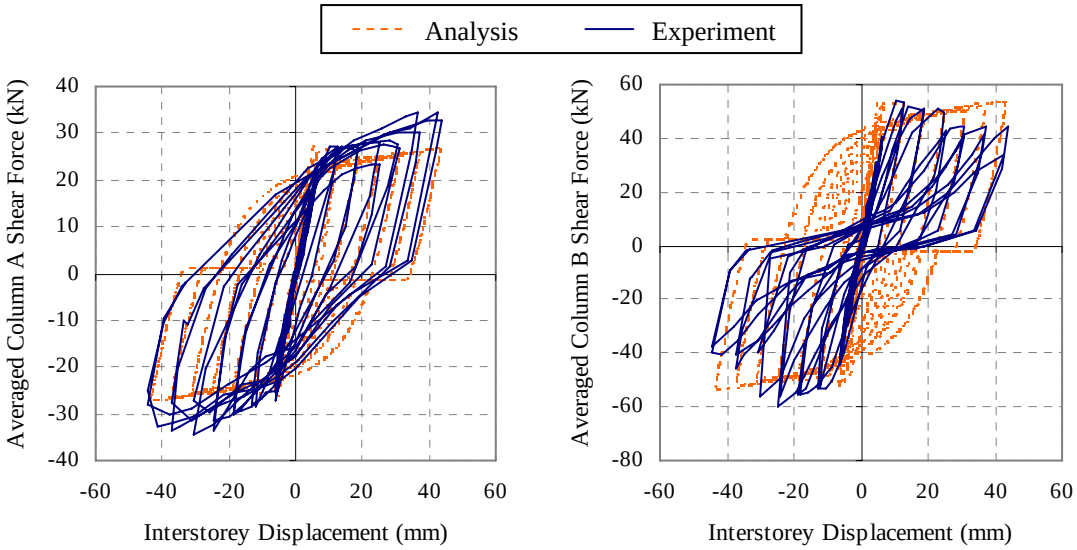

(a) *Column A* (b) *Column B*

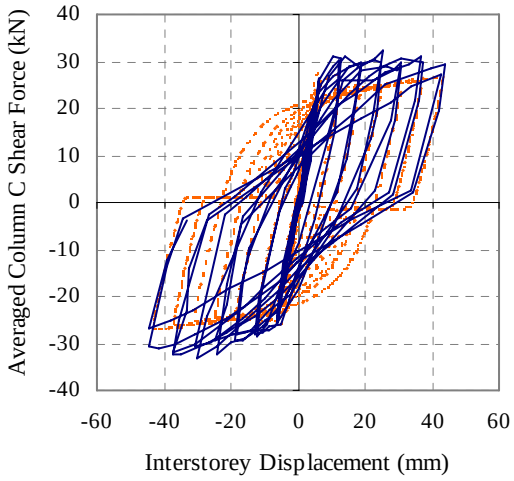

(c) *Column C*

Figure 4-14. Force-displacement relationship in each individual column in the two-bay frame

Comparison of the analytical and experimental elongation is plotted in Figure 4-15. It can be seen that the analysis predicts elongation satisfactorily. The predicted elongation is larger than the experimentally measured value in *Beam AB* after 1.5% drift. It was found the beam in the experiment was subjected to an axial compression force, whereas no axial force was induced in the analysis. Therefore, the axial compression force in the experiment led to a smaller measured elongation. The predicted elongation is smaller than the experimentally measured value in *Beam BC* after 3% drift. This is because the beam in the experiment was under some axial tension force.

The elongation measured in the cantilever beams with no axial force, examined in Section 2.7.1, was about 3.2% of the member depth. As the predicted elongation was also 3.2% of the member depth, it is believed that the model provides a reasonable elongation prediction. The discrepancies between the analytical and experimental results arise mainly due to different boundary conditions.

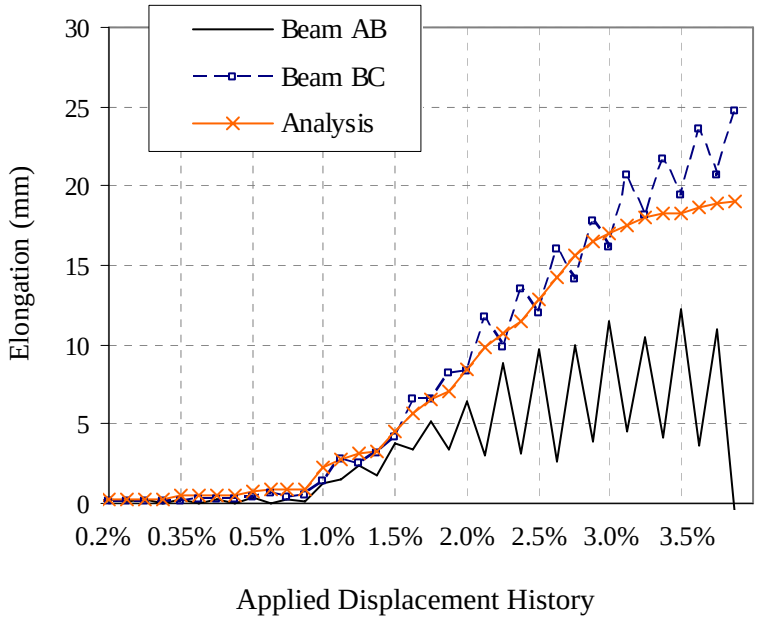

Figure 4-15. Elongation response in the two-bay frame

4.2.4 Sensitivity Analysis

A sensitivity study was carried out to examine the effect of incremental displacement step size and the beam-column joint stiffness on the analytical predictions.

4.2.4.1 Incremental step size

As reported in Section 2.4.1, the amount of pinching in the force-displacement relationship and the level of elongation are sensitive to the incremental displacement step size used in the analysis. As joint rotation was fed into the analysis instead of beam displacement, three different incremental rotation step sizes (10^{-7}, 10^{-6} and 10^{-5} radians) were examined. The force-displacement and elongation response are plotted in Figures 4-16 and 4-17. It can be seen that the solution converges when the

incremental step size reaches 1E-6 radians. This is similar to that found in Section 2.4.1.

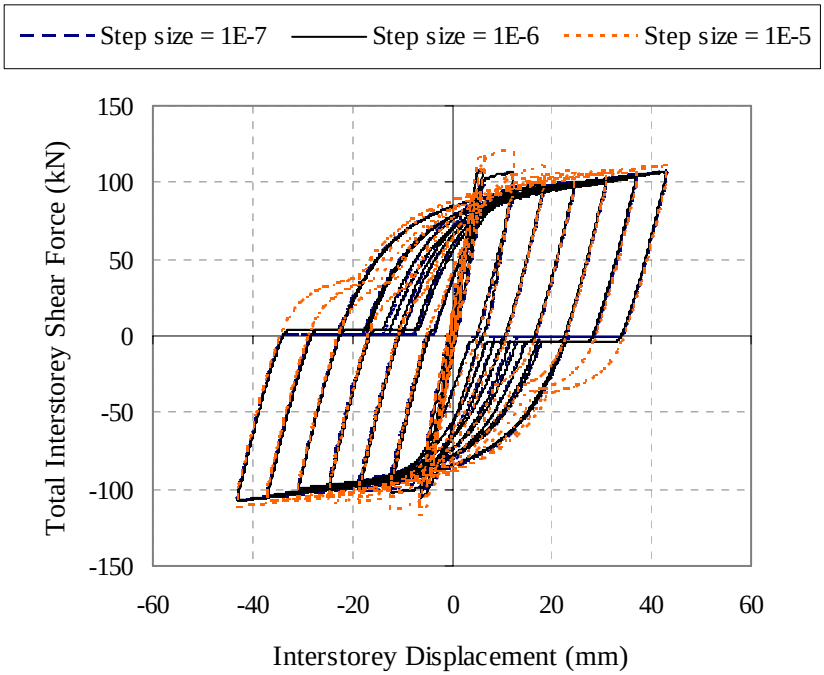

Figure 4-16. Effect of incremental step size on the predicted force-displacement response

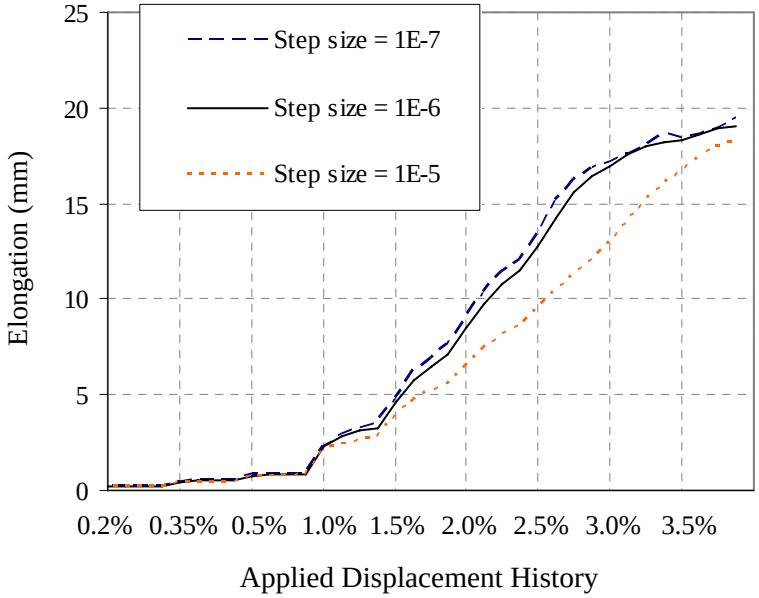

Figure 4-17. Effect of incremental step size on the predicted elongation

4.2.4.2 Stiffness of beam-column elements

The effect of beam-column joint stiffness on the analytical predictions was investigated. The force-displacement and elongation responses are plotted in Figures 4-18 and 4-19, respectively. In the flexible beam-column joint model, the effective moment of inertia of the joints was set to be twice of the effective moment of inertia of the elastic beam, whereas in the rigid beam-column joint model, it was set as 10 times the effective moment of inertia of the beam.

It can be seen from the force-displacement comparison that the frame response is not sensitive to the stiffness of the beam-column joint. The initial stiffness of the hysteresis curve obtained using the rigid beam-column joint model is slightly higher than that in the flexible beam-column joint model. As the plastic hinge element in the rigid beam-column joint model sustained larger deformation/rotation, elongation is slightly greater in the rigid beam-column joint model as shown in Figure 4-19.

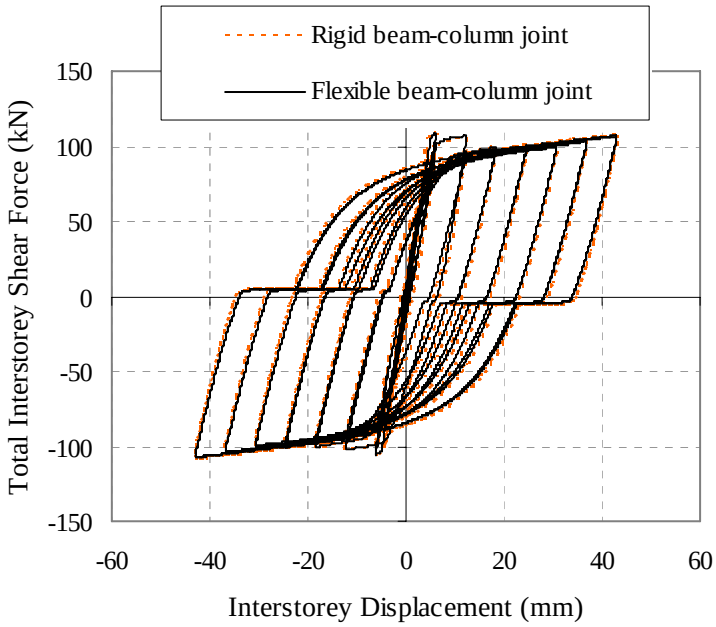

Figure 4-18. Effect of beam-column stiffness on the predicted force-displacement response

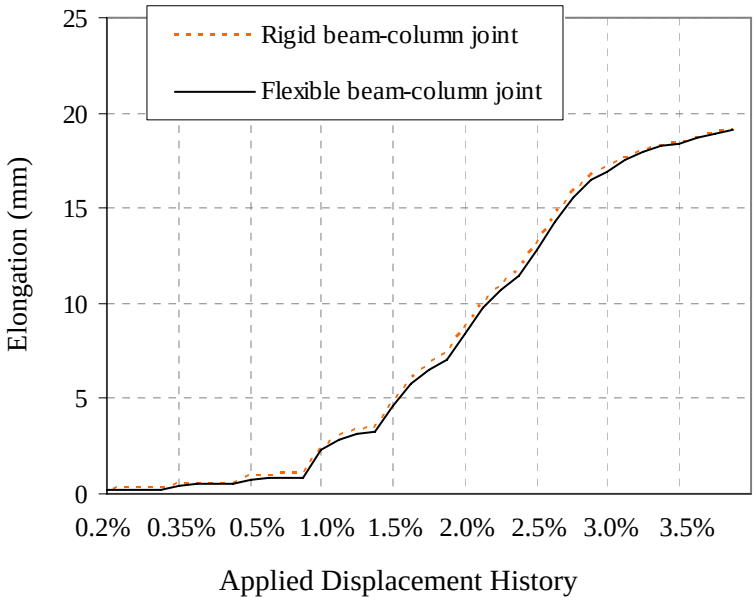

Figure 4-19. Effect of beam-column stiffness on the predicted elongation history

4.3 THREE-BAY ONE-STOREY MOMENT RESISTING FRAME

4.3.1 Experimental Program

An experimental study of a three-bay one-storey moment resisting frame was conducted by McBride et al. (1996). The specimen was approximately one-third scale model of a moment resisting frame. The test setup and the section details are shown in Figures 4-20 and 4-21, where (HT) in Figure 4-21 indicates heat treated bars. These bars were heat treated so that the yield stress and the ultimate strain characteristics were more ductile. Additional 10mm bars were welded to the flexural reinforcement in the beam-column joints to prevent yield penetration into the joints. These additional bars were extended 25mm out from the column face. The columns were designed to remain elastic throughout the test and were pinned at the bottom and connected to four hydraulic actuators at the top as shown in Figure 4-20.

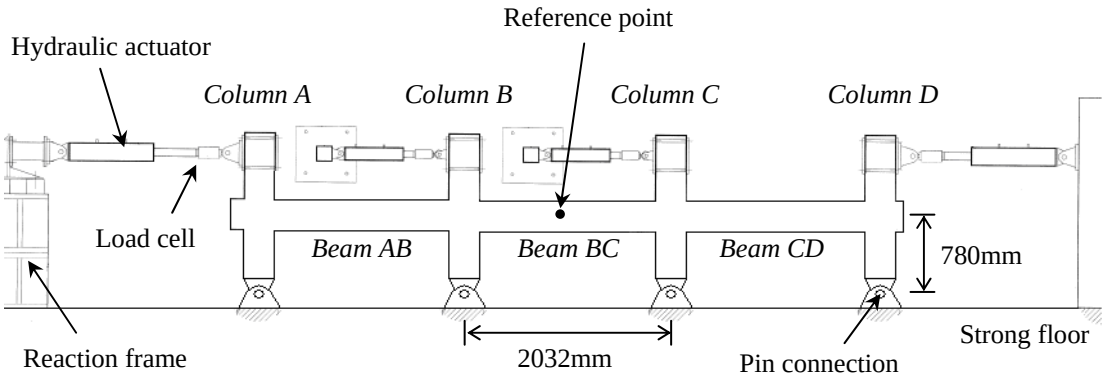

Figure 4-20. Test set up of the three-bay one-storey frame (McBride et al. 1996)

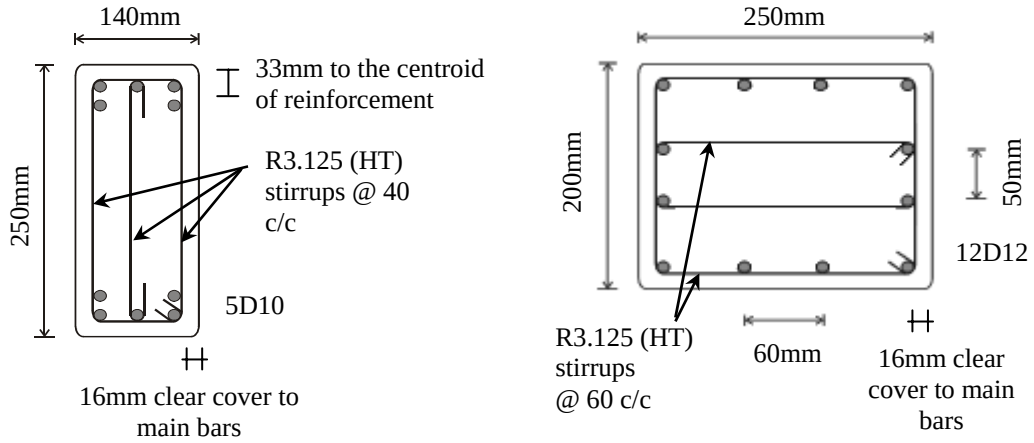

(a) Beam section (b) Column section

Figure 4-21. Member details in the three-bay one-storey frame

The applied lateral force was kept at a constant ratio of 1:2:2:1 in the four columns throughout the test. This was done to minimize the axial compression force induced in the beam so that elongation could develop freely. Cyclic displacements were applied to the frame by monitoring the movement at the reference point, which is shown in Figure 4-20. The force in each column was increased slightly in the aforementioned ratio until the target displacement at the reference point was reached. The displacement histories applied in the test are summarised in Figure 4-22. The displacement corresponding to the displacement ductility of 1, *D1*, measured in the test was 7.4mm.

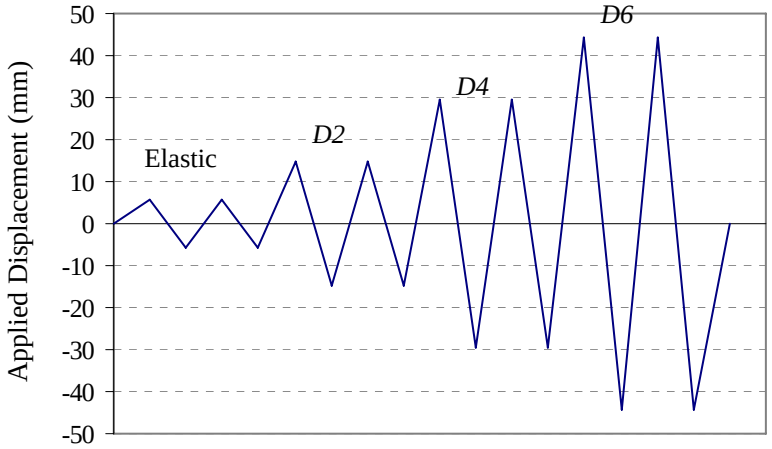

Figure 4-22. Experimental loading protocol for the three-bay one-storey frame

It should be noted that with this loading scheme, there is no guarantee that the axial force in the beam was zero. In addition, the loading arrangement results in elongation of the beams pushing the external columns apart; thereby inducing a larger drift on the external columns and increasing the inelastic actions in the associated plastic hinges.

The measured and calculated material properties for the frame are summarised in Tables 4-7 and 4-8.

Table 4-7. Stirrup arrangement and measured material properties in the three-bay one-storey frame

Member	**Stirrups arrangement**	f_{vy} **(MPa)**	f_y **(MPa)**	f_u **(MPa)**	f_c' **(MPa)**
Beam	3R3 (HT) @ 40c/c	295	320	457	33

Table 4-8. Calculated material and section properties for the three-bay one-storey frame

Member	f_t **(MPa)**	E_c **(GPa)**	$f_{c\,(D)}'$ **(MPa)**	M_{yc} **(kNm)**	L **(mm)**	V_{yc} **(kN)**	ε_{sh} / ε_y	ε_u / ε_y
Beam	2.1	26.0	11.2	23.1	866	26.7	10*	94

* The value is not available from the report, a value is assumed here.

4.3.2 Analytical Model

The analytical model, which is illustrated in Figure 4-23, was set up in RUAUMOKO2D. The top of the columns were free to move and rotate whereas the

bottom of the columns was locked in position but free to rotate. The beams were divided into elastic and plastic hinge regions. The elastic regions were modelled using elastic elements and the plastic regions were modelled using the modified elongating plastic hinge element as described in Chapter 3. The beam-column joints and the columns were modelled using elastic elements. The input parameters for the plastic hinge element are summarised in Table 4-9.

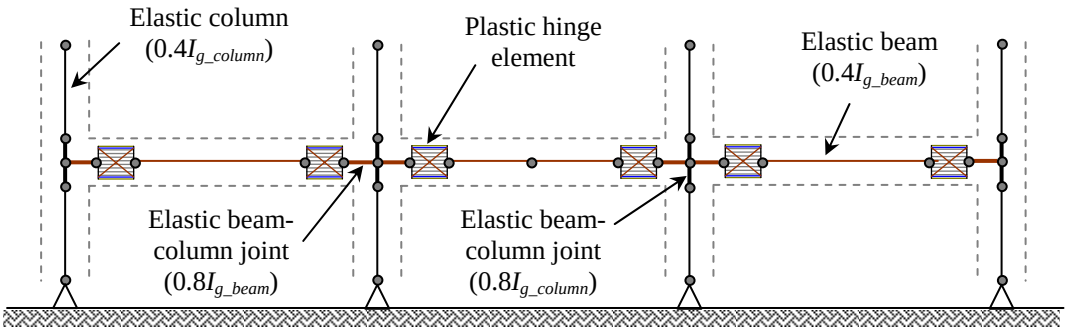

Figure 4-23. Analytical three-bay one-storey frame model

Table 4-9. Calculated plastic hinge properties for the three-bay one-storey frame

L_p (mm)	θ (degree)	D (mm)	M_{max} (kNm)	M_{y1} (kNm)	L_t (mm)	L_{yield} (mm)
155	50	119	27.4	24.1	92	228

The effective moment of inertia of the elastic beams and columns was taken as $0.4I_g$, as recommended in the New Zealand code (Standards New Zealand 2006). The effective moment of inertia of the beam-column joint was assumed to be twice of the effective moment of inertia of the beam and column as shown in Figure 4-23. The shear deformation was considered in all of the elastic members. The shear modulus of concrete was calculated based on NZS 3101:2006 and the shear area of the elastic beams and columns was taken as *bd*.

Difficulties were encountered when deciding on the loading system to be used in the analysis to try and best compare with the experiment. It was not feasible to apply directly the column displacement in the analysis, as it would artificially generate the same elongation as in the experiment. It was also not feasible to apply the experimentally measured force directly in the analysis, as a small variation in the column shear force (at inelastic level) could lead to a huge difference in the frame

displacement. The loading method used to model Lau's test (see Section 4.2.2), where rotation was applied to the centre of beam-column joints, could not be adopted here as the bottom of the columns were fixed and applying rotation would fix the elongation. To resolve this problem, the analysis was carried with the following steps:

1) The shear force in each column was increased incrementally at a 1:2:2:1 ratio until the ultimate capacity of the frame in the positive drift was reached.
2) The force-displacement response was analysed and the column shear force corresponding to the reference point reaching its target displacement was identified.
3) The analysis was then restarted and the column shear force was increased incrementally at 1:2:2:1 ratio until the force identified above was reached. The column shear force was then reversed into the opposite direction until the ultimate capacity in the negative drift was reached.
4) Again, the column shear force corresponding to the reference point reaching the next target displacement in the opposite direction was identified.
5) The analysis was then restarted and the column shear force was increased cyclically until the forces identified in the previous steps were reached in sequence and a new force corresponding to the reference point reaching the next target displacement was identified.
6) Steps 1-5 were repeated until all the displacement cycles were reached.

It should be noted that the analytical predictions were made only up to the end of *D4* cycles. This is because the longitudinal reinforcement buckled severely in the experiment after this displacement cycle and the behaviour became highly non-linear. As the frame response is very sensitive to the size of the incremental step size applied in the analysis, two different force increments, 0.1N and 0.01N, were used in the analysis. The smaller force increment was applied over the regions where shear pinching in the analysis was expected to occur.

4.3.3 Analytical and Experimental Comparisons

The analytical and experimental force-displacement relationships of the frame are illustrated in Figure 4-24. The dashed lines represent the response at *D6* cycles. It can be seen that the analysis predicts the loading and unloading stiffness together with

the yield and ultimate force satisfactorily. Pinching in the unloading loop is predicted reasonably well.

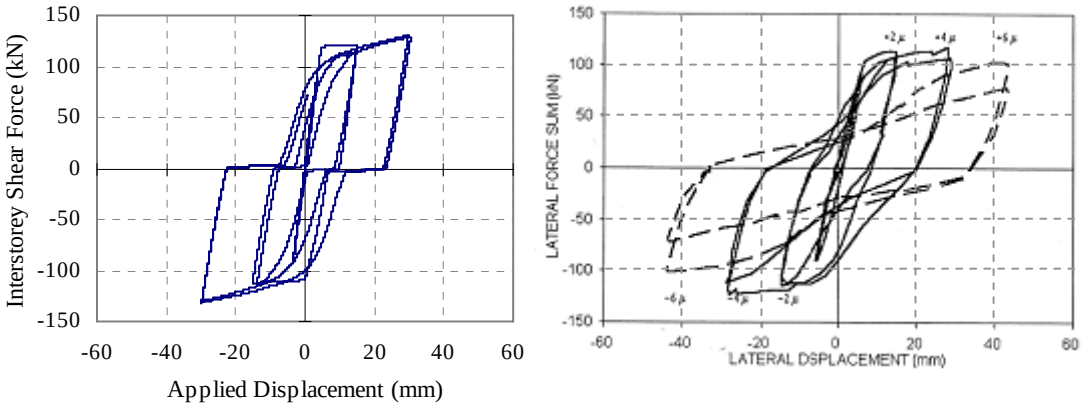

(a) Analytical prediction (b) Experiment (McBride et al. 1996)

Figure 4-24. Total force-displacement response of the three-bay one-storey frame

The force-displacement comparisons of each individual column are illustrated in Figure 4-25. It can be seen that the applied displacements in the positive drift cycles are smaller than the applied displacements in the negative drift cycles in *Column A*. This is due to elongation of the beam plastic hinges pushing the columns outwards as shown in Figure 4-26. Similar behaviour can be observed in *Column B*, but to a lesser extent, because *Column B* was only affected by one elongating plastic hinge.

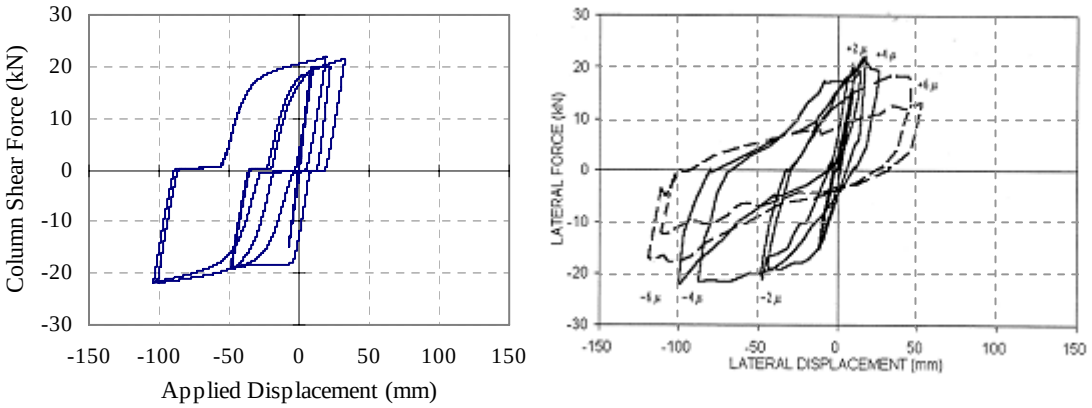

(a) *Column A* (analysis) (b) *Column A* (McBride et al. 1996)

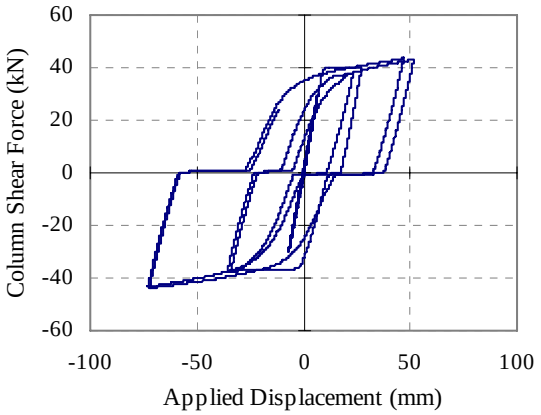

(c) *Column B* (analysis)

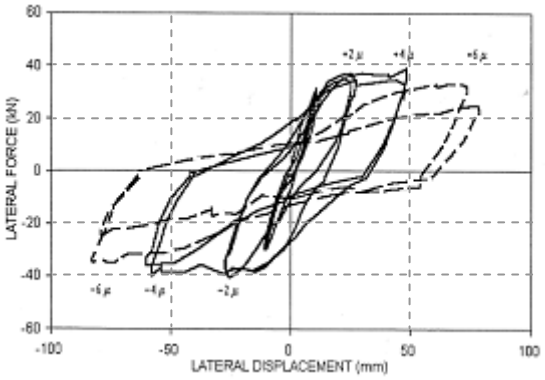

(d) *Column B* (McBride et al. 1996)

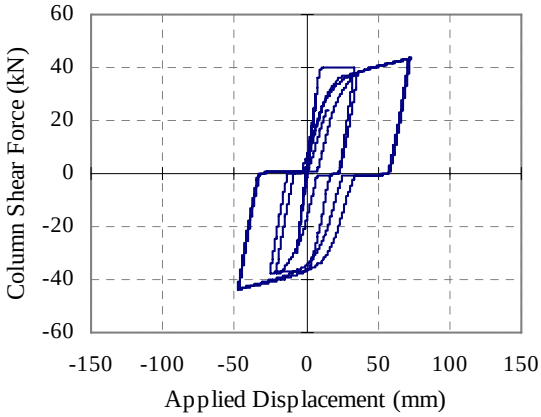

(e) *Column C* (analysis)

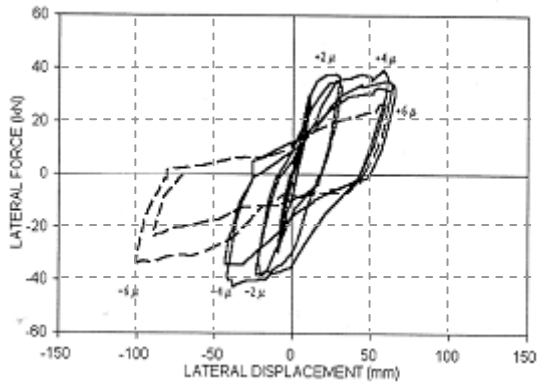

(f) *Column C* (McBride et al. 1996)

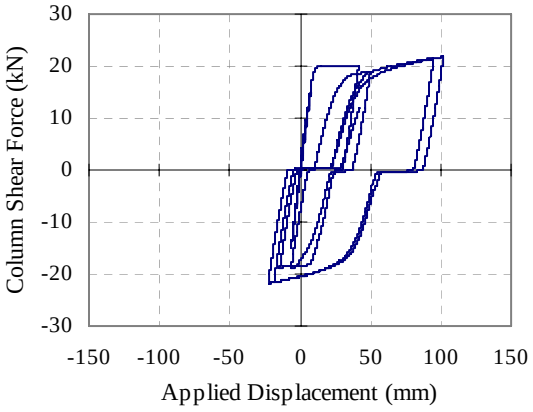

(g) *Column D* (analysis)

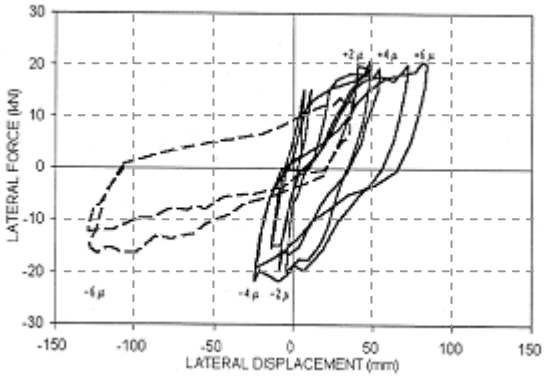

(h) *Column D* (McBride et al. 1996)

Figure 4-25. Force-displacement response of individual columns in the three-bay one-storey frame

The analytically predicted and experimentally observed deformed shapes of the frame, at the peak of the first *D4* cycle, are shown in Figure 4-26. It can be seen from Figure 4-26 that elongation in the plastic hinges pushed the external column outwards forcing the outer columns to undergo larger deformation. Consequently, the plastic hinges next to the external columns were sustaining larger inelastic actions compared to those next to the internal column. Despite the global ductility demand of the frame at the reference point being four, much higher rotational ductility demands were imposed on the exterior plastic hinges than in the interior plastic hinges.

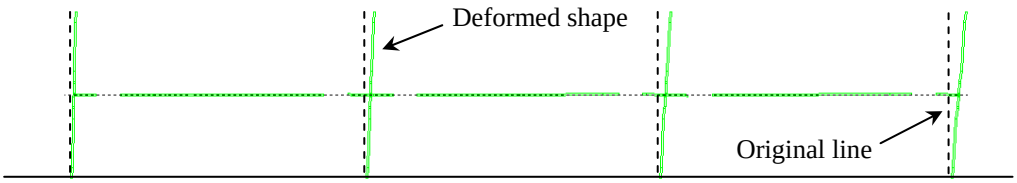

(a) Analysis

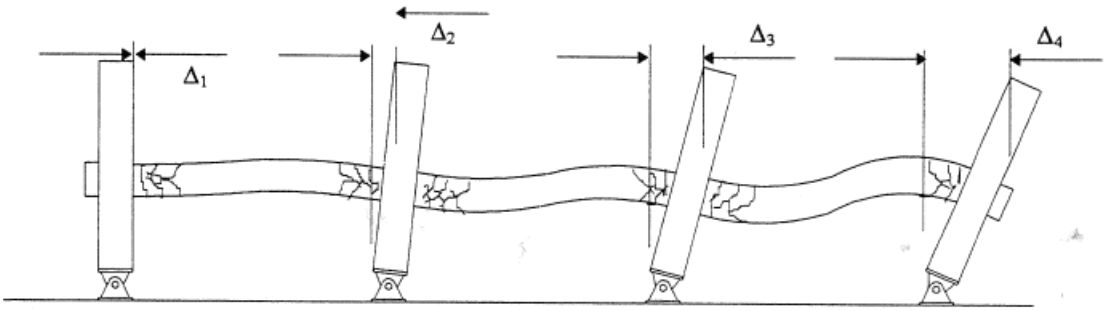

(b) Experiment (McBride et al. 1996)

Figure 4-26. Deformed shape in the three-bay one-storey frame at the peak of first positive *D4* cycle

Analytical and experimental elongation within the frame is summarised in Figure 4-27; elongation within each beam bay is summarised in Figure 4-28. The comparisons in these figures show that the predicted elongation matches satisfactorily with the experimental values up to the first *D4* cycle. After these cycles, the reinforcing bars in the exterior plastic hinges buckled in the experiment. This was due to large rotational demands placed on the exterior plastic hinges as a result of beam elongation. As the analytical model does not consider buckling of reinforcement, elongation was over-estimated at large displacement cycles in the exterior plastic hinges. Elongation in *Beam BC* was over-predicted at early drift cycles. It is

postulated that this is due to an under-estimation of the axial compression force in the analysis.

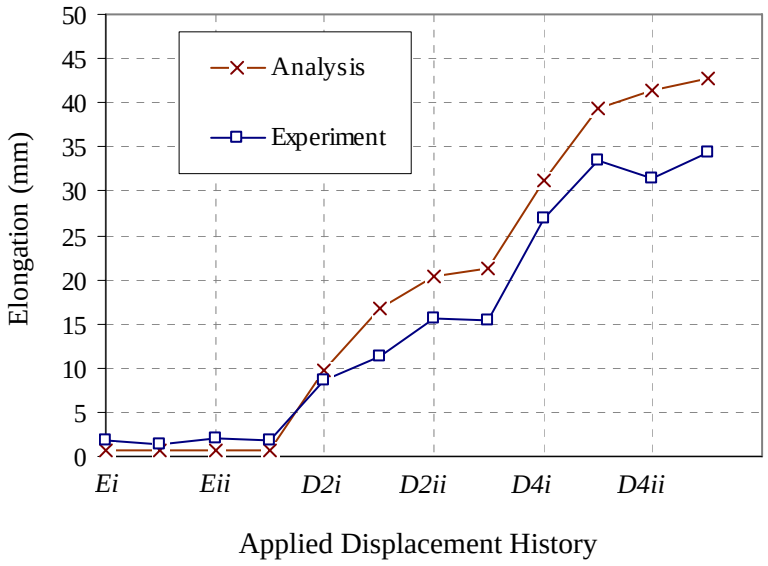

Figure 4-27. Comparison of the analytical and experimental elongation for three-bay one-storey frame

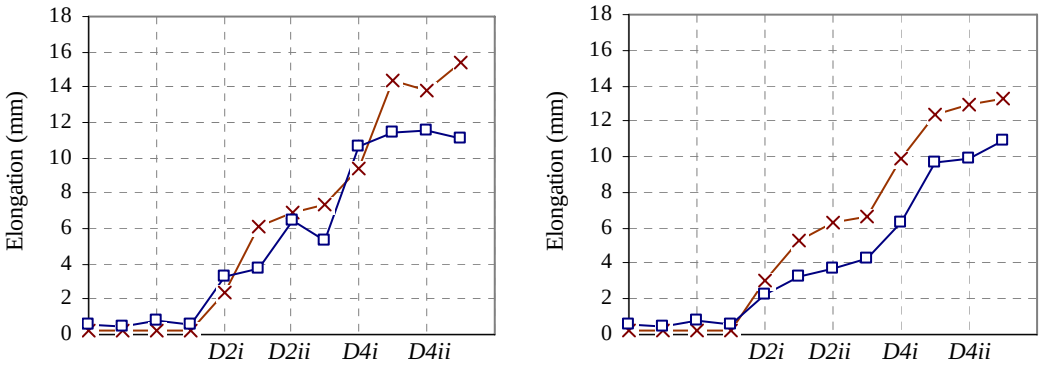

(a) *Beam AB*

(b) *Beam BC*

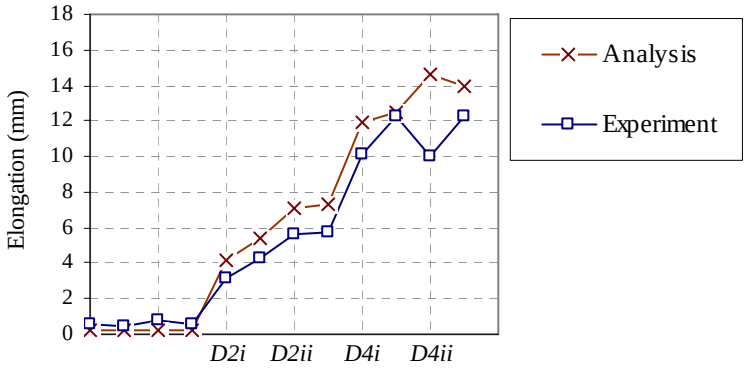

(c) *Beam CD*

Figure 4-28. Analytical and experimental elongation in each beam for the three-bay one-storey frame

As indicated in Section 2.7.1, elongation of plastic hinges with no axial force is about 3.2% of the beam depth, which corresponds to a total elongation of 48mm in this frame. This is much greater than the experimentally measured value which implies that the beam plastic hinges in the experiment may have sustained some axial compression force. The predicted axial force history in the beams is shown in Figure 4-29. It can be seen that a small level of axial compression force was predicted in the analysis. It is observed that the axial compression force sustained in the internal beam was twice the axial compression force sustained in the external beams. This explains why elongation is smaller in the centre beam compared to the two outer beams as observed in Figure 4-28.

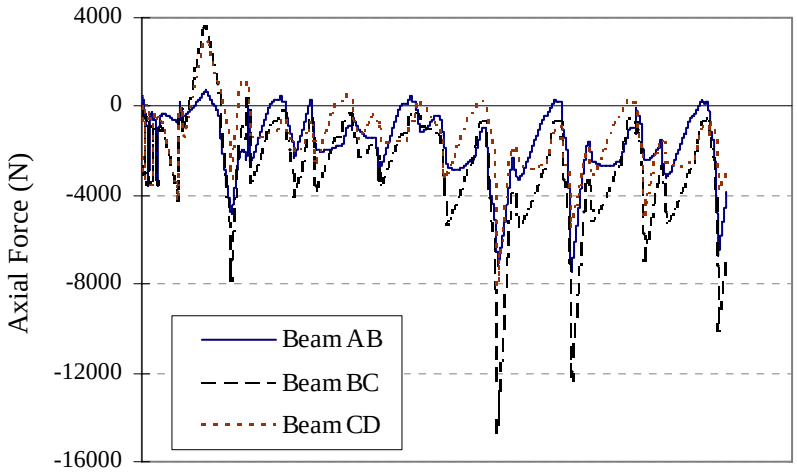

Figure 4-29. Predicted axial force in the beams of three-bay one-storey frame

It should be noted that elongation of plastic hinges and its effect on the deformed shape and induced axial force in the beams cannot be predicted unless the analysis can capture elongation of plastic hinges. Therefore, the plastic hinge element proposed in this study offers a more objective tool for conducting analytical performance assessments of RC structures than the conventional lumped plasticity approach.

4.4 THREE-BAY TWO-AND-A-HALF STOREY MOMENT RESISTING FRAME

4.4.1 Experimental Program

An experimental test of a three-bay, two-and-a-half story moment resisting frame was carried out by Wuu (1996). The test was approximately a one-third scale model of a moment resisting frame. This model represents the situation near the base of a multi-storey frame where elongation of the beams at the first floor level is partially restrained by the foundation, columns, and the second floor beams. The test setup and the member sections are shown in Figures 4-30 and 4-31.

The plastic hinges were designed to form in the beams at the column faces and in the columns just above the foundation beam. The foundation beam was stressed down to the strong floor. Additional R6 bars were welded to the longitudinal beam bars passing through the beam-column joints to ensure that inelastic deformation was

confined to the beam plastic hinges. These additional reinforcing bars extended 50mm into the beams on each side of the joints.

The lateral force was kept at a constant ratio of 1:2:2:1 in the four columns throughout the test. The overall loading system is similar to the one used in McBride's experiment described earlier. Cyclic displacement was applied to the frame by monitoring the displacement at the reference point as illustrated in Figure 4-30. The force in each column was increased slightly in the aforementioned ratio until the target displacement at the reference point was reached. The displacement histories applied in the test are summarised in Figure 4-32. The applied lateral force corresponding to the theoretical yield and ultimate strength of the frame was 156kN and 192kN, respectively. The ductility 1 displacement at the reference point was 16.5mm.

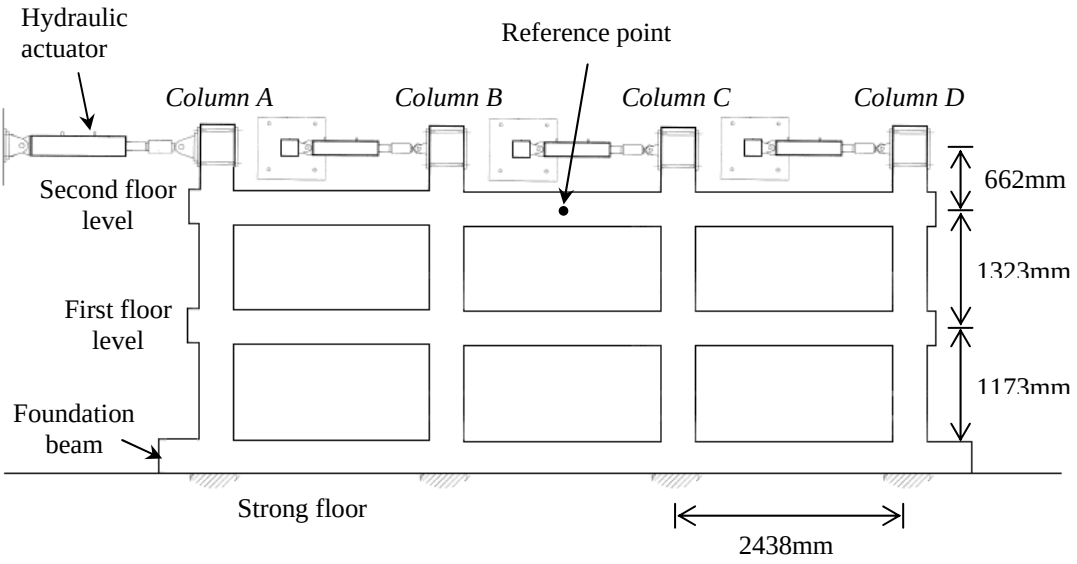

Figure 4-30. Three-bay, two and a half storey frame test arrangement (Wuu 1996)

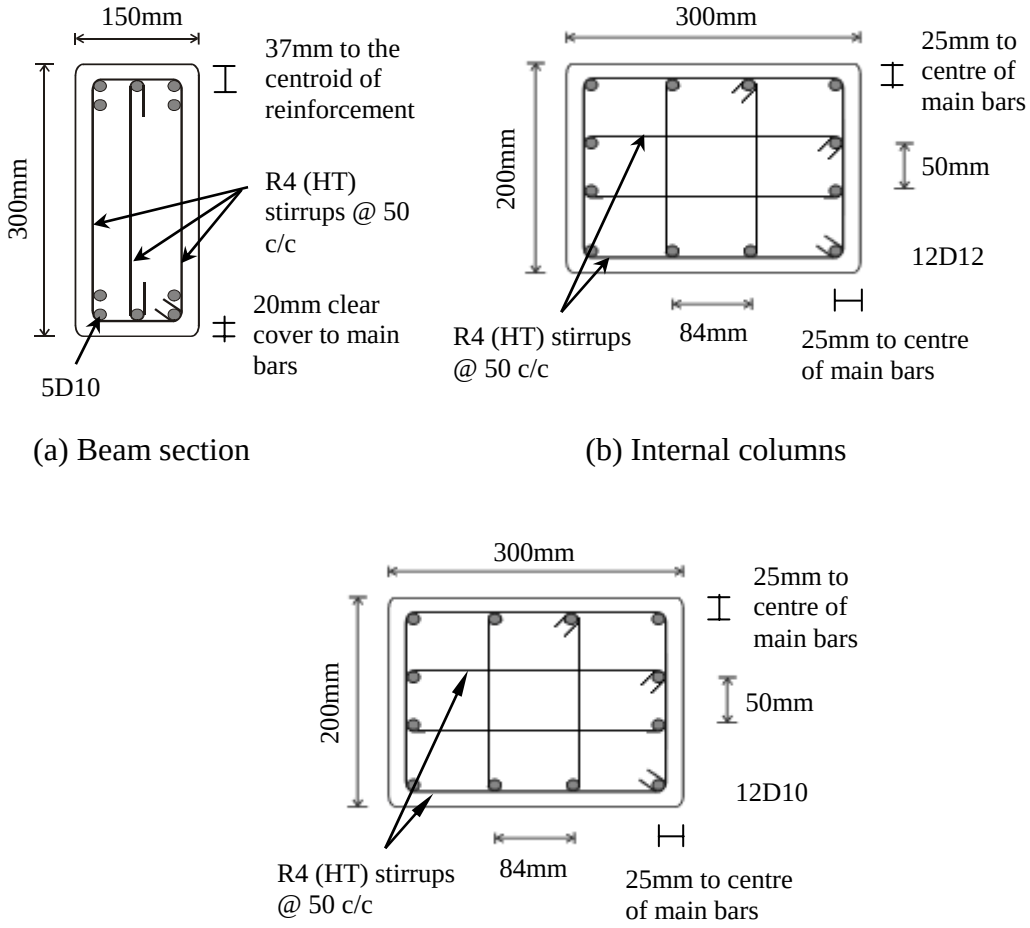

Figure 4-31. Member details in the three-bay two-and-a-half storey frame

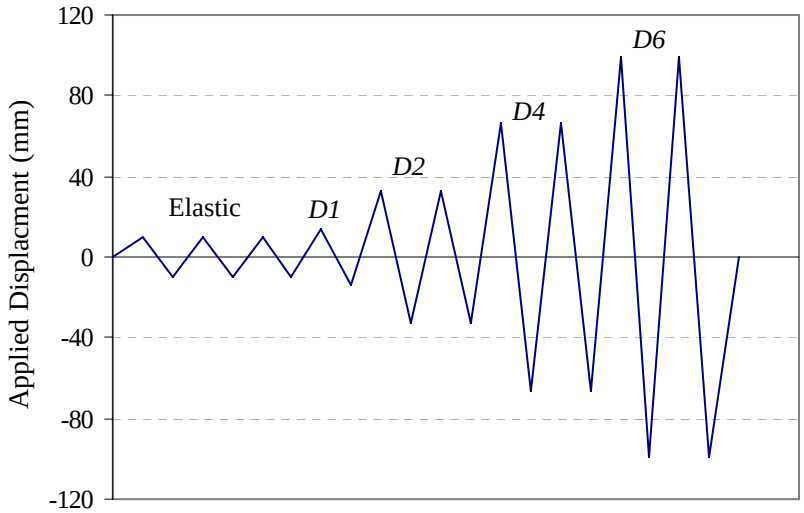

Figure 4-32. Displacement history applied in the three-bay two-and-a-half storey frame test

The measured and calculated material properties for this frame are summarised in Tables 4-10 and 4-11.

Table 4-10. Stirrup arrangement and measured material properties in the three-bay two-and-a-half storey frame

Member	Stirrups arrangement	f_{vy} (MPa)	f_y (MPa)	f_u (MPa)	f_c' (MPa)
Beam	3R4 (HT) @ 50c/c	250	331	468	27.8
External Column	4R4 (HT) @ 50c/c	250	331	468	27.8
Internal Column	4R4 (HT) @ 50c/c	250	336	471	27.8

Table 4-11. Calculated material and section properties for the three-bay two-and-a-half storey frame

Member	f_t (MPa)	E_c (GPa)	$f_{c\,(D)}'$ (MPa)	M_{yc} (kNm)	L (mm)	V_{yc} (kN)	ε_{sh} / ε_y	ε_u / ε_y
Beam	1.9	24.4	9.5	29.4	1019	28.9	17	114

4.4.2 Analytical Model

Two different analytical models, one with the elongating plastic hinge element and one without it, were set up in RUAUMOKO2D to investigate the effect of elongation on the cyclic performance of RC frames. The analyses were also used to highlight the deficiency associated with an analytical model not allowing for beam elongation.

4.4.2.1 With Elongating Plastic Hinge Elements

The layout of the analytical model is illustrated in Figure 4-33. The top of the columns were free to move and rotate. The beams were divided into elastic regions and plastic hinge regions. The elastic regions were modelled using elastic elements and the plastic hinge regions were modelled using the modified plastic hinge element as described in Chapter 3. The beam-column joints were modelled using elastic elements. The input parameters for the plastic hinge are summarised in Table 4-12. L_{yield} was calculated assuming that the maximum moment, M_{max}, is 1.2 times the yield moment, M_{yc}.

The effective moment of inertia for the elastic beams and columns was taken as $0.4I_g$ recommended in NZS 3101:2006. The effective moment of inertia of the beam-

column joints was assumed to be twice the effective moment of inertia of elastic beams and columns as illustrated in Figure 4-33. The shear deformation was considered in all of the elastic members with the shear modulus of concrete calculated based on NZS 3101:2006 and the shear area taken as *bd*.

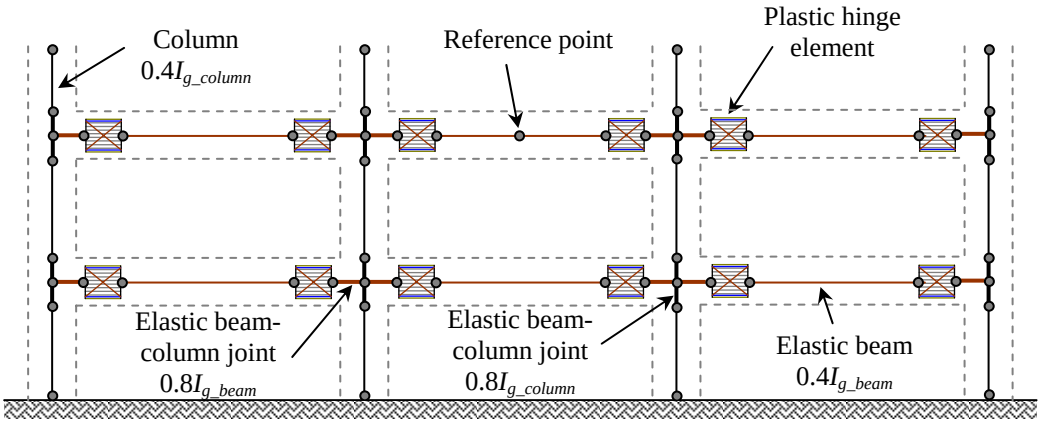

Figure 4-33. Analytical frame model with elongating plastic hinge element

Table 4-12. Calculated plastic hinge properties for the three-bay two-and-a-half storey frame

L_p (mm)	θ (degree)	D (mm)	M_{max} (kNm)	M_{y1} (kNm)	L_t (mm)	L_{yield} (mm)
153	55.9	127	35.3	30.5	113	283

The columns were modelled using the existing 'Concrete Beam-Column' element in RUAUMOKO2D which allows for axial force-moment interaction with lumped plasticity at the member ends. "Modified TAKEDA Hysteresis" rule with unloading stiffness parameter, α, equal to 0.3 and reloading stiffness parameter, β, equal to 0.0 was adopted to simulate the moment-curvature relationship of the columns (Carr 2008a). The reloading stiffness power factor was taken as 1.0 and the unloading loop followed the *DRAIN-2D* model (Carr 2008a) where the stiffness of the unloading loop is defined as such shown in Figure 4-34. The bilinear factor was set as 0.01 and the plastic hinge length in the column was assumed to be *H/2* where *H* is the section depth. The nominal section capacities of the external and internal columns with no axial force were 40.4kNm and 58.0kNm, respectively. The moment capacities at the balance point were 81kNm and 93.9kNm, respectively, and the corresponding axial compression forces were 740kN and 750kN.

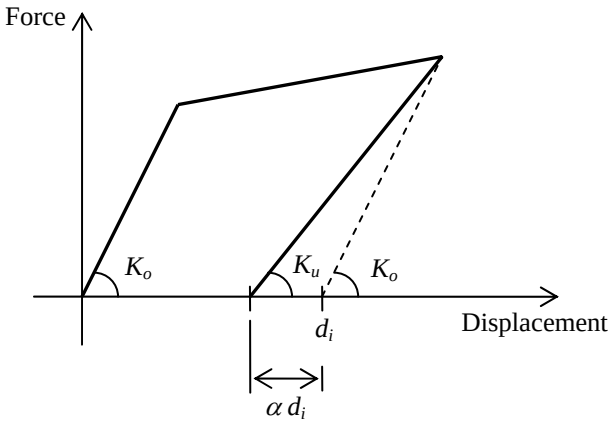

Figure 4-34. Drain-2D unloading model in Modified Takeda Hysteresis

The loading scheme adopted in this analysis was similar to that adopted for McBride's test (see Section 4.3.2), where the analysis was initially carried out in several steps to determine the shear force corresponding to the target displacements. The shear forces applied to the top of the columns were kept constant at a 1:2:2:1 ratio throughout the test. The complete loading history with the pre-determined column shear force was then applied in the final analysis. Two different force increments, 0.1N and 0.01N, were used in the analysis. The smaller increment was applied over the regions where shear pinching in the analysis is expected to occur.

4.4.2.2 Without Elongating Plastic Hinge Elements

The analytical model without elongating plastic hinge elements is illustrated in Figure 4-35. The main difference between this model and the one described above is how the beams were modelled. Here, the beam was modelled using Giberson beam elements with lumped plasticity at the member ends. A Modified TAKEDA hysteresis was adopted to simulate the moment-curvature relationships of the plastic hinges. The nominal flexural strength of the beam was 32kNm. The moment capacity was assumed to be independent of axial force. The length of the plastic hinge was assumed to be *H/2* where *H* is the section depth.

Unlike the plastic hinge element developed in this research, the parameters used in this lumped plasticity model need to be calibrated so that the moment-rotation/force-displacement characteristics match with the experiment. The bilinear factor of the

beam plastic hinges was set as 0.3% and the unloading and reloading stiffness parameters for the hysteresis loop was set as 0.3 and 0.0, respectively.

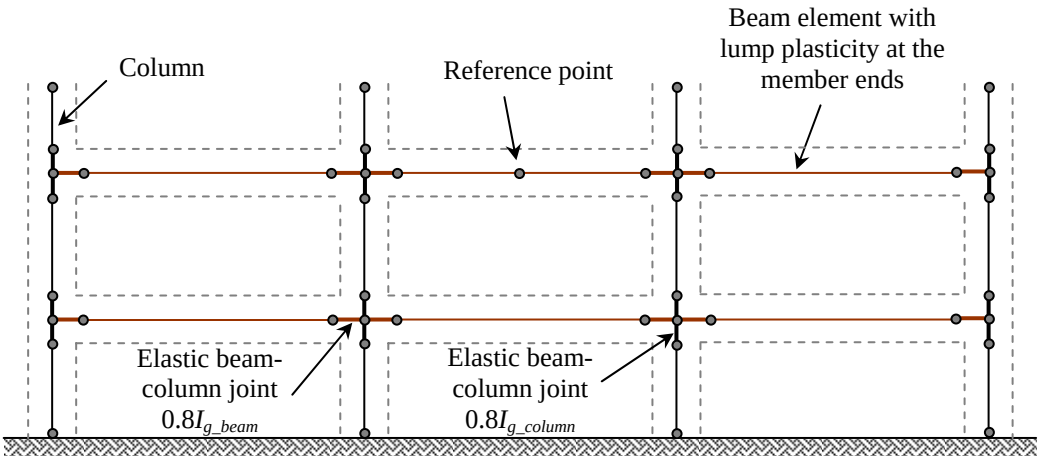

Figure 4-35. Analytical frame model without elongating plastic hinge element

4.4.3 Analytical and Experimental Comparisons

4.4.3.1 With Elongating Plastic Hinge Elements

The analytical and experimental force-displacement response of the frame is illustrated in Figure 4-36. The comparisons show that the analysis predicts the loading and unloading stiffness, as well as the yield and ultimate force, accurately. Pinching was predicted accurately up to the first *D6* cycle. Strength degradation observed in the experiment after this cycle was not captured accurately in the analysis. This is likely due to buckling of reinforcement not being considered and shear deformation being under-estimated in the analysis. It is emphasised here that the analytical model was not calibrated to fit the experimental results. The springs in the plastic hinge elements are based on stress-strain relationships of concrete and reinforcing bars which do not require calibration.

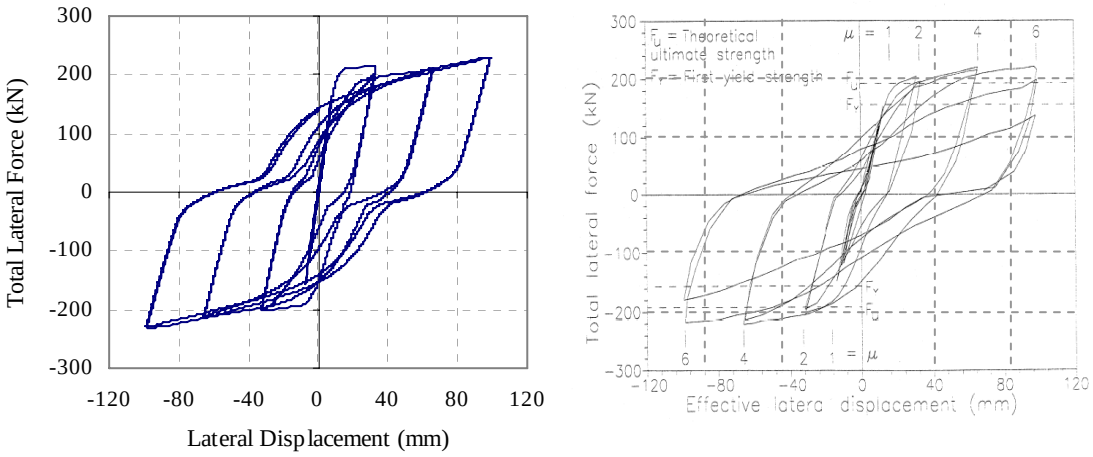

(a) Analytical prediction (b) Experimental results (Wuu 1996)

Figure 4-36. Total force-displacement response of the frame with elongating plastic hinge element

The predicted deformation of the frame at the first positive *D6* cycle is shown in Figure 4-37. It can be seen that the inter-storey drift increases from *Column A* to *Column D* due to elongation of the plastic hinges. This implies that the plastic hinges next to the external columns and at the external column base may sustain much greater inelastic actions compared to those adjacent to the internal columns under inelastic cyclic loading. Despite the global ductility demand of the frame at the reference point being six; this may correspond to a much higher local ductility demand in the specific plastic hinges.

The plastic hinges formed in the beams, next to the column faces, are represented by the empty gap and the plastic hinges formed in the columns are represented by the blue lines as shown in Figure 4-37. The figure shows that uni-directional plastic hinges were predicted to form in the external columns immediately above level 1 and reversing plastic hinges were predicted to form in the internal columns immediately above level 1. These predicted plastic hinges were observed in the experiment. It should be noted that these plastic hinges were not designed to occur. They formed due to elongation of the plastic hinges, which is explained in detail in Section 4.4.3.3.

Figure 4-38 shows that an axial compression force was induced in the beams at level 1 and an axial tension force was induced in the beams in level 2, due to elongation of the beam plastic hinges. As the columns were fixed to the foundation beam, the

columns provide some axial restraint against elongation of the beam plastic hinges at level 1 and hence an axial compression force was induced in beams at level 1. To satisfy force equilibrium of a free body of a column section, a tension force must be induced in the beams at level 2. Similar behaviour was also observed in the experiment.

The axial force induced in the beams would change the shear force and hence moment distributions in the columns as well as the moment capacities of the beams. This is described further in Section 4.4.3.3.

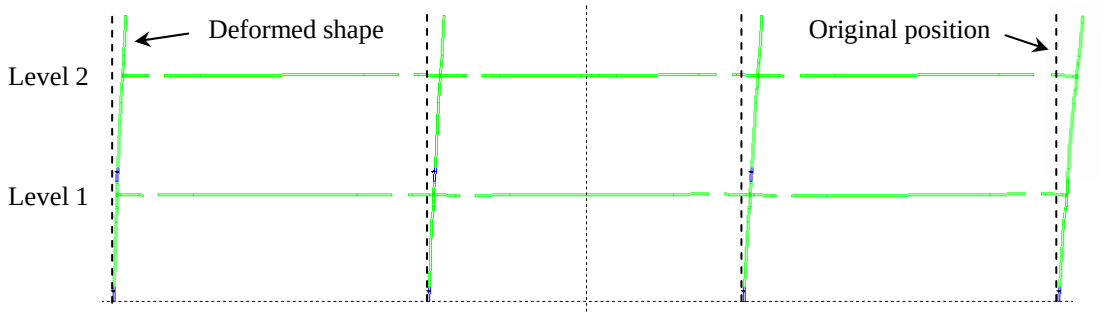

Figure 4-37. Predicted deformed shape of the frame with elongating plastic hinge element at first positive *D6* cycle

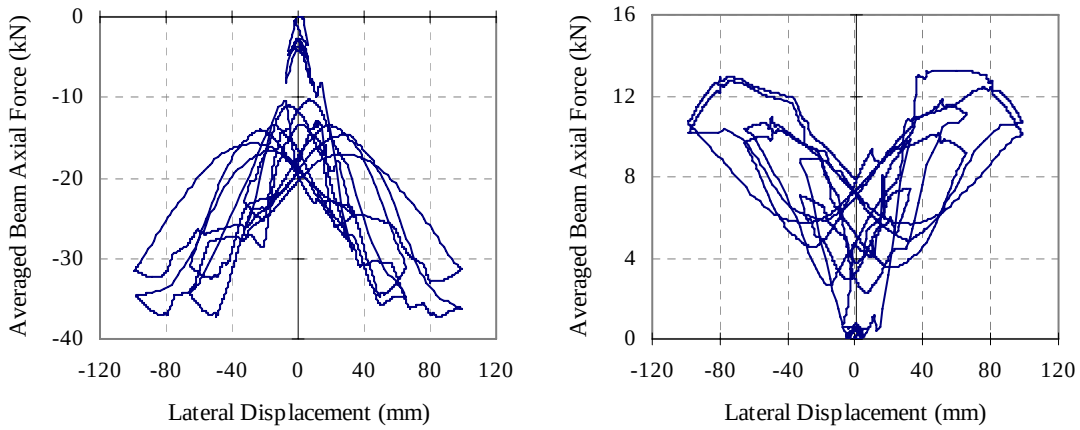

(a) Level 1 (b) Level 2

Figure 4-38. Predicted axial force in the beams with elongating plastic hinge element

The analytical and experimental total beam elongations in levels 1 and 2 are plotted in Figure 4-39. Elongation in level 2 was greater than that in level 1. This is due to an

axial tension force being induced in beams at level 2 and an axial compression force being induced in beams at level 1, as observed earlier. The analysis predicts elongation in beams at level 1 and level 2 accurately up to the second *D4* cycle and the first *D4* cycle, respectively. At large displacement ductility cycles, flexural reinforcement in the plastic hinges buckled in the experiment and hence, elongation measured in the experiment was smaller than that predicted in the analysis.

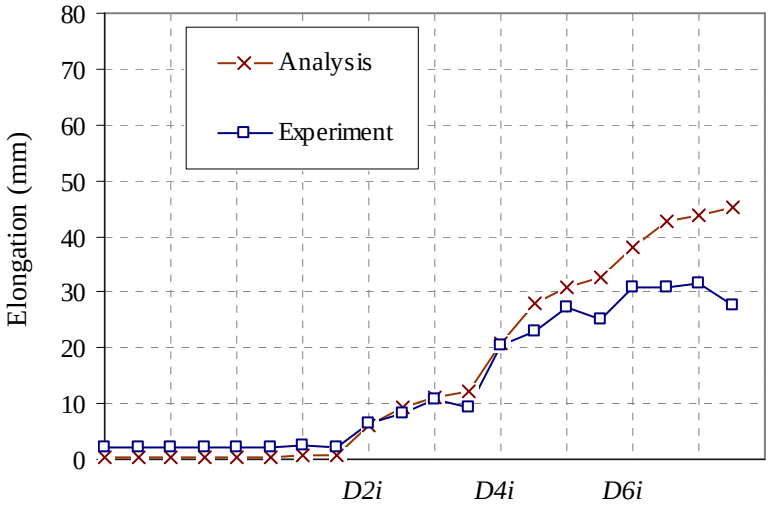

(a) Level 1

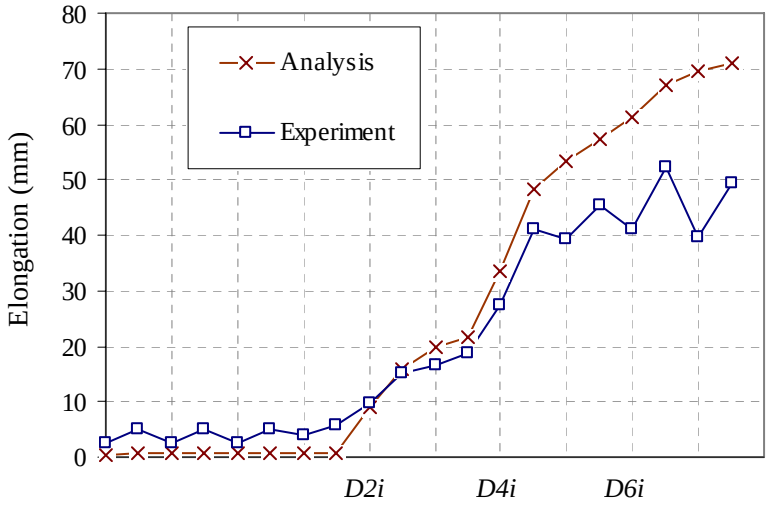

(b) Level 2

Figure 4-39. Elongation history in the analysis with elongating plastic hinge element

4.4.3.2 Without Elongating Plastic Hinge Elements

The analytical and experimental force-displacement comparisons of the frame are shown in Figure 4-40. As the model was calibrated to fit the experimental results, the yield and peak force as well as the loading and unloading loops correlate well with the experiment.

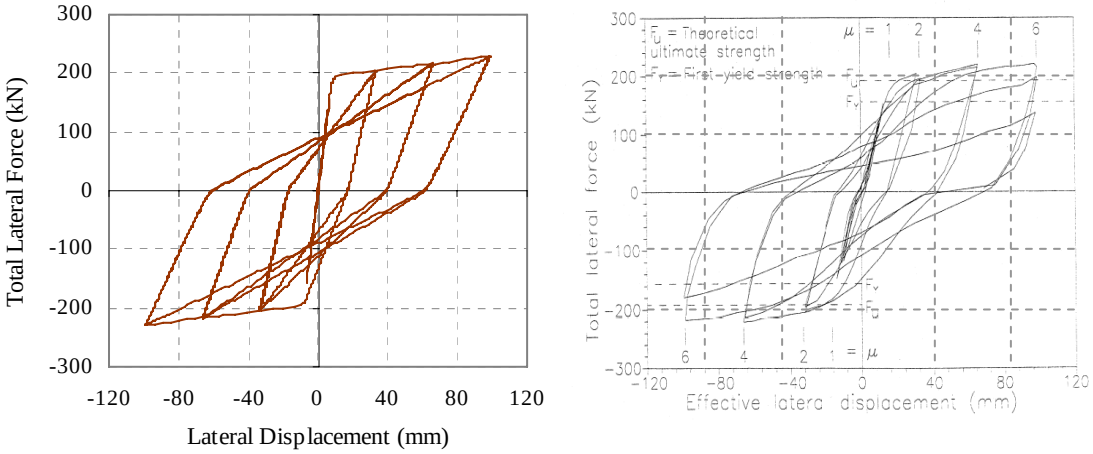

(a) Analytical prediction (b) Experimental results (Wuu 1996)

Figure 4-40. Total force-displacement relationship of the frame without elongating plastic hinge element

The predicted deformation of the frame at the first positive *D6* cycle is illustrated in Figure 4-41. The inter-storey drift of each column is the same in the analysis. The plastic hinges were only forming in the beams next to the column faces and in the columns directly above the foundation. These predictions were quite different to those observed in the experiment. Plastic hinges were not predicted to form in the columns immediately above level 1 in this analysis because elongation was not captured using the conventional lumped plasticity model.

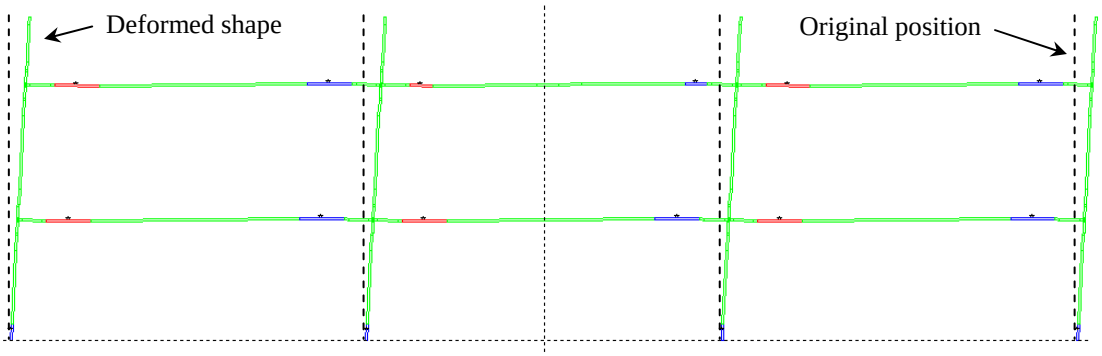

Figure 4-41. Predicted deformed shape of the frame without elongating plastic hinge element at first positive D6 cycle

The average axial force of the three beams in each storey, predicted in the analysis, is plotted in Figure 4-42. It can be seen that before yielding occurs in the frames, there was no axial force exerted in the beams. However, as plastic hinges develop in the columns and beams, shear force and moment redistribution occurred within the frame which induced axial forces in the beams. Unlike that predicted in the analysis with elongating plastic hinge element, the top storey was under axial compression force and the bottom storey was under axial tension force in this case. This behaviour is different to that observed in the experiment.

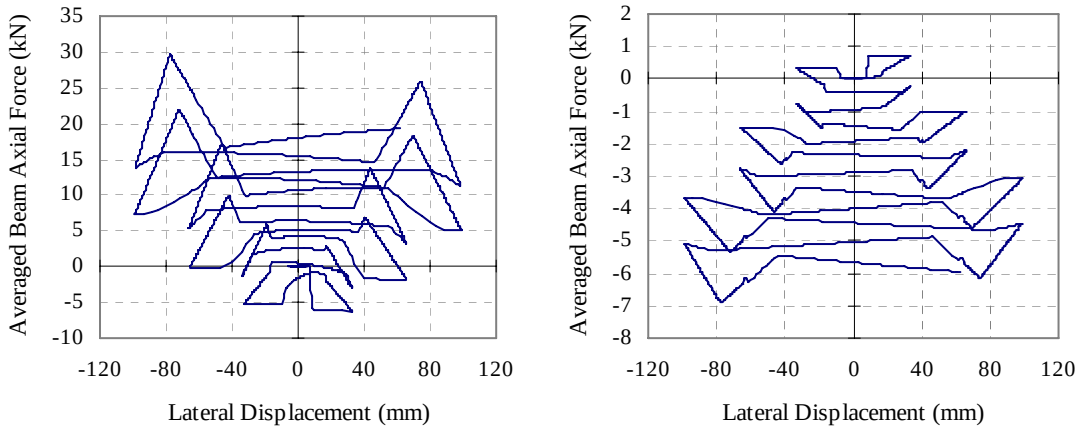

(a) Level 1 (b) Level 2

Figure 4-42. Predicted axial force in the beams without elongating plastic hinge element

4.4.3.3 Discussions

The predicted moment, shear and axial force distributions at the first positive *D6* cycle from analyses with and without elongating plastic hinge elements are plotted in Figures 4-43 to 4-45. It can be seen from Figure 4-43 that the moment in the columns above level 2 were similar in these two analyses. However, larger moments were induced in the columns above level 1 for *Columns A* to *C* in the analysis with the elongating plastic hinge element compared to the conventional approach. The moment was 43% higher in the analysis with the elongating plastic hinge element. An increase in the moment at these locations caused *Columns A-C* to yield just above level 1. This increase in the column moment demand in the analysis with the elongating plastic hinge element was due to a change in the column shear force as shown in Figure 4-45. As the moment in the columns immediately below level 2 cannot alter significantly, an increase in the column shear force between levels 1 and 2 increases the moments in the columns immediately above level 1.

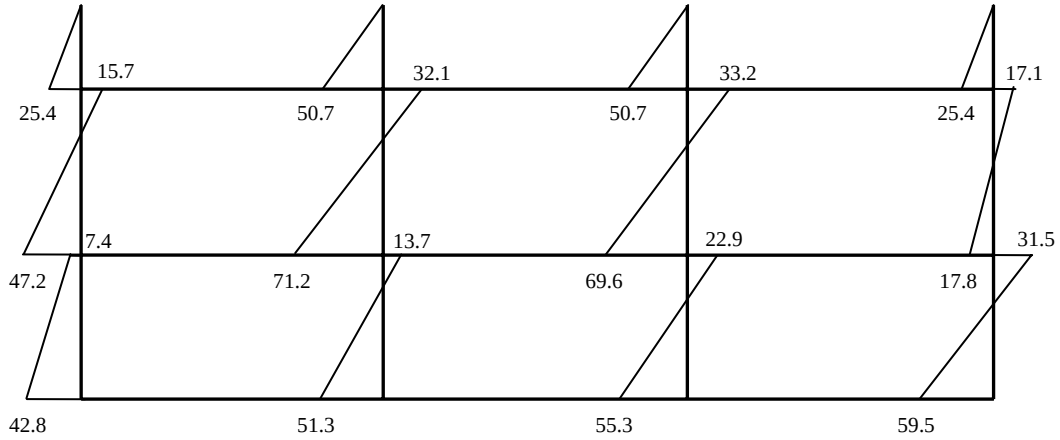

(a) With elongating plastic hinge elements

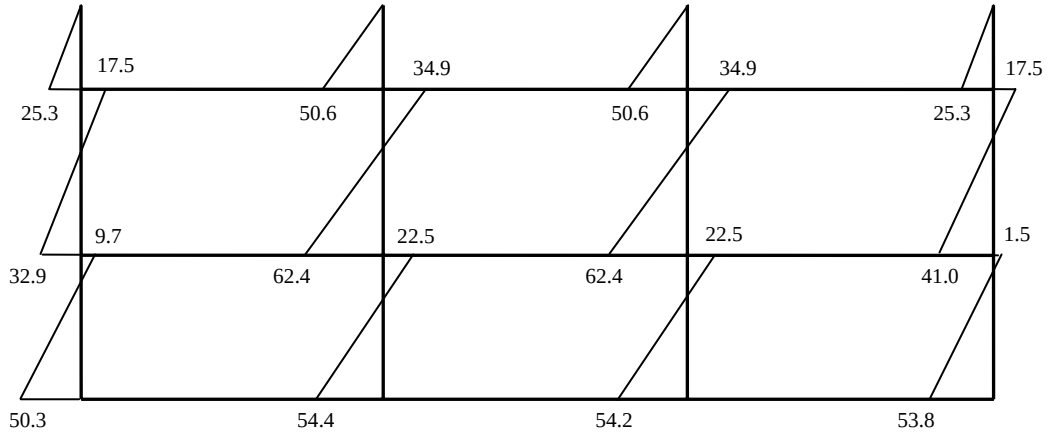

(b) Without elongating plastic hinge elements

Figure 4-43. Predicted moment distribution in the columns at first positive *D6* cycle (units in kNm)

The moment distribution in the beams plotted in Figure 4-44 shows that the predicted moment in the beams at level 2 are similar between these two analyses. However, as a larger axial compression force was induced in level 1 in the beams with the elongating plastic hinge element, the beam moment next to *Column D* was 16% higher in the analysis with the elongating plastic hinge element.

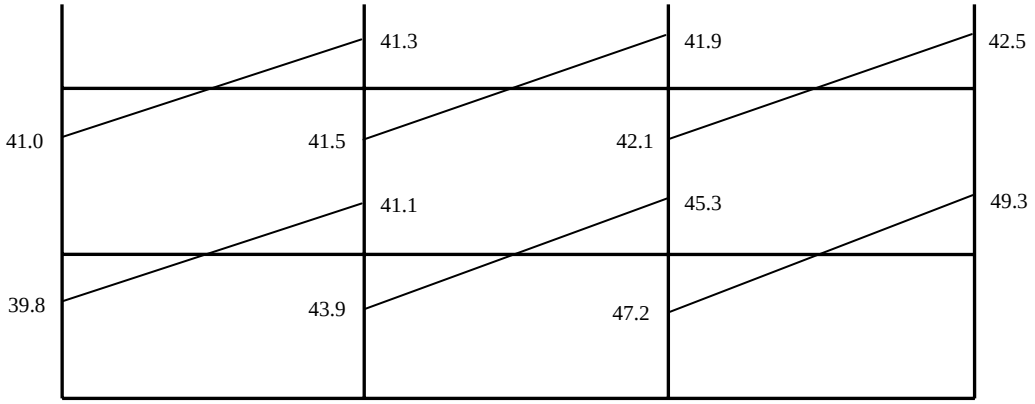

(a) With elongating plastic hinge elements

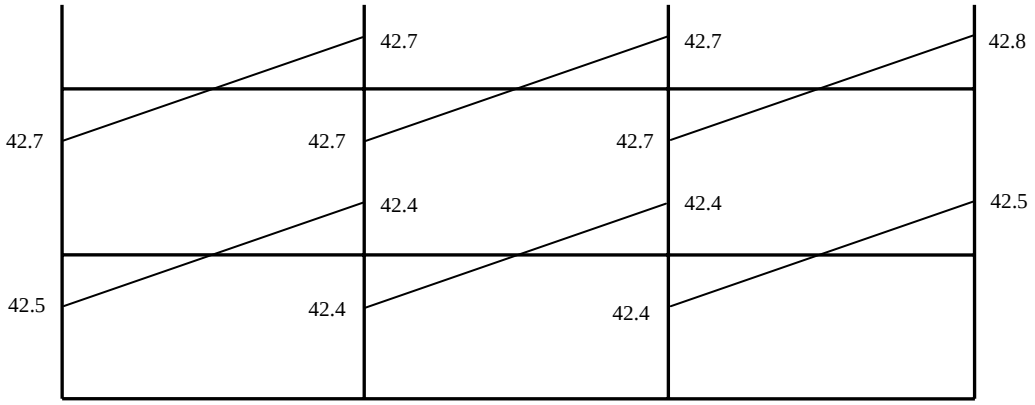

(b) Without elongating plastic hinge elements

Figure 4-44. Predicted moment distribution in the beams at first positive *D6* cycle (units in kNm)

The column shear force and beam axial force comparisons are shown in Figure 4-45. The maximum column base shear occurred in the internal columns in the analysis without elongation, whereas it occurred in the external columns in the analysis with elongation. The predicted axial force in the beams is quite different between these analyses. The magnitude of axial force sustained in the beams with the elongating plastic hinge element is much larger than that without it. The change in column shear force distribution is a result of the induced axial force in beams arising from elongation of the beam plastic hinges.

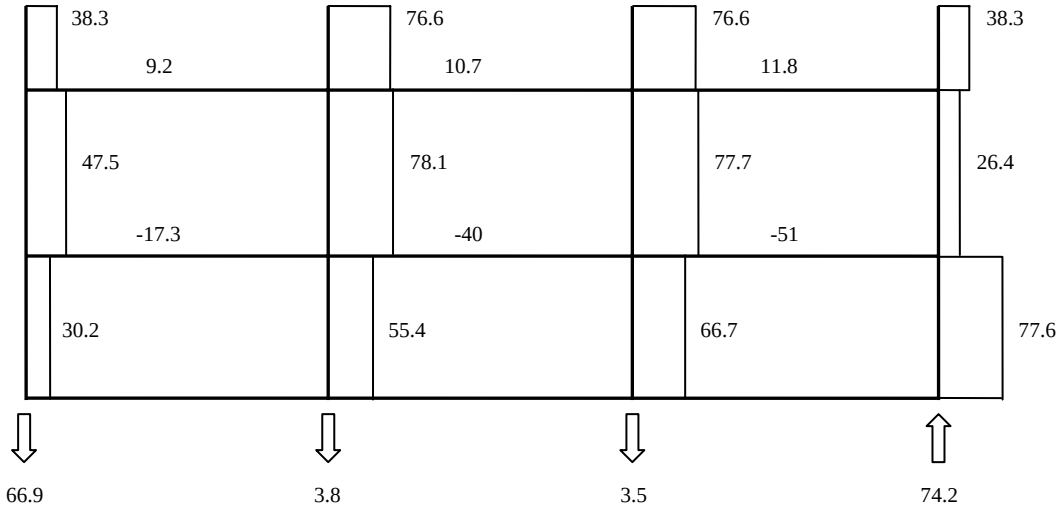

(a) With elongating plastic hinge elements

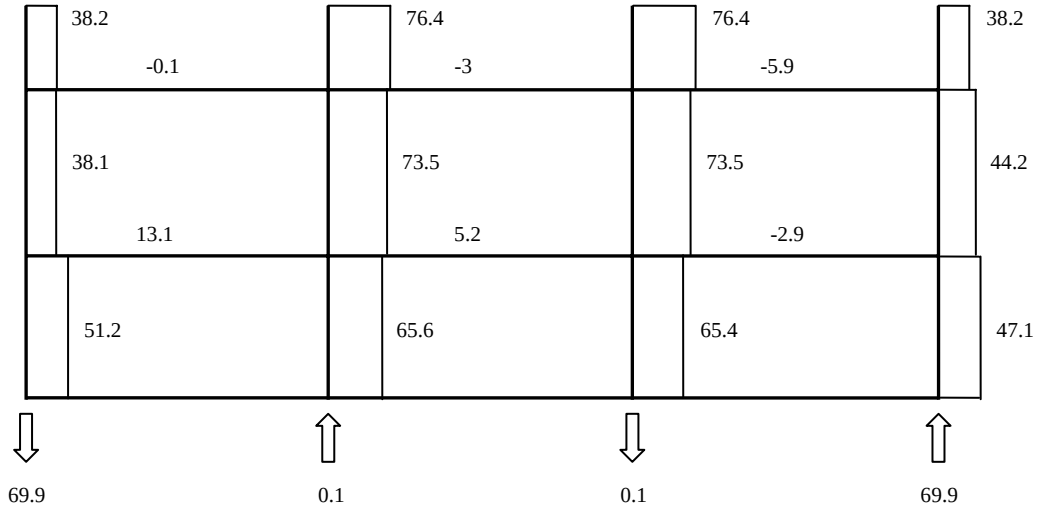

(b) Without elongating plastic hinge elements

Figure 4-45. Predicted shear and axial force distribution at first positive *D6* cycle (units in kN)

The above comparisons of the analytical predictions, with and without the elongating plastic hinge element, have highlighted the importance of beam elongation on the seismic response of RC frames. It was found that elongation of beam plastic hinges changes the axial force induced in the beams, thereby changing the shear force and moment distributions in the columns. In some cases, the changes in the internal forces may lead to column hinging at regions in which was not expected to occur. It was also observed that elongation increases the column drift and rotational demand of plastic hinges on one side of the frame while reducing drift and rotational demand on the other side.

It has been shown both in analysis and experiment that elongation can have a significant effect on the seismic behaviour of RC frames. As the conventional analysis technique using lumped plasticity model does not capture elongation of plastic hinges, it cannot be used to assess the seismic behaviour of frames accurately.

4.5 CONCLUSIONS

In this chapter, the modified elongating plastic hinge element described in Chapter 3 was implemented in 2D frame analyses to predict the cyclic response of: (i) an interior beam-column joint sub-assembly; (ii) a two-bay one-storey determinate frame; (iii) a three-bay one-storey indeterminate frame; and (iv) a three-bay two-and-a-half storey indeterminate frame. The comparisons of the analytical and experimental results have shown that analyses carried out with the elongating plastic hinge elements were able to capture beam elongation and its effect on the cyclic response of frame satisfactorily. Important hysteretic behaviour such as pinching in the force-displacement relationship was also captured in the analysis. It was also observed that in general, elongation is being over-estimated at large displacement cycles. This may be due to buckling of beam reinforcement not being modelled in the analysis.

The analytical predictions together with the experimental results have highlighted the effect of elongation on the seismic response of RC frames. Elongation of the plastic hinges may induce significant axial compression forces in beams at level 1 and axial tension forces in beams at level 2 of a RC frame building. These axial forces in beams

change the moment capacity of the beams, which lead to an increase in shear force and moment demands in the columns. In some cases, it may lead to column yielding at regions which was not expected to occur, based on conventional capacity design philosophy. Elongation of the plastic hinges also changes the deformed shape of the frame and increases the deformation demand on the external columns.

Conventional analytical methods with lumped plasticity line elements to model RC beams cannot predict elongation and its effect on RC structures. Therefore, the proposed plastic hinge element offers a significant advancement in the assessment of RC frame behaviour. The use of the proposed plastic hinge element, unlike the conventional analytical approach, has the added advantage of not requiring any calibration of the modelling parameters.

4.6 REFERENCES

Carr, A. J. (2008a). "RUAUMOKO2D - Inelastic dynamic analysis." Department of Civil Engineering, University of Canterbury, Christchurch, New Zealand.

Carr, A. J. (2008b). "RUAUMOKO3D - Inelastic dynamic analysis." Department of Civil Engineering, University of Canterbury, Christchurch, New Zealand.

Fenwick, R. C., and Nguyen, H. T. (1981). *Reinforced concrete beam-column joints for seismic loading*, Department of Civil Engineering, University of Auckland, Auckland, New Zealand.

Lau, D. B. N. (2007). "Influence of precast prestressed flooring on the seismic performance of reinforced concrete perimeter frame buildings." *Report Number 653*, Dept. of Civil and Environmental Engineering, University of Auckland, Auckland, New Zealand.

McBride, A., Fenwick, R. C., and Davidson, B. J. (1996). "The influence of slabs on the lateral cyclic behaviour of ductile concrete frames." *Report No. 566*, Department of Civil and Resource Engineering, University of Auckland, Auckland, New Zealand.

Standards New Zealand. (2006). *Concrete structures standard: NZS 3101:2006*, Standards New Zealand, Wellington.

To, N. H. T., Ingham, J. M., and Sritharan, S. (2001). "Monotonic non-linear analysis of reinforced concrete knee joints using strut-and-tie computer models."

Bulletin of the New Zealand Society for Earthquake Engineering, 34(3), 169-190.

Wuu, P. J. Y. (1996). "Deformations in plastic hinge zone of RC beam in ductile frame structures subjected to inelastic cyclic loading," Master Thesis, University of Auckland, Auckland, New Zealand.

5 DESIGN OF 3D FRAME-FLOOR SUB-ASSEMBLY TEST

A three dimensional, approximately half-scale, one-storey, two-bay reinforced concrete (RC) frame with floor consisting of prestressed units and cast-in-situ concrete topping was designed and tested in this study. The focus of the test was to investigate the interaction between prestressed flooring system and elongation of beam plastic hinges. The experimental results are also used as a basis for validating the proposed 3D frame-floor analytical model described in Chapter 7.

This chapter describes the design and construction of the sub-assembly test. Previous experimental studies are critically examined with their merits and shortcomings highlighted in Section 5.1. The design considerations and the overall layout of the sub-assembly are described in Section 5.2. The construction process is detailed in Section 5.3. The test setup and the loading arrangement are provided in Section 5.4. Finally, the detailed instrumentation plan is shown in Section 5.5.

5.1 LITERATURE REVIEW

5.1.1 Determinate and Indeterminate Sub-assembly Tests

Many experiments have been carried out in the past on components of ductile frame structures such as beam, column, and beam-column joint sub-assemblies. Most of these tests were carried out under statically determinate conditions so that the structural actions could be determined easily and their construction costs could be minimised. More recently, experimental studies on indeterminate frame sub-assemblies (Zerbe and Durrani 1989; Qi and Pantazopoulou 1991) have shown that these determinate components do not allow for internal redistribution of forces associated with elongation of plastic hinges. In addition, these actions were shown to have significant influence on the seismic performance of RC structures.

An example is the seven storey indeterminate building tested by the joint U.S. – Japan cooperative research program (Wight 1985). This test, with a combined RC frame-

wall system showed that elongation of plastic hinges at the base of the wall caused the transverse beams that were attached to the wall to lift up. This movement was restrained by the columns in the frames attached to the transverse beams on the other side of the structure. As a result, large axial compression force was induced in the wall and large axial tension force was induced in the columns. These actions significantly increased the moment capacity of the wall and hence the overall lateral strength of the system.

To ensure actions induced in the indeterminate frame structures are captured, an indeterminate gravity dominated RC portal frame was tested by Meggett and Fenwick (1989) to study the seismic performance of RC frames containing uni-directional plastic hinges. As illustrated in Figure 5-1, reversing lateral displacements were applied at the top of left column to simulate the seismic action, and two constant point loads were applied on the beam to simulate the gravity action. It was found that as uni-directional plastic hinges formed in the beam (see Section 2.1.1 for definition), the rotational demand in each plastic hinge accumulated under inelastic displacements. Consequently, these plastic hinges were required to sustain higher rotational demands than those in equivalent reversing plastic hinges. This was reflected by sagging of the beam at the mid-span region observed in the experiment. The accumulated inelastic rotations also caused the beam to elongate. The vertical deflection and elongation of the beam measured at the end of the test were roughly 15 and 8 percent of the beam depth respectively.

It should be noted that as the possibility of uni-directional hinges forming in the lower storey of a moment resisting frame is relatively small compared to the formation of reversing plastic hinges (due to the magnitude of seismic moment increases from the top of building to the bottom of building). Most of the analytical and experimental models examined in the past were focused on the behaviour of reversing plastic hinges.

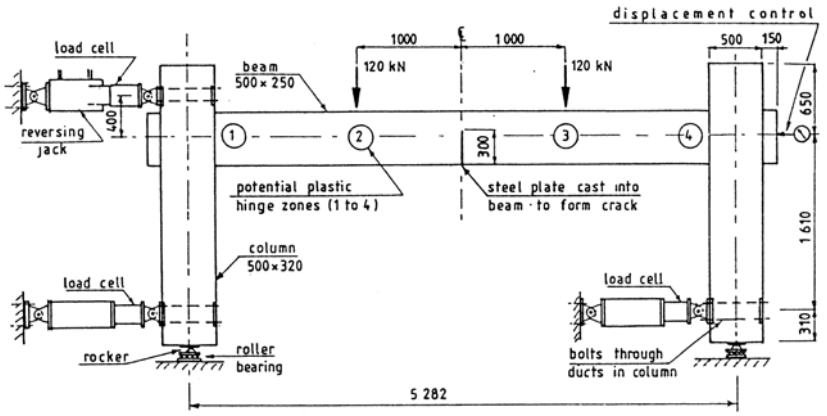

Figure 5-1. Test set up of Meggett and Fenwick (1989)

5.1.2 Indeterminate RC Frame Tests with/without Cast-in-Situ Floor Slabs

Cast-in-situ one-way or two-way concrete floor slabs have been widely used in the construction industry. Experimental studies over the last three decades with cast-in-situ floor slabs (Zerbe and Durrani 1990; Qi and Pantazopoulou 1991; Fenwick et al. 1995) have highlighted the importance of floor slabs on the lateral strength and stiffness of frame structures. It was shown that the presence of floor slabs can increase the negative flexural strength of beams significantly. Design recommendations in New Zealand, NZS 3101:1995 (Standards New Zealand 1995), were made to estimate the level of floor participation by specifying an effective flange width that should be considered when calculating the flexural strength of beams (Cheung 1991).

Zerbe and Durrani (1989; 1990) tested a number of indeterminate two-bay, one storey RC frame structures with and without a floor slab. In these indeterminate frames, the top and bottom of each column was pinned to the support, which is able to rotate but not translate as shown in Figure 5-2. With this arrangement, elongation of plastic hinges in the beam was restrained by the external columns. Consequently, an artificially high axial compression force was induced in the beams which increased their flexural strength and improved the performance of the beam-column joints. It should be noted that this kind of restraint cannot be expected to form in a real structure and therefore it is difficult to draw any firm conclusion from their results other than that elongation can have a significant influence on the seismic performance of frames.

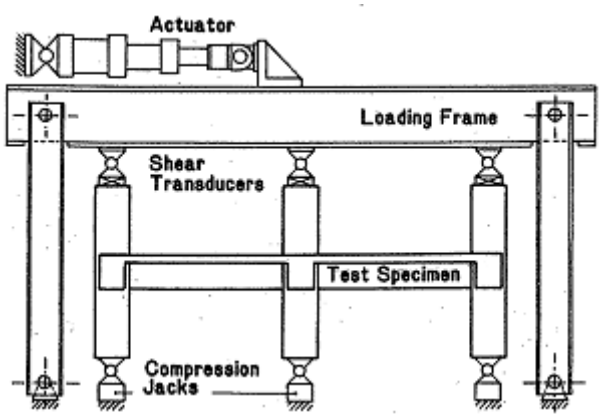

Figure 5-2. Test set up of Zerbe and Durrani (1989; 1990)

Qi and Pantazopoulou (1991) tested a single storey, two-bay sub-assembly with cast-in-situ floor slab as shown in Figure 5-3. The test setup was representative of a first storey floor beam where the columns were fixed to the foundation. In order to minimise the artificial restraint arising from the experimental set-up and the applied loading; the displacement of the MTS actuators was set equal to the measured beam growth within the respective span. The test results have shown that the floor slab contributed significantly to the flexural strength of the main beam particularly at the internal column. At the external columns, slab participation was limited by the torsional resistance of the transverse beams. Based on their results, an effective flange width of two beam depths (for the interior plastic hinges) and one beam depth (for the exterior plastic hinges) was recommended for calculating the negative flexural strength of the beam.

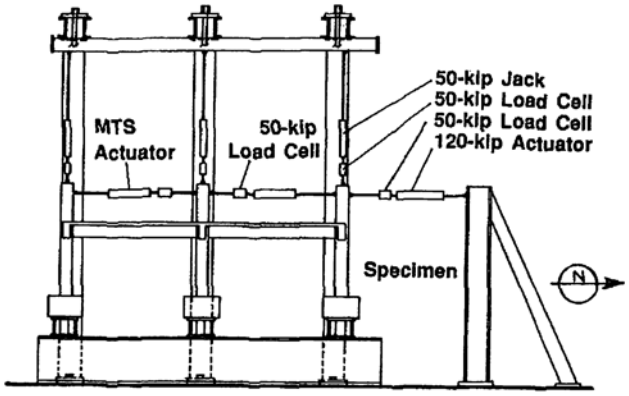

Figure 5-3. Test set up of Qi and Pantazopoulou (1991)

Two three-bay, one-storey internal RC moment resisting frames with and without a floor slab were tested by McBride et al. (1996). The bottom of each column was fixed to the strong floor by a one way pin and the lateral force was applied to the unit by four hydraulic jacks connected to the top of columns as shown in Figure 5-4. A different loading regime to that of Qi and Pantazopoulou was used in an attempt to minimise the artificial restraint in the main beams. The force in each of the four columns was kept at a constant ratio of 1:2:2:1 between one another. From their tests, it was found that the existence of the slab increased both the initial stiffness and the overall strength of the system; however, it had little influence on the amount of elongation in beam plastic hinges.

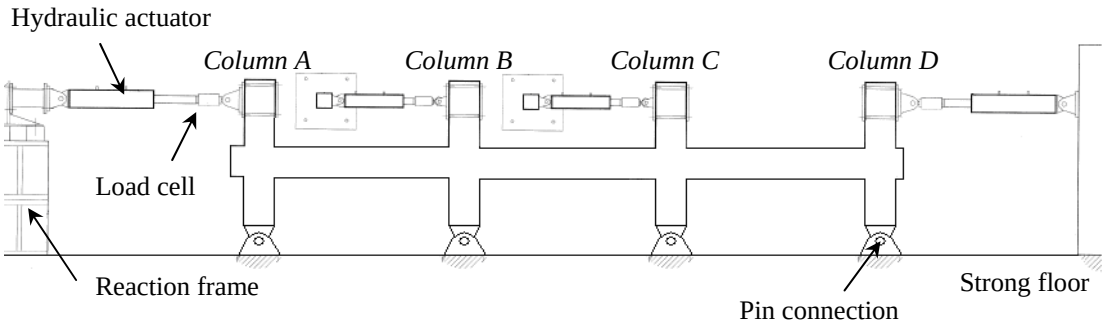

Figure 5-4. Test set up of McBride (1996)

Following on from these two tests, Wuu (1996) tested a three-bay, two-and-a-half storey RC frame to further investigate the effect of beam elongation on the cyclic response of moment resisting frame. The sub-assembly represents the lower part of a multi-storey frame. To reduce the cost and complexity of the test unit, the slabs were omitted in the experiment. The force applied to each of the four columns was again kept at a constant ratio of 1:2:2:1. The overall test arrangement is shown in Figure 5-5. The experimental results indicated that elongation, which developed in the plastic hinges, had a marked influence on the behaviour of the frame. It changed the distribution of shears and moments in the columns and induced axial compression and axial tension in the beams at the first and second storey, respectively. It also induced higher deformational demands on the external columns where additional plastic hinges were formed in the columns just above the first storey beam.

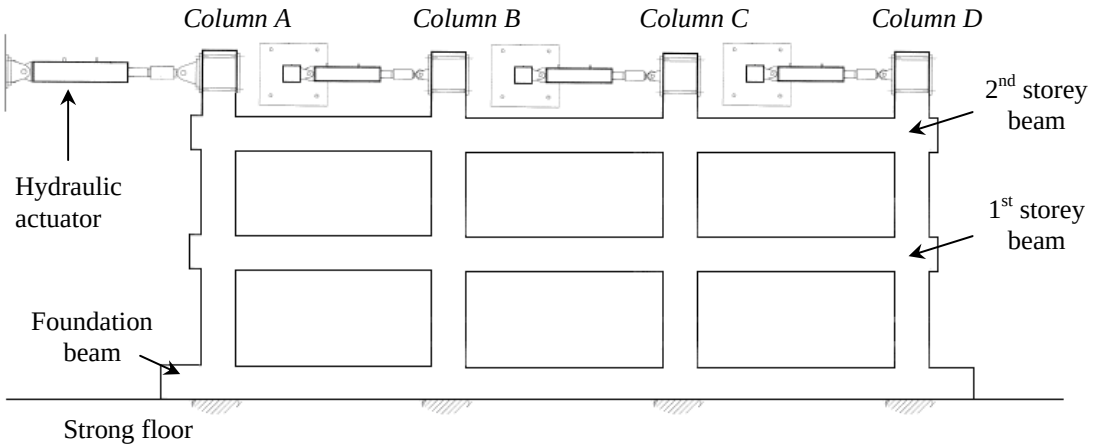

Figure 5-5. Test setup of Wuu (1996)

5.1.3 Indeterminate RC Frame Tests with Floor Slab Consisting of Prestressed Floor Units

Prestressed floors have been widely used in long span structures. Recent experimental studies in New Zealand have highlighted the effect of prestressed floor units on the lateral strength and stiffness of moment resisting frames. It was found that the presence of prestressed floor units increases the flexural strength of beams much more than that specified in the codes.

Matthews (2004), Lindsay (2004) and MacPherson (2005) carried out a series of large scale experimental tests in which the influence of different connection details between the prestressed floor units and the surrounding frames were examined. The tests were built to represent a mid-height storey of a multi-storey frame. The layout and setup of the tests is shown in Figure 5-6. The loading system consisted of a primary loading frame and a secondary frame working together to ensure that elongation in the beam plastic hinges was not exaggerated nor restrained and that the columns remained parallel throughout the test.

The test results have shown that NZS 3101:1995, significantly under-estimates the strength of the beams when coupled with prestressed floor units. A method for assessing the strength of beam plastic hinges where the prestressed floor unit span passes the column, as indicated by crosses in Figure 5-6(a), was developed by

Fenwick et al. (2006). However, the method required the effective flange width of floor slab to be estimated.

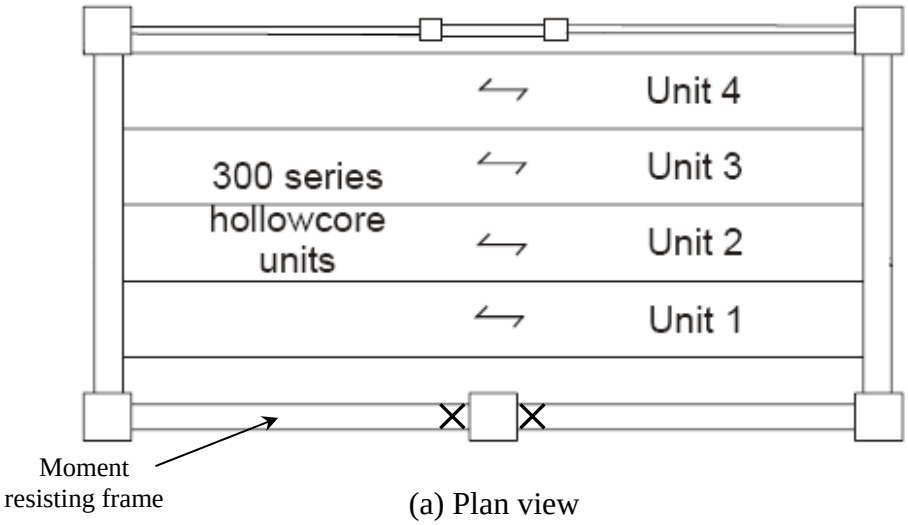

(a) Plan view

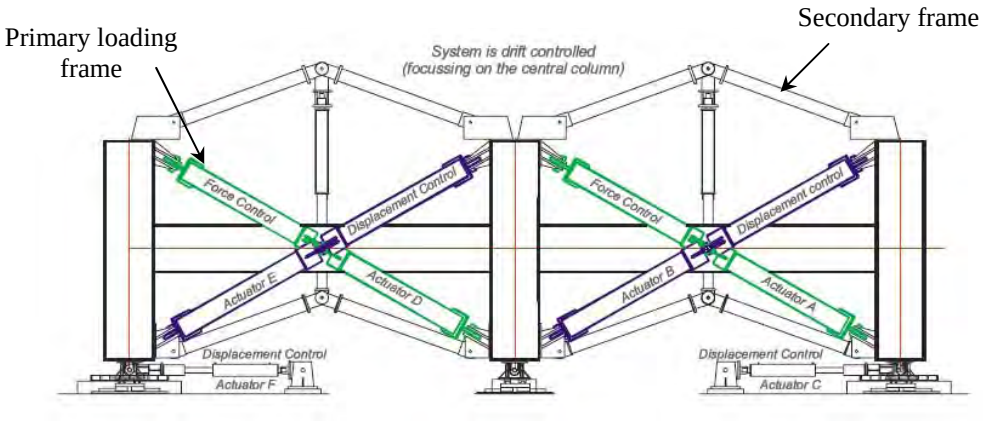

(b) Test arrangement

Figure 5-6. Setup of McPherson's experiment (2007)

Lau (2007) tested one three-bay frame with floor slab containing precast prestressed floor units to investigate the interaction between beams and prestressed floors under cyclic displacements. The test was built to represent the mid-height storey of a multi-storey frame. As shown in Figure 5-7, cyclic displacements were applied at the top and bottom of each column through six hydraulic actuators. In order to minimise the restraint arising from the test set-up and the loading arrangement; the displacement of each actuator was incremented so that the distance between the top and bottom of each column is equal to the measured beam growth within the respective span. However, this loading regime cannot control the magnitude of the applied forces at

the top and bottom of each column. Therefore, an artificial restraining force may still be exerted to the beam which may restrain or exaggerate beam elongation.

The experimental results have shown that NZS 3101:1995 under-estimates the over-strength of beams by a considerable margin. This may shift the designed ductile beam sway mechanism to an undesirable column sway mechanism in an event of a major earthquake. The level of strength enhancement was found to vary between different structural arrangements, for example: (i) where prestressed floor units span past a column, i.e., Column A and Column C in Figure 5-7(a); and (ii) where prestressed floor units are supported on a transverse beam connected to a column, i.e., Column B in Figure 5-7(a). The measured strength enhancement was significant in both cases and it was concluded that a practical analytical method is required to establish design rules for the interaction between moment frames and floor slabs containing prestressed units, especially where prestressed floor units are supported on transverse beams connected to an internal column.

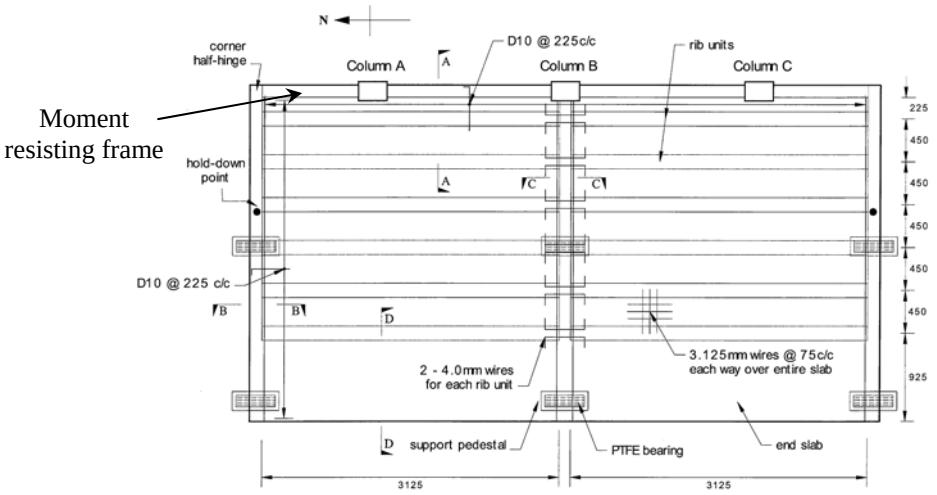

(a) Plan view

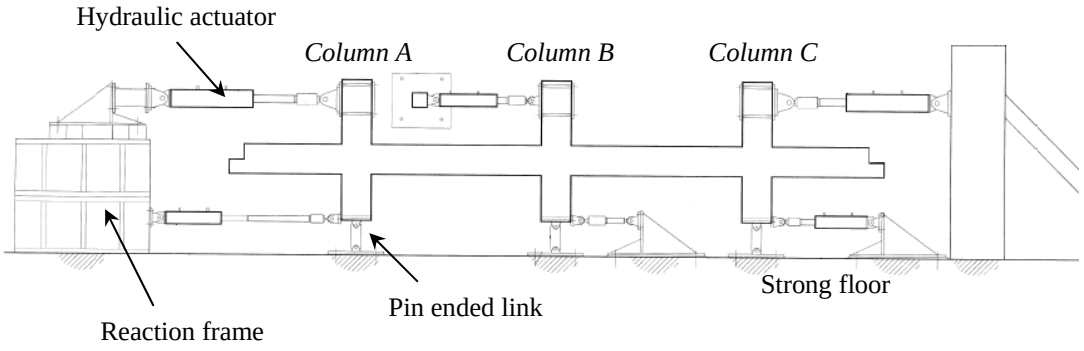

(b) Test arrangement

Figure 5-7. Setup of Lau's experiment (2007)

5.1.4 Summary

Based on the experimental research examined above, the following key observations can be drawn:

1) Response of indeterminate frame sub-assemblies is different from the combined response of its determinate components. This is primarily due to redistribution of internal forces that may occur as a result of plastic hinge elongation in the indeterminate system, which does not develop in the individual determinate tests.
2) The presence of a floor slab can increase the stiffness and strength of beams significantly. This may alter the column-to-beam flexural strength ratio and the designed strength hierarchy.

3) Experimental setup, boundary conditions, loading arrangement, and loading history can affect the inelastic cyclic response of the indeterminate frame system. Hence, the experiment should be designed carefully to represent realistic conditions.
4) The presence of floor slabs containing prestressed floor units can increase the negative flexural strength of beams much more than that specified in the design codes around the world. The level of strength enhancement varies between different structural arrangements. A practical method of assessing the strength enhancement where prestressed floor units are supported on transverse beams connected to an internal column is yet to be developed.

5.2 DETAIL OF THE SUB-ASSEMBLY

A one-storey, two-bay, half-scale frame-floor sub-assembly was constructed and tested in this research project. The sub-assembly is designed to represent a portion of the mid-height storey of a ductile moment resisting frame as shown in Figure 5-8. The perimeter of the building consists of moment resisting frames in one direction and structural walls on the other direction. The rest of the internal structure consists of gravity frames.

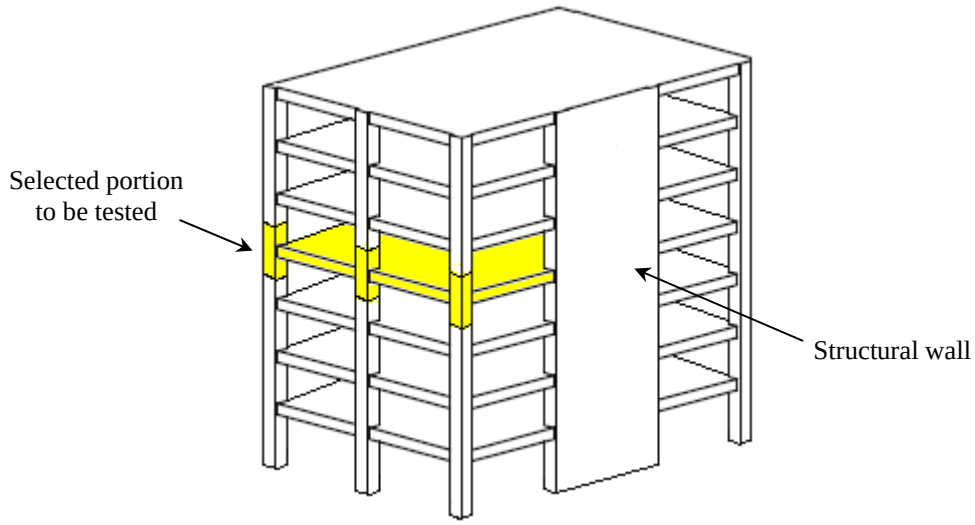

Figure 5-8. Prototype building

The members in the sub-assembly were designed and detailed in accordance to NZS 3101:1995. The columns were designed to remain elastic throughout the test to ensure

that the maximum strength of the beam plastic hinges could be developed. Figure 5-9 summarises the details of the sub-assembly. The specimen had a bay length of 3.05m and a bay width of 6.1m. In the prototype building, the beams in the gravity frames are much smaller in depth compared to the beams in the moment resisting frames; consequently, beam elongation is expected to be much smaller in the gravity frames. In addition, the gravity frames would remain essentially elastic under seismic action. Therefore, to represent the stiff continuation of floor diaphragm in the rest of the building, the floor was connected to a 175mm thick heavily reinforced end slab as shown in Figure 5-9(a). It can also be seen from Figure 5-9(a) that the bay width was purposely designed to be wider so that the cracks can propagate further into the floor. This also prevented the stiff end slab from artificially restraining elongation of beam plastic hinges.

The details of the key structural members are shown in Figure 5-10. The columns were 500mm square and the longitudinal and transverse beams were 200mm wide by 400mm deep. The transverse beams had a seating ledge of 40mm on each side. The flooring system consisted of 100mm deep precast prestressed Stahlton^{TM} ribs spaced at 500mm centres with 45mm thick cast-in-situ concrete topping. The prestressed floor units were supported on three transverse beams connected to the columns. The typical reinforcement details in a floor with prestressed floor units are Grade 500 deformed 12mm diameter bars at 300mm centres in 75mm thick topping. To preserve the stress levels between the sub-assembly and a typical structure, Grade 300 deformed 10mm diameter bars were used in the topping at 210mm centres in both directions in this test. These bars were lapped with the same size starter bars along the perimeter beams. The length over which the bars are lapped was calculated based on NZS 3101:1995.

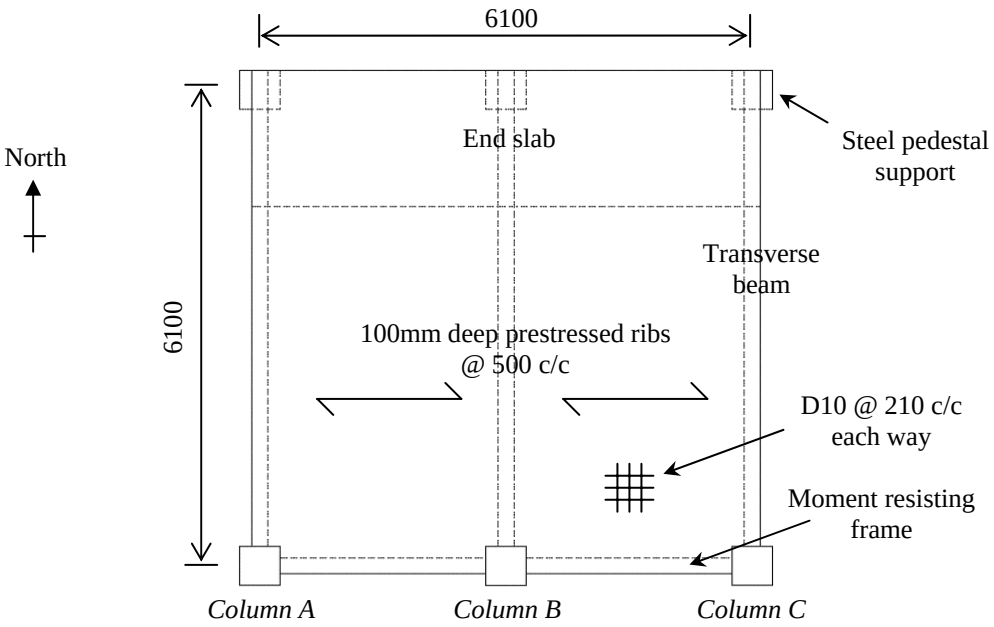

(a) Plan view

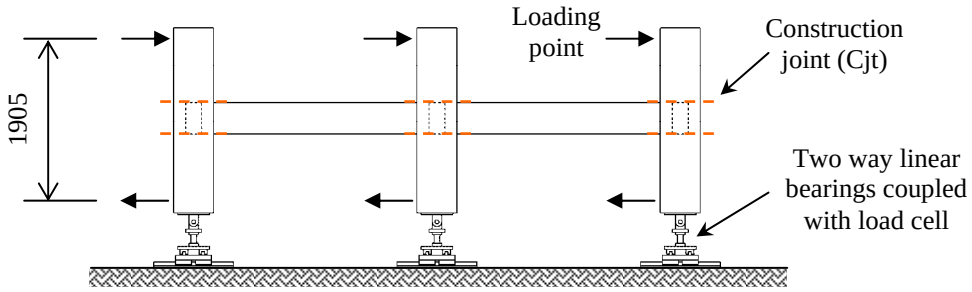

(b) Front elevation

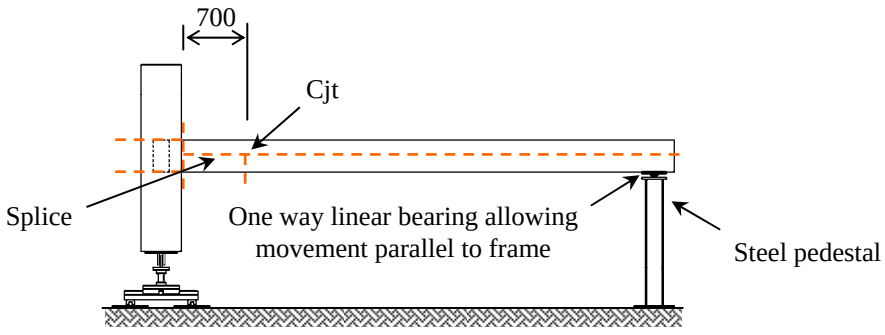

(c) Side elevation

Figure 5-9. Dimension and layout of the sub-assembly (units in mm)

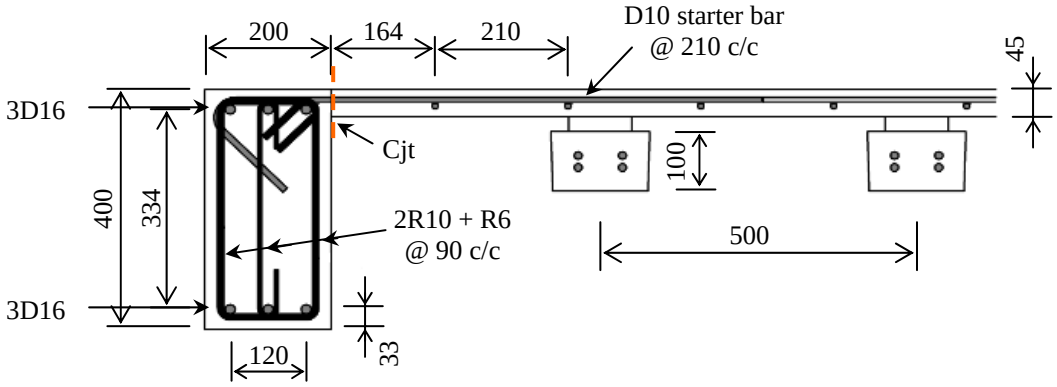

(a) Longitudinal beam

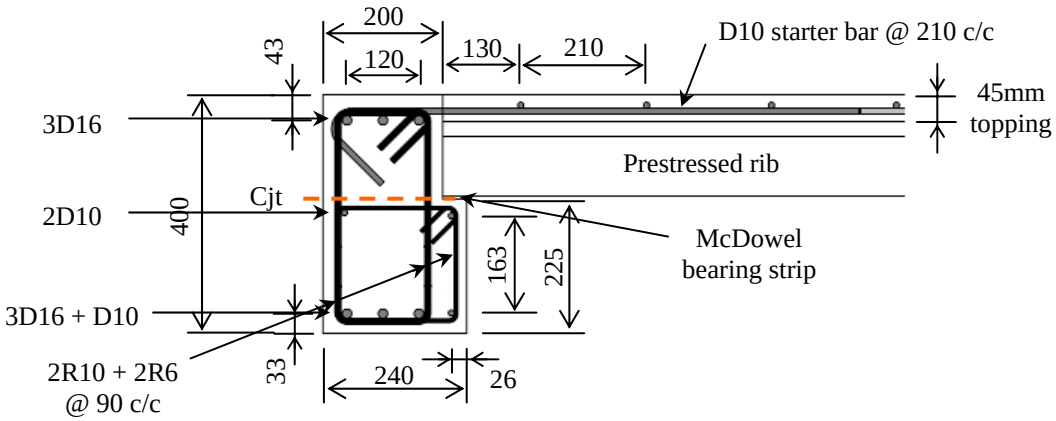

(b) External transverse beam

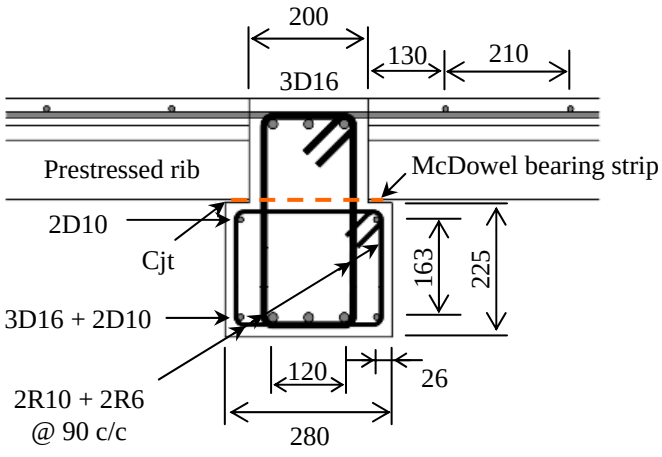

(c) Internal transverse beam

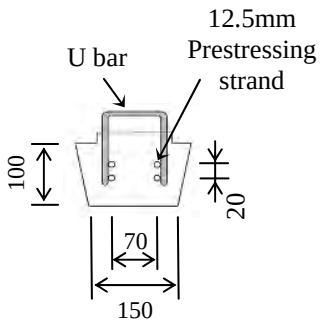

(d) Stahlton™ prestressed rib

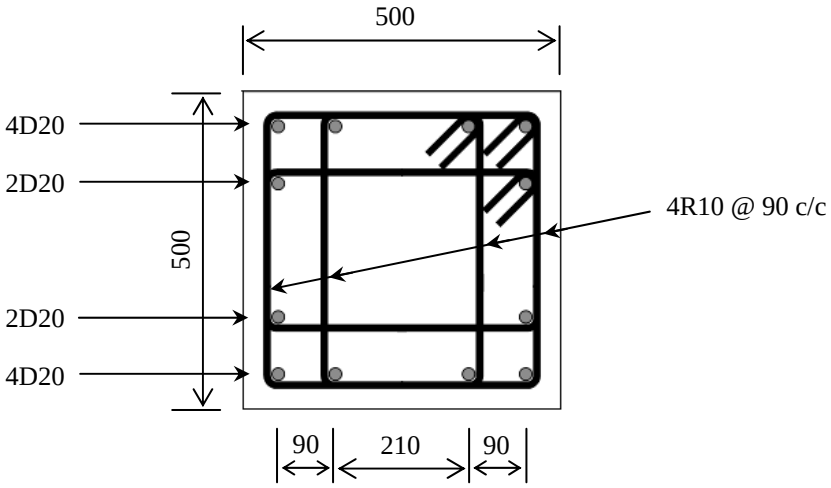

(e) Column

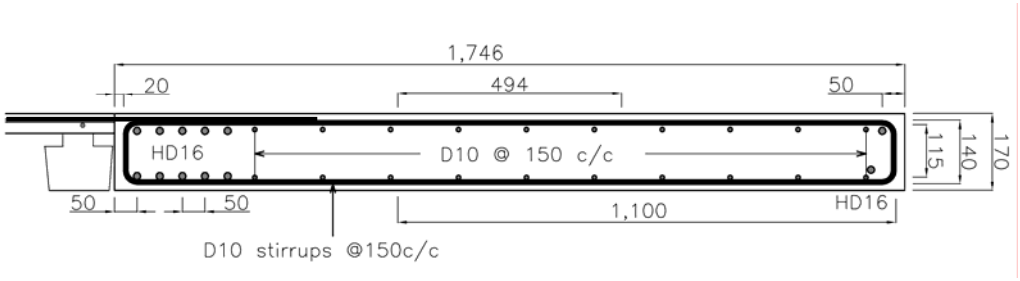

(f) End slab

Figure 5-10. Cross section details of the key structural members (units in mm)

5.3 CONSTRUCTION SEQUENCE

The sub-assembly was built in four different stages. First, the three bottom columns with reinforcing bars protruding to the top; full depth longitudinal beam including beam-column joints with floor and transverse beam starter bars overhanging to the side; and three half-height transverse beams were precast in the laboratory, as shown in Figure 5-11. The beam-column joints contained ducts that allowed the protruding column reinforcing bars to pass through the joint.

These precast members were then erected and the beam-column joints were grouted by local contractors, as shown in Figure 5-12. Next, the top of columns and the lap splices between the transverse beams and beam-column joints were cast-in-place (see Figure 5-13). Finally, the prestressed ribs were placed between the transverse beams;

and the floor topping, the end slab and the top half of the transverse beams were poured (see Figure 5-14).

It should be noted that in practice, the timber infill for the slab formwork would remain underneath the floor slab. However, it was removed in this test to simplify the model and to prevent the formwork from contributing to the overall response of the system. This also enabled cracks to be observed on the lower surface of the slab. To ensure that the floor slab formwork can be removed easily, the edge of the formwork was rounded and the formwork was pre-cut, as shown in Figures 5-14(c) and (d). The test specimen at the completion of construction is shown in Figure 5-15.

The reinforcing bars were purchased and bent from a local reinforcing steel supplier. 30MPa concrete, 13mm aggregate particles with 100mm slump was ordered from a local ready mix company for each cast. The concrete surface was cured with wet sacks and tarpaulins for seven days. Twelve concrete cylinders were prepared for each cast using the standard technique.

(a) Column cage

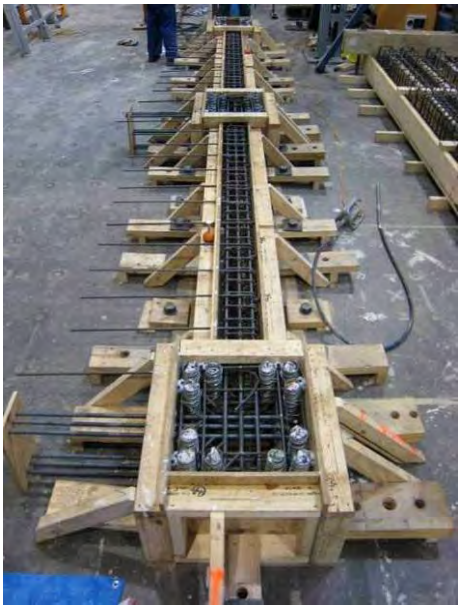

(b) Main beam unit ready for casting

(c) Pouring transverse beams

(d) Columns after being trowelled

(e) Water blasting the construction joint

(f) Roughened the construction joint

Figure 5-11. Photos of first stage of construction

(a) Two way linear bearings underneath the columns of the moment resisting frame

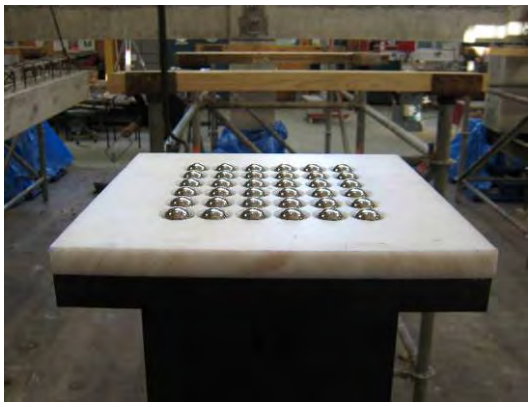

(b) Ball bearings for the central back pedestal

(c) Lowering the column in place

(d) Lowering the precast beam unit in place

(e) Lowering the transverse beam in place

(f) Linear bearing for the external back pedestal

(g) Dry pack the perimeter of beam-column joint

(h) Pressure grouting

Figure 5-12. Photos of second stage of construction

(a) Transverse beam cage

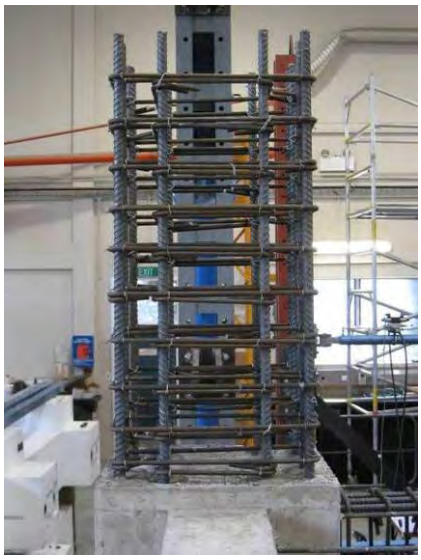

(b) Column cage

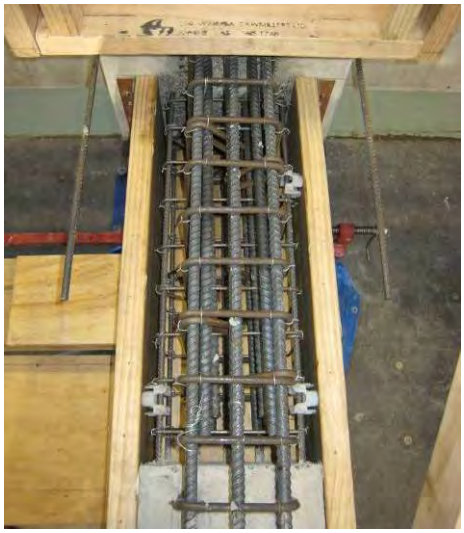

(c) Transverse beam splice ready to cast

(d) Top of column ready to cast

(e) Pouring transverse beam splice

(f) Curing the concrete

Figure 5-13. Photos of third stage of construction

(a) Lowering prestressed ribs in place

(b) Scaffolding for the end slab

(c) Rounded edge for floor slab formwork

(d) Transverse beam and slab formwork

(e) Caging for the end slab

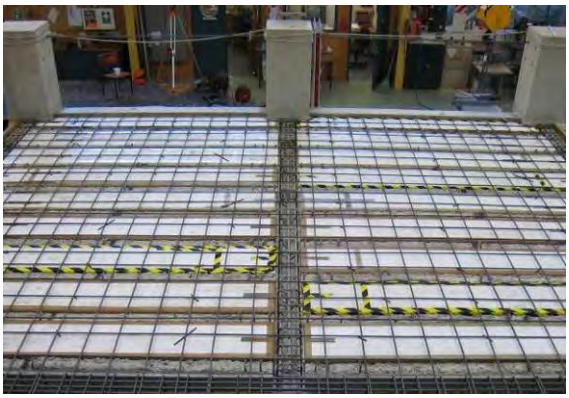

(f) Caging for the floor topping

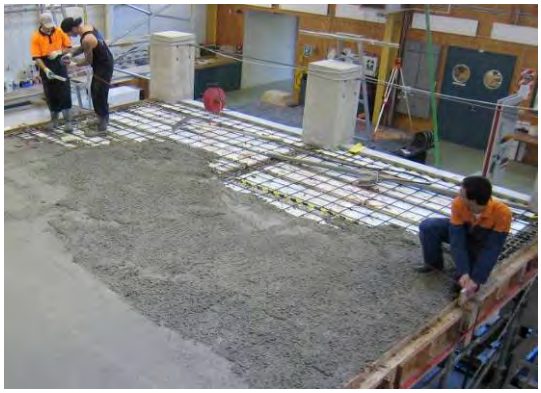

(g) Taking the floor level while pouring

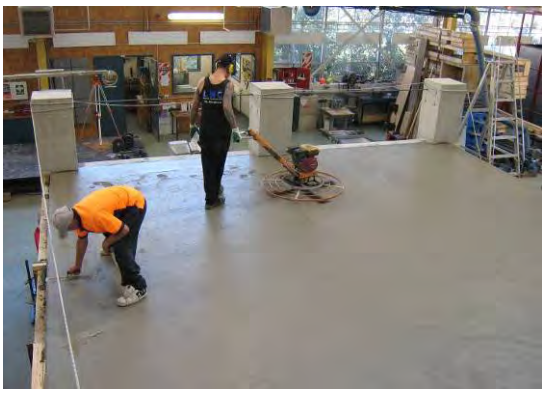

(h) Trowelling/floating the floor slab

Figure 5-14. Photos of final stage of construction

(a) Front view

(b) Side view

(c) View from underneath the floor

Figure 5-15. Completed test specimen

5.4 TEST SETUP AND LOADING ARRANGEMENT

Figure 5-16 shows the setup of the sub-assembly test. Uni-directional cyclic displacements were applied in-plane to the moment resisting frame at the top and bottom of each column. The columns were linked together by hydraulic actuators. Column drift was driven by a pair of hydraulic actuators between the reaction frame and *Column A*. With this loading arrangement the axial force accumulates in the actuators from *Column C* towards the reaction frame. Consequently, the axial force is the highest in *Rams A* and *B* and smallest in *Rams E* and *F*. Subsequently, two different sizes of actuators were used; 1000kN axial capacity actuator was applied to *Rams A* to *D* and 250kN axial capacity actuator was applied to *Rams E* and *F*. Extension brackets were made for the smaller hydraulic actuators as shown in Figure 5-16. All the pin connections in the experiment, as shown in Figure 5-16, contained spherical bearings that allow out-of-plane rotation to develop.

The columns were supported on two way linear bearings allowing movement in the horizontal plane. The external transverse beams, below the end slab, were supported on steel pedestals with one way linear bearings allowing floor movement parallel to frame, as shown in Figure 5-16(b). The central transverse beam, below the end slab, was supported on a steel pedestal with ball bearings allowing movement in the horizontal plane, as shown in Figure 5-12(b). With this setup, the exterior transverse beams are restrained against rotation near the end slab. The torsional strength of the exterior transverse beams may provide additional lateral resistance to the moment resisting frame. It should also be noted that if the exterior transverse beams are not restrained against rotation near the end slab, the precast units and concrete topping may still provide some torsional resistance to the transverse beams. This is elaborated in Chapter 6.

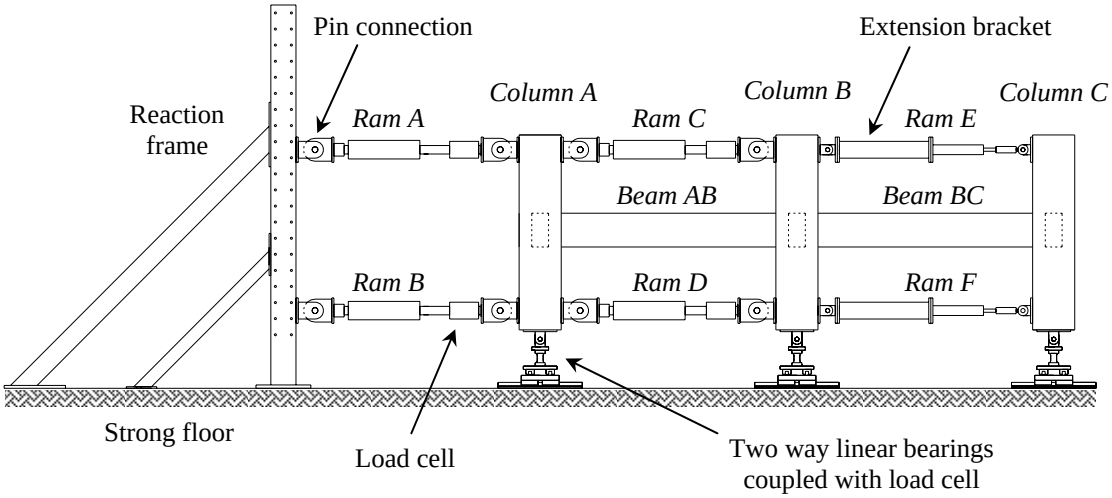

(a) Front view

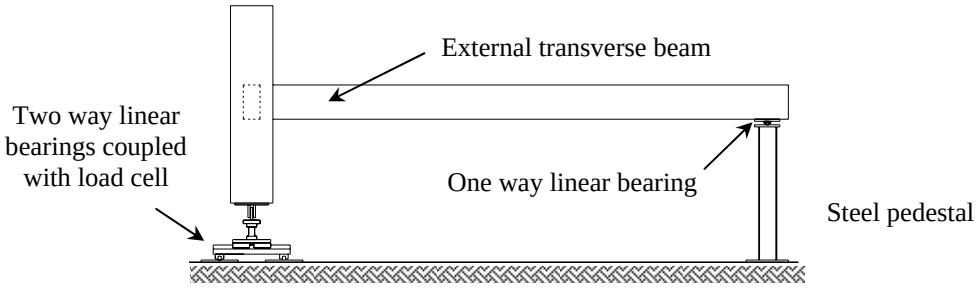

(b) Side view

Figure 5-16. Test arrangement and loading setup

5.4.1 Loading Protocol

The loading was displacement controlled; quasi-static cyclic loading was applied to the top and bottom of each column through six hydraulic rams as illustrated in Figure 5-16(a). The loading history started with one elastic cycle at ±0.15% drift. This was done to check the loading regime, control system, instrumentation, and data loggers. Two cycles at ±0.25%, ±0.35% and ±0.5% drifts were then applied to obtain the elastic behaviour of the frame.

Following these elastic cycles, two cycles at ±0.75% and ±1% drifts were applied; in subsequent cycles the peak displacements were increased in increments of 0.5% drift until the peak lateral force in a cycle was less than 65% of the maximum force

sustained. In between each peak drift magnitude, a small cycle equal to 30% of the peak cycle amplitude was applied. The overall loading history is plotted in Figure 5-17.

It should be noted that due to the scale of this experiment, testing was carried out over several weeks. Consequently, testing was stopped over night. The test was stopped at zero storey shear such that the stress induced in the system was minimised.

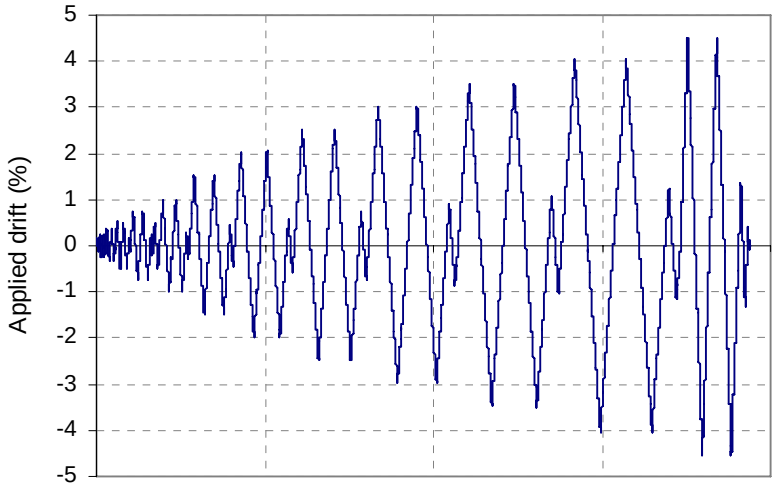

Figure 5-17. Experimental loading history

Within each displacement increment, the displacements at the top and bottom of each column were corrected iteratively to ensure that the columns remained parallel to each other; beam elongation was not restrained nor exaggerated; and the centre beam-column joint remained close to the original position. In order to control the six hydraulic actuators simultaneously, a valve controller programme was developed in LabVIEW, a graphical programming environment that uses intuitive graphical icons and wires that resemble a flowchart.

To allow beam elongation to develop freely, the forces applied at the top and bottom of each column must be equal and opposite. This can be achieved by extending/retracting the pair of actuators in each column depending on the combined forces. For example, if the combined forces in the column induce compression force to the beam, the pair of actuators will extend by the same amount until the forces are equal and opposite.

During the elastic cycles, it was found that *Columns B* and *C* did not move as much as the displacement applied at *Column A*. For example, when 0.75% drift was applied to *Column A*; *Columns B* and *C* were only sustaining 0.6% and 0.5% drift respectively. This reduction in column drift was found to arise due to slop and elastic movement within the fittings connecting the actuators to the columns. The controller program was modified so that additional drift was added to *Columns B* and *C* such that all three columns remained parallel. The additional drift was expressed as a function of the averaged shear force within each column. The relationship is described in detail in Section 6.2.2.

To ensure the internal beam-column joint remained close to the original position during the test, elongation arising in *Beam AB* was subtracted from the applied displacement in *Column A*. The iterative procedure for calculating the column displacement within each incremental step is summarised in Figure 5-18. Here, compression force and ram extension are taken as positive values.

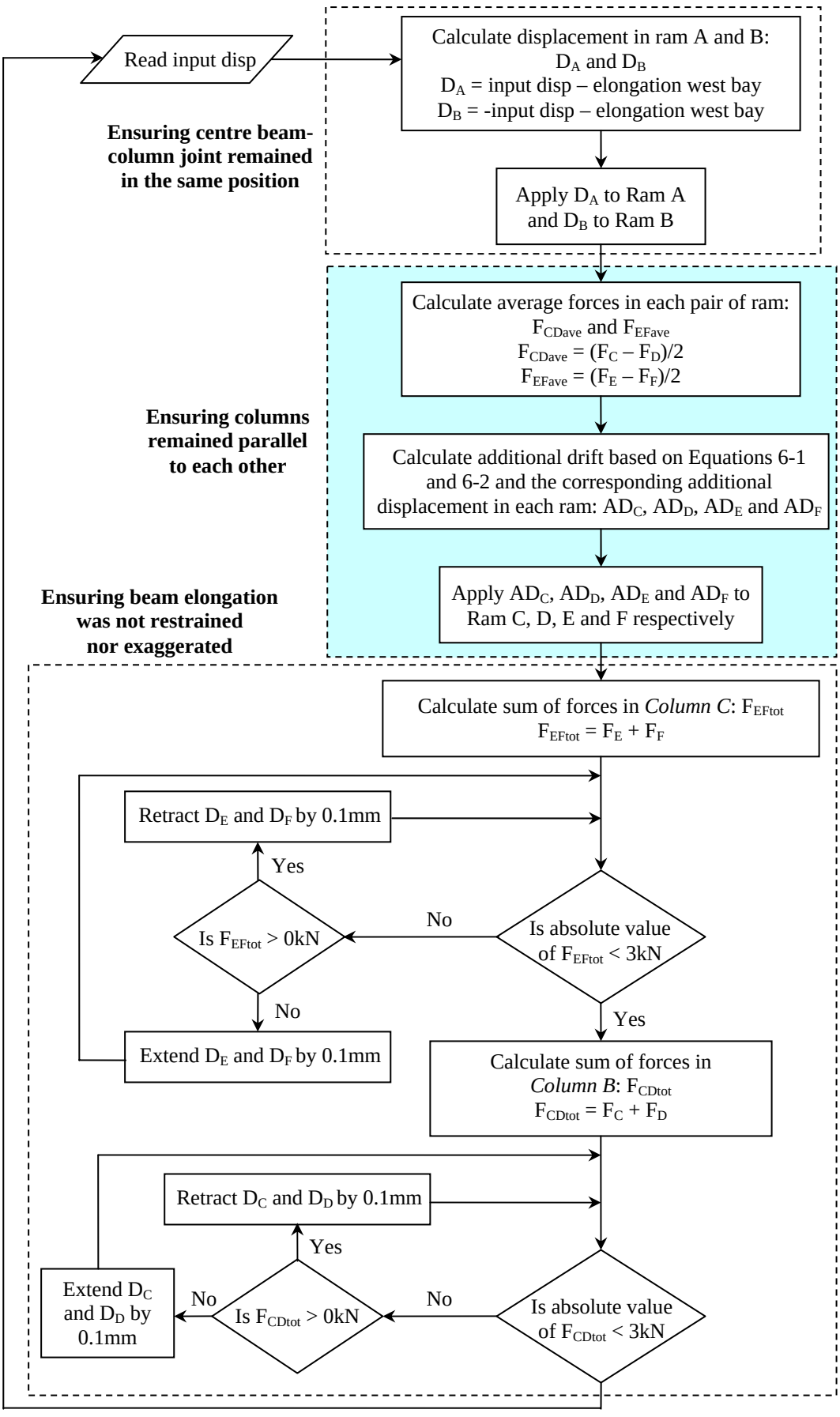

Figure 5-18. Flow chart showing the iterative procedure within each incremental step

5.5 INSTRUMENTATION

The sub-assembly was extensively instrumented with load cells, linear and rotary potentiometers, inclinometers, DEMEC points and sonic displacement transducers to gather as much information as possible on the force and deformation responses of the sub-assembly. The deformation measured in the tests includes: inclination of columns in two directions; flexural rotation, shear deformation, and elongation in the beams and columns; shear distortion of the beam-column joints; in-plane floor deformation; relative movement between floor and longitudinal beams; twisting in the transverse beams; and movement of the supports. A total of 253 channels were used to record the experimental data. In addition, 1100 DEMEC readings were taken on the floor at the selected peak displacement cycles. Figure 5-19 shows the instrumentation on the frame.

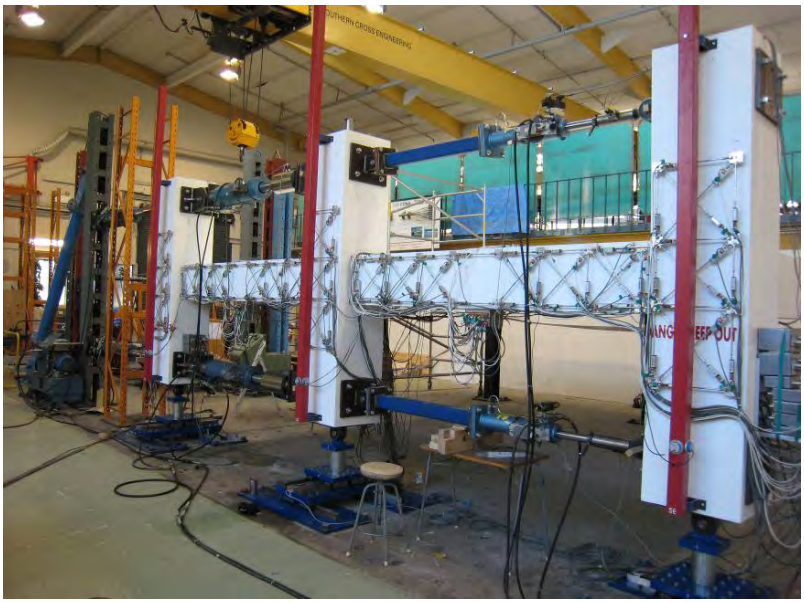

Figure 5-19. Overall instrumentation on the moment resisting frame

5.5.1 Measurement of Forces

Each hydraulic actuator was coupled with a load cell to monitor the shear force applied to the columns. Load cells were also placed at the bottom of each column to measure the axial force induced in the column. These load cells were made of hollow cylinders, machined from high strength steel, with four strain gauges on four

quadrants of each load cell that measure strain. The load cells were calibrated so that the axial force can be converted from strain measurements directly.

5.5.2 Measurement of Frame Deformations

Inclinations of *Columns A* and *C* were interpolated using measurements from rotary potentiometers connected between instrumentation towers and the top and bottom of each column as shown in Figure 5-20. Two inclinometers were also mounted on each column to monitor the average column drifts both parallel and transverse to the moment resisting frame.

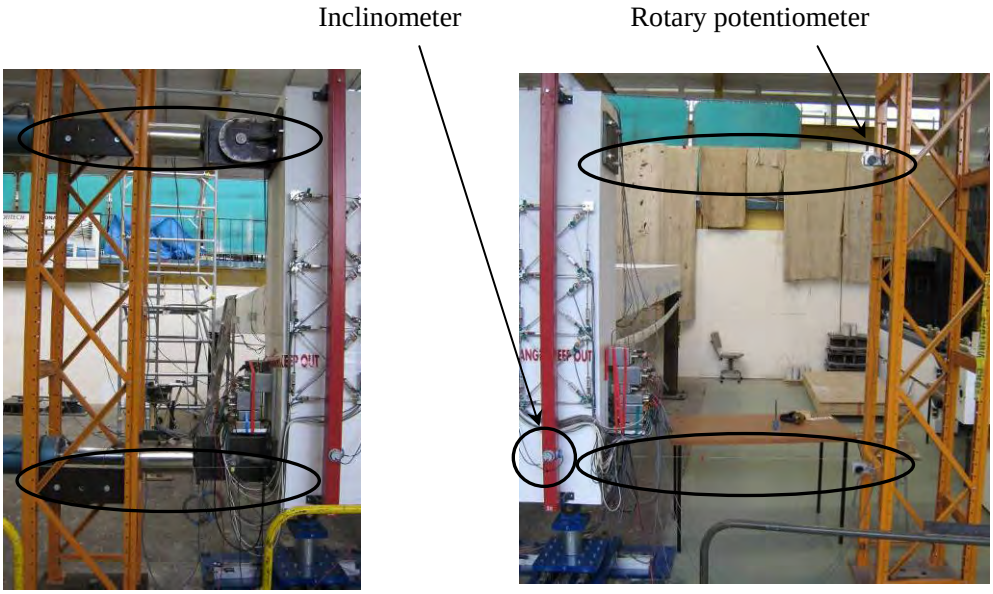

(a) Rotary potentiometers on *Column A* (b) Rotary potentiometers on *Column C*

Figure 5-20. Rotary potentiometers used to calculate column drift

Flexural rotation, shear deformation and elongation of beams, columns and beam-column joints were measured via the linear potentiometer rosettes, as illustrated in Figure 5-21. In this figure, the blue lines represent potentiometers with 50mm measuring length and the black lines represent potentiometers with 30mm measuring length. The longer potentiometers were placed over the plastic hinge region where large displacement is expected to occur. Rotary potentiometers mounted between the columns were also used to monitor elongation in each beam bay.

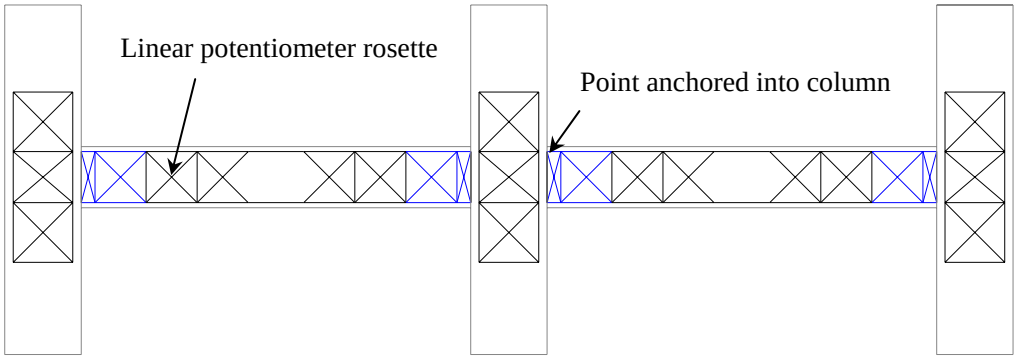

Figure 5-21. Linear potentiometer layout on the moment resisting frame

Figure 5-22(a) shows the connection detail of the linear potentiometers in the column. The end connections for the potentiometers in the column consist of a square plate, a 70mm threaded rod, and three nuts. The threaded rod was embedded in the pre-drilled 20mm deep hole and was fixed in place with an anchor using epoxy glue. The square plate was secured at the specified height by tightening the two adjacent nuts and the linear potentiometers were fastened to the plate using 6mm bolts. This arrangement ensured that the potentiometers were kept at the same level so that error associated with out-of-plane movement of the rods could be minimised. Also to minimise the error, the linear potentiometers were mounted as close as possible to the concrete surface.

Figure 5-22(b) shows the connection detail of the linear potentiometers between the beam to column face region. The connection for the potentiometers in the beam-column face consisted of an angle plate, a 150mm threaded rod and two nuts. The threaded rod was embedded in the pre-drilled 120mm deep holes and was fixed in place using epoxy glue. The angle plate was secured close to the column face by tightening the adjacent nuts. The linear potentiometers were fastened to the plate using 6mm bolts.

Figure 5-22(c) shows the connection detail for the potentiometers in the beam. 70mm threaded rod was screwed into the stud welded onto the beam reinforcement. An additional stud was added to tighten the rod. The square plate was then secured at the specified level by tightening two adjacent nuts. The linear potentiometers were fastened to the plate using 6mm bolts.

(a) Side view of column with potentiometers (b) Beam-column junction

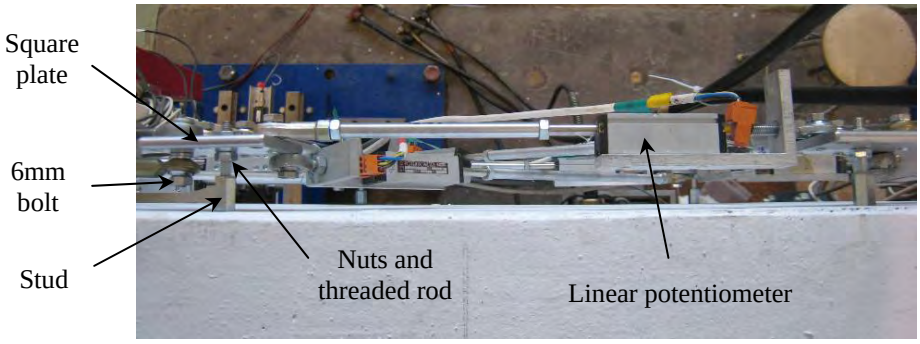

(c) Plan view on main beam

Figure 5-22. Connection details of the linear potentiometers

The rosette arrangement, as shown in Figure 5-23, allows the averaged flexural rotation, θ, shear deformation, S, and beam elongation, E, to be determined using Equations 5-1 to 5-3, where δa, δb, δdb, δdt, are the deformation in member a, b, db, and dt respectively and ϕ is the angle of the diagonals to the horizontal plane. It can be seen from Figure 5-23(b) that flexural rotation does not change the sum of the lengths of the diagonals; it increases the longitudinal length on one side and reduces the length on the other side. On the other hand shear deformation, as shown in Figure 5-23(c), does not change the longitudinal length in the rosette; it increases the length of one diagonal and decreases the length of the other. When elongation occurs, both the diagonal and longitudinal length increases.

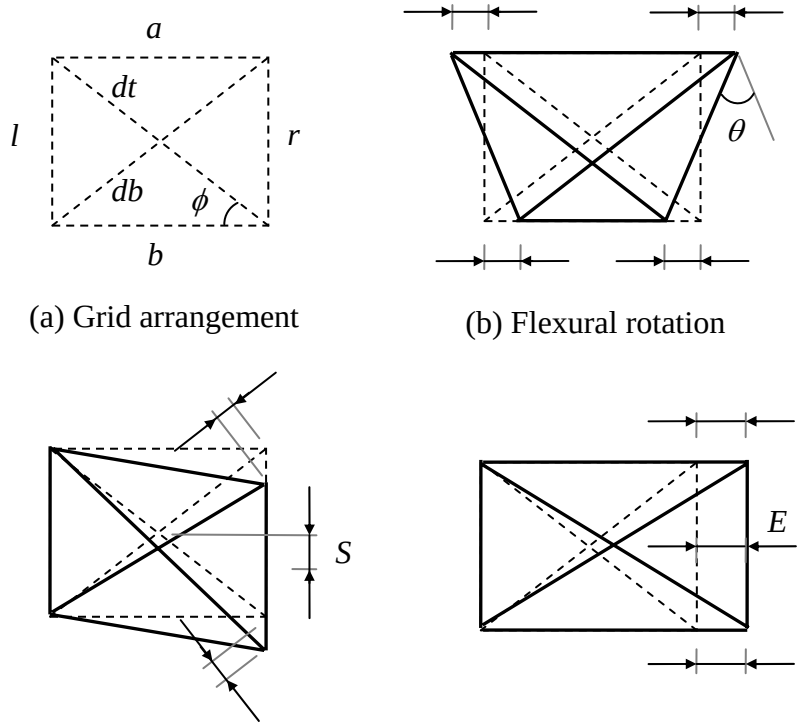

(a) Grid arrangement (b) Flexural rotation

(c) Shear deformation (d) Elongation

Figure 5-23. Schematic diagram showing deformation of beam from the rosette measurement

$$\theta = 2\frac{\delta a - \delta b}{l + r} \tag{5-1}$$

$$S = \frac{\delta db - \delta dt}{2\sin\phi} \tag{5-2}$$

$$E = \frac{\delta a + \delta b}{2} \tag{5-3}$$

5.5.3 Measurement of Floor Deformations

The in-plane deformation of the floor slab was measured using electronic DEMEC (demountable extensometer) gauges. The gauge is a hand-held instrument used to measure displacement between two DEMEC points. The gauge is sensitive to temperature variation and was calibrated prior to the test. Two different sizes of DEMEC grids, 250mm and 500mm, were laid on the floor surface as illustrated in Figure 5-24.

The DEMEC points were glued onto the floor surface using 24 hour epoxy. The grids were labelled and numbered so they could be easily identified. Longitudinal, transverse and diagonal readings were taken for the 250mm grid using a 250mm and a 353.6mm custom made DEMEC gauges. Longitudinal and transverse readings were taken for the 500mm grid using the 500mm custom made DEMEC gauge.

Complete DEMEC readings were taken several times prior to the test to obtain an accurate datum. During testing, DEMEC readings were taken at the selected peak cycles. The difference between the initial readings and the readings at the peak cycles gives the in-plane deformation of the floor slab.

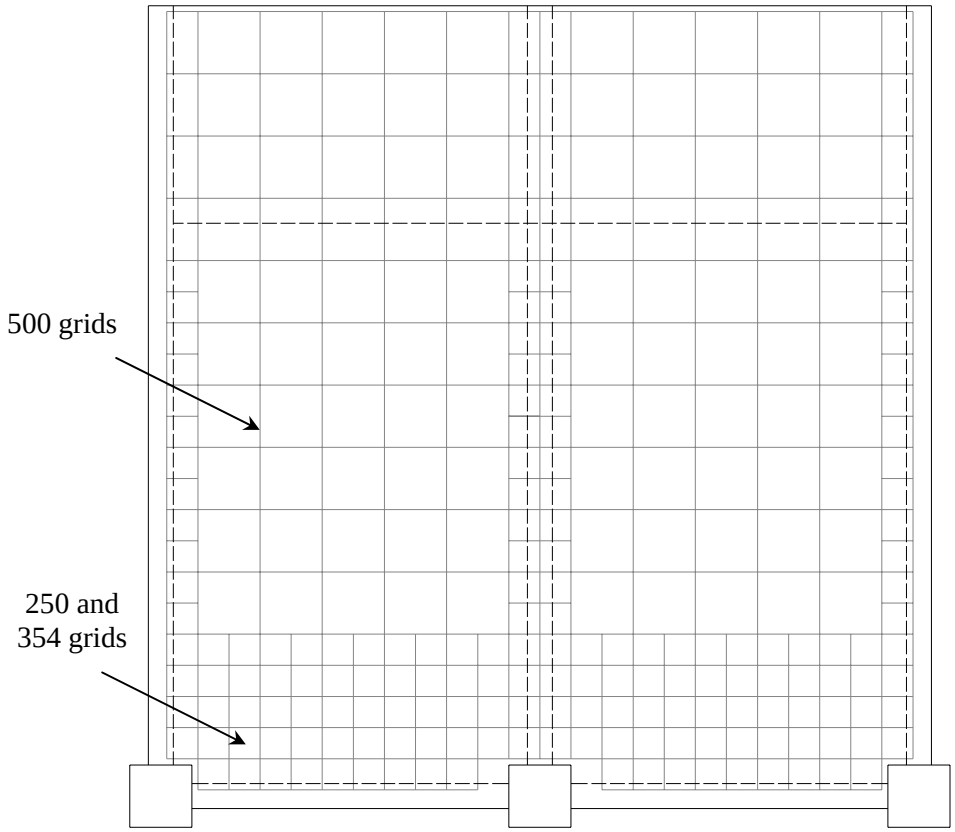

Figure 5-24. DEMEC grid layout on floor surface

In addition to the DEMEC points on the floor surface, linear potentiometers were placed at the critical locations (i.e., interface between the perimeter beams and floor slab) where the change in displacement is expected to be large. A triangular arrangement as shown in Figure 5-25 was used to measure the movement between the slab and the beams.

To reduce the error associated with the potentiometer readings, the potentiometers were mounted as close as possible to the floor without touching the surface. The potentiometers were kept at the same height so that the error associated with the out-of-plane movement of the rods could be minimised.

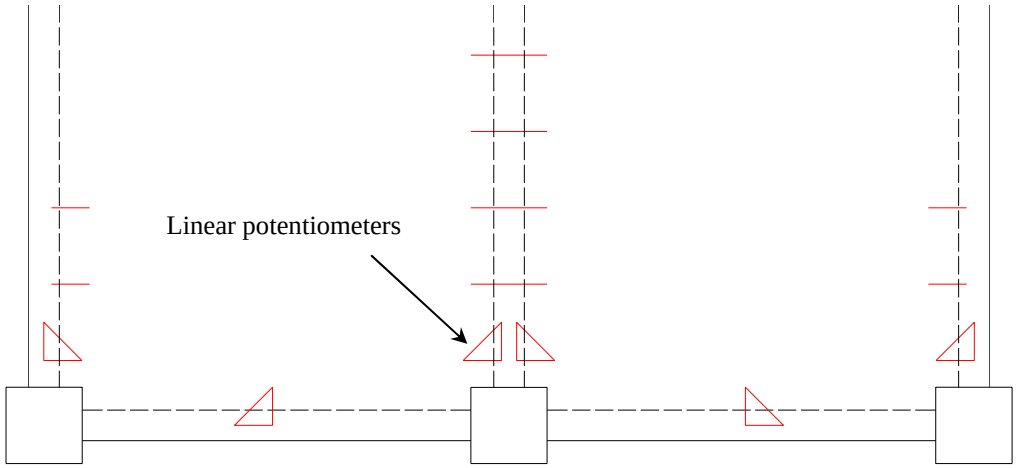

Figure 5-25. Arrangement of linear potentiometers on the floor

To measure the differential movement between the longitudinal beams and the first set of prestressed ribs, five linear potentiometers were installed underneath the floor slab along each beam, as illustrated in Figure 5-26. These potentiometers were located at the centre and at 550mm and 1050mm from the centre of the beams. The potentiometers were attached on an angle that was fixed to the prestressed ribs. It can be seen that the measuring end of the potentiometers were attached to the underside of the floor (for the ones next to the columns), whereas the others were attached to the side of the longitudinal beam. This was done to prevent damage in the beam plastic hinges from affecting the measurements. To account for the movement arising from rotation of the rib units, an inclinometer was mounted on the angle.

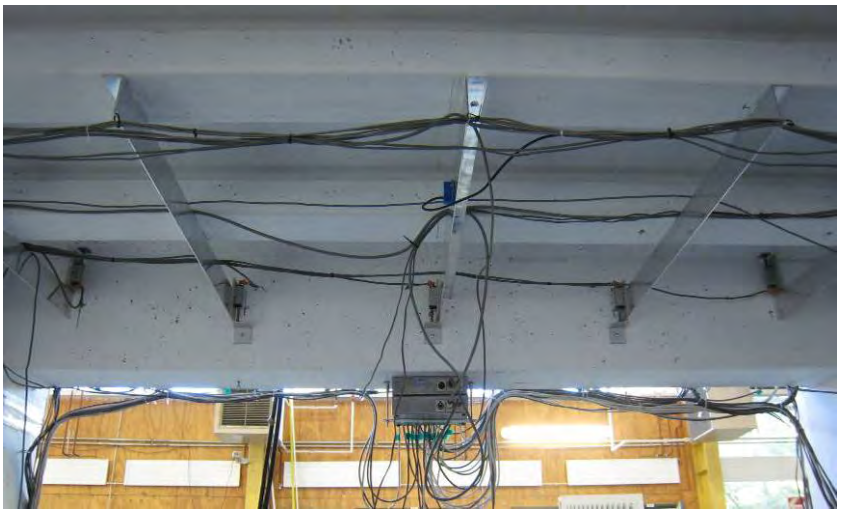

Figure 5-26. Instrumentation underneath the floor slab

5.5.4 Measurement of Transverse Beam Deformations

To measure twists in the transverse beams, five inclinometers were mounted onto each transverse beam as illustrated in Figure 5-27. The inclinometers were approximately 1000mm apart with the first unit located 100mm out from the column face.

Figure 5-27. Inclinometers on transverse beams

5.5.5 Measurement of Support Movements

Linear potentiometers and sonic displacement transducers were mounted on the column bearings to monitor the support movements.

5.5.6 Interpolating Frame Deformations

Lateral displacement at the top and bottom of each column arises from several components: flexure and shear deformation of the beams; flexure and shear deformation of the columns; and beam-column joint distortions. Each of these deformation components is discussed in detail in the following sections.

5.5.6.1 Flexure and Shear Deformation of Beam

Assuming the columns and beam-column joints are rigid, flexure deformation of the West beam induces rotation in *Columns A* and *B*, denoted as θ_{CWf} and θ_{CCf} respectively, as shown in Figure 5-28. The induced rotation/drift can be expressed using Equations 5-4 and 5-5 respectively, where L is the distance between the column centreline and Δ_{B1}, Δ_{B2} are specified in Equations 5-6 and 5-7. In these equations, N is the number of potentiometer segments in a bay, θ_{BWn} is the rotation in the n^{th} segment, and x_{BWn} is the distance from the centre of the n^{th} segment to the centre of *Column B*. Note that *Column B* in the experiment has two different rotation readings, one from each bay. In this case, the rotation is taken as the average of the two. Note that clockwise rotation in the column is taken as positive and a positive rotation in the beam implies tension on the bottom.

$$\theta_{CWf} = \frac{\Delta_{B1}}{L} \tag{5-4}$$

$$\theta_{CCf} = -\frac{\Delta_{B2}}{L} \tag{5-5}$$

$$\Delta_{B1} = \sum_{n=1}^{N} \theta_{BWn} \times x_{BWn} \tag{5-6}$$

$$\Delta_{B2} = \sum_{n=1}^{N} \theta_{BWn} \times \left(L - x_{BWn}\right) \tag{5-7}$$

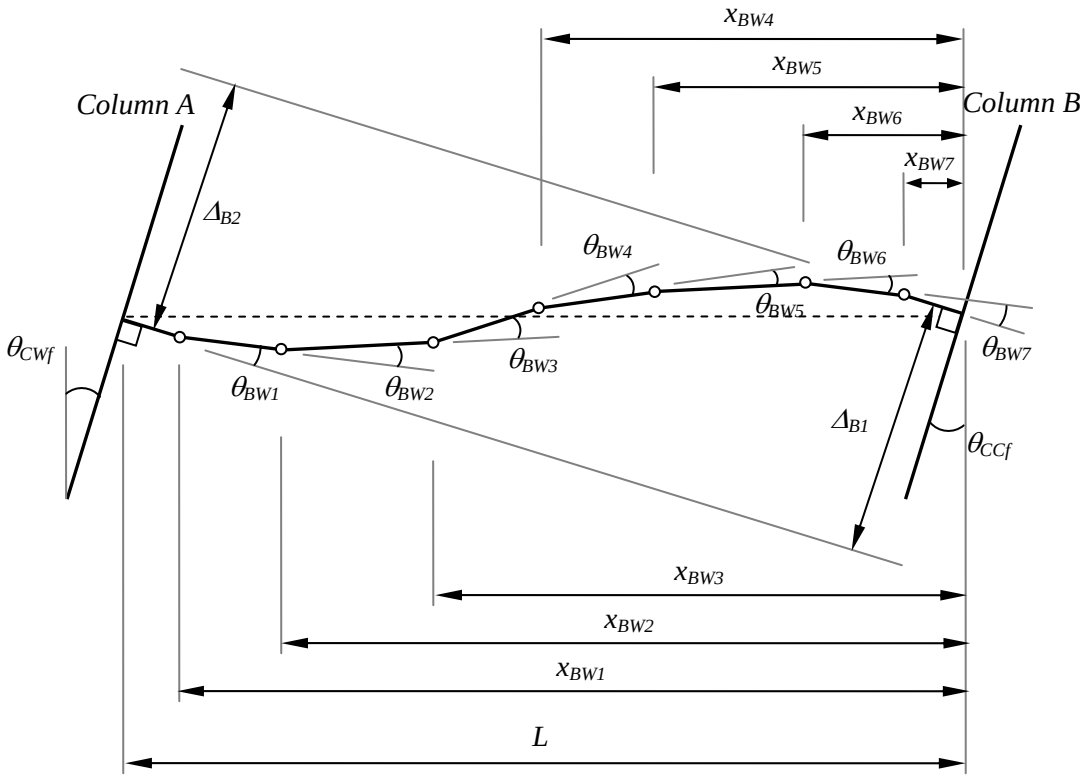

Figure 5-28. Schematic diagram showing column rotation from flexure deformation of beam

Shear deformation of the beam also induces rotation in the column as shown in Figure 5-29. The rotation/drift in *Columns A* and *B* due to shear deformation of the West beam, denoted as θ_{CWs} and θ_{CCs} respectively, can be expressed using Equations 5-8, where L is the distance between the column centreline, N is the number of potentiometer segments in a bay, and δ_{BWn} is the shear displacement over the n^{th} segment. Again, *Column B* in the experiment has two rotation readings, one from each bay. Therefore, the rotation in *Column B* is taken as the average of the two. Here, a positive shear deformation is moving up.

$$\theta_{CWs} = \theta_{CCs} = \sum_{n=1}^{N} \frac{\delta_{BWn}}{L} \tag{5-8}$$

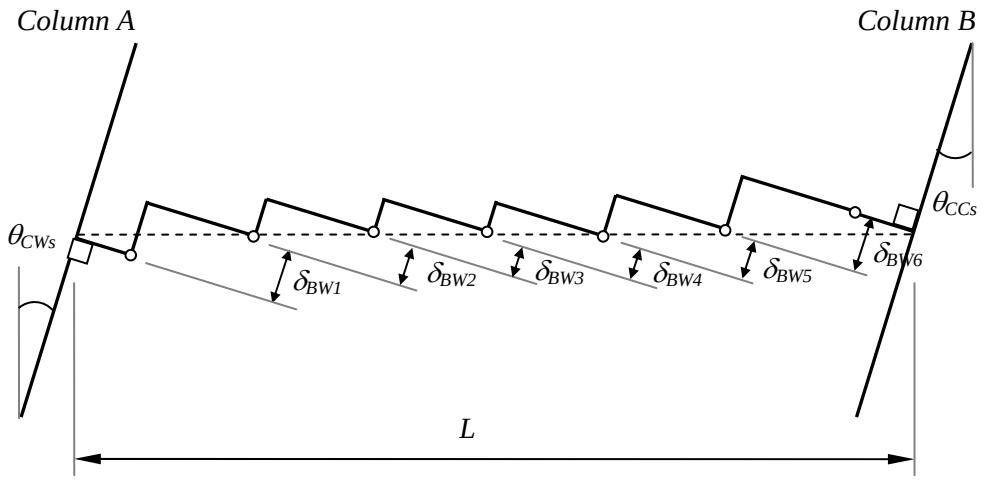

Figure 5-29. Schematic diagram showing column rotation from shear deformation of beam

The total displacement at the top and bottom of *Column A* due to flexural and shear deformation of the West beam, $(\Delta_{CWtop})_{beam}$ and $(\Delta_{CWbot})_{beam}$ is simply the total rotation multiplied by the half height of the column, h_c, as shown in Equation 5-9 and Figure 5-30.

$$(\Delta_{CWtop})_{beam} = -(\Delta_{CWbot})_{beam} = (\theta_{CWf} + \theta_{CWs}) \times h_c \tag{5-9}$$

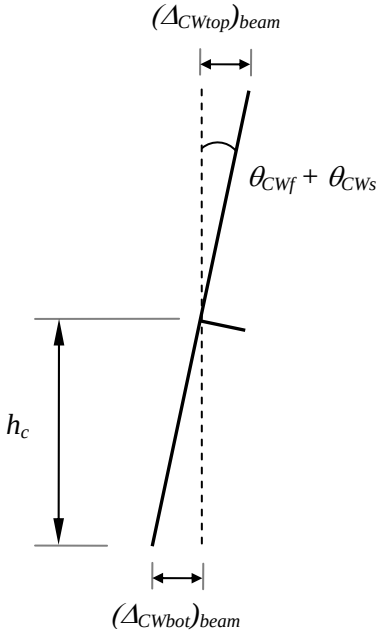

Figure 5-30. Lateral displacement of *Column A* due to shear and flexural deformation of the West beam

5.5.6.2 Flexure and Shear Deformation of Column

The displacement at the top and bottom of *Column A* due to column flexural deformation, $(\Delta_{CWtop})_f$ and $(\Delta_{CWbot})_f$ respectively, can be calculated using Equations 5-10 and illustrated in Figure 5-31, where θ_{CWt} and θ_{CWb} are the rotations at the top and bottom column segment and y_{CWt} and y_{CWb} are the distance from the centre of these segments to the top and bottom line of action in the column. Here, clockwise rotation is positive.

$$(\Delta_{CWtop})_f = -(\Delta_{CWtop})_f = \frac{\theta_{CWt} \times y_{CWt} + \theta_{CWb} \times y_{CWb}}{2} \quad (5\text{-}10)$$

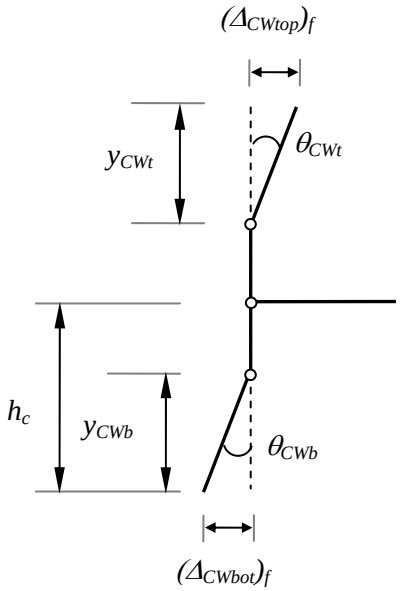

Figure 5-31. Schematic diagram showing flexural deformation of *Column A*

The displacement at the top and bottom of *Column A* from column shear deformation, $(\Delta_{CWtop})_s$ and $(\Delta_{CWbot})_s$ respectively, can be calculated using Equation 5-11 and is illustrated in Figure 5-32, where δ_{CWt} and δ_{CWt} are the shear displacement at the top and bottom column segment. Here, shear deformation to the right is positive.

$$(\Delta_{CWtop})_s = -(\Delta_{CWbot})_s = \frac{\delta_{CWt} - \delta_{CWb}}{2} \quad (5\text{-}11)$$

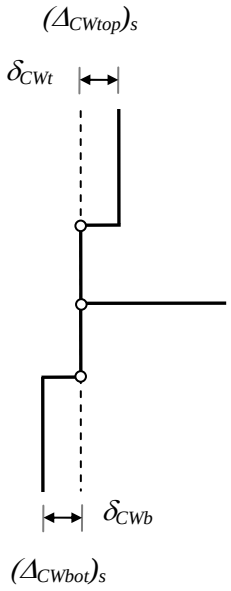

Figure 5-32. Schematic diagram showing shear deformation of column of *Column A*

The total displacement at the top and bottom of *Column A* due to flexural and shear deformation of column, $(\Delta_{CWtop})_{col}$ and $(\Delta_{CWbot})_{col}$ is given by Equation 5-12.

$$(\Delta_{CWtop})_{col} = -(\Delta_{CWbot})_{col} = (\Delta_{CWtop})_f + (\Delta_{CWtop})_s \quad (5\text{-}12)$$

5.5.6.3 Beam-Column joint distortion

With reference to Figure 5-33, the total shear distortion in the joint, γ, can be estimated using Equation 5-13, where Δ_{d1} and Δ_{d2} are the change in length of the diagonals, l_d is the original length of the diagonals and ϕ is the original angle between the diagonals to the horizontal plane (Cheung 1991).

$$\gamma = \gamma_1 + \gamma_2 = \frac{\Delta_{d1} - \Delta_{d2}}{2l_d}\left(\tan\phi + \frac{1}{\tan\phi}\right) \quad (5\text{-}13)$$

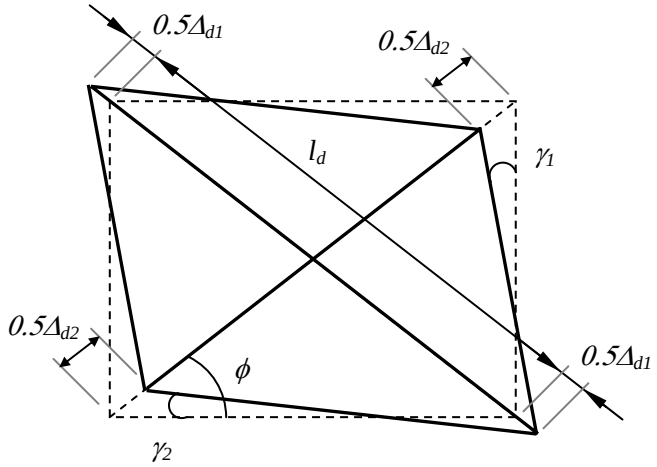

Figure 5-33. Schematic diagram showing beam-column joint shear distortion

With reference to Figure 5-34, the beam deformation due to joint shear distortion, δ_{js}, can be expressed as Equation 5-14.

$$\delta_{js} = l_b \times \gamma - h_b \times \gamma \times \frac{0.5L}{2h_c} \tag{5-14}$$

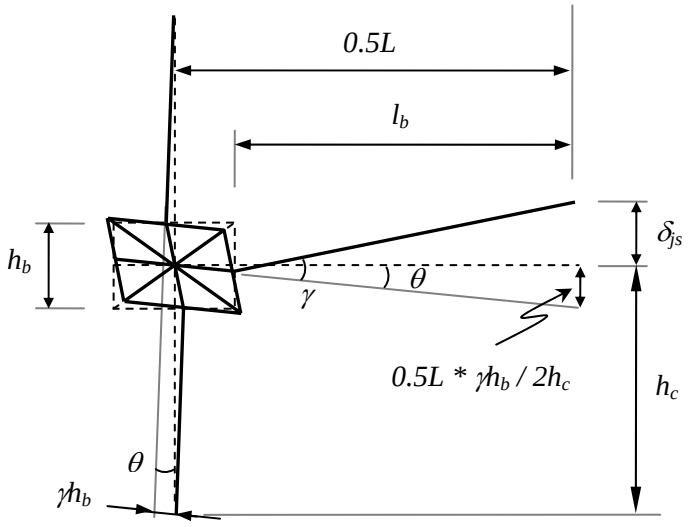

Figure 5-34. Lateral storey displacement due to joint shear distortion

Therefore, the corresponding displacement at the top and bottom of *Column A*, $(\Delta_{CWtop})_{js}$ and $(\Delta_{CWbot})_{js}$, is given by Equation 5-15.

$$(\Delta_{CWtop})_{js} = -(\Delta_{CWbot})_{js} = \frac{\delta_{js}}{0.5L} \times h_c \quad (5\text{-}15)$$

5.5.6.4 Total Deformation

The total deformation at the top and bottom of *Column A* is equal to the sum of the deformations from beam, column and beam-column joints as shown in Equation 5-16. Similar approach can be used to calculate the total deformation at the top and bottom of other columns.

$$(\Delta_{CWtop})_{total} = -(\Delta_{CWbot})_{total} = (\Delta_{CWtop})_{beam} + (\Delta_{CWtop})_{col} + (\Delta_{CWtop})_{js} \quad (5\text{-}16)$$

5.5.7 Interpolating Floor Deformations from Potentiometer Measurements

Linear potentiometers were set up in a triangular grid arrangement, as shown in Figure 5-35, on the floor to measure the deformation across the main cracks at the weak sections between beam and floor slab interface. This arrangement allowed the opening of the cracks, Δ_o, as well as shear deformation, Δ_s, to be calculated using Equations 5-17 and 5-18 respectively. Here, δ_L is the change in length of the horizontal potentiometer and δ_D is the change in length of the diagonal potentiometer.

$$\Delta_o = \delta_L \quad (5\text{-}17)$$

$$\Delta_s = -\frac{\delta_D}{\sin\theta} + \frac{\Delta_o}{\tan\theta} \quad (5\text{-}18)$$

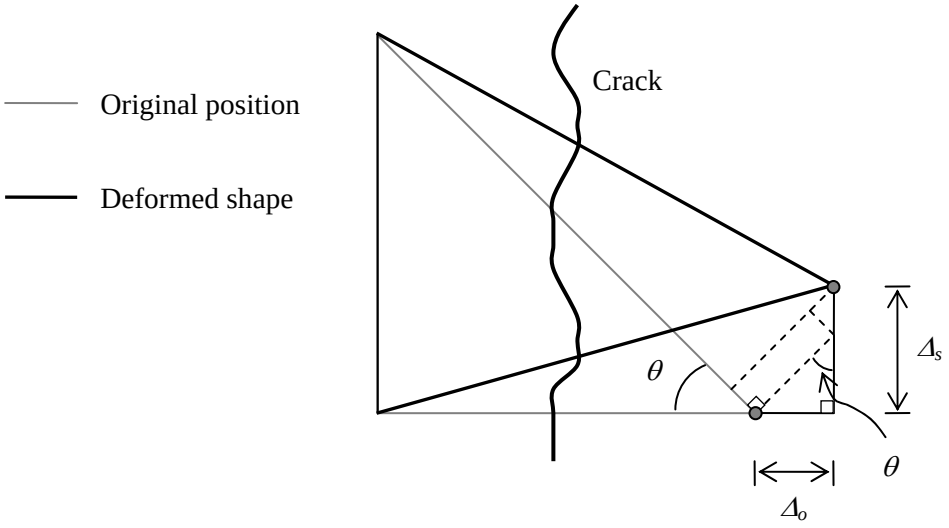

Figure 5-35. Deformation of floor slab calculated from potentiometers with triangular arrangement

5.6 CONCLUSIONS

Based on the research carried out in the past, it is evident that indeterminate frame tests provide more realistic results than those tested under individual determinate conditions. The experimental setup, loading protocol and boundary conditions were found to have marked influence on the overall behaviour of indeterminate systems.

A three dimensional frame-floor sub-assembly test was designed and constructed to enable the interaction between prestressed floor units and the surrounding frames to be investigated. The loading arrangement was detailed such that elongation of beam plastic hinges was not restrained nor exaggerated by the loading system and the columns remained parallel to each other throughout the entire loading.

The test specimen was heavily instrumented with linear and rotary potentiometers, inclinometers, sonic displacement transducers, DEMEC points and load cells to monitor the deformations and internal actions of the sub-assembly. Methods for determining the frame and floor deformations from linear potentiometer measurements are provided.

5.7 REFERENCES

Cheung, P. C. (1991). "Seismic design of reinforced concrete beam-column joints with floor slab," PhD. Thesis, Department of Civil Engineering, University of Canterbury, Christchurch, New Zealand.

Fenwick, R. C., Bull, D. K., MacPherson, C., and Lindsay, R. "The influence of diaphragms on strength of beams." *New Zealand Society for Earthquake Engineering Conference 2006*.

Fenwick, R. C., Davidson, B. J., and McBride, A. "The influence of slabs on elongation in ductile seismic resistant frames." *New Zealand National Society for Earthquake Engineering Conference 1995*, 36-43.

Lau, D. B. N. (2007). "Influence of precast prestressed flooring on the seismic performance of reinforced concrete perimeter frame buildings." *Report Number 653*, Dept. of Civil and Environmental Engineering, University of Auckland, Auckland, New Zealand.

Lindsay, R. (2004). "Experiments on the seismic performance of hollow-core floor systems in precast concrete buildings," Master Thesis, University of Canterbury, Christchurch, New Zealand.

MacPherson, C. (2005). "Seismic performance and forensic analysis of a precast concrete hollow-core floor super-assemblage," Master Thesis, University of Canterbury, Christchurch, New Zealand.

Matthews, J. (2004). "Hollow-core floor slab performance following a severe earthquake," PhD. Thesis, University of Canterbury, Christchurch, New Zealand.

McBride, A., Fenwick, R. C., and Davidson, B. J. (1996). "The influence of slabs on the lateral cyclic behaviour of ductile concrete frames." *Report No. 566*, Department of Civil and Resource Engineering, University of Auckland, Auckland, New Zealand.

Megget, L. M., and Fenwick, R. C. (1989). "Seismic behaviour of a reinforced concrete portal frame sustaining gravity loads." *Bulletin of the New Zealand National Society for Earthquake Engineering*, 22(1), 39-49.

Qi, X., and Pantazopoulou, S. J. (1991). "Response of RC frame under lateral loads." *Journal of Structural Engineering-ASCE*, 117(4), 1167-1188.

Standards New Zealand. (1995). *Concrete structures standard: NZS 3101:1995*, Standards New Zealand, Wellington.

Wight, J. K. (1985). *Earthquake effects on reinforced concrete structures: U.S. - Japan research*, American Concrete Institute, Detroit, Michigan.

Wuu, P. J. Y. (1996). "Deformations in plastic hinge zone of RC beam in ductile frame structures subjected to inelastic cyclic loading," Master Thesis, University of Auckland, Auckland, New Zealand.

Zerbe, H. E., and Durrani, A. J. (1989). "Seismic response of connections in two-bay reinforced concrete frame sub-assemblies." *Journal of Structural Engineering*, 115(11), 2829-2844.

Zerbe, H. E., and Durrani, A. J. (1990). "Seismic response of connections in two-bay reinforced concrete frame sub-assemblies with a floor slab." *ACI Structural Journal*, 87(4), 406-415.

6 EXPERIMENTAL RESULTS

This chapter summarizes the experimental results obtained from the 3D sub-assembly test described in Chapter 5. A general description of the visual observations and the significant events observed during the test is provided in Section 6.2. The global and local hysteretic response of the sub-assembly as well as the deformation of the frame, transverse beams and floor slab is presented and discussed in Section 6.3. Torsional response of the transverse beams is described in Section 6.4. Finally, the experimentally measured storey shear force is compared with the shear force calculated based on New Zealand and ACI codes. Mechanisms that cause the difference in these values are described in Section 6.5.

6.1 MATERIAL PROPERTIES

The averaged concrete compressive strengths, f_c', for the three different concrete batches used in the construction of the test unit are summarised in Table 6-1. The concrete strengths were found by tests on 100mm diameter by 200mm deep cylinders. Two cylinders, which were cured in a temperature controlled fog room, were tested at 7 days as a preliminary indication of the concrete strength. Three cylinders were tested at 28 days; and three were tested at the start of the test and three more were tested at the end of the test. The results are attached in Appendix C. These cylinders were cured alongside the sub-assembly. It should be noted that the main test was carried out over a period of two months.

Table 6-1 Summary of the concrete compressive strength

Member	**Averaged Compressive stress f_c' (MPa)**			
	7 Days	**28 Days**	**Start of test**	**End of test**
Longitudinal beam, lower half of transverse beams, columns below the main beams, and beam-column joints	21.4	26.6	31.2	30.6
Transverse beam lap-splice and the rest of columns	32.0	39.4	42.4	50.1
Floor slab, top half of transverse beams and end slab	24.1	30.7	33.0	33.4

The averaged properties of the reinforcement used in the test are summarised in Table 6-2, where f_y and f_u are the yield and ultimate stress respectively; ε_y and ε_{sh} are the yield and strain hardening strains respectively; ε_u is the strain at maximum stress; *R* and *D* stand for Grade 300 round and deformed bars respectively; and *HD* stands for Grade 500 deformed bar. The number following the letters represents the diameter of the reinforcing bar in millimetre. Three samples were tested for each type of reinforcement. The stress-strain relationships of the reinforcing bars are shown in Appendix C.

The longitudinal reinforcement in the main beam was broken out of the member at the end of the main test. These bars were extracted away from the plastic hinge zone. The stress-strain relationships of these reinforcing bars are also given in Appendix C. It was found that these bars behaved quite differently to the ones tested prior to the test and other Grade 300 bars tested in the laboratory. The yield and ultimate stress of the reinforcement extracted from the main beam is 11% and 7% higher than the ones tested prior to the main test. The yield strain of the reinforcement extracted from the main beam is higher than the ones tested prior to the main test, while the strain hardening and ultimate strains are much smaller. It is uncertain why there is a difference between the properties of the reinforcement. In this research, the properties of the ones tested prior to the test have been used for calculations.

Table 6-2 Summary of the reinforcing bars properties

Steel	f_y **(MPa)**	f_u **(MPa)**	ε_y	ε_{sh}	ε_u
R6	444.7	557.1	0.0022	-	0.0916
R10	395.2	490.5	0.0020	0.0174	0.1355
D10	372.5	477.1	0.0019	0.0189	0.1209
D16	325.4	454.9	0.0016	0.0253	0.2084
D20	319.1	455.5	0.0016	0.0243	0.2065
HD12	541.4	668.1	0.0027	0.0191	0.1118
HD16	551.4	684.8	0.0028	0.0165	0.1158
D16[*]	359.4	486.2	0.0043	0.0081	0.1086
D16[**]	365.1	484.3	0.0033	0.0089	0.0990

[*] Steel bars extracted from the top of the longitudinal beam at the end of the test
[**] Steel bars extracted from the bottom of the longitudinal beam at the end of the test

6.2 GENERAL OBSERVATIONS

6.2.1 Cracks in the Sub-Assembly Prior to Test

Some cracks were observed in the floor slab prior to test as shown in Figure 6-1. These were believed to be caused by shrinkage of the floor topping and creep of the prestressed rib units. These cracks formed mostly perpendicular to the frame. This may partially be due to creep of the highly eccentric prestressed ribs inducing tensile strains in the topping concrete parallel to the frame. In addition, it is postulated that the potential shrinkage movement in the East-West direction was more effectively restrained by the prestressed rib units. Therefore, the tensile stress built up over a shorter distance and caused the cracks to develop perpendicular to the frame. On the other hand, the shrinkage movement in the North-South direction was less effectively restrained by the surrounding transverse beams. Therefore, the tensile stress in the concrete built up over a longer distance and the stress level was insufficient to cause cracking parallel to the frame.

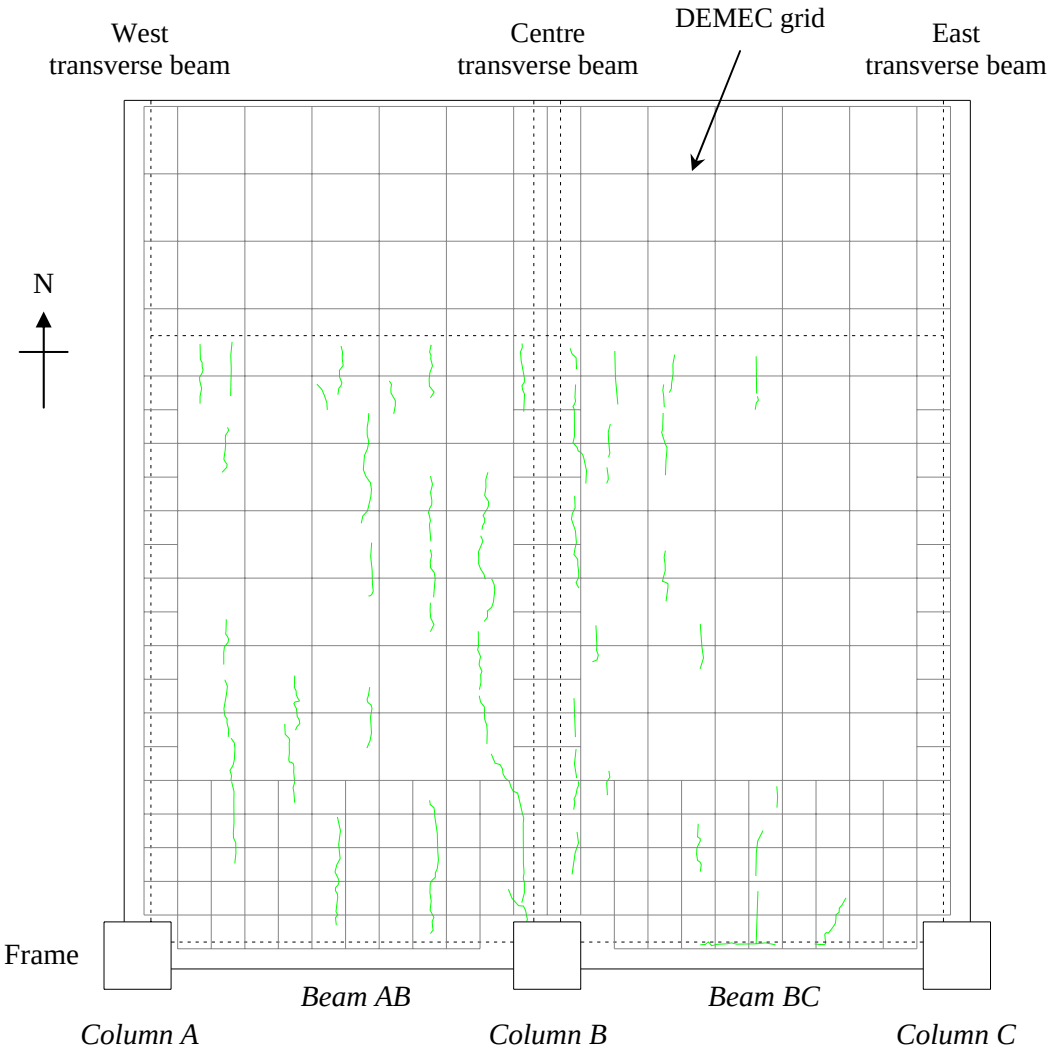

Figure 6-1. Crack pattern on the floor slab prior to test

Some cracks were observed at the bottom of the transverse beams. These were believed to be caused by a combination of gravity load bending and shrinkage.

6.2.2 Observations Made During the Main Test

A list of the important events observed during the main test is summarised below.

Minor flexural cracks first appeared in the longitudinal beams and floor slab at ±0.25% drift. During the ±0.35% drift cycles, some of the flexural cracks in the longitudinal beams became inclined diagonally towards the column as shown in Figure 6-2(a). Minor cracks appeared at the interface between the precast sections of the columns, immediately above and below the beam-column joints, as highlighted in Figure 6-2(b). Cracks were also apparent at the connection interface between the

prestressed rib units and the transverse beams as shown in Figure 6-2(d). These cracks initiated from the rib soffit and propagated upwards. These cracks were thought to be caused by rotation of the transverse beam relative to the rib units as illustrated in Figure 6-3. All of the cracks closed when the displacement was reversed to zero.

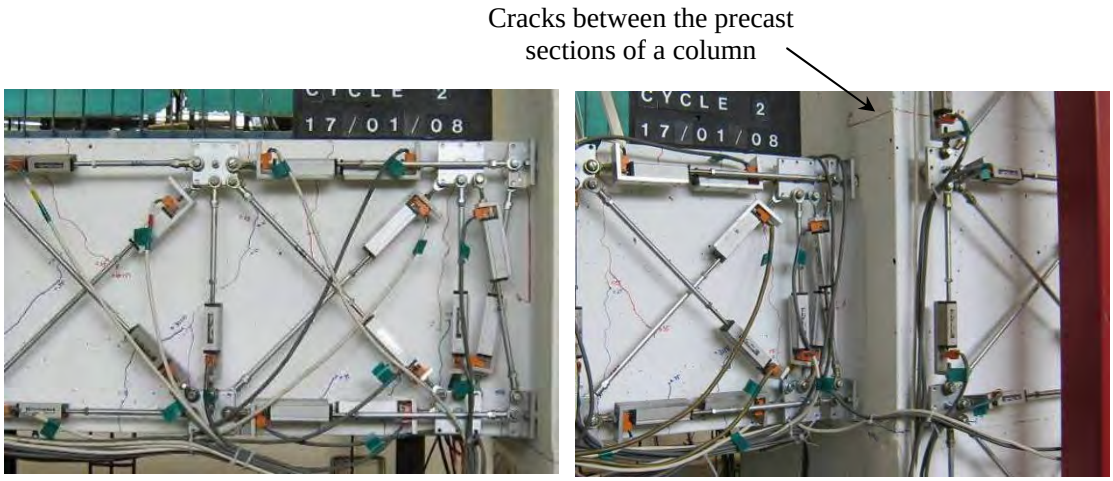

(a) Cracks in a longitudinal beam

(b) Cracks in the central column

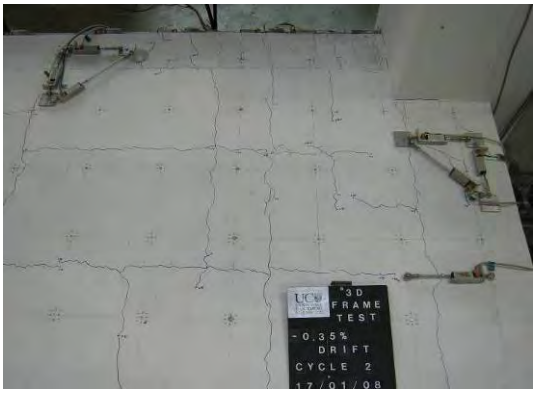

(c) Cracks in the topping next to *Column A*

(d) Cracks at the interface of a rib connecting to a transverse beam

Figure 6-2. Visual observations during the ±0.35% drift cycles

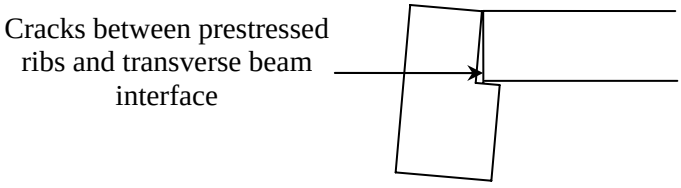

Figure 6-3. Rotation of the transverse beam relative to the floor ribs

During the ±0.5% drift cycles, additional flexural cracks appeared in the columns and longitudinal beams. A greater number of cracks occurred in the central column than the outer columns because the central column was sustaining greater moment from the two adjacent beams. Minor cracks at the level of beam reinforcement also developed in the central beam-column joint.

Discontinuity cracks in the topping, as highlighted in Figure 6-4(b) and Figure 6-20(c), clearly show the weak section between the interface of transverse beams and prestressed ribs. These cracks extended about 2.5m along the transverse beams. Diagonal cracks, which were all inclined towards the centre column, became apparent in the floor topping.

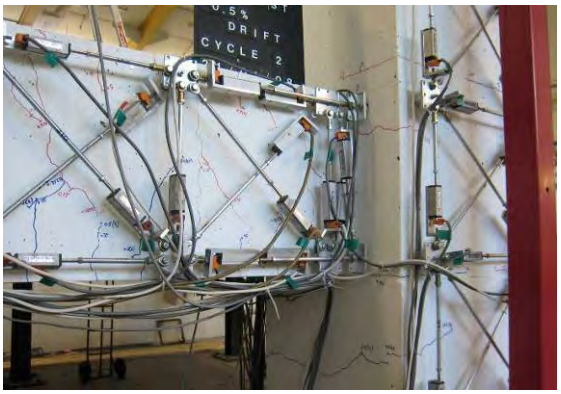

(a) Cracks in the centre column and longitudinal beam

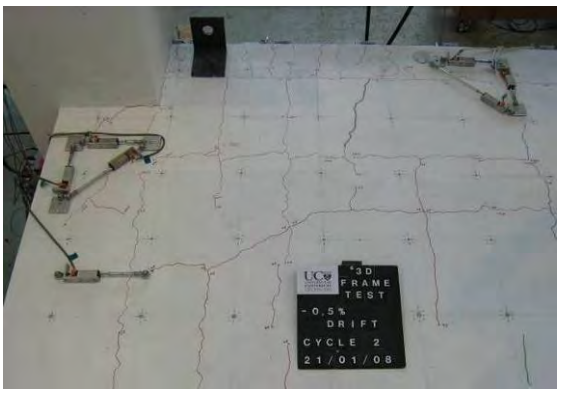

(c) Diagonal cracks in the floor slab next to *Column C*

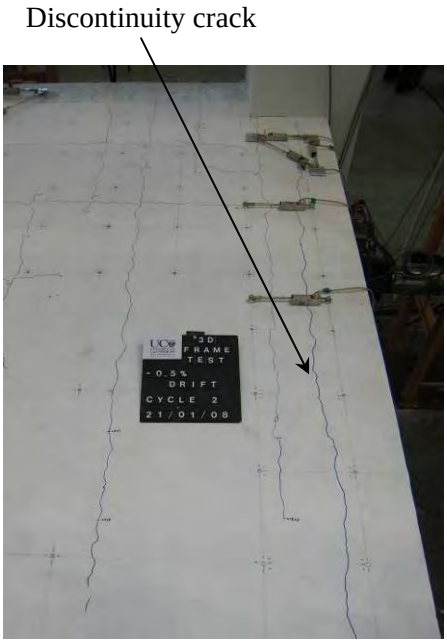

(b) Discontinuity cracks in the floor slab along the west external transverse beam

Figure 6-4. Visual observations during the ±0.5% drift cycles

A number of photographs showing cracking at ±0.75% drift cycles are reproduced in Figure 6-5. It can be seen that at this stage more flexural and diagonal cracks had developed in the longitudinal beams and floor. Minor diagonal cracks also became

apparent in the central beam-column joint. The flexural cracks in the longitudinal beam next to *Column A* remained open, by 0.5mm as shown in Figure 6-5(c), when the storey shear force reversed to zero, indicating the first sign of yielding in the flexural reinforcement. It was also apparent from the total force-displacement diagram, as illustrated in Figure 6-22, that the structure had yielded at this stage.

The discontinuity cracks in the topping extended further along the transverse beams. The extension at the external transverse beams was further than that at the internal transverse beam, as shown in Figure 6-20(d). This may be due to the difference in elongation between the exterior and interior plastic hinges.

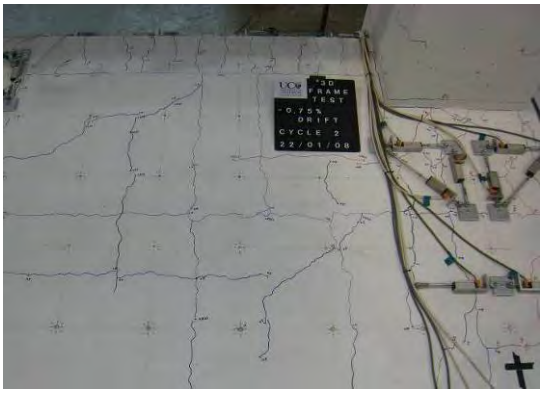

(a) Cracks in the topping next to *Column B*

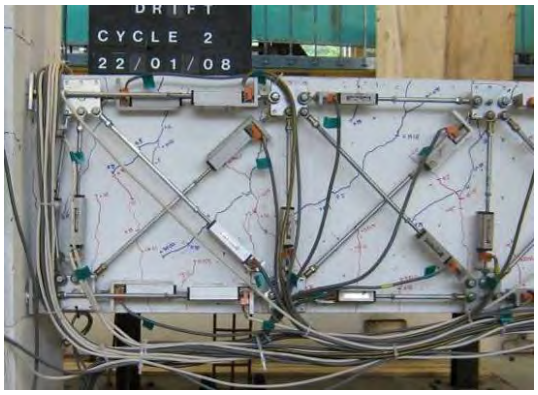

(b) Cracks in a longitudinal beam

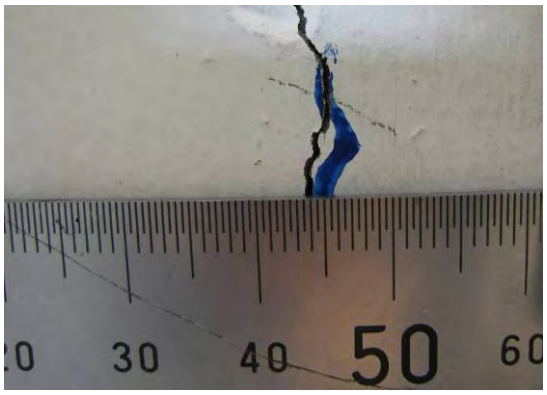

(c) Permanent cracks in the longitudinal beam next to *Column A*

(d) Cracks in the central column

Figure 6-5. Visual observations during the ±0.75% drift cycles

Figure 6-6 shows the calculated displacement at top of the columns during the first ±0.75% drift cycle, interpreted using the inclinometer measurements. The displacement at the bottom of the columns is the same as the top of the column except with an opposite sign; hence it is not shown in the figure.

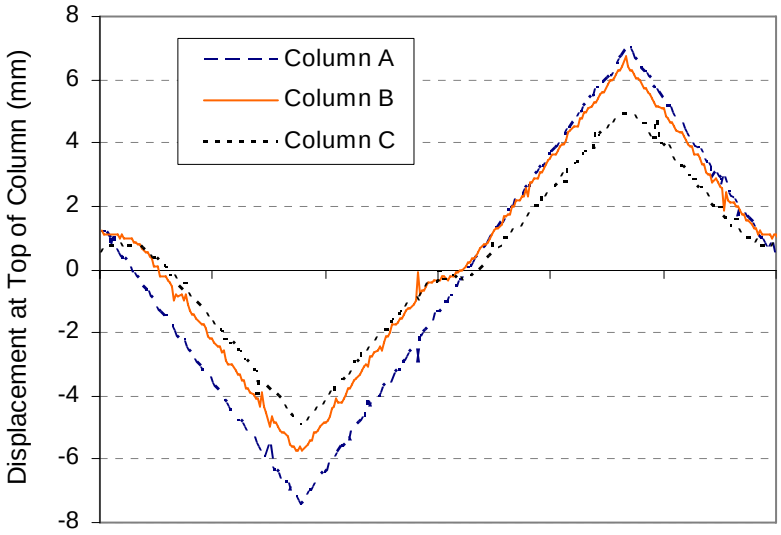

Figure 6-6. Measured displacement at top of the columns during the 0.75% drift cycle

It can be seen that *Column B* and *Column C* did not move as much as *Column A*. Columns *B* and *C* sustained an equivalent of 0.6% and 0.5% drift respectively when 0.75% drift was applied to *Column A*. The differences in the movement between *Columns A* and *B* and *Columns B* and *C* are plotted against the corresponding column shear force, as illustrated in Figure 6-7. The differences in the column movement were found to arise from:

1. Slop in the fittings which took up at a small column shear force;
2. Elastic deformation of actuators and connection fittings, which increased with applied lateral force, as illustrated in Figure 6-7.

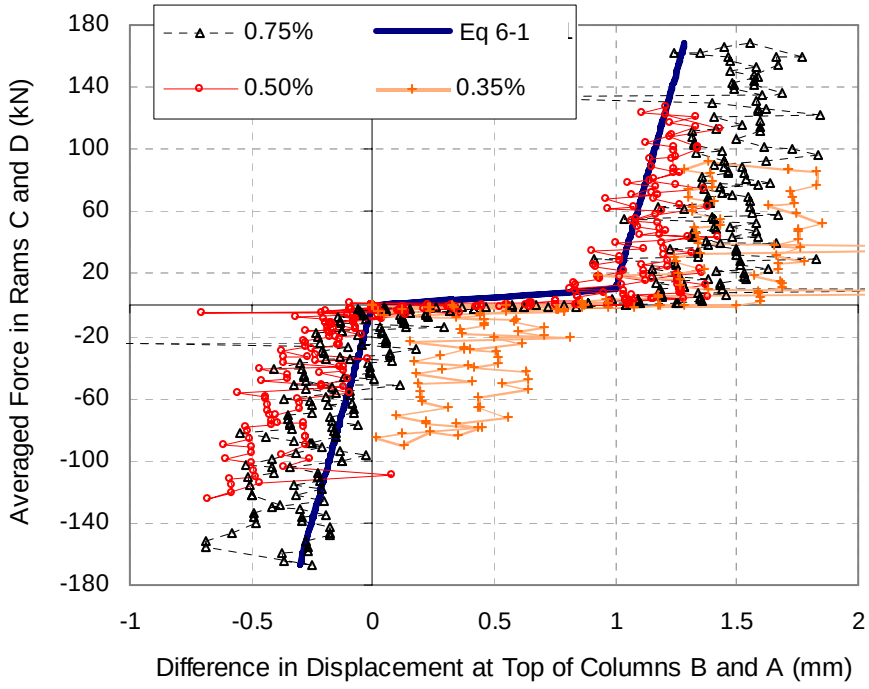

(a) *Column B*

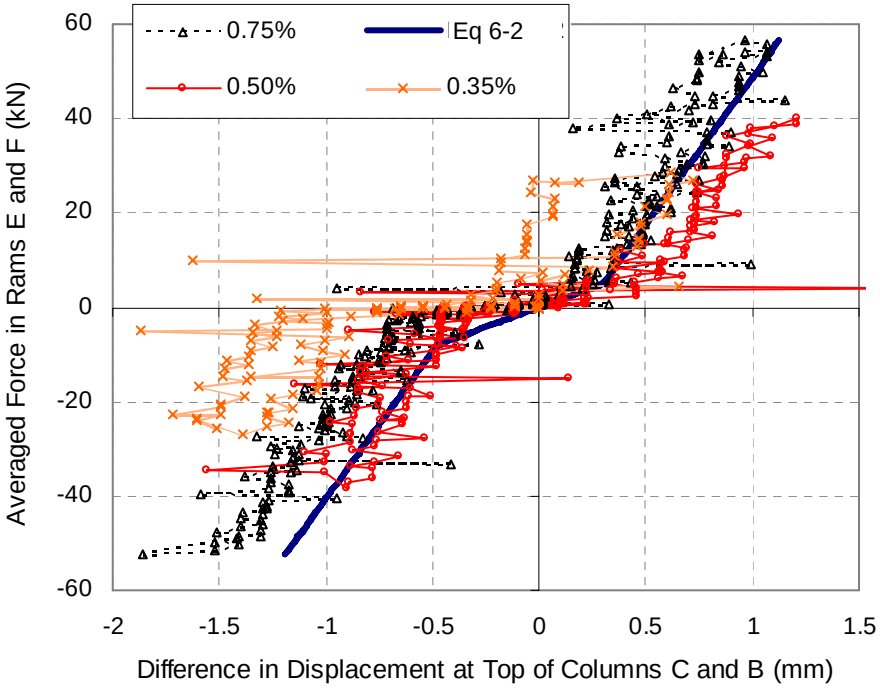

(b) *Column C*

Figure 6-7. Out of parallel movements of the columns

The controller program was modified with additional displacements added to the actuators for *Columns B* and *C* in an attempt to keep the columns parallel. The

additional displacements, Δ_{add}, applied to *Columns B* and *C* are specified in Equations 6-1 and 6-2 respectively, where F_{aveCD} and F_{aveCD} are the averaged force in *Rams C* and *D* and Rams *E* and *F*, respectively. These were also plotted in Figure 6-7 using the thick solid line. The modified programme was tested with an additional ±0.5% drift cycle. The difference in the movement between these columns, during the 1% drift cycle using the modified programme, is plotted in Figure 6-8. It can be seen that with the modified program, the out of parallel movement between each columns at 1% drift cycle are within 0.5mm, which corresponds to a discrepancy of 0.05% drift.

$$\begin{aligned} \Delta_{add} &= (F_{aveCD} - 10) \times 0.0018 + 1 && \text{when} && F_{aveCD} > 10 \\ \Delta_{add} &= 0.1 \times F_{aveCD} && \text{when} && 0 \le F_{aveCD} \le 10 \\ \Delta_{add} &= 0.0018 \times F_{aveCD} && \text{when} && F_{aveCD} < 0 \end{aligned} \qquad (6\text{-}1)$$

$$\begin{aligned} \Delta_{add} &= (F_{aveEF} - 5) \times 0.016 + 0.3 && \text{when} && F_{aveEF} > 5 \\ \Delta_{add} &= 0.06 \times F_{aveEF} && \text{when} && -8 \le F_{aveEF} \le 5 \\ \Delta_{add} &= (F_{aveEF} + 8) \times 0.016 - 0.48 && \text{when} && F_{aveEF} < -8 \end{aligned} \qquad (6\text{-}2)$$

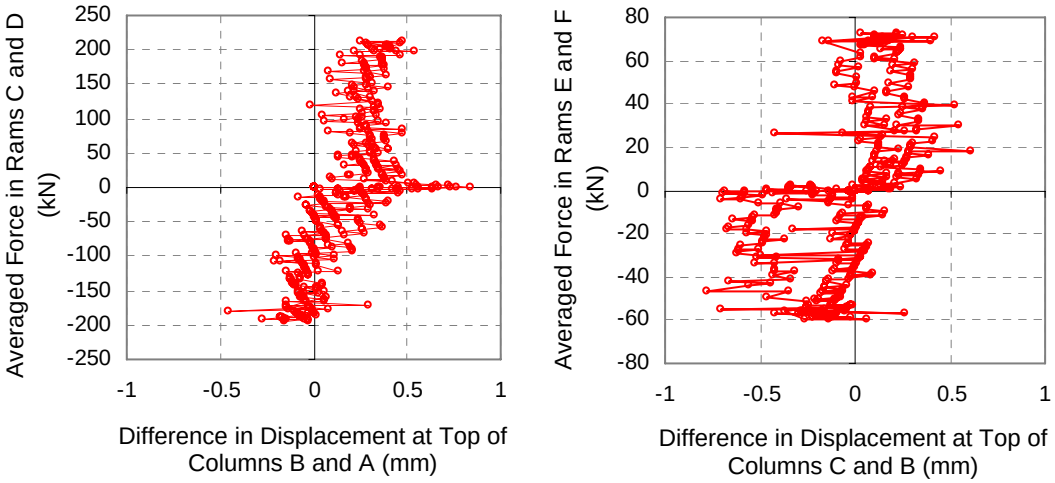

(a) *Column B* (b) *Column C*

Figure 6-8. Out of parallel movements of the columns after correction during 1% drift cycle

During the ±1.0% drift cycles, diagonal cracks appeared in the transverse beams as shown in Figure 6-9(a). Cracks appeared in all the connection interfaces between the

prestressed ribs and external transverse beams. Some of these cracks opened up to 3mm at the peak applied displacement as shown in Figure 6-9(b). In this figure, there were two cracks forming at the end of the prestressed rib.

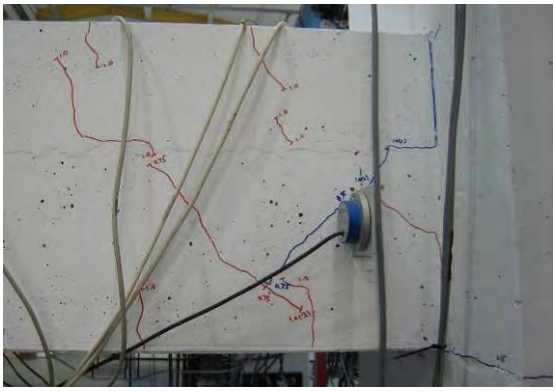

(a) Shear cracks in a transverse beam

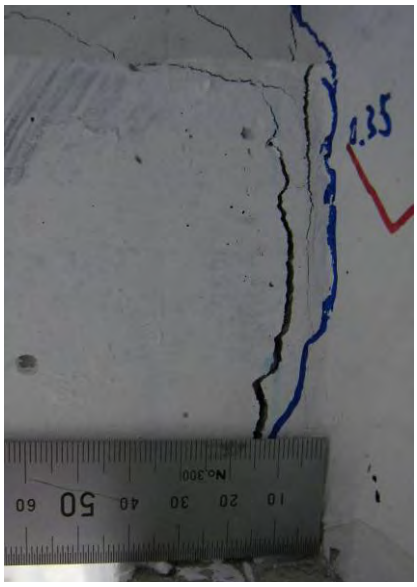

(b) Cracks at the end of a rib unit

Figure 6-9. Visual observations during the ±1.0% drift cycles

At the peaks of ±1.5% drift cycles, differential horizontal movement of roughly 4mm between the longitudinal beam and floor slab became apparent as shown in Figure 6-10(a). This movement is due to elongation of beam plastic hinges. Differential vertical movement of approximately 2mm between the transverse beams and floor slab was observed near the column as shown in Figure 6-10(b). It is postulated that this arises due to relative rotation at the interface between the transverse beam and floor slab as shown in Figure 6-11. Torsional cracks were observed in the transverse beams as shown in Figure 6-10(c).

(a) Differential horizontal movement between longitudinal beam and floor

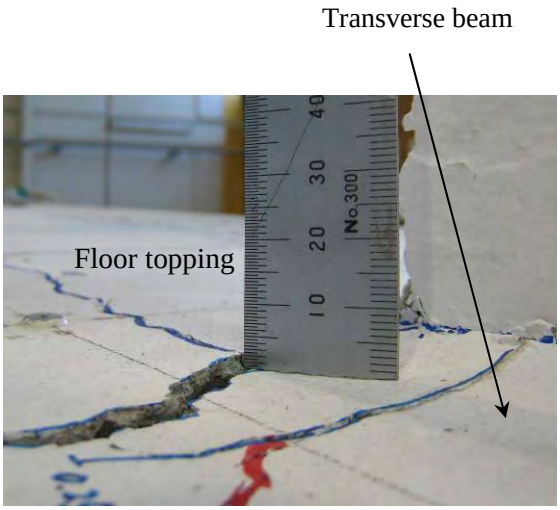

(b) Differential vertical movement between transverse beam and floor

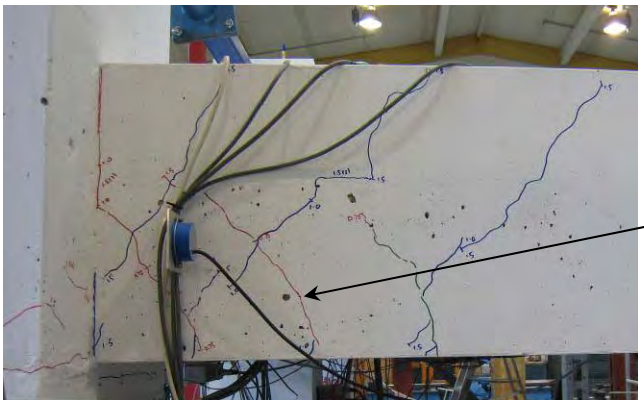

(c) Torsional cracks in a transverse beam

Figure 6-10. Visual observations during the ±1.5% drift cycles

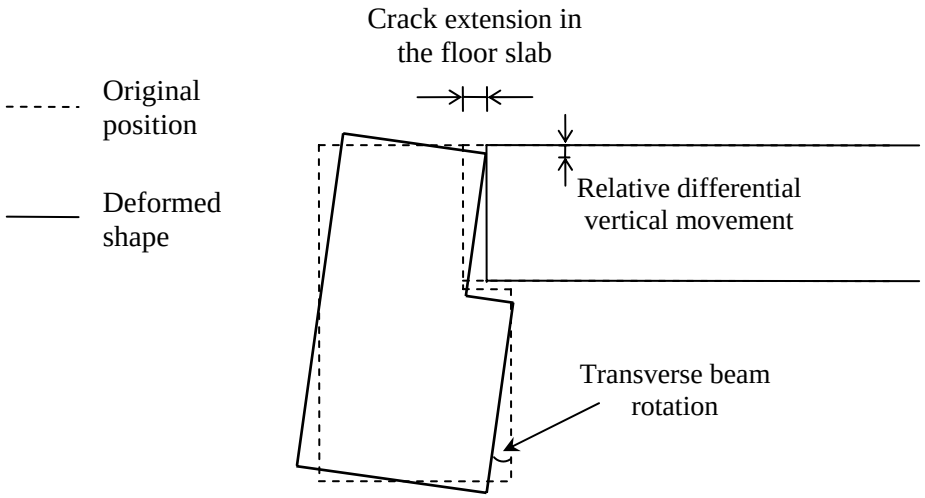

Figure 6-11. Schematic diagram showing the vertical differential movement between transverse beam and floor slab

Cracking observed around the exterior and interior plastic hinges at the end of 2.0% drift cycles is shown in Figure 6-12. It can be seen from these comparisons that cracking around the exterior plastic hinges was more severe than the cracking around the interior plastic hinges. Minor spalling was observed around the exterior plastic hinges.

The differential vertical and horizontal movement between the beams and the floor slab increased further and the discontinuity cracks in the floor slab extended to 3.5m along the transverse beams. The external columns were observed to twist relative to the beams as shown in Figure 6-13. The figure shows the eccentric forces arising from elongation of plastic hinges and shear resistance of transverse beams, which caused the column to twist.

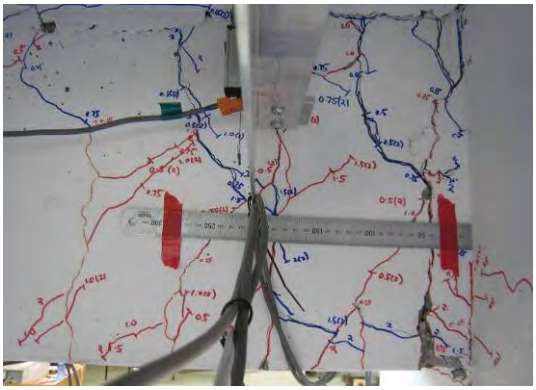

(a) Cracking in an exterior plastic hinge

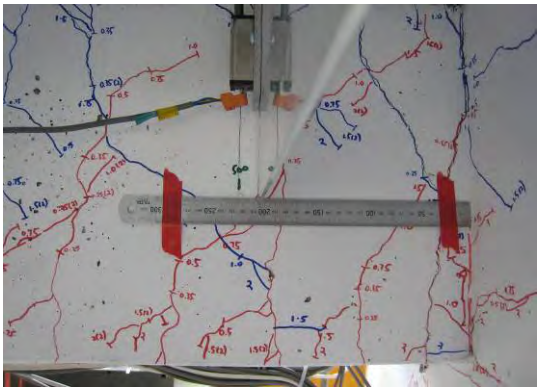

(b) Cracking in an interior plastic hinge

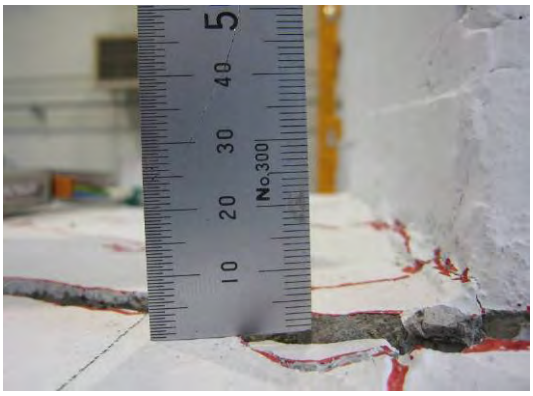

(c) Differential vertical movement near an exterior plastic hinge

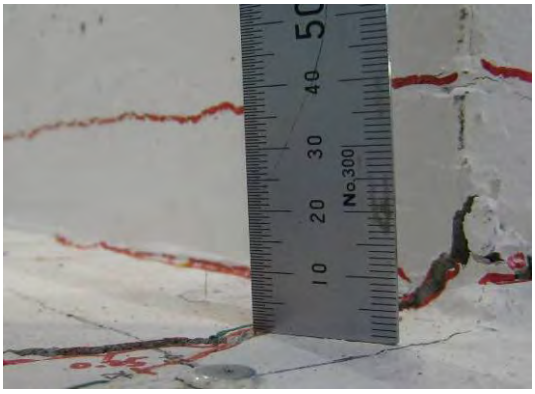

(d) Differential vertical movement near an interior plastic hinge

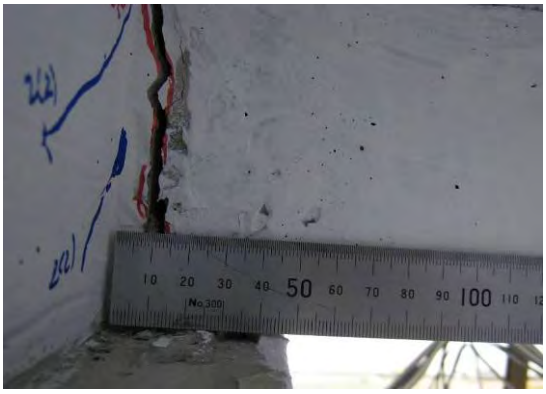

(e) Rib connection next to an exterior plastic hinge

(f) Rib connection next to an interior plastic hinge

Figure 6-12. Visual observations during the ±2.0% drift cycles

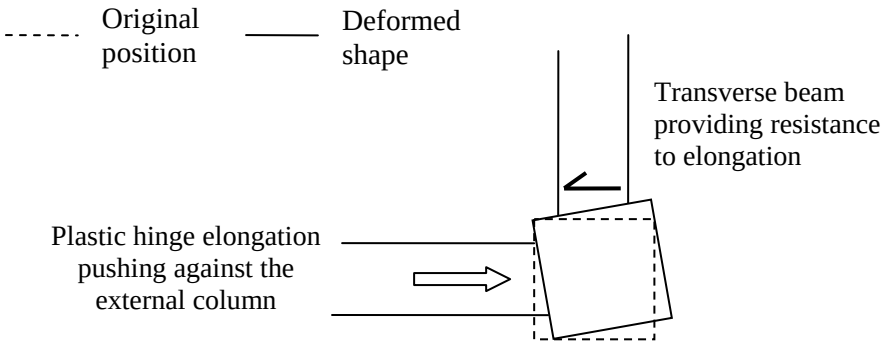

Figure 6-13. Twisting of an external column

During the ±2.5% drift cycles, minor flexural cracks appeared at the bottom surface, on the southern side, of the end slab as shown in Figure 6-14(a). Spalling was observed underneath the floor slab near the exterior plastic hinges as shown in Figures 6-14(b) and (c).

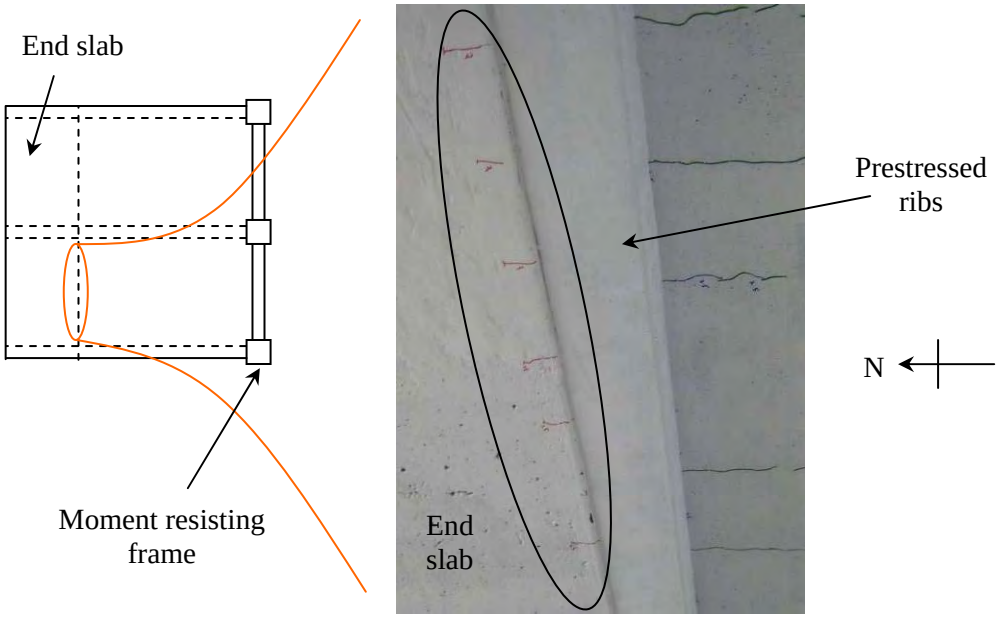

(a) Cracking underneath the end slab

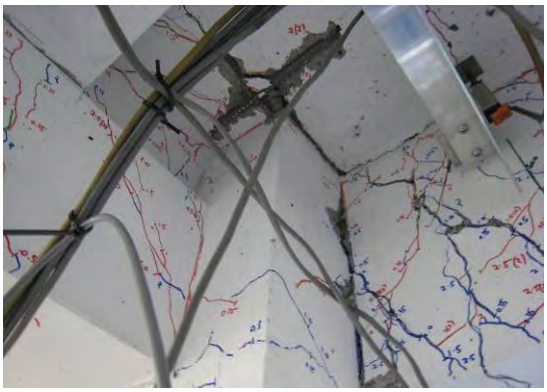

(b) Cracking around *Column C* underneath the floor slab

(c) Cracking around *Column A* underneath the floor slab

Figure 6-14. Visual observations during the ±2.5% drift cycles

Damage and permanent inelastic deformations such as differential movement between the beams and floor slab, twisting of external columns, cracking in the moment resisting frame, and torsional cracks in the transverse beams, all increased during the ±3.0% drift cycles. Some of these inelastic deformations are shown in Figure 6-15. It can be seen that the exterior plastic hinges lost concrete cover exposing the buckled bottom reinforcement.

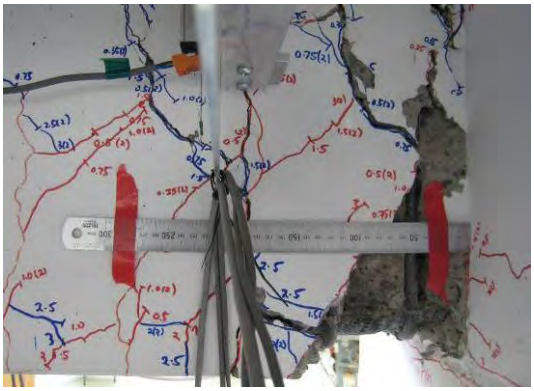

(a) Damage in an exterior plastic hinge

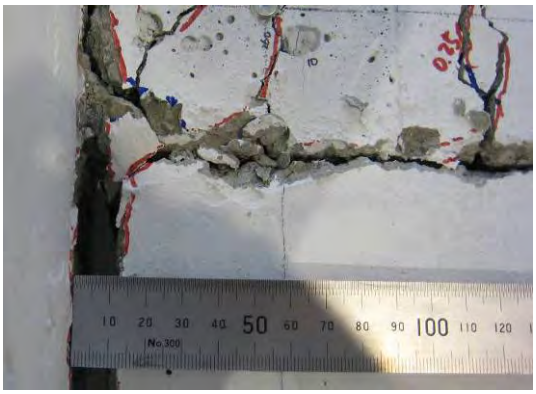

(b) Differential horizontal movement

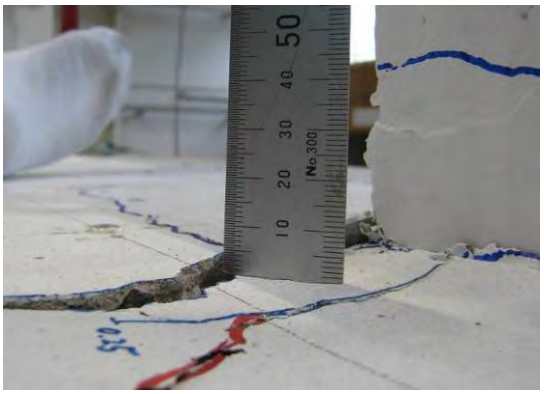

(c) Differential vertical movement

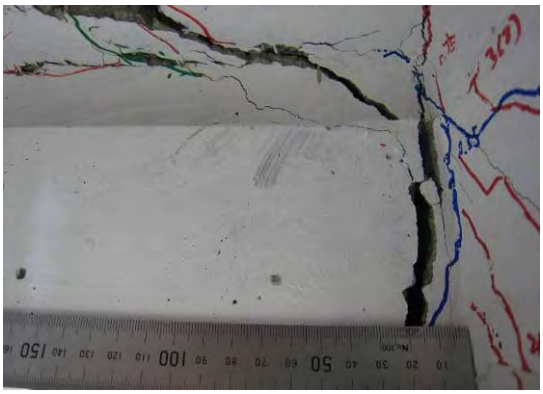

(d) Cracking at a rib connection

Figure 6-15. Visual observations during the ±3.0% drift cycles

At the end of 3.5% drift cycles, one of the bottom bars in the West end exterior plastic hinge fractured. The ribs near the moment resisting frame were lifted off their supports as shown in Figure 6-16(b). This is partially due to differential vertical movement between the floor and the transverse beam and partially due to the longitudinal beam increasing in depth. This increase in depth of the beam can be as high as 12mm, as shown in Figure 6-27. Figure 6-16(c) shows the large shear deformation observed in the exterior plastic hinge next to *Column A*.

(a) Fracture of reinforcing bars in the west end exterior plastic hinge

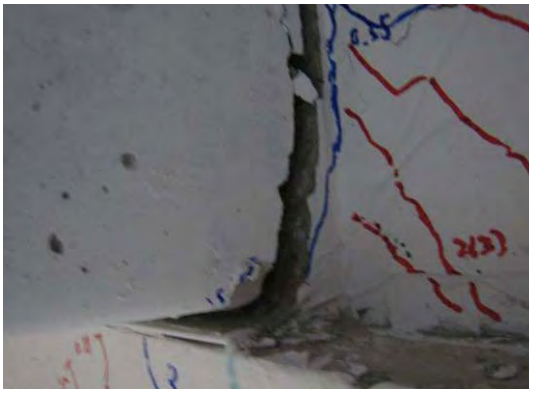

(b) Uplift of prestressed rib from the support

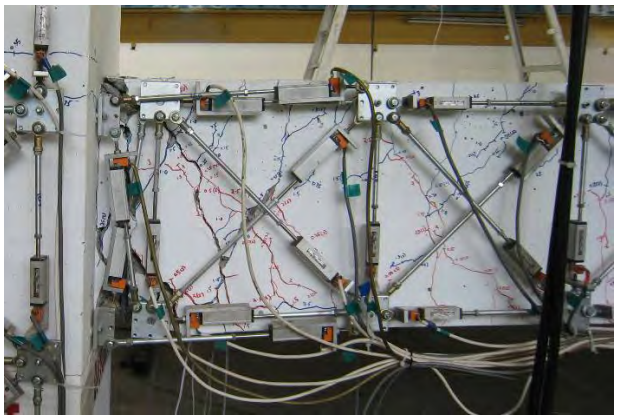

(c) Shear deformation in the exterior plastic hinge next to *Column A*

Figure 6-16. Visual observations during the ±3.5% drift cycles

During the ±4.0% drift cycles, the rest of the bottom reinforcement in the West end exterior plastic hinge fractured. The bottom reinforcement in the East end exterior plastic hinge buckled severely. The internal plastic hinge lost some concrete cover. The physical condition of the specimen at the end of 4% drift cycles is shown in Figure 6-17.

(a) Fracture of reinforcing bars in the west end exterior plastic hinge

(b) Reinforcement buckled in the east end exterior plastic hinge

(c) Partial lost of cover in an interior plastic hinge

(d) Torsional cracks in a transverse beam

Figure 6-17. Visual observations during the ±4.0% drift cycles

During the ±4.5% drift cycles, all of the bottom reinforcement in the East end exterior plastic hinge fractured and consequently, the test was terminated.

6.2.3 Observed Damage at the End of the Test

Photos showing the damage in the sub-assembly at the end of the test are reproduced in Figures 6-18 and 6-19. It can be seen from Figure 6-18 that the columns remained elastic, with minor cracking in the beam-column joints. Figures 6-19(a) and (b) show the crack patterns around the exterior and interior plastic hinges. It can be seen that the region around the exterior plastic hinges sustained much more damage than that around the interior plastic hinges. This is because elongation of interior plastic hinges was partially restrained by the floor slab. This is also reflected by the permanent crack widths at the interface between the ribs and transverse beams as shown in Figures 6-

19(c) and (d). The crack width around the exterior plastic hinges was of the order of 10mm, which is more than double the crack width around the interior plastic hinges. Shear and torsional cracks were observed in the transverse beams as shown in Figure 6-19(f).

(a) Cracking in the west bay moment resisting frame

(b) Cracking in the east bay moment resisting frame

Figure 6-18. Cracking observed in the frame at the end of the test


(a) Damage around an exterior plastic hinge

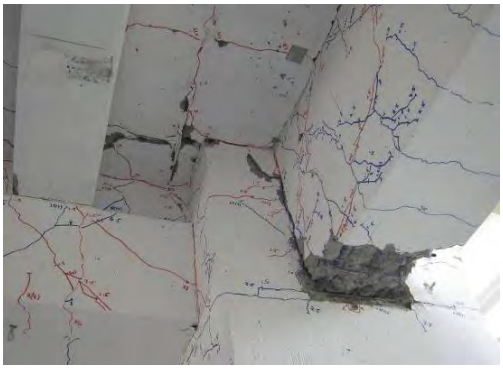
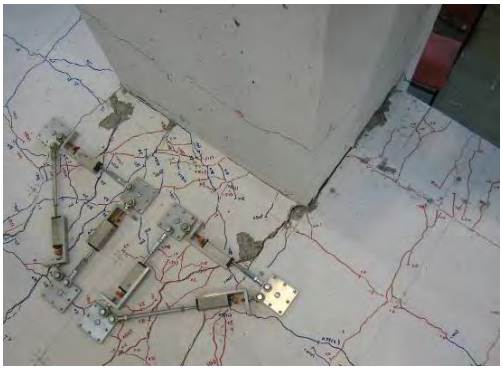

(b) Damage around an interior plastic hinge

(c) Prestressed rib connection next to exterior plastic hinge

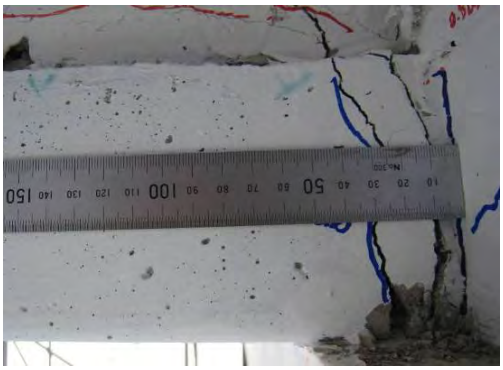

(d) Prestressed rib connection next to interior plastic hinge

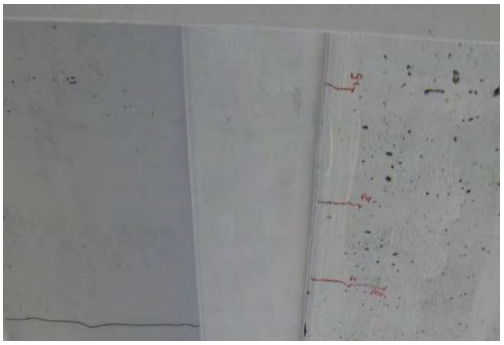

(e) Cracking in the end slab

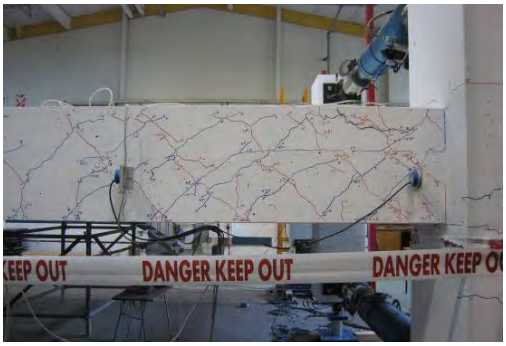

(f) Shear and torsional cracks in a transverse beam

Figure 6-19. Damage observed at the end of the test

6.2.4 Crack Patterns on the Floor Slab

A series of diagrams showing the crack patterns on the floor slab at the end of each drift magnitude are given in Figure 6-20. The green lines represent shrinkage cracks that developed prior to the test, the red lines represent cracks that developed during the positive drift cycles, and the blue lines represent cracks that developed during the negative drift cycles. Here, a positive drift implies a clockwise column rotation.

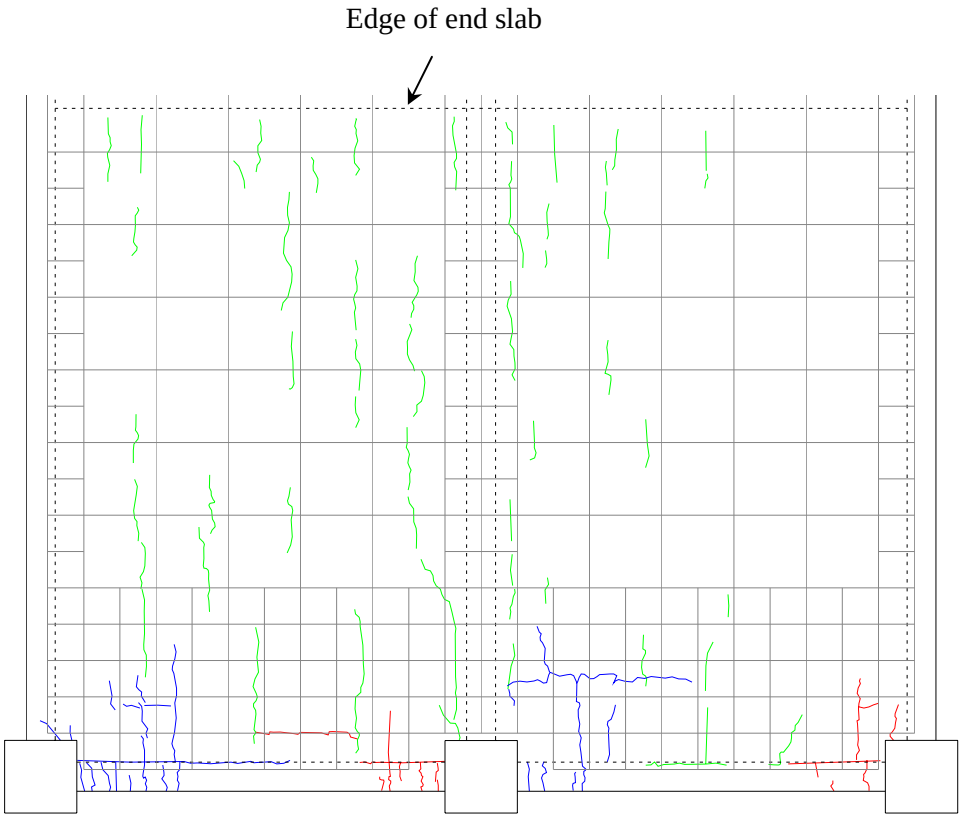

(a) 0.25% drift

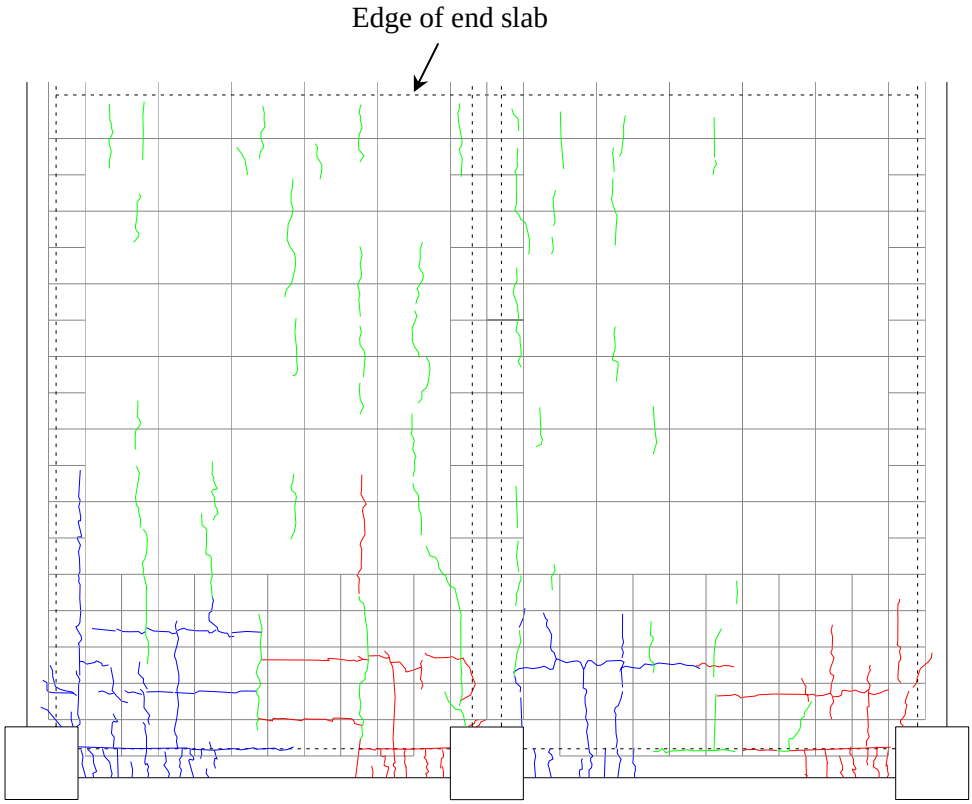

(b) 0.35% drift

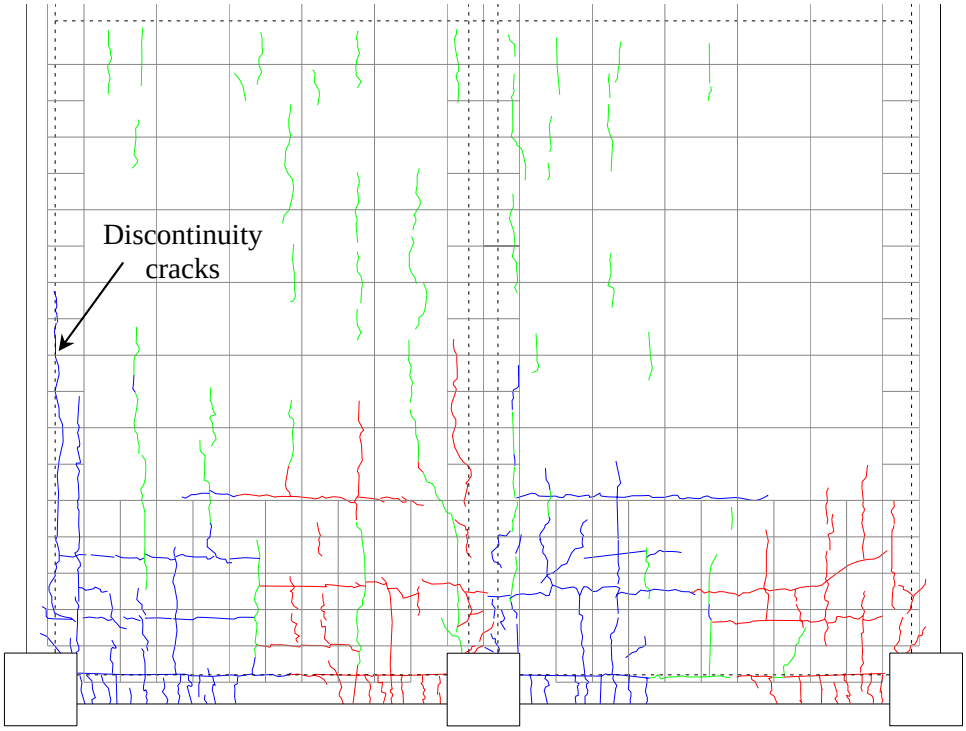

(c) 0.5% drift

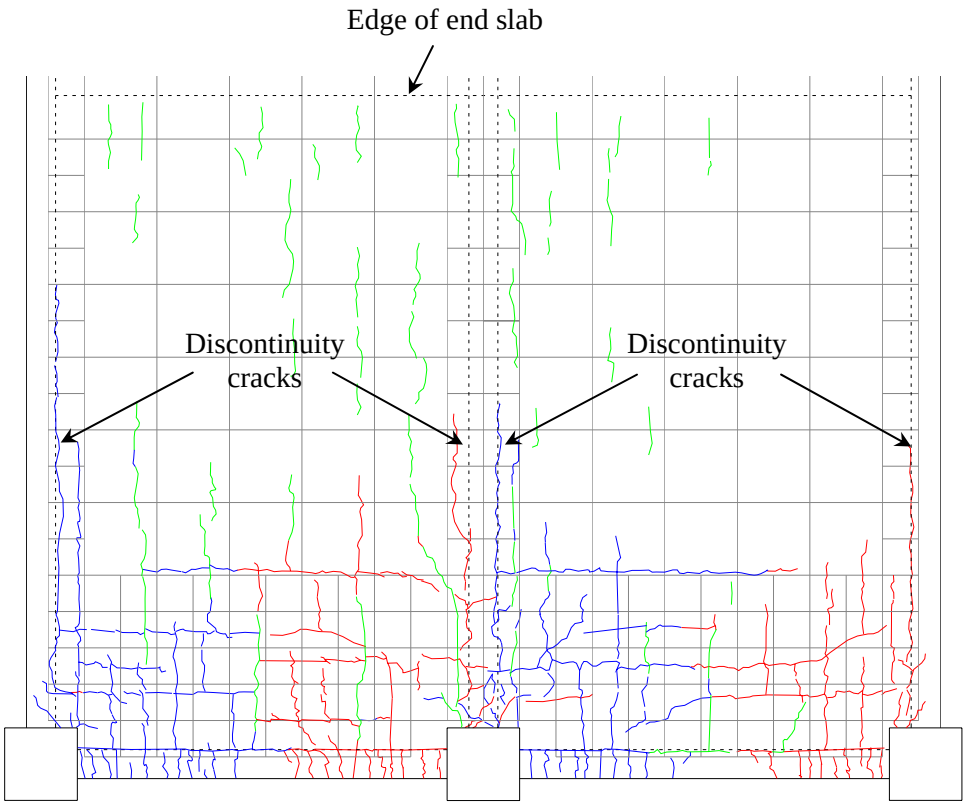

(d) 0.75% drift

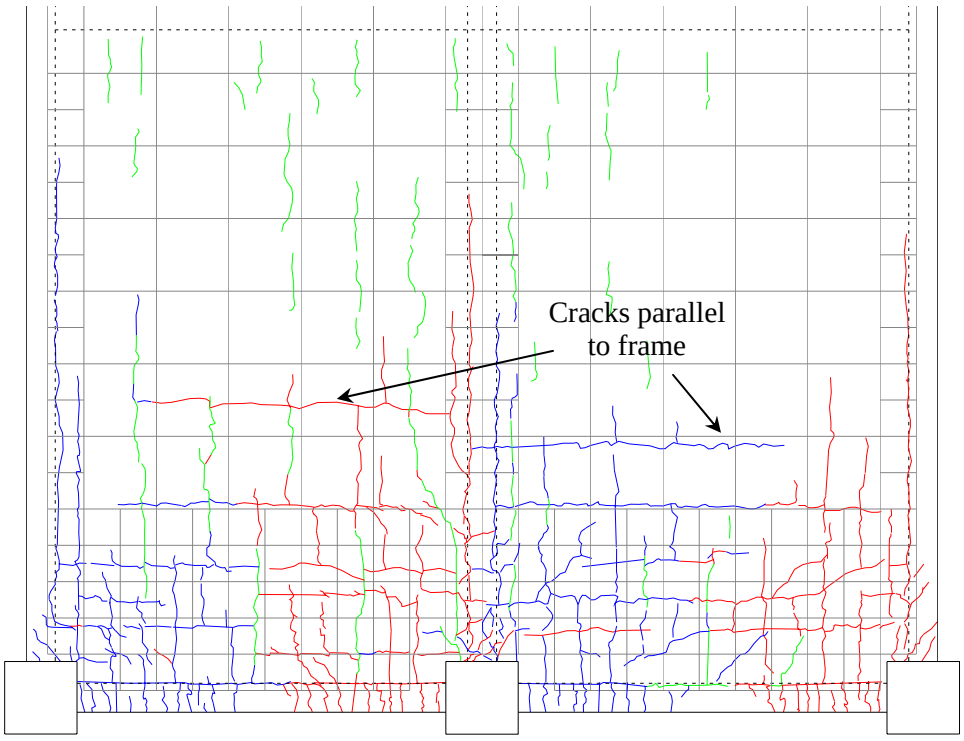

(e) 1.0% drift

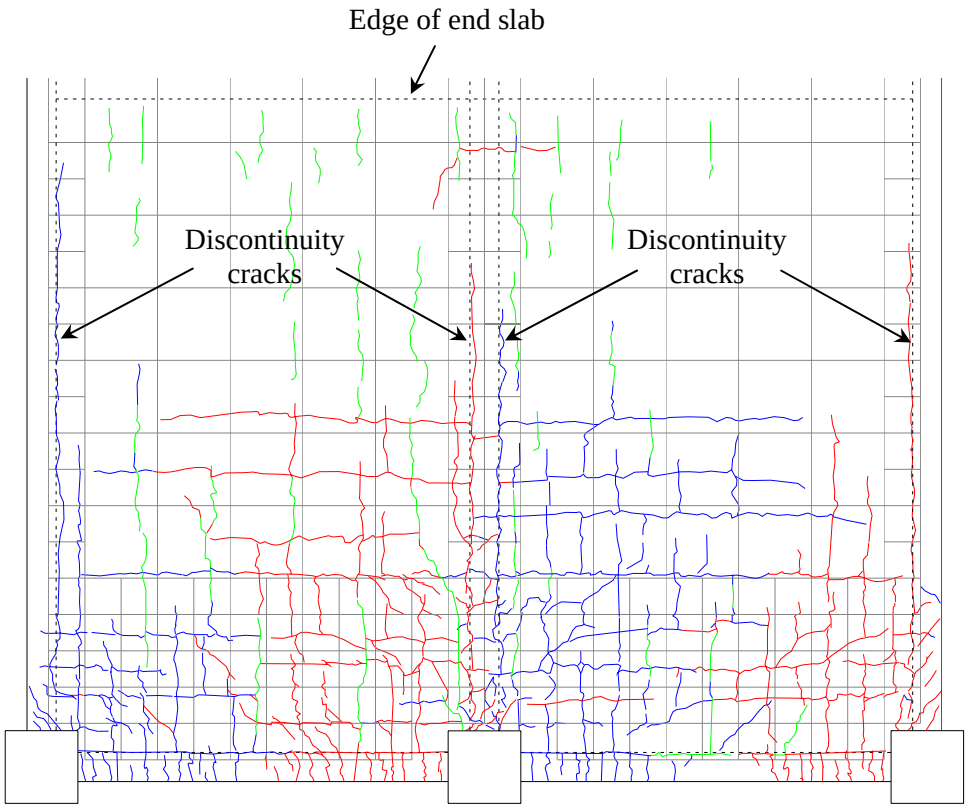

(f) 1.5% drift

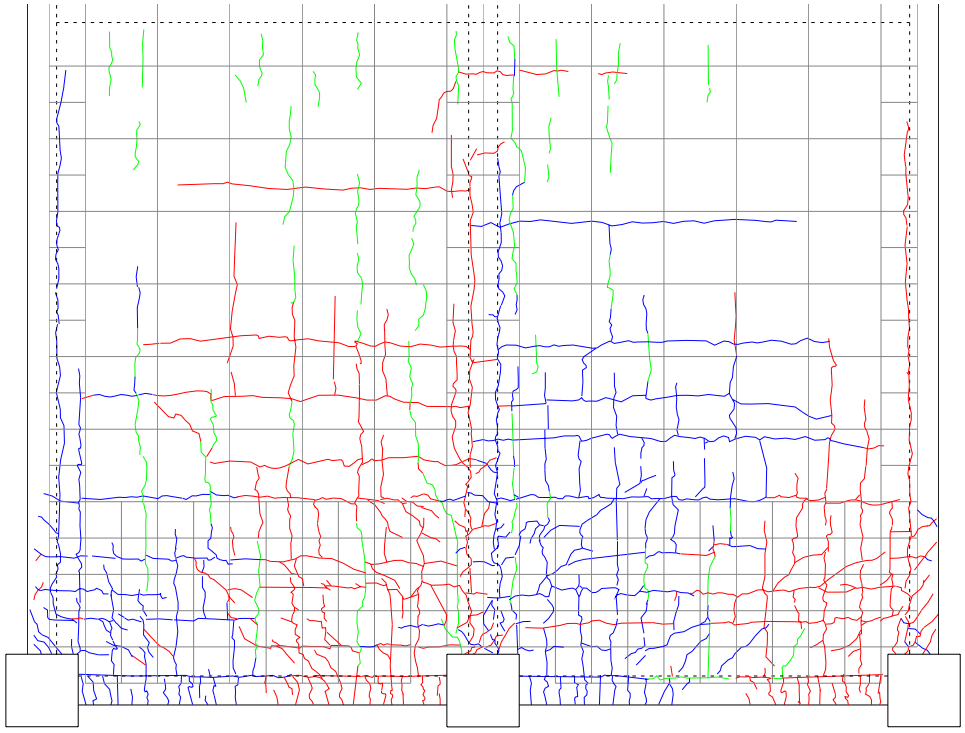

(g) 2.0% drift

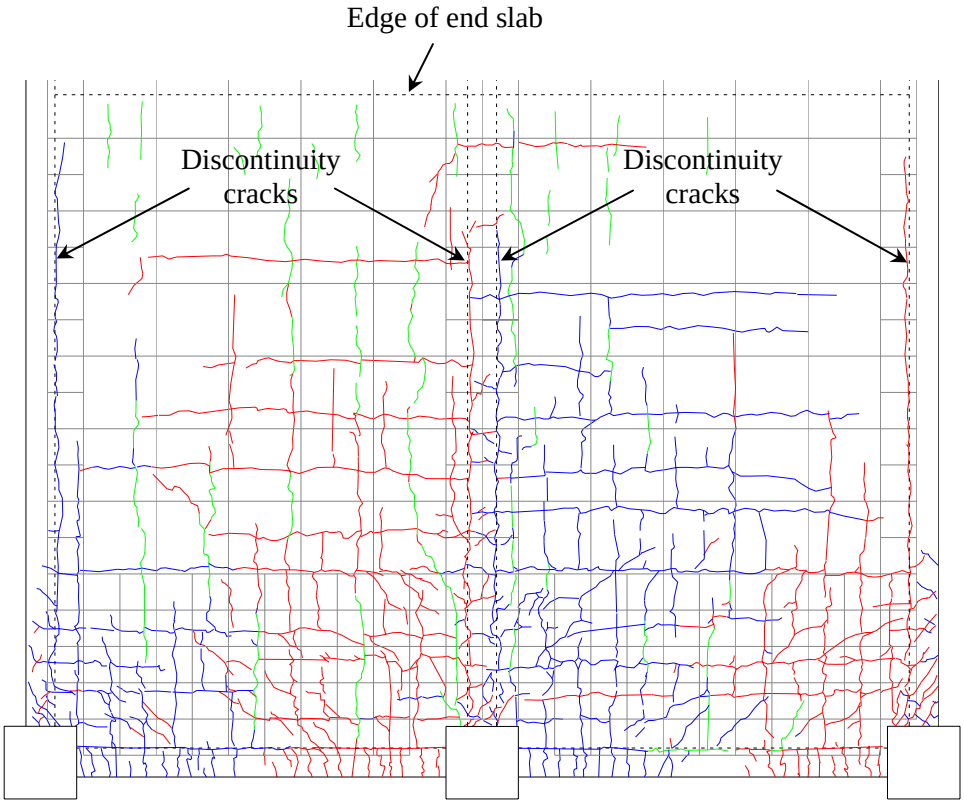

(h) 2.5% drift

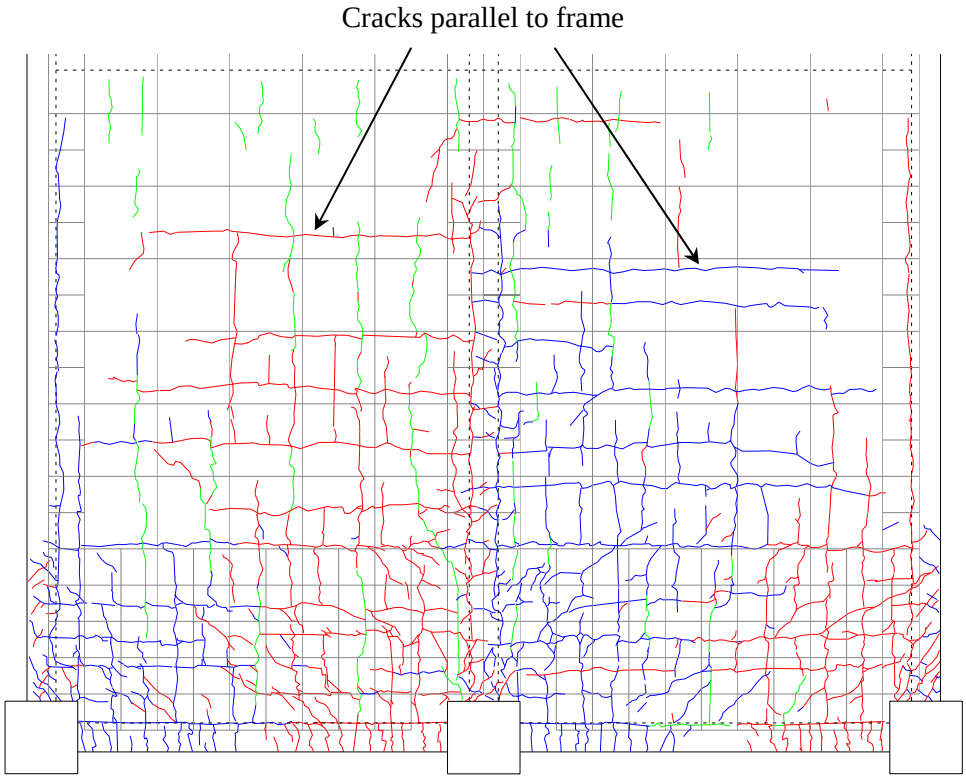

(i) 3.0% drift

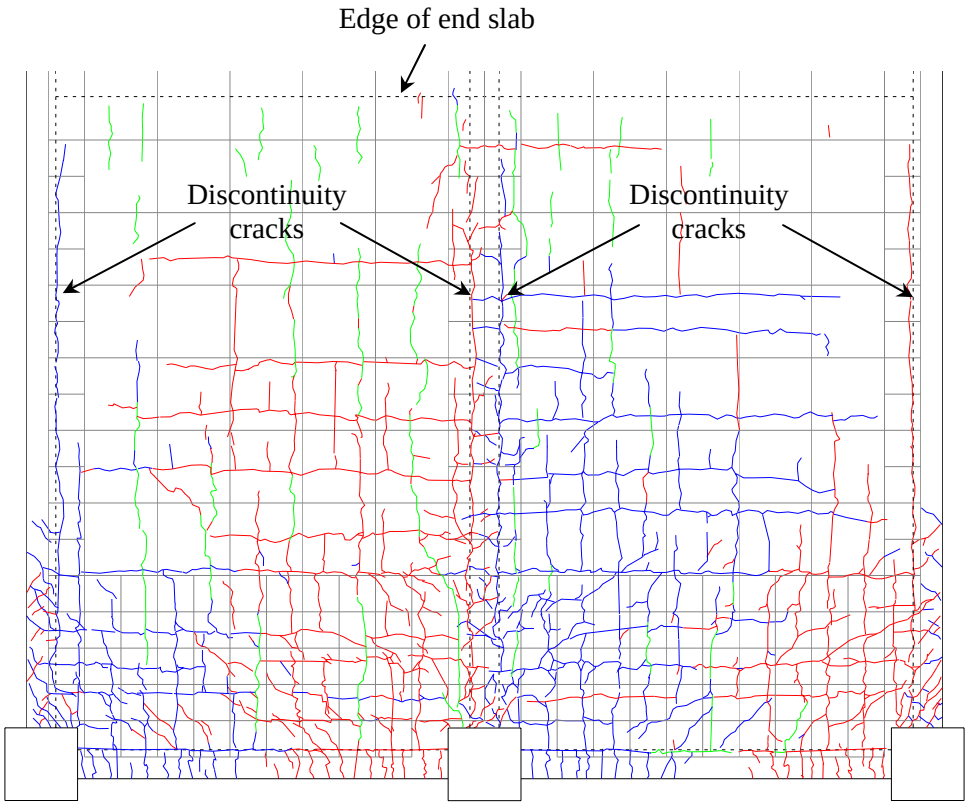

(j) 4.0% drift

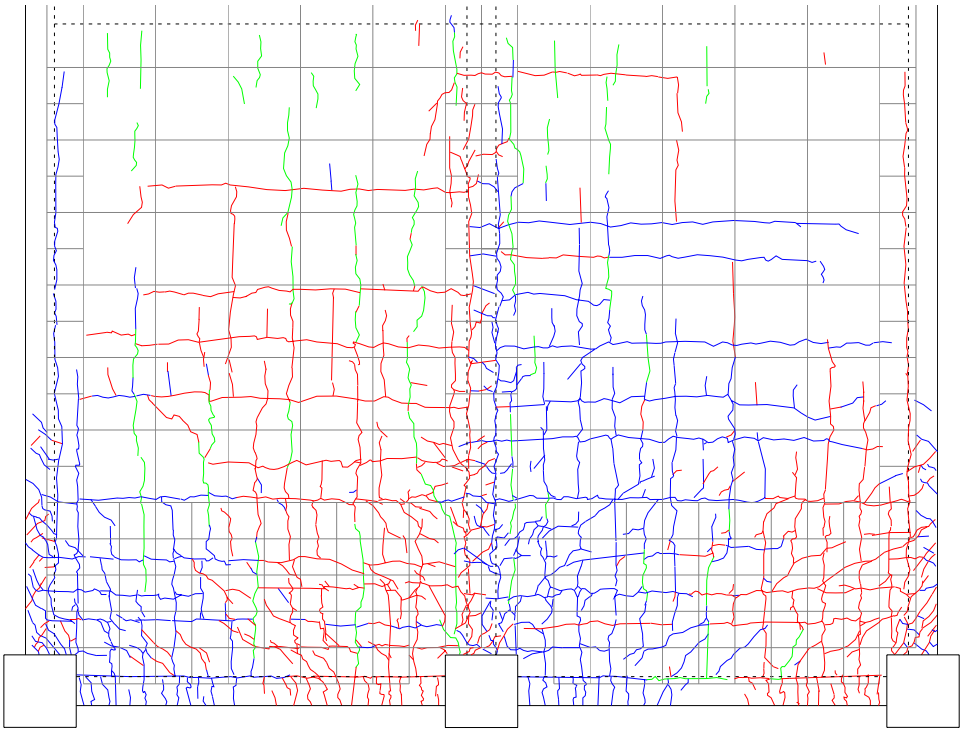

(k) 4.5% drift

Figure 6-20. Cracks pattern on the floor slab

It can be seen from Figure 6-20 that many cracks formed parallel, perpendicular and diagonal to the frame. The diagonal cracks were all inclined towards the internal column. The angle of these diagonal cracks to the horizontal plane ranged from 31 degree to 45 degree. The cracks parallel to the frame were initiated close to the internal transverse beam and extend across the floor slab. The overall crack pattern and the way they developed imply that the floor slab was restraining elongation of interior plastic hinges through shear and bending actions, with the slab on each side of the internal transverse beam acting as a deep beam as shown in Figure 6-21.

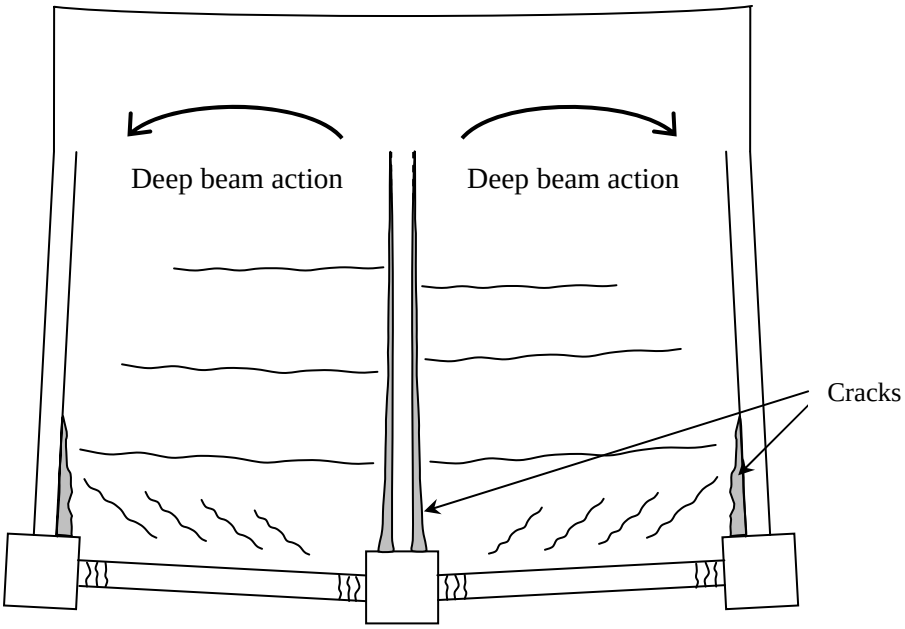

Figure 6-21. Deep beam action of floor slab restraining elongation of interior plastic hinges

6.3 GENERAL RESULTS

6.3.1 Force-Displacement Response

The total force-displacement response of the frame is plotted in Figure 6-22. The force was obtained from the load cells and the applied drift was interpreted from the rotary potentiometers mounted on *Column A*. Overall, the structure behaved in a ductile manner with high energy dissipation. Yielding of the longitudinal reinforcement in the exterior plastic hinges occurred close to 0.75% drift. Maximum

lateral forces of 334kN and 318kN were reached at the peak of positive and negative 3% drift cycle respectively.

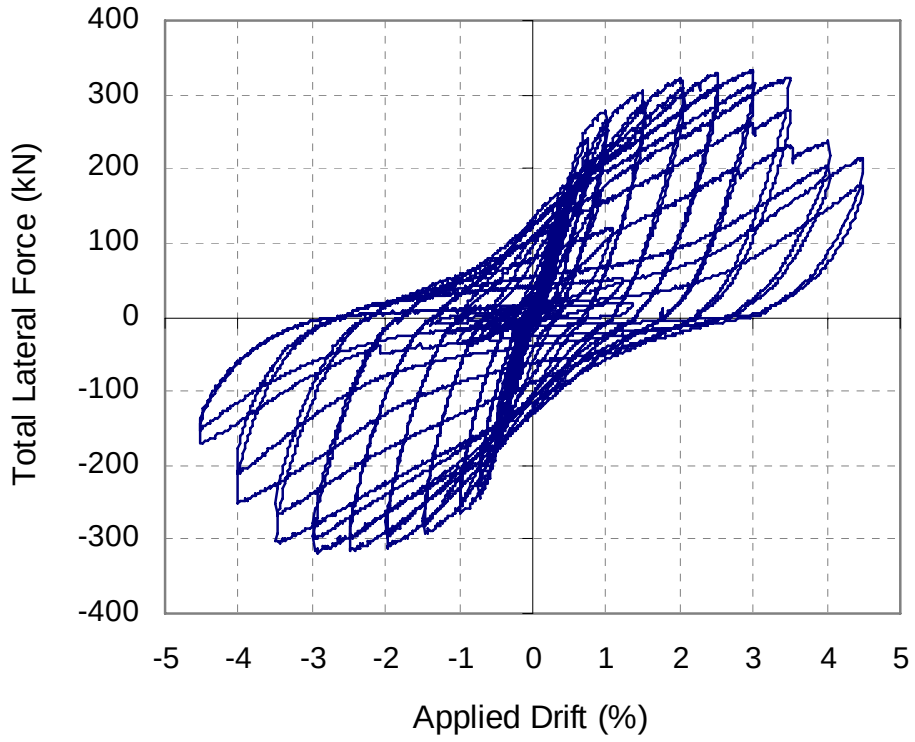

Figure 6-22. Total force-displacement relationship of the sub-assembly

As mentioned in Chapter 5, the displacements applied at the top and bottom of each column were adjusted iteratively until the forces at the top and bottom of each column were equal and opposite. However, the forces applied at the top and bottom of each column in reality were not necessarily equal, but were always within the tolerance of ±3kN from each other. Figure 6-23 plots the averaged top and bottom column forces against the applied drift for each individual column.

It can be seen that the external columns experienced less pinching than the internal column. This is believed to be due to the difference in anchorage of the beam flexural reinforcement within the beam-column joints, which affects the bond condition of the reinforcing bars. The reinforcing bars were hooked in the external beam-column joints, which provide sufficient anchorage to the flexural reinforcement. However, in the central beam-column joint, the reinforcing bars passed straight through the joint. In this case, the bond was insufficient for the flexural tension and compression forces to

be anchored in the column at large inelastic drift cycles. Consequently, the bars slipped through the joint zone, which resulted in the pinched hysteresis loop as observed in Figure 6-23(b). It should be noted that the diameter of the reinforcing bars passing through the central beam-column joint was 16mm, which was well within the design requirement to prevent premature bond slip, as specified in NZS 3101:2006 (Standards New Zealand 2006), where a 24mm bar would have been permitted.

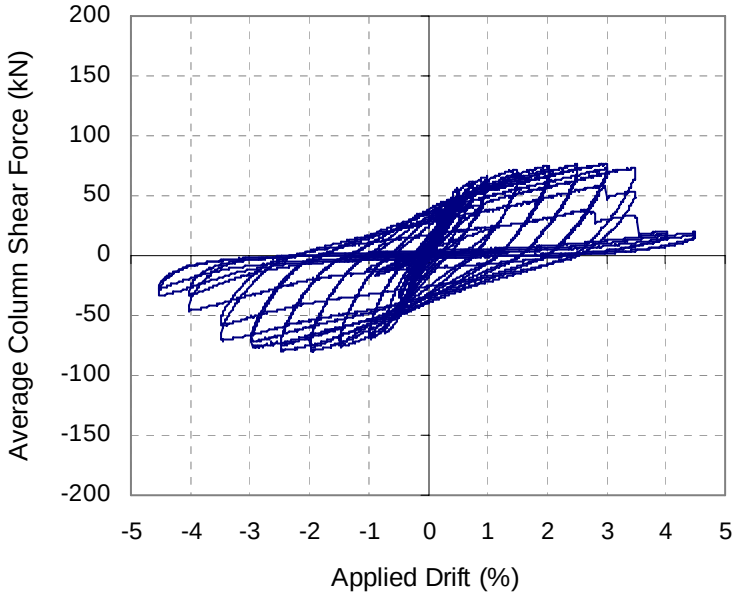

(a) *Column A*

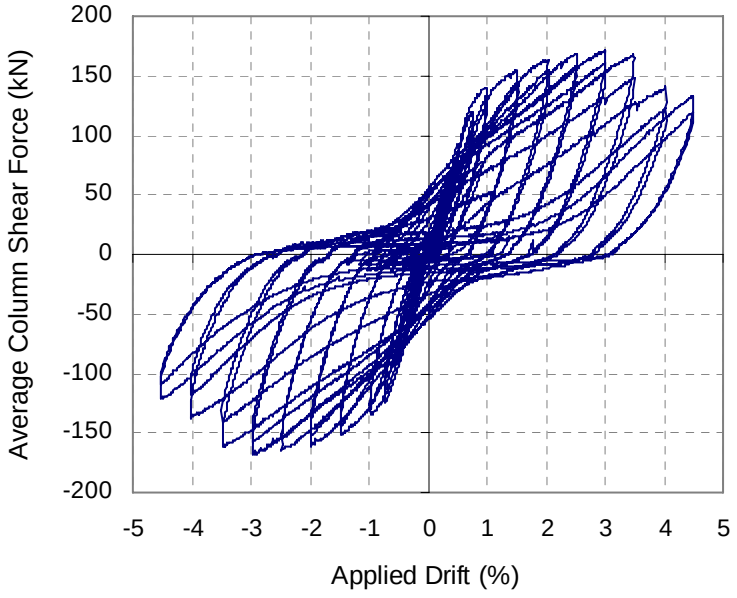

(b) *Column B*

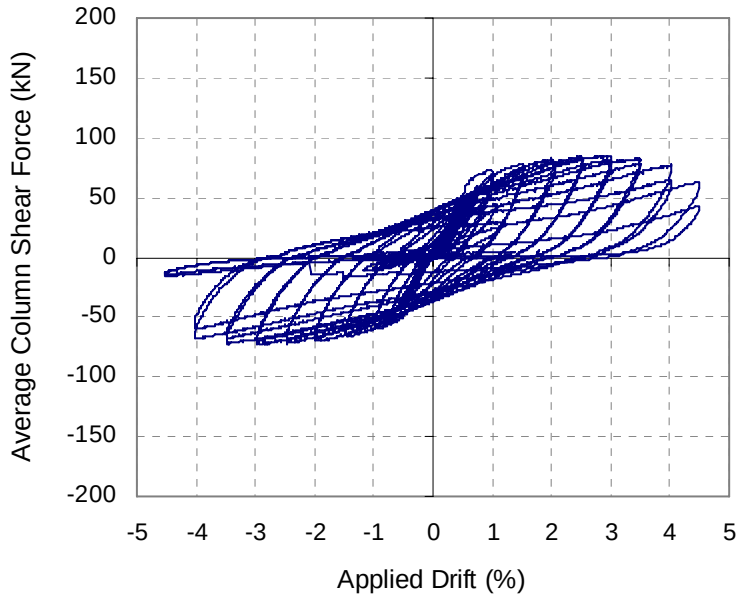

(c) *Column C*

Figure 6-23. Averaged force-displacement relationship of individual column

A plot of the reinforcement movement on one side minus the movement on the other versus the total lateral force for the internal beam-column joint is shown in Figure 6-24. The slip may be identified in regions where there is a significant change in the difference of reinforcement movement with little change in force. These regions are circled in Figure 6-24. It can be seen that slip generally occurred when the lateral force changed sign. The magnitude of slip in the internal beam-column joint is of the order of 2mm at 3% drift.

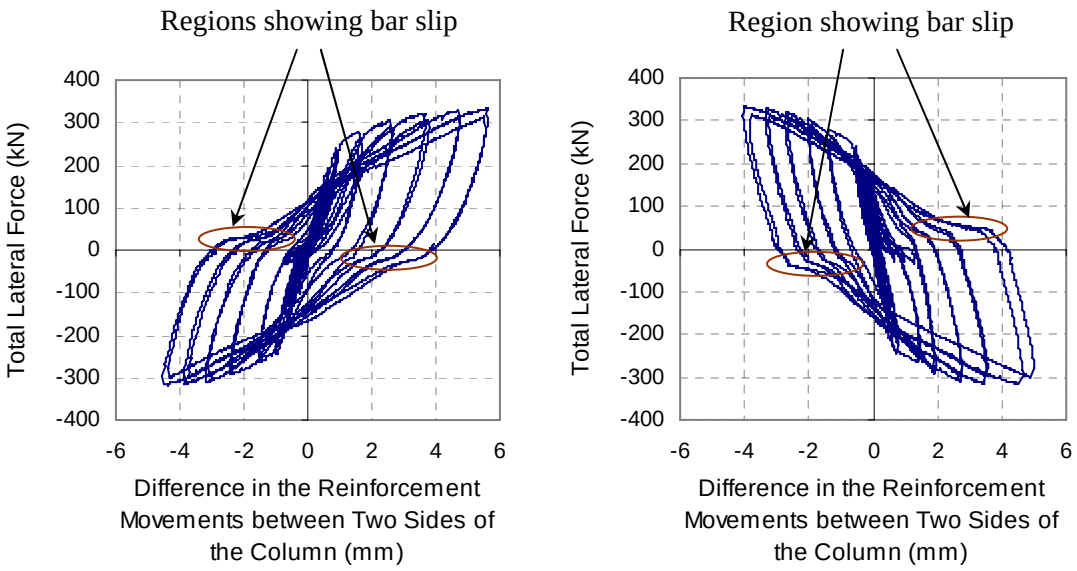

(a) Top reinforcement level (b) Bottom reinforcement level

Figure 6-24. Slipping of reinforcement in the central beam-column joint up to 3% drift

The averaged lateral force sustained at the peaks of the positive and negative displacement cycles in each column is given in Tables 6-3 and 6-4. In general, the total storey shear force in the positive peaks was larger than that in the negative peaks. This may be due to damage sustained in the frame at the positive drift cycles reducing the load carrying capacity of the frame in the negative drift cycles.

Table 6-3. Averaged column shear force at the peak positive drift cycles

	Averaged column shear force (kN)			**Total shear force (kN)**
	Column *A*	**Column *B***	**Column *C***	
1st cycle at +0.5 %	56.3	93.2	43.2	192.7
1st cycle at +0.75 %	62.4	119.1	59.7	241.2
1st cycle at +1.0 %	65.5	139.1	72.9	277.5
1st cycle at +1.5 %	71.5	155.3	78.9	305.7
1st cycle at +2.0 %	74.7	163.3	82.9	320.9
1st cycle at +2.5 %	76.3	167.9	85.5	329.7
1st cycle at +3.0 %	76.4	171.6	85.6	333.6
1st cycle at +3.5 %	73.3	166.6	83.5	323.4
1st cycle at +4.0 %	20.3	140.0	77.7	238.0
1st cycle at +4.5 %	19.1	131.9	63.7	214.7

Table 6-4. Averaged column shear force at the peak negative drift cycles

	Averaged column shear force (kN)			Total shear force (kN)
	Column *A*	**Column *B***	**Column *C***	
1st cycle at -0.5 %	50.9	91.1	40.8	182.8
1st cycle at -0.75 %	65.1	124.8	55.7	245.6
1st cycle at -1.0 %	69.5	133.8	61.1	264.4
1st cycle at -1.5 %	75.5	150.5	67.3	293.3
1st cycle at -2.0 %	79.8	159.6	71.2	310.6
1st cycle at -2.5 %	79.7	163.6	72.7	316
1st cycle at -3.0 %	76.2	168.1	73.6	317.9
1st cycle at -3.5 %	70.5	160.8	72.9	304.2
1st cycle at -4.0 %	46.3	137.0	68.6	251.9
1st cycle at -4.5 %	34.0	120.1	17.1	171.2

6.3.2 Beam Elongation

As described in Section 5.5.2, elongation was measured using linear potentiometers, which were fixed to studs welded to the beam flexural reinforcement. Elongations in the exterior and interior plastic hinges are plotted in Figures 6-25 and 6-26 respectively. Elongation is only plotted up to 3% drift because the reinforcing bars started to buckle at that cycle, which reduced the accuracy of the measurements.

From these figures, we can see that elongation in the interior plastic hinges is much smaller than that in the exterior plastic hinges. This is likely due to a difference in the axial compression force sustained in the beams. The averaged elongation in the exterior plastic hinges at the end of 3% drift is 15mm, which corresponds to 3.8% of the section depth. The averaged elongation in the interior plastic hinges at the end of 3% drift is 5mm, which corresponds to 1.3% of the section depth.

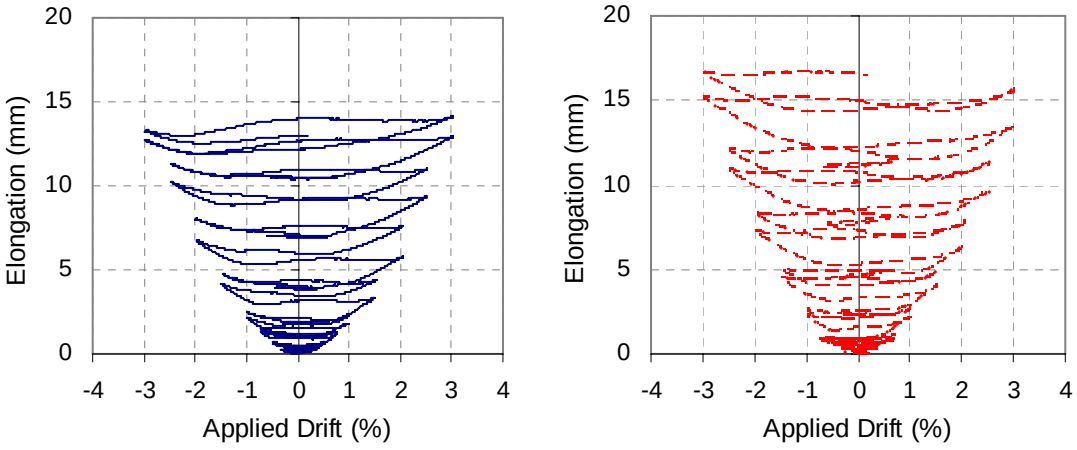

(a) West bay (b) East bay

Figure 6-25. Elongation in the exterior plastic hinges

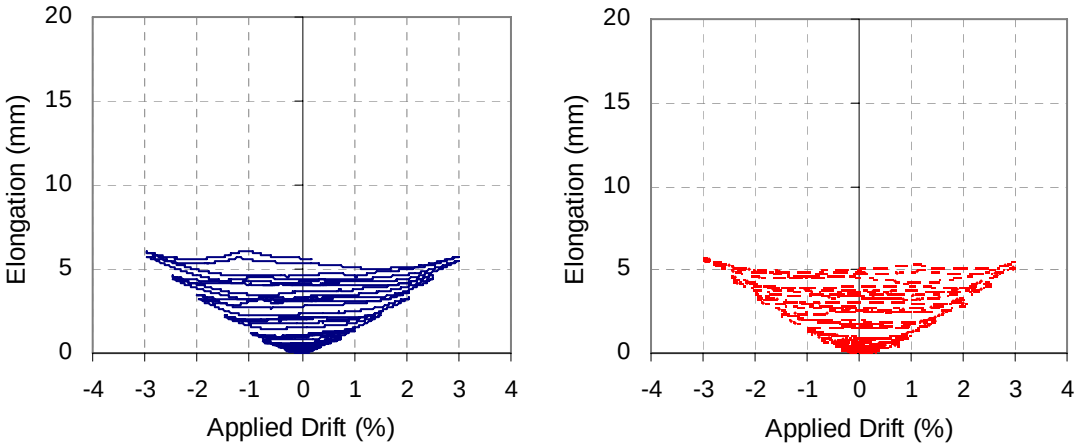

(a) West bay (b) East bay

Figure 6-26. Elongation in the interior plastic hinges

6.3.3 Increase in Beam Depth within the Plastic Hinges

It was described in Chapter 3 that part of the shear deformation in plastic hinges arises due to inelastic extension of stirrups. As stirrups extend the beam inevitably increases in depth. The increase in the beam depth measured from the first set of the vertical potentiometer, 90mm out from the column face, is shown in Figures 6-27 and 6-28. It can be seen that the increase in beam depth varies significantly between different plastic hinges. The averaged growth of the two exterior hinges and two interior hinges at the end of 3% drift is 7.8mm and 2.3mm, respectively. It has been shown in Chapter 3 that shear deformation from stirrup extensions decreases as axial compression force increases. This matches with the test results observed in this test,

where the increase in depth in the exterior plastic hinges (with smaller axial compression force) is much greater than that in the interior plastic hinges. The growth was less than 1mm in the second set of vertical potentiometers, 420mm out from the column face. This indicates that the growth in the beam depth is localised in the plastic hinges.

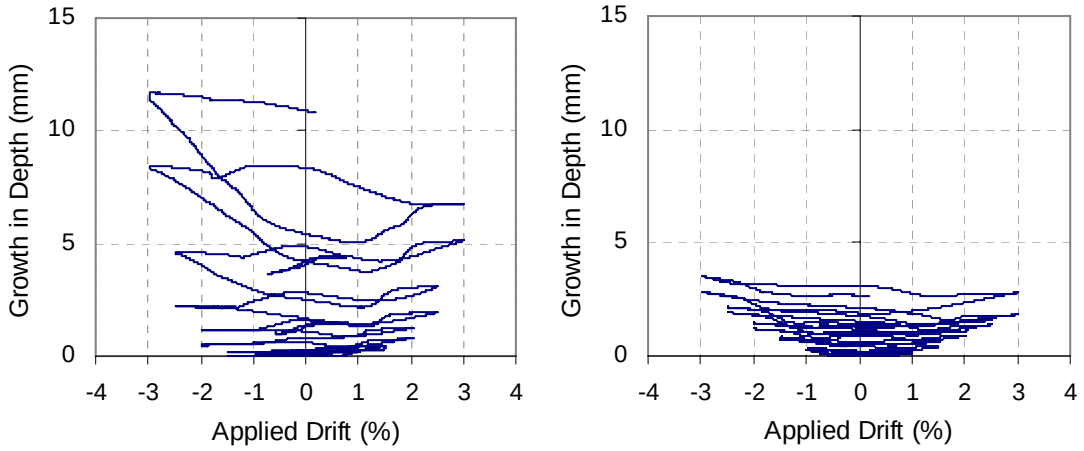

(a) West bay (b) East bay

Figure 6-27. Increase in beam depth in the exterior plastic hinges

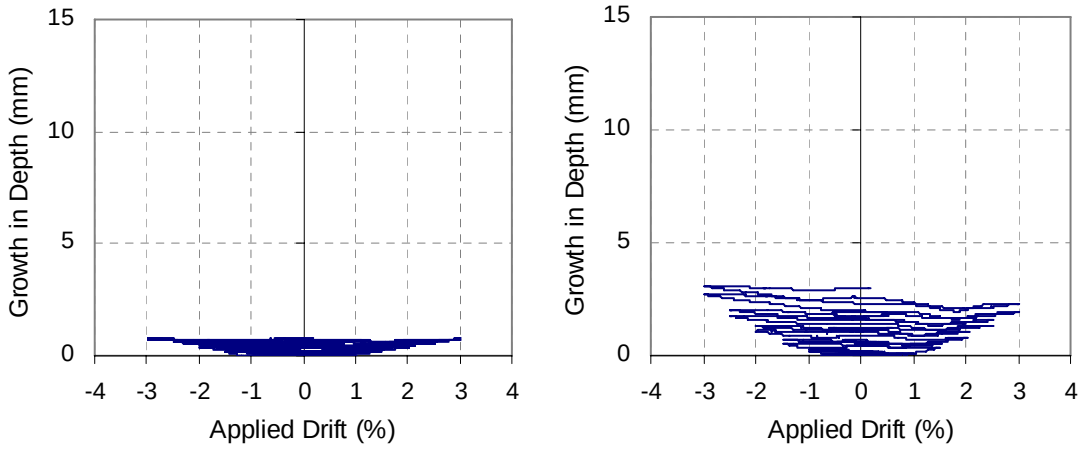

(a) West bay (b) East bay

Figure 6-28. Increase in beam depth in the interior plastic hinges

6.3.4 Frame Response

Figure 6-29 plots the absolute value of the applied column displacement at the peak positive and negative drift cycles. The displacements were measured using column inclinometers, rotary potentiometers. These values are compared with displacements

calculated from the linear potentiometer measurements made on the frame. The comparison between the calculated and directly measured displacements gives an indication of the accuracy of the instrumentation, especially the linear potentiometer measurements. In general, the displacements calculated from the potentiometers are in satisfactory agreement with the direct measured displacements from the rotary potentiometers and inclinometers. The error increases after 3% drift due to buckling of beam reinforcement. A method for interpreting column displacements from linear potentiometers in the frame is described in Section 5.5.6.

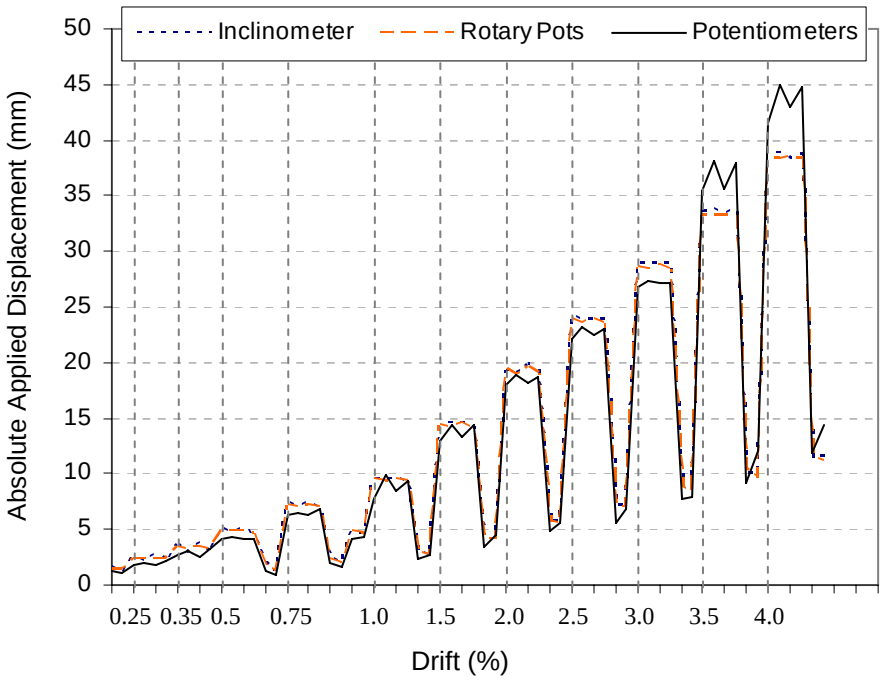

(a) *Column A*

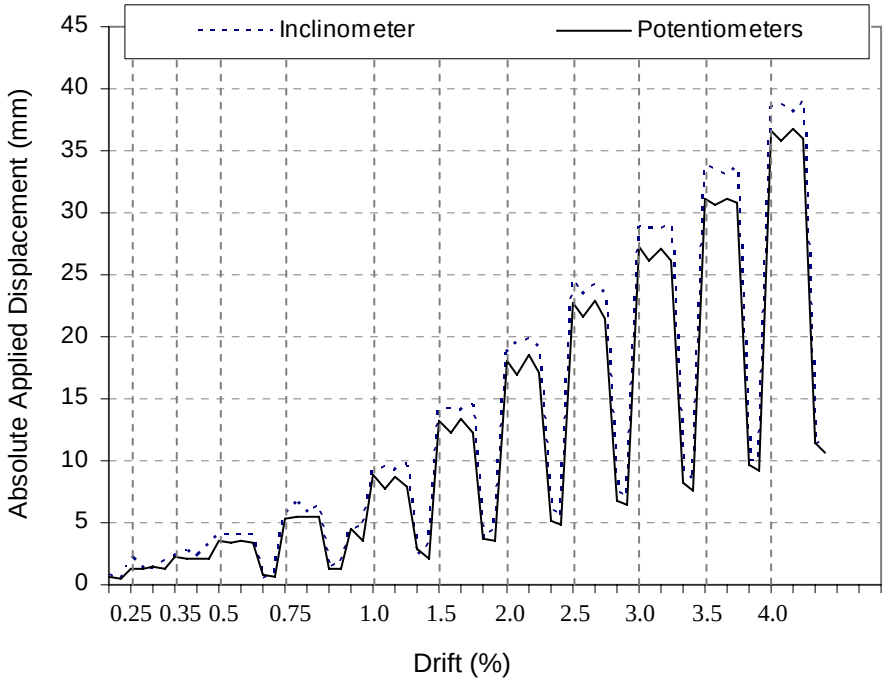

(b) *Column B*

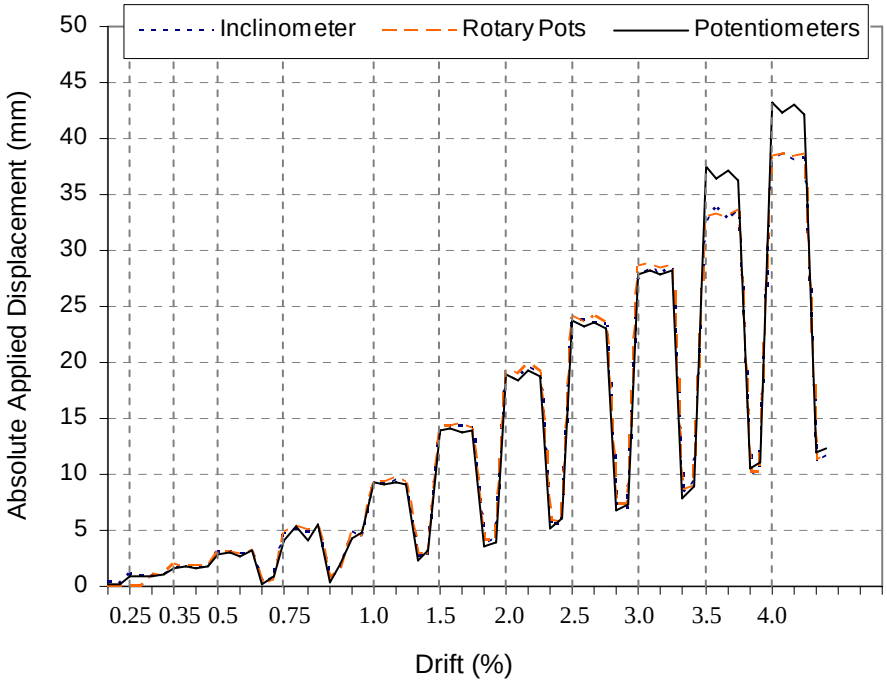

(c) *Column C*

Figure 6-29. Comparison of the applied and calculated column displacement

Figure 6-30 plots the contribution of member deformations to the displacement at the top and bottom of each column deduced from the linear potentiometer measurements on the frame. The member deformations are separated into four categories; beam

flexure rotation, beam shear deformation, column flexure rotation and column and beam-column joint shear deformation. For a simpler representation, the member deformations were averaged at the peaks of each positive and negative drift magnitude.

The diagram shows that the majority of frame deformation arises from beam flexure rotation. The amount of beam shear deformation increases as the displacement amplitude increases. The combined column and beam-column joint deformations are generally less than 10% of the total deformation in the external columns, whereas in the central column, they are generally less than 15% of the total deformation.

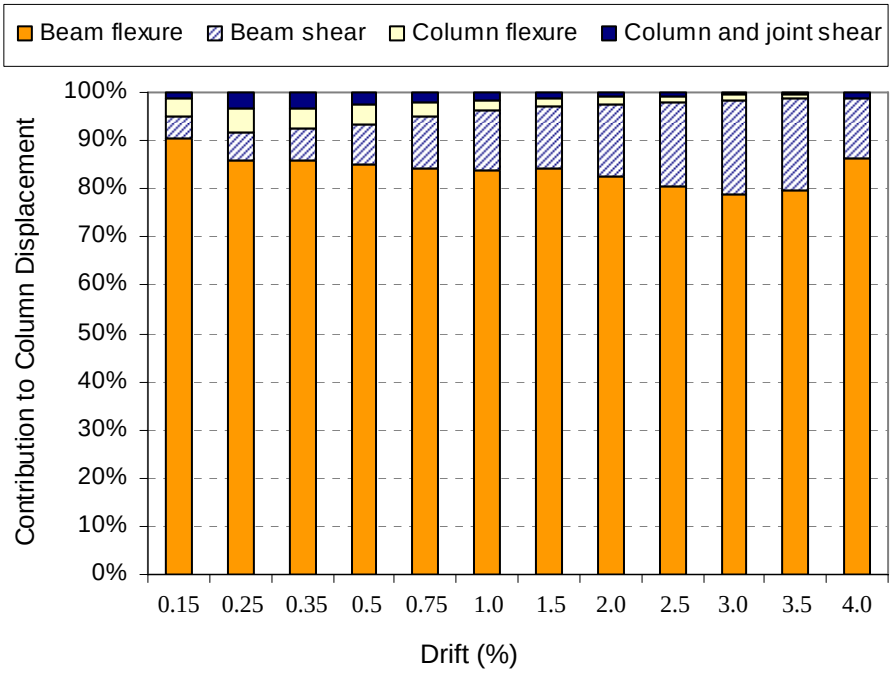

(a) *Column A*

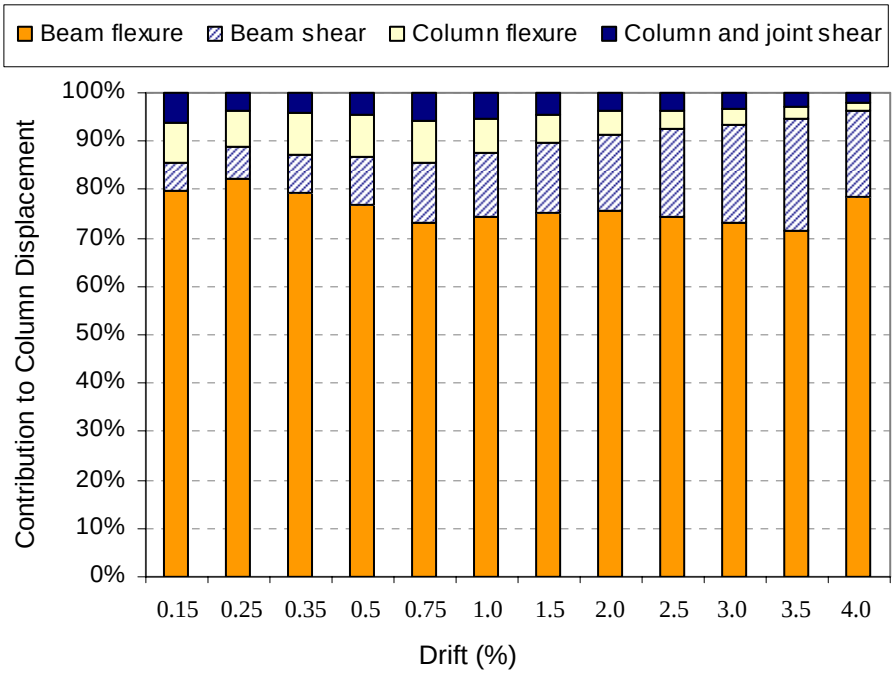

(b) *Column B*

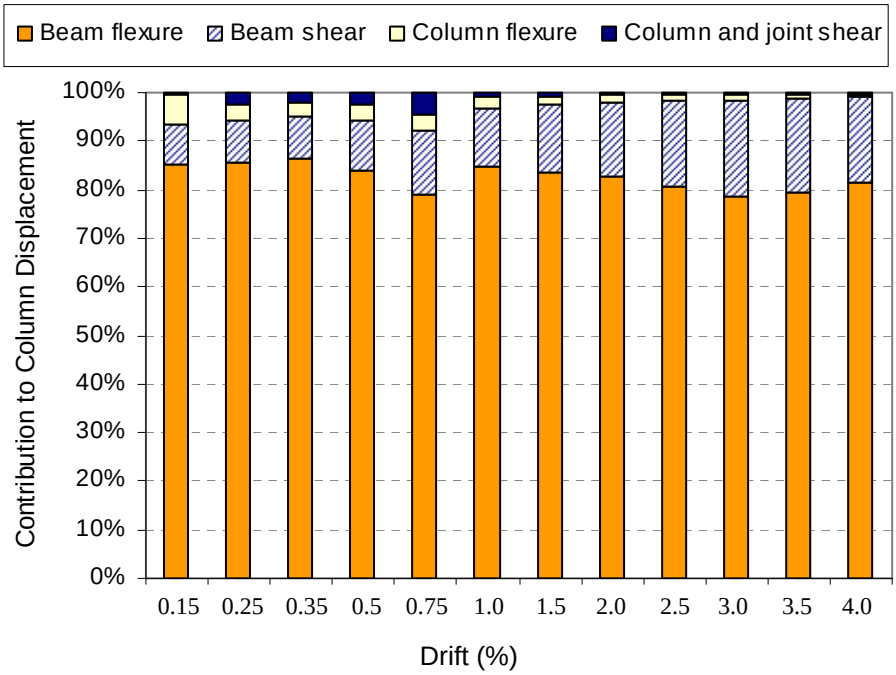

(c) *Column C*

Figure 6-30. Contribution of the member deformations to the applied column displacement

6.3.5 Transverse Beam Rotation

Figure 6-31 plots the torsional rotation at different sections along the transverse beams up to 4% drift, where 'CF' is short for column face. It can be seen that the

transverse beams were twisting. This is because the end closer to the end slab was restrained against rotation, whereas the other end (connected to the column) was rotating with the column.

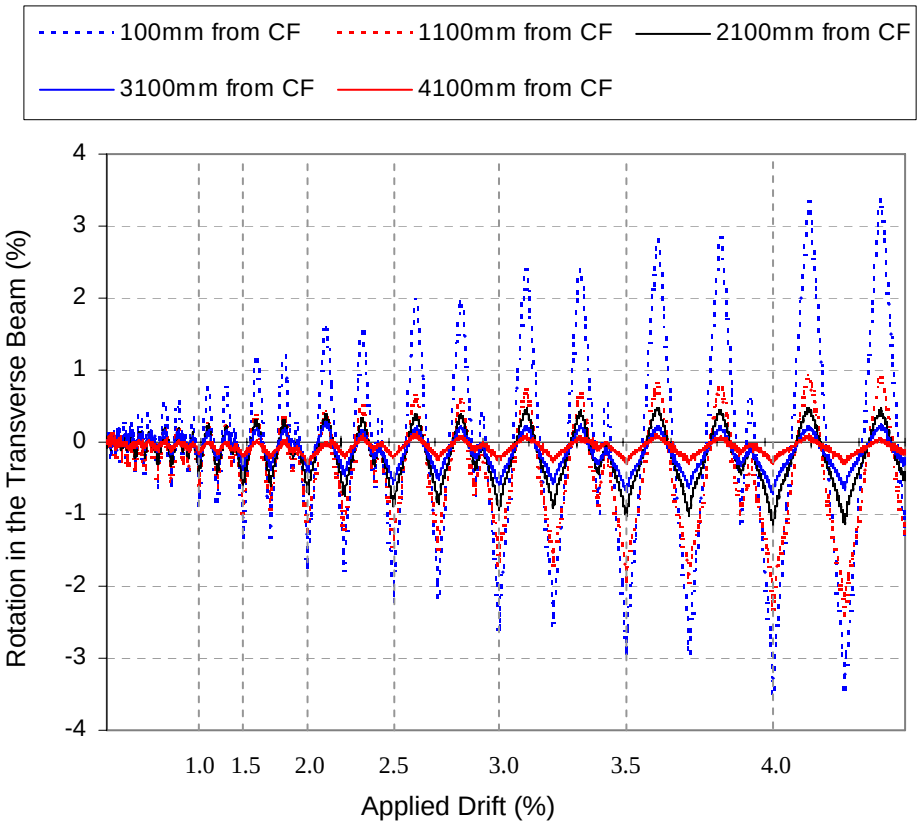

(a) West transverse beam

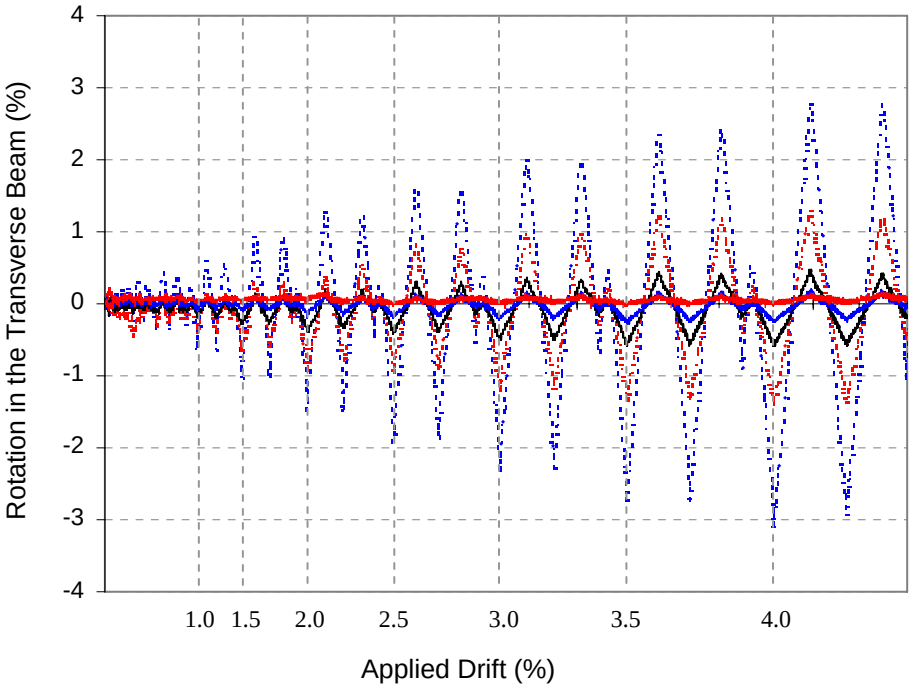

(b) Centre transverse beam

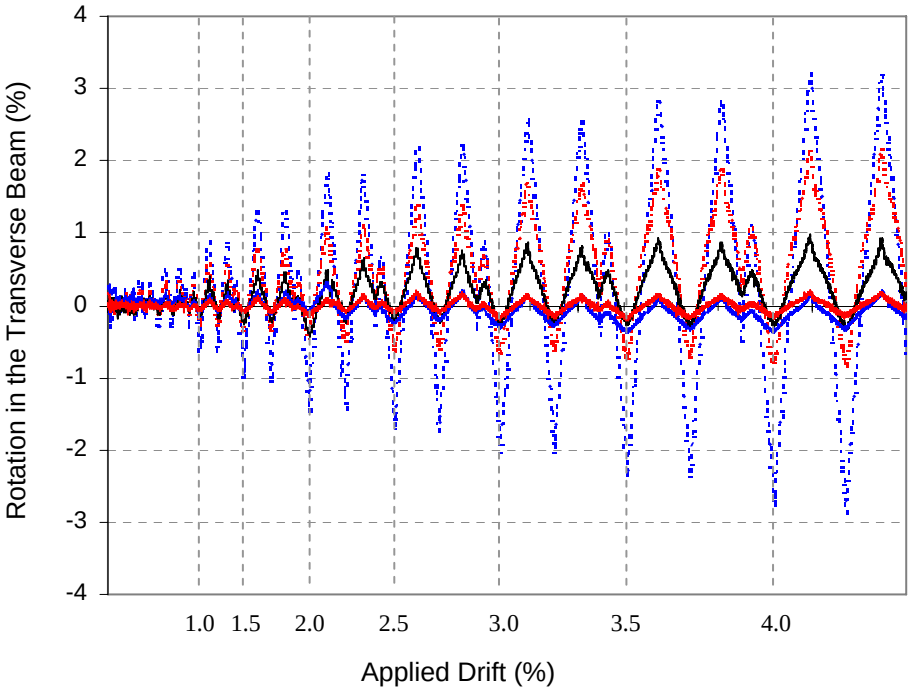

(c) East transverse beam

Figure 6-31. Twist at different sections along the transverse beams

For a better visualisation, a schematic diagram showing the deformation along the top of the transverse beam centreline, induced by the transverse beam rotation, at the peaks of ±4% drift cycles is plotted in Figure 6-32. It should be noted that as the

transverse beam rotation at the column face is equal to the rotation of the column, the deformation at the column face is not plotted in the figure. The following observations can be drawn from this figure:

1. Torsional rotation in the external transverse beams is smaller in one direction than in the other, except for the measurements taken at 100mm from the column face;
2. Twist in the external transverse beams decreases more rapidly when it imposed compression to the floor slab.

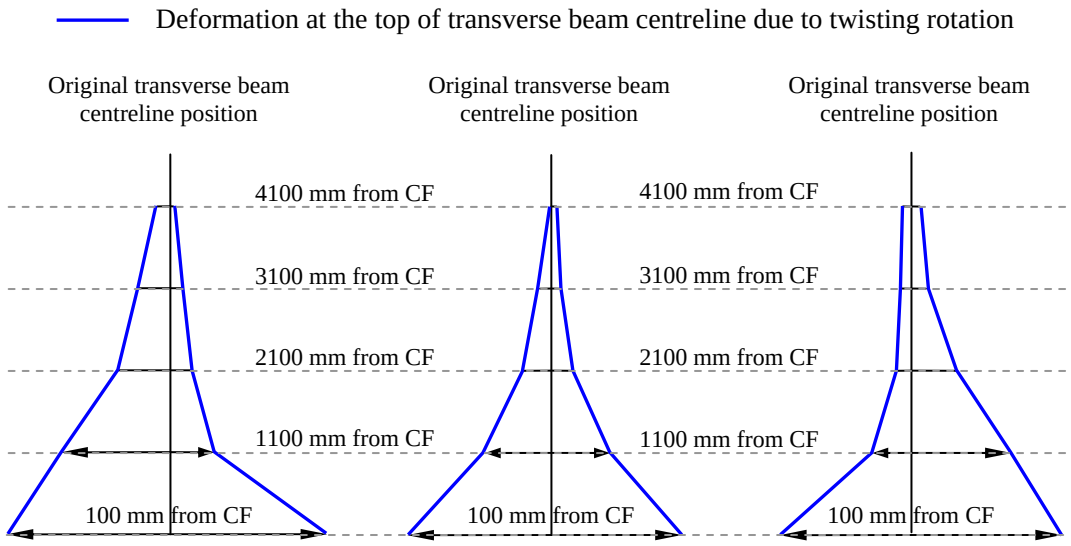

(a) West transverse beam (b) Centre transverse beam (c) East transverse beam

Figure 6-32. Schematic diagram showing the deformation along the top of transverse beam centreline due to transverse beam rotation at the peaks of ±4% drift cycles

6.3.6 Floor-Beam Interface Deformation Derived from Potentiometers

6.3.6.1 Extension between Transverse Beams and Floor Slab

Extensions in the East-West direction between the transverse beams and floor slab interfaces at different sections along the transverse beam are plotted in Figure 6-33. It can be seen that although the crack extensions are greater in the external transverse beams near the column face, the crack extensions carry on further along the internal transverse beam than the external transverse beams. This implies that the crack extensions were more localised near the column face of the external transverse beams than for the internal transverse beam.

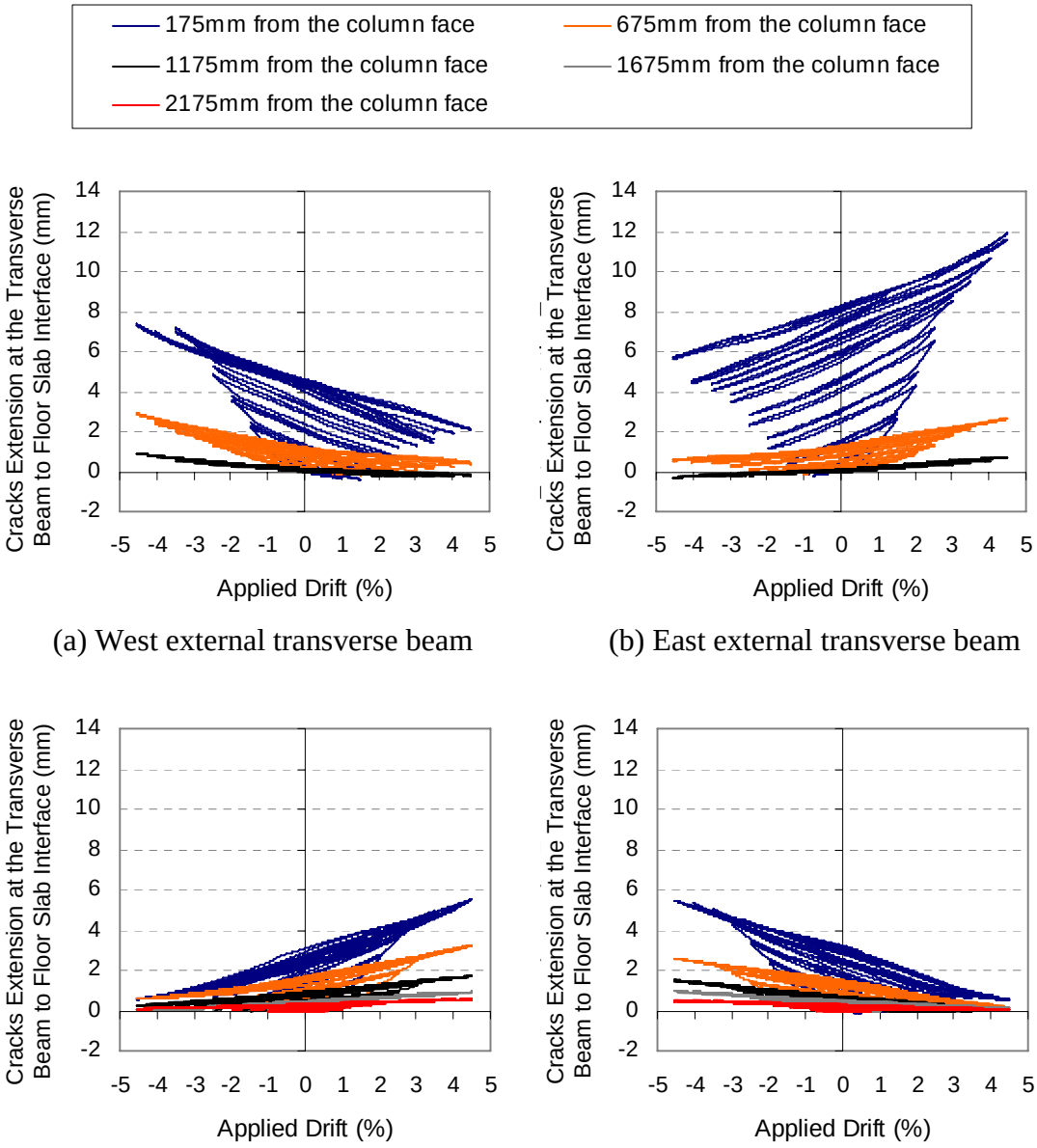

(a) West external transverse beam (b) East external transverse beam

(c) West end of internal transverse beam (d) East end of internal transverse beam

Figure 6-33. Crack extension at the transverse beams and floor slab interface

6.3.6.2 Shear Deformation between Beams and Floor Slab

Shear deformation across the main cracks at the weak section between the transverse beams and floor slab interface and between the longitudinal beam and floor slab interface is plotted in Figure 6-34 and Figure 6-35 respectively. The shear displacement was calculated based on the triangular potentiometer measurements made on the floor slab as described in Section 5.5.7. These potentiometers were located at 175mm from the column face on the transverse beams and in the middle of

the beam bay on the longitudinal beam. Here, a positive shear displacement implies that the floor is moving North relative to the transverse beams, and East relative to the longitudinal beam.

The following observations can be made from these figures:

1. Shear movement is generally larger on the external transverse beams than on the internal transverse beam.
2. The difference in the shear displacement at positive and negative drifts is larger next to the internal transverse beam than next to the external transverse beams.
3. Shear displacement between the longitudinal beam and floor slab is similar in each bay.

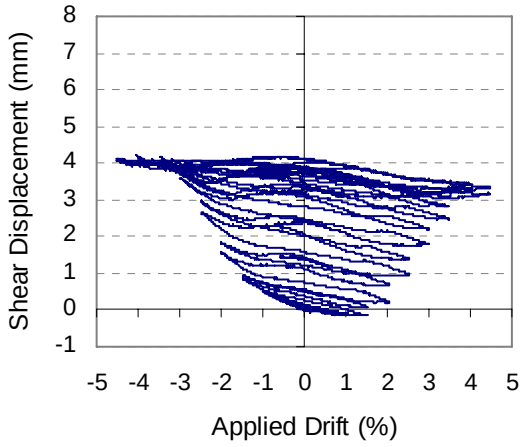

(a) West external transverse beam

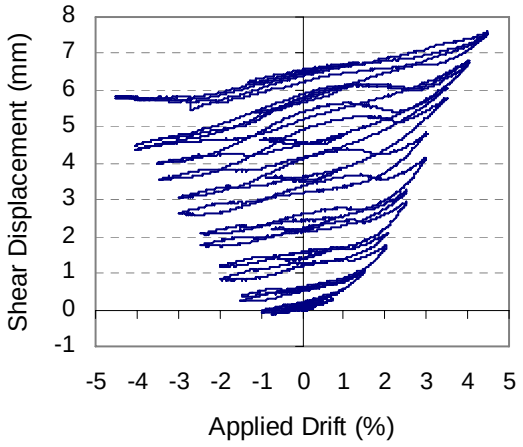

(b) East external transverse beam

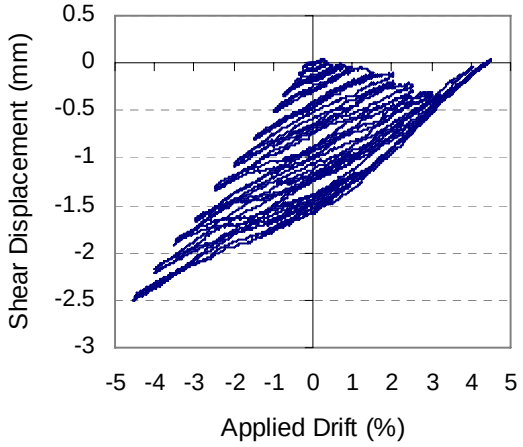

(c) West end of internal transverse beam

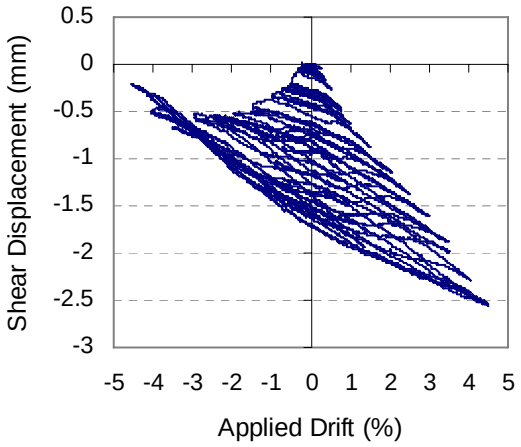

(d) East end of internal transverse beam

Figure 6-34. Shear deformation between the transverse beams and floor slab interface

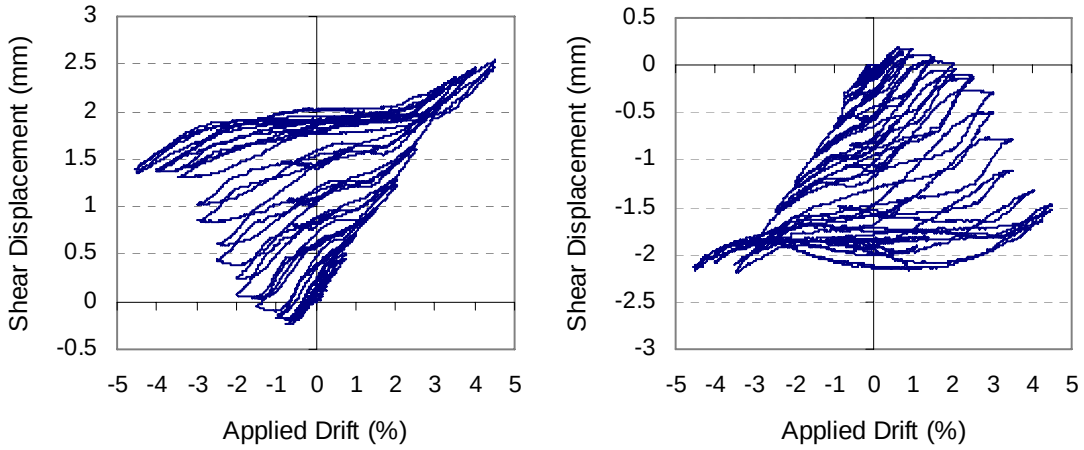

(a) West bay longitudinal beam (b) East bay longitudinal beam

Figure 6-35. Shear deformation between the longitudinal beam and floor slab interface

A schematic diagram showing the overall shear deformation pattern at the cracks along the floor to beam interface is shown in Figure 6-36. The shear displacement across the floor slab and longitudinal interface indicates that the floor slab is restraining elongation of interior plastic hinges. This implies that large axial compression force may be induced in the interior plastic hinge. The shear displacement across the floor slab and transverse beams indicates that an axial compression force is induced in the external transverse beams and an axial tension force is induced in the internal transverse beam. From this shear deformation pattern, it can be inferred that the floor slab was restraining elongation of plastic hinges through bending and shear actions.

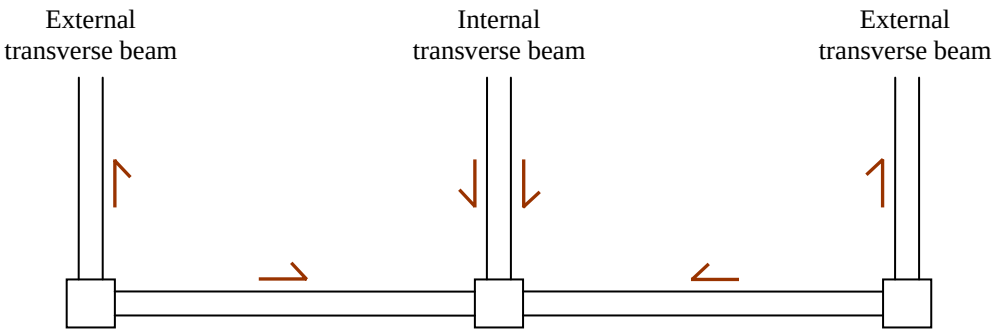

Figure 6-36. Shear deformation pattern along the beam and floor slab interface

6.3.7 Floor Response Derived from DEMEC Measurements

Floor deformations parallel and transverse to the frame as well as shear deformation calculated from the DEMEC measurements are summarised in the following sections.

6.3.7.1 Deformation Parallel to Frame

Deformation of the floor slab parallel to the frame measured at the peaks of various drift cycles is shown in Figure 6-37. The key observations are summarised below:

1) The cracks opened up across the external transverse beams and floor slab interface were localised close to the external columns.
2) The cracks opened up across the internal transverse beam and floor slab interface propagated further than those observed across the external transverse beams and floor slab interface.
3) At larger drift cycles, deformations in some regions along the external transverse beams and floor slab interface, behind the positive moment plastic hinges, were shortening.
4) At larger drift cycles, the length on the North side of the end slab was shortening, and on South side was lengthening. This deformation pattern implies that the end slab was under minor bending action.

A similar deformation behaviour between the transverse beams and floor slab interface was observed from the potentiometer results described earlier in Section 6.3.6.1.

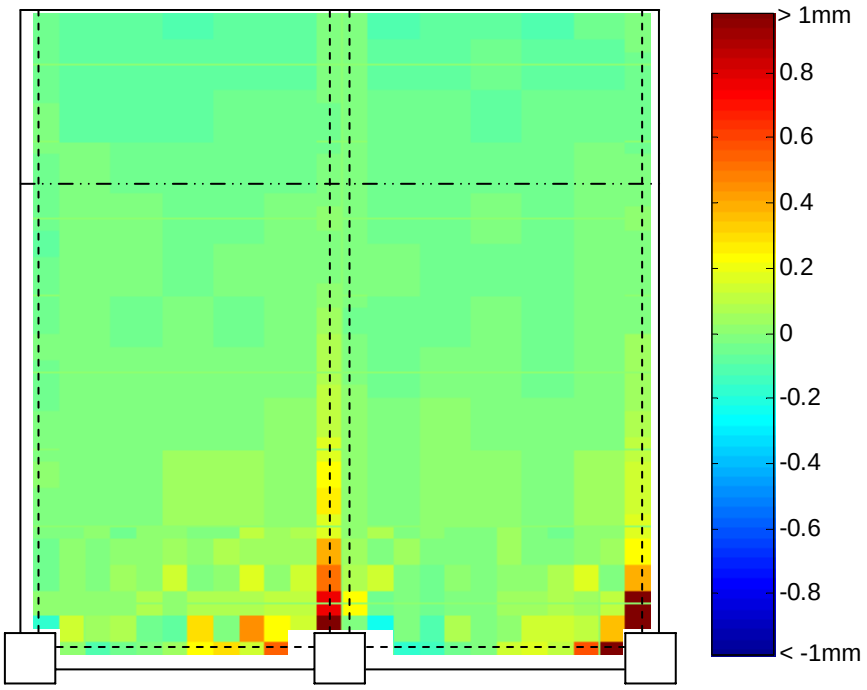

(a) At the peak of second 1% drift cycle

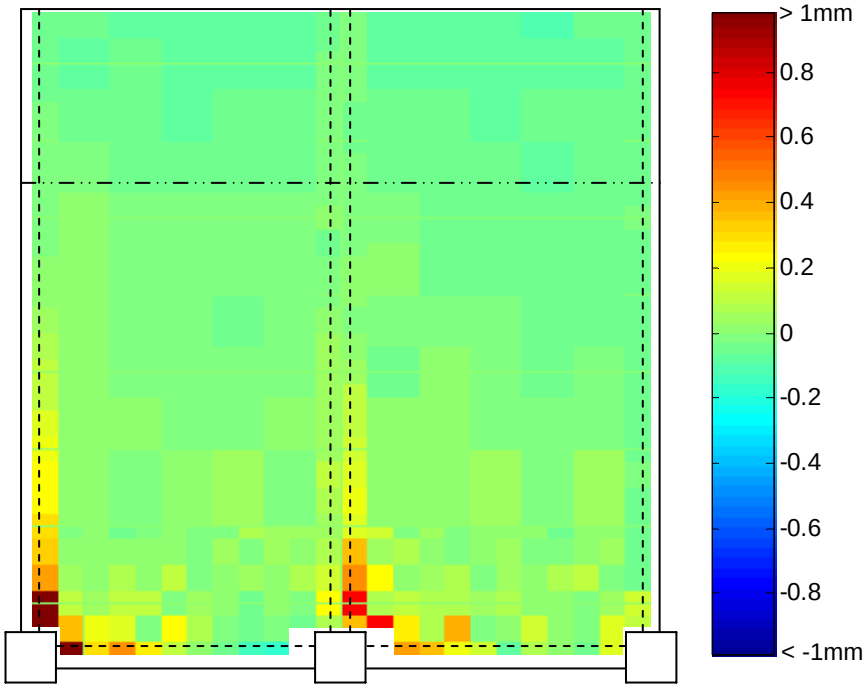

(b) At the peak of second -1% drift cycle

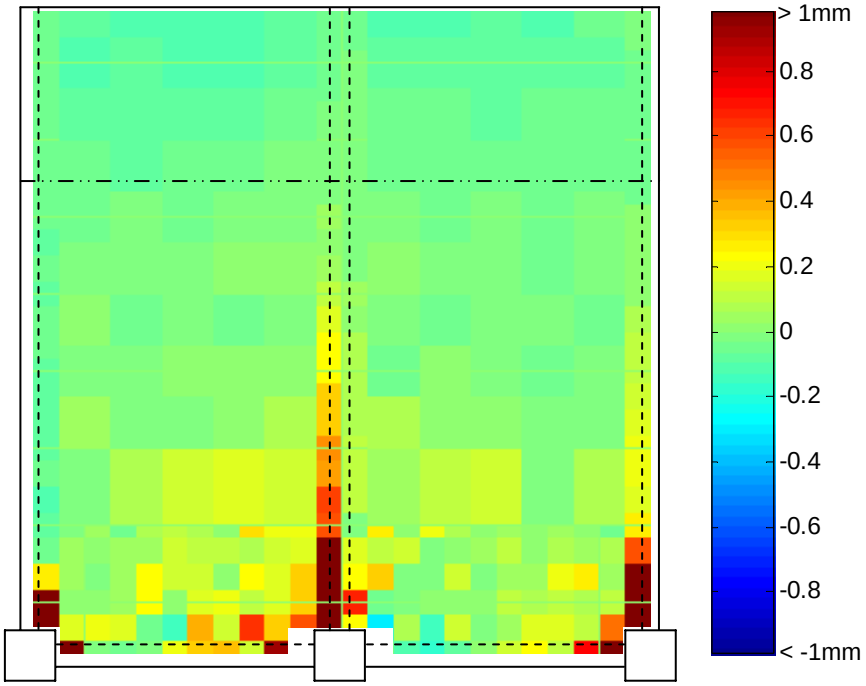

(c) At the peak of second 2% drift cycle

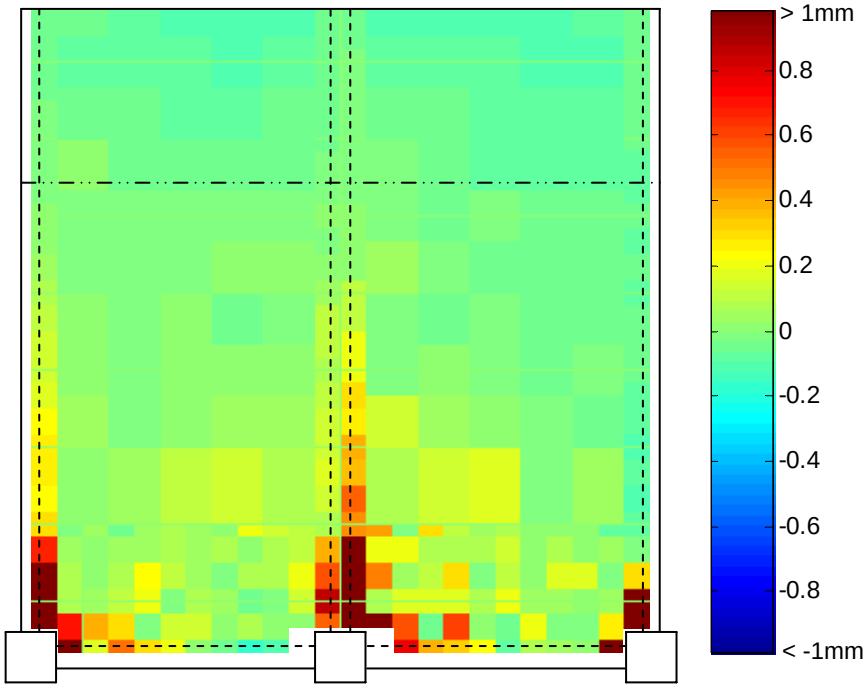

(d) At the peak of second -2% drift cycle

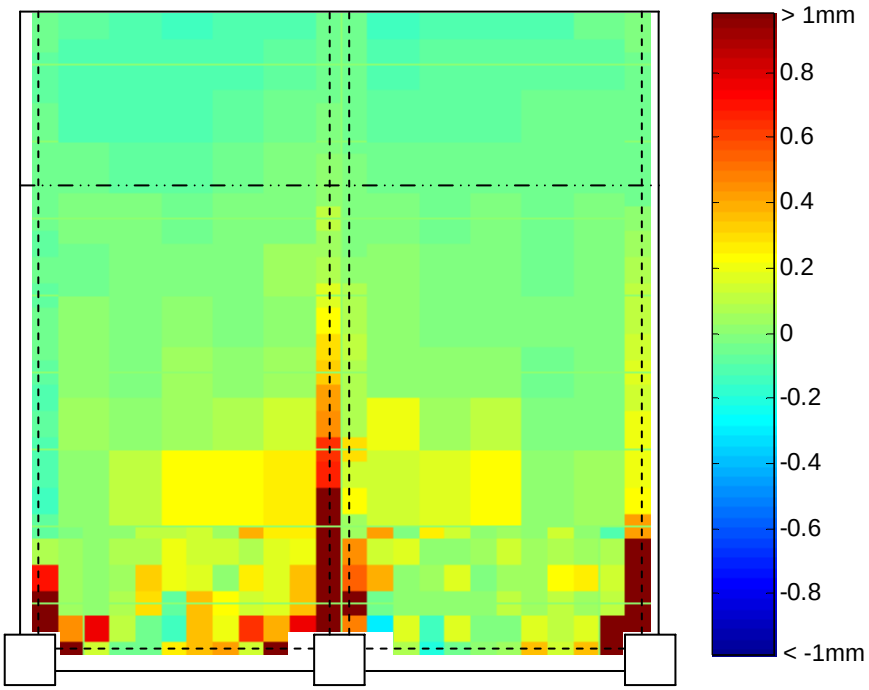

(e) At the peak of second 3% drift cycle

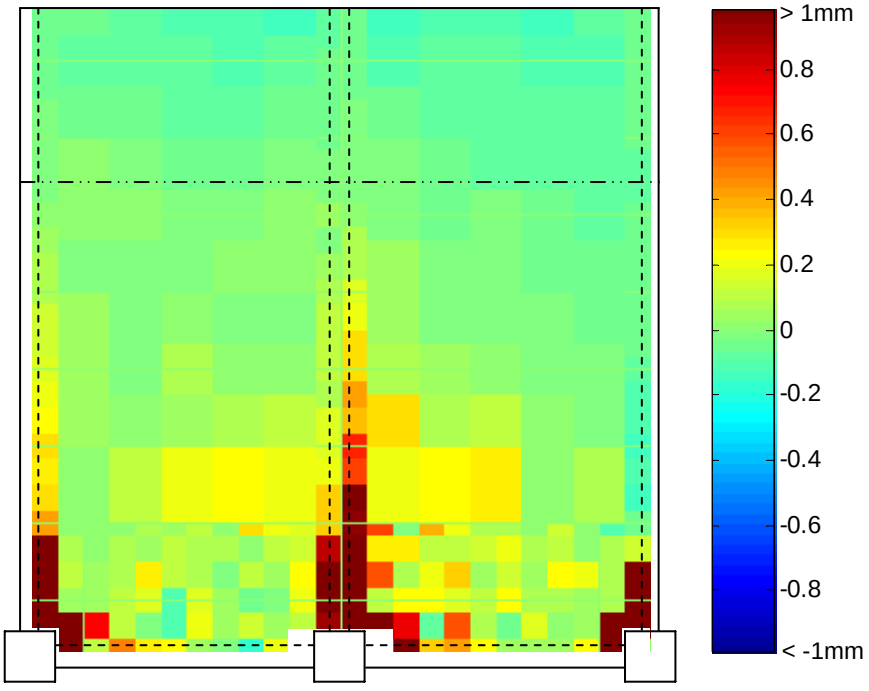

(f) At the peak of second -3% drift cycle

Figure 6-37. Floor deformation pattern parallel to frame from DEMEC measurements

The overall floor deformation parallel to the frame, at the peaks of various drift cycles, is shown in Figure 6-38. The overall floor deformation is calculated by summing the DEMEC measurements across different sections along the transverse beam. The results are compared with the measurements taken at zero force before the 0.35% drift cycle. This is because before the commencement of the 0.35% drift cycle, the specimen was un-tested for more than a month, and during this period substantial shrinkage deformation could be anticipated.

The time delay between when the initial readings were taken and the measurements taken at zero force before the 0.35% drift cycle was 43 days. Based on the study carried out by Bryant et al. (1984) for a 200mm deep slab, the shrinkage strains over the period would be expected to be of the order of 110 micro-strain, and the corresponding shrinkage deformation is 0.67mm over the length of the end slab. This value correlates well with the measurements taken before 0.35% drift where the deformation in the end slab, 5050mm from the column face, is 0.7mm, as shown in Figure 6-38(b). It should be noted that a further shrinkage of 0.25mm is expected to occur over the period from 0.35% drift to 3% drift based on Bryant et al shrinkage values.

The following observations can be drawn from Figure 6-38:

1) Elongation of plastic hinges in the frame causes the floor slab close to the frame to increase in length parallel to frame but it causes the floor slab further away from the frame (beyond 4550mm from the column face) to reduce in length.
2) The length of the floor slab parallel to frame at a distance 4550mm from the column face is approximately constant.
3) The increase in length of the floor slab parallel to frame reduces sharply within the first 2 meters from the column face. The increase in length of the floor slab decreases approximately linearly from the 3 meter mark to the end of the floor slab.

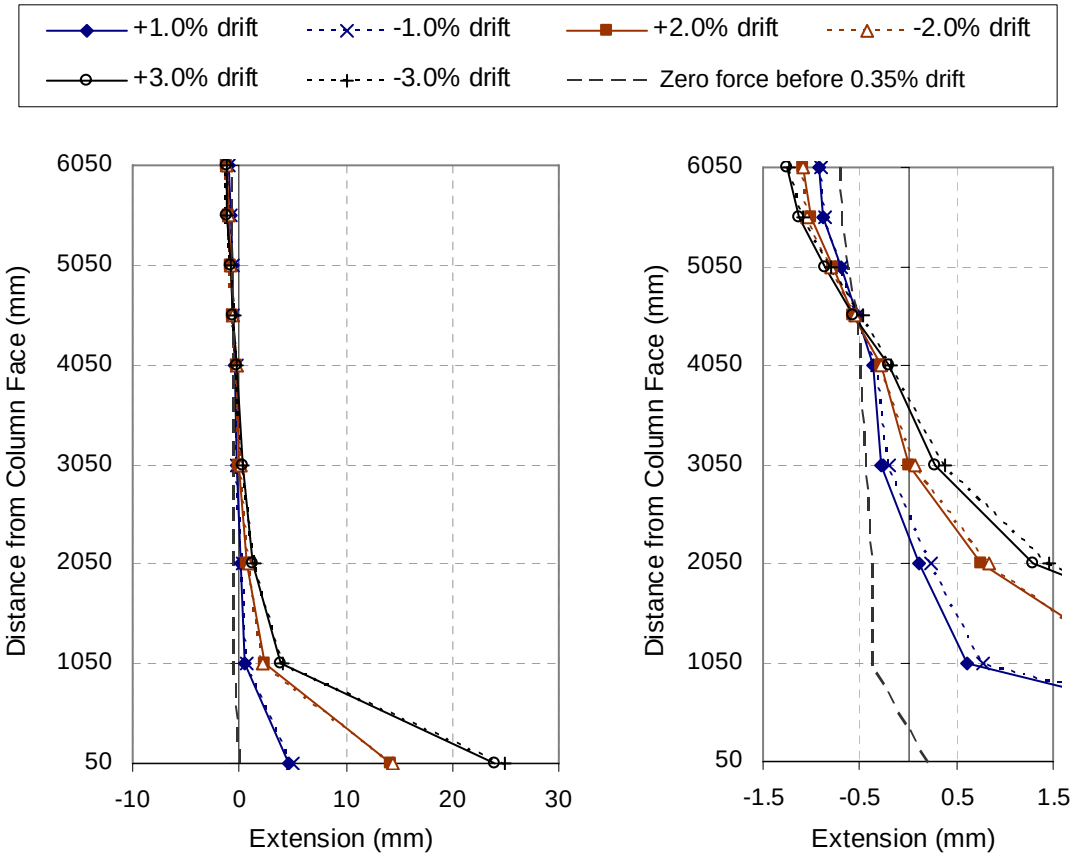

(a) Floor extension (b) Close-up of the floor extension

Figure 6-38. Sum of the floor extension parallel to frame at different locations

The crack widths measured at the peak of the positive 3% drift cycle is summarised in Table 6-5. To account for the effect of concrete shrinkage, the amount of shrinkage deformation over the measured gauged length, estimated based on shrinkage results of Bryant et al. (1984), is added to the measured value and is given in Table 6-5 as the interpreted values. The shrinkage strain incurred from the initial reading to 3% drift is approximately 150 micro-strains for the deep beam and 80 micro-strains for the floor slab and the corresponding length is 0.04mm and 0.02mm, respectively.

Table 6-5. Crack widths along the transverse beams and floor slab interface at the peak of second 3.0% drift cycle

Distance from the column face (mm)	East transverse beam		West side of internal transverse beam	
	Crack widths (mm)		Crack widths (mm)	
	Measured	Interpreted	Measured	Interpreted
50	10.3	10.3	4.76	4.78
300	5.97	5.99	3.72	3.74
550	2.54	2.56	2.72	2.74
800	1.06	1.08	2.20	2.22
1050	0.422	0.44	1.19	1.21
1300	0.223	0.24	1.07	1.09
1550	0.217	0.24	0.663	0.68
1800	0.207	0.23	0.655	0.68
2050	0.196	0.22	0.461	0.48
2300	0.149	0.17	0.437	0.46
2550	0.165	0.19	0.318	0.34
2800	0.147	0.17	0.289	0.31
3050	0.119	0.14	0.222	0.24
3300	0.096	0.12	0.174	0.19
3550	0.069	0.09	0.082	0.10
3800	0.036	0.06	0.036	0.06
4050	0.026	0.05	0.097	0.12
4550	-0.040	-0.00	0.002	0.02
5050	-0.046	-0.01	-0.029	-0.01
5550	-0.049	-0.01	-0.043	-0.02
6050	-0.057	-0.02	-0.053	-0.03

From these crack width measurements, the amount of slab reinforcement that yielded across the cracks can be estimated using the method described below. It should be noted that as the DEMEC points were not mounted on the reinforcing bars. Hence the DEMEC measurements do not directly correspond to the reinforcement extensions.

The postulated stress distribution in the reinforcement when it first yields at the crack section is shown in Figure 6-39, where L_{db} is the development length calculated based on the New Zealand Concrete Structures Standard, NZS 3101:2006, f_y is the reinforcement yield stress, and 180mm represents the length of hook reinforcement in the exterior transverse beams. The strain associated with the stress distribution in Figure 6-39 causes localised extension at the crack section. Therefore, the crack width

corresponding to yielding of the slab reinforcement is the sum of the area under the strain distribution, which is equal to approximately 0.5mm. Based on the this value, it can be seen from Table 6-5 that the slab reinforcement had yielded at a distance up to 1050mm behind the external columns and up to 2050mm behind the internal columns. However, it should be emphasised here that not all of the tension force in the slab reinforcement is contributing to the negative flexural strength of beam plastic hinges. This is elaborated more in Section 7.3.7.

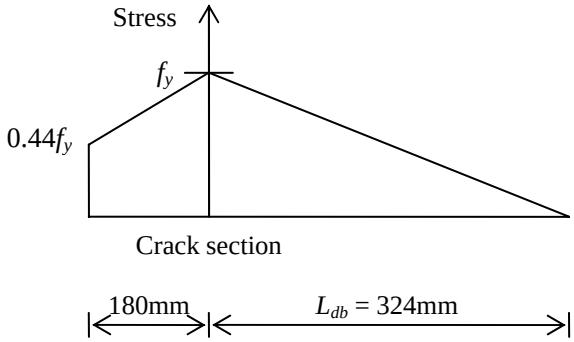

Figure 6-39. Schematic diagram showing the stress distribution of the floor reinforcement connected to exterior transverse beam

6.3.7.2 Deformation Transverse to Frame

Floor deformation transverse to the frame measured at the peaks of various drift cycles is illustrated in Figure 6-40. It can be seen that the region near the internal transverse beam, away from the frame, was extending and the region near the external transverse beams, away from the frame, was contracting. This action is consistent with bending of the floor slab as described earlier in Section 6.2.4.

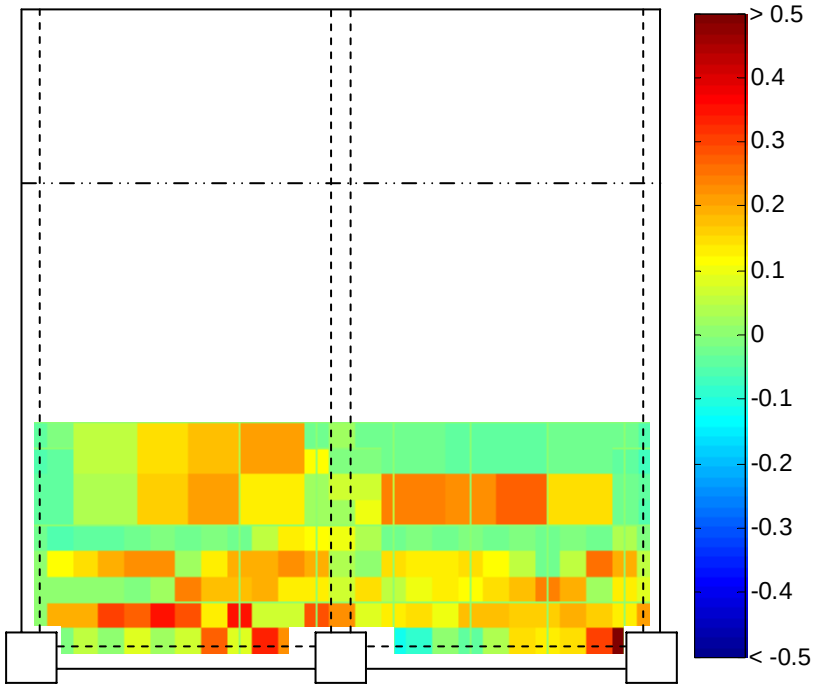

(a) At the peak of second 1% drift cycle (units in mm)

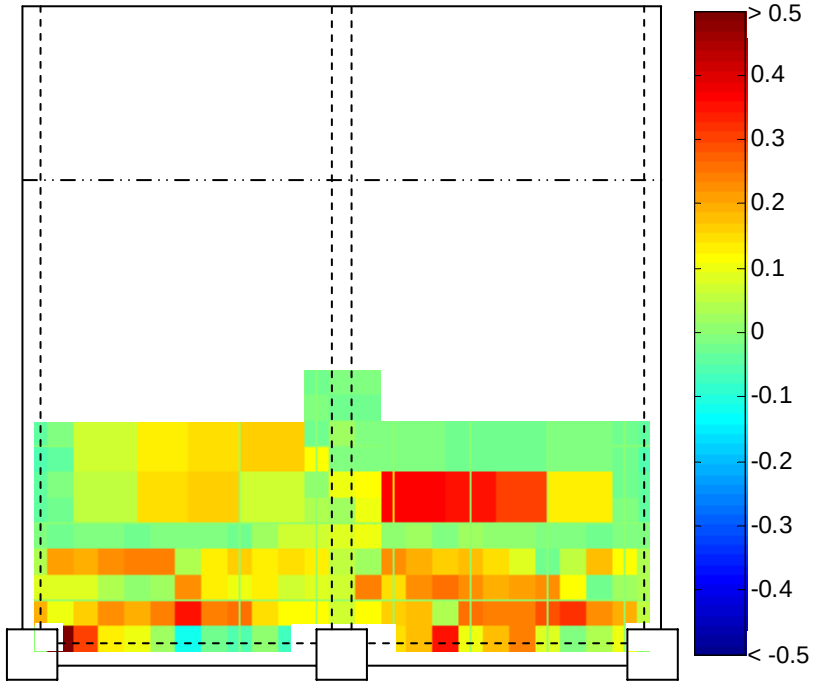

(b) At the peak of second -1% drift cycle (units in mm)

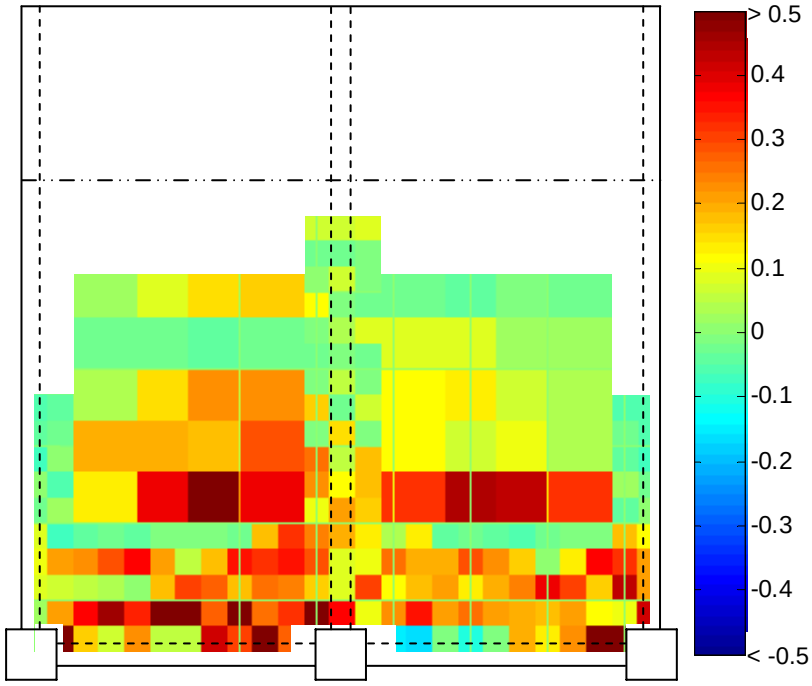

(c) At the peak of second 2% drift cycle (units in mm)

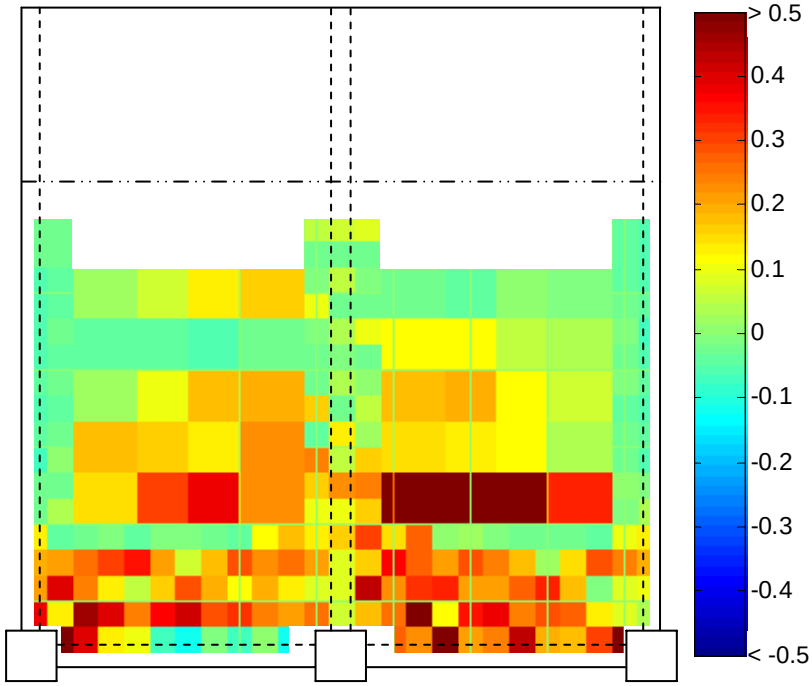

(d) At the peak of second -2% drift cycle (units in mm)

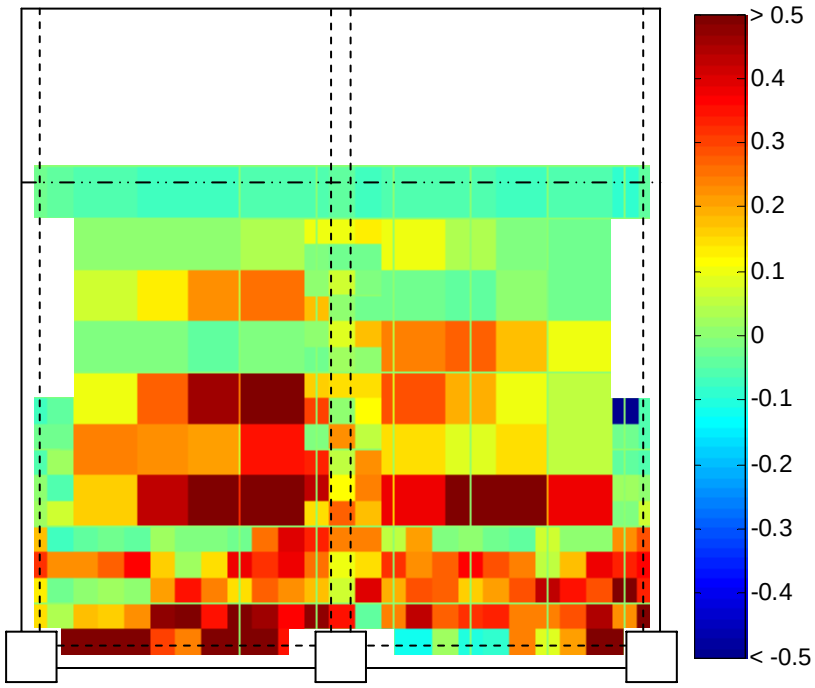

(e) At the peak of second 3% drift cycle (units in mm)

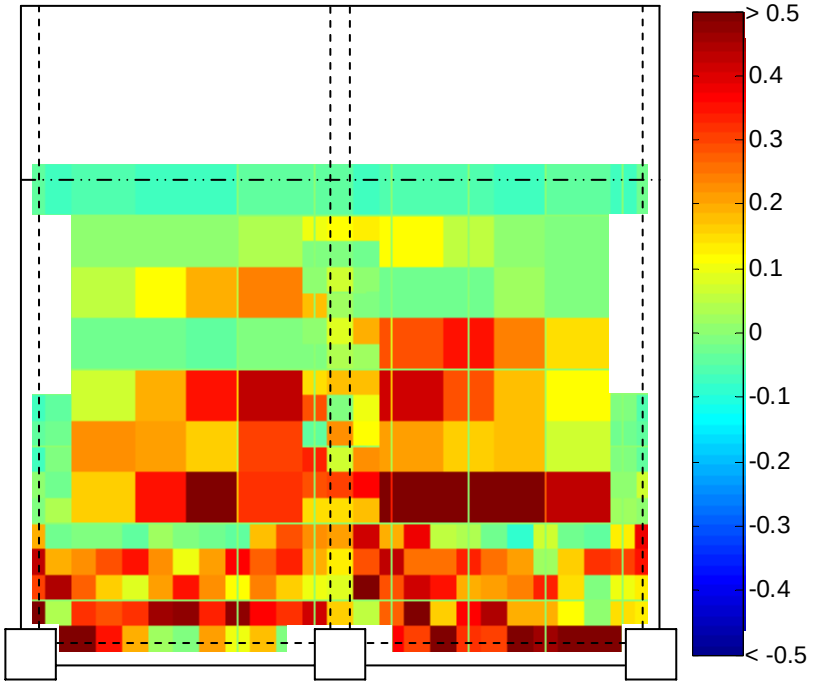

(f) At the peak of second -3% drift cycle (units in mm)

Figure 6-40. Floor deformation pattern transverse to frame from DEMEC measurements

The floor extension transverse to the frame at different locations, interpreted from DEMEC measurements, is shown in Figure 6-41, where part (a) sums the extension over 1.5m South of the end slab and part (b) sums the extension over 2m North of column face. This is done because not all of the DEMEC measurements were taken transverse to the frame. As mentioned earlier, the results are compared with the measurements taken at zero force before the 0.35% drift cycle. Based on the study carried out by Bryant et al. (1984) for a 100mm deep slab, the expected shrinkage strain over the period of 43 days is roughly 60 micro-strain.

In Figure 6-41(a), the results is only plotted at -2.0% drift. This is because the measurements were not complete at other drift levels as shown in Figure 6-40. It can be seen from Figure 6-41(a) that the external transverse beams were shortening and the internal transverse beam were lengthening near the end slab. This deformation pattern implies that the floor is bending like two deep beams as described earlier in Section 6.2.4.

Figure 6-41(b) shows that the floor slab near the internal transverse beam lengthened more than the floor slab near the external transverse beams, whereas the length of the internal and external transverse beams appears to increase by a similar amount. This is probably due to torsion effect of the transverse beams. The transverse beams would lengthen when they were being twisted under torsional action.

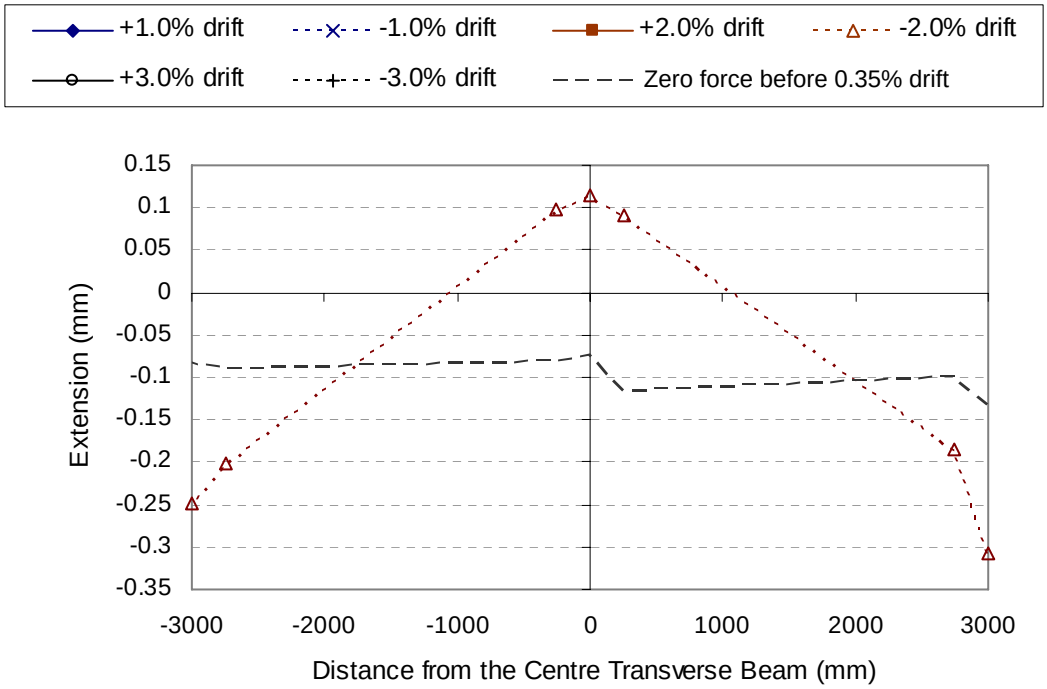

(a) Extension from the south edge of end slab to a distance 1.5m south of the end slab

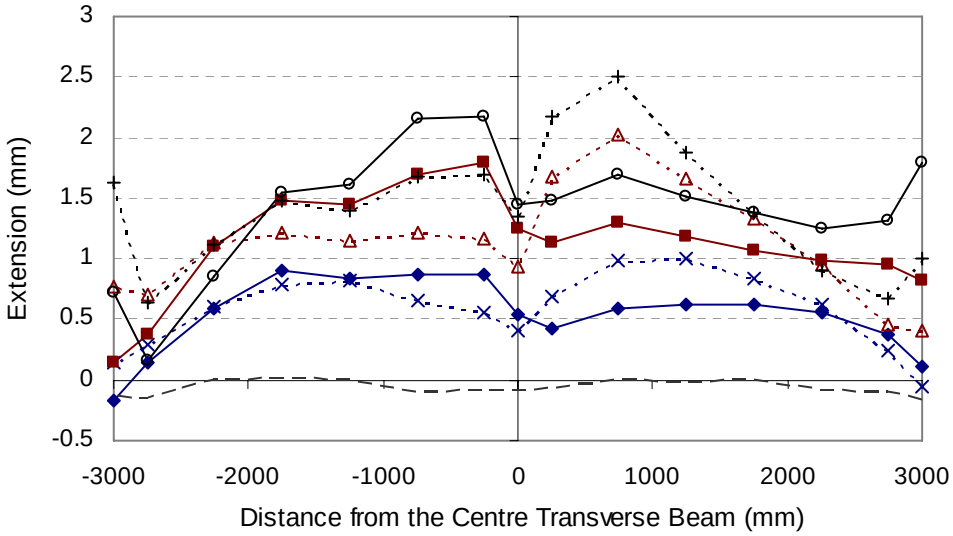

(b) Extension from the column face to a distance 2m north of the column face

Figure 6-41. Sum of the floor extension transverse to frame at different locations

6.3.7.3 Shear Deformation

Shear deformations were calculated from the two diagonal measurements within each DEMEC grid. The calculation is based on Equation 6-3, where ΔD_1 is the change in length in the top left to bottom right diagonal, ΔD_2 is the change in length in the bottom left to top right diagonal, and θ is the angle of the diagonals to the axis parallel

to frame. Based on this equation, a positive value represents shear movement illustrated in Figure 6-42(a) and a negative value represents shear movement illustrated in Figure 6-42(b).

$$S = \frac{\Delta D_2 - \Delta D_1}{2\cos\theta} \tag{6-3}$$

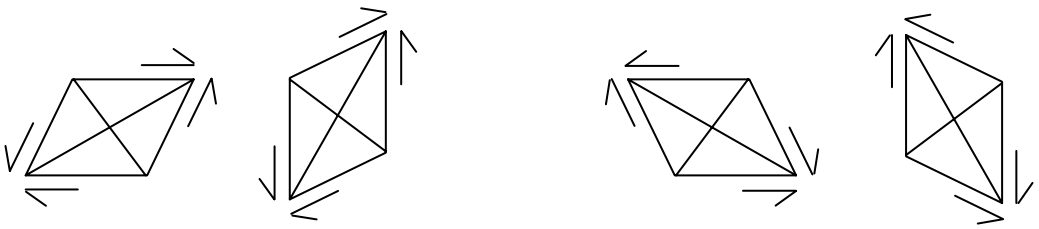

(a) Positive shearing mode (b) Negative shearing mode

Figure 6-42. Schematic diagram showing shearing sign convention in the floor slab

Shear deformation of the floor slab is plotted in Figure 6-43. The white regions represent area where no readings were taken. A few observations can be made from the observed shear deformation pattern in Figure 6-43:

1) Elongation of interior plastic hinge was restrained by the floor slab; consequently shear deformation was induced in the interface between the floor slab and the longitudinal beam.
2) Shear deformation is smaller in the floor slab than the regions along the beams to floor slab interface.
3) Shear deformation along the external transverse beams and floor slab interface is greater than that along the internal transverse beam and floor slab interface.

A similar shear deformation behaviour between the beam and floor slab interface was observed from the potentiometer results as discussed earlier in Section 6.3.6.2.

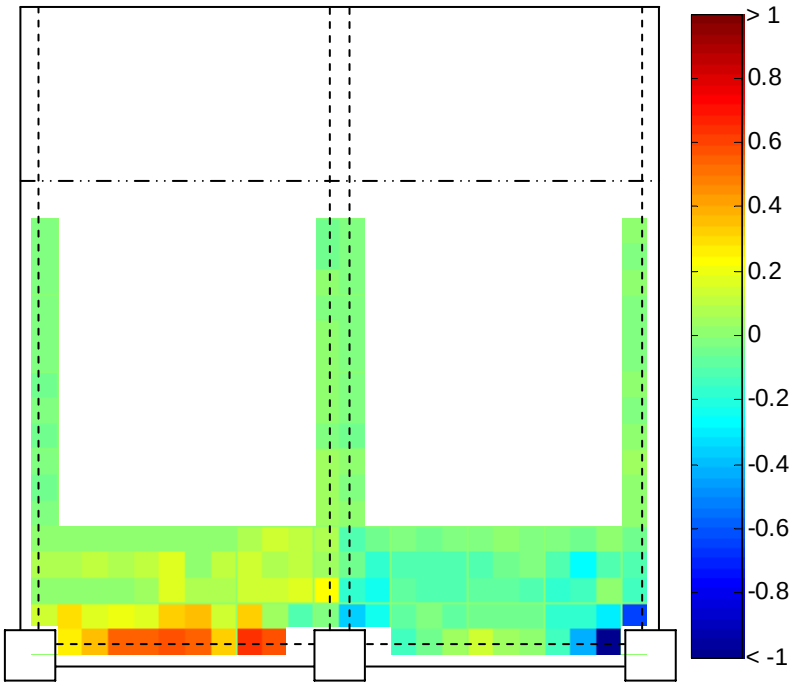

(a) At the peak of second 1% drift cycle (units in mm)

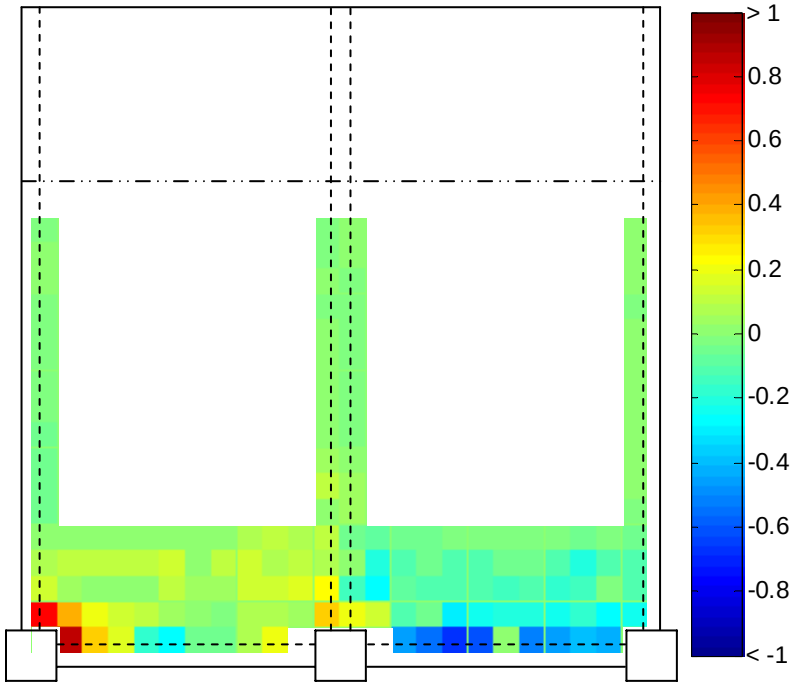

(b) At the peak of second -1% drift cycle (units in mm)

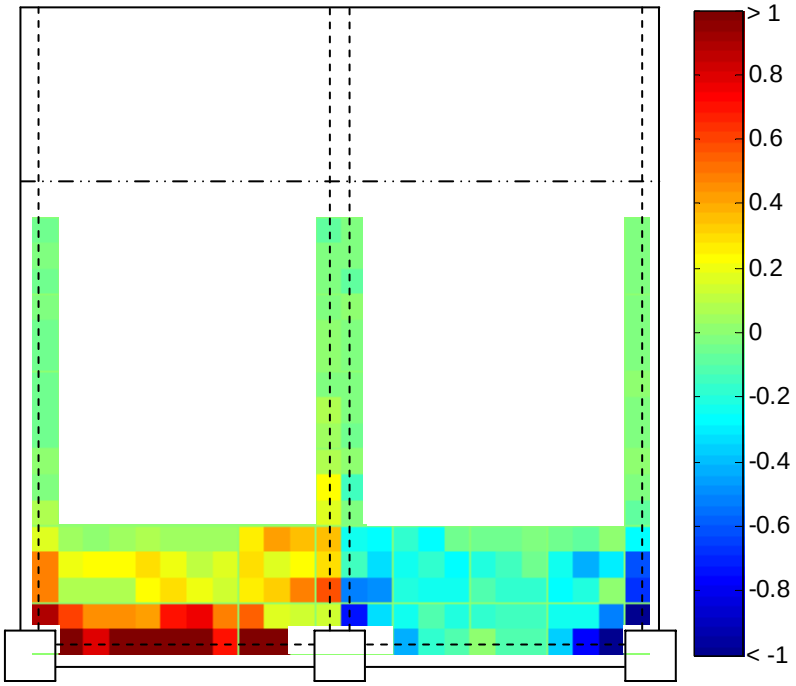

(c) At the peak of second 2% drift cycle (units in mm)

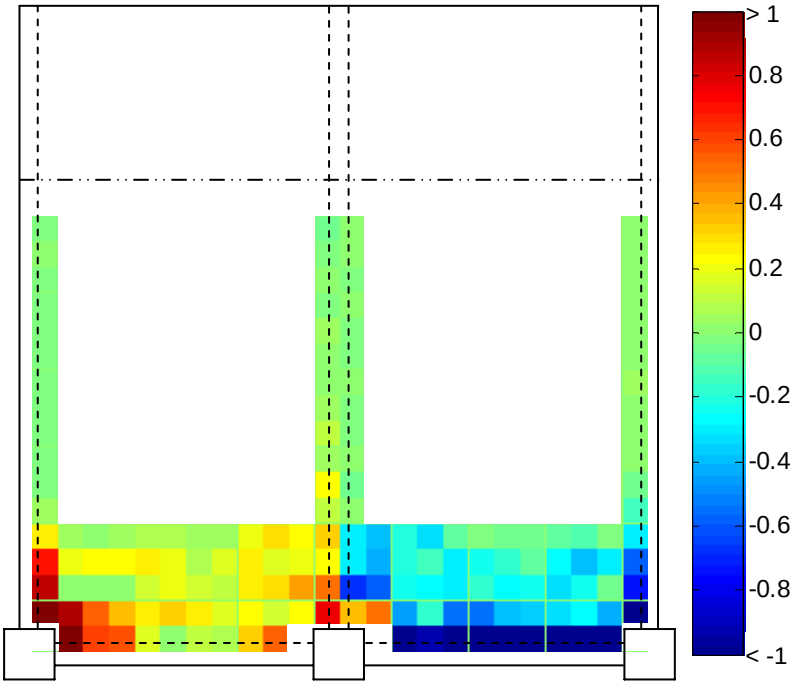

(d) At the peak of second -2% drift cycle (units in mm)

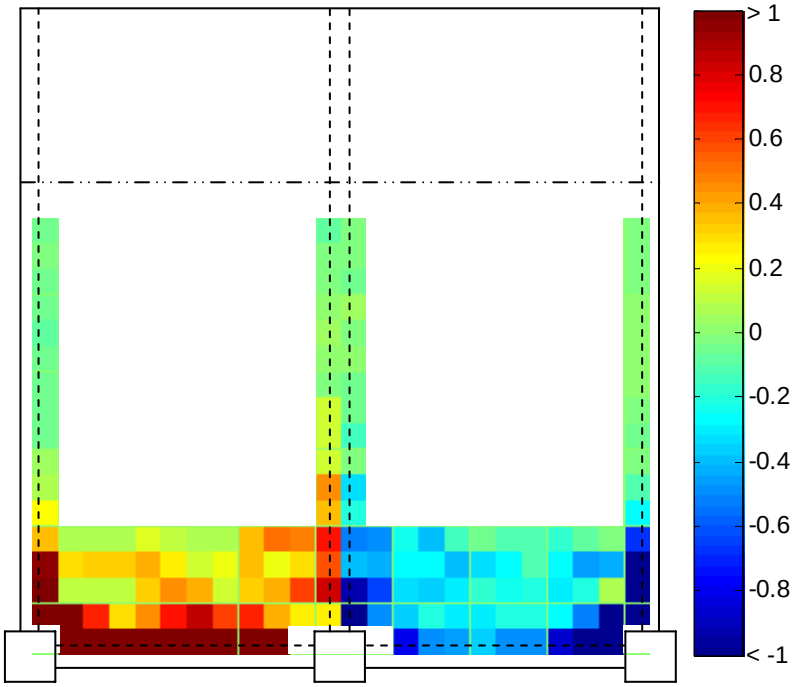

(e) At the peak of second 3% drift cycle (units in mm)

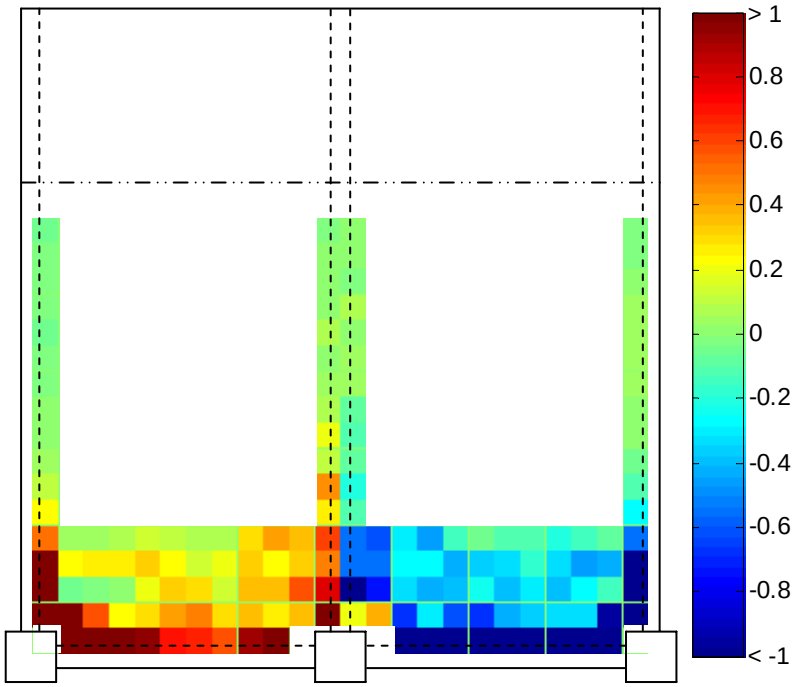

(f) At the peak of second -3% drift cycle (units in mm)

Figure 6-43. Floor shear deformation pattern from DEMEC measurements

6.3.8 Overall Floor Deformation Mechanisms

Based on the floor deformation measurements reported in Sections 6.3.6 and 6.3.7, a schematic free body diagram showing the forces in the two slabs, one on each side of the internal transverse beam, at a peak positive drift cycle is shown in Figure 6-44. The internal forces of the floor slab are drawn as dotted lines and the forces in the slab to beam interface, induced by elongation of plastic hinges, are drawn as solid lines. The shaded area represents the stiff end slab.

By examining the free body diagram of the slab on the left hand side, it can be seen that shear force along the longitudinal beam and slab interface as well as tension force across the internal transverse beam and slab interface are induced due to elongation of the interior plastic hinge, on the left hand side of the internal column. To satisfy horizontal force equilibrium, a horizontal compression force may be induced in the end slab. These forces induce a moment, which is resisted by the end slab.

The shear force along the longitudinal beam and slab interface is resisted by a series of compression struts developed in the floor slab. These compression struts are then resisted by slab reinforcement acting as ties both parallel and transverse to the longitudinal beam. For simplicity, only one set of ties is shown in the diagram. The magnitude of the tie forces, parallel to the longitudinal beam, decreases towards the end slab and the magnitude of the tie forces, transverse to the longitudinal beam, decreases towards the West column. These forces are consistent with the slab deformation measurements as observed in Sections 6.3.6 and 6.3.7.

The forces induced in the slab on the right hand side are more complex. Elongation of the interior plastic hinge, on the left hand side of the internal column, induces shear force along the longitudinal and slab interface as well as tension force across the transverse beam and slab interface. Elongation of the exterior plastic hinge next to the East column tends to push the column and external transverse beam outwards as they are less effectively restrained by the external transverse beam. Consequently, only a small portion of shear force, if any, is induced along the longitudinal beam. These forces induce a net counter-clockwise moment, which is resisted by the moment developed in the end slab.

Similarly, shear force along the longitudinal beam and slab interface is resisted by a series of compression struts developed in the floor slab. These compression struts are then resisted by slab reinforcement acting as ties both parallel and transverse to the longitudinal beam. For simplicity, only one set of ties is shown in the diagram. The magnitude of the tie forces (parallel to the longitudinal beam) decreases towards the end slab and the magnitude of the tie forces (transverse to the longitudinal beam) decreases towards the East column. These forces are consistent with the slab deformation measurements as observed in Sections 6.3.6 and 6.3.7.

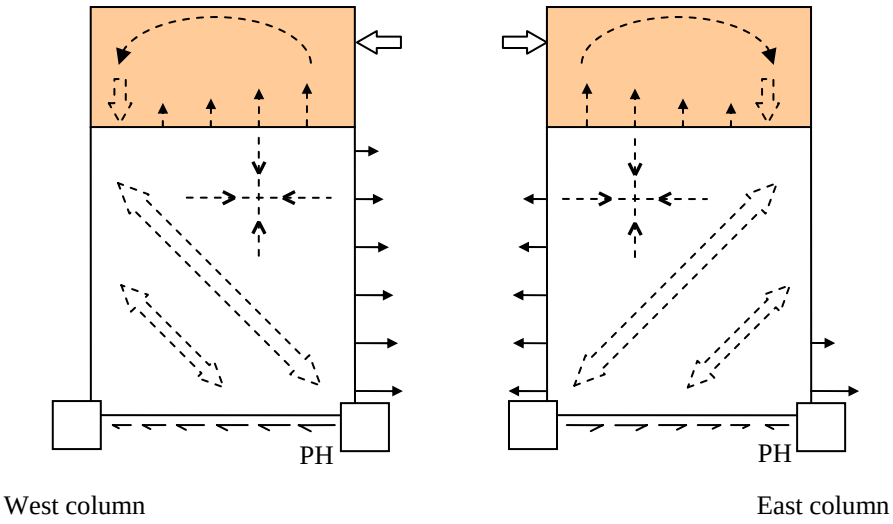

Figure 6-44. Equilibrium criteria for each slab at the peak of a positive drift cycle

6.3.9 End Slab Deformation

The change in length of the end slab at the line of the back supports was calculated by taking the difference between the potentiometer measurements from each support. This is plotted in Figure 6-45, where a positive value implies extension. It can be seen that the end slab at the line of back support shortened as the drift level increased. This observation matches well with the DEMEC results described in Section 6.3.7.1.

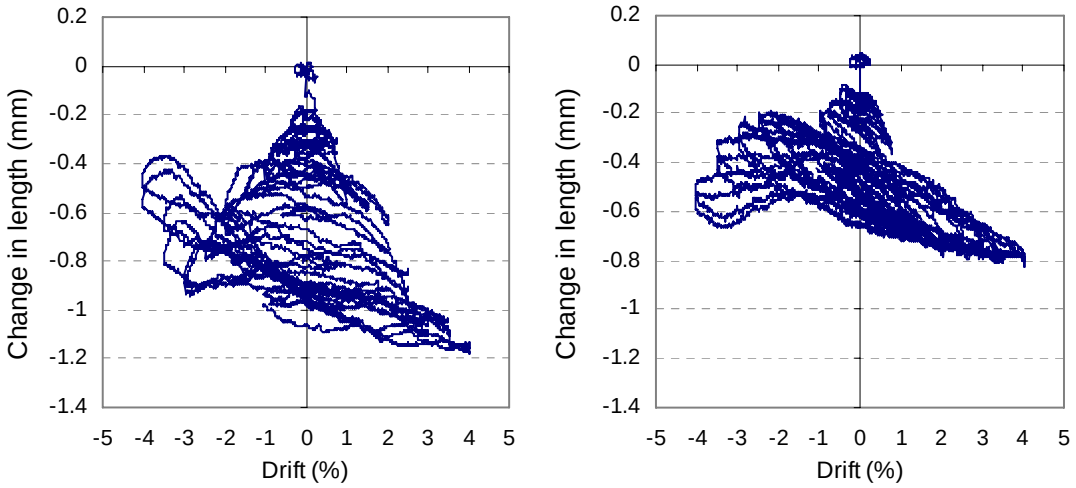

(a) West bay (b) East bay

Figure 6-45. Change in length of the end slab parallel to frame at the location of support

6.4 TORSIONAL TEST

At the end of the test, the longitudinal beams were removed from the sub-assembly and the applied displacement history was re-applied to the columns to measure the torsional resistance of the transverse beams. The total column force-displacement relationship is shown in Figure 6-46. The total shear force measured at 3% drift was 25kN.

Figure 6-47 plots the averaged force-displacement relationship of each individual column. It can be seen that:

1) despite the external and internal transverse beams have similar cross section, the torsional resistance of the internal transverse beam is about the same order as the combined torsional resistance of the external transverse beams. This may be due to the internal transverse beam being more effectively restrained by the surrounding floor slab.
2) the torsional resistance of the external transverse beams is higher when the transverse beam is rotating away from the floor slab. It is postulated that the increase in the torsional strength arises from the tension force in the slab reinforcement.

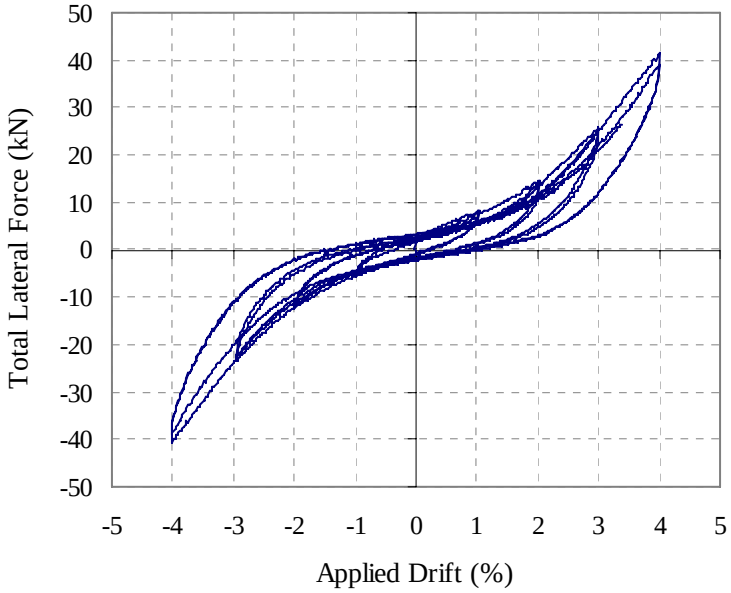

Figure 6-46. Total force-displacement relationship without the longitudinal beam

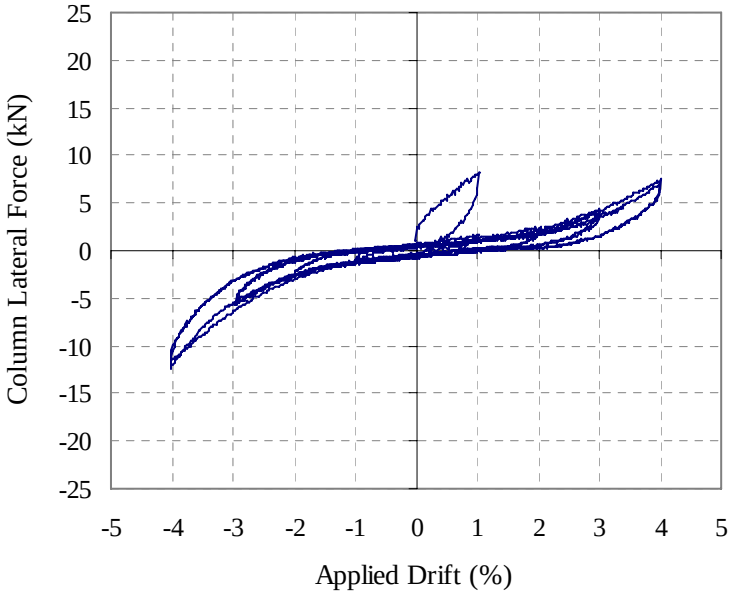

(a) *Column A*

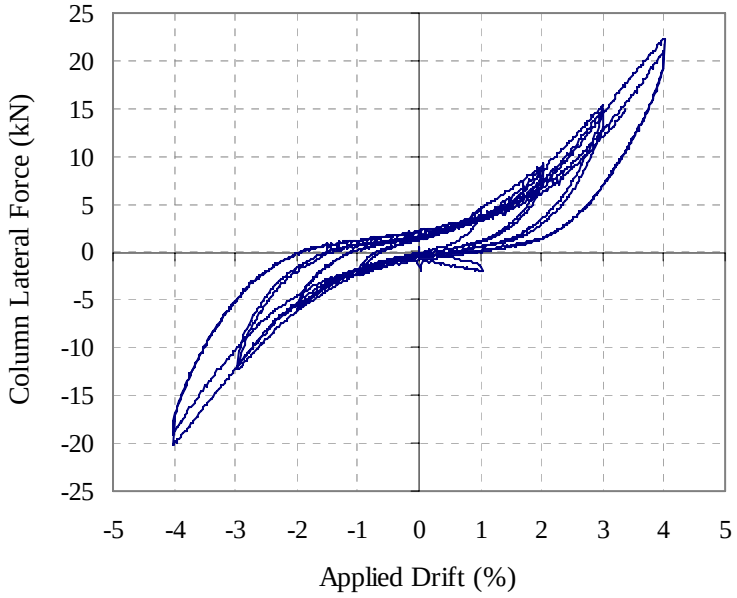

(b) *Column B*

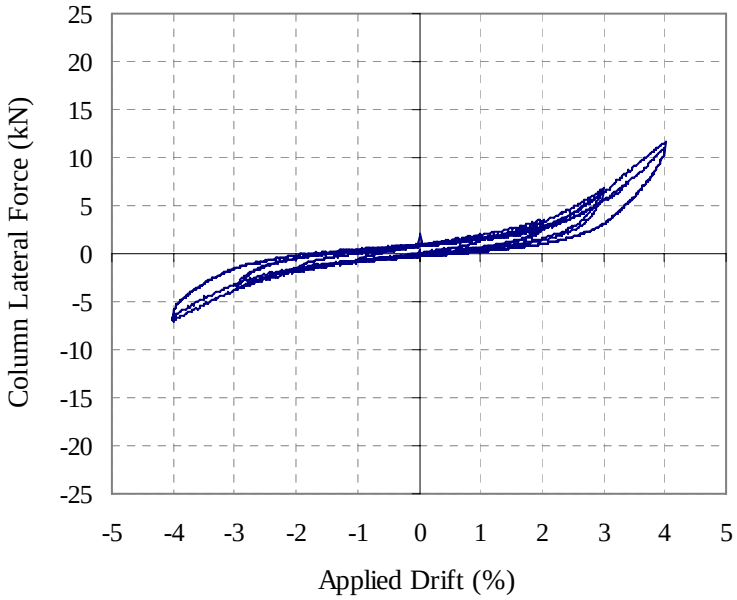

(c) *Column C*

Figure 6-47. Averaged force-displacement relationship of each column without the longitudinal beam

The nominal theoretical torsional strength of beam, T_n, as specified in the New Zealand Concrete Structures Standard, NZS 3101:2006, is based on the tensile strength of the reinforcement in the beam. It can be expressed by Equation 6-4 where A_o is the gross area enclosed by shear flow path, A_t is the area of one leg of closed stirrup, s is the spacing of stirrup, A_l is the area of longitudinal bars, P_o is the length of

the perimeter of the section measured between centres of the corner reinforcing bars, and f_y and f_{vy} are the yield stresses of longitudinal and transverse reinforcement.

$$T_n = 2A_o\sqrt{\frac{A_t f_{vy}}{s}\frac{A_l f_y}{P_o}} \tag{6-4}$$

The reinforcement in the floor slab would have partially restrained axial extension of the transverse beam and hence may have contributed to A_l in Equation 6-4. However, it is hard to quantify the contribution of the slab reinforcement to A_l, and for simplicity, this effect is neglected in the calculation. The calculated nominal torsional capacity of external and internal transverse beams is 35.5kNm and 40.5kNm, respectively. This corresponds to a storey shear force of 59kN, which is more than twice the measured value at ±3% drifts. However, it should be noted that the transverse beams had been extensively cracked prior to the torsional test and the actual torsional resistance of the transverse beams could have been higher than that indicated by this test.

6.5 BEAM STRENGTH COMPARISON

The experimentally measured shear force in each column at the peaks of positive and negative drift cycles is summarized in Tables 6-6 and 6-7. These were compared with the values calculated based on the New Zealand code, NZS 3101:2006, and the ACI code, ACI 318-05 (American Concrete Institute 2005). In Table 6-6, the shear forces in *Columns A* and *C* correspond to the positive (tension on the bottom) and negative (tension on the top) strengths of the plastic hinges respectively, whereas the shear force in *Column B* corresponds to the combination of positive and negative strengths of the plastic hinges in the two sides of the column. It should be noted that prior to the 1.0% drift cycle, *Columns B* and *C* were displaced less than the actual intended drift due to slop in the loading system.

Assuming gravity load imposed on the longitudinal beam is the self weight plus the 150mm wide topping slab, this gives a shear force of 2.65kN at the column face. The flexural strength of the beam (neglecting flange effects) is 68.4kNm. The

corresponding column shear force is given in Tables 6-6 and 6-7. As gravity load is taken into account when calculating the shear force in the frame, the shear force in *Columns A* and *C* is different. However, the total storey shear force would not be affected by the gravity load.

The effective flange width for calculating the theoretical flexural strength of the beam, specified in Clauses 9.3.1.2 and 9.3.1.4 in NZS 3101:2006, is 360mm. It should be noted that in the experiment, the first set of the floor slab reinforcement parallel to frame is located at 50mm from the column face. Therefore, only one slab reinforcing bar would contribute to the negative flexural strength of the beams. Consequently, the corresponding additional tension force is 29.3kN. The corresponding negative and positive flexural strength of the beam is 78.3kNm and 72.6kNm respectively and the column shear force is given in Tables 6-6 and 6-7.

The effective flange width for calculating the negative over-strength of the beam plastic hinge is specified in Clause 9.4.1.6.2. The effective flange width for the exterior and interior plastic hinges in this test is 900mm and 1200mm, respectively. This corresponds to four and five slab reinforcing bars contributing to the exterior and interior plastic hinges, respectively.

In addition, the code specifies that the stress of the slab reinforcement be taken as $1.1\phi_o f_y$ where ϕ_o is the over-strength factor equal to 1.25 for Grade 300 steel. The additional 1.1 factor on top of the over-strength factor is to account for slab reinforcement under very high tensile strain. The over-strength value in the code assumes a 15% increase in yield stress to account for the statistical variation of the reinforcement yield stress in addition to an approximate strain-hardening effect of 10%. In the experiment, the actual material yield stress was measured and hence an over-strength value of 1.1 was used for calculating the over-strength of the beams.

The corresponding additional tension force from the slab reinforcement in the exterior and interior plastic hinges is 142kN and 177kN, respectively. The calculated negative over-strength moment of the exterior and interior plastic hinges is 122.4kNm and 134.1kNm respectively and the positive over-strength of the plastic hinge is 79.2kNm.

The corresponding column shear force for positive and negative drifts is given in Table 6-6 and Table 6-7, respectively. It should be noted that the dynamic magnification and modification factors, stated in Appendix CD of NZS 3101:2006, were not included in these calculations.

The provision for calculating the flexural strength of T-beams, with a flange on one side only, in ACI 318-05 building code resulted in an effective flange width of 254mm. This provision was based on experimental beam-column results at 2% drift (Jirsa 1991). The corresponding negative and positive flexural strength of the beam, based on the measured material properties is 78.3kNm and 71.5kNm respectively. To design the flexural strength of columns under seismic actions, the ACI code specifies that the sum of nominal flexural strengths of columns, evaluated at the faces of the joint, should be greater than 1.2 times the sum of the nominal flexural strengths of the beams, evaluated at the faces of the joint. The column shear forces corresponding to the positive and negative drifts are given in Table 6-6 and Table 6-7, respectively.

Table 6-6. Comparisons of the experimental measured and code specified strength for positive drift cycles

	Averaged column shear force (kN)			**Total shear force (kN)**
	Column *A*	**Column *B***	**Column *C***	
	Positive hinge	**Combined**	**Negative hinge**	
Theoretical strength with no flange effect	42.6	85.9	43.3	171.8
ACI 318-05	56.6	119.0	62.4	238
NZS 3101:2006 theoretical strength	45.5	94.8	49.2	189.5
NZS 3101:2006 over-strength	52.2	133.3	75.0	260.5
1st cycle at +0.75 %	62.4	119.1	59.7	241.2
1st cycle at +2.0 %	74.7	163.3	82.9	320.9
1st cycle at +3.0 %	76.4	171.6	85.6	333.6

Table 6-7. Comparisons of the experimental measured and code specified strength for negative drift cycles

	Averaged column shear force (kN)			Total shear force (kN)
	Column *A*	**Column *B***	**Column *C***	
	Negative hinge	**Combined**	**Positive hinge**	
Theoretical strength with no flange effect	43.3	85.9	42.6	171.8
ACI 318-05	62.4	119.0	56.6	238
NZS 3101:2006 theoretical strength	49.2	94.8	45.5	189.5
NZS 3101:2006 over-strength	75.0	133.3	52.2	260.5
1st cycle at -0.75 %	65.1	124.8	55.7	245.6
1st cycle at -2.0 %	79.8	159.6	71.2	310.6
1st cycle at -3.0 %	76.2	168.1	73.6	317.9

It can be seen from the comparisons in Tables 6-6 and 6-7 that both the ACI and NZ codes under-estimate the strength of the beams significantly. The ACI code under-predicts the strength of the beam by 35% and 31% at positive and negative 2% drift respectively and 40% and 34% at positive and negative 3% drift respectively. Similarly, the NZ code under-predicts the over-strength of the beam by 28% (73kN) and 22% (57kN) respectively at positive and negative 3% drift.

Breaking it down to each individual column, the ACI code under-estimates the positive and negative strength of the exterior beam plastic hinges by an average of 29% and 30% at positive and negative 2% drifts, respectively and under-estimates the combined positive and negative plastic hinges next to the internal column by an average of 36%. On the other hand, the NZ code under-estimates the positive and negative over-strength of the exterior plastic hinges by an average of 44% and 8% respectively at positive and negative 3% drifts and under-estimates the combined positive and negative plastic hinges next to the internal column by an average of 27%.

If the nominal torsional strength of the transverse beams, calculated based on NZS 3101:2006, is subtracted from the test results, the ACI code under-predicts the strength of the beam by 8% and 5% at positive and negative 2% drift respectively and 12% and 7% at positive and negative 3% drift respectively; while, the NZ code under-

predicts the over-strength of the beam by an average of 2% at positive and negative 3% drift.

6.5.1 Strength Enhancement Mechanisms

The enhancement in the column shear force arises due to two main mechanisms: Firstly, torsional resistance of the transverse beams increased the column shear force in both directions. It is difficult to separate out the torsional resistance of transverse beams directly from the experimental results. The nominal torsional strength, calculated based on the New Zealand Code, is 35.5kNm and 40.5kNm for the external and internal transverse beams, respectively. Therefore, the torsional resistance of the transverse beams increases the total storey shear by 59kN. The torsional resistance of the transverse beams would reduce significantly if plastic hinges formed in the transverse beams. It should be noted that the current New Zealand code does not explicitly specify that the contribution from the torsional resistance of the transverse beam should be considered when determining the lateral strength of the moment resisting frame. Therefore, it is believed that this is often neglected in design. Based on the nominal torsional strength of the transverse beam specified in NZS 3101:2006, it would contribute approximately 18% of the inter-storey shear force in the columns in this test.

Secondly, reinforcement in the slab contributes to the negative flexural strength of the beam. The slab contribution can be visualised as an additional tension force, T_{slab}, acting at the mid-height of the slab as shown in Figure 6-48 where T_{beam} is the flexural tension force in the beam reinforcement and C is the flexural compression force. The amount of slab reinforcement participating in the negative flexural strength of the beam depends on the location of the plastic hinge (i.e., exterior or interior plastic hinges).

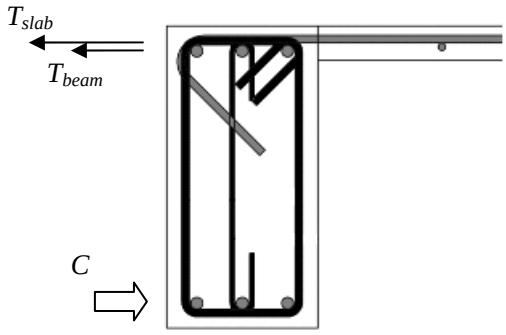

Figure 6-48. Strength increase in beam under negative bending

6.5.1.1 Interpreting Slab Reinforcement Contribution from Column Shear Force

The additional tension force, T_{slab}, can be interpreted using the experimentally measured column shear force as described below:

1. Moment at the centre of each beam-column joint can be calculated from the column shear force measured in the experiment.
2. Torsional resistance of the transverse beam, calculated based on the recommended value in the NZ code as described above was subtracted from the beam-column joint moment obtained in 1. The resultant moment, M_{C1} to M_{C3}, as shown in Figure 6-49(a), represents the sum of the column moment at the beam-column joint without the torsional contribution from the transverse beams. In this case, the resultant moment at positive 3% drift is M_{C1} = 110.0kNm, M_{C2} = 286.4kNm and M_{C3} = 127.6kNm.
3. The sum of the beam and column moment at the centre of beam-column joint should be equal and opposite. Hence, the resultant beam moment M_{B1}, (M_{B2} + M_{B3}), and M_{B4} can be determined. In this case, M_{B1} = 110.0kNm, (M_{B2} + M_{B3}) = 286.4kNm and M_{B4} = 127.6kNm as shown in Figure 6-49(b).
4. The magnitude of moment M_{B2} and M_{B3} can be solved using simultaneous equations assuming that the positive plastic hinge moments in the beams at the column face on the West and centre column, M_{CF1} and M_{CF3}, as shown in Figure 6-49(b), are the same. Therefore, M_{B2} = 182kNm and M_{B3} = 104kNm.
5. The negative moment at the column face can then be found and is equal to 158kNm and 109kNm for the interior and exterior plastic hinges, respectively.
6. The additional tension force from the slab participation, T_{slab}, was varied until the calculated moment at the section is equal to the moment interpreted from

the experiment in step 5. The moment was calculated using the standard rectangular stress block described in the New Zealand code with stress of the beam reinforcement taken as 1.1 times the measured value to take into account strain hardening effect. The corresponding T_{slab} in the interior and exterior plastic hinges are found to be 250kN and 100kN, respectively.

It can be seen that the level of T_{slab} varies significantly between the exterior and interior plastic hinges. This is because the mechanisms associated with the floor and plastic hinge interactions are different. The additional tension force in the interior plastic hinge depends on the deep beam action (i.e., the strength and stiffness of the floor slab), whereas the additional tension force in the exterior plastic hinges is limited by the out-of-plane bending and torsional strength of the transverse beams connected to the column.

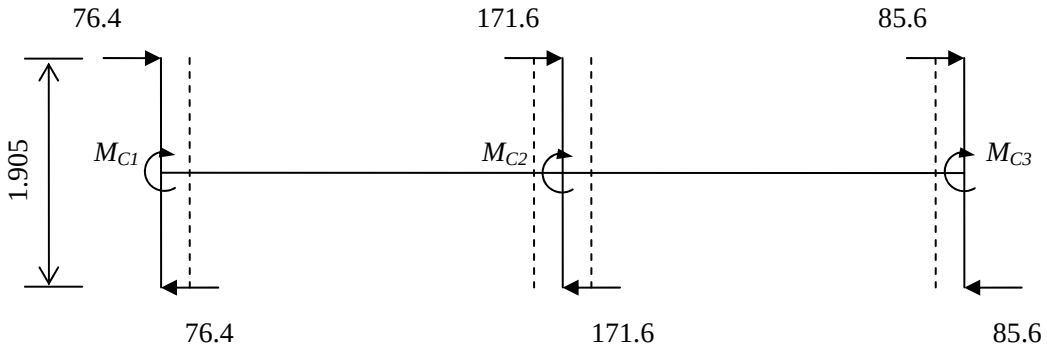

(a) Beam-column moment interpreted from column shear force

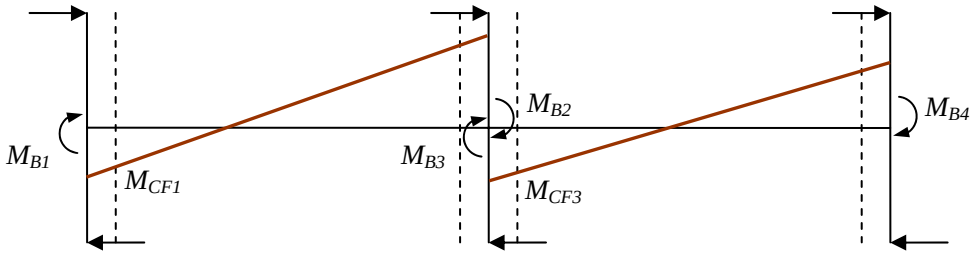

(b) Bending moment diagram in the beam

Figure 6-49. Moment distribution in the frame at the peak of the first positive 3% drift

A similar method can be used to calculate the additional tension force, T_{slab}, at the peak of the negative 3% drift cycle. The corresponding additional tension force in the

interior and exterior plastic hinges are 250kN and 50kN respectively. Therefore, the averaged T_{slab} in the interior and exterior plastic hinges is 250kN and 75kN respectively. Comparing these values with 177kN and 142kN recommended by NZS 3101:2006, the slab reinforcement contribution to the interior plastic hinges is significantly under-estimated by the code, whereas the slab reinforcement contribution to the exterior plastic hinges is significantly over-estimated by the code. Based on the experimental results, the effective flange widths, with stress of $1.1\phi_o f_y$, for calculating the negative over-strength of interior and exterior plastic hinges are 1670mm and 620mm, respectively (compared to 1200mm and 900mm specified in the code).

6.5.1.2 Method of Estimating Slab Reinforcement Contribution to Over-Strength of Beam Plastic Hinges

The additional tension force, T_{slab}, acting in the plastic hinges can be calculated considering force and moment equilibrium at a transverse beam section where the shear force, V, is zero (i.e., the moment, M, is maximum/minimum), as illustrated in Figure 6-50. If the moment capacity of the section is known, the additional tension force acting in the plastic hinges can be solved iteratively.

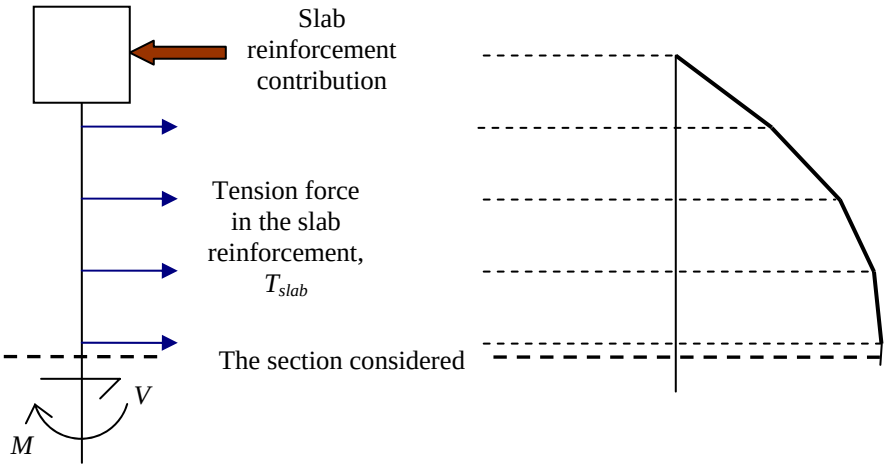

(a) Free body diagram of (b) Bending moment diagram

Figure 6-50. Schematic diagram showing the force distribution along the weak section between the floor slab and transverse beam

The out-of-plane moment capacity of the external transverse beams under eccentric loading, which induces both bending and torsional actions in the transverse beams as shown in Figure 6-51(a), cannot be calculated easily. Instead, an upper bound value (assuming the whole section can resist bending) and a lower bound value (assuming only about half of the section can resist bending as illustrated in Figure 6-51(b)) are specified. The corresponding upper and lower bound moment capacities of the transverse beam are 31kNm and 16kNm, respectively.

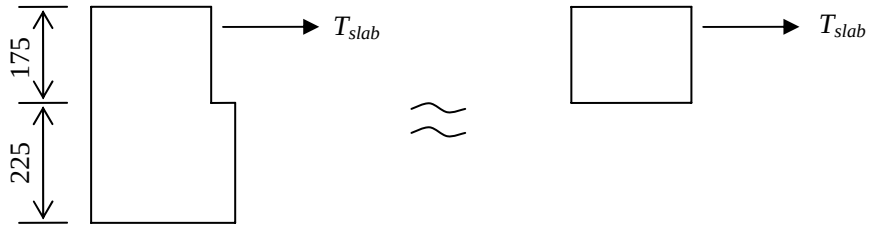

(a) Transverse beam (b) Equivalent section

Figure 6-51. Slab reinforcement acting on the external transverse beam

The location of zero shears for the upper and lower bound yield moments calculated using the method described above is 470mm and 260mm from the column face respectively and the corresponding T_{slab} in the exterior plastic hinge is 75kN and 45kN, respectively. It should be noted that the slab reinforcement contribution interpreted from the experimental results, described in Section 6.5.1.1, falls within the calculated values herein.

As the moment resistance of the internal transverse beam and floor slab is unknown, the additional tension force in the interior plastic hinge cannot be determined accurately using this approach. An attempt was made based on the moment resistance corresponding to the first yield moment of the floor slab without considering the transverse beams. The first yield moment of the floor slab only is 314kNm. The location of zero shears calculated using the method described above is 1940mm from the column face and the corresponding T_{slab} in the interior plastic hinge is 270kN. This value matches well with the interpreted experimental results described in Section 6.5.1.1.

6.6 CONCLUSIONS

From the experimental investigation that has been presented in this chapter, the following conclusions can be made:

1. Cracking and damage sustained at regions around the exterior plastic hinges is much more than that around the interior plastic hinges. This was due to differences in confinement provided by the floor slab restraining elongation of plastic hinges.
2. The observed crack patterns and DEMEC measurements made on the floor show that the floor was under combined bending and shear actions. The floor slab on each side of internal transverse beam acts like a deep beam restraining elongation of interior plastic hinges.
3. The moment demand of columns from beam over-strength calculated using ACI code under-estimates the experimentally measured value by 33% at 2% drift. This was attributed to torsional resistance of transverse beams not being taken into consideration and an under-estimation of the effective flange width. If the nominal torsional resistance of transverse beams, calculated from NZS 3101:2006, is subtracted from the test results, the ACI code under-estimates the test results by 7%. The levels of torsional resistance of the transverse beams depend on the boundary conditions, the beam properties and the connection details between the flooring system and the transverse beams.
4. The moment demand on columns from beam over-strength calculated using the New Zealand code under-estimates the experimental measured value by 28%. The difference arises mainly due to the torsional resistance of the transverse beams not being taken into consideration in the New Zealand code. If the nominal torsional resistance of transverse beams, calculated from NZS 3101:2006, is subtracted from the test results, the New Zealand code under-estimates the test results by 2%. The torsional contribution of the transverse beams should be specified more explicitly in the New Zealand code.
5. The experimental results show that the effective flange width for calculating the negative over-strength of beam plastic hinges, specified in the New Zealand code, is significantly under-estimated for the interior plastic hinges and is significantly over-estimated for the exterior plastic hinges. The experimentally interpreted additional tension force arising from slab

reinforcement contribution in the interior and exterior plastic hinges was 250kN and 75kN, respectively (compared to 177kN and 142kN specified by the code).

6. Strength enhancement of the plastic hinges was found to arise due to two main actions: (i) torsional resistance of the transverse beams; and (ii) additional tension force from slab reinforcement contribution. The amount of slab reinforcement that participates in the flexural strength of plastic hinges depends on its location, the floor slab arrangement and the strength of transverse beams surrounding the plastic hinges.
7. A method of assessing the slab reinforcement contribution to the negative flexural over-strength of exterior plastic hinges is proposed in Section 6.5.1.2. This method was validated with the experimental results obtained in this study.

6.7 REFERENCES

American Concrete Institute. (2005). *Building code requirements for structural concrete and commentary (ACI 318M-05)*, American Concrete Institute, Farmington Hills, Michigan.

Bryant, A. H., Wood, J. A., and Fenwick, R. C. (1984). *Creep and shrinkage in concrete bridges*, National Roads Board, Wellington, New Zealand.

Jirsa, J. O. (1991). *Design of beam-column joints for seismic resistance, ACI SP-123*, American Concrete Institute, Detroit, Michigan.

Standards New Zealand. (2006). *Concrete structures standard: NZS 3101:2006*, Standards New Zealand, Wellington.

7 MODELLING OF 3D FRAME-FLOOR SUBASSEMBLY

To simulate the behaviour of structures under earthquake excitations, three-dimensional effects of the key members, such as frame-floor interaction, torsion, in-plane and out-of-plane bending response, should be incorporated into the analysis program. A plastic hinge element that can capture elongation of ductile RC members was developed, validated and applied to two-dimensional cantilever beam and frame sub-assembly tests as described in Chapters 2 to 4. However, the model must possess the ability to simulate the out-of-plane bending as well as torsional response of the plastic hinges when being applied to the three-dimensional (3D) framework.

In this chapter, an equivalent 3D plastic hinge element is developed and implemented into a 3D time-history analysis program, RUAUMOKO3D, by Professor Athol Carr (Carr 2008). The 3D plastic hinge element is verified against the 2D plastic hinge element for accuracy in Section 7.1. This element is then combined to form a 3D analytical model to predict the cyclic response of the floor-frame sub-assembly test described in Chapters 5 and 6. The development of the analytical model for the sub-assembly is described in Section 7.2. Validation of the analytical model with the experimental results is discussed in Section 7.3. A sensitivity study on some of the modelling parameters used in the analytical model is presented in Section 7.4.

7.1 3D PLASTIC HINGE ELEMENT

The extended 3D plastic hinge element is illustrated in Figures 7-1 and 7-2. It consists of a series of longitudinal and diagonal axial springs connected between the rigid planes at the two ends to represent the flexural, shear, torsional and axial response of the plastic hinges.

A total of eight diagonal springs are located at the faces of the x-y and x-z plane as shown in Figure 7-1. The diagonal springs on the x-y plane are used to represent the diagonal compression struts under in-plane bending and shear actions; whereas the

diagonal springs on the x-z plane are used to represent the diagonal struts under out-of-plane bending and shear actions.

The area of each diagonal spring in the x-y plane is simply half of the width of the beam, *b/2*, multiplied by the effective depth of the compression strut, D_y, and the area of each diagonal spring in the x-z plane is equal to half of the depth of the beam, *h/2*, multiplied by the effective depth of the compression strut, D_z. The effective depths, D_y and D_z, are taken as the perpendicular distance from the diagonal strut to the end-point of the reinforcement spring as illustrated in the figure below.

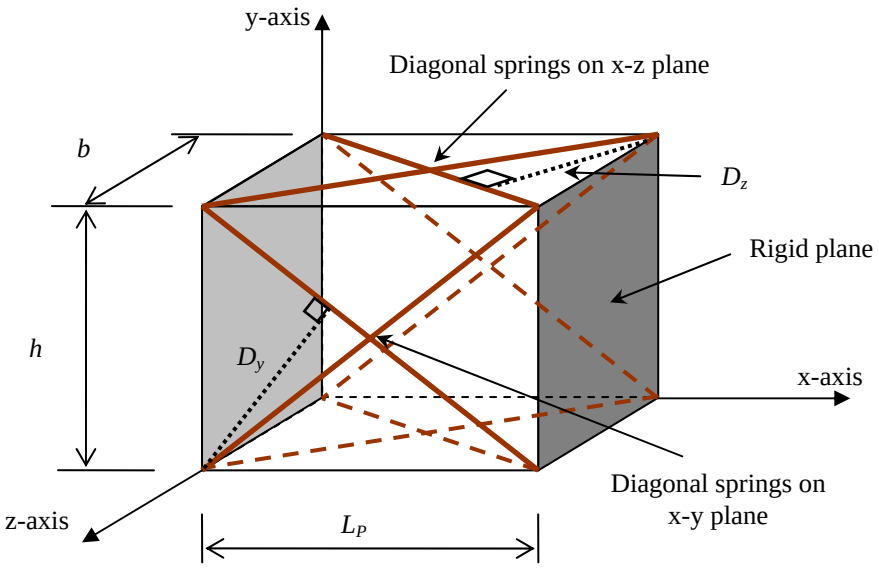

Figure 7-1. 3D plastic hinge element

A total of 72 longitudinal concrete and steel springs are distributed over the cross section of the element as shown in Figure 7-2. Of these, 28 springs are spaced around the cover to represent the unconfined concrete; 36 springs are located between the centroids of the reinforcement to represent the confined concrete; and 8 springs are located at the circumference of the core section to represent the reinforcing bars. It should be noted that the reinforcement content at each location can vary depending on the actual reinforcement layout. The proposed plastic hinge element does not allow for different cover depths on each face and it does not allow for reinforcing bars with different material properties.

The parameters controlling the response of plastic hinges, such as the length of the plastic hinge element, L_P, and the length of the steel spring, L_{yield}, are calculated based on the method described in Section 2.2.

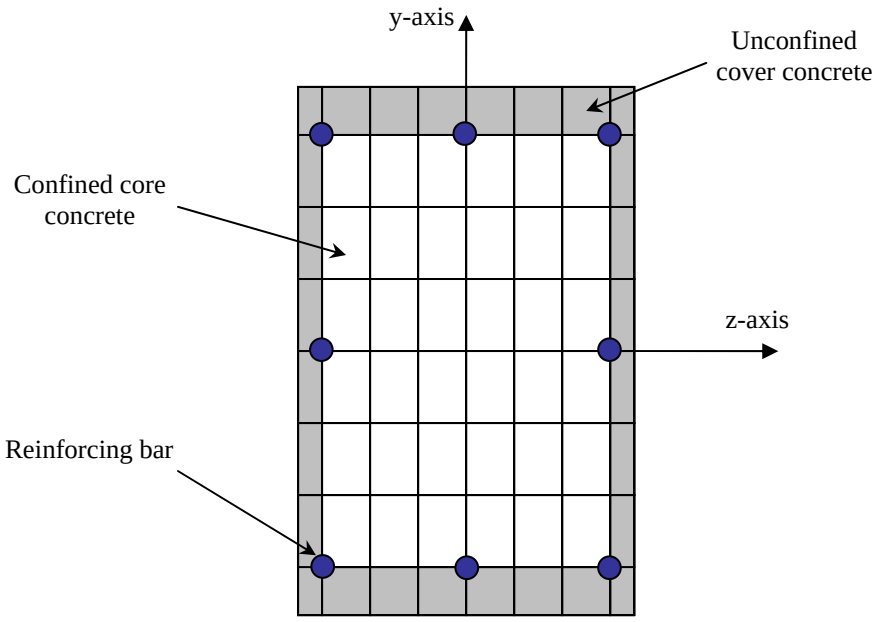

Figure 7-2. Cross-section of 3D plastic hinge element

It should also be noted that the diagonal springs on the top and bottom x-z plane are uncoupled with the rotation about the z-axis, but are coupled with the axial deformation, whereas the diagonals on the vertical x-y plane are uncoupled with the rotation about the y-axis. This is done to prevent the diagonals from adding unrealistic flexural strength and stiffness to the plastic hinge element. More research may be required to examine the validity of the plastic hinge element under bi-axial loading.

With this arrangement, the diagonal springs on the x-z plane arbitrarily increase the concrete area in the section. For most of the applications in this study, the plastic hinge is predominantly under in-plane actions. Consequently, the compressive and tensile strength of the diagonals on the x-z plane are minimised to diminish their effect on the axial response.

7.1.1 Comparison between 2D and 3D Analyses

To verify the newly developed 3D plastic hinge element under in-plane bending and shear actions, analyses of a cantilever beam were carried out using both the 2D and 3D plastic hinge element. Figure 7-3 shows the force-displacement and elongation responses obtained from these analyses. It can be seen that the hysteretic and elongation responses of the two analyses are in good agreement. It should be noted that in the 2D element, the concrete springs between the top and bottom reinforcement are assumed to be confined over the width; however in the 3D element, the concrete springs (at the member face) are modelled as unconfined concrete, where the contact stress effect is less significant. However, this does not appear to have a significant influence on the analytical predictions.

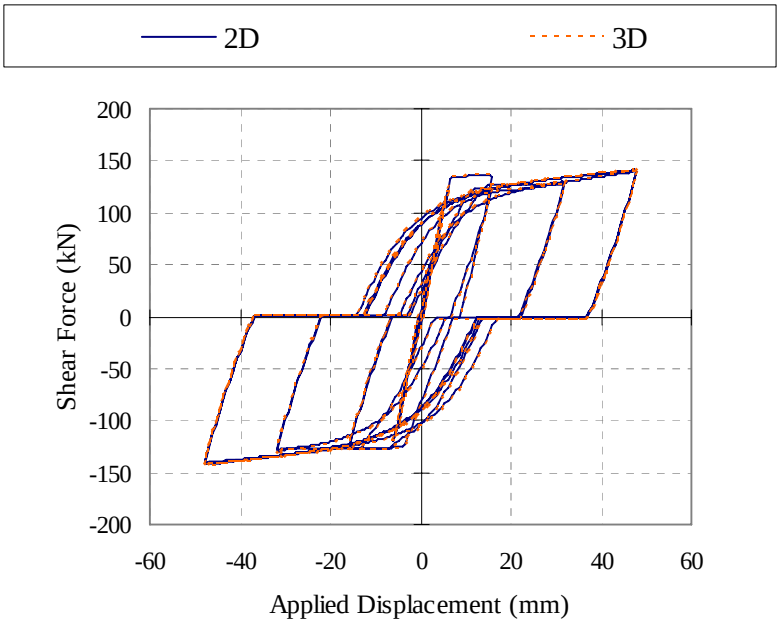

(a) Force displacement

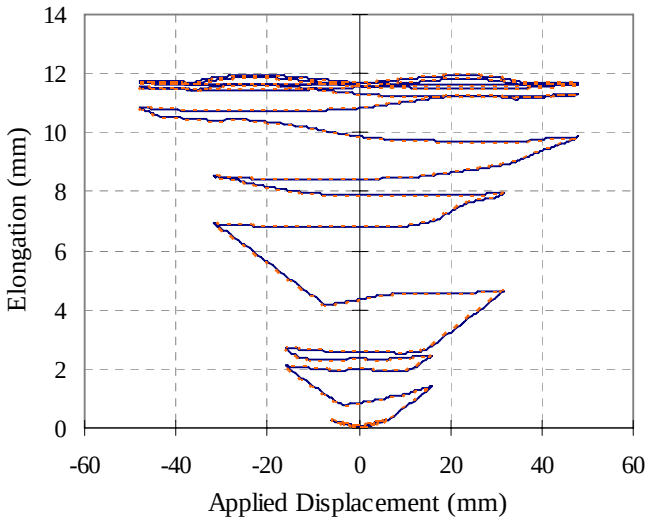

(b) Elongation

Figure 7-3. Comparison between 2D and 3D plastic hinge models

7.2 ANALYTICAL MODEL FOR THE FRAME-FLOOR SUB-ASSEMBLY

7.2.1 Literature Review

In order to capture the interactions between the floor slab and its surrounding frame, important mechanisms such as elongation of plastic hinges and inelastic floor

deformation must be modelled. A few analytical models have been attempted in the past to include these actions. These models are discussed below.

Shahrooz et al. (1992) were the first to propose an analytical model to simulate the slab contribution to the flexural strength of beams. The model was developed based on kinematic relations between beam deformations and the state of strain in the slab. The slab was modelled using rigid links with axial springs and it accounted for the support movement such as reinforcement slip, twist, weak axis rotation and elongation of the transverse beams. The model was verified against test results of individual determinate beam-column joint sub-assemblies under monolithic loading. However, its applicability in indeterminate structures or structures under cyclic loading is uncertain.

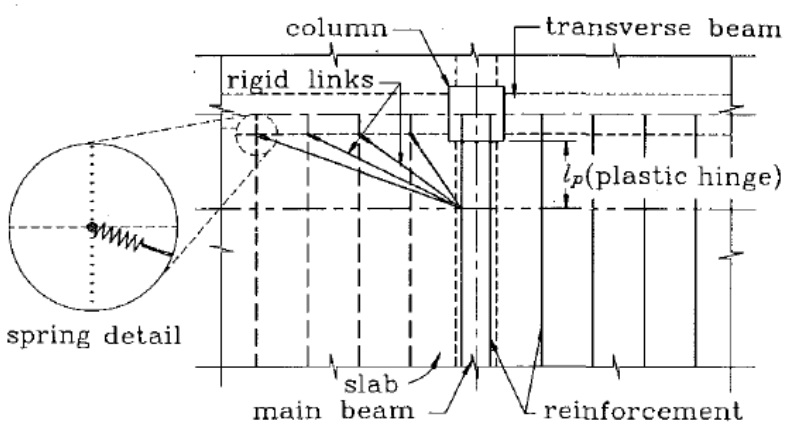

Figure 7-4. Proposed floor slab model by Shahrooz et al. (1992)

MacRae and Gunasekaran (2006) proposed a simple 2D analysis method to model the floor slab which was used in conjunction with the elongating plastic hinge element developed by Kim (2002). The slab was modelled using strut elements as shown in Figure 7-5. This model is relatively simple and it has several limitations, some of which are listed below:

1. The slab elements need to be calibrated prior to analysis in order to represent the slab behaviour accurately;
2. Interaction between the slab and the column is ignored as the element strut is not connected to the column; and

3. 3D effects such as torsional and flexural response of the transverse beam and out-of-plane bending of the slab are ignored.

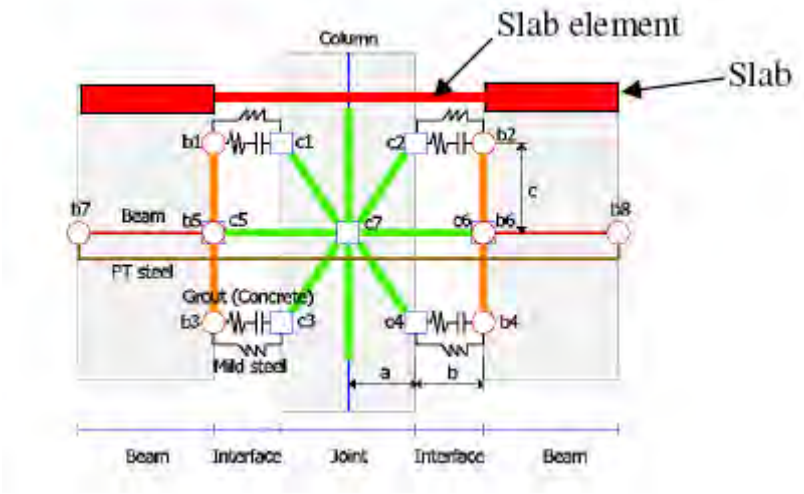

Figure 7-5. MacRae's beam-column joint model including beam elongation and slab effect (MacRae and Gunasekaran 2006)

Lau (2007) developed a complex 3D floor model to simulate the response of a linking slab (region connecting the first pre-stressed floor unit to the frame). The linking slab was modelled using a series of struts, connected both in parallel and in series, to simulate the horizontal shear transfer in the plane of the floor slab as well as out-of-plane bending of the floor slab, as illustrated in Figure 7-6. As the model is very sophisticated, it requires large computational effort. It should also be noted that despite the relative complexity of the model, there were some discrepancies between the analytical predictions and the experimental results. The errors were mainly due to elongation of plastic hinges not being captured accurately.

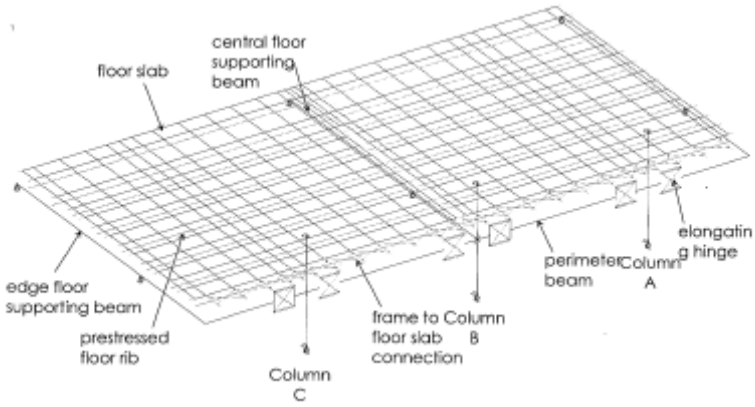

(a) Overall modelling layout

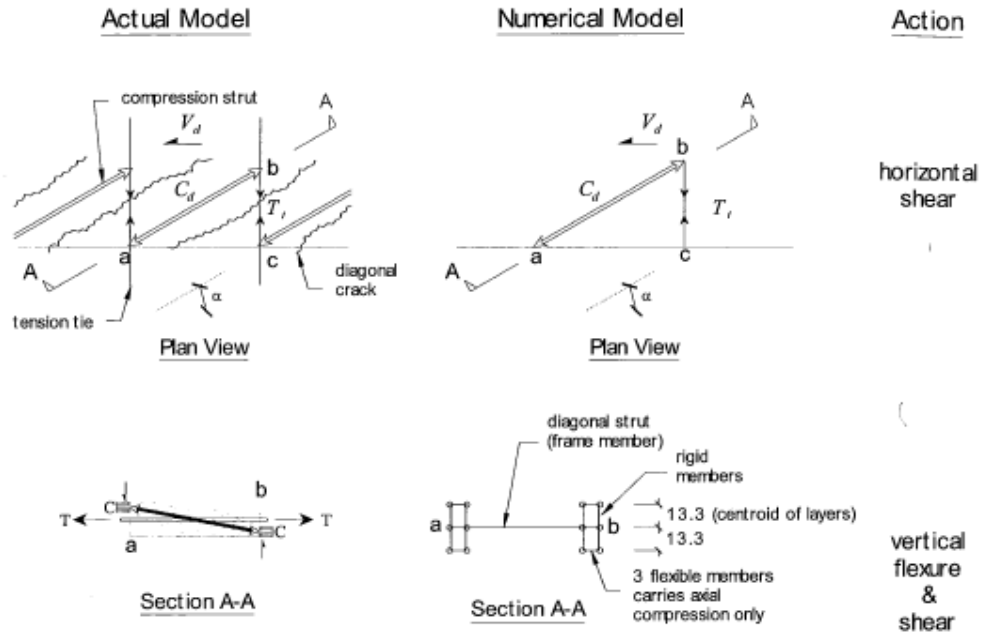

(b) Modelling of linking slab

Figure 7-6. Analytical model developed by Lau (2007)

7.2.2 Set-up of the Proposed 3D Model

An analytical model was set up in RUAUMOKO3D to simulate the behaviour of the sub-assembly test described in Chapter 4. The model consists of the newly developed 3D plastic hinge element described in Section 7.1, which can capture the flexural, axial, shear and elongation response of plastic hinges in beams subjected to inelastic cyclic actions with varying axial load levels. The plastic hinge element takes into account shear deformation from both elongation and stirrup extensions as described in Chapter 3.

A small displacement analysis scheme where the member stiffness is not affected by the deformations of the structure and the nodal coordinates remain unchanged was assumed in the analysis. This was chosen to avoid instability in the analysis. As pseudo-static analysis was carried out, no mass and damping coefficients were assigned to the structure so that no inertial and damping forces were considered. Three Newton-Raphson iterations were initially used as a maximum limit and the norm of the out-of-balance force vector relative to the incremental force vector was set as 1%. However, it was found that in some situations the iterations disturbed the stress-strain relationships of some axial spring elements. Therefore, iterations were turned off in the subsequent analyses and a very small incremental displacement step was used.

The overall layout of the frame-floor analytical model is shown in Figure 7-7. The model consists of several layers of nodes and elements located at the centre line of each member section. The columns, beam column joints, transverse beams, elastic portion of the longitudinal beams, prestressed ribs and end slab were modelled using elastic elements. The plastic hinges in the longitudinal beams were modelled using the newly developed 3D plastic hinge element. Axial truss members were used to model the “linking slab” (floor slab between the first prestressed rib unit and the longitudinal beam) and along the interface between the floor topping and transverse beams where large non-linearity is expected to occur. The rest of the floor topping was modelled using elastic quadrilateral shell elements, which take into account plane stress and plate bending. The details of these members are described later in the chapter. It should be noted that non-linear shell elements are currently not available in RUAUMOKO3D.

The boundary conditions adopted in the model represent the conditions applied in the experiment. The base of each column in the moment resisting frame was restrained against vertical movement only, and the beam-column joint in the centre column was restrained against movement parallel to the frame. The far end of the external transverse beams, close to the end slab, were free to move parallel to the moment frame only and the far end of centre transverse beam was free to move in a horizontal plane and free to rotate in all directions.

Figure 7-7(c) shows the mid-height level of floor slab, ribs, end slab and longitudinal/transverse beams; these members were connected to the floor via rigid links. At the column centre line, the end node of diagonal trusses representing the linking slab were connected to the beam-column joint via rigid links (i.e., centre of beam column joint is the external node and the end of the diagonal truss at the floor level is the internal node). The steel and concrete truss elements between the transverse beams and the floor were located at the mid-height of the floor slab. The RUAUMOKO input file for this frame-floor model is given in Appendix B.

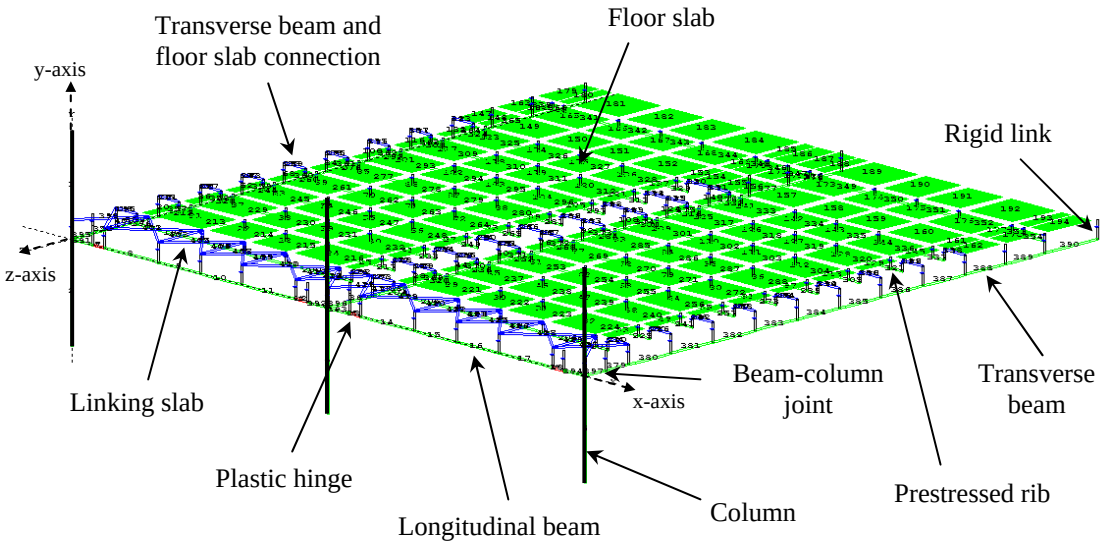

(a) Isometric view

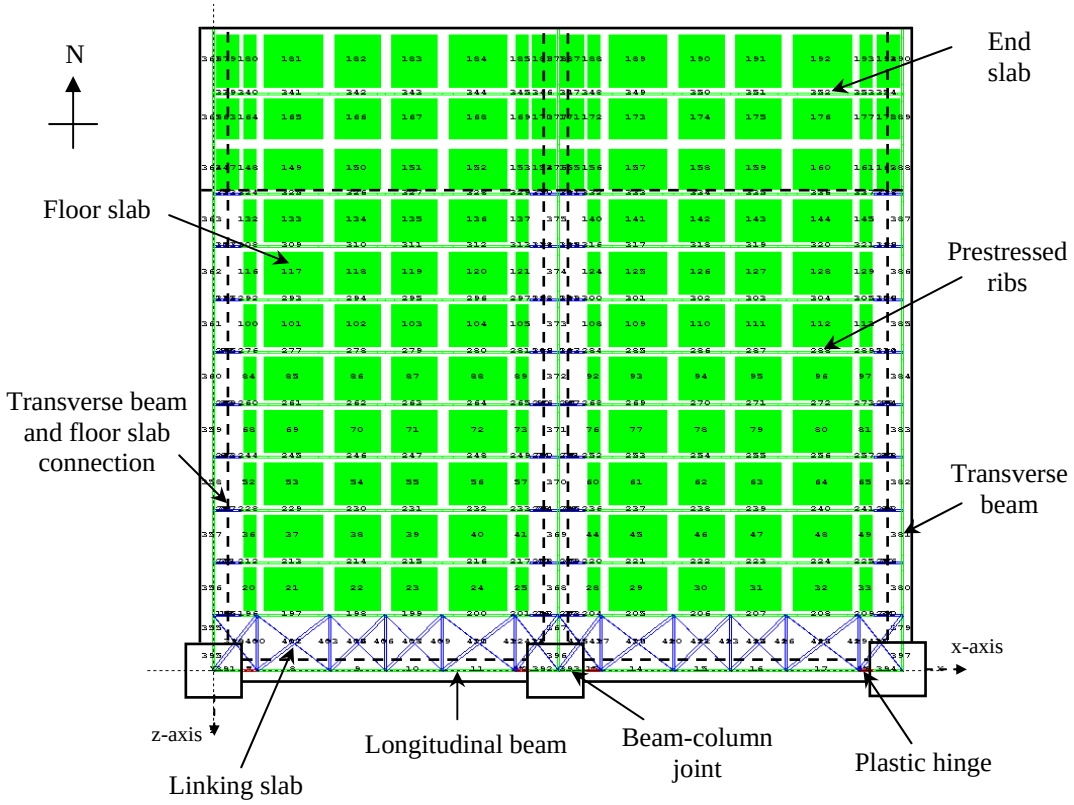

(b) Plan view

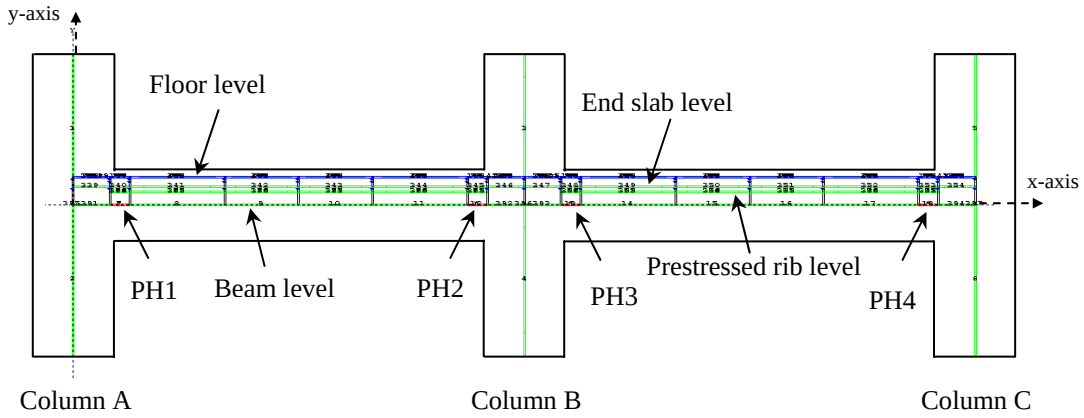

(c) Elevation showing relative levels of element centroids

Figure 7-7. Layout of the 3D analytical model

7.2.3 Loading arrangement

As the displacements applied at the top and bottom of each column in the experiment were corrected iteratively to allow elongation of beam plastic hinges to develop freely, the same displacement history could not be directly fed into the analysis. This is because it would artificially generate the same elongation as in the test. To resolve

this problem, the flexural and shear deformation of each column was assumed to be negligible, and hence rotation was applied to the centre of each beam-column joint. The rotation applied to each column followed the same rotation history applied in the experiment (see Section 5.4.1). It should be noted that the column deformation measured in the experiment was less than 10% of the total deformation as shown in Section 6.3.4. Therefore, the assumption is reasonable in this case.

7.2.4 Member Types and Properties

7.2.4.1 Beam Plastic Hinges

As described in Section 2.2, the plastic hinge element is controlled by two key parameters: the length of the plastic hinge element, L_P, and the effective length of the steel spring, L_{steel}. The length of the plastic hinge element is chosen to represent the inclination of the diagonal compression struts in the plastic hinge. It depends on the shear force in the beam corresponding to yielding of the plastic hinges. As it is difficult to calculate the yield strength of the beams interacting with the floor slab, the averaged yield strength is obtained from the measured experimental column shear force at 1% drift where all the plastic hinges have yielded. The corresponding averaged shear force in the beam is 87kN and the length of the plastic hinge element is 105mm.

The effective steel length in the plastic hinge element is taken as the length over which the reinforcement yields, L_{yield}, as described in Section 2.2 and is expressed in Equation 7-1. It depends on the ratio between the maximum strength, M_{max}, and yield strength, M_{yc}, of the plastic hinges; moment to shear ratio, M/V; the length of tension shift, L_{ts}; and the length of yield penetration into the support, L_e. In this case, the averaged maximum strength in the plastic hinges measured in the experiment, was 1.2 times the measured averaged yield strength. The length of the tension shift is taken as $0.5(d - d')$ where $(d - d')$ is the distance between the centroids of tension and compression reinforcement. The length of yield penetration into the support is based on Equation 7-2 and is illustrated in Figure 7-8 where L_{db} is the development length specified in the New Zealand code. It is an approximate value because it is difficult to determine accurately the stress distribution of the longitudinal

reinforcement in the beam-column joint. The calculated effective steel length in this case is 458mm.

$$L_{yield} = \frac{M}{V}\frac{M_{max} - M_{yc}}{M_{max}} + L_{ts} + L_e \quad (7\text{-}1)$$

$$L_e = \frac{M_{max} - M_{yc}}{M_{max}} \times L_{db} \quad (7\text{-}2)$$

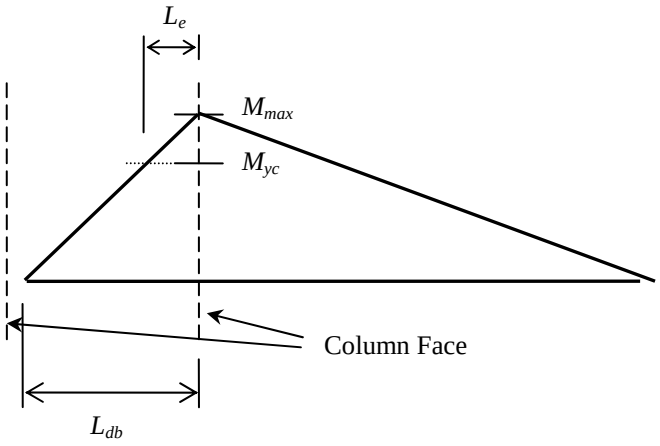

Figure 7-8. Schematic diagram showing tension force profile in the beam-column joint

The compressive strength of the confined concrete in the plastic hinge element was calculated based on the equations proposed by Mander et al. (1988), which gave a value of $1.2f_c'$. The tensile strength of concrete is calculated from Clause 5.2.6 in NZS 3101:2006 (Standards New Zealand 2006) and it is shown in Equation 7-3. It should be noted that the equation specified here is based on the lower characteristic value; therefore it is acknowledged that the average tensile strength of concrete should be slightly higher.

$$f_t = 0.36\sqrt{f_c'} \quad (7\text{-}3)$$

The compressive strength of the diagonal springs on the vertical face was set to $0.34f_c'$, as recommended by To et al. (2001). It is thought that once the concrete cracked in flexure, the diagonal would not be able to sustain any tensile stress. Therefore, the tensile strength of these diagonal springs was set to a very small value.

It should be noted that if the tensile strength is set to zero, the analysis becomes unstable.

7.2.4.2 Elastic Beams, Columns, Beam-Column Joints, Prestressed Ribs and End Slab

The elastic portion of the longitudinal beam, transverse beams, beam-column joints, prestressed ribs and end slab were modelled using Giberson beam elements with lumped plasticity at the member ends. The moment of inertia of the elastic beams and columns was taken as $0.4I_{gross}$, where I_{gross} is the second moment area of the gross section. The 0.4 factor was used to represent the loss of stiffness due to flexural cracking (in-line with the value recommended in the NZ code). The elastic modulus of the section was taken as Young's modulus of concrete, E_c, estimated by Equation 7-4, and the shear modulus of member, G, was taken as $0.4E_c$. These values are consistent with the New Zealand Standard, NZS 3101:2006. The torsional second moment of area, J, was calculated based on Equation 7-5 where b and h are the width and depth of the section. Shear deformation in the elastic members was neglected in the analysis.

$$E_c = 3320\sqrt{f_c'} + 6900 \tag{7-4}$$

$$J = \frac{1}{12}bh\left(b^2 + h^2\right) \tag{7-5}$$

A few assumptions were made to simplify the analysis. The concrete compressive strength of the prestressed ribs was assumed to be 40MPa, as this value was not specified by the manufacturer. The portion of the seating ledge in the transverse beams was not taken into account when calculating the effective moment of inertia (i.e., the second moment of area). The effective moment of inertia of the beam-column joint element was assumed to be twice the effective moment of inertia of the elastic beam.

The nominal torsional capacity of the transverse beams, T_n, was calculated based on Clause C7.6.2 of NZS 3101:2006 and is given in Equation 7-6, where A_o is the gross

area enclosed by shear flow path, A_t is the area of one leg of the closed stirrup, f_{yt} and f_y are the yield stress of the stirrups and longitudinal bars respectively, s is the spacing of the stirrup, A_l is the area of the longitudinal bars and p_o is the length of perimeter of the section measured between centres of reinforcing bars in corners of the member. This relationship was developed for members without axial restraint. However, in the test, the transverse beams were restrained by the floor slab and the longitudinal beam. Therefore, the value calculated using Equation 7-6 is likely to be on the low side.

$$T_n = 2A_o\sqrt{\frac{A_t f_{yt}}{s}\frac{A_l f_y}{p_o}} \tag{7-6}$$

A schematic diagram showing the relationship between torsional strength and twist is plotted in Figure 7-9, where GK and GK_{cr} are the un-cracked and cracked torsional stiffness, respectively. After diagonal cracking occurs, concrete resistance to torsion reduces and the stiffness decreases. An equation to calculate the post-cracking stiffness of the transverse beam was described by Park and Paulay (1975). For a beam under axial restraint, the stiffness would increase; for simplicity, the torsional stiffness of the member is taken as the un-cracked section and a bilinear factor of 0.02 was used to prevent instability in the analysis.

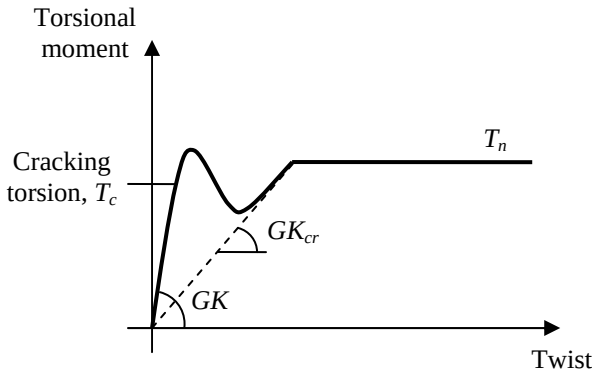

Figure 7-9. Schematic relationship between torsional moment and twist

7.2.4.3 Floor Topping

As there is currently no inelastic shell element available in RUAUMOKO3D, the floor topping was modelled using 'Hybrid Stress Type 2' quadrilateral finite element

(elastic shell element which considers plane stress and plate bending). The stress distribution in the element is assumed to have a cubic variation along the edge. The tangential displacements are assumed to vary linearly along the edge and the normal displacements are assumed to have cubic variation along the edge. Three points Guassian quadrature is used in each direction to integrate the flexibility matrix. Shear deformation of the element was considered. The elastic modulus of member was taken as the Young's modulus of concrete, E_c, given by Equation 7-4. The Poisson's ratio was taken as 0.2.

7.2.4.4 Linking Slab

The linking slab was modelled using a strut-and-tie analogy. The diagonal struts were modelled using concrete springs and the transverse ties were modelled using steel springs. These axial springs were located at the mid-height of the floor slab and were connected between the centre of the first prestressed rib and the centre of the perimeter frame as shown in Figure 7-10. With this arrangement, the model cannot resist out-of-plane bending in the linking slab. It is appropriate for this experiment, where the out-of-plane bending actions in the linking slab arising from differential vertical movements between the longitudinal beams and the first set of prestressed rib units are small.

In this layout, the first set of the diagonals next to the columns are connected to the end of the plastic hinge element; hence, the angle of these diagonals was fixed at 56^0 to match with the position and length of the plastic hinge element. The angle of the next set of diagonals was set equal to the average angle measured in the experiment, which was equal to 38 degree. For symmetry, the angle of the remaining diagonals was set at 46 degree. These dimensions are illustrated in Figure 7-10(b).

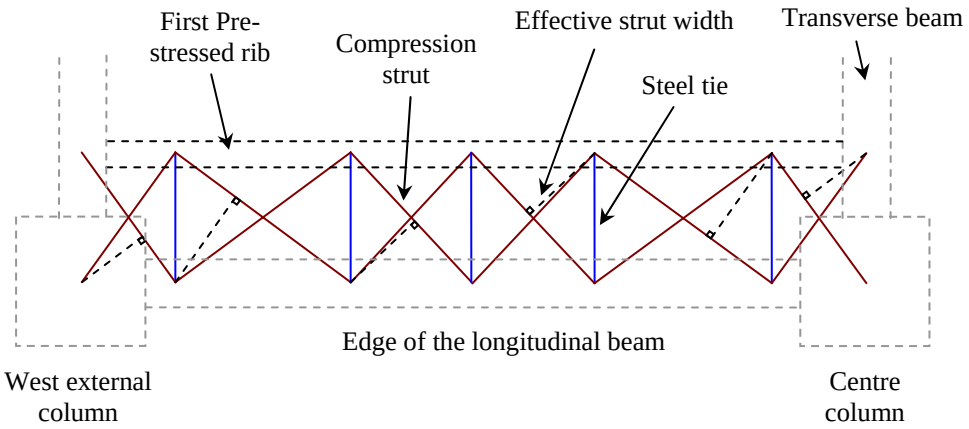

(a) Modelling layout

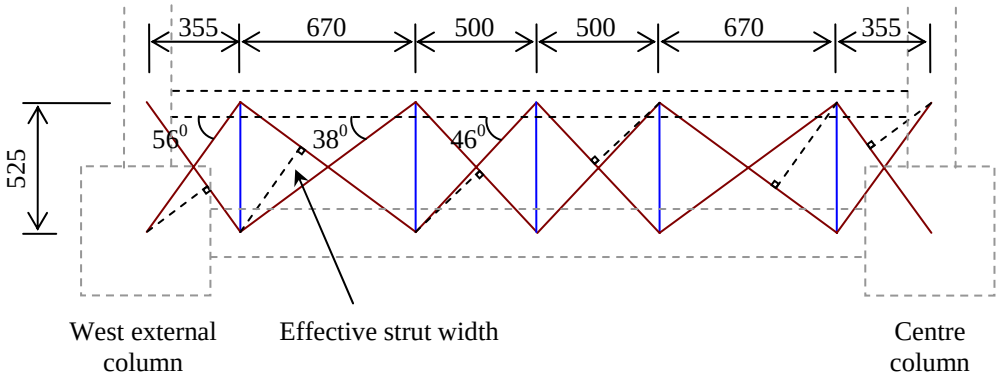

(b) Modelling dimension

Figure 7-10. Analytical model of linking slab

The length of the diagonal concrete spring in Figure 7-10 was taken as the length of the element. The length of the steel spring was approximated as the clear width of the linking slab plus half of the development length into the floor slab plus a portion of the anchorage length in the longitudinal beam as illustrated in Figure 7-11. It should be noted that the exact stress profile is not linear as assumed here, however for simplicity, the linear approximation was used. The development length was calculated based on NZS 3101:2006, and is expressed in Equation 7-7. As the equation was developed based on the lower characteristic value, it is acknowledged that the actual development length should be slightly smaller. The calculated length for the steel spring is 640mm.

$$L_{db} = \frac{0.5\alpha_a f_y d_b}{\sqrt{f_c'}} \qquad (7\text{-}7)$$

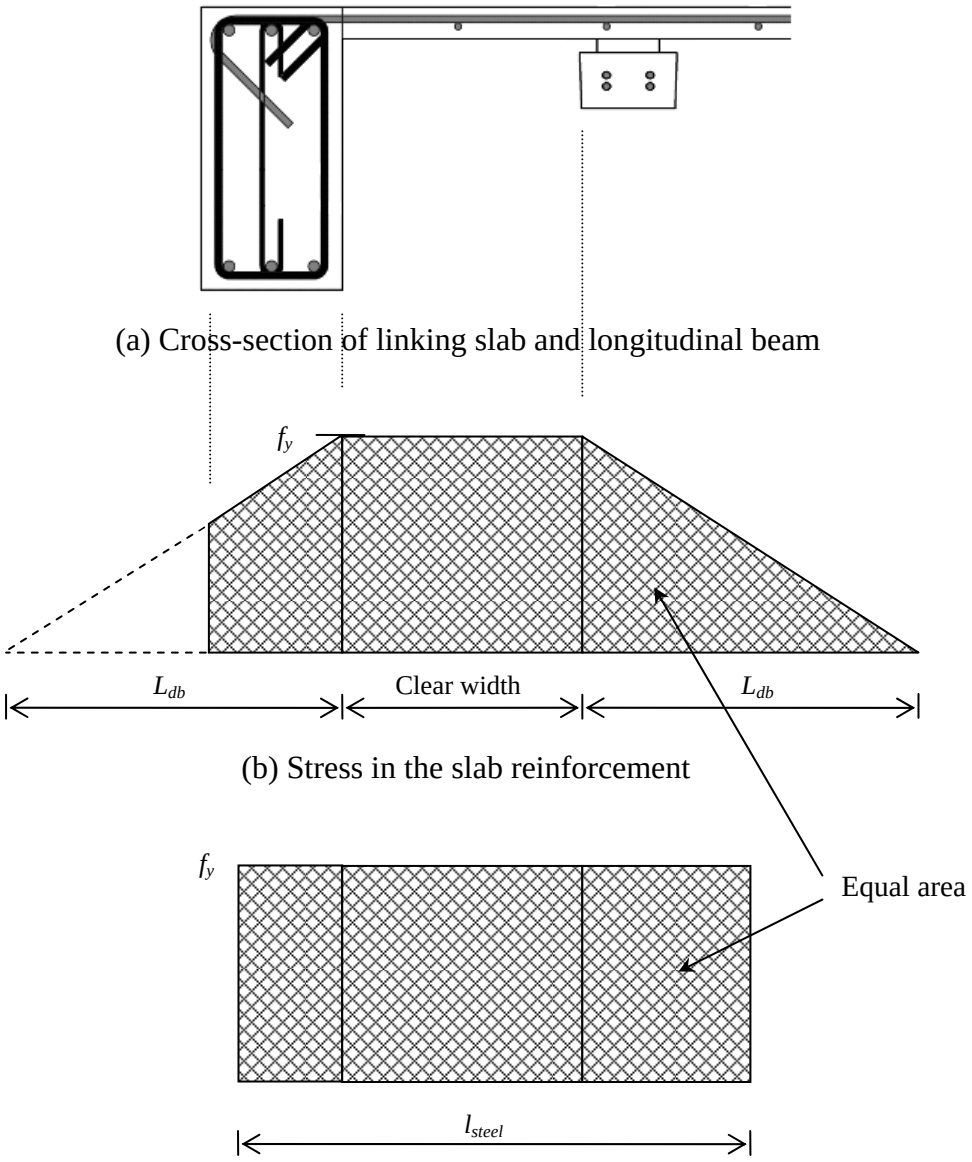

Figure 7-11. Schematic diagram showing length of steel spring for the linking slab model

The area of the concrete strut was taken as the effective strut width, as shown in Figure 7-10(a), multiplied by the thickness of the slab. A very small value was assigned for the tensile strength of the diagonal struts so they acted as contact elements.

7.2.4.5 Floor Topping-Transverse Beam Interfaces

It was assumed that the moment capacity of the interface between the floor topping and the transverse beams was negligible due to the small topping depth and also due to wide cracks developing as a result of plastic hinge elongation. With this assumption, the interface is modelled by a series of axial steel and concrete springs located at the mid-height of the floor topping along the transverse beams.

The length of the concrete spring was taken as the actual length of the element, equal to 250mm. The area of the concrete spring in the analysis only modelled the area of the floor topping. The tensile strength of concrete was calculated using Equation 7-3. The contact stress parameters for the concrete springs were set as default value in RUAUMOKO.

The length of the steel spring was approximated as half of the development length into the floor slab plus a portion of the anchorage length in the transverse beams as shown in Figure 7-12. Note that the portion of the anchorage length in the internal transverse beams was taken as 100mm (half of the transverse beam width). Thus the steel length for the external and internal transverse beam interface was 290mm and 262mm respectively.

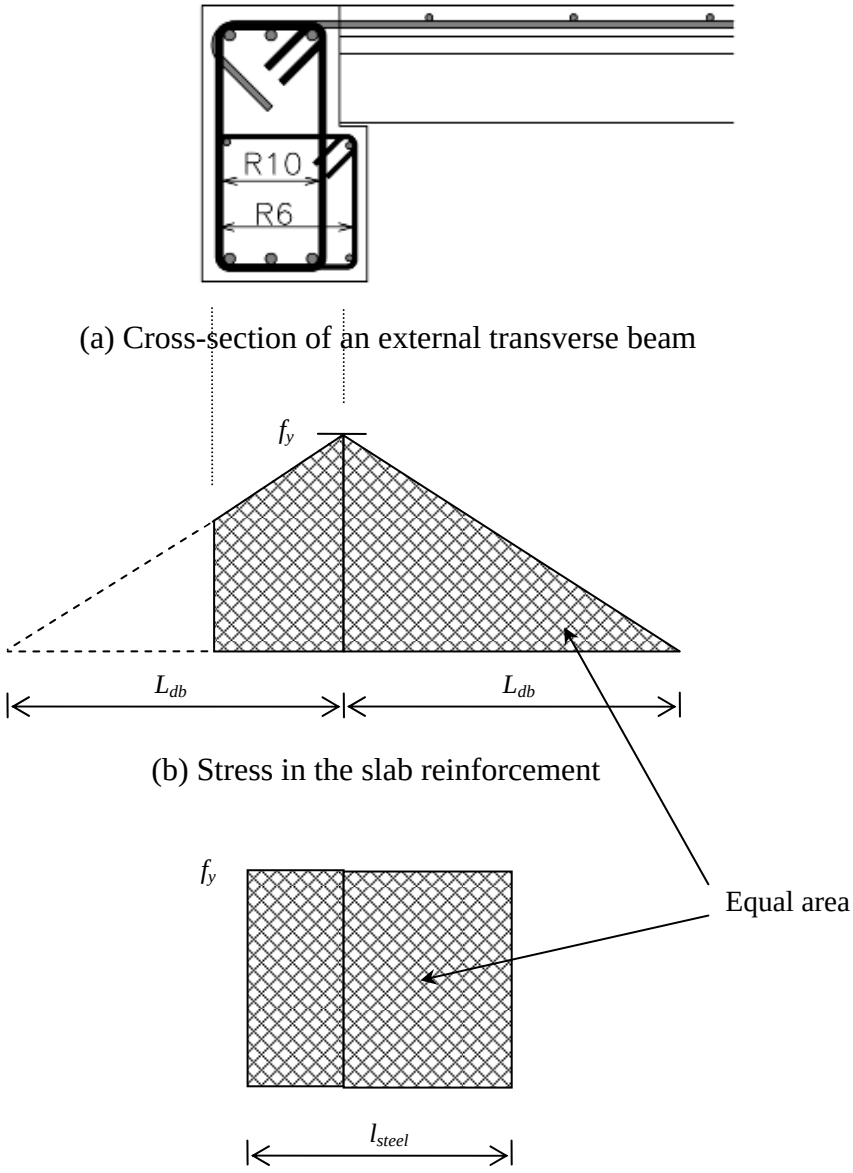

Figure 7-12. Schematic diagram showing the length of steel spring for the transverse beam interface element

7.3 ANALYTICAL PREDICTIONS AND COMPARISONS WITH EXPERIMENTAL RESULTS

7.3.1 Force-Displacement Response

The analytical and experimental force-displacement relationships of the overall frame, up to 3% drift, are shown in Figure 7-13. It can be seen that the analysis predicts

both the loading and unloading stiffness together with the yield force and the peak force accurately. Pinching was under-estimated in the analysis. It is believed that this was due to bond degradation and slipping of reinforcing bars in the central beam-column joints, which were observed in the experiment, but not considered in the analysis.

It should be noted that this model has not been calibrated to fit the experimental results. The main difference between this model and other conventional frame models is that it contains the newly developed plastic hinge elements as well as truss like floor elements that allow floor slabs to interact with the frame. These elements are based on stress-strain relationships of concrete and reinforcing bars which do not require calibration.

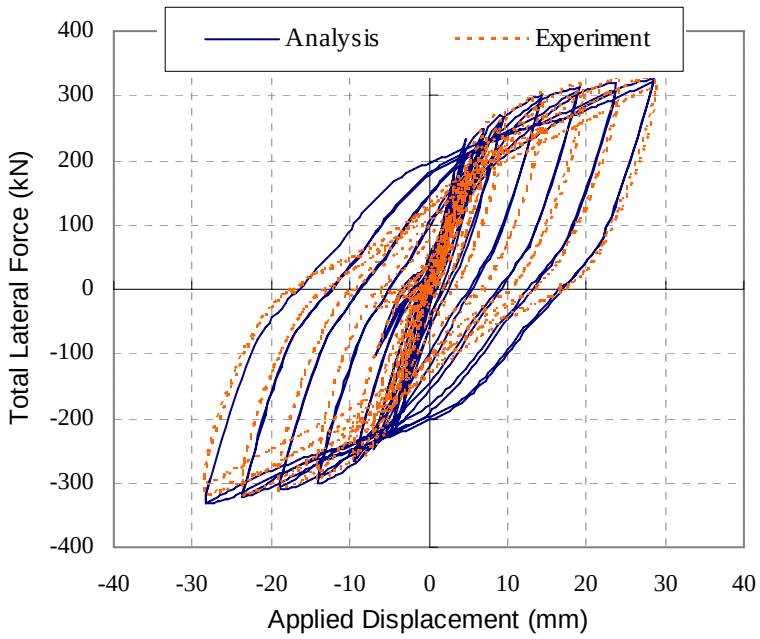

Figure 7-13. Total force-displacement comparisons

Figure 7-14 shows the averaged force-displacement relationships of each individual column. Pinching is generally being under-estimated in the analysis, this is partially due to the pinched torsional response of the transverse beams, observed in the test (see Section 6.4), not being modelled correctly in the analysis. Pinching is under-estimated more in Column B. It is believed that this is due to bond degradation and

slipping of reinforcing bars in the beam-column joints, which were observed in the test, but not modelled in the analysis.

Also plotted in Figure 7-14 is the column shear force corresponding to the flexural over-strength of the beam plastic hinges calculated using NZS 3101:2006 as described in Section 6.5. It should be noted that the torsional resistance of the transverse beam has not been included in these values. The corresponding additional shear force associated with the nominal torsion strength of the transverse beams for the external and internal columns is 19kN and 21kN, respectively.

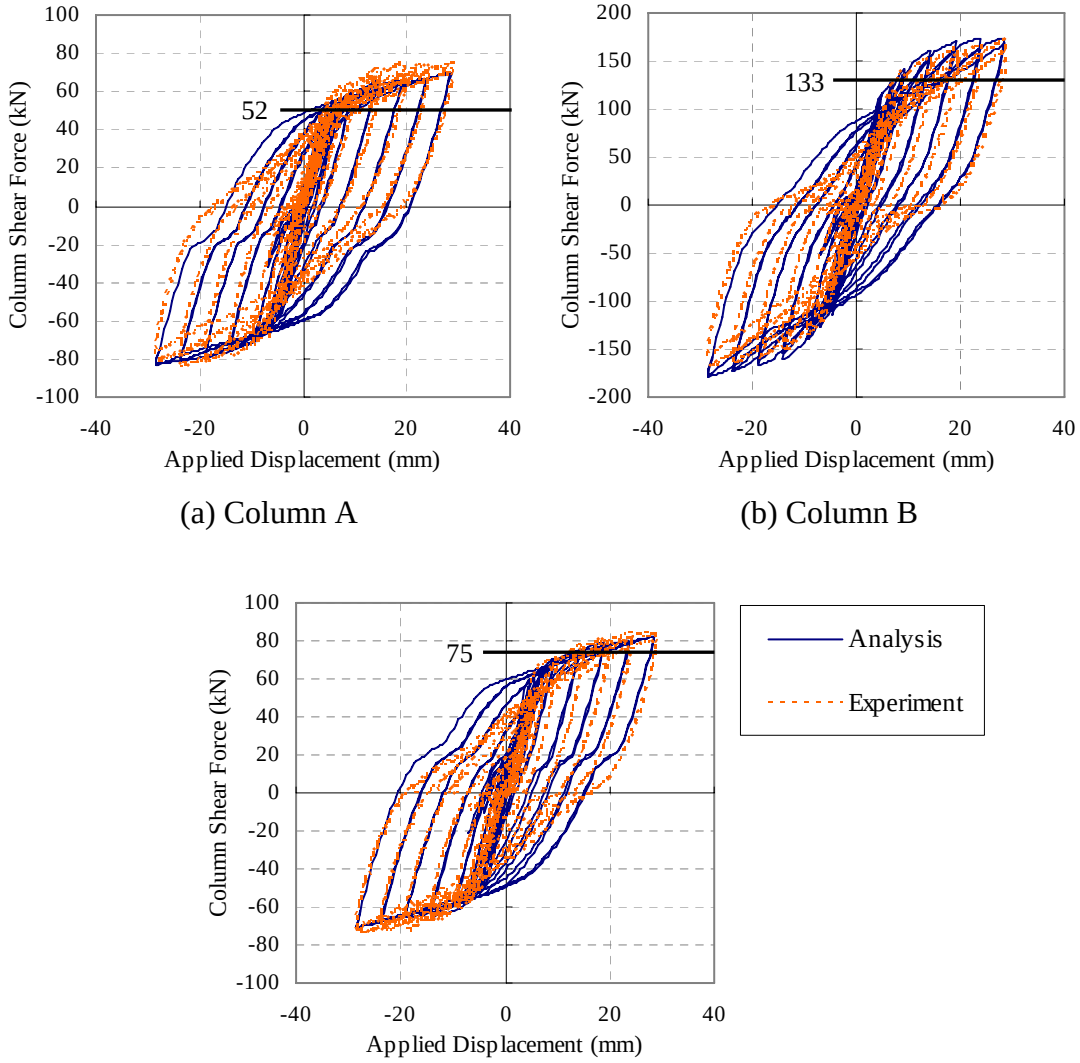

(a) Column A

(b) Column B

(c) Column C

Figure 7-14. Force-displacement comparisons for each column

7.3.2 Predicted Moment-Applied Column Displacement Response

Figure 7-15 shows the predicted moment against the column displacement (or drift) for the West end exterior plastic hinge (PH1) and the East end interior plastic hinge (PH3). As the behaviours of PH1 and PH3 are similar to the behaviours of PH4 and PH2 respectively, only the responses of PH1 and PH3 are illustrated. The flexural over-strength of the plastic hinges, calculated based on NZS 3101:2006, are also plotted in this figure. A few key observations can be drawn from the figure:

1. The predicted positive moment decreases as the drift cycle increases in the interior plastic hinge, whereas the predicted positive moment remains relatively constant in the exterior plastic hinge. The reduction in the positive moment of interior plastic hinges is believed to arise due to the additional participation of the tension force from the slab reinforcement, which effectively reduces the lever arm between the centorids of compression and tension forces. Consequently, the positive moment induced in the interior plastic hinge decreases;
2. The code recommended negative over-strength value for the exterior plastic hinge is quite conservative, whereas the code recommended negative over-strength value for the interior plastic hinge is un-conservative. Similar conclusions were drawn based on the comparisons with the experimental results, as described earlier in Section 6.5.1.1;
3. The code recommended positive over-strength value is slightly conservative for both the exterior and interior plastic hinges.

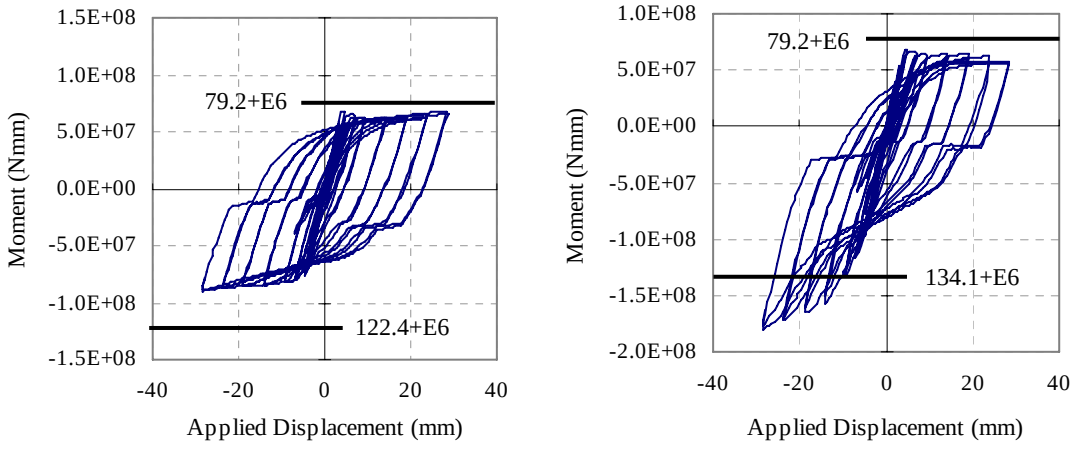

(a) West end exterior plastic hinge (b) East end interior plastic hinge

Figure 7-15. Predicted moment response in the plastic hinges

7.3.3 Predicted Axial Force in the Plastic Hinges

The predicted axial force in the plastic hinges is shown in Figure 7-16, where a negative force implies axial compression. It can be seen that the plastic hinges sustained appreciable axial compression force. This arises due to the contribution of slab reinforcement from elongation of plastic hinges. It should be noted that the axial compression force identified in this figure is acting at the same level as the slab reinforcement (i.e., at the mid-height of the concrete topping). The axial force sustained in the interior plastic hinges is much higher than that in the exterior plastic hinges. This implies that the interior plastic hinges were restrained more by the surrounding floor slab than the exterior plastic hinges.

The axial force response in Figure 7-16 also shows that the slab reinforcement provides additional tension force to both the negative and positive bending of interior plastic hinges, whereas it only provides additional tension force to the negative bending of exterior plastic hinges. As the additional tension force was acting at the mid-height of the concrete topping, it increases the negative strength of plastic hinges significantly. It should be noted that the additional tension force reduces the positive strength of the interior plastic hinges slightly, as shown in Figure 7-15(b).

The level of axial force predicted in the analysis is similar to that interpreted from the experimental results as described in Section 6.5.1. The maximum axial compression force predicted in the exterior and interior plastic hinges was 75kN and 370kN, respectively; whereas the interpreted experimental axial force in the plastic hinges was 75kN and 250kN, respectively. The difference in the interior plastic hinge is partially due to an over-estimation of the floor slab stiffness, as discussed later in Section 7.4.7.

It should be noted that the axial force interpreted from the experimental results was calculated assuming that the positive over-strength moments of interior and exterior plastic hinges are the same. However, Figure 7-15 shows that the positive moment of interior plastic hinge reduces due to additional tension force in the slab. As the interpreted experimental results did not take this into account, the negative over-

strength of interior plastic hinges is under-estimated in the calculation. Therefore, the axial force is expected to be greater than 250kN as calculated in Section 6.5.1.1.

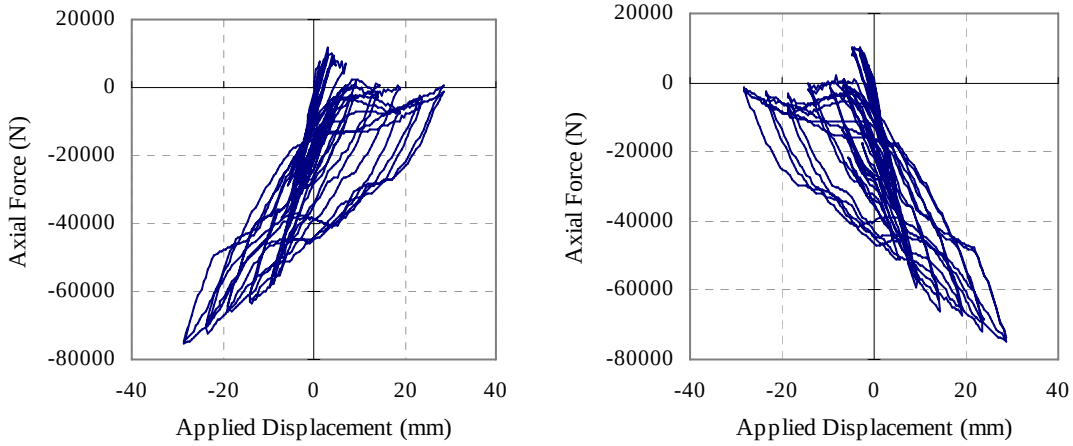

(a) West end exterior plastic hinge

(b) East end exterior plastic hinge

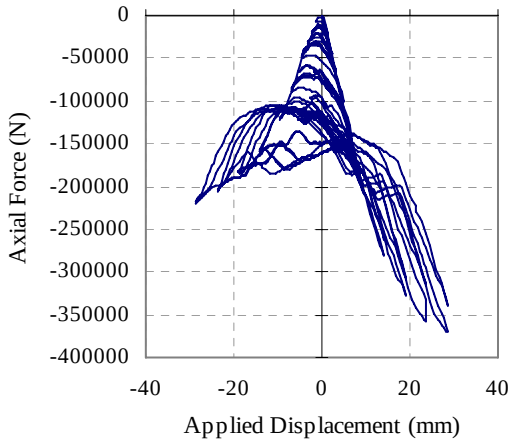

(c) West end interior plastic hinge

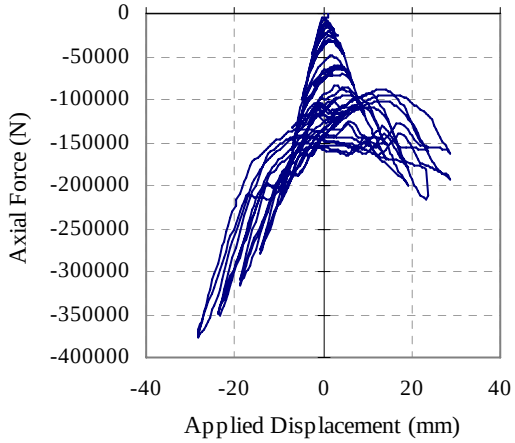

(d) East end interior plastic hinge

Figure 7-16. Predicted axial force response in the plastic hinges

7.3.4 Beam Elongation

Figure 7-17 shows the analytical and experimental elongation histories for the exterior and interior plastic hinges. The analysis predicts elongation of the interior and exterior plastic hinges accurately up to 2% drift. After which, elongation is under-estimated in the analysis. A similar trend, in which elongation is much greater in the exterior plastic hinges than the interior plastic hinges, was observed in the analytical and experimental results. This is because the interior plastic hinges sustained larger axial compression forces than the exterior plastic hinges.

It can be seen from Figures 7-17(a) and (d) that the predicted elongation is smaller in the negative drifts than that in the positive drifts for the West end exterior and East end interior plastic hinges. This is because in these plastic hinges, a larger axial compression force was induced in the negative drift than in the positive drift cycles. Therefore, elongation of these plastic hinges should theoretically be smaller in the negative drift cycles. However, in the experimentally measured results, the difference between elongation in the positive and negative drifts are not obvious. It is uncertain at this stage why this is the case.

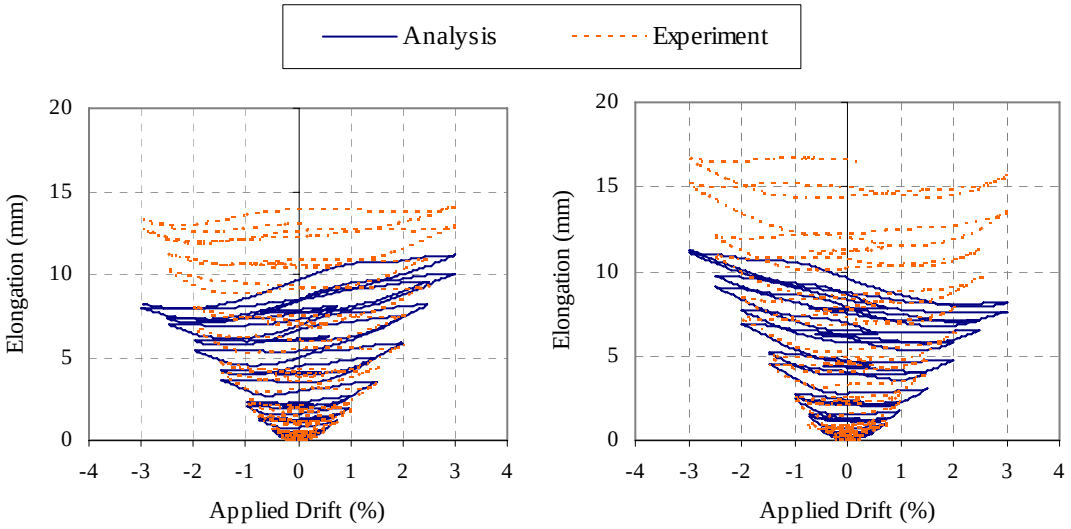

(a) West end exterior plastic hinge (b) East end exterior plastic hinge

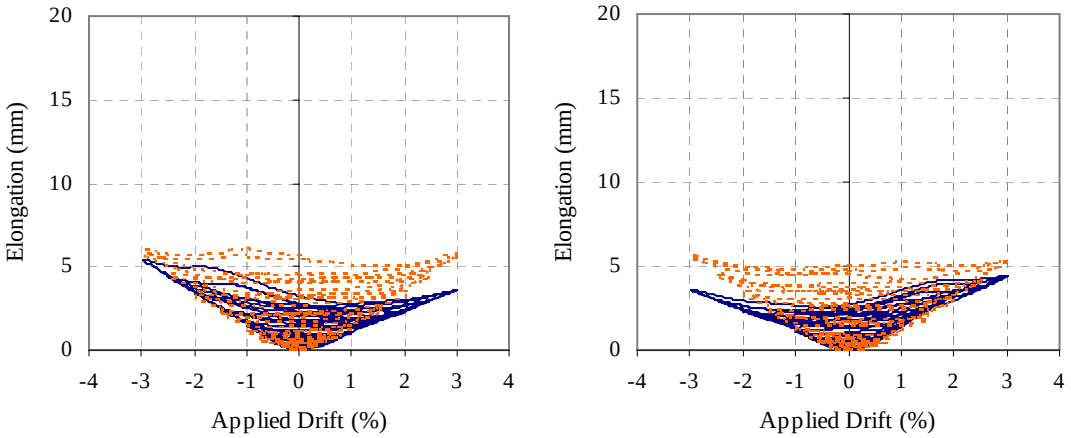

(c) West end interior plastic hinge (d) East end interior plastic hinge

Figure 7-17. Elongation in the plastic hinges

7.3.5 Predicted Transverse Beam Response

Figure 7-18 shows the predicted torque in the transverse beams versus the applied column displacement. The nominal torque capacity of the external and internal transverse beams was 35.5kNm and 40.5kNm, respectively calculated based on Equation 7-6. It can be seen that the torque in the external transverse beams is higher in one direction and lower in the other. This is because twisting in the external transverse beams was greater in one direction than the other. A similar trend was observed in the experiment where twisting of the transverse beam was greater when the column was rotating away from the floor slab.

Unlike the torsional response predicted in the analysis, the observed torsional response in the test is highly pinched (see Section 6.4). Despite acknowledging that the bi-linear hysteretic rule is not accurate in predicting the torsional response of the transverse beams, it is adopted here because RUAUMOKO3D currently does not allow for different hysteresis rules to be used for axial and torsional response.

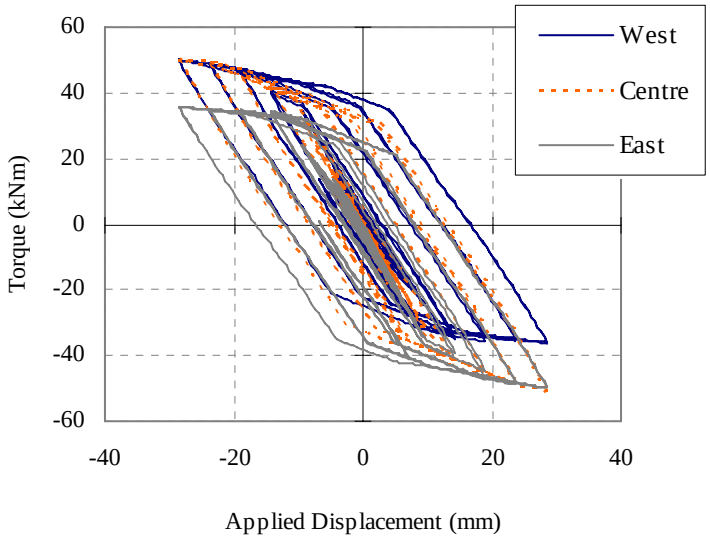

Figure 7-18. Predicted torsional response in the transverse beams

7.3.6 Predicted Column Twisting

The predicted twists in the external columns (i.e., rotation about the vertical axis) are plotted in Figure 7-19. It can be seen that the predicted twist in the external column increases as the applied displacement increases. The West column was twisting in the

clockwise direction and the East column was twisting in the counter-clockwise direction. Similar behaviour was observed in the experiment as described in Section 6.2.2.

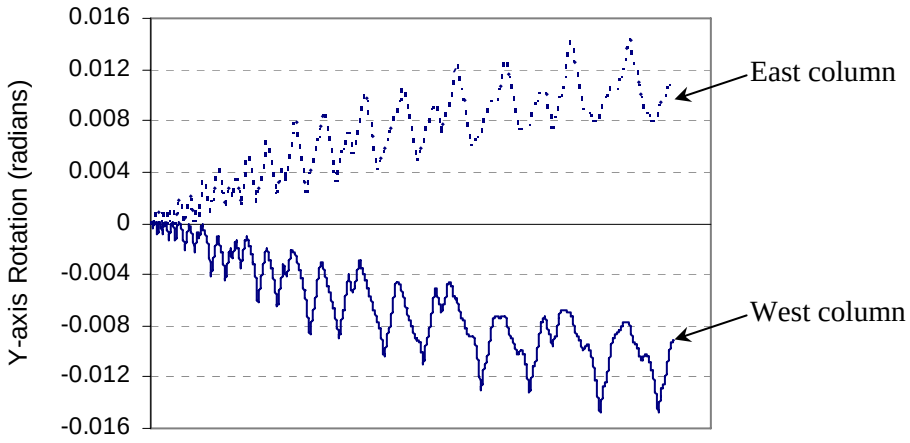

Figure 7-19. Predicted twisting response in the columns

7.3.7 Predicted Floor Response

7.3.7.1 Predicted Crack Widths between Transverse Beams and Floor Slab Interface

The crack widths between the transverse beam and floor slab interface are important as they control the amount of slab reinforcement participating to the negative flexural strength of the beam. Crack widths along the transverse beam and floor slab interface at the peak of the second positive 3% drift cycle are summarised in Table 7-1. Comparison between the analytical and experimental results shows that the analysis predicted the crack widths accurately along the internal transverse beam. However, the crack widths along the external transverse beam were under-estimated in the analysis. This was due to elongation being under-estimated in the exterior plastic hinges.

Table 7-1. Crack widths along the transverse beams and floor slab interface at the peak of the second positive 3% drift

Distance from the column face (mm)	Crack widths along East transverse beam (mm)		Crack widths along West side of internal transverse beam (mm)	
	Experiment	Analysis	Experiment	Analysis
275	6.0	4.5	3.7	3.0
775	1.1	0.2	2.2	1.9
1275	0.24	-0.01	1.1	1.3
1775	0.23	-0.00	0.68	0.75
2275	0.17	-0.00	0.46	0.45
2775	0.17	-0.00	0.31	0.31
3275	0.12	0.00	0.19	0.16
3775	0.06	0.00	0.06	0.02

Based on the crack widths comparison in Table 7-1, it is reasonable to think that the slab reinforcement participation and the induced axial force in the interior plastic hinge predicted in the analysis would match better with the experimental results than the exterior plastic hinge. However, this was not the case. It was found in Section 7.3.3 that the axial force predicted in the exterior plastic hinges matches better with the interpreted experimental results calculated in Section 6.5.1.

Figure 7-20 shows the predicted crack widths along the interfaces between the floor slab and the East transverse beam and between the floor slab and the West side of the internal transverse beam. It can be seen that the crack widths along the external transverse beam interface were localised around the column, whereas the crack widths along the internal transverse beam interface propagated further into the floor slab. It is observed that the crack widths along the West side of internal transverse beam interface do not necessarily reach a minimum value at the peak of each negative drift cycle. In fact, the crack widths generally decrease slightly then increase before reaching the peak of the negative drift cycles, except for that at 275mm from the column face. This indicates that the slab reinforcement along the internal transverse beam provides additional tension force to both the negative and positive strength of interior plastic hinges.

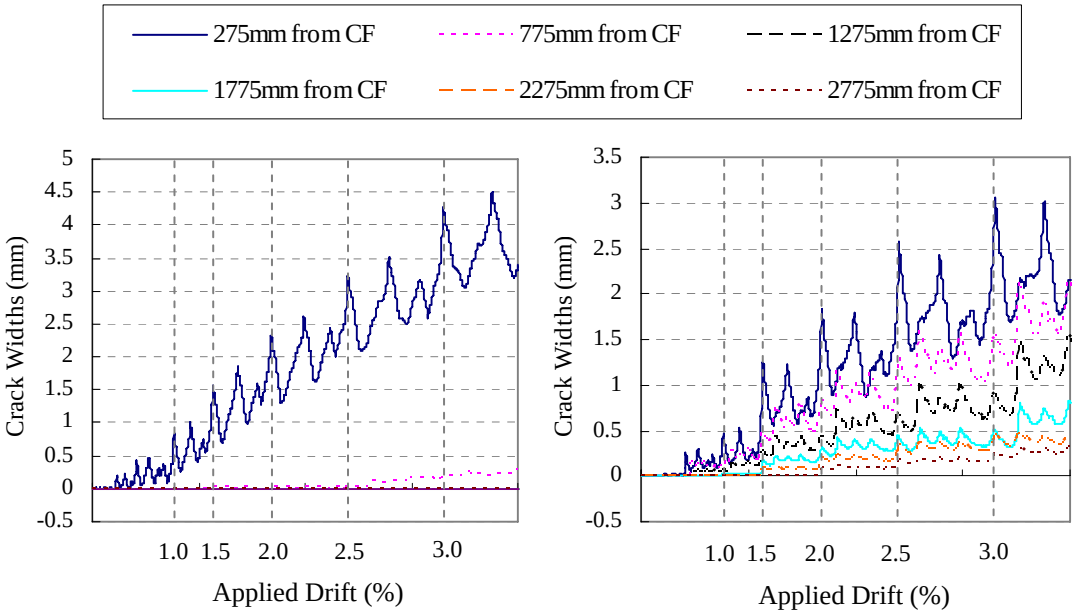

(a) Along an external transverse beam (b) Along an internal transverse beam

Figure 7-20. Predicted crack widths along the transverse beams and floor slab interface

The axial force of the slab reinforcement across the interface along the internal transverse beam versus the applied drift is plotted in Figure 7-21. It can be seen that the axial force in the slab reinforcement is at its maximum at the peak of both positive and negative drift cycles, except for the reinforcement at 275mm from the column face. This implies that these slab reinforcing bars induce an axial compression force to the interior plastic hinges at the peak of both positive and negative drift cycles. It also highlights that attention is required when interpreting the crack widths listed in Table 7-1. The magnitude of crack widths does not directly represent the magnitude of the tension force in the slab reinforcement. It also depends on the cyclic history of the reinforcing bars.

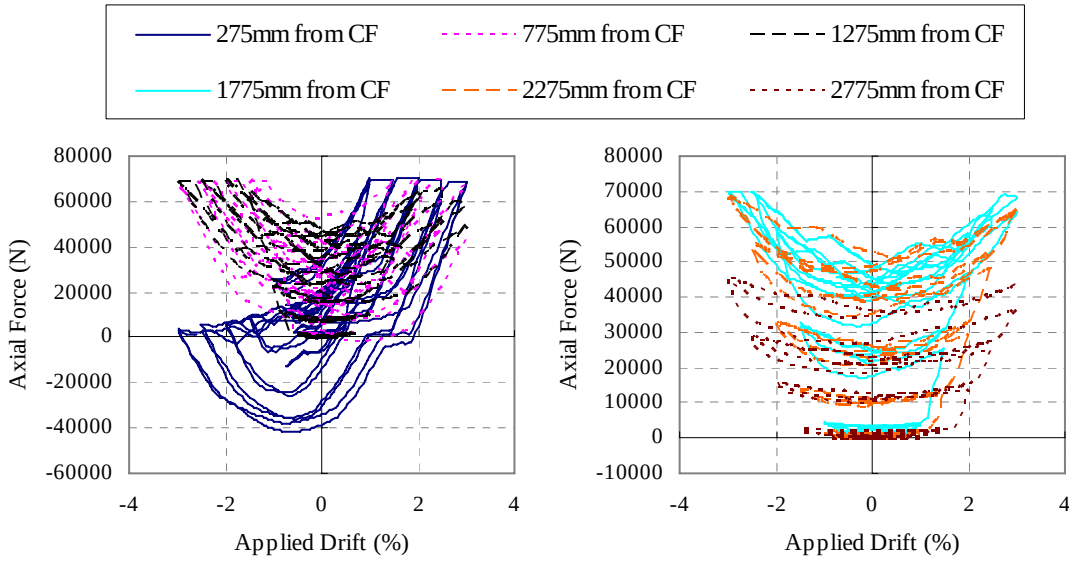

Figure 7-21. Predicted forces in the slab reinforcement along the internal transverse beam versus the applied column drift

7.3.7.2 Predicted Forces in the Linking Slab

Figures 7-22 and 7-23 show the forces in the linking slab predicted in the analysis at the peaks of the first positive and negative 3% drift cycle. The forces in the figure do not appear to be in equilibrium. This is because shear and axial force in the longitudinal beams are not plotted in the figure. It should be noted that the predicted tension force in the ties did not exceed the yield strength of the slab reinforcement but was very close to yield.

From these two figures, it can be seen that the truss action predicted in the linking slab behaves similarly to that observed in the experiment. The diagonal compression struts in the two bays were always inclined towards the centre column. This implies that the floor slabs are restraining elongation of interior plastic hinges. Also plotted in these diagrams is the shear deformation in the linking slab. The predicted shear deformation pattern is compatible with that observed in the experiment.

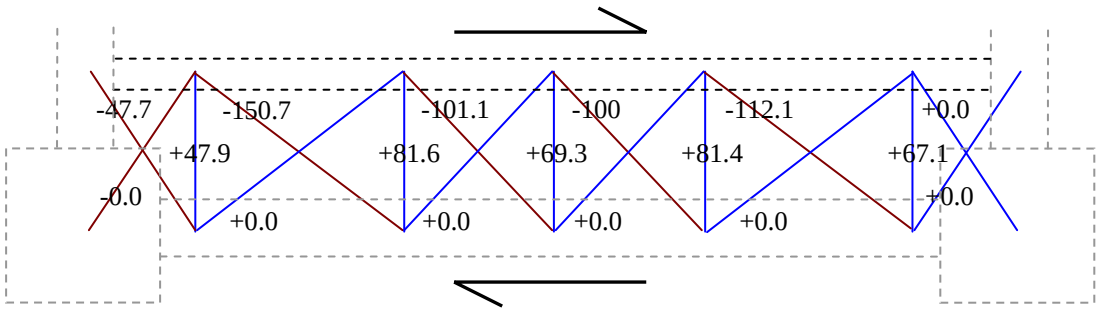

(a) West bay

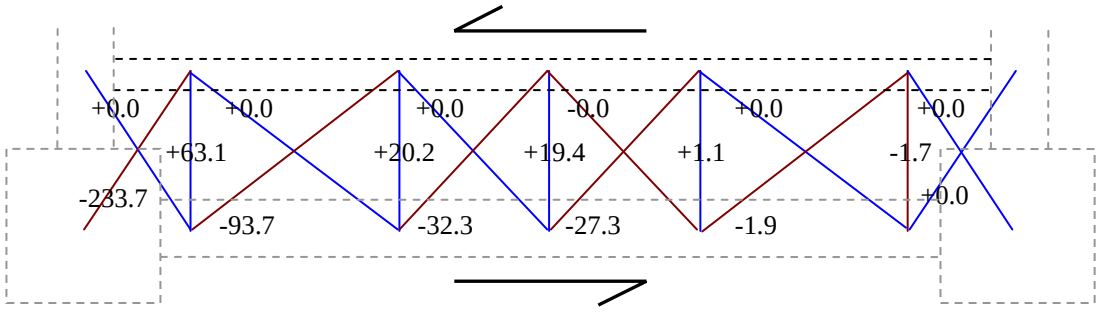

(b) East bay

Figure 7-22. Predicted actions in the linking slab at the peak of the first positive 3% drift

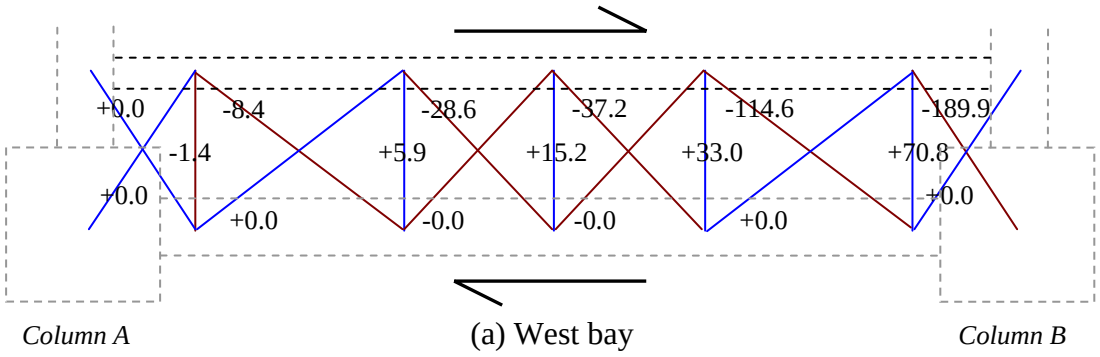

(a) West bay

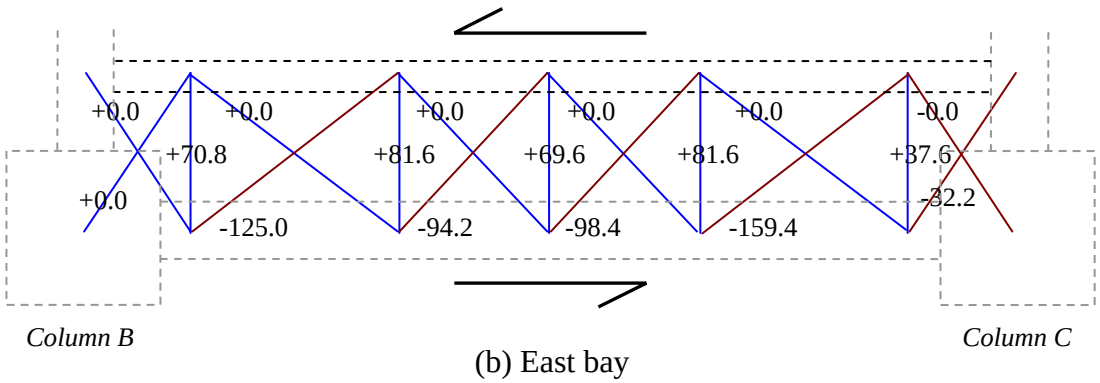

(b) East bay

Figure 7-23. Predicted actions in the linking slab at the peak of the first negative 3% drift

7.3.7.3 Predicted In-Plane Bending Action in the Floor Slab

Figure 7-24 shows the predicted forces per unit length (N/mm) in the floor slab at a distance 4025mm from the centre line of moment resisting frame at the peak of second positive 3% drift cycle. These values were the direct nodal outputs within each shell element from RUAUMOKO. There are four nodes located at the four corners of each shell element; therefore two readings are shown in each shell element from the two nodes.

It can be seen from Figure 7-24 that the floor slab near the internal transverse beam was subjected to tensile forces while the floor slab near the external transverse beams was subjected to compressive forces. In addition, the external columns were moving towards the end slab and the internal column was moving away from the end slab. The corresponding movement in the z-direction predicted in the analysis at the peak of the second 3% drift cycle was -0.04mm, 0.9mm and 0.01mm, respectively. The overall force and displacement pattern implies that the slab on each side of the internal transverse beam was bending like a deep beam restraining elongation of the interior plastic hinges. Similar behaviour was observed in the experiment, as described in Sections 6.2.4 and 6.3.8.

It should be noted that as the floor slabs are currently modelled using elastic shell elements with the gross section properties, the stiffness and strength of the floor slab are over-predicted in the analysis. Consequently, the axial force in the interior plastic hinges is over-estimated in the analysis. Despite, acknowledging that this is a problem, more accurate analysis (with reduced stiffness) could not be performed with RUAUMOKO3D because the analysis became unstable when the stiffness was reduced. More research is required to resolve this issue.

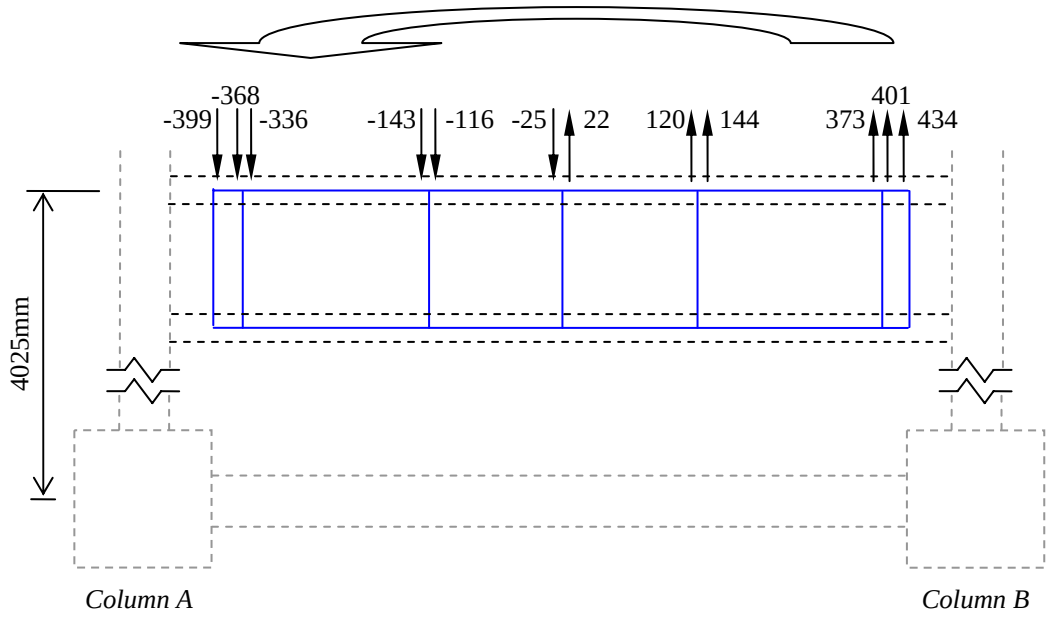

(a) West bay

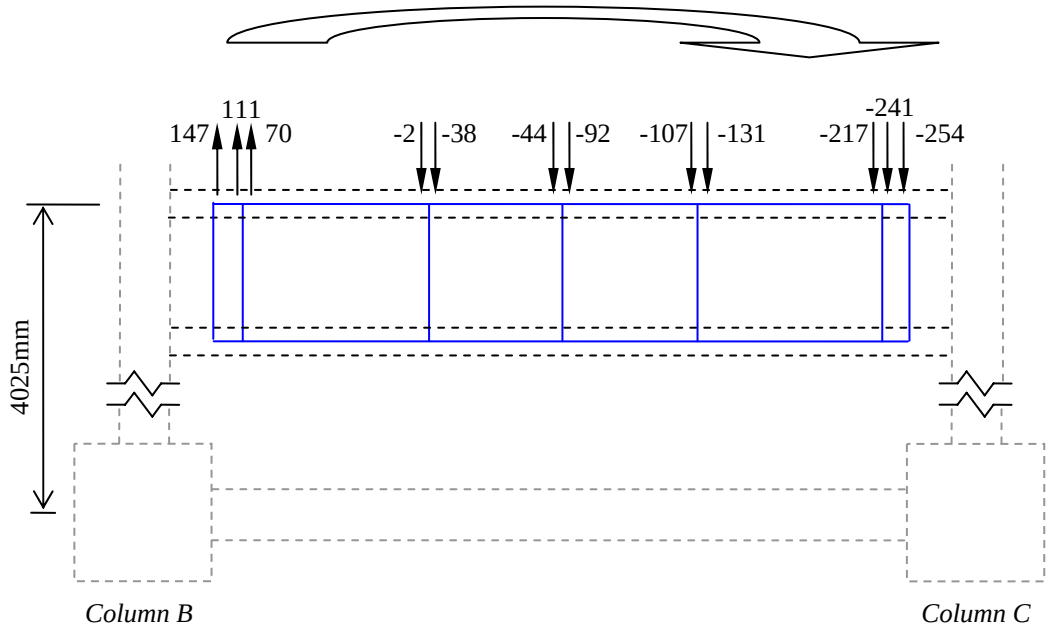

(b) East bay

Figure 7-24. Predicted force per unit length in the floor slab at the peak of the second positive 3% drift (units in N/mm)

7.3.8 Mechanisms Contributing to Axial Force in the Interior Plastic Hinges

As described in Sections 6.2.4 and 6.5.1.2, the axial compression force in the interior plastic hinges arises from the tension force in the slab reinforcement across the cracks

between the transverse beam and floor slab interface, which depends on the moment resistance of internal transverse beam and floor slabs acting as deep beams. This is schematically shown in Figure 7-25. A free body diagram taken along the cracks is shown in Figure 7-25(b), where C_{beam} is the axial compression force sustained in the beam plastic hinge, ΣT is the sum of the tension forces transmitted across the cracks and M_{deep_beam} and F_{deep_beam} are the moment and force contribution from the floor acting as a deep beam. From force equilibrium condition along the cracks, F_{deep_beam} is equal to $(\Sigma T - C_{beam})$.

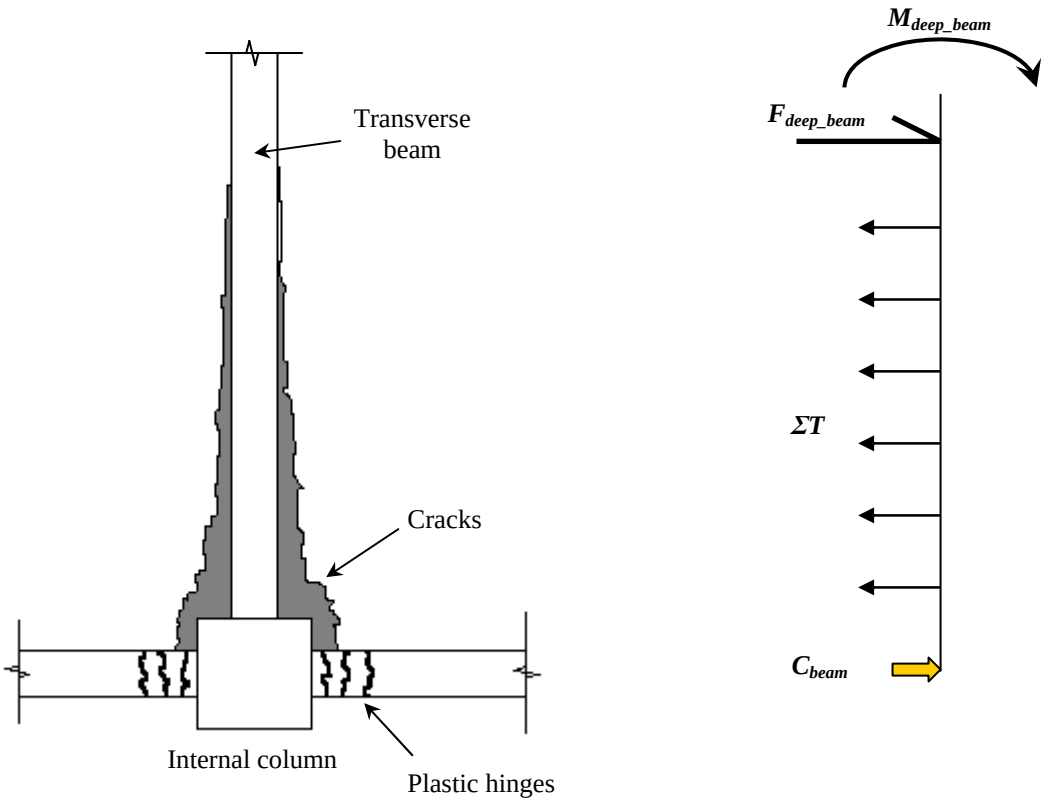

(a) Action induced next to the interior plastic hinge (b) Free body diagram

Figure 7-25. Mechanisms contributing to axial force in the interior plastic hinges

As the terms ΣT and C_{beam} are available from the analysis, the deep beam action can be readily calculated. The internal forces are summarised in Table 7-2. It can be seen that the contribution from deep beam action increases as the drift magnitude increases. At the peak of second positive 3% drift cycle, deep beam action contributed to about 32% of the total tension force in the slab. At the peak of other 3% drift cycles, the contribution of deep beam action was also approximately 32%.

Table 7-2. Contribution of axial force in the interior plastic hinges

Internal forces	Column drift			
	3.0% (2)	**2.5% (2)**	**2.0% (2)**	**1.5% (2)**
ΣT (kN)	499	458	427	341
C_{beam} (kN)	340	313	307	261
F_{deep_beam} (kN)	159 (32%)	145 (32%)	120 (28%)	80 (23%)

7.4 SENSITIVITY STUDY

Analyses were carried out to examine the effects of some modelling parameters on the analytical predictions. These parameters include the diagonal angle in the linking slab, the out-of-plane bending strength of transverse beams, the floor mesh size, the modelling area, the stiffness of steel springs in the linking slab, the stiffness of core concrete springs in the plastic hinges and the stiffness of the elastic floor slab.

7.4.1 Diagonal Angle in the Linking Slab

The angle of the diagonals in the linking slab was altered to investigate its effect on the analytical predictions. As the first set of the diagonals next to the columns are connected to the end of the plastic hinge elements, the angle of these diagonals could not be altered. The angle of the rest of the diagonals was kept constant at 42 degree as shown in Figure 7-26. This is denoted as “constant angle” analysis in Figure 7-27.

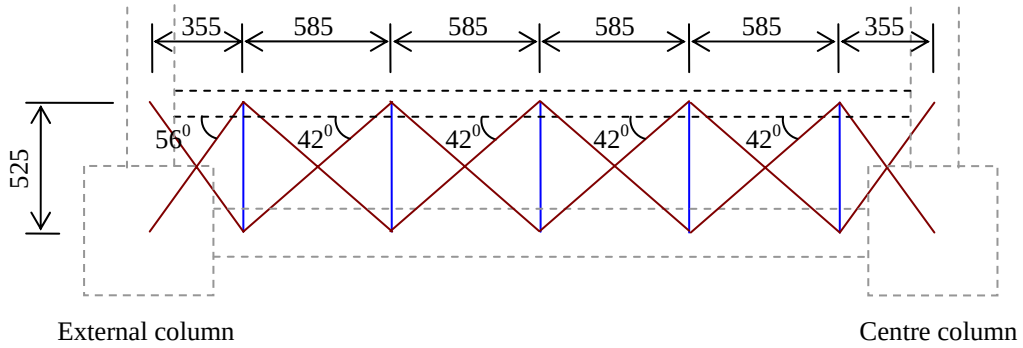

Figure 7-26. Sensitivity study on the diagonal angle in the linking slab

Figure 7-27 plots the predicted force-displacement response of the original model and the modified model with constant angle. It can be seen that the force-displacement relationships between these two models are almost identical. Thus, it can be concluded that provided the diagonal angle in the model is in the range of 30 to

45 degree, the force-displacement response is not sensitive to the diagonal angle used in the analysis.

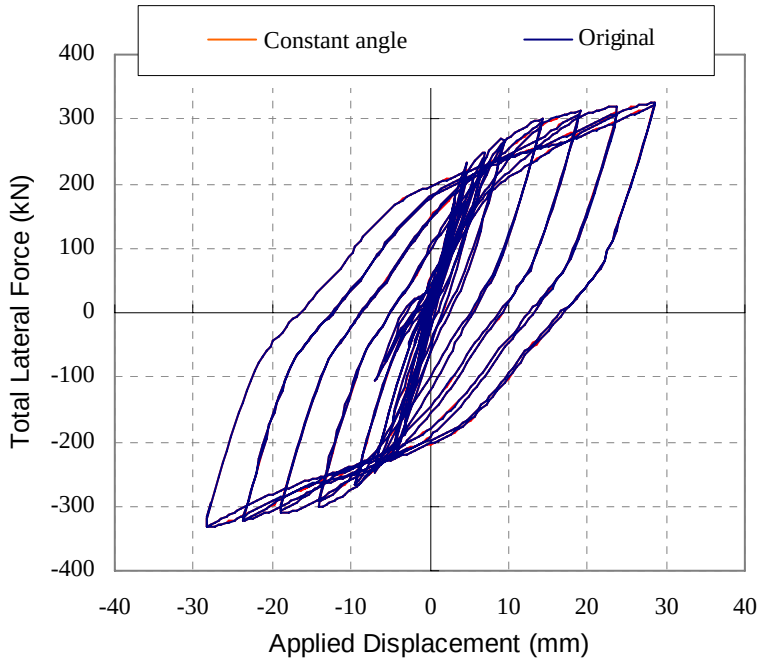

Figure 7-27. Force-displacement comparison for models with different diagonal angles

A similar conclusion can be drawn from the elongation comparison in Figure 7-28. It can be seen that the angle of the diagonals has little effect on the elongation response of the plastic hinges.

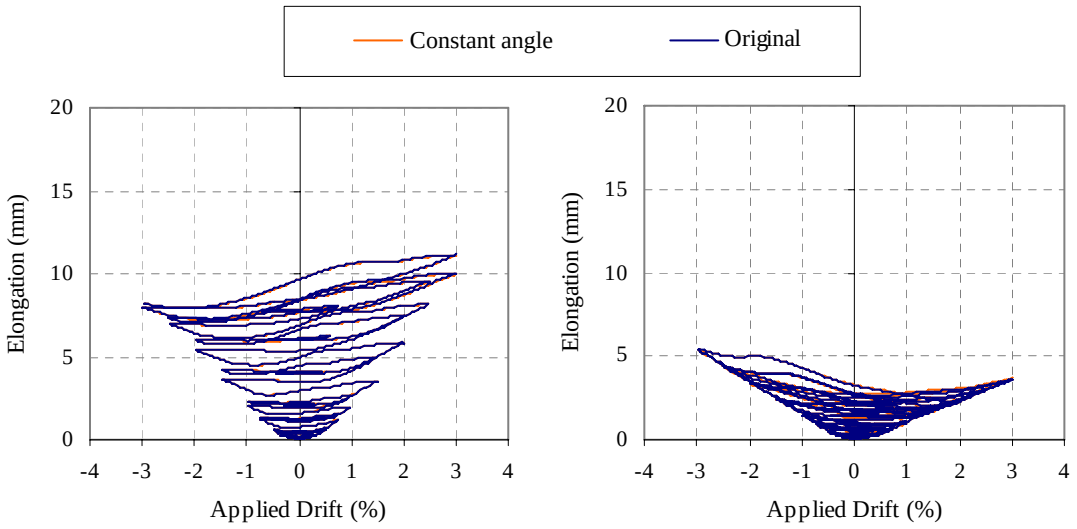

(a) West end exterior plastic hinge (b) West end interior plastic hinge

Figure 7-28. Elongation comparison for models with different diagonal angles

7.4.2 Out-of-Plane Bending Strength of the Transverse Beams

The effect of transverse beam out-of-plane bending strength on the analytical predictions is examined. Two additional analyses with different out-of-plane bending strengths were carried out on top of the original elastic transverse beam model. One of these was calculated based on the whole transverse beam section and the other was calculated based on half of the transverse beam section. The half section was done as a rough approximation to consider moment-torsion interaction. The corresponding flexural strengths are 31kNm and 16kNm, respectively. These values can be seen as upper bound and lower bound solutions. A bilinear factor of 0.02 was used for the post yielding strength. A plastic hinge length of 0.5*b* was chosen where *b* is the width of the transverse beam.

The force-displacement relationships of the frame and each column predicted using these two strengths together with the original model are shown in Figures 7-29 and 7-30. It can be seen that the strength of the transverse beam has little effect on the overall force-displacement response of the frame. It has more influence on the force-displacement response of the external columns than the internal column.

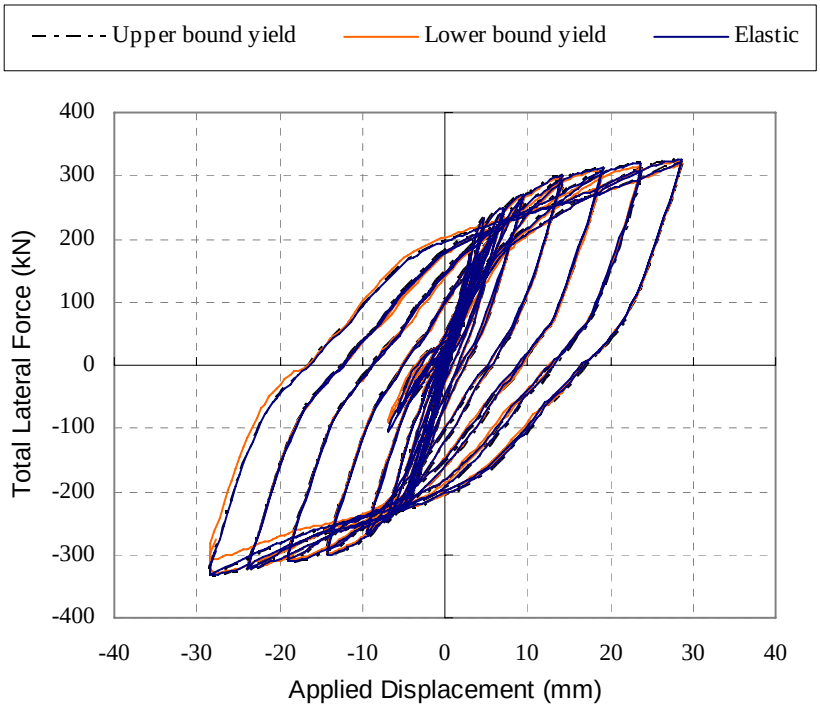

Figure 7-29. Force-displacement comparison for models with different transverse beam properties

It can be seen from Figure 7-30 that the negative strength of the exterior plastic hinges is sensitive to the out-of-plane bending strength of the transverse beam. This is because yielding of the transverse beam would cause the crack extensions to localise near the column face. Consequently, as the out-of-plane bending strength of the transverse beam decreases the slab reinforcement contribution and the axial compression force sustained in the plastic hinges decreases. This can be observed in Figure 7-31. These findings complement well with the theory described in Section 6.5.1.2.

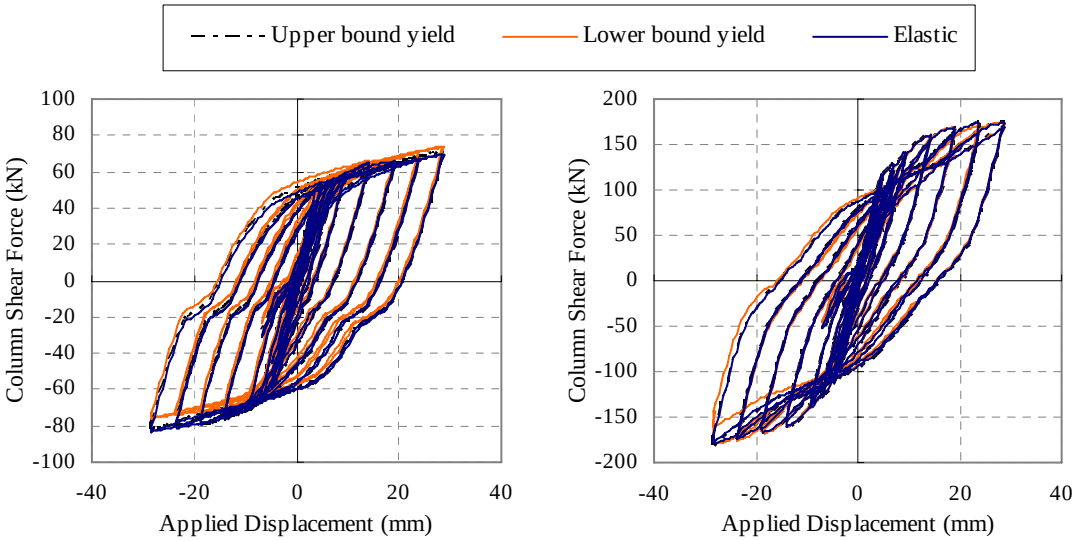

(a) Column A

(b) Column B

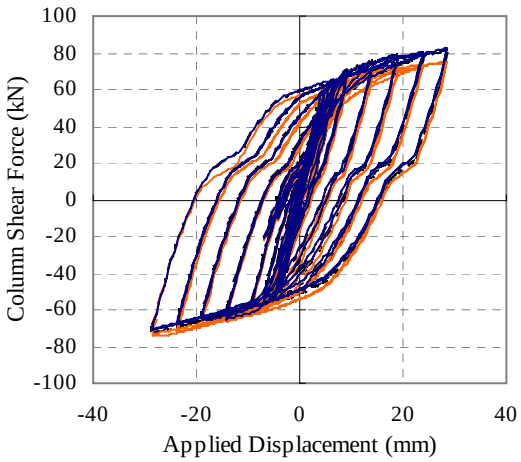

(c) Column C

Figure 7-30. Force-displacement comparison of each column for models with different transverse beam properties

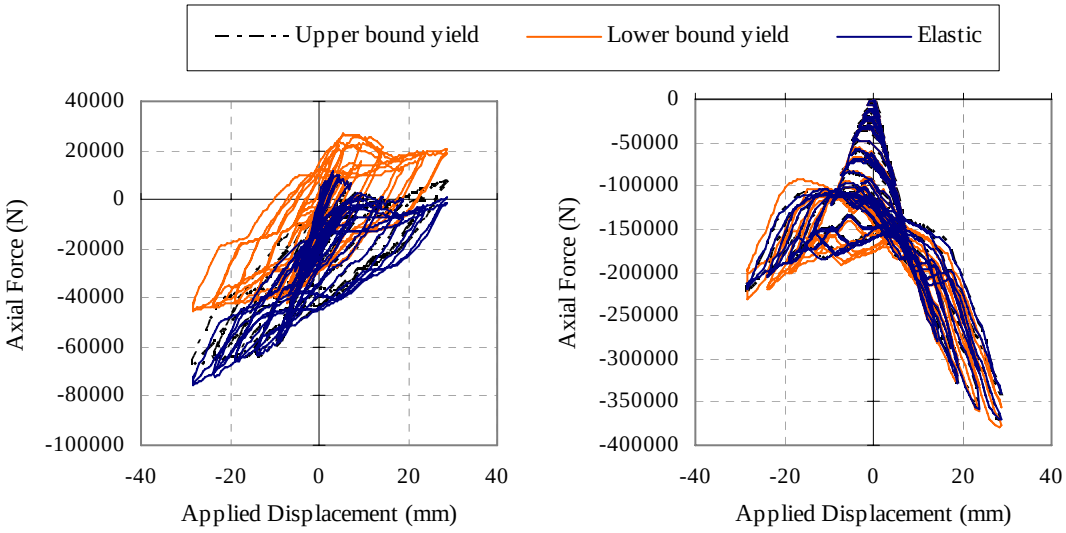

(a) West end exterior plastic hinge (b) West end interior plastic hinge

Figure 7-31. Axial force comparison for models with different transverse beam properties

Figure 7-32 shows the predicted crack widths at the external transverse beam and floor slab interface at a distance 275mm from the column face. Also plotted in this figure is the crack widths measured using the DEMEC gauge. It can be seen that the crack widths predicted in the analysis with elastic transverse beam were the closest to the experimental results, whereas the crack widths predicted in the lower bound transverse beam yielding model gave the poorest comparison. Crack widths were smaller with lower bound analysis because yielding of the transverse beam tends to confine the inelastic actions close to the column face. It should be noted that yielding of the transverse beam in the lower bound analysis occurred at 1% drift. This behaviour was not observed in the experiment and hence, analysis carried out with the upper bound yield strength is believed to be more realistic.

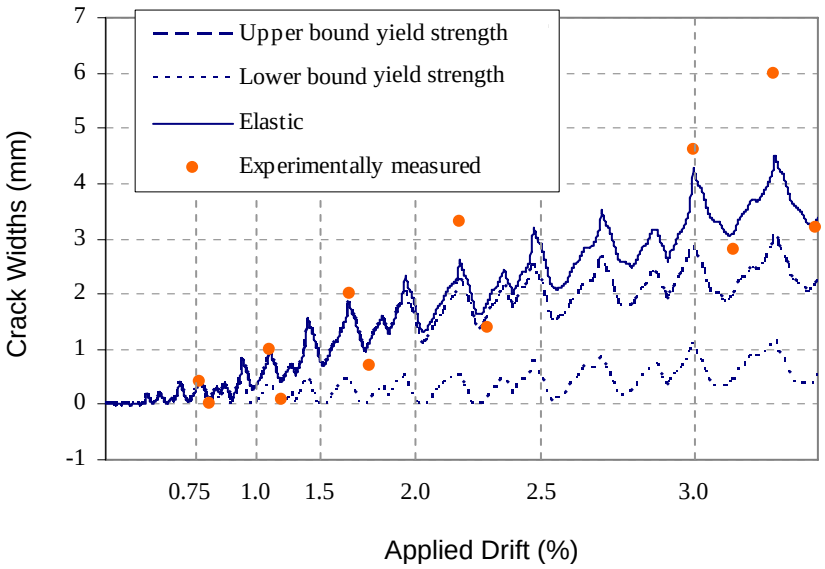

Figure 7-32. Comparison of crack extension between external transverse beam and floor slab interface at a distance 275mm from the column face

Elongation response of these three models is compared in Figure 7-33. It can be seen that elongation response of interior plastic hinges is not sensitive to the out-of-plane bending strength of the transverse beams. Elongation of the exterior plastic hinges in the analyses where transverse beams were allowed to yield is higher than that in the original model. This is because once the external transverse beams yield; the stiffness decreases and thus the axial restraint to elongation of exterior plastic hinge decreases. In addition, as the predicted axial compression force in the exterior plastic hinge is smaller in the models with transverse beam yielding, the predicted elongation is expected to be greater than that in the original model.

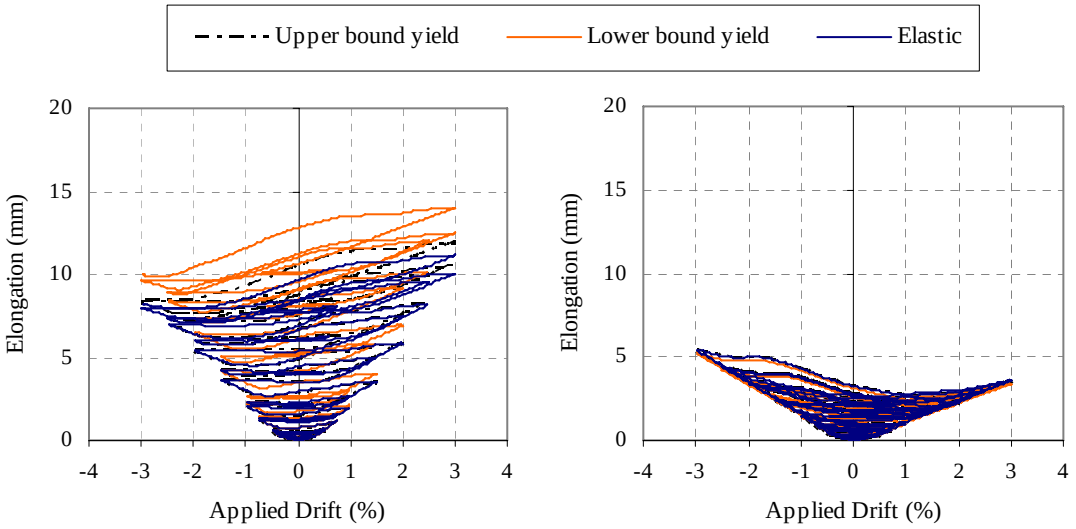

(a) West end exterior plastic hinge (b) West end exterior plastic hinge

Figure 7-33. Elongation comparison for models with different transverse beam properties

7.4.3 Mesh Size

As each analysis takes 16 hours to complete in an Intel Pentium M processor 1.73GHz, it is desirable to reduce the analytical time by effectively simplifying the mesh discritization. The first attempt was to reduce the number of nodes in the beam and its corresponding nodes in the floor. The number of nodes in the beam was reduced from seven to five. However, the analysis terminated in the first few steps due to numerical instability.

The second attempt was to increase the mesh size at regions far away from the moment resisting frame as shown in Figure 7-34. It can be seen that the displacement compatibility requirement may not be satisfied along the line indicated in the diagram. This is because two smaller shell elements were connecting to a larger shell element on one edge. Nevertheless, the analysis was carried out with this set up. The analysis time was reduced to 10 hours.

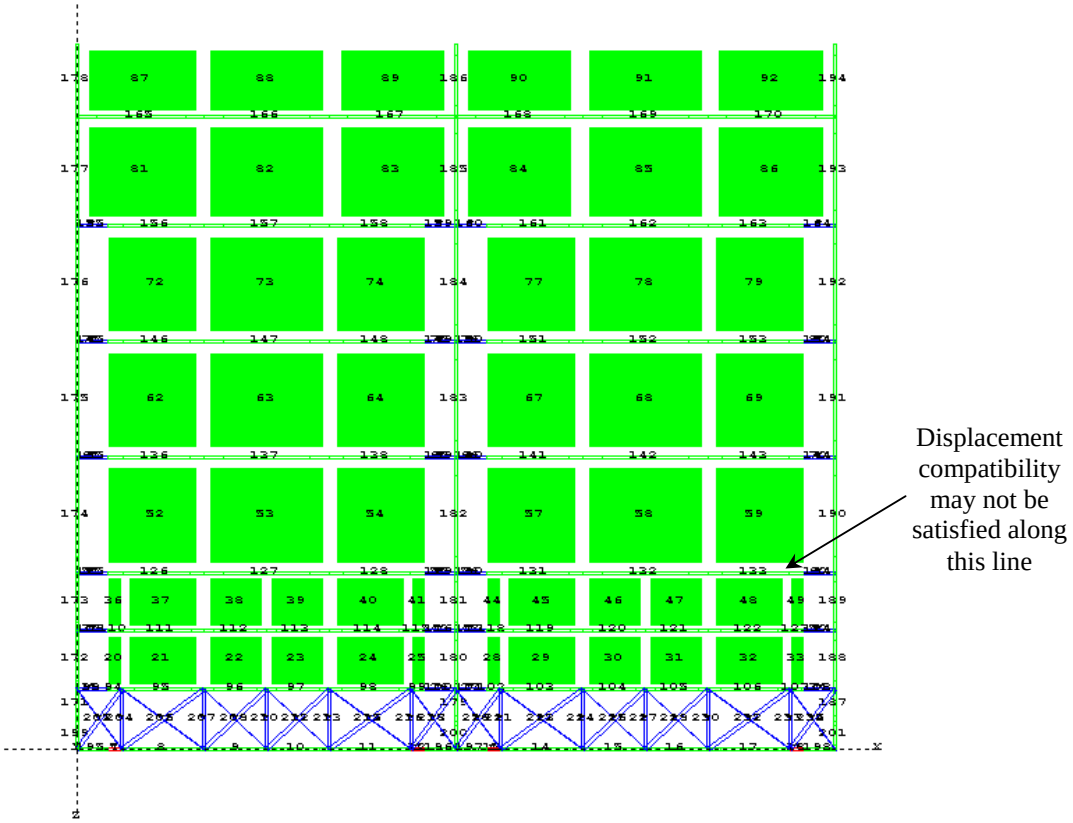

Figure 7-34. Plan view of the modified analytical model (bigger mesh size)

The difference between the predicted force-displacement relationships, axial force and elongation responses of plastic hinges are illustrated in Figures 7-35 to 7-38. It can be seen from Figure 7-36 that the effect of mesh size is more significant for the internal column than for the external columns. The model with a larger mesh size gives a slightly higher peak shear force. This is due to a larger predicted axial compression force in the interior plastic hinges as shown in Figure 7-37(b). As the axial compression force in the interior plastic hinge is higher in the model with a larger mesh size, elongation is smaller as illustrated in Figure 7-38(b).

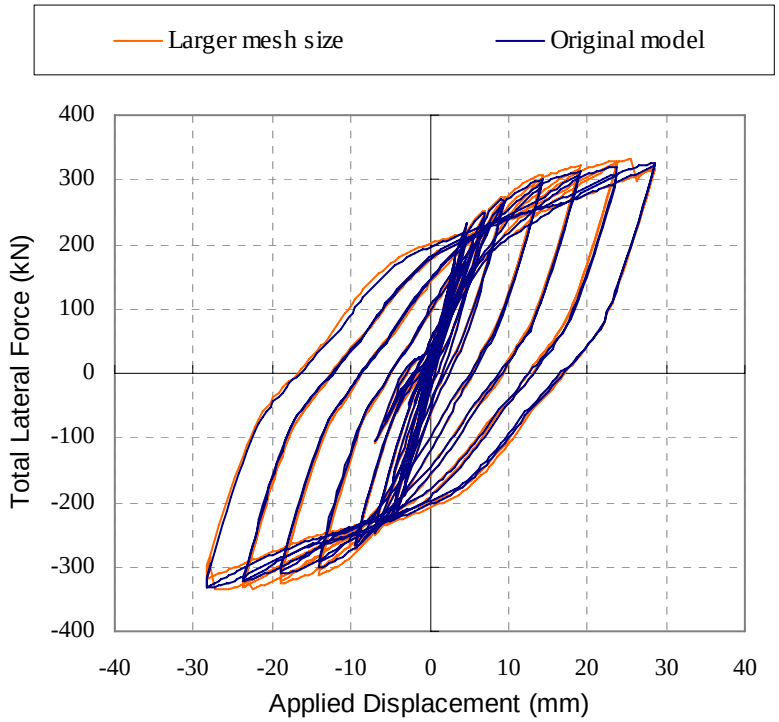

Figure 7-35. Force-displacement comparison for models with different mesh sizes

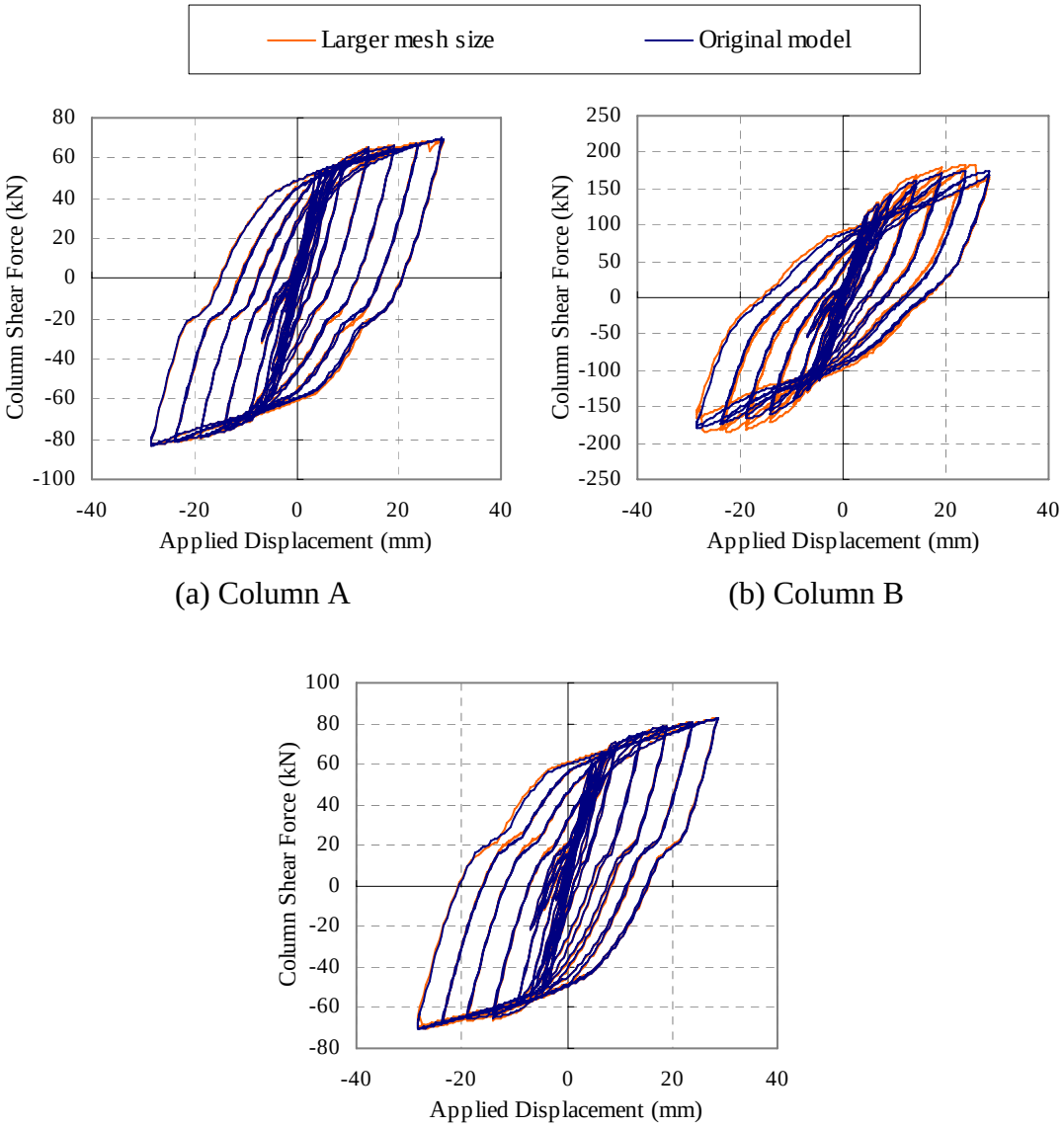

(a) Column A

(b) Column B

(c) Column C

Figure 7-36. Force-displacement comparison of each column for models with different mesh sizes

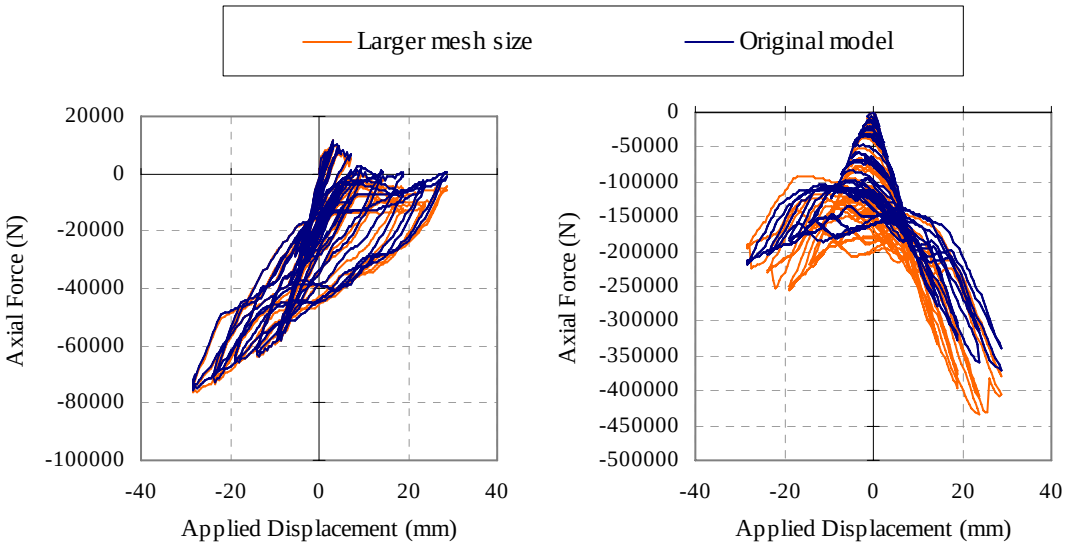

(a) West end exterior plastic hinge (b) West end interior plastic hinge

Figure 7-37. Axial force comparison for models with different mesh sizes

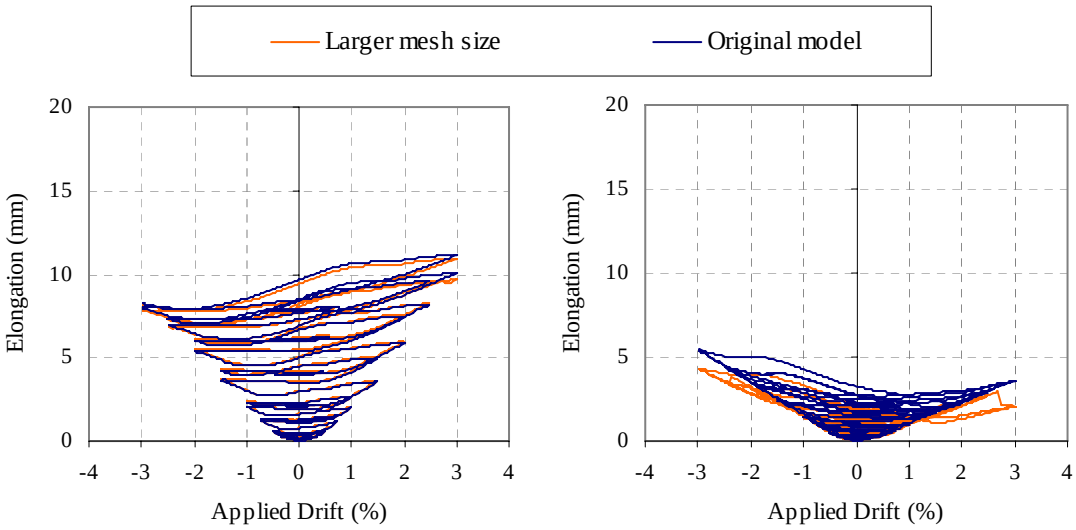

(a) West end exterior plastic hinge (b) West end interior plastic hinge

Figure 7-38. Elongation comparison for models with different mesh sizes

7.4.4 Modelling Floor Area

As the floor deformation far away from the moment resisting frame is relatively small, it is reasonable to assume that the floor is relatively rigid at a certain distance from the frame. Consequently, a smaller width of the floor slab was considered in the analysis as shown in Figure 7-39. In the modified model, the floor width up to 2775mm from the column face was taken into account. This width was chosen because the predicted

deformation between the floor slab and transverse beam interface element in the original model is small at this location (see Table 7-1). The predicted crack widths were 0.00mm and 0.31mm for the external and internal transverse beams, respectively. Therefore, the floor diaphragm is assumed to be effectively rigid beyond this point. The boundary conditions of the floor edge in the modified model were chosen such that it satisfies the rigid floor diaphragm assumption. The x-translational movement of the boundary line was slaved to the centre node, so that the floor can translate with the frame but no elongation is allowed in the rigid diaphragm. All of the other degrees of freedom were fixed to simulate the rigid diaphragm assumption. The analysis time was reduced to 8 hours.

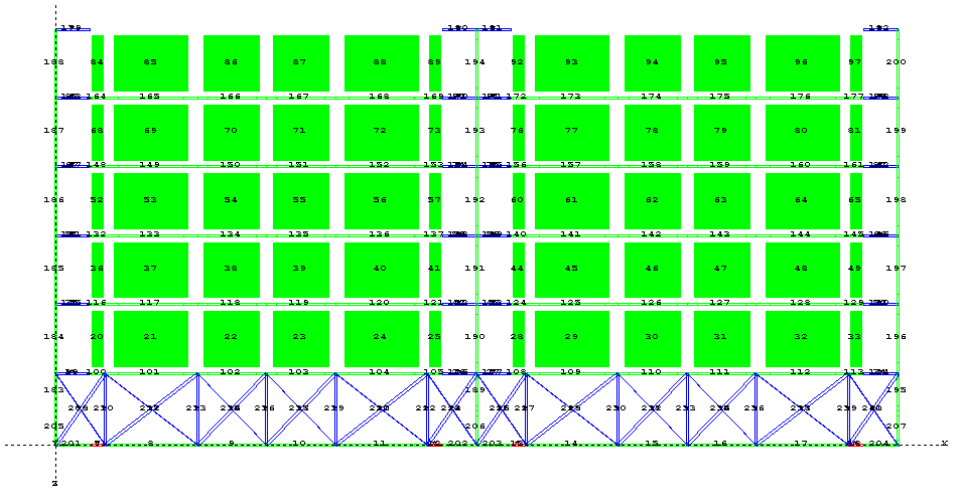

Figure 7-39. Plan view of the modified analytical model (reduce modelling floor area)

The force-displacement response of the modified model is compared with the original model in Figure 7-40. It can be seen that the force-displacement relationship varies slightly between the two models. The modified model gives a higher yield and peak force and a smaller shear pinching response. The difference in the shear pinching prediction is due to torsional response of the transverse beams, which is discussed in a later section.

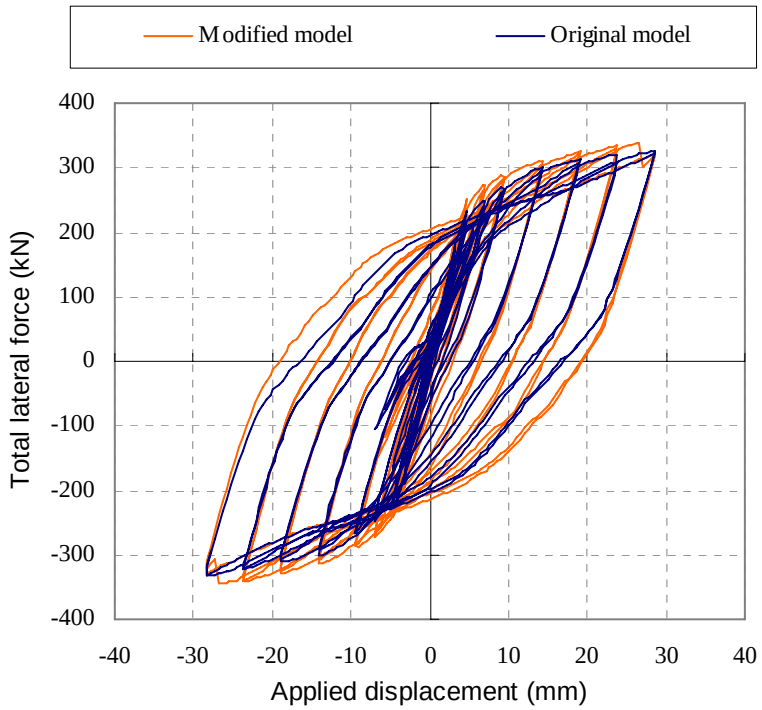

Figure 7-40. Force-displacement comparison for beams with different modelling areas

An increase in column shear force in the modified model is expected as the modified boundary condition artificially restrained the growth between the transverse beam and floor slab interface, therefore effectively providing greater axial restraint to elongation of plastic hinges. This can be observed in Figure 7-41(b), where the predicted axial force increased by 19% in the interior plastic hinges. It should be noted that as the predicted growth at the external transverse beam to floor slab interface was zero in the original model, restraining the growth would not make a significant difference to the axial force induced in the exterior plastic hinges as shown in Figure 7-41(a).

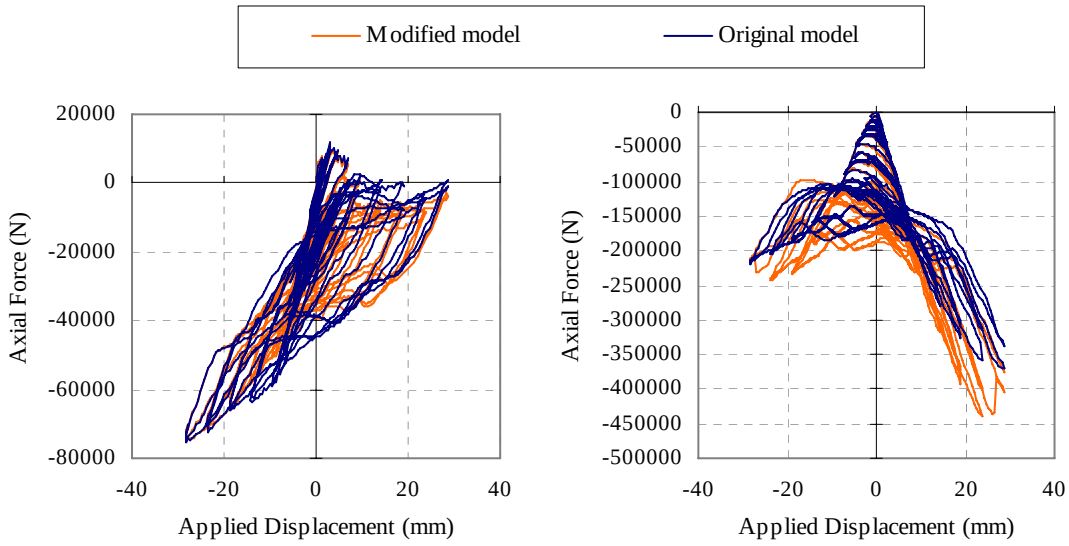

(a) West end exterior plastic hinge (b) West end interior plastic hinge

Figure 7-41. Elongation comparison for models with different modelling floor areas

The force-displacement relationships of each column from the two models are compared in Figure 7-42. It can be seen that the modified model predicts a slightly higher peak shear force in the internal column. This is because the predicted axial force in the interior plastic hinges increases in the modified model. As the predicted axial force remained constant in the exterior plastic hinges, the peak shear force in the external columns does not change.

Figure 7-42 also shows that the shear pinching behaviour in the force-displacement response is delayed in the modified model. This is because the effective torsional stiffness of the transverse beams in the modified model is more than twice of that in the original model as shown in Figure 7-43. The torsional stiffness of the transverse beams increases because the length of the transverse beam in the modified model was about half of that in the original model.

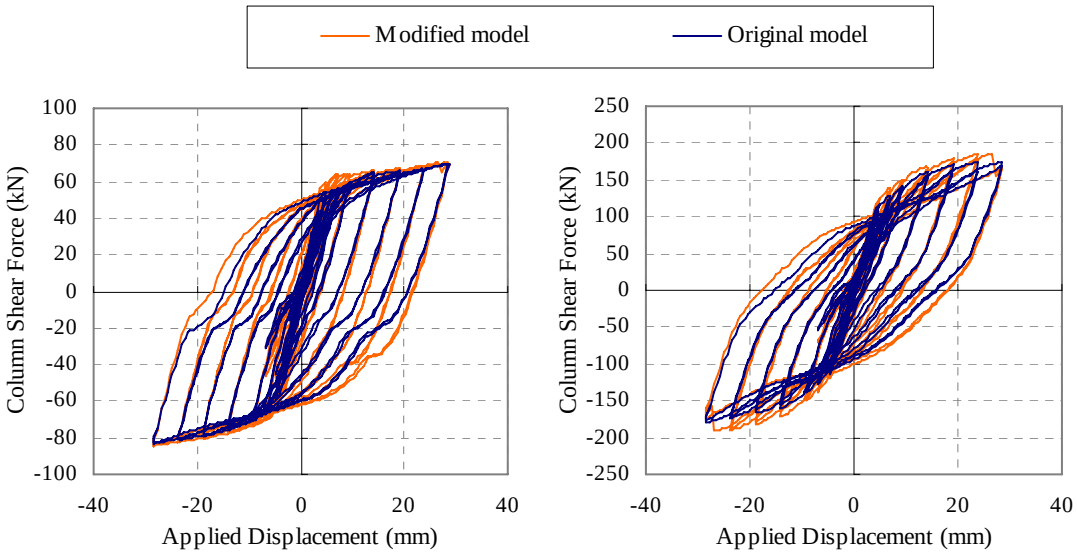

(a) Column A

(b) Column B

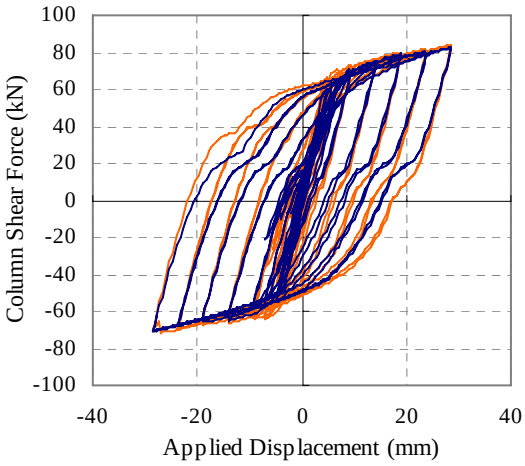

(c) Column C

Figure 7-42. Force-displacement comparison of each column for models with different modelling floor areas

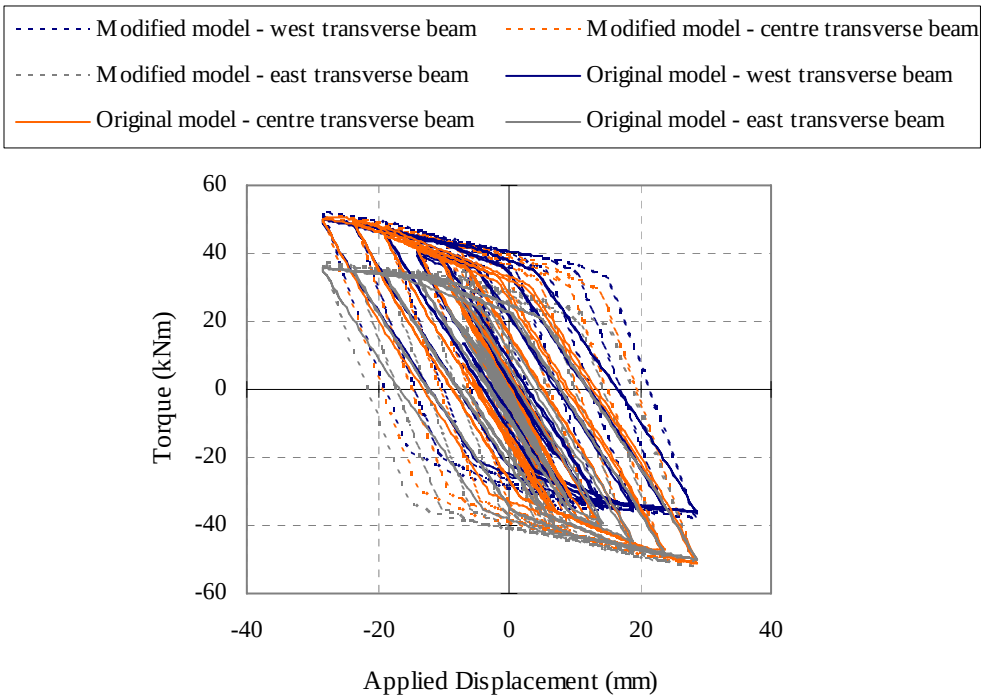

Figure 7-43. Transverse beam torque and column displacement relationship for models with different modelling floor areas

Figure 7-44 shows that the modelling floor area has little effect on the elongation response of the exterior plastic hinges. However, it reduces elongation of interior plastic hinges in one direction at the later cycles.

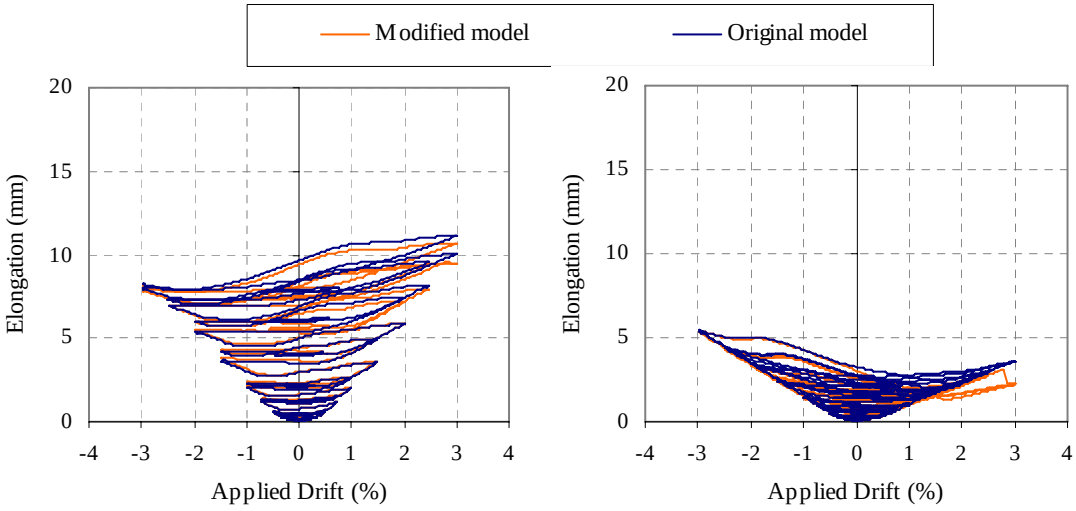

(a) West end exterior plastic hinge (b) West end interior plastic hinge

Figure 7-44. Elongation comparison for models with different modelling floor areas

7.4.5 Stiffness of Steel Springs in the Linking Slab

A sensitivity study was carried out to examine the stiffness of steel springs in the linking slab on the analytical predictions. Figures 7-45 and 7-46 show the force-displacement response of the frame and the elongation response of plastic hinges predicted using models with two different linking slab reinforcement stiffness. In the modified model, the stiffness of the steel spring in linking slab was doubled. The comparison shows that the predicted hysteric and elongation response of the frame is not sensitive to the stiffness of the steel springs in the linking slab.

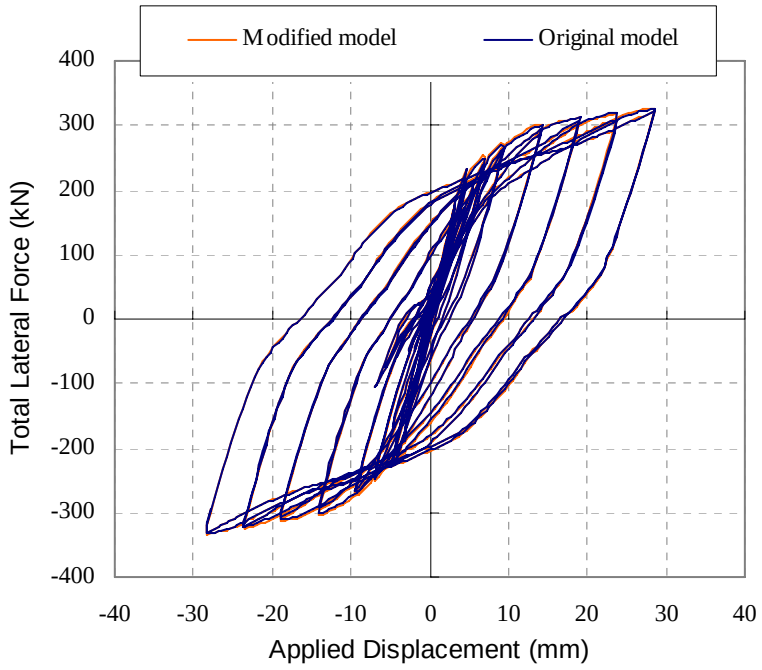

Figure 7-45. Force-displacement comparison for models with different linking slab steel stiffness

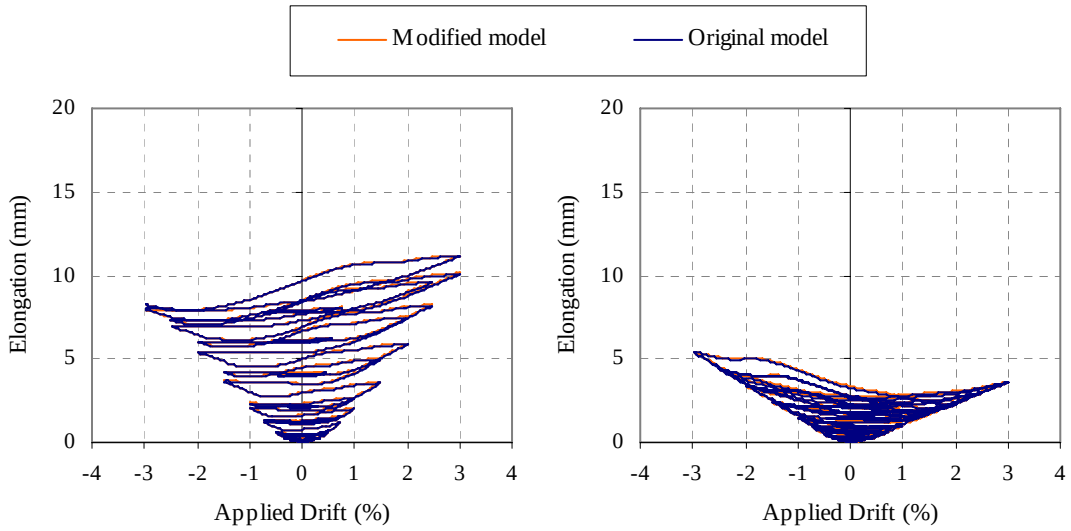

(a) West end exterior plastic hinge (b) West end interior plastic hinge

Figure 7-46. Elongation comparison for models with different linking slab steel stiffness

7.4.6 Stiffness of Core Concrete Springs in the Plastic Hinge Elements

With the current concrete model adopted in the plastic hinge element, it is difficult to increase the compressive strain at which the compressive strength is reached, as well as prolonging compressive strength beyond the crushing strain without changing the concrete stiffness. Therefore, the effect of confinement in the core concrete was not modelled in the previous analysis.

One analysis was carried out with the core concrete stiffness reduced by half so that the concrete compressive strain at the maximum strength is increased and the compressive stress does not drop significantly after compressive strength is reached. Figure 7-47 shows the monotonic stress-strain relationship of concrete model adopted in this study for cover concrete and for confined concrete with reduced stiffness together with Mander's confined concrete model (1988). The comparisons show that the stress dropped away much more rapidly beyond the peak strength in the confined concrete model adopted in this study than that in the Mander's model. This could affect the analytical predictions when the core concrete compressive strain is large.

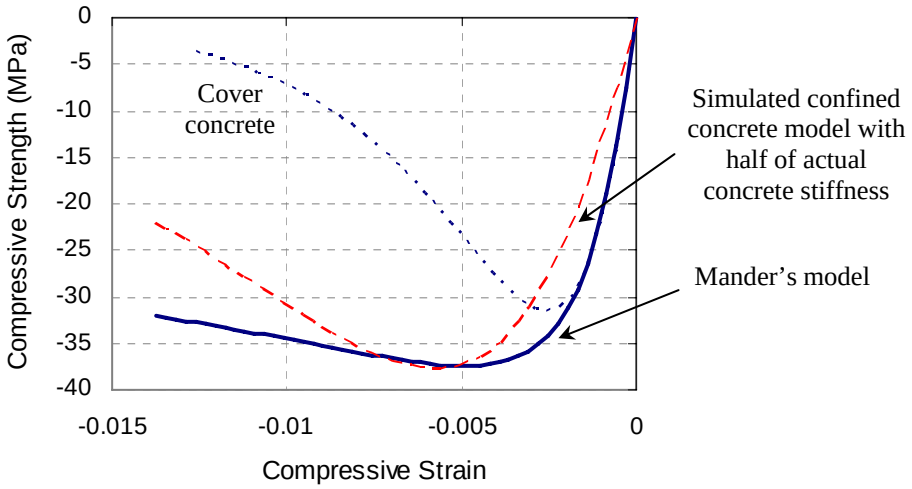

Figure 7-47. Comparison of different concrete models

Figures 7-48 and 7-49 show the predicted force-displacement and elongation response of the sub-assembly with different core concrete stiffness. It can be seen from these comparisons that the core concrete stiffness in the plastic hinge element has little effect on the overall response of the frame. This is expected as the response of plastic hinges in the inelastic range, where significant elongation has occurred, is predominantly controlled by the behaviour of the reinforcing bars. The effect of concrete stiffness on the predicted response of frames could be more significant in cases where the beam plastic hinges are sustaining large axial compression forces. In these cases, a more realistic confined concrete model is required.

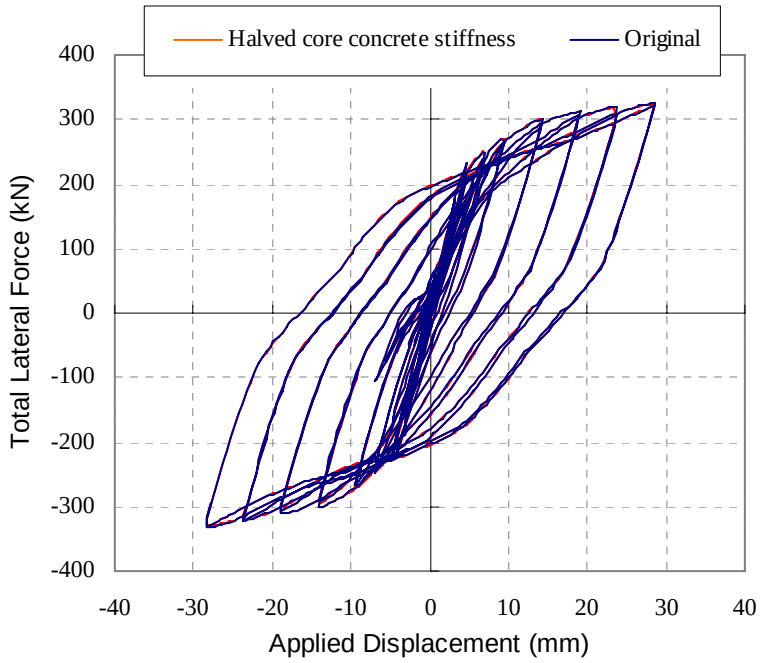

Figure 7-48. Force-displacement comparison for models with different core concrete stiffness in the plastic hinge elements

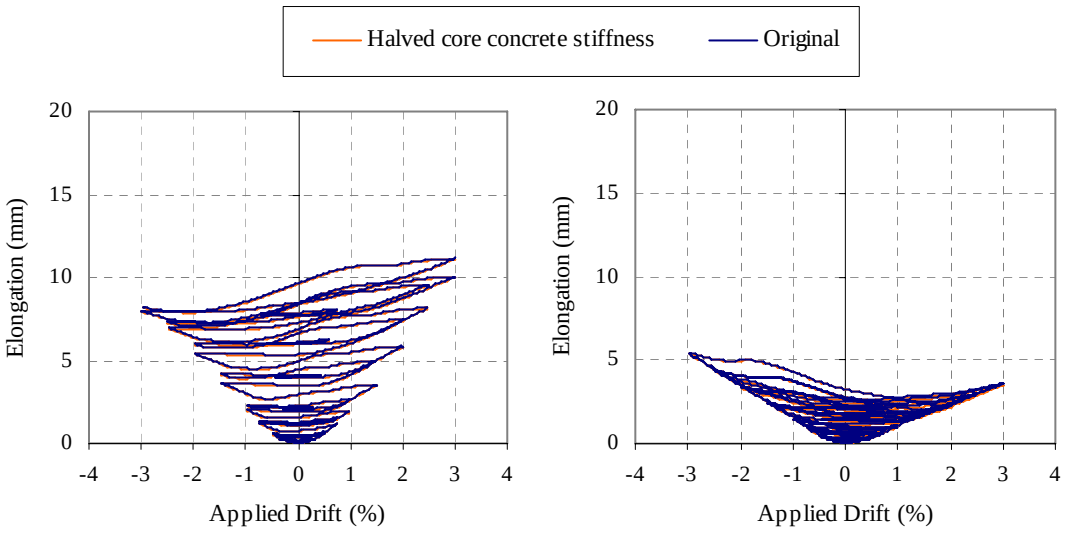

(a) West end exterior plastic hinge (b) West end interior plastic hinge

Figure 7-49. Elongation comparison for models with different core concrete stiffness in the plastic hinge elements

7.4.7 Stiffness of Floor Slab

In the original model, the floor slab was modelled using elastic shell elements, and the stiffness was calculated based on the gross section. As minor cracks were observed in the floor slab, the stiffness may have been over-estimated in the analysis. To take into account a reduction in the stiffness of the floor slab due to cracking Young's modulus for the member was halved. Other means of reducing the stiffness (i.e., reducing the thickness of the floor slab) was also tested. However, the analysis became unstable for all these cases. Consequently, the stiffness of the floor slab was doubled to investigate its effect on the analytical predictions.

The force-displacement response of the sub-assembly, predicted using the modified model with the floor slab stiffness being doubled, is compared with the original model in Figure 7-50. The comparison shows that increasing the floor slab stiffness has little effect on the overall force-displacement response.

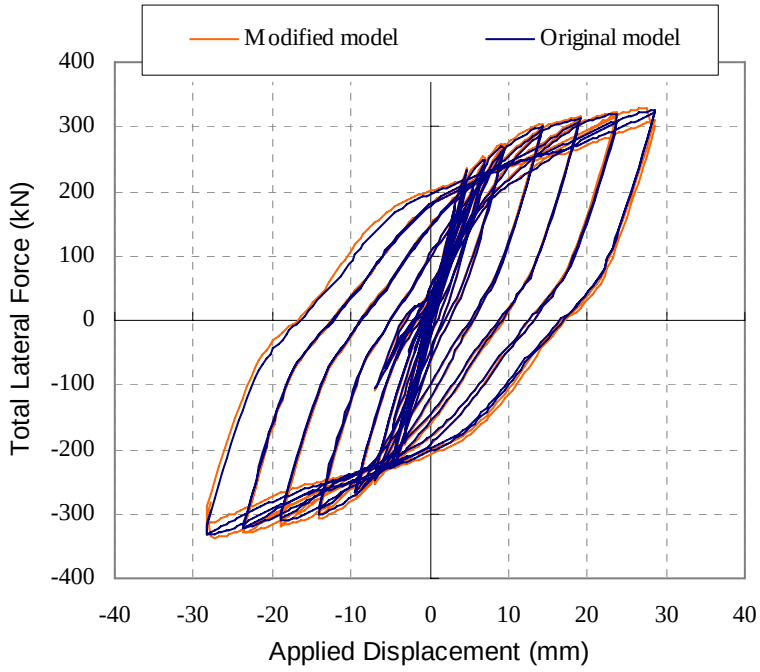

Figure 7-50. Force-displacement comparison for models with different floor slab stiffness

Figures 7-51 and 7-52 show the predicted elongation history and axial force response of plastic hinges. It can be seen that doubling the stiffness of the floor slab has little influence on the response of the exterior plastic hinges. However, it increases the

axial compression force in the interior plastic hinges and therefore reduces the elongation.

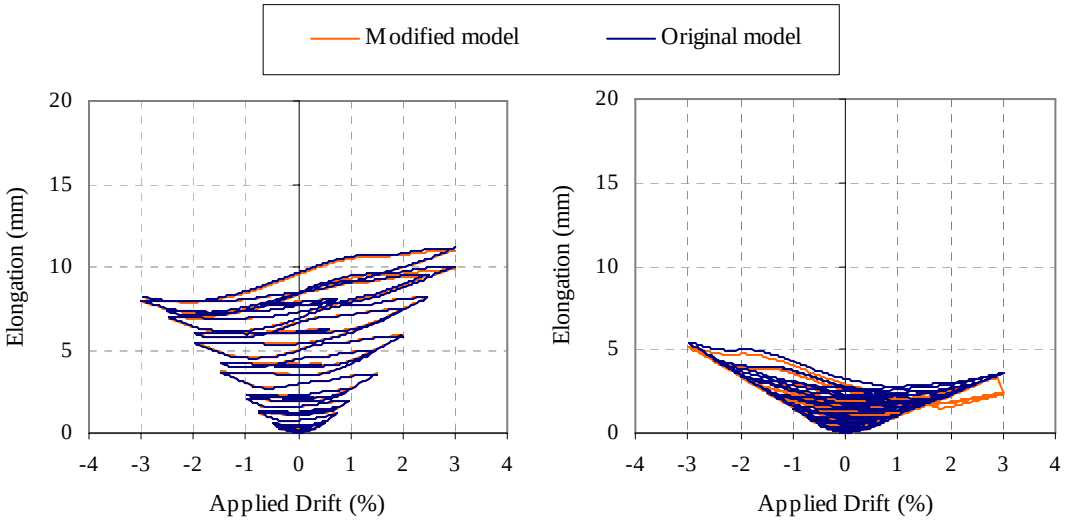

(a) West end exterior plastic hinge (b) West end interior plastic hinge

Figure 7-51. Elongation comparison for models with different floor slab stiffness

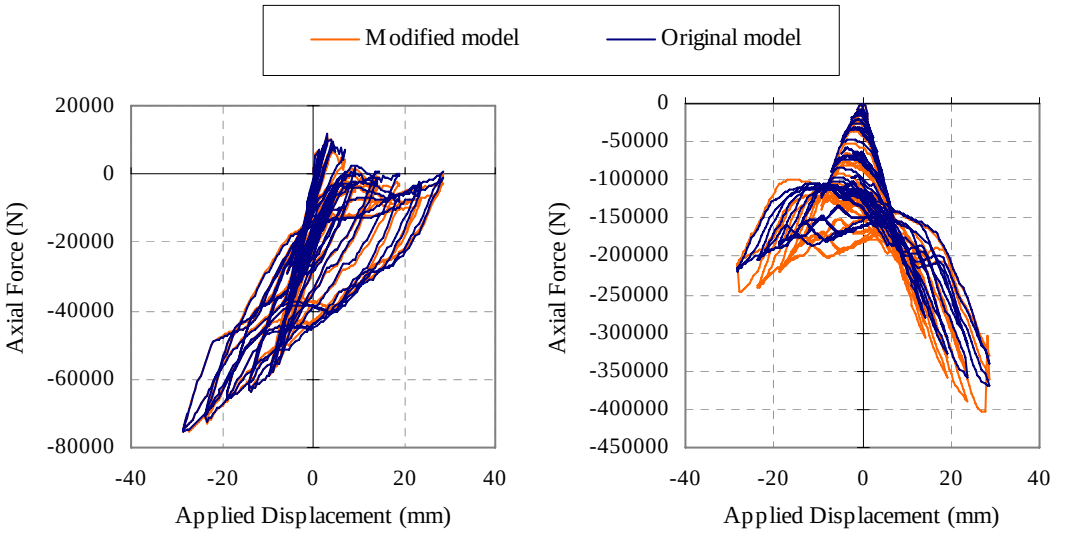

(a) West end exterior plastic hinge (b) West end interior plastic hinge

Figure 7-52. Axial force comparison for models with different floor slab stiffness

As the floor slab stiffness in the original model is over-estimated, the predicted axial force (i.e., the predicted slab reinforcement participation) in the interior plastic hinges, reported in Section 7.3.3, may have been over-estimated. It is important to note that as the analysis became unstable when a smaller stiffness value was used, the exact

reduction in the predicted axial force could not be quantified in this study. Based on the observations above, it is postulated that when the stiffness of the floor slab is halved, the axial force in the interior plastic hinge may peak at 300kN. This value is closer to that interpreted from the experimental results as described in Section 6.5.1.1.

7.4.8 Summary

Based on the findings in the sensitivity studies, the following recommendations for the modelling parameters are made:

- The analysis is not sensitive to the angle of the diagonal struts in the linking slab provided the diagonal angle in the model is in the range of 30 to 45 degree. It is recommended that the angle be kept at 38 degree based on the experimental observation.
- Out-of-plane bending strength of the transverse beams can affect the response of the external columns, but it has little influence on the response of the internal columns. For simplicity, moment-torsion interaction is neglected in the analysis and the out-of-plane bending strength is calculated based on the gross section.
- Large mesh discretization may cause instability in the analysis. For reliable predictions, it is recommended to divide each beam into 6 sections.
- Any simplification made by reducing the modelling area can affect the force-displacement response of the frame. It is recommended to model the whole area in the analysis.
- The effective length of steel spring in the linking slab has negligible effect on the overall response of the frame. It is recommended to calculate the steel length using the method described in Section 7.2.4.4.
- The stiffness of core concrete spring in the plastic hinge element has little influence on the overall response of the frame. However, for beam plastic hinges sustaining large axial compression forces, its effect may be more significant. With the limitation of the concrete model adopted in this study, it is recommended to reduce the stiffness of the core concrete spring to represent the confined concrete behaviour. For this particular case, the stiffness was reduced by half.

- The stiffness of floor slabs has little influence on the force-displacement response of the sub-assembly. However, it can have a significant effect on the predicted axial force in the interior plastic hinges. Increasing the stiffness would increase the predicted axial force in the interior plastic hinges.

7.5 LIMITATIONS

The analytical 3D frame-floor model developed in this research has shown some promising results. However, there are limitations in the current model where further research and refinement may be required. These limitations are summarised below:

- Bond failure and slip within the beam column-joints were not taken into account in the analytical model. This appears to have resulted in an under-estimation of the pinching behaviour in the force-displacement predictions. A more accurate beam-column joint element allowing for the effect of bond degradation between concrete and reinforcement could improve the hysteresis behaviour.
- Apart from the linking slab, the rest of the floor was modelled using elastic shell elements as there was no non-linear shell element available in RUAUMOKO3D. This has inherently increased the stiffness of the floor slab and hence increased the axial force induced in the interior plastic hinges. More research is required to develop an appropriate element to model the rest of the floor slab.
- The truss elements developed to model the linking slab do not allow for out-of-plane moment and shear actions to be considered in the analysis. This is appropriate for cases where the prestressed units are supported on transverse beams connected to the columns where the vertical differential movement between the prestressed floor units and the main beam is relatively small and the linking slab is relatively flexible. However, this model is not appropriate for cases where the prestressed units are spanning past a column, where significant differential vertical movements are expected to occur. In this case, the level of tension force contributing to the negative flexural strength of plastic hinges depends on the out-of-plane flexural and shear capacities of the linking slab (Fenwick et al. 2006). A linking slab element was developed by Lau (2007) to model this behaviour.

- The plastic hinge element has not been validated against beam tests with bi-directional loading. Its accuracy in predicting the bi-axial actions should be tested in the future.
- The torsional response of the transverse beams was modelled using bi-linear hysteresis rule. A more appropriate hysteretic model should be used in the future to improve the analytical predictions.

7.6 CONCLUSIONS

The proposed 2D plastic hinge element was transformed into a 3D plastic hinge element. The validity of the 3D plastic hinge element was first confirmed by comparing the predictions with the 2D plastic hinge elements. The 3D plastic hinge element was then combined with other elements to form an analytical model to predict the cyclic response of the frame-floor sub-assembly test carried out in this research. Comparisons of the analytical and experimental results have shown that the 3D model with elongating plastic hinge element can predict the hysteretic behaviour of frame satisfactorily. Deformation mechanisms such as elongation of plastic hinges, opening of cracks at the transverse beam-floor slab interface, shear deformation in the linking slab and bending of floor slab were also captured qualitatively by the analysis.

Sensitivity study has provided insight into the parameters that affect the analytical results. It was found that the angle of the diagonal concrete struts and the stiffness of the steel ties in the linking slab have little influence on the analytical predictions. The core concrete stiffness in the plastic hinge element does not effect the analytical predictions in the case examined here. However, this may not be generic to all other cases. The out-of-plane bending strength of the transverse beams affects mainly the response of exterior plastic hinges whereas the mesh size, modelling area and stiffness of floor slab affect mainly the response of interior plastic hinges.

Based on the outcomes of this chapter, it can be concluded that the analytical model developed in this study can be used as a tool to assess the seismic performance of frames with different structural arrangements where prestressed floor units are supported on transverse beams connected to columns.

7.7 REFERENCES

Carr, A. J. (2008). "RUAUMOKO3D - Inelastic dynamic analysis." Department of Civil Engineering, University of Canterbury, Christchurch, New Zealand.

Fenwick, R. C., Bull, D. K., MacPherson, C., and Lindsay, R. "The influence of diaphragms on strength of beams." *New Zealand Society for Earthquake Engineering Conference 2006*.

Kim, J. (2002). "Behaviour of hybrid frames under seismic loading," PhD. Thesis, University of Washington, Washington, USA.

Lau, D. B. N. (2007). "Influence of precast prestressed flooring on the seismic performance of reinforced concrete perimeter frame buildings." *Report Number 653*, Dept. of Civil and Environmental Engineering, University of Auckland, Auckland, New Zealand.

MacRae, G. A., and Gunasekaran, U. "A concept for consideration of slab effects on building seismic performance." *NZSEE Conference 2006*, Napier.

Mander, J. B., Priestley, M. J. N., and Park, R. (1988). "Theoretical stress-strain model for confined concrete." *Journal of Structural Engineering*, 114(8), 1804-1826.

Park, R., and Paulay, T. (1975). *Reinforced concrete structures*, Wiley, New York.

Shahrooz, B. M., Pantazopoulou, S. J., and Chern, S. P. (1992). "Modeling slab contribution in frame connections." *Journal of Structural Engineering*, 118(9), 2475-2494.

Standards New Zealand. (2006). *Concrete structures standard: NZS 3101:2006*, Standards New Zealand, Wellington.

To, N. H. T., Ingham, J. M., and Sritharan, S. (2001). "Monotonic non-linear analysis of reinforced concrete knee joints using strut-and-tie computer models." *Bulletin of the New Zealand Society for Earthquake Engineering*, 34(3), 169-190.

8 PARAMETRIC ANALYSIS ON 3D FRAME-FLOOR SUB-ASSEMBLIES

An analytical model developed to predict the cyclic response of a frame with an associated floor slab containing precast-prestressed floor units was validated with experimental results in Chapter 7. In this chapter, the effect of different structural configurations on the cyclic response of moment resisting frame with prestressed floor units is investigated using the proposed analytical technique. The main focus of this chapter is to quantify the extent of beam elongation and floor contribution to the flexural strength of beam plastic hinges.

Four different case studies are examined. These include a 2-bay perimeter moment resisting frame with half of the slab reinforcement as that investigated in Chapter 5; a 3-bay and a 4-bay perimeter moment resisting frames; and a 2-bay internal moment resisting frame. These case studies were purposely selected to attempt to answer the following questions:

1. Is the effective flange width an appropriate parameter for prescribing the slab reinforcement contribution to the negative flexural strength of beams? Will the effective flange width be the same for two identical frames where one has half of the slab reinforcement ratio of the other?
2. Does slab reinforcement contribution increase as the number of bays in the moment resisting frame increases? Is there simple relationship that can be specified for design engineers to follow in this regard?
3. Will significantly different beam-slab interaction phenomena be observed when a moment resisting frame is located within the building rather than on the building's perimeter?

The generic modelling parameters used in all of the aforementioned case studies are given in Section 8.1. A description of the analytical layout and predictions for each case is summarised in Sections 8.2 to 8.5.

8.1 GENERAL MODELLING PARAMETERS

8.1.1 Model Set-up

The analytical models for different case studies are based on the method proposed in Chapter 7. The columns, beam-column joints, transverse beams, elastic portion of longitudinal beams, prestressed ribs and end slab are modelled using Giberson beam elements with lumped plasticity at the member ends. The potential plastic hinges in the longitudinal beams are modelled using the elongating plastic hinge element described in Chapters 2 and 3. The linking slab (the floor slab between the first prestressed rib unit and the longitudinal beam) is modelled using strut-and-tie analogy with axial concrete springs representing the diagonal compression struts and axial steel springs representing the steel ties. The interface between the floor topping and transverse beams are modelled using axial concrete and steel truss elements. The rest of the floor topping is modelled using elastic quadrilateral shell elements. The modelling parameters used in these analyses follow those recommended in Section 7.4.8.

Similar boundary conditions as those imposed in Chapter 7 are adopted for these analyses. The bases of columns in the moment resisting frame are restrained against vertical movement only, and the mid-point of moment resisting frame is restrained against movement parallel to frame. The far end of the external transverse beams, close to the end slab, are only free to move parallel to the moment frame and the far end of the internal transverse beams are free to move in a horizontal plane and rotate in all directions.

8.1.2 Applied Loading

Loading in all of the case studies examined was displacement controlled, in which cyclic rotation was applied to the centre of each beam-column joint. The column drift history applied in all of the case studies herein follows that adopted in Section 7.2.3. This method of load application prevents inconsistencies between the analytical prediction and experimental observations arising from different displacement histories, and allows comparisons to be made between the analyses.

8.2 2-BAY PERIMETER MOMENT RESISTING FRAME WITH REDUCED SLAB REINFORCEMENT RATIO

8.2.1 Model Set-up

The layout of the 2-bay perimeter frame-floor model is shown in Figure 8-1, where PH stands for plastic hinge. This frame is identical to the 2-bay frame that was examined in Section 7.2 except that the slab reinforcement ratio in this model is halved.

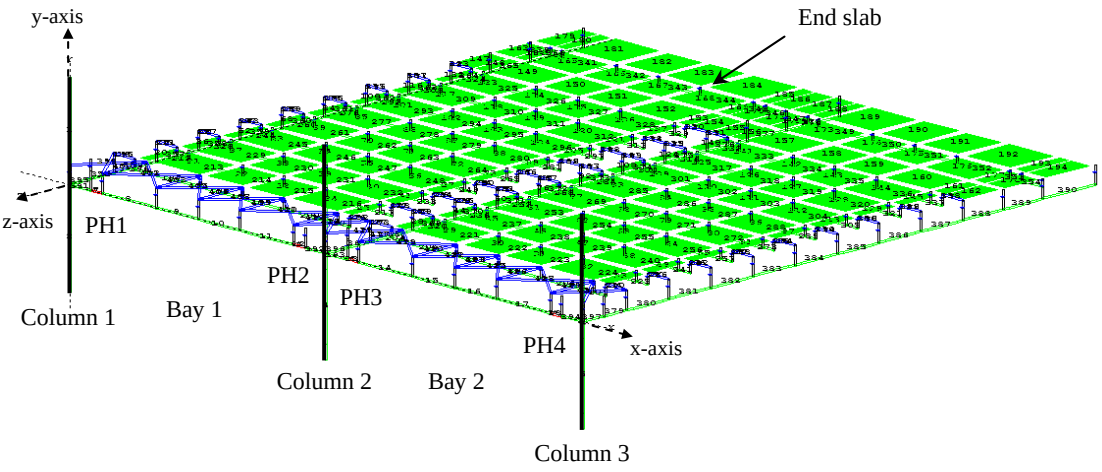

Figure 8-1. Layout of the 2-bay perimeter frame-floor model with the slab reinforcement being halved

8.2.2 Analytical Predictions

As the analytically predicted behaviour of PH1 and PH3 is similar to the behaviour of PH4 and PH2, respectively, discussion in the following sections concentrates on the behaviour of PH1 and PH3 only.

8.2.2.1 Predicted Axial Force in the Plastic Hinges

The predicted axial force comparisons for models with different slab reinforcement contents is shown in Figure 8-2, where the original model represents the analysis set up based on Section 7.4.8 and the modified model represents the analysis with slab

reinforcement contents reduced by half. Here, a positive drift implies a clockwise column rotation.

The axial force comparison in Figure 8-2 shows that as the slab reinforcement ratio decreases, the level of slab contribution reduces (i.e., the axial compression force sustained in the plastic hinges decreases). However, the reduction in axial forces sustained in the plastic hinges is not equal to the reduction in the slab reinforcement ratio. The reduction in axial force in the exterior and interior plastic hinges is approximately 20% and 35%, respectively. This implies that specifying a constant effective flange width, such as the method adopted in the New Zealand Concrete Structures Standard, NZS 3101:2006 (Standards New Zealand 2006), may not be adequate and may lead to an un-conservative design by under-estimating the level of slab contribution.

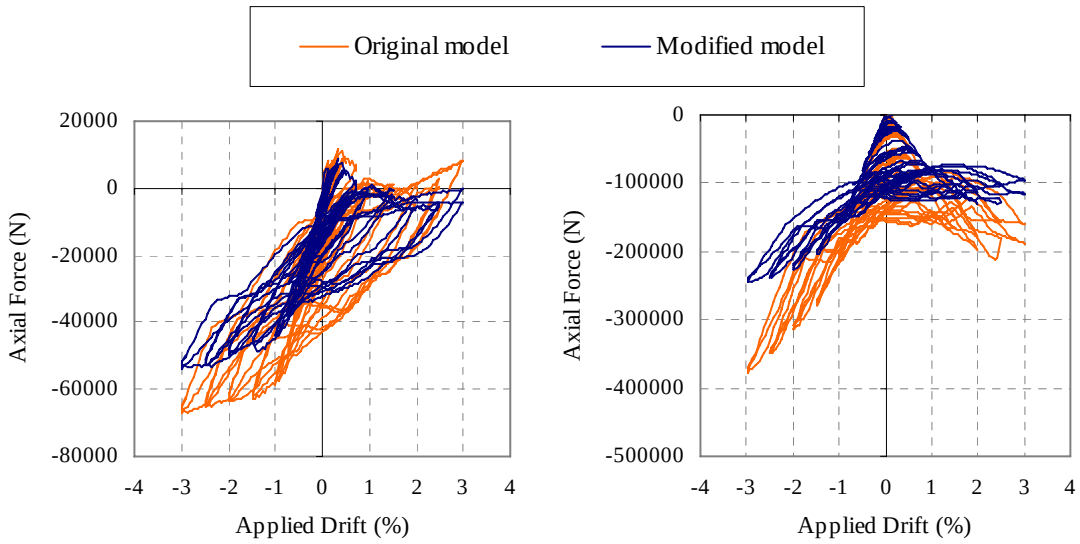

(a) PH1 (b) PH3

Figure 8-2. Predicted axial force comparison for models with different slab reinforcement ratios

The maximum level of axial compression force sustained in the exterior plastic hinge (i.e., PH1) can be estimated using the method proposed in Section 6.5.1.2. Based on the proposed method, the location of zero weak-axis shear force in the transverse beam is located between 775mm and 1275mm from the column face, and the axial compression force in the exterior plastic hinge is estimated to be 48kN. This matches

satisfactorily with the analytical prediction of 53kN. The predicted axial force in the analytical model is higher than that obtained from the hand analysis method. This is because a bilinear factor of 0.02 was specified for the out-of-plane flexural strength of the transverse beam in the analytical model, which may have increased the strength of the transverse beam more than that assumed in the hand analysis method. Consequently, axial force predicted by the hand analysis method is smaller.

8.2.2.2 Predicted Elongation in the Plastic Hinges

Figure 8-3 shows the elongation comparison for models with different slab reinforcement contents. It can be seen that the slab reinforcement content has a bigger effect on the elongation response of interior plastic hinge, (i.e., PH3) than exterior plastic hinge (i.e., PH1). This is because the difference in the predicted axial force between these two models is greater in the interior plastic hinge. As the level of axial compression force in the plastic hinge reduces, elongation of plastic hinge increases. This can be observed in Figure 8-3(b), where a smaller predicted axial force in the modified model with half of the slab reinforcement content leads to a greater elongation prediction. Elongation in the interior plastic hinges increased from 1% to 1.5% of the member depth when the reinforcement ratio is halved.

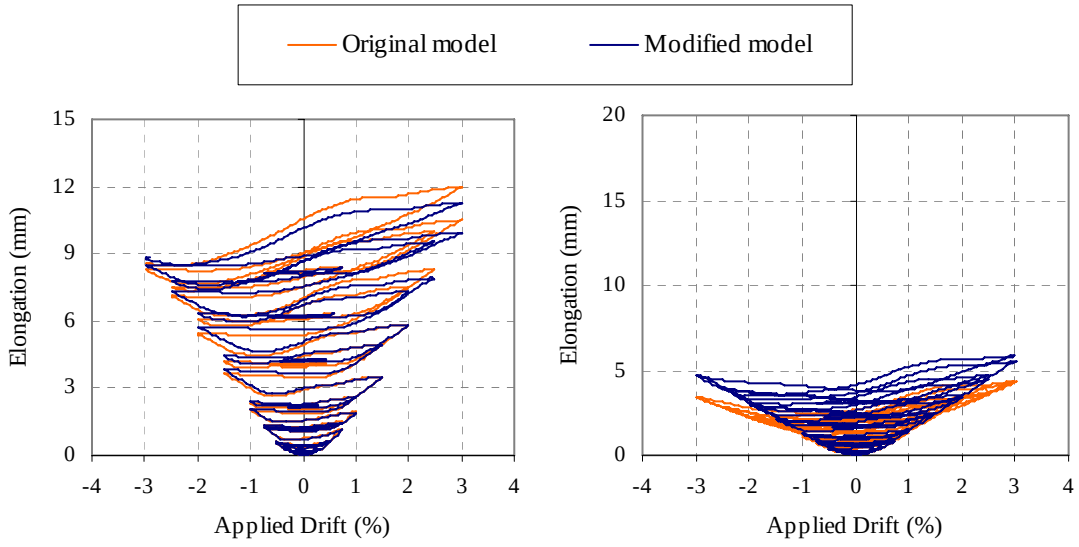

(a) PH1 (b) PH3

Figure 8-3. Predicted elongation comparison for models with different slab reinforcement ratios

It should be noted that in PH1, the predicted elongation in the modified model is smaller than that in the original model at the peak of the positive drift cycles. This is because the axial compression force predicted in the modified model is larger than that in the original model.

8.2.2.3 Predicted Crack Widths between Transverse Beams and Floor Slab Interface

The predicted crack widths between the transverse beams and floor slab interfaces at the peak of the first negative 3% drift cycle, from the two models, are shown in Table 8-1. The crack widths in the modified model, with half of the slab reinforcement content, are greater than those in the original model. This is expected because as the slab reinforcement decreases the stiffness of the slab reinforcement connecting the floor slab and transverse beam decreases. Therefore, elongations are less restrained by the floor slab, and consequently the cracks propagate further along the transverse beams.

Table 8-1. Predicted crack widths along the transverse beams and floor slab interface at the peak of the first negative 3% drift cycle for models with different slab reinforcement ratios

Distance from the column face (mm)	**Crack widths along transverse beam (mm)**			
	Bay 1 behind column 1		**Bay 2 behind column 2**	
	Original model	**Modified model**	**Original model**	**Modified model**
275	2.24	6.46	1.67	3.12
775	0.01	0.55	0.95	1.87
1275	-0.01	-0.01	0.67	1.44
1775	-0.00	-0.00	0.41	1.26
2275	-0.00	-0.00	0.20	0.90
2775	-0.00	-0.00	0.04	0.46

8.2.2.4 Mechanisms Contributing to Axial Force in the Interior Plastic Hinges

A summary of the predicted internal forces along the internal transverse beam and floor slab interface from the two models are summarised in Table 8-2 and Table 8-3, where ΣT is the sum of the tension forces across the cracks, C_{beam} is the axial

compression force sustained in the plastic hinge, and F_{deep_beam} is the force contribution from the floor acting as a deep beam as defined in Section 7.3.8.

It can be seen that the contribution of F_{deep_beam} increases as the sum of slab reinforcement tension force increases. At the -3% drift, F_{deep_beam} contributes to about 33% of the total force across the transverse beam and floor slab interface. The comparison between these two models shows that the ratio of F_{deep_beam} to ΣT is approximately the same. Despite this general trend in the ratio of these forces, it is difficult to propose a design recommendation as the magnitude of ΣT changes for different slab reinforcement contents. Further parametric studies with different slab reinforcement contents are required before generalised recommendations should be made.

Table 8-2. Contribution of axial force for PH3 in the modified model

Internal forces	**Column drift**				
	-3.0% (1)	**-2.5% (1)**	**-2.0% (1)**	**-1.5% (1)**	**-1.0%(1)**
ΣT (kN)	365	358	336	293	214
C_{beam} (kN)	244	235	226	203	160
F_{deep_beam} (kN)	121 (33%)	123 (34%)	110 (33%)	90 (31%)	54 (25%)

Table 8-3. Contribution of axial force for PH3 in the original model

Internal forces	**Column drift**				
	-3.0% (1)	**-2.5% (1)**	**-2.0% (1)**	**-1.5% (1)**	**-1.0%(1)**
ΣT (kN)	552	505	443	374	269
C_{beam} (kN)	378	349	315	278	210
F_{deep_beam} (kN)	174 (32%)	156 (31%)	128 (29%)	96(26%)	59 (22%)

8.3 3-BAY PERIMETER MOMENT RESISTING FRAME

8.3.1 Model Set-up

The layout of the 3-bay perimeter frame-floor model is shown in Figure 8-4. The specimen is identical to the 2-bay perimeter frame that was examined in Section 7.2 except that an additional bay has been added to the frame. The midpoint of the centre beam bay is restrained against movement parallel to frame to act as an anchored point.

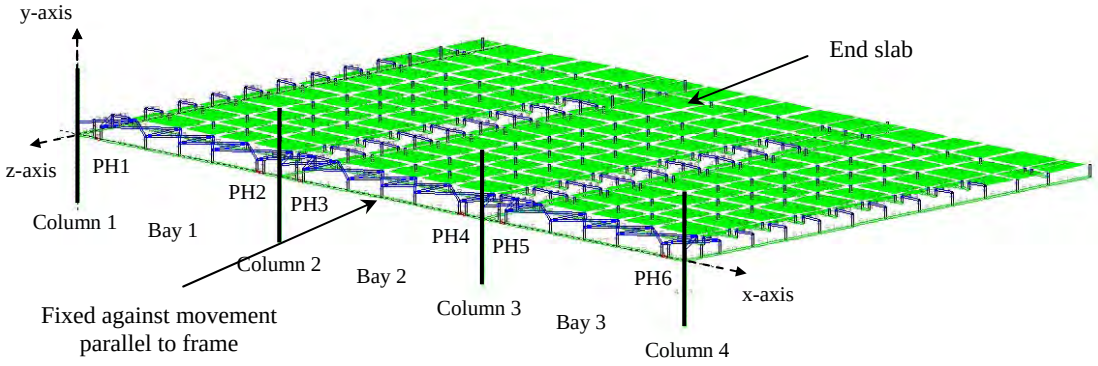

Figure 8-4. Layout of the 3-bay perimeter frame-floor model

8.3.2 Analytical Predictions

8.3.2.1 Predicted Axial Force in the Plastic Hinges

The predicted axial force in the plastic hinges from this analysis, together with the predictions from the 2-bay frame-floor model using the recommended parameters specified in Section 7.4.8, are shown in Figure 8-5. Here, a positive drift implies a clockwise column rotation. As the behaviour of PH1, PH3 and PH5 are similar to the behaviour of PH6, PH4 and PH2, respectively, only PH1, PH3 and PH5 are discussed in the following sections. The predicted axial force in the 3-bay frame model shows that the force sustained in PH3 at the peak of each displacement cycle is greater than that in PH5. This is due to PH3 being confined more by the surrounding columns and floor slab. Here, PH3 is confined by two columns and one slab whereas PH5 is confined by only one column and one slab.

The behaviour of PH1 in the 3-bay frame is compared with that of PH1 in the 2-bay frame and the behaviour of PH3 and PH5 in the 3-bay frame are compared with that of PH3 in the 2-bay frame in Figure 8-5. The following observations can be made based on these comparisons:

1) The axial force-drift relationships between: PH5 in the 3-bay frame, PH3 in the 2-bay frame and PH1 in the 2-bay and 3-bay frames are similar, whereas the axial force-drift response of PH3 in the 3-bay frame is much stiffer than that of PH3 in the 2-bay frame.

2) The peak axial compression force sustained in the plastic hinge next to the external column (i.e., PH1) stays the same, whereas the peak axial compression force sustained in the plastic hinges next to the internal columns (i.e., PH3 and PH5) increases slightly from 370kN to 420kN and 390kN, respectively.

3) There is a significant increase in the predicted axial compression force in PH3 at the peak of each positive drift cycle. It should be noted that as this force is acting relatively close to the centroid of the compression stress block, it has little influence on the positive moment of plastic hinges.

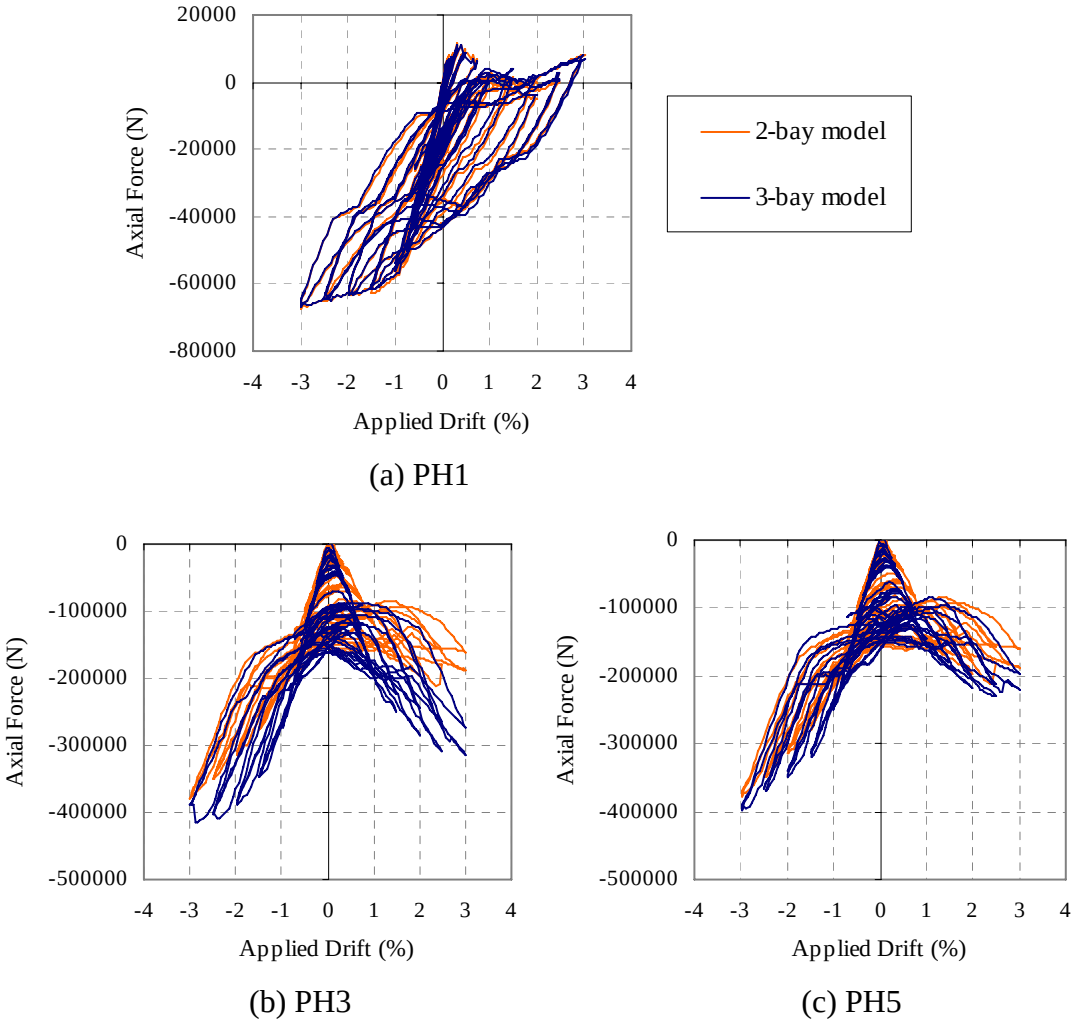

(a) PH1

(b) PH3

(c) PH5

Figure 8-5. Predicted axial force in the plastic hinges in 2-bay and 3-bay frames

8.3.2.2 Predicted Elongation in the Plastic Hinges

The predicted elongation in the plastic hinges for the 2-bay and 3-bay frame models are plotted in Figure 8-6, where the behaviour of PH1 in the 3-bay frame is compared with PH1 in the 2-bay frame, and the behaviour of PH3 and PH5 is compared with PH3 in the 2-bay frame.

In PH3 of the 3-bay frame, there is an abrupt reduction in elongation during the first negative 3% drift. This is due to crushing of concrete springs in the analysis, which also leads to a loss in axial load carrying capacity, as shown in Figure 8-5(b). It should be noted that in the core concrete model used in the analysis, the compressive strength decreases more rapidly than that recommended in the Mander's model (see Section 7.4.6 for detail). Therefore, crushing of concrete predicted in the analysis may not have occurred in reality. The comparisons between the 2-bay and 3-bay frame models show that increasing the number of bays in a frame has negligible effect on the elongation response of the plastic hinges. The difference in the peak elongation of PH3 is less than 0.2mm.

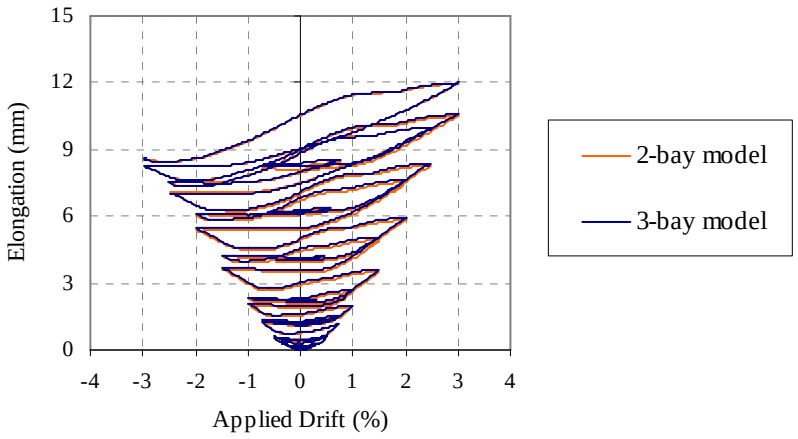

(a) PH1

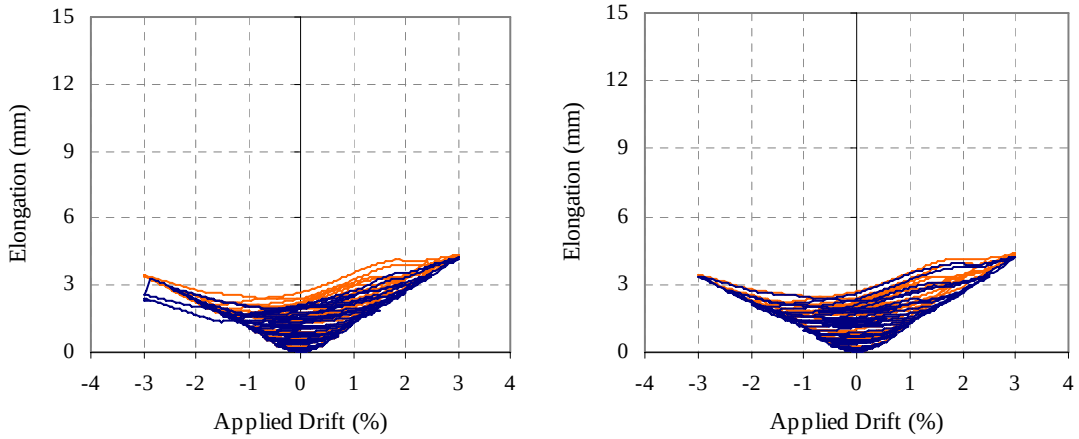

(b) PH3 (c) PH5

Figure 8-6. Predicted elongation in the plastic hinges in 2-bay and 3-bay frames

8.3.2.3 Predicted Crack Widths between Transverse Beams and Floor Slab Interface

Table 8-4 compares the predicted crack widths along the transverse beams and floor slab interface at the peak of the first negative 3% drift cycle. Crack widths behind PH1 (i.e., along the external transverse beam) in the 3-bay frame are compared with those behind PH1 in the 2-bay frame, and crack widths behind PH3 and PH5 (i.e., along the two internal transverse beams) in the 3-bay frame are compared with those behind PH3 in the 2-bay frame. The comparisons show that the predicted crack widths along the external transverse beam are similar in both the 2-bay and 3-bay frame analyses, whereas the crack widths along the internal transverse beams are quite different. In general, crack widths behind PH3 in the 3-bay frame are smaller than those behind PH3 in the 2-bay frame, whereas crack widths behind PH5 in the 3-bay

frame are greater than those behind PH3 in the 2-bay frame, except for regions close to the column face.

As mentioned earlier in Sections 7.3.7.1 and 7.3.8, the magnitude of crack widths does not directly represent the magnitude of the slab reinforcement contributing to the negative flexural strength of beam plastic hinges. The magnitude of slab reinforcement contributing to the flexural strength of beam plastic hinges depends on the distribution of the internal forces. The amount of tension force in the slab reinforcement crossing the cracks also depends on the cyclic history of the reinforcing bars. This explains why, despite the crack widths being greater behind PH5 than those behind PH3 in the 3-bay frame, the axial force sustained in PH5 is smaller.

Table 8-4. Crack widths along the transverse beams and floor slab interface at the peak of first negative 3% drift cycle in the 2-bay and 3-bay frames

Distance from the column face (mm)	**Crack widths along transverse beam (mm)**				
	2-bay (behind PH1)	**3-bay (behind PH1)**	**2-bay (behind PH3)**	**3-bay (behind PH3)**	**3-bay (behind PH5)**
275	2.92	3.10	3.00	2.98	2.67
775	0.01	0.09	1.80	1.41	1.99
1275	-0.01	-0.01	1.38	0.83	1.95
1775	-0.00	-0.00	1.09	0.54	1.66
2275	-0.00	-0.00	0.68	0.44	1.07
2775	-0.00	-0.00	0.33	0.45	0.54

8.3.2.4 Predicted Deformation in the Linking Slab

Figures 8-8 and 8-9 show the axial deformation in the truss elements used to model the linking slab and the corresponding averaged shear deformation across the linking slab, as interpreted from each pair of diagonals and ties using Equation 8-1. The symbols in this equation are illustrated in Figure 8-7, where D_1, D_2, Δ_1 and Δ_2 are the axial deformation in the diagonals and ties, respectively. In this equation, axial extension of the truss element is positive and a positive shear deformation implies the slab is moving to the right relative to the beam. The units for these values are in millimetres.

$$S = \frac{D_1 - D_2}{2\cos\theta} + \left(\frac{\Delta_2 - \Delta_1}{2}\right)\tan\theta \qquad (8\text{-}1)$$

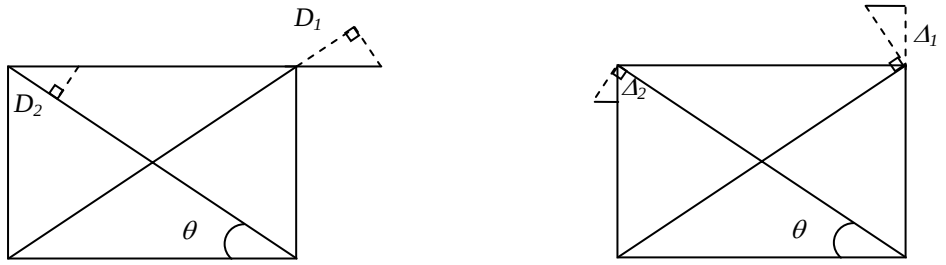

(a) Deformation in the diagonal struts (b) Deformation in the ties

Figure 8-7. Schematic diagram showing shear displacement across the linking slab calculated from the truss deformations

The interpreted shear deformation in the linking slab at ±3% drift in Figures 8-8 and 8-9 show that the shear deformation behaviour is similar between the positive and negative drifts. Hence, the discussion below focuses on the negative drift cycle (see Figure 8-8). The deformation pattern shows that in the outer bays (Bays 1 and 3) the diagonal compression struts were all inclined towards the internal columns. This behaviour is similar to that observed in the 2-bay frame. The deformation pattern of the middle bay (Bay 2) is more complex. When the frame was displaced in the negative drift cycles, diagonal struts formed predominantly towards Column 2. When the frame was displaced in the positive drift cycles, diagonal struts formed predominantly towards Column 3.

The direction of the compression struts formed in the linking slab is believed to be dependent on the axial compression force sustained in the plastic hinges at the two ends of the beam. For example, at the peak of the negative drift cycles, the axial compression force sustained in PH3 is much greater than that in PH4, as shown in Figure 8-5. Therefore, the majority of the diagonal struts are inclined towards Column 2 in Bay 2. Also, at the peak of the negative drift cycles, the axial compression force sustained in PH2 is much greater than that in PH1, as shown in Figure 8-5. Therefore, the diagonal struts are inclined towards Column 2 in Bay 1.

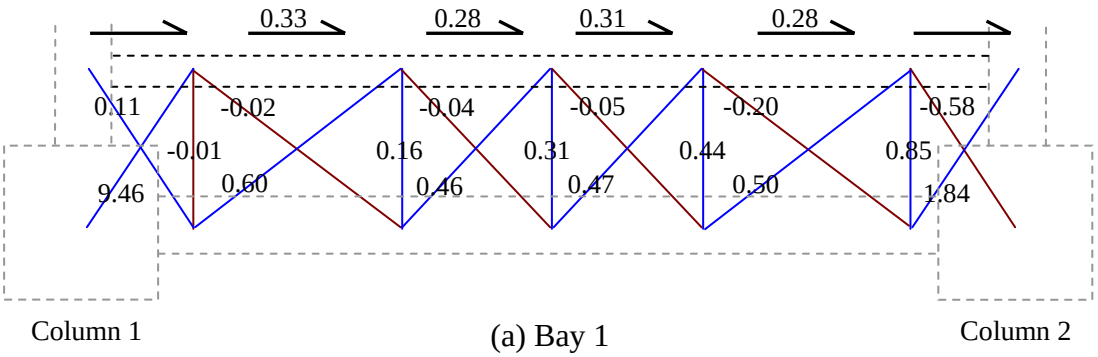

(a) Bay 1

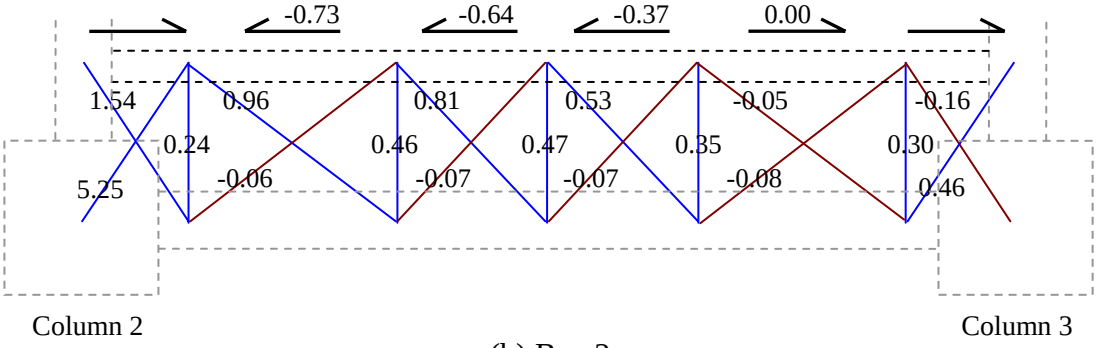

(b) Bay 2

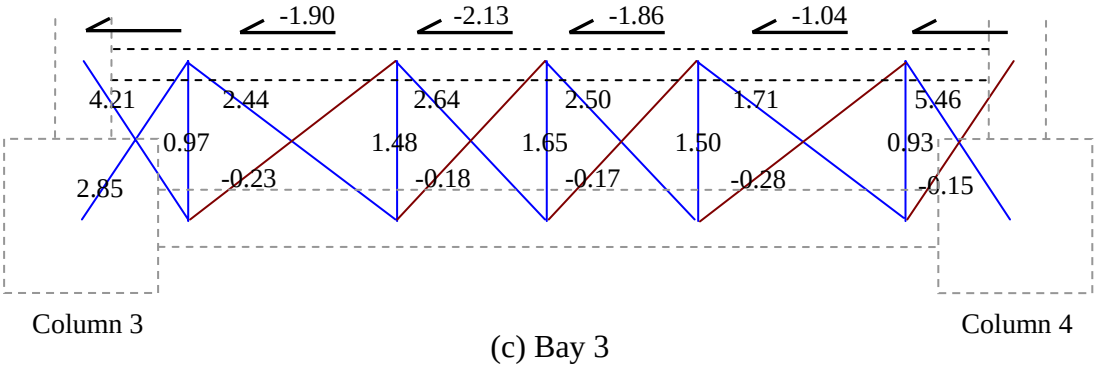

(c) Bay 3

Figure 8-8. Axial deformations in the truss elements modelling the linking slab at the peak of first negative 3% drift cycle (units in mm)

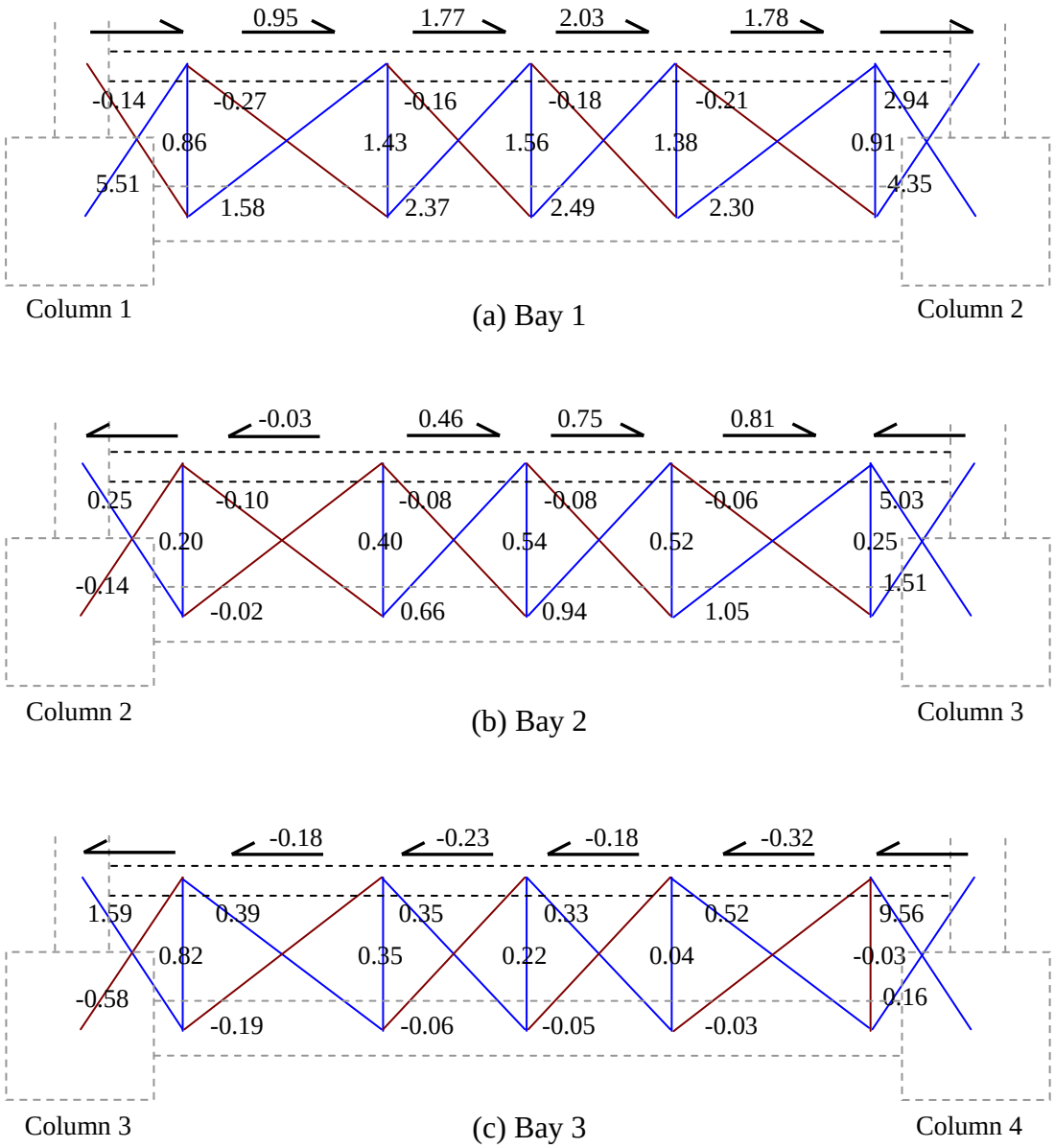

Figure 8-9. Axial deformations in the truss elements modelling the linking slab at the peak of second positive 3% drift cycle (units in mm)

Figures 8-10 and 8-11 show schematic diagrams of diagonal cracks developed in the linking slab. It is postulated that the diagonal cracks will develop when one diagonal is under compressive strain while the other diagonal reaches the tensile cracking strain of concrete. The tensile cracking strain of concrete is taken as two times the strain at which the tensile stress is reached as specified in Shima et al. (1987). In this case, the cracking strain of concrete is 1.6E-4 strain and the corresponding cracking extensions for the three diagonals are 0.10mm, 0.14mm and 0.12mm, respectively. It should be

noted that the angle of the diagonal cracks drawn in the figures below does not necessarily represent the angle of the diagonal cracks that are expected to occur in reality.

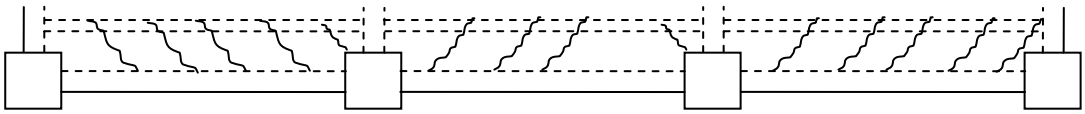

Figure 8-10. Diagonal crack pattern in the linking slab at the peaks of negative 3% drift cycles

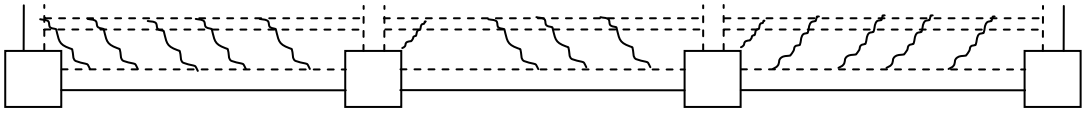

Figure 8-11. Diagonal crack pattern in the linking slab at the peaks of positive 3% drift cycles

8.3.2.5 Predicted In-Plane Bending Action in the Floor Slab

Figure 8-12 shows the predicted force per unit length in the floor slab at a distance 4025mm from the centre line of the moment resisting frame at the peak of first negative 3% drift cycle. These values are the direct nodal outputs within each shell element from RUAUMOKO. There are 4 nodes located at the 4 corners of each shell element; therefore 2 readings are shown in each shell element from the 2 nodes. The units for these values are in N/mm.

It can be seen that a clockwise moment is induced in the floor slab at Bays 2 and 3, whereas a counter-clockwise moment is induced in the floor slab at Bay 1. With reference to the free body diagram in Section 6.3.8, the magnitude of the moment induced in the floor slab depends on the level of axial force sustained in the plastic hinges at the two ends of the beam. For example at the peak of the first negative 3% drift cycle, the axial force sustained in PH1 to PH6 is -65kN, -215kN, -390kN, -310kN, -400kN and 5kN, respectively, where a negative value implies axial compression force. As the difference in the level of axial force between the two plastic hinges is the greatest in Bay 3, the bending action induced in the floor slab of Bay 3 is also the largest. As the difference in the level of axial force between the two

plastic hinges is the smallest in Bay 2, the bending action induced in the floor slab of Bay 2 is also the smallest, as observed in Figure 8-12.

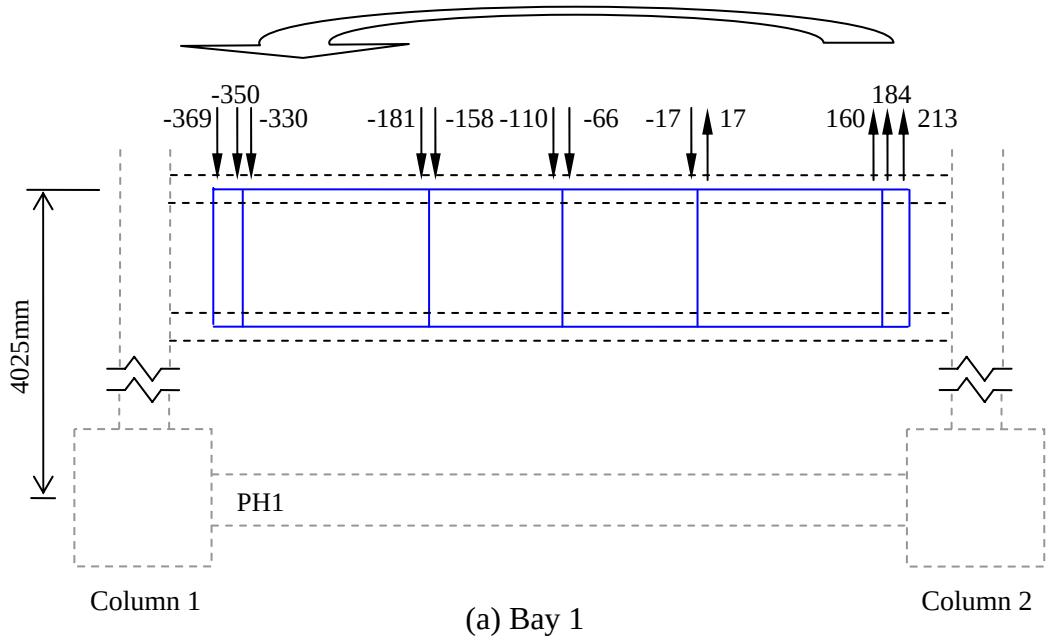

(a) Bay 1

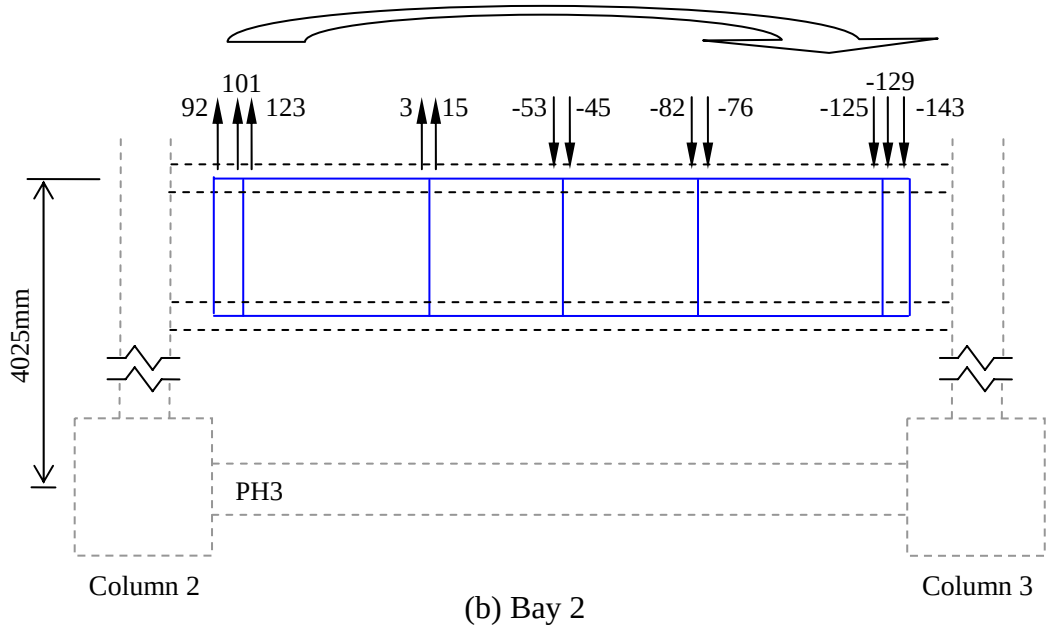

(b) Bay 2

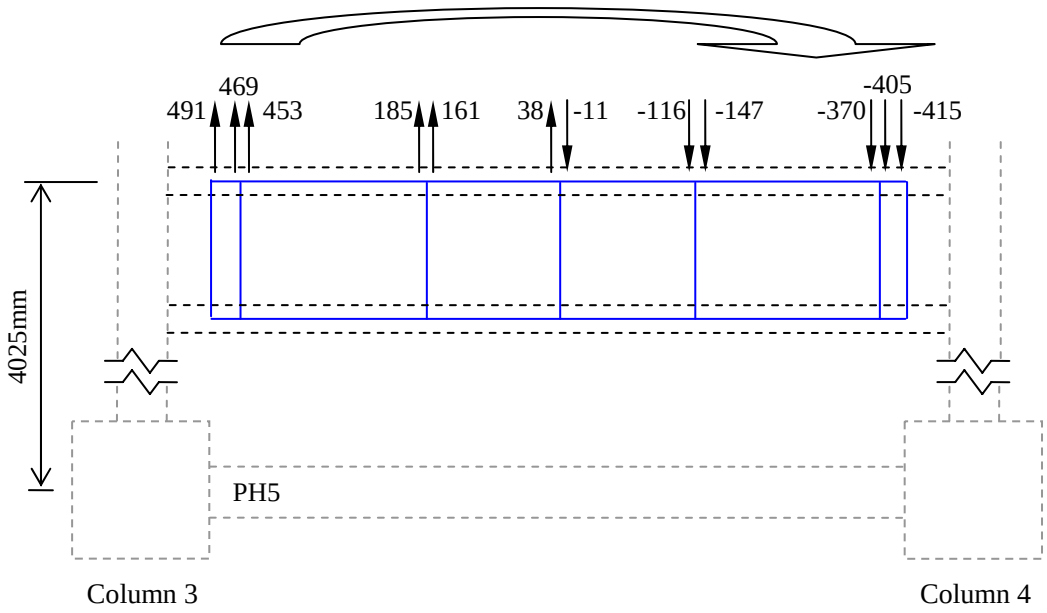

(c) Bay 3

Figure 8-12. Force per unit length in the floor slab at the peak of first negative 3% drift (units in N/mm)

8.3.2.6 Mechanisms Contributing to Axial Force in the Interior Plastic Hinges

A breakdown of the internal forces in the interior plastic hinges, C_{beam}, along the transverse beam and floor slab interface, ΣT, and deep beam action F_{deep_beam} are summarised in Table 8-5 and Table 8-6. It can be seen that the deep beam action increases as the drift increases. The sum of the tension force in the floor slab, ΣT, is greater in PH3 than in PH5, except at the peak of negative 3% drift. This is because the concrete crushes in PH3 and hence, the load carrying capacity reduces during the 3% drift cycle.

Comparing these results with the predictions from 2-bay frame in Section 7.3.8, the magnitude of F_{deep_beam} has increased significantly for PH3 and PH5 as a result of increasing ΣT.

Table 8-5. Contribution of axial force in PH3 in the 3-bay frame

Internal forces	Column drift				
	-3.0% (1)	**-2.5% (1)**	**-2.0% (1)**	**-1.5% (1)**	**-1.0%(1)**
ΣT (kN)	582	611	585	510	376
C_{beam} (kN)	390	399	389	348	271
F_{deep_beam} (kN)	192 (33%)	212 (35%)	196 (34%)	162 (32%)	105 (28%)

Table 8-6. Contribution of axial force in PH5 in the 3-bay frame

Internal forces	Column drift				
	-3.0% (1)	**-2.5% (1)**	**-2.0% (1)**	**-1.5% (1)**	**-1.0%(1)**
ΣT (kN)	610	578	532	474	357
C_{beam} (kN)	399	370	348	319	248
F_{deep_beam} (kN)	211 (35%)	208 (36%)	184 (35%)	155 (33%)	109 (31%)

8.4 4-BAY PERIMETER MOMENT RESISTING FRAME

8.4.1 Model Set-up

The layout of the 4-bay perimeter frame-floor model is shown in Figure 8-13. The specimen is similar to the 3-bay perimeter frame examined earlier except that an additional bay has been added to the frame. In this model, the beam-column joint in the central column (Column 3) is restrained against movement parallel to frame.

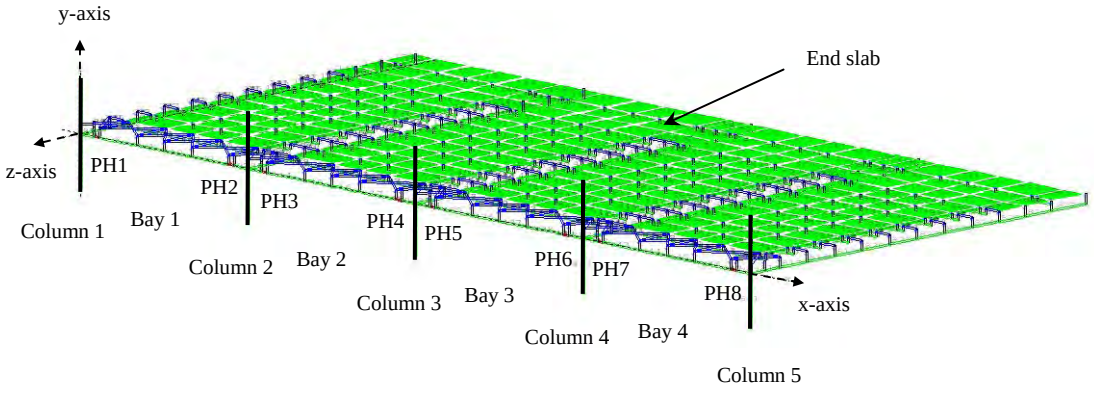

Figure 8-13. Layout of the 4-bay perimeter frame-floor model

8.4.2 Analytical Predictions

8.4.2.1 Predicted Axial Force in the Plastic Hinges

The predicted axial forces in the plastic hinges in this model together with the predictions from the 2-bay and 3-bay frame models are shown in Figure 8-14. As the behaviour of PH1, PH3, PH5 and PH7 are similar to the behaviour of PH8, PH6, PH4 and PH2, respectively, only PH1, PH3, PH5 and PH7 are discussed herein. The comparisons include: (i) the axial force in PH1 in this frame with PH1 in the 2-bay and 3-bay frames; (ii) the axial forces in PH3 and PH5 in this frame with that of PH3 in the 2-bay and 3-bay frames; and (iii) the axial force of PH7 in this frame with PH5 in the 3-bay frame and PH3 in the 2-bay frame. The following observations can be made based on these comparisons:

1) The peak axial compression force sustained in the plastic hinges next to the external columns (i.e., PH1) remains the same. This further emphasises that the strength of plastic hinges next to the external transverse beams is mainly a function of the out-of-plane bending and torsional strength of the transverse beams.
2) The stiffness and the peak axial compression force in PH7 is similar to PH5 in the 3-bay frame, and the stiffness and the peak axial force in PH3 is similar to PH3 in the 3-bay frame. This implies that the strength of interior plastic hinges depends mainly on the locations of plastic hinges and the number of bays and columns that are effectively confining the plastic hinges. For example, PH5 in the 3-bay frame and PH7 in the 4-bay frame are both confined by 1 floor slab and 1 column to the right of the plastic hinge. Consequently, their behaviours are similar.
3) The stiffness and the peak axial compression force induced in PH5 (450kN) is considerably higher than those in the interior plastic hinges in the 2-bay and 3-bay models. This is expected as PH5 is more confined by the surrounding columns and floor slabs. The increase in the axial force in this plastic hinge is approximately 22% compared to PH3 in the 2-bay frame.
4) There is a significant increase in the axial compression force in PH5 of the 4-bay frame at the peak of the positive drift cycles. It should be noted that as this force is acting relatively close to the centroid of the compression stress block, it has little influence on the positive moment of the plastic hinge.

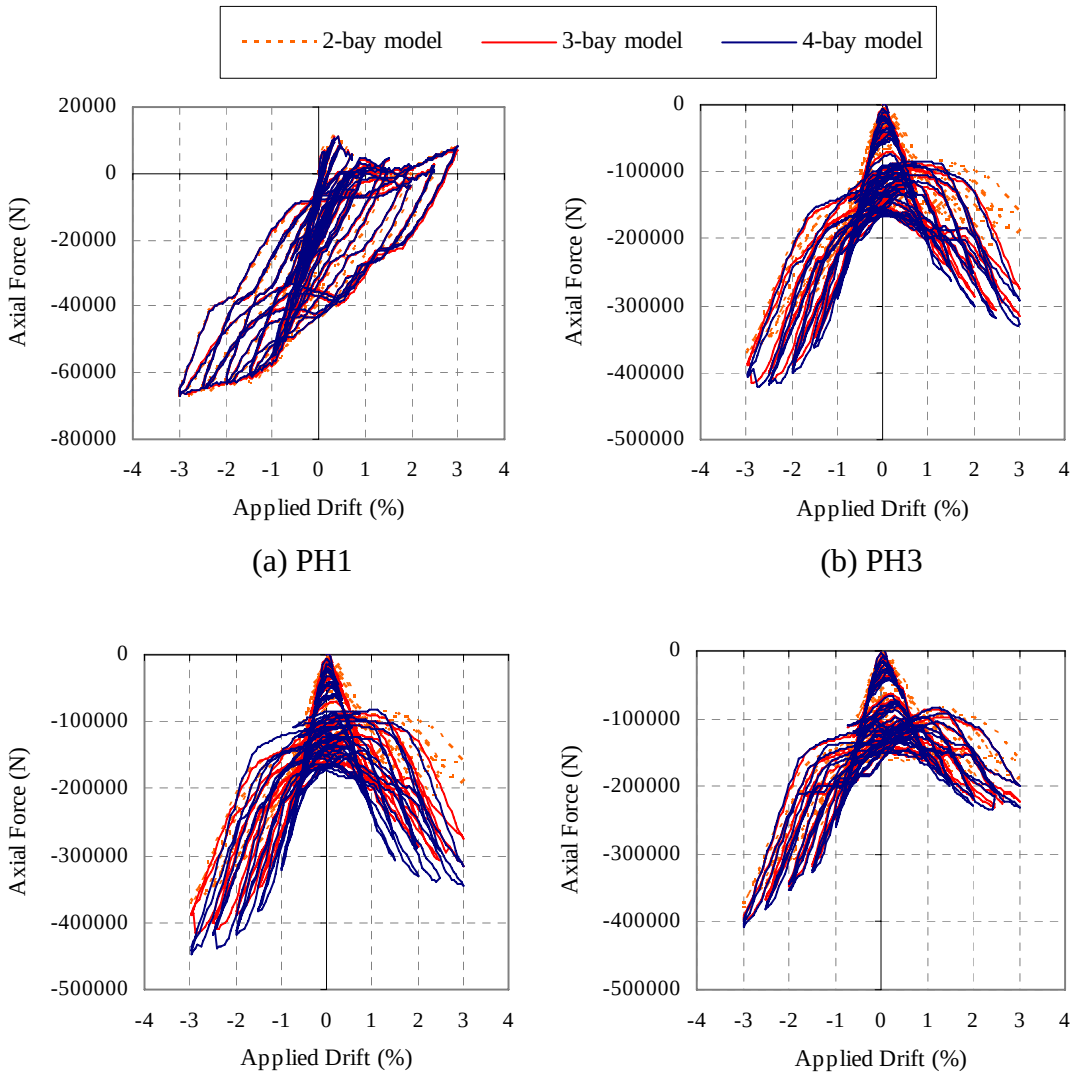

Figure 8-14. Predicted axial force in the plastic hinges in 2-bay, 3-bay and 4-bay frames

8.4.2.2 Predicted Elongation in the Plastic Hinges

The predicted elongation in the plastic hinges in this analysis is compared with the corresponding elongation in the 2-bay and 3-bay frame models in Figure 8-15. The behaviour of PH1 in this frame is compared with PH1 in the 2-bay and 3-bay frames; the behaviour of PH3 and PH5 in this frame are compared with PH3 in the 2-bay and 3-bay frames; and the behaviour of PH7 in this frame is compared with PH3 in the 2-bay frame and PH5 in the 3-bay frame. It can be seen from these comparisons that elongation of exterior plastic hinges remained constant in all three cases. However, elongation in the interior plastic hinges decreased slightly as a result of a larger

predicted axial compression force. There is an abrupt decrease in elongation in PH3 during the first negative 3% drift cycle and in PH5 during the first negative 2.5% drift cycle. As mentioned earlier, this is due to crushing of core concrete. In general, increasing the number of bays in moment resisting frames is found to have little influence on the elongation response of plastic hinges.

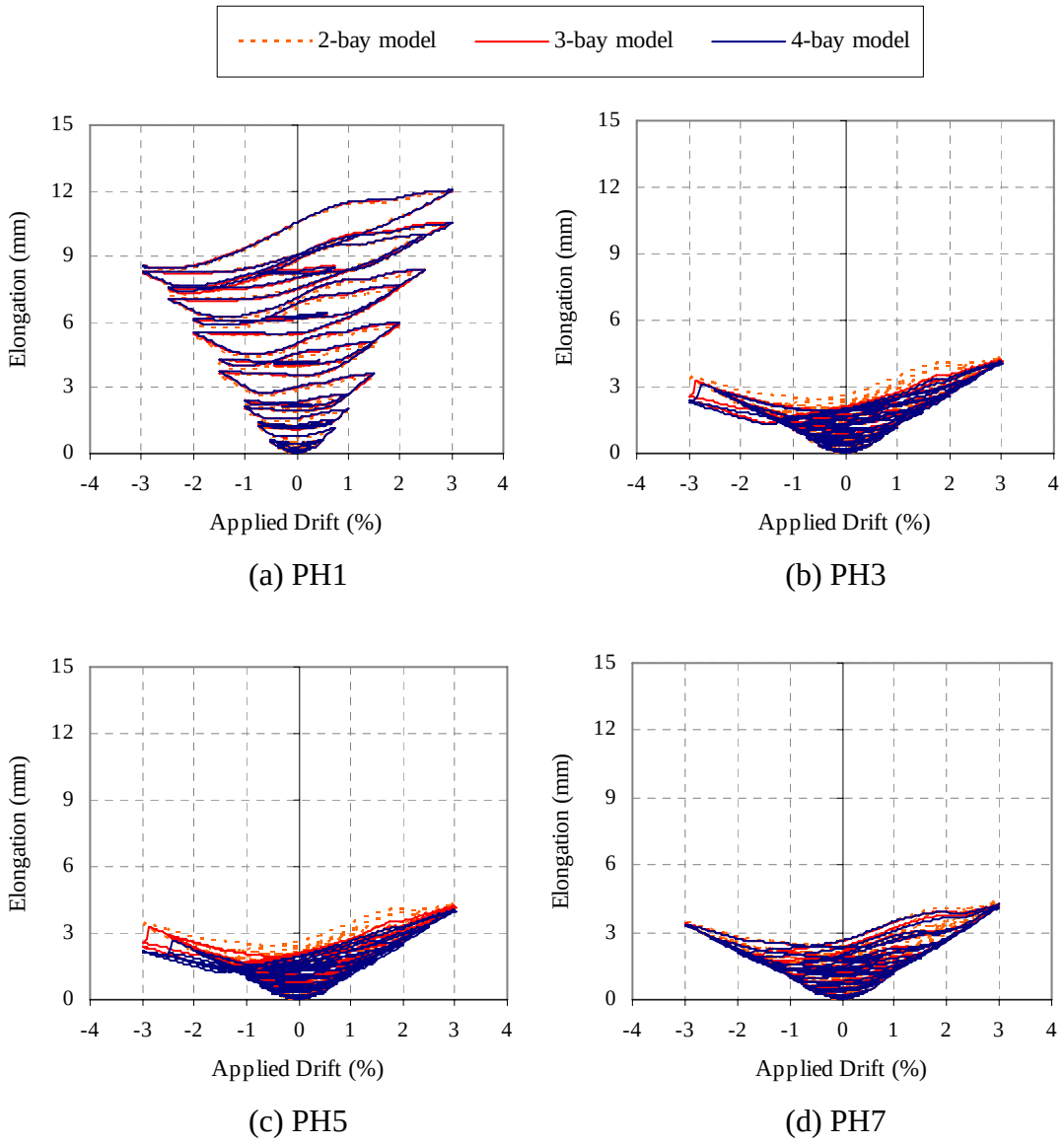

Figure 8-15. Predicted elongation in the plastic hinges in 2-bay, 3-bay and 4-bay frames

8.4.2.3 Predicted Deformation in the Linking Slab

Figure 8-16 shows the axial deformation in the truss elements used to model the linking slab and the corresponding averaged shear deformation across the linking slab

interpreted from each pair of diagonals and ties using Equation 8-1. A positive shear deformation implies that the slab is moving to the right relative to the beam. The units in these graphs are in millimetres. As the deformation is similar between the positive and negative drifts, only the behaviour at the peak of the negative 3% drift cycle is shown here.

The deformation pattern observed in this frame is similar to that observed in the 3-bay frame. In general, the diagonal compression struts in the floor slab in the outer bays (Bays 1 and 4 in this case) are all inclined towards the internal columns; whereas the diagonal compression struts in the floor slab between the internal columns developed in different directions during the positive and negative drift cycles. The diagonal struts develop mainly towards the plastic hinges where the flexural tension is on the top. This is because within an internal beam bay, the axial compression force sustained in the plastic hinge at one end (where flexural tension is on the top), is generally larger than the plastic hinge on the other end (where flexural tension is on the bottom).

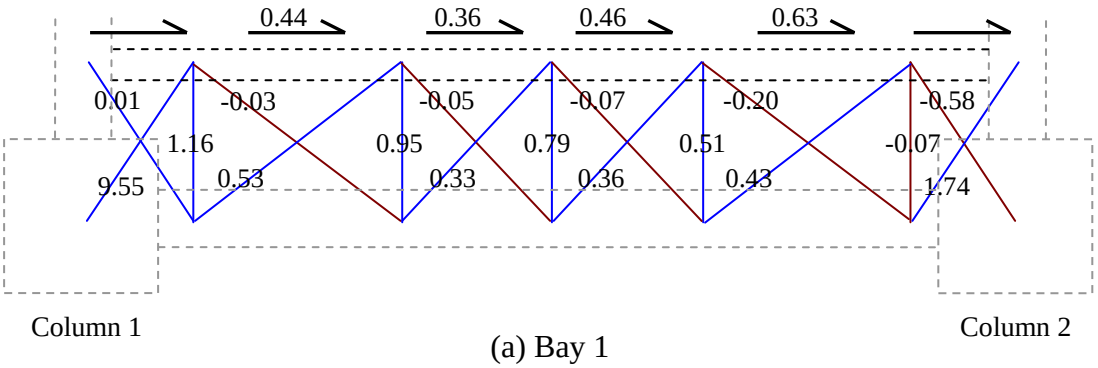

Column 1 Column 2

(a) Bay 1

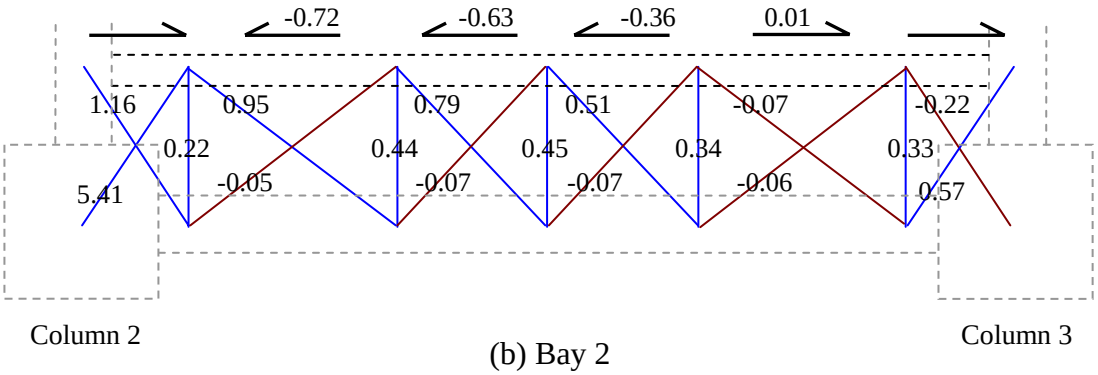

Column 2 Column 3

(b) Bay 2

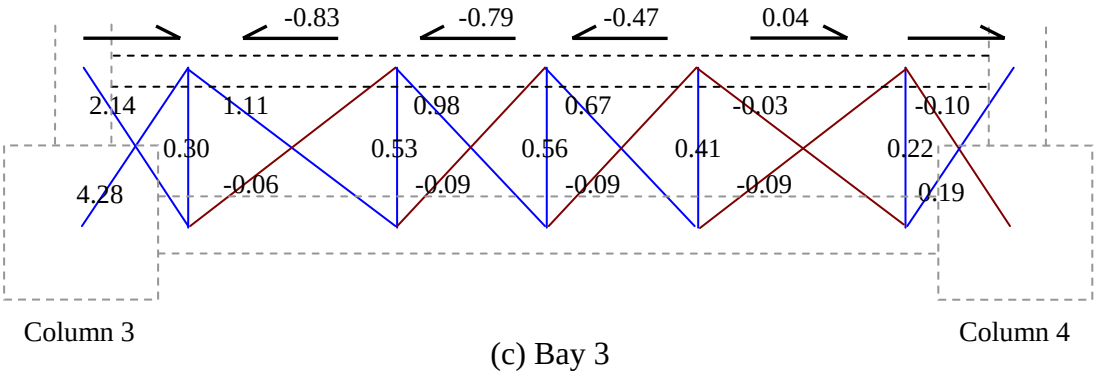

Column 3 Column 4

(c) Bay 3

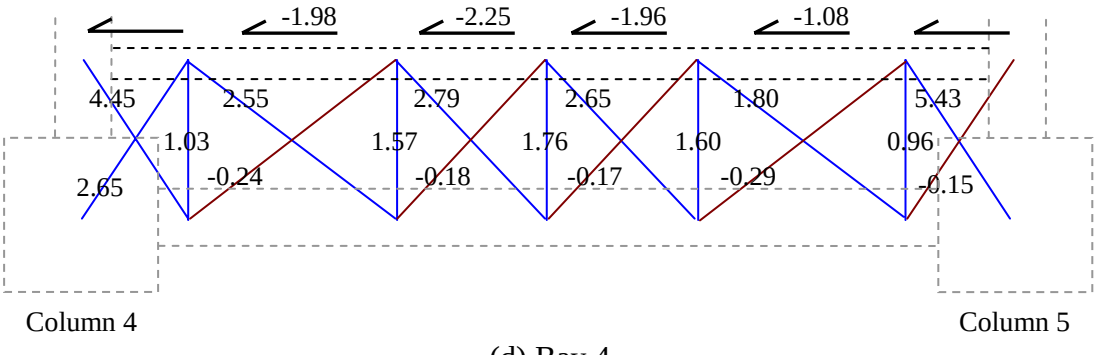

Column 4 Column 5

(d) Bay 4

Figure 8-16. Axial deformations in the truss elements modelling the linking slab at the peak of first negative 3% drift cycle (units in mm)

Figures 8-17 and 8-18 show schematic diagrams of the diagonal cracks developed in the linking slab. The method for deciding whether diagonal cracks form in the floor slab is described earlier in Section 8.3.2.4. It should be noted that the angle of the diagonal cracks drawn in the figures below does not necessarily represent the angle of the diagonal cracks that are expected to occur in reality.

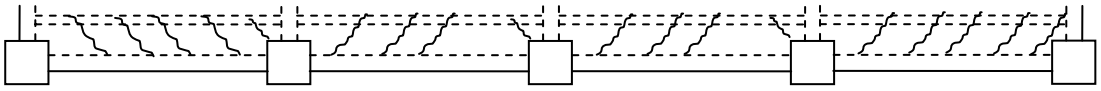

Figure 8-17. Diagonal crack pattern in the linking slab at the peaks of negative 3% drift cycles

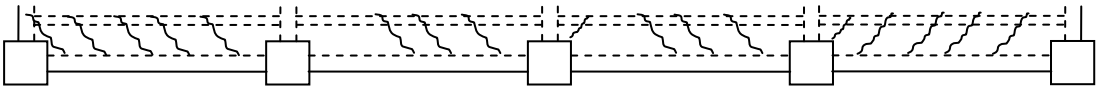

Figure 8-18. Diagonal crack pattern in the linking slab at the peaks of positive 3% drift cycles

8.4.2.4 Predicted In-Plane Bending Action in the Floor Slab

Figure 8-19 shows the predicted force per unit length in the floor slab at a distance 4025mm from the centre line of the moment resisting frame at the peak of first negative 3% drift. The figure shows that a clockwise moment is induced in Bays 2, 3 and 4, whereas a counter-clockwise moment is induced in Bay 1. It is observed that the bending actions of the floor slab follow closely with the truss actions in the linking slab. This observation is expected, as both of these actions depend on the level of axial force sustained in the plastic hinges at the two ends of a beam.

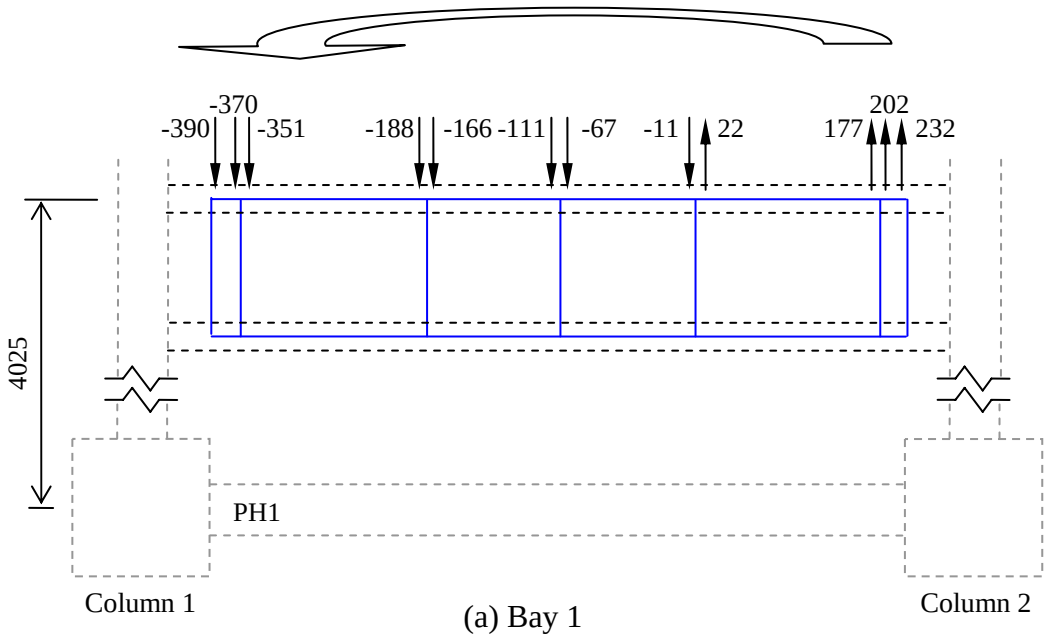
-370
-390
-351
-188
-166
-111
-67
-11
22
202
177
232
4025
PH1
Column 1
Column 2

(a) Bay 1

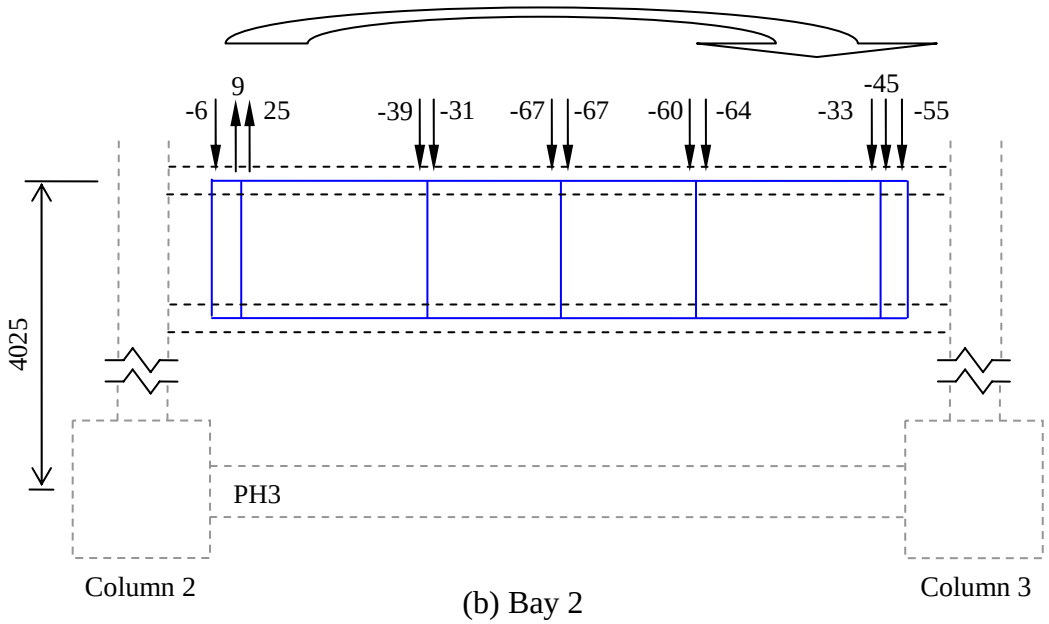
9
-6
25
-39
-31
-67
-67
-60
-64
-45
-33
-55
4025
PH3
Column 2
Column 3

(b) Bay 2

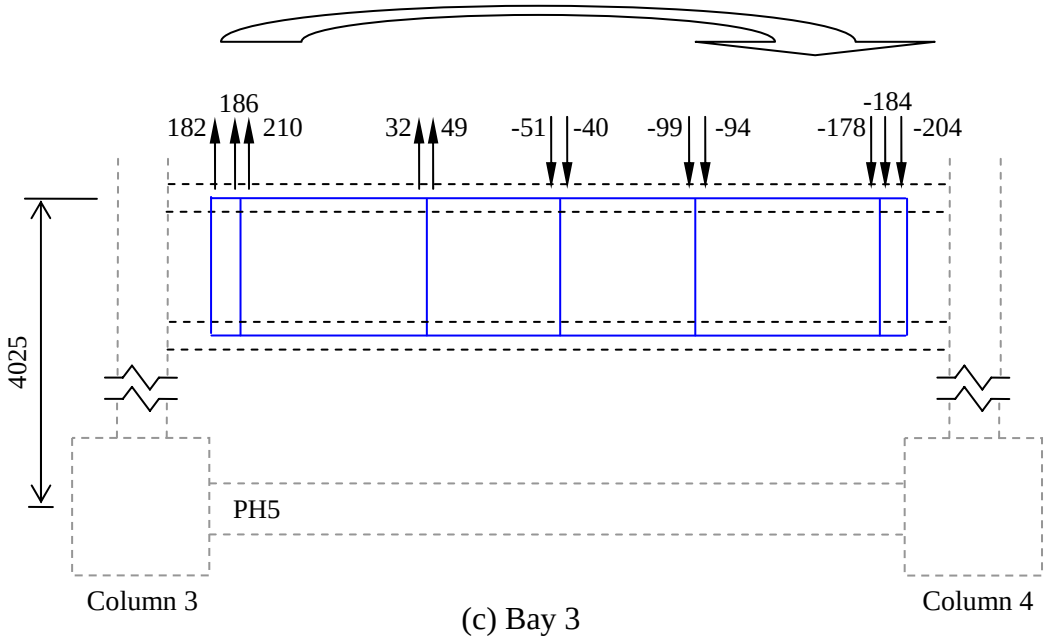

(c) Bay 3

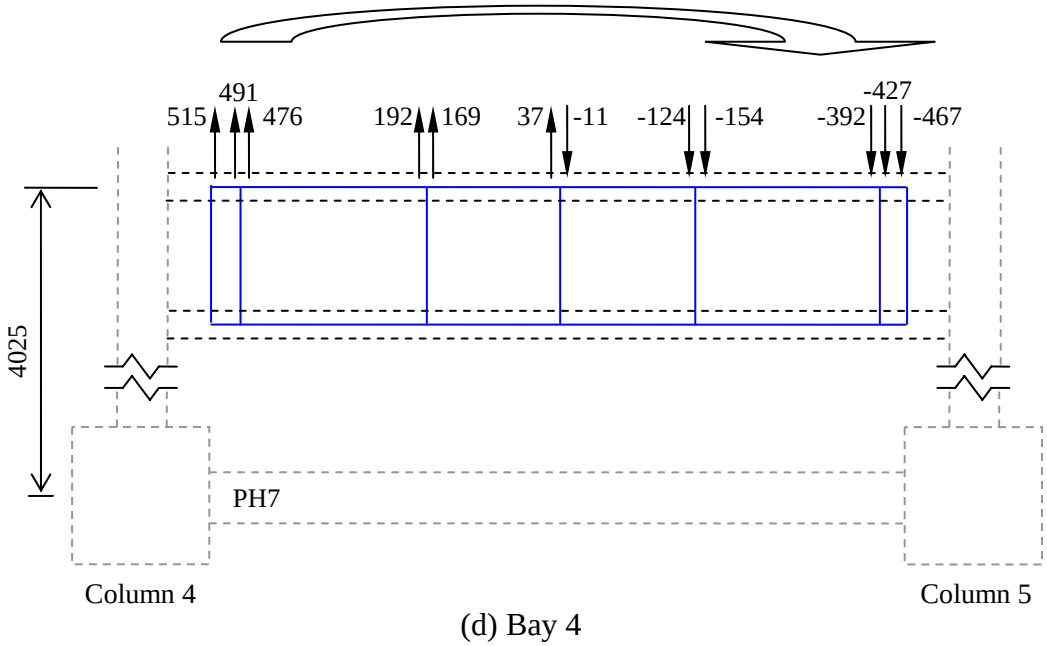

(d) Bay 4

Figure 8-19. Force per unit length in the floor slab at the peak of first negative 3% drift (units in N/mm)

8.4.2.5 Mechanisms Contributing to Axial Force in the Interior Plastic Hinges

A breakdown of the internal forces in the interior plastic hinges, C_{beam}, along the transverse beam and floor slab interface, ΣT, and deep beam action F_{deep_beam} are

summarised in Table 8-7 to Table 8-9. The following observations can be made from these results:

1) The maximum force of the deep beam action is approximately 215kN. The force starts to decrease when this value is reached.
2) The magnitude of F_{deep_beam} increases much faster in PH5. The maximum F_{deep_beam} is reached at 1.5% drift.
3) The magnitude of C_{beam} increases with the magnitude of ΣT.

These results are compared with those predicted for the 3-bay frame in Section 8.3.2.6. It can be seen that the maximum proportion of F_{deep_beam} is similar between PH3 in the 3-bay and 4-bay frames and between PH7 in the 4-bay frame and PH5 in the 3-bay frame. Comparing the behaviour of PH5 in the 4-bay frame with PH3 in the 3-bay frame, the magnitude of the axial compression force sustained in the 4-bay frame is much higher. This arises mainly due to an increase in the slab force, ΣT. The maximum magnitude of F_{deep_beam} is reached at a much smaller drift cycle in the 4-bay frame.

Table 8-7. Contribution of axial force in PH3 in the 4-bay frame

Internal forces	**Column drift**				
	-3.0% (1)	**-2.5% (1)**	**-2.0% (1)**	**-1.5% (1)**	**-1.0%(1)**
ΣT (kN)	598	627	608	543	413
C_{beam} (kN)	407	413	400	363	286
F_{deep_beam} (kN)	191 (32%)	214 (34%)	208 (34%)	182 (34%)	127 (31%)

Table 8-8. Contribution of axial force in PH5 in the 4-bay frame

Internal forces	**Column drift**				
	-3.0% (1)	**-2.5% (1)**	**-2.0% (1)**	**-1.5% (1)**	**-1.0%(1)**
ΣT (kN)	637	615	631	603	487
C_{beam} (kN)	447	416	419	385	318
F_{deep_beam} (kN)	190 (30%)	199 (32%)	212 (34%)	218 (36%)	169 (35%)

Table 8-9. Contribution of axial force in PH7 in the 4-bay frame

Internal forces	**Column drift**				
	-3.0% (1)	**-2.5% (1)**	**-2.0% (1)**	**-1.5% (1)**	**-1.0%(1)**
ΣT (kN)	614	578	546	499	377
C_{beam} (kN)	408	376	354	327	258
F_{deep_beam} (kN)	206 (34%)	202 (35%)	192 (35%)	172 (34%)	119 (32%)

8.4.3 Summary

Based on the comparisons of the analytical results for frames with different number of bays examined in Sections 8.3 and 8.4, the following conclusions can be drawn:

1) The response of exterior plastic hinges is independent of the number of bays in the moment resisting frame. It depends mainly on the out-of-plane bending and torsional strength of the external transverse beams. A method for calculating the slab contribution to the negative flexural over-strength of the exterior plastic hinge proposed in Section 6.5.1.2 and hence is applicable to all cases regardless of the number of bays.
2) The response of interior plastic hinges depends on their locations within the frame. The behaviour depends mainly on the minimum number of bays and columns that are confining the plastic hinge. This is illustrated in Figure 8-20, where the plastic hinges marked with the same symbol behave in a similar manner.
3) Number of bays in the moment resisting frame was found to have little effect on the elongation of exterior and interior plastic hinges. For the sub-assemblies investigated herein, elongation of interior and exterior plastic hinges is approximately 3% and 1% of the beam depth, respectively at 3% drift. However, these values were found to change with the slab reinforcement ratio.

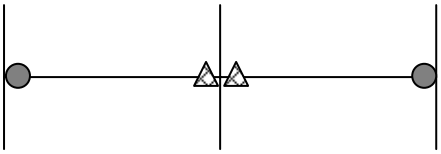

(a) 2-bay perimeter frame

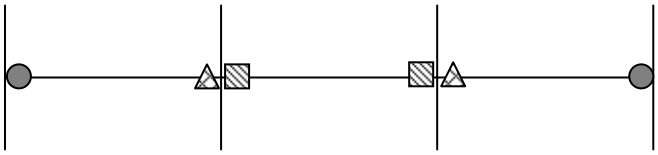

(b) 3-bay perimeter frame

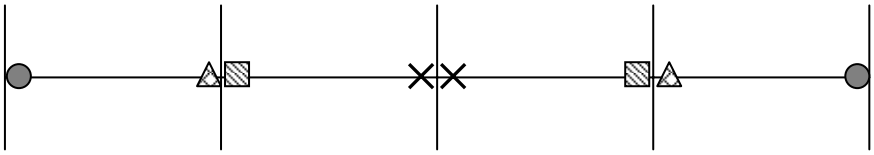

(c) 4-bay perimeter frame

Figure 8-20. Schematic diagram identifying plastic hinges with similar behaviour

8.5 2-BAY INTERNAL MOMENT RESISTING FRAME

8.5.1 Model Set-up

The layout of the 2-bay internal frame-floor model is shown in Figure 8-21. It is similar to the 2-bay perimeter frame examined in Section 7.2 except that additional floor slabs and transverse beams were added on the other side of the main beam to simulate the behaviour of an internal moment-resisting frame. The model is symmetrical about the x-axis. This modelling setup assumed the continuity effect at the two ends of the floor slab is stiff similar to that assumed in the experiment. This implies a seismic moment resisting frame is located between laterally flexible frames designed to resist gravity loads, which do not form plastic hinges in the beams.

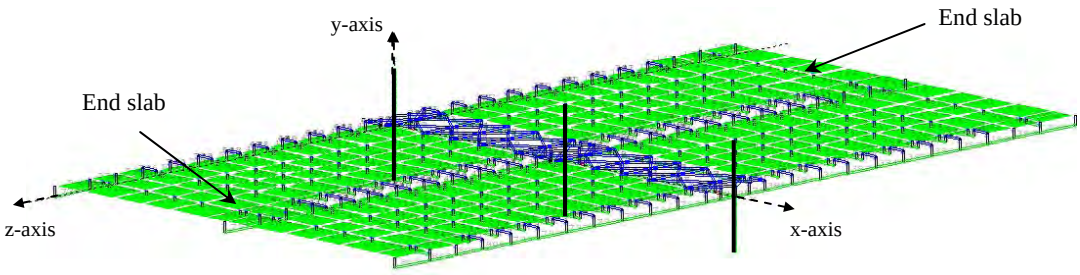

Figure 8-21. Layout of the 2-bay internal frame-floor model

It should be noted that the cases examine above is an unusual case, which would seldom arise in practice. In cases where there are several moment resisting frames immediately adjacent to each other, such as the one shown in Figure 8-22. The end slab should be replaced by moment-resisting frame and modelled accordingly. This case is not examined in this dissertation.

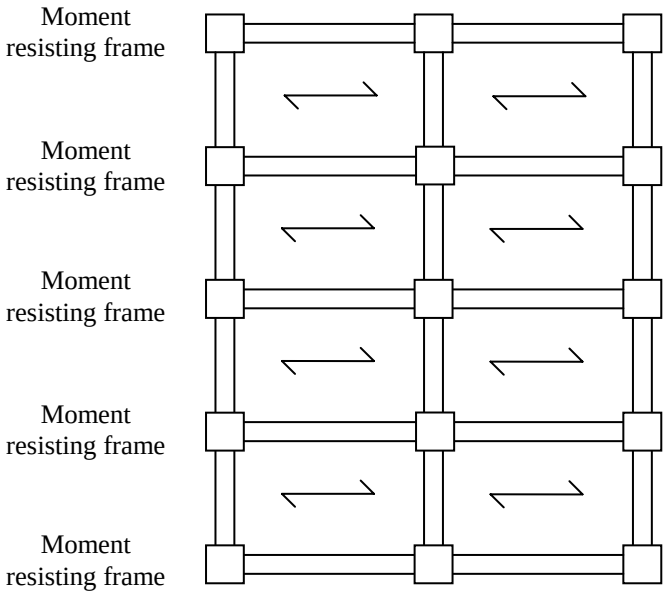

Figure 8-22. Physical layout of a schematic building

8.5.2 Analytical Predictions

8.5.2.1 Predicted Axial Force in the Plastic Hinges

Figure 8-23 compares the predicted axial forces in the plastic hinges in the internal and perimeter frame models. As the behaviours of PH1 and PH3 are similar to the behaviours of PH4 and PH2, respectively, only PH1 and PH3 are discussed herein. It can be seen that the axial force sustained in the interior plastic hinges in the internal frame are about twice of that in the corresponding perimeter frame. The analytical predictions were only plotted up to the first complete cycle at 2.5% drift. This is because the results became ambiguous due to crushing of core concrete in the interior plastic hinges in the internal frame model.

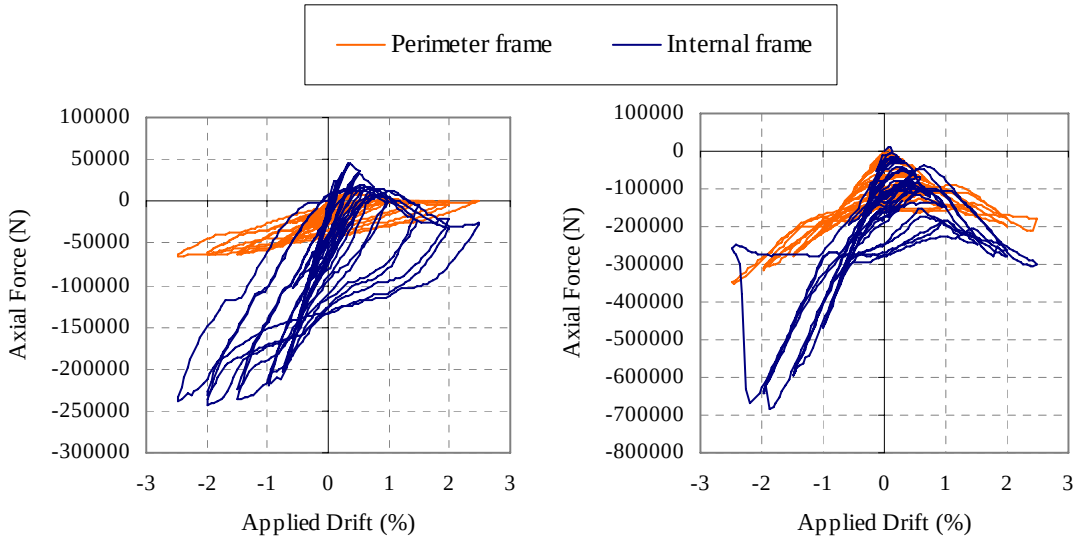

(a) PH1 (b) PH3

Figure 8-23. Predicted axial force in the plastic hinges in 2-bay internal and perimeter frames

The peak axial compression force sustained in the exterior plastic hinges in the internal frame is approximately 4 times of that in the perimeter frame. This is because the continuous transverse beam connected to the external column allows out-of-plane moment to develop in the beam-column joint due to continuity effect. Therefore, the axial force that can be sustained in the exterior plastic hinges increases. This is illustrated schematically in the figure below.

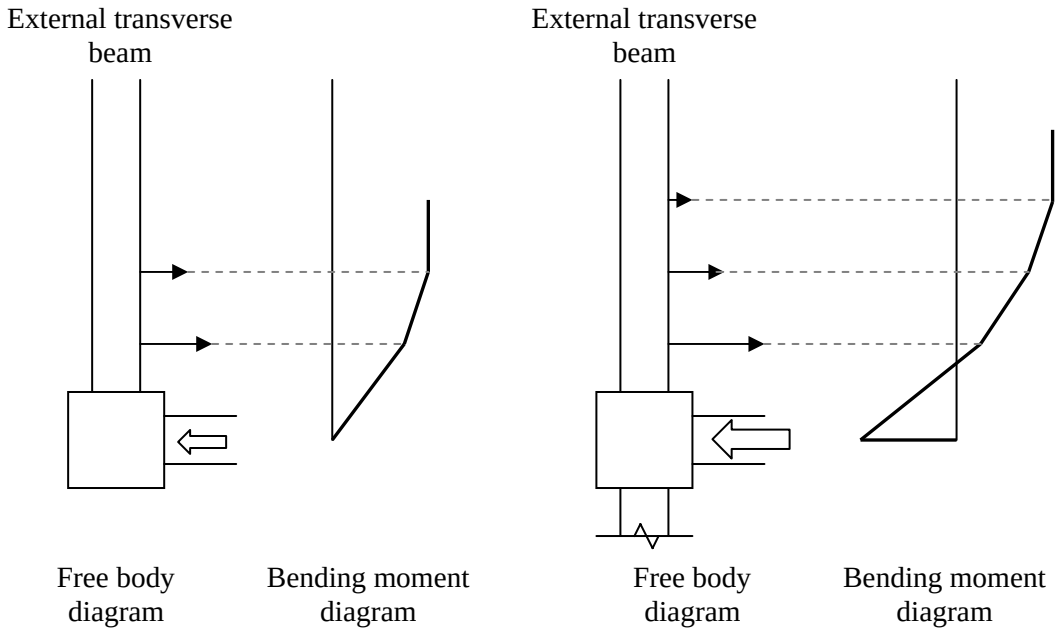

Figure 8-24. Schematic diagram showing the moment distributions in the external transverse beam in a perimeter frame and an internal frame

The maximum axial compression force sustained in the exterior plastic hinge of the internal frame, estimated using the method proposed in Section 6.5.1.2, is 250kN. This matches satisfactorily with the analytical predictions of 240kN.

8.5.2.2 Predicted Elongation in the Plastic Hinges

The predicted elongation in the plastic hinges for internal and perimeter frame models are plotted in Figure 8-25. It can be seen that the predicted elongation of plastic hinges is much smaller in the internal frame. This is expected as the predicted axial compression force in the plastic hinges is larger in the internal frame. The average elongation in the exterior and interior plastic hinges in the internal frame is 1.5% and 0.5%, respectively (roughly half of those in the perimeter frame).

In PH3, there is a sharp decrease in elongation during the first negative 2% drift cycle. This is due to crushing of core concrete, which also corresponds to a loss in axial load carrying capacity, as observed in Figure 8-23(b).

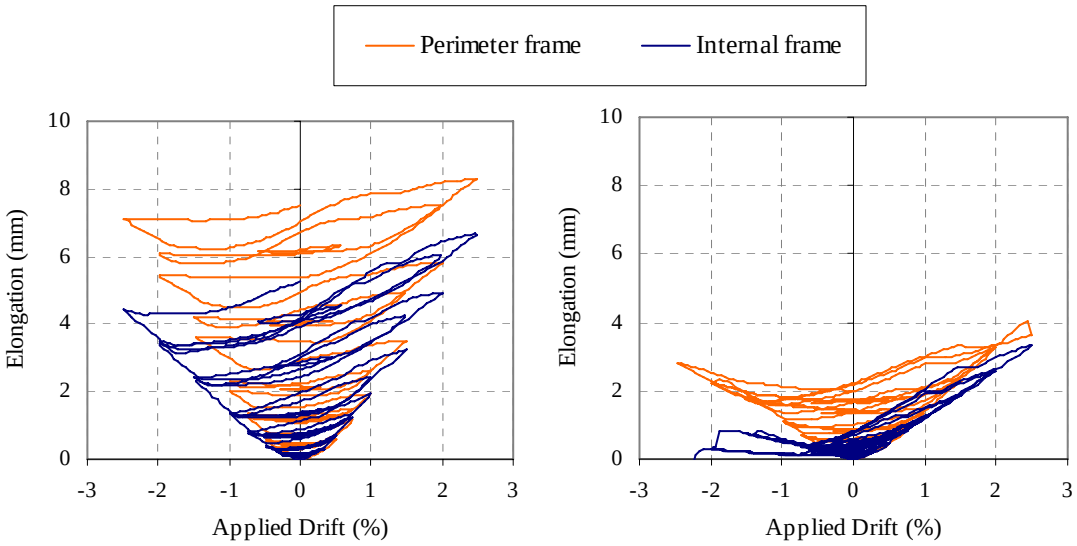

(a) PH1 (b) PH3

Figure 8-25. Predicted elongation in the plastic hinges in 2-bay internal and perimeter frames

8.5.2.3 Predicted Crack Widths between Transverse Beams and Floor Slab Interface

The predicted crack widths along the transverse beams and floor slab interface at the peak of first negative 2% drift are summarised in Table 8-10. As the behaviour is symmetrical about the longitudinal beam, the predictions only one side of the floor slab is given in this table. It can be seen that the crack widths along the internal transverse beam are smaller in the internal frame than those in the perimeter frame. This is because elongation of interior plastic hinges is much smaller in the internal frame. The crack widths along the external transverse beam are greater in the internal frame than those in the perimeter frame, despite elongation in the plastic hinge being smaller in the internal frame. It is postulated that this is due to the different deflected shapes as shown in Figure 8-26.

Table 8-10. Crack widths along the transverse beams and floor slab interface at the peak of first negative 2% drift cycle in 2-bay internal and perimeter frames

Distance from the column face (mm)	Crack widths along transverse beam (mm)			
	Behind PH1		Behind PH3	
	Perimeter frame	Internal frame	Perimeter frame	Internal frame
275	2.24	2.62	1.67	1.15
775	0.01	0.44	0.95	0.57
1275	-0.01	-0.01	0.67	0.32
1775	-0.00	-0.00	0.41	0.20
2275	-0.00	-0.00	0.20	0.11
2775	-0.00	-0.00	0.04	0.02

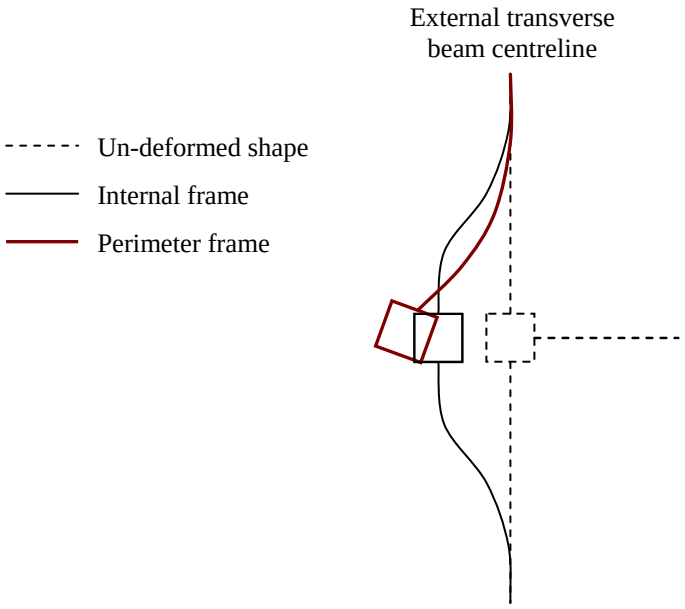

Figure 8-26. Deflected shapes of the external transverse beam in the internal and perimeter frames

8.5.2.4 Predicted Deformation in the Linking Slab

Figure 8-27 shows the axial deformation in the truss elements used to model the linking slab and the corresponding averaged shear deformation across the linking slab interpreted from each pair of diagonals and ties at the peak of the first negative 2% drift cycle. The units for these values are in millimetres. The deformation pattern observed in this frame is quite different to that observed in the perimeter 2-bay frame.

The diagonal compression struts in the floor slab developed in different directions during the positive and negative drift cycles.

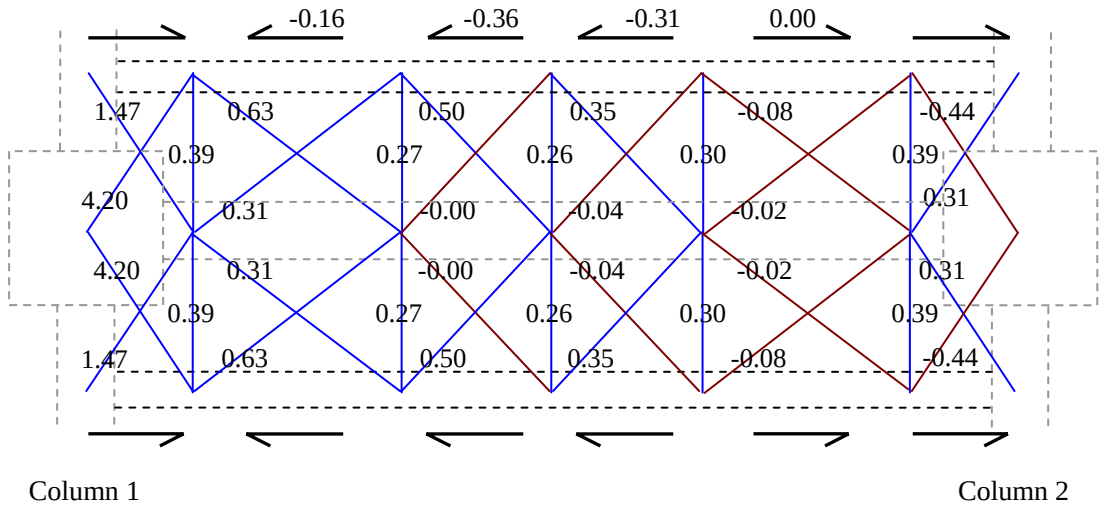

(a) Bay 1

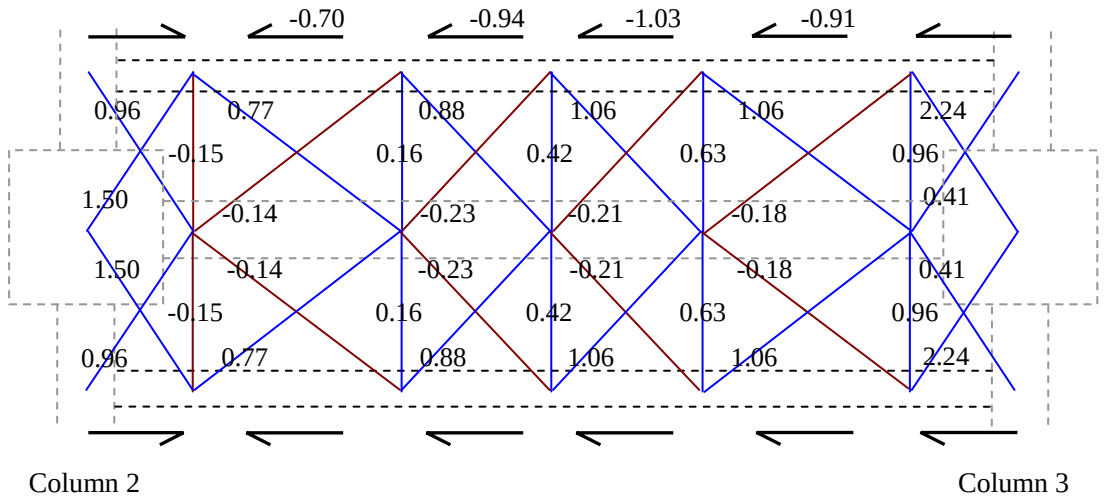

(b) Bay 2

Figure 8-27. Axial deformations in the truss elements modelling the linking slab at the peak of first negative 2% drift cycle (units in mm)

Figures 8-28 and 8-29 show the schematic diagrams of the diagonal cracks developed in the linking slab. The method for deciding whether diagonal cracks form in the floor slab is described earlier in Section 8.3.2.4. It should be noted that the angle of the diagonal cracks drawn in the figures below does not necessarily represent the angle of the diagonal cracks that are expected to occur in reality. It can be seen that the

diagonal cracks developed in the floor slab in Bay 1 are predominantly inclined towards the left column in the negative drift cycle. This is very different to the behaviour of the perimeter frame where the diagonal cracks were all pointing towards the internal column.

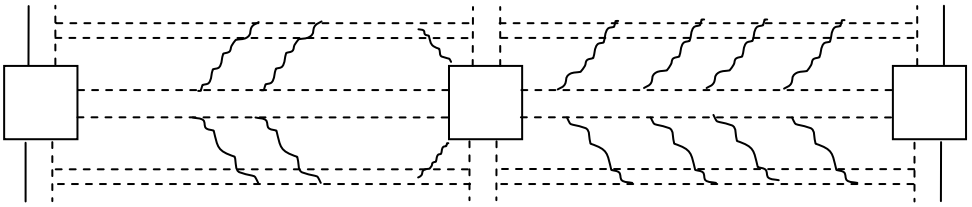

Figure 8-28. Diagonal crack pattern in the linking slab at the peaks of negative 2% drift cycles

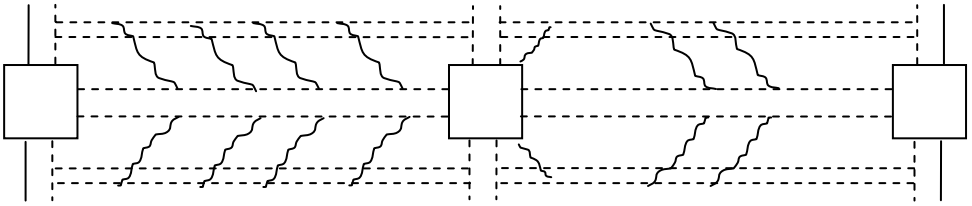

Figure 8-29. Diagonal crack pattern in the linking slab at the peaks of positive 2% drift cycles

8.5.2.5 Predicted In-Plane Bending Action in the Floor Slab

Figure 8-30 shows the predicted force per unit length in the floor slab at a distance 4025mm from the centre line of the moment resisting frame at the peak of first negative 2% drift cycle. It can be seen that there is a small bending action in Bay 2. This is because elongation of PH3 is pushing the beam in Bay 2 outwards. The bending action is not apparent in Bay 1. This is because the difference in the level of axial force sustained in PH1 and PH2 is small.

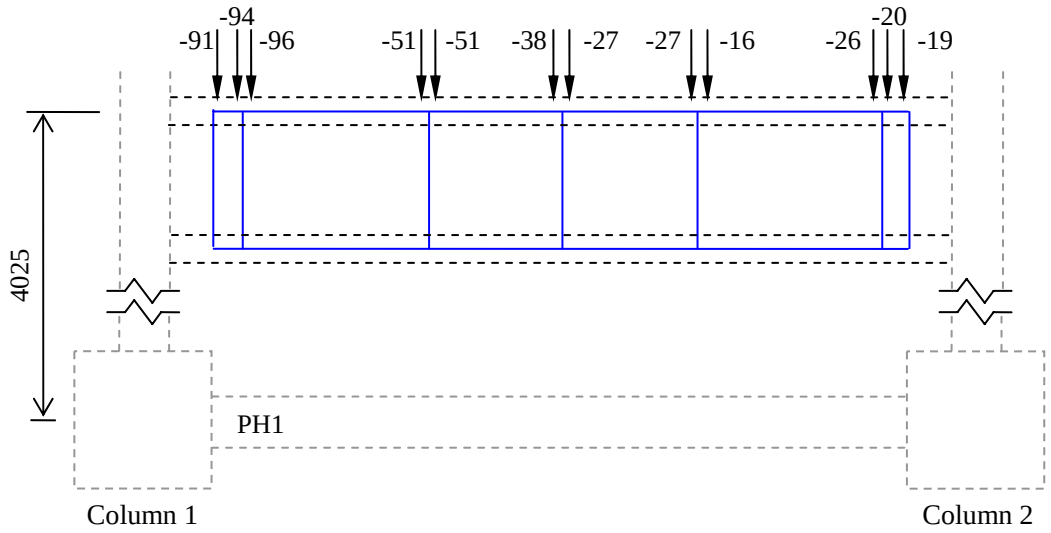

(a) Bay 1

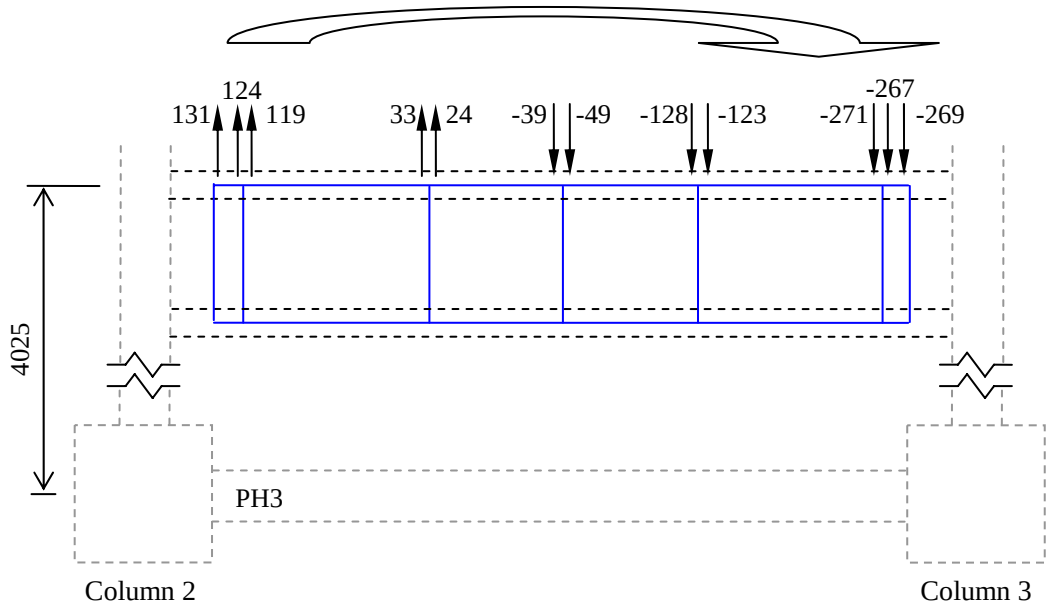

(b) Bay 2

Figure 8-30. Force per unit length in the floor slab at the peak of first negative 2% drift cycle (units in N/mm)

8.5.2.6 Mechanisms Contributing to Axial Force in the Interior Plastic Hinges

A summary of the internal forces along the internal transverse beam and floor slab interface is summarised in Table 8-11 where ΣT is the sum of the tension force across the cracks on both side of the frame, C_{beam} is the axial compression force sustained in the plastic hinge, and F_{deep_beam} is the force contribution from the floor

acting as a deep beam on both side of the frame, as defined in Section 7.3.8. It can be seen that despite the axial compression force in the interior plastic hinge being doubled that in the perimeter frame in Section 7.3.8, the magnitude of F_{deep_beam} is much smaller. It is believed that this is due to different floor deformation mechanisms as shown in Figure 8-31.

Similar to that described in Section 6.3.8, elongation of interior plastic hinge induces shear force along the longitudinal beam and floor slab interface as well as tension force in the slab reinforcement across the transverse beam and floor slab interface. These forces induce a counter-clockwise moment which is believed to be resisted predominantly by the moment in the floor slab across the longitudinal beam due to deformation compatibility requirement. This is different to the mechanisms in the perimeter frame where the moment is resisted solely by the end slab.

Table 8-11. Contribution of axial force in PH3 in the 2-bay internal frame

Internal forces	**Column drift**			
	-2.5% (1)	**-2.0% (1)**	**-1.5% (1)**	**-1.0%(1)**
ΣT (kN)	270	698	654	510
C_{beam} (kN)	256	638	594	463
F_{deep_beam} (kN)	14 (5%)	60 (9%)	60 (9%)	47 (9%)

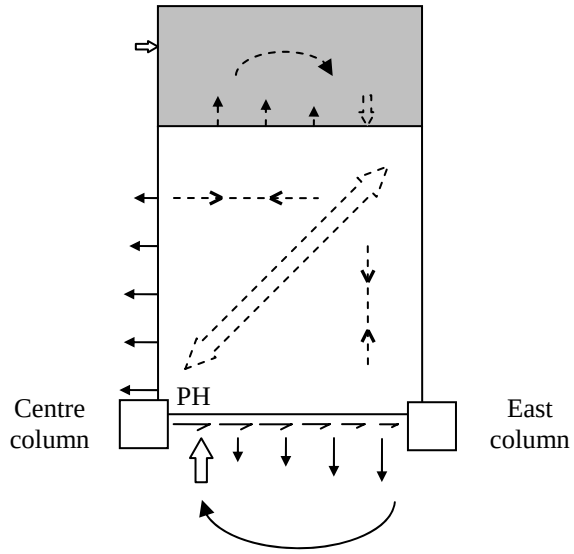

Figure 8-31. Equilibrium criteria of a floor slab in an internal frame at the peak of a negative drift cycle

8.6 CONCLUSIONS

The effect of different structural configurations on the cyclic response of the frame-floor sub-assembly was examined through several case studies. The following conclusions can be drawn based on the analytical results:

1. The analysis has shown that by reducing the slab reinforcement ratio by half, the slab contribution to the plastic hinges only reduces by 20% and 35% in the exterior and interior plastic hinges, respectively. Consequently, considering the slab contribution by specifying a constant effective flange width such as that adopted in the code is not appropriate especially for cases where different slab reinforcement ratios are used. More analytical studies are required to develop a simple relationship that can be used by the design engineers.
2. The amount of slab reinforcement content was found to have a significant effect on the elongation of interior plastic hinges, whereas its effect on the elongation of exterior plastic hinges were less appreciable. Reducing the reinforcement content reduced axial compression force and hence increased elongation in the plastic hinges. More analytical studies are required to develop a simple relationship to quantify the magnitude of elongation in the interior plastic hinges with different slab reinforcement ratios.
3. The slab contribution to the negative flexural over-strength of exterior plastic hinges appeared to be independent of the number of bays in the moment resisting frame. However, the slab contribution to the negative flexural over-strength of interior plastic hinge was found to vary with its location relative to the frame. For the cases examined in this chapter, the behaviour depends mainly on the minimum number of bays and columns that were confining the plastic hinges. In the 4-bay frame, the axial compression force in the interior plastic hinges increased by 22%. More analytical studies are required to develop a simple relationship between the number of bays to the slab reinforcement contribution of the interior plastic hinges.
4. The number of bays in the moment resisting frame has little effect on the elongation of exterior and interior plastic hinges. For the sub-assemblies examined herein, elongation of interior and exterior plastic hinges was approximately 1% and 3% of the member depth, respectively. However, this value was found to change with the slab reinforcement ratio.

5. For the structural arrangement investigated herein, the slab reinforcement contribution to the exterior plastic hinges in an internal frame was approximately four times of that in a perimeter frame. Whereas the slab contribution to the interior plastic hinges in an internal frame was approximately twice of that in a perimeter frame. Higher axial forces sustained in plastic hinges of internal frames led to smaller elongations compared to those in a perimeter frame. This may also cause the concrete in the interior plastic hinges to crush before reaching the design limit of 2% drift. More analytical studies are required to develop simple relationships to quantify elongation of plastic hinges and the slab reinforcement contribution of plastic hinges in internal frames.
6. The method proposed in Section 6.5.1.2 for calculating the slab contribution to the negative flexural over-strength of the exterior plastic hinge has been validated with the finite element results. This method can be adopted to determine the slab reinforcement contribution to the negative over-strength of exterior plastic hinges.

8.7 REFERENCES

Shima, H., Chou, L., and Okamura, H. (1987). "Micro and macro models for bond behaviour in reinforced concrete." *Journal of Faculty of Engineering, University of Tokyo*, 39(2), 94-133.

Standards New Zealand. (2006). *Concrete structures standard: NZS 3101:2006*, Standards New Zealand, Wellington.

9 CONCLUSIONS AND RECOMMENDATIONS

In this dissertation, the seismic behaviour of reinforced concrete (RC) frames with floor slabs containing precast-prestressed floor units has been investigated. The study focused on four distinct parts: (i) development of a plastic hinge element to predict elongation response of RC plastic hinges; (ii) experimental investigation on frame-floor interaction and its effect on the flexural strength of beam plastic hinges; (iii) development of an analytical model to simulate the interaction between RC frames with floor slabs in a single storey; and (iv) analytical investigation on the key parameters that affect the level of slab participation to the strength of RC beams. The main findings and limitations from this study are described in this chapter together with recommendations for future research.

9.1 KEY FINDINGS

9.1.1 Development of Plastic Hinge Element

In order to analytically predict the interaction between RC beam plastic hinges and floor slabs, elongation of plastic hinges must be captured by analytical models. A two-dimensional multi-spring plastic hinge element capable of predicting elongation response was proposed and verified in Chapter 2 and refined in Chapter 3. This element consists of a series of longitudinal and diagonal springs connected between rigid links at two ends. The longitudinal springs, representing concrete and reinforcing bars, were used to model flexural and axial load response, and the diagonal springs were used to model the diagonal compression struts in the plastic hinges, and to provide shear resistance.

Sensitivity studies on the parameters associated with the proposed plastic hinge element have shown that the predicted response of plastic hinges depends on the length of the plastic hinge element, the length of the steel springs and the amount of “contact stress effect” in the concrete springs. However, it is not sensitive to the stiffness of the diagonal struts. Equations to quantify these parameters were developed based on the mechanisms observed in the tests. Comparisons of analytical predictions

with experimentally measured results from cantilever beams and frames sub-assemblies have shown that the proposed plastic hinge element generally predicts the flexural, shear and elongation response of ductile RC plastic hinges satisfactorily. It should be noted that considerable scatter in elongation measurements is observed on tests of similar beams. Limitations associated with the plastic hinge element are elaborated in Section 9.2.1

Tests on cantilever beams, which are examined in Chapter 2, showed that plastic hinge in a beam, with no axial force, elongated 3.2% of the member depth before strength degradation occurred. The amount of elongation varies with the level of axial force in the beam. For a beam with an axial compression force of $0.14A_g f_c'$, where A_g is the cross sectional area and f_c' is the concrete compressive strength, elongation reduced to 1.1% of the member depth before strength degradation occurred. For a beam with an axial tension force of $0.13A_s f_y$, where A_s and f_y are the area and yield stress of the longitudinal reinforcement respectively, elongation increased to 4.4% of the member depth before strength degradation occurred.

Shear deformation of plastic hinges was examined in more detail in Chapter 3. Two main mechanisms were identified to contribute to shear deformation: (i) elongation of plastic hinges, and (ii) inelastic extension of shear reinforcement due to plastic hinge rotation. Experimental data collected from the literature on ductile RC beams has shown that shear deformation from elongation of plastic hinges contributes approximately half of the total shear deformation prior to strength degradation. Hence, as an approximation, the modified plastic hinge element assumes the total shear deformation is twice the shear deformation due to elongation.

Comparisons of the proposed elongating plastic hinge element with conventional lumped plasticity models have shown the following advantages:

1. Elongation of plastic hinges during reversed inelastic cyclic deformation can be predicted by the proposed plastic hinge element while elongation cannot be captured at all using the conventional approach. Elongation can have a significant effect on the seismic performance of RC frames, especially when subjected to repetitive inelastic cyclic loadings. It can alter the moment and shear force distributions in frames and increase the moment capacity of beams.

2. The proposed plastic hinge element does not require calibration of any modelling parameters. The intended modelling framework together with the generic path-dependent cyclic material models used for the plastic hinge element generally gives a satisfactory prediction of the cyclic response of RC beams. This is not the case for the conventional approach where the members need to be calibrated prior to the analysis to yield the desired hysteretic response. In the absence of experimental results, the analyst has to use subjective judgment to assign values for the hysteresis parameters.
3. Different mechanisms contributing to the global deformation of plastic hinges (i.e., flexural, shear and elongation deformations) can be separated from the analytical results and traced back to the deformations of each material spring at the element level. This is not possible using the conventional approach.

9.1.2 Effect of Elongation on the Cyclic Response of 2D Frames

The plastic hinge element developed in this research has been implemented in the analyses of two-dimensional frames in Chapter 4. In these analyses, the potential beam plastic hinges in the frame were modelled using the refined plastic hinge element developed in Chapter 3 and the elastic portion of the members were modelled using linear elastic elements. The analytical predictions of these frames were compared with the experimental results obtained from literature. The comparisons have shown that the proposed approach allows elongation of plastic hinges to be captured in the analysis, thereby enabling the effect of elongation on the cyclic response of RC frames to be predicted.

The analytical and experimental results highlighted the importance of elongation on the seismic response of RC frames. Elongation was shown to change the moment, shear force and axial force distributions in frames. In some cases, it increases the moment capacity of beams and consequently the associated structural actions in the columns, which may lead to column yielding instead of the intended beam yielding.

Analytical prediction of a frame, modelled without the elongating plastic hinge elements has predicted different behaviour to that observed in a test of the frame. This

highlights the need to consider elongation of plastic hinges for accurate assessment of the seismic performance of RC frame buildings.

9.1.3 Experimental Investigation of Frame-Floor Interaction

A three dimensional, two-bay, one-storey, half-scale RC frame with floor slabs containing prestressed floor units was constructed and tested in this study. The crack pattern, deformation measurements in the floor slab and the beam plastic hinges, and the actions applied to the columns provided insight into the elongation of plastic hinges and its interaction with the surrounding floor slabs.

It was found that the behaviour of interior and exterior plastic hinges is different. The level of elongation and damage sustained in the interior plastic hinges was much smaller than that observed in the exterior plastic hinges. This was mainly due to difference in the level of restraint provided by the surrounding floor slab to the plastic hinges. The level of restraint imparted on the exterior plastic hinges was limited by the out-of-plane bending and torsional resistance of external transverse beams, whereas the level of restraint imparted on the interior plastic hinges was limited by the slab reinforcement content and the strength of the surrounding floor slab.

The test results indicated that the total moment demand imposed on columns from beam over-strength may be under-estimated by the current New Zealand Standard, NZS 3101:2006 (Standards New Zealand 2006), and the American Concrete code, ACI 318-05 (American Concrete Institute 2005). The increase in bending moments imposed on the columns, in this test, was found to arise due to two main actions: (i) torsional resistance of transverse beams; and (ii) additional tension force from slab reinforcement contributing to the negative flexural strength of beams due to the interaction between elongating plastic hinges and the surrounding floor slabs.

The torsional resistance of transverse beams contributed to approximately 18% of the total lateral resistance of the frame in this experiment. It should be noted that as one end of the transverse beams are restrained against twisting, it is expected that the contribution would be smaller in a real building. While it may be argued that the contribution would reduce significantly under bi-directional loading once plastic

hinges have formed in the transverse beams, the strength enhancement from torsional resistance of transverse beam should be explicitly specified in the code to ensure that an adequate column to beam strength hierarchy is maintained under the worse case scenario.

The additional slab reinforcement tension force contributing to the negative flexural over-strength of beams, specified in NZS 3101:2006, was found to be under-estimated for the interior plastic hinges and over-estimated for the exterior plastic hinges. The experimentally interpreted effective flange widths, for calculating the negative over-strength of interior and exterior plastic hinges were 1670mm and 620mm respectively, compared to 1200mm and 900mm specified in the code. However, the parametric study in Chapter 8 has shown that the effective flange widths changes with the amount of reinforcement content in the slab. It should be noted that the test was carried out under uni-directional loading. For bi-directional loading, the slab participation to the over-strength of beam plastic hinges may be lower than that observed in this experiment.

A method for assessing the slab reinforcement contribution to the negative over-strength of exterior plastic hinges is proposed in Chapter 6. The method was developed based on force and moment equilibrium considerations of the transverse beams and was validated against the experimental and analytical results obtained in this study. The proposed method provides a direct estimation on the amount of slab reinforcement participating to the negative over-strength of exterior plastic hinges and can be adopted for design purposes.

9.1.4 Development of 3D Frame-Floor Analytical Model

A computational model was set up in Chapter 7 to predict the cyclic response of the frame-floor sub-assembly tested in this project. The model contained the newly developed plastic hinge element representing potential plastic hinges, and axial strut-and-tie elements representing the linking slab between the longitudinal beams and the first prestressed floor unit. These allow beam plastic hinges to interact with floor. The model was shown to predict adequately the strength and hysteretic response of the sub-assembly. It captured the deformation mechanisms such as elongation of plastic

hinges, crack opening at the transverse beam-floor slab interface, and shear deformation in the linking slab.

The internal forces acting across the transverse beam-floor slab interfaces and the corresponding axial forces in the seismic beams and end slabs were extracted from the analysis. These actions provide insight into the interaction between the floor slab and elongation of plastic hinges, which could not be determined from the experimental results. The actions around the internal column showed that the slab reinforcement provides additional tension force, which increases the axial restraint to the interior plastic hinges when subjected to both negative and positive bending. These additional forces were acting in the same line as the slab reinforcement, i.e., at the mid-height of the concrete topping. Consequently, it has a more significant effect on the negative flexural strength than the positive flexural strength of the interior plastic hinges. The actions around the external column showed that the slab reinforcement provides additional tension force which increases the axial restraint to the exterior plastic hinges when subjected to negative bending only. This increased the negative flexural strength of exterior plastic hinges.

9.1.5 Effect of Structural Arrangement of RC Frames on the Strength and Elongation of Plastic Hinges

Analytical studies were carried out to examine the effects of different structural configurations on the cyclic response of RC frames. It was shown that the effective flange width changes with different slab reinforcement ratios. Therefore, specifying a constant effective flange width to consider the slab contribution to the negative flexural strength of beams, as recommended by the New Zealand and ACI codes, may not be adequate. The effective flange width was found to increase as the slab reinforcement ratio decreases.

Case studies of frames with different numbers of bays have shown that the level of slab contribution to the strength of beam plastic hinges depends on the location of plastic hinges within the frame. The number of bays was found to have negligible influence on the strength of exterior plastic hinges. However, the strength of interior plastic hinges was found to depend on the location of the plastic hinges, in particular,

the minimum number of bays and columns that are confining the plastic hinges. It was found that the number of bays in a frame has little influence on elongation response of both interior and exterior plastic hinges. In general, elongations of interior and exterior plastic hinges at 3% drift are approximately 1% and 3% of the member depth, respectively.

The extent of slab contribution to the negative over-strength of interior plastic hinges increases as the number of bay increases. The slab contribution increased by 22% from 2-bay to 4-bay frames and may increase further with more bays. The method proposed to calculate the negative over-strength of exterior plastic hinges in Chapter 6 has shown good agreement with the analytical predictions in Chapter 8.

For the internal frame examined in this study, the predicted slab contribution to the exterior plastic hinges in an internal frame is approximately four times of that in a perimeter frame. On the other hand, the slab contribution to the interior plastic hinges in an internal frame is approximately twice of that in a perimeter frame. This is expected as the interior plastic hinges in the internal frame are confined by floor slabs on both sides of the beams. The maximum level of slab contribution may depend on the confinement of the core concrete (i.e., when the crushing strain of core concrete is reached) and it is anticipated that the applied displacement history may also be important. It should be noted that as there could be many different structural arrangements available in practice, the values stated above do not represent the generic value for all cases.

9.2 LIMITATIONS AND RECOMMENDAITONS FOR FUTURE RESEARCH

9.2.1 Plastic Hinge Element

Although significant advances have been made with the development of the plastic hinge element in this study, there are limitations associated with the current model where further research and refinement may be required:

1. The proposed plastic hinge element is based on mechanisms typical of ductile RC beams, where the amount of shear deformation from stirrup extension is

smaller than the flexural deformation. In this situation, the shear deformation in the plastic hinge element was approximated as a function of elongation. However, for nominally ductile or non-ductile beams, elongation was found to be smaller and the proportion of shear deformation from stirrup extensions was found to be much greater than those observed in the ductile beams. Consequently, the proposed shear deformation model may not be applicable to nominally ductile or non-ductile beams. Further research is required to verify the applicability of the proposed plastic hinge element in predicting elongation and shear response of beam plastic hinges with limited ductility.

2. The length of the plastic hinge element is calculated assuming that the shear resistance of concrete in plastic hinges is negligible. This may not be the case when significant axial compression is applied to the beam. As there are currently no results available in literature, more research is required to examine the shear contribution of concrete in plastic hinges with different levels of axial force.
3. The length of tension shift is required for calculating the stiffness of the steel springs. This is currently taken as a constant value. In reality, the length of tension shift would change with different levels of axial force. As there is currently no literature available on this inter-relationship, more studies are required to quantify the effect of axial force on the length of tension shift.
4. The plastic hinge element developed in this study does not take into account localised bond slip between concrete and reinforcing bars and pull-out of reinforcing bars from the beam-column joints. Consequently, the plastic hinge element by itself cannot predict the additional pinched hysteretic response from these effects. To accurately assess the force-displacement response of ductile moment resisting frames, additional joint/interface/bond element considering these localised effects needs to be developed and implemented into the analytical framework.
5. Buckling and low-cycles fatigue of longitudinal reinforcement in the plastic hinge is not modelled in the analysis. Consequently, strength degradation cannot be predicted with the current model. As most of the bar buckling models were developed based on uni-axial cyclic tests, these models cannot be used to accurately predict the buckling phenomenon in RC plastic hinges, where local yielding of stirrups in a plastic hinge causes the longitudinal

reinforcement to bent, which reduces the buckling resistance of the bars. More research is required to developed a bar buckling model that can be implemented into the plastic hinge element.

6. Shear deformation is generally under-estimated at large displacement cycles for beams with applied tension. As a result, rotation and elongation are over-estimated in the analysis. Further research is required to enable the post-peak response of the plastic hinges to be captured in the analytical model.
7. The plastic hinge element has not been validated against beam tests with bi-directional loading. Its accuracy in predicting the combined flexural and torsional responses of plastic hinges should be examined in the future.

9.2.2 Application of the Plastic Hinge Element

Most conventional RC frame analysis models represent beams by line elements with lumped plasticity at the member ends. This approach cannot capture elongation and its effect on the seismic response of RC frames. With the elongating plastic hinge element developed in this project, elongation and its effect on frame response can be captured analytically. Further studies with time-history analyses are required to quantify the effects of elongation on the seismic performance of RC frame buildings.

9.2.3 3D Frame-Floor Model

In the 3D frame-floor model, a major portion of the floor slab was modelled using elastic shell elements, as non-linear shell elements are not available in RUAUMOKO3D (Carr 2008). In the sub-assembly test, cracks developed in the floor slab decreased the stiffness and hence reduced its resistance to elongation at the interior plastic hinges. As the slab was modelled using elastic shell elements, the slab contribution to the negative over-strength of interior plastic hinges was over-estimated in the analysis. The accuracy of the prediction should improve if non-linear shell elements were available.

The torsional response of the transverse beams was modelled using bi-linear hysteresis rule in the analysis due to the limitation with the current RUAUMOKO3D.

To capture the highly pinched torsional response of the transverse beams as observed in the test a more appropriate analytical model is required.

The current truss model developed for linking slab does not allow for out-of-plane moment and shear actions in the slab. This is applicable in cases where the prestressed floor units are supported on transverse beams connected to the columns and the linking slab is sufficiently flexible so that relatively small differential vertical displacement between the prestressed floor units and the main beam does not damage the precast floor units. However, this model needs to be modified to represent cases where the prestressed floor units span past a column, or where the linking slab is short and stiff such that the force transfer due to the vertical differential movement can damage the precast units. In these situations, the level of tension force contributing to the negative flexural strength of plastic hinges, next to the column, is influenced by the out-of-plane flexural and shear capacities of the linking slab and prestressed floor units. A method for modelling this effect has been proposed by Lau (2007) and over-strength calculations based on this action are included in NZS 3101:2006.

For frames coupled with floor slabs, it is difficult to determine the flexural strength and over-strength of plastic hinges. Therefore, the length of the plastic hinge element and the length of steel springs are difficult to predetermine without experimental data. Consequently, these lengths must be assumed. For accurate analytical predictions, the plastic hinge parameters should be revised based on the analytical prediction after an analysis to ensure that the initial assumptions are correct.

9.2.4 Parametric Study on 3D Frame-Floor Sub-Assemblies

The slab reinforcement ratio and the number of bays in a frame have been identified as important parameters that influence the cyclic behaviour of RC frames containing prestressed floor units. More research with time-history analyses are required to quantify the effect of these parameters on the cyclic response of frames and to develop simple relationships that are suitable for design purposes.

9.3 REFERENCES

American Concrete Institute. (2005). *Building code requirements for structural concrete and commentary (ACI 318M-05)*, American Concrete Institute, Farmington Hills, Michigan.

Carr, A. J. (2008). "RUAUMOKO3D - Inelastic dynamic analysis." Department of Civil Engineering, University of Canterbury, Christchurch, New Zealand.

Lau, D. B. N. (2007). "Influence of precast prestressed flooring on the seismic performance of reinforced concrete perimeter frame buildings." *Report Number 653*, Dept. of Civil and Environmental Engineering, University of Auckland, Auckland, New Zealand.

Standards New Zealand. (2006). *Concrete structures standard: NZS 3101:2006*, Standards New Zealand, Wellington.

APPENDIX A. CONCRETE CONSTITUTIVE MODEL

To formulate an accurate reinforced concrete plastic hinge model, reliable cyclic path-dependent stress-strain (i.e., axial force-displacement) relationship of reinforcing steel and concrete are required. Development of generalised material models based on extensive research is not within the scope of this project. Therefore, existing material models, published in peer reviewed literature, are adopted for this study. The material models are coded in computer language FORTRAN so that it can be incorporated into RUAUMOKO (Carr 2004), a non-linear dynamic time history analysis program. Minor modifications were made to simplify the concrete model and to allow users to vary the contact stress effect. Background related to the material models adopted in this study as well as the modifications made to the concrete model are summarised below.

A.1 REINFORCED CONCRETE MODEL

It is known that reinforced concrete (RC) member behaves non-linearly due to cracking and bond between concrete and reinforcing bars. The development of the concrete model adopted in this study is described in detail in *'Nonlinear Analysis and Constitutive Models of Reinforced Concrete'* by Okamura and Maekawa (1991) and *'Nonlinear Mechanics of Reinforced Concrete'* by Maekawa et al. (2003).

The model was developed and verified against uni-axial experimental tests conducted at the University of Tokyo. It was derived using fixed crack theory where cracks are regarded as being geometrically fixed, once occurred. Smeared crack approach was used to obtain an averaged-stress/averaged-strain relationship. The model is path-dependent which can take into account any cyclic history.

The overall concrete model consists of four distinct parts as outlined in the following sections.

i) Compression envelope, which is based on Elasto-Plastic and Fracture (EPF) model, developed by Maekawa and Okamura (1983)

ii) Tension envelope, which is based on tension stiffening model developed by Shima et al. (1987)

iii) Re-contact stress model developed by Maekawa et al. (2003).

iv) Cyclic behaviour for tension-compression loading and compression-tension loading.

A.1.1 Compression Model

The compression model is based on Elasto-Plastic and Fracture theory. The theory idealises reinforced concrete, as a continuum of sliders and elastic springs as illustrated in Figure A-1(a). The sliders represent the permanent plastic deformation of concrete and the elastic springs represent the stress bearing mechanism and stiffness of concrete. As shown in Figure A-1(b), the concrete damage is represented by the fracture of the elastic spring, which leads to a loss in stiffness when the load reverses, as shown in Figure A-1(c) where ε is the average concrete strain, σ is the average concrete stress, K_0 is the fracture parameter that represents the reduction in stiffness, and E_{C0} is the initial concrete stiffness. Compression is defined as negative in this section.

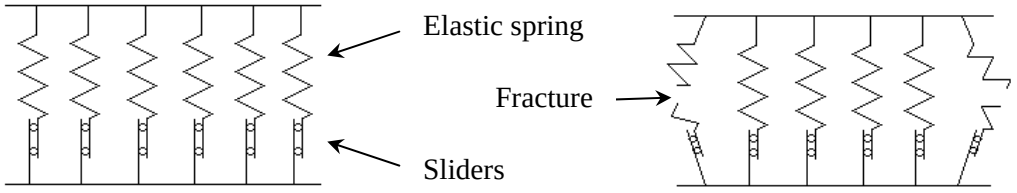

(a) Initial condition (b) Concrete damage under axial force

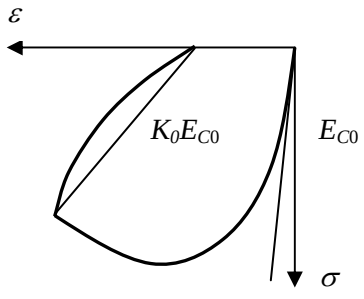

(c) Concrete hysteresis in compression

Figure A-1. Elasto-plastic and fracture model for concrete in compression

The effect of compressive strength reduction due to orthogonal tensile strain of concrete under cyclic actions, observed by Collins and Vecchio (1982) is neglected in the modified model as it requires the magnitude of tensile strain in the orthogonal direction to be computed. As this is not taken into account, the concrete capacity may be over-estimated under reversing cyclic analysis.

A schematic concrete compression hysteresis is shown in Figure A-2. It consists of compression loading, un-loading and re-loading loops. These path dependent compressive stress-strain loops are described in the following sections.

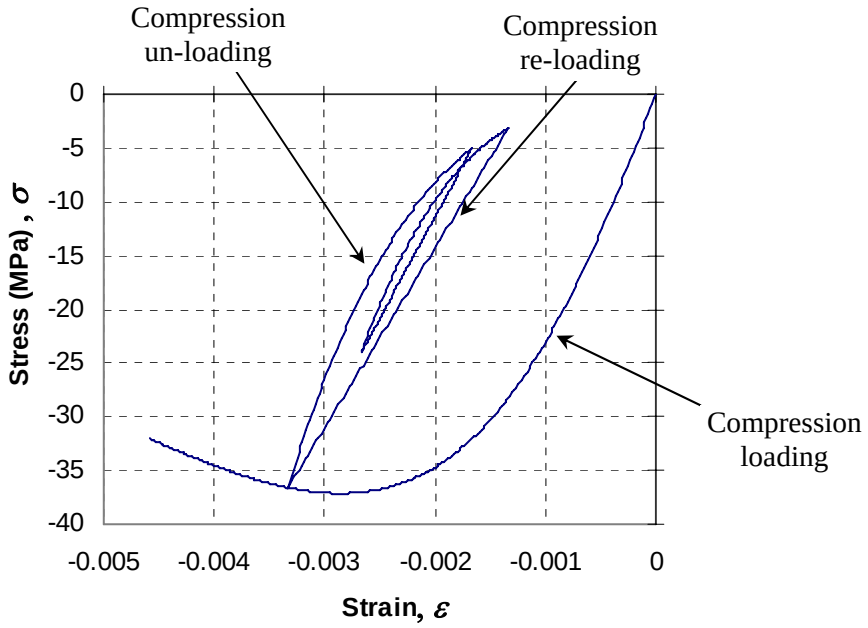

Figure A-2. Schematic concrete hysteresis in compression

A.1.1.1 Compression Loading Envelope where $\varepsilon \le \varepsilon_{C\max}$

The compression loading envelope is described by the equations below. A schematic diagram showing some of the parameters in these equations is plotted in Figure A-3.

$$\sigma = K_0 E_{C0}\left(\varepsilon - \varepsilon_P\right) \tag{A-1}$$

$$K_0 = exp\left\{-0.73\frac{\varepsilon}{\varepsilon_C}\left[1 - exp\left(-1.25\frac{\varepsilon}{\varepsilon_C}\right)\right]\right\} \tag{A-2}$$

$$E_{C0} = 2\frac{f_c^{'}}{\varepsilon_C} \tag{A-3}$$

$$\varepsilon_P = \beta\left\{\frac{\varepsilon}{\varepsilon_C} - \frac{20}{7}\left[1 - exp\left(-0.35\frac{\varepsilon}{\varepsilon_C}\right)\right]\right\}\varepsilon_C \tag{A-4}$$

where

ε is the average concrete strain, $\varepsilon_{C\ max}$ is the maximum compressive strain in the previous cyclic history, σ is the average concrete stress, K_0 is the fracture parameter that represents the reduction in stiffness, E_{C0} is the initial concrete stiffness, ε_p is the plastic strain when the stress is reversed to zero, ε_C is the strain at concrete compressive strength, $f_c^{'}$, and β is the strain rate factor (taken as 1 for dynamic loading and 1.5 to 2 for static loading).

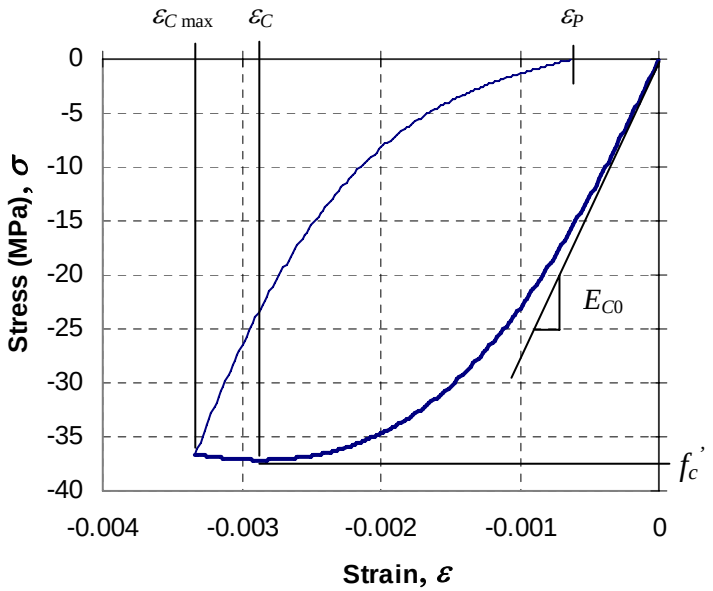

Figure A-3. Schematic concrete compression loading envelope

A.1.1.2 Compression Un-loading Loop where $\varepsilon > \varepsilon_0$

The unloading curve is formulated using polynomial function connecting the unloading point to (ε_p, 0) given by Equations A-5 and A-6. The stress-strain relationship is prescribed by the compression un-loading loop when the current strain, ε, is greater than the strain at previous step, ε_0. It can be seen from Figure A-4 that the shape of the unloading curve is governed by the parameters *PN* and *Slop*.

$$\sigma = K_0 E_{C0} (\varepsilon - \varepsilon_P) \alpha \tag{A-5}$$

$$\alpha = slop + \left(\frac{\sigma_{unl}}{K_0 E_{C0} (\varepsilon_{unl} - \varepsilon_P)} - slop \right) \left(\frac{\varepsilon - \varepsilon_P}{\varepsilon_{unl} - \varepsilon_P} \right)^{PN} \tag{A-6}$$

where

slop and *PN* are unloading parameters taken as K_0^2 and 2 respectively, σ_{unl} and ε_{unl} are stress and strain at the unloading point. Note that the value of K_0 and ε_P are calculated only at the unloading point.

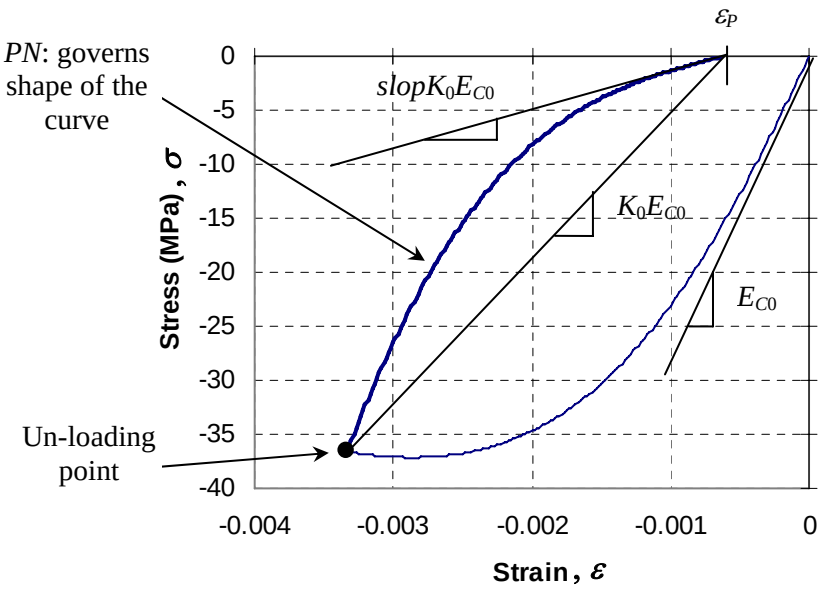

Figure A-4. Schematic concrete compression un-loading envelope

A.1.1.3 Compression Re-loading Loop where $\varepsilon \le \varepsilon_0$ *and* $\varepsilon > \varepsilon_{C\max}$

The reloading loop is a straight line connecting the reloading point to ($\varepsilon_{C\max}$, $\sigma_{C\max}$) as illustrated in Figure A-5 where $\sigma_{C\max}$ is the stress at the maximum compressive strain, $\varepsilon_{C\max}$.

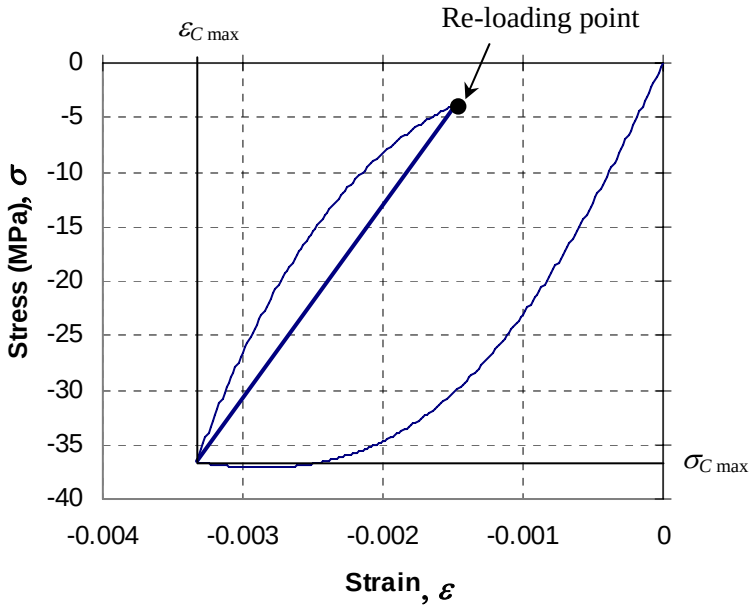

Figure A-5. Schematic concrete compression re-loading envelope

A.1.2 Tension Model

Experimental studies have shown that concrete in RC members can support some tensile force even after cracking. This is referred to as “tension stiffening” effect. The tension resistance after cracking arises mainly due to bond transfer between concrete and reinforcing bar where lugs in the deformed bars push against the surrounding concrete when subjected to tension.

A schematic concrete tension hysteresis is illustrated in Figure A-6. Similar to the compression model, the tension model consists of tension loading un-loading and reloading loops. These path-dependent tensile stress-strain loops are described below.

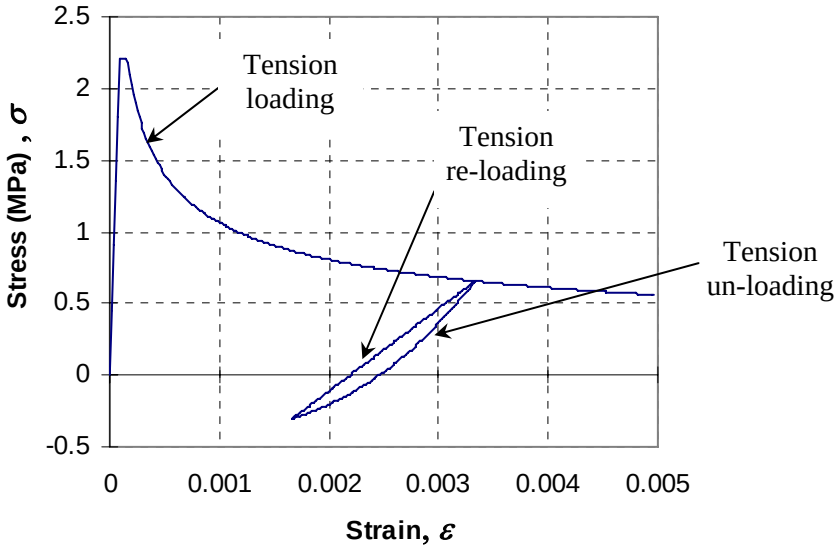

Figure A-6. Schematic concrete hysteresis in tension (Default with beta = 1)

A.1.2.1 Tension Loading Envelope $\varepsilon \geq \varepsilon_{t\max}$

The tension loading envelope consists of initial elastic branch, yield plateau, and tension stiffening curve. The tension stiffening curve is developed based on uni-axial pull-out tests of one dimensional RC member conducted by Shima et al. (1987). The model is independent of crack spacing, element size, and reinforcement orientation and was verified against RC containing two-way reinforcing bars with reinforcement ratios up to 2%. The model also considers the reduction in tensile strength due to concrete damage/fracture in the previous compression history. These loops are described by the equations below. A schematic diagram illustrating the parameters in these equations is shown in Figure A-7.

Elastic branch $0 \leq \varepsilon \leq \varepsilon_t$

$$\sigma = E_{C0} \times \varepsilon \ \leq R_f \times f_t \tag{A-7}$$

Yield plateau $\varepsilon_t \leq \varepsilon \leq \varepsilon_{tu}$

$$\sigma = f_t \ \leq R_f \times f_t \tag{A-8}$$

Tension stiffening $\varepsilon \geq \varepsilon_{tu}$

$$\sigma = f_t \left(\frac{\varepsilon_{tu}}{\varepsilon} \right)^C \ \leq R_f \times f_t \tag{A-9}$$

where

ε_t is the strain when tensile strength of concrete, f_t, is reached, R_f is the tensile strength reduction factor taken as K_0^3 calculated at the maximum compressive strain, f_t is uni-axial tensile strength of concrete taken as $0.36\sqrt{f_c'}$ specified in NZS3101:2006 (Standards New Zealand 2006), ε_{tu} is cracking strain taken as $2\varepsilon_t$, and C is the stiffening parameter that controls the shape of the unloading curve (taken as 0.4 for deformed bars).

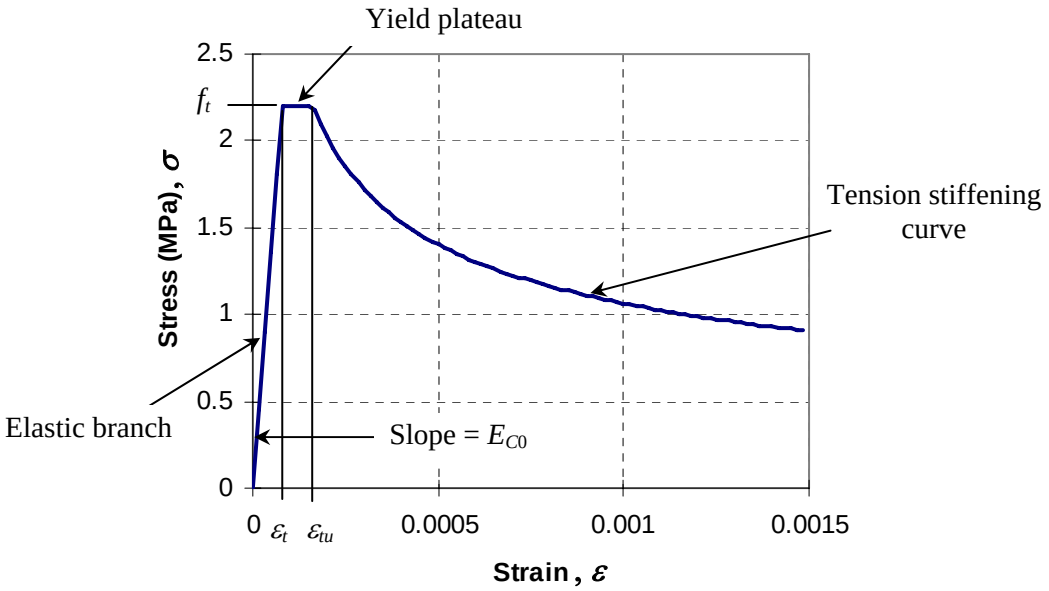

Figure A-7. Schematic concrete tension loading envelope

Note that an averaged-stress/averaged-strain relationship is used for the tension stiffening curve because the stress in concrete is not uniform along the section as illustrated in Figure A-8. It can be seen that the concrete stress is maximum between the cracks and zero at the crack surface.

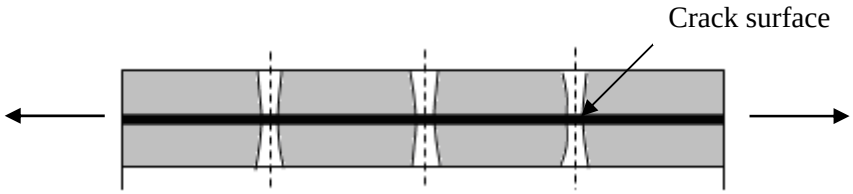

(a) Cracking in reinforced concrete

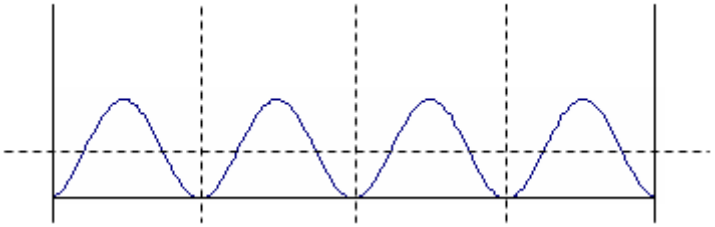

(b) Stress distribution in reinforced concrete

Figure A-8. Stress distribution of concrete under tension when cracks form

A.1.2.2 Tension Un-loading Loop $\varepsilon < \varepsilon_0$

The tension unloading curve is similar to the compression unloading curve where it is also represented by a polynomial function. The unloading envelope is defined by the equations below and is plotted in Figure A-9.

$$\sigma = E_{b0}(\varepsilon - \varepsilon_P)\alpha + \sigma_{b0} \tag{A-10}$$

$$\alpha = slop + \left(\frac{\sigma_{unl} - \sigma_{b0}}{E_{b0}(\varepsilon_{unl} - \varepsilon_P)} - slop\right)\left(\frac{\varepsilon - \varepsilon_P}{\varepsilon_{unl} - \varepsilon_P}\right)^{PN} \tag{A-11}$$

$$E_{b0} = \frac{\sigma_{t\,max} - \sigma_{b0}}{\Delta\varepsilon_{t\,max}} \tag{A-12}$$

$$\sigma_{b0} = -f_t\left(0.05 + 0.15\frac{\Delta\varepsilon_{t\,max}}{5\varepsilon_{tu}}\right) > -0.2\,f_t \tag{A-13}$$

where

E_{b0} is the unloading stiffness, σ_{b0} is the residual compressive bond stress, s*lop* and *PN* are unloading parameters that govern the shape of the unloading curve taken as 0 and 3 respectively, $\sigma_{t\ \max}$ is the stress at maximum tensile strain and $\Delta\varepsilon_{t\ \max}$ is the maximum incremental tensile strain taken as - ε_P, where $\varepsilon_{t\,\max}$ is the maximum tensile strain in previous steps.

Modification was made for calculating the residual compressive bond stress. This is because the original equation, Equation A-13, did not have an upper bound limit, where the value could become unrealistic for concrete in the plastic hinges where significant tensile strain is expected to occur. Hence, for simplicity, the compressive bond stress was limited to -0.2f_t.

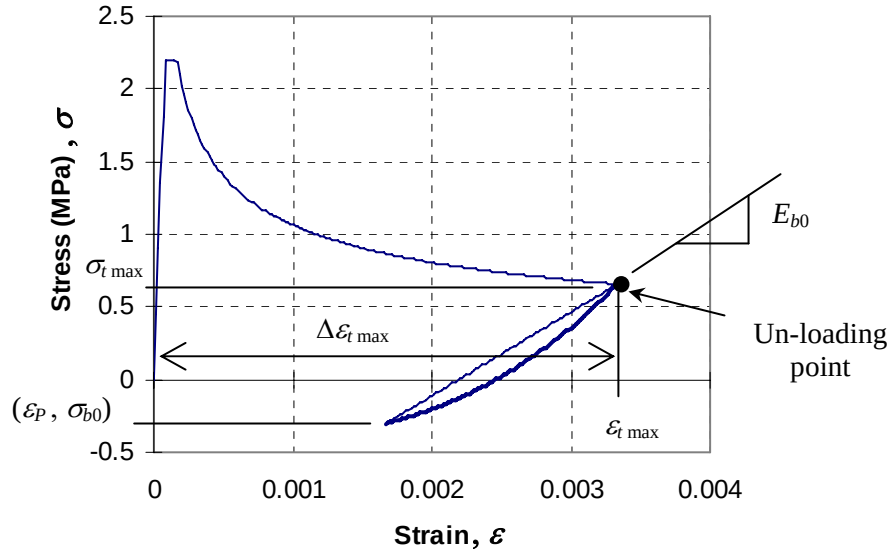

Figure A-9. Schematic concrete tension un-loading envelope

A.1.2.3 Tension Re-loading Loop $\varepsilon \geq \varepsilon_0$ *and* $\varepsilon < \varepsilon_{t\max}$

The reloading loop is a straight line connecting the reloading point to ($\varepsilon_{t\max}$, $\sigma_{t\max}$) as shown in Figure A-10.

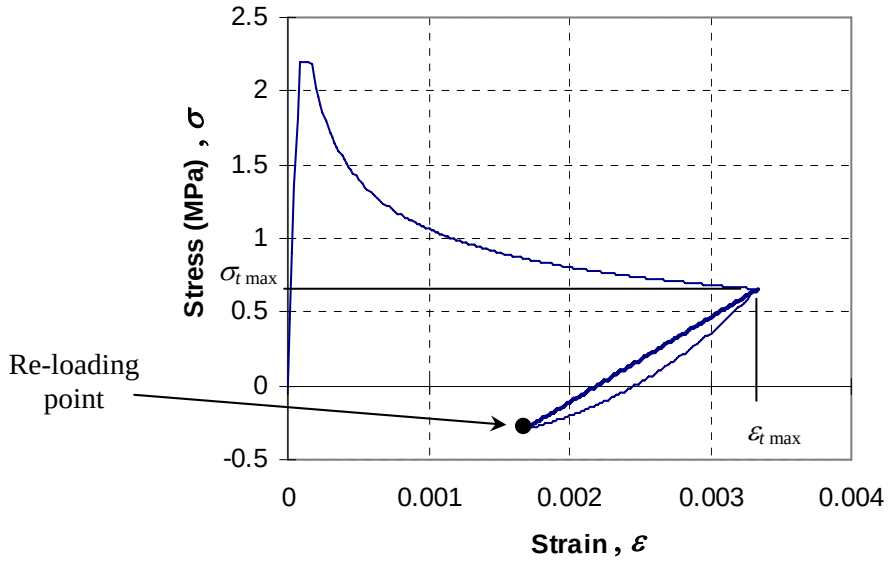

Figure A-10. Schematic concrete tension re-loading envelope

A.1.3 Re-contact Model

Reversing cyclic tests have shown that small amount of compressive stress would develop in RC members as they unload from tension into compression even before the cracks close completely. This is due to rough nature of the crack surface, dislocation of the aggregate particles falling into cracks and aggregate interlock actions. As a result, premature contact occurs before the average tensile strain of concrete reverses to zero.

A simple linear relationship connecting the start of the contact strain, ε_{tl}, to the end of the contact strain, ε_{cl}, is used instead of the complicated relationships proposed by Maekawa et al. (2003), to represent the contact stress effect as illustrated in Figure A-11. As the original model is developed based on uni-directional push pull tests, modifications were also made to allow for the magnification of the contact stress effects for concrete in plastic hinges where concrete are under combined tensile and shear actions. Note that currently there has been no study looking at the magnitude of contact stresses for concrete under combined tensile and shear actions. Research in this area is required for a precise contact stress model.

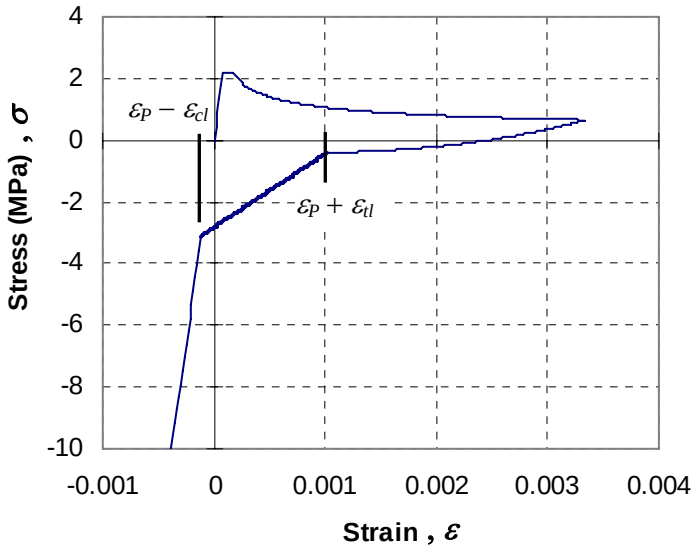

Figure A-11. Schematic concrete re-contact envelope

The parameters ε_{tl} and ε_{cl} are functions of the maximum incremental tensile strain as shown in Figure A-12 where *CLIMIT* and *TLIMIT* are parameters controlling the maximum ε_{tl} and ε_{cl}. To take into account the magnification of the contact stress effect for concrete under tensile and shear actions, *CFACTOR* and *TFACTOR* are introduced as multiplying factors on the parameters ε_{tl} and ε_{cl}, respectively. The effect of *CFACTOR* and *TFACTOR* are shown in Figure A-12.

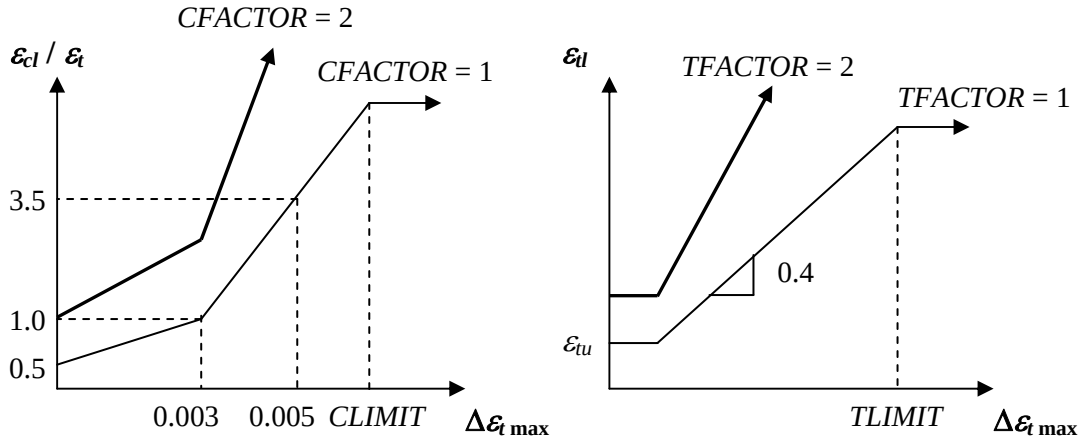

(a) Parameter ε_{cl} (b) Parameter ε_{tl}

Figure A-12. Re-contact parameters ε_{tl} and ε_{cl} in concrete model

A.1.4 Cyclic Compression-tension Model

The unloading/reloading behaviour of concrete is different, as shown in Figure A-13, depending on whether it undergoes tension or compression first. If loading starts in the compression region first, as the load reverses to zero the strain will not return to the origin but will have a permanent plastic strain, ε_P, and the tension profile will start from (ε_P, 0). This is referred to as compression-tension loop as illustrated in Figure A-13(a). Whereas if the loading starts in the tension region, it will start from the origin as illustrated in Figure A-13(b) and this is referred to as tension-compression loop.

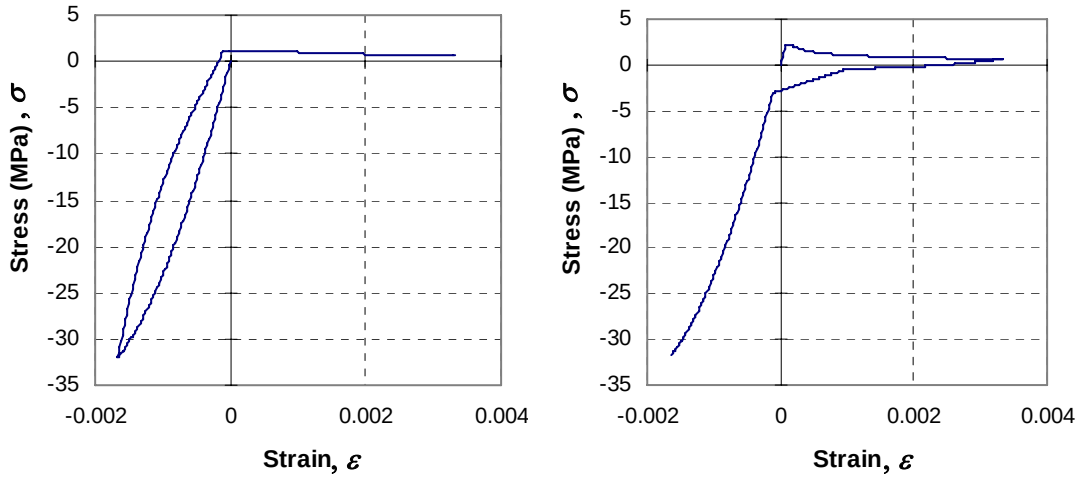

(a) Compression-tension loop (b) Tension-compression loop

Figure A-13 Schematic concrete cyclic model

The effects of changing the parameters *TLIMIT* and *CLIMIT* are shown in Figure A-14(a) and the effects of altering the parameters *TFACTOR* and CFACTOR are shown in Figure A-14(b).

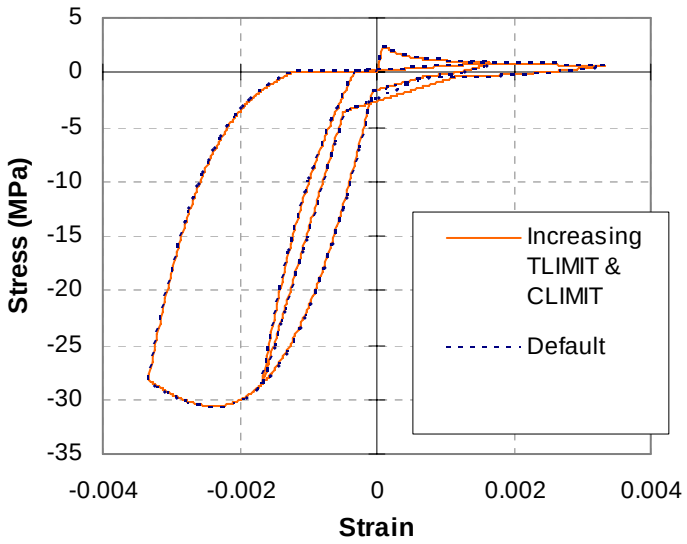

(a) Increasing the parameters *TLIMIT* and *CLIMIT*

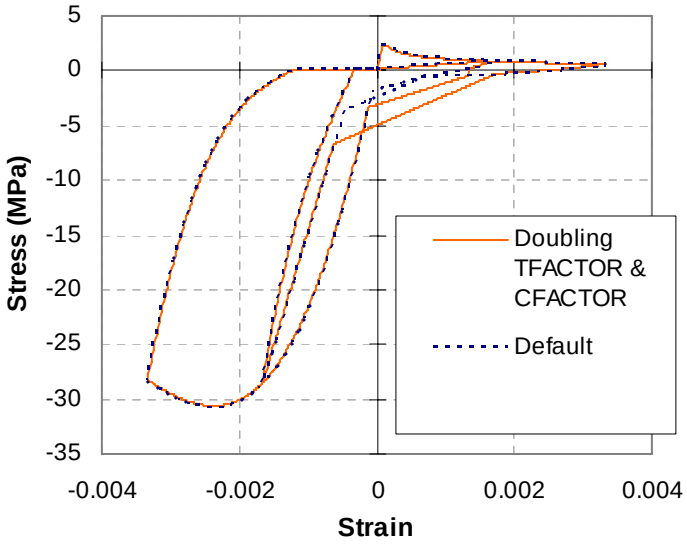

(b) Doubling the parameters *TFACTOR* and *CFACTOR*

Figure A-14 Effect of changing the contact stress parameters

A.2 REFERENCES

Carr, A. J. (2004). "RUAUMOKO2D - Inelastic Dynamic Analysis." Department of Civil Engineering, University of Canterbury, Christchurch, New Zealand.

Collins, M. P., and Vecchio, F. (1982). "The response of reinforced concrete to In-plane shear and normal stresses." University of Toronto, Toronto, Canada.

Maekawa, K., and Okamura, H. (1983). "The Deformation Behaviour and Constitutive Equation of Concrete using Elasto-Plastic and Fracture Model."

Journal of Faculty of Engineering, University of Tokyo (B), Vol. 37(No. 2), pp. 253-328.

Maekawa, K., Pimanmas, A., and Okamura, H. (2003). *Nonlinear Mechanics of Reinforced Concrete*, Spon Press, London.

Okamura, H., and Maekawa, K. (1991). *Nonlinear Analysis and Constitutive Models of Reinforced Concrete*, Gihodo-Shuppan Co., Tokyo.

Shima, H., Chou, L., and Okamura, H. (1987). "Micro and Macro Models for Bond Behaviour in reinforced Concrete." *Journal of Faculty of Engineering, University of Tokyo (B)*, Vol. 39(No. 2), pp.133-94.

Standards New Zealand. (2006). *Concrete structures standard: NZS 3101:2006*, Standards New Zealand, Wellington.

APPENDIX B. RUAUMOKO INPUT FILES

B.1 CANTILEVER BEAM 2A

```
2D model for cantilever beam 2A                    !TITLE (units in mm, N, and second)
8 0 1 0 0 -1 0 0 0 0 0                             !PRINCIPAL ANALYSIS OPTIONS
3 2 2 1 1 5 9810 2 4 0.01 24000 1                  !FRAME CONTROL PARAMETERS
0 1000 1000 0 1 1 100 100 1 1 0                    !PLOTTING CONTROL PARAMETERS
3 0 0.0001 0 0 0 0 0 0 0 0                         !ITERATION CONTROL

NODES 1                                            !NODAL POINT INPUT
1       0       0       1       1       1       0       0       0       1
2       220     0       0       0       0       0       0       0       1
3       1500    0       0       0       0       0       -1      0       1

DRIFT                                              !INTER-STOREY DRIFT INPUT
1

ELEMENTS 1                                         !MEMBER GEOMETRY
1       1       1       2       0       0       1
2       2       2       3       0       0       1

PROPS
1 Reinforced                                       !PLASTIC HINGE ELEMENT
! Type  Width   Depth   Cover   Length  Weight  Theta   Isteel  Iconcrete
1       200     500     58      220     0       0       0       0
! Confined concrete     Cover concrete  Shear concrete
! Ec    f'c     ft  Ec      f'c     ft  Ec      f'c     ft  Effective width
27300 -37.6 2.2 27300 -37.6 2.2 27300 -12.8 0.01 190.5
! Es      fy-   fy+   Atop    Abot   Effective length
200000  -306  306  1570.5  1570.5  463
1 0 1 0.01 1 1.5 1 0                               !CONFINED CONCRETE HYSTERESIS
1 0 1 0.01 1 1 1 0                                 !COVER CONCRETE HYSTERESIS
1 0 1 13 1.5 130 0.018 0 0 0                       !REINFORCING STEEL HYSTERESIS
0 0 1 0.01 1 1 1 8E-5                              !DIAGONAL CONCRETE HYSTERESIS

2 FRAME         !ELASTIC_BEAM
1 0 0 2 0 0 0 0 0                                  !11A SECTION PARAMETERS
27300 10900 100000 88400 1170E+6 0 0 0 0           !11B SECION PROPERTIES
0.01 0.01 0 0                                      !11C BILINEAR FACTORS
0 0 0 -0 0 -0                                      !11F BEAM YIELD CONDITIONS

WEIGHTS 0
1       0       0       0
2       0       0       0
3       0       0       0

LOADS
1       0       0       0
2       0       0       0
3       0       0       0

EQUAKE 2A.eqf
3 1 1 1 -1 0 0 1
```

B.2 3D FRAME-FLOOR MODEL

```
3D original model for the floor-frame sub-assembly      !TITLE (units in mm, N, and second)
8 1 0 1 -1 0 0 0 0 0                                    !PRINCIPAL ANALYSIS OPTIONS
545 431 20 1 1 5 9810 5 10 0.005 10250                  !FRAME CONTROL PARAMETERS
0 1000 0 1 0 0 0 0 2 2 0 0                              !PLOTTING CONTROL PARAMETERS
DEFAULT                                                 !PLOT AXES TRANSFORMATION
0 0 0.0001 0 0 0 0 0 0 0 0 0                            !ITERATION CONTROL

NODES 1                                                 !NODAL POINT INPUT
1     0     952.5   0     0     0     0     0     0     0     0     1
2     0     0       0     0     0     0     0     0     -1    0     1
3     0     -952.5  0     0     1     0     0     0     0     0     1
4     3050  952.5   0     0     0     0     0     0     0     0     1
5     3050  0       0     1     0     0     0     0     -1    0     1
6     3050  -952.5  0     0     1     0     0     0     0     0     1
7     6100  952.5   0     0     0     0     0     0     0     0     1
8     6100  0       0     0     0     0     0     0     -1    0     1
9     6100  -952.5  0     0     1     0     0     0     0     0     1
10    250   0       0     0     0     0     0     0     0     0     1
11    355   0       0     0     0     0     0     0     0     0     1
12    1025  0       0     0     0     0     0     0     0     0     1
13    1525  0       0     0     0     0     0     0     0     0     1
14    2025  0       0     0     0     0     0     0     0     0     1
15    2695  0       0     0     0     0     0     0     0     0     1
16    2800  0       0     0     0     0     0     0     0     0     1
17    3300  0       0     0     0     0     0     0     0     0     1
18    3405  0       0     0     0     0     0     0     0     0     1
19    4075  0       0     0     0     0     0     0     0     0     1
20    4575  0       0     0     0     0     0     0     0     0     1
21    5075  0       0     0     0     0     0     0     0     0     1
22    5745  0       0     0     0     0     0     0     0     0     1
23    5850  0       0     0     0     0     0     0     0     0     1
24    250   177.5   0     0     0     0     0     0     0     0     1
25    355   177.5   0     0     0     0     0     0     0     0     1
26    1025  177.5   0     0     0     0     0     0     0     0     1
27    1525  177.5   0     0     0     0     0     0     0     0     1
28    2025  177.5   0     0     0     0     0     0     0     0     1
29    2695  177.5   0     0     0     0     0     0     0     0     1
30    2800  177.5   0     0     0     0     0     0     0     0     1
31    3300  177.5   0     0     0     0     0     0     0     0     1
32    3405  177.5   0     0     0     0     0     0     0     0     1
33    4075  177.5   0     0     0     0     0     0     0     0     1
34    4575  177.5   0     0     0     0     0     0     0     0     1
35    5075  177.5   0     0     0     0     0     0     0     0     1
36    5745  177.5   0     0     0     0     0     0     0     0     1
37    5850  177.5   0     0     0     0     0     0     0     0     1
38    0     0       0     0     0     0     0     0     0     0     0
39    0     0       0     0     0     0     0     0     0     0     0
40    0     177.5   -250  0     0     0     0     0     0     0     1
41    250   177.5   -250  0     0     0     0     0     0     0     1
42    355   177.5   -250  0     0     0     0     0     0     0     1
43    1025  177.5   -250  0     0     0     0     0     0     0     1
44    1525  177.5   -250  0     0     0     0     0     0     0     1
45    2025  177.5   -250  0     0     0     0     0     0     0     1
46    2695  177.5   -250  0     0     0     0     0     0     0     1
47    2800  177.5   -250  0     0     0     0     0     0     0     1
48    3050  177.5   -250  0     0     0     0     0     0     0     1
49    3300  177.5   -250  0     0     0     0     0     0     0     1
50    3405  177.5   -250  0     0     0     0     0     0     0     1
```

51	4075	177.5	-250	0	0	0	0	0	0	0	1
52	4575	177.5	-250	0	0	0	0	0	0	0	1
53	5075	177.5	-250	0	0	0	0	0	0	0	1
54	5745	177.5	-250	0	0	0	0	0	0	0	1
55	5850	177.5	-250	0	0	0	0	0	0	0	1
56	6100	177.5	-250	0	0	0	0	0	0	0	1
57	0	0	0	0	0	0	0	0	0	0	0
58	0	0	0	0	0	0	0	0	0	0	0
59	0	0	0	0	0	0	0	0	0	0	0
60	0	177.5	-525	0	0	0	0	0	0	0	1
61	250	177.5	-525	0	0	0	0	0	0	0	1
62	355	177.5	-525	0	0	0	0	0	0	0	1
63	1025	177.5	-525	0	0	0	0	0	0	0	1
64	1525	177.5	-525	0	0	0	0	0	0	0	1
65	2025	177.5	-525	0	0	0	0	0	0	0	1
66	2695	177.5	-525	0	0	0	0	0	0	0	1
67	2800	177.5	-525	0	0	0	0	0	0	0	1
68	3050	177.5	-525	0	0	0	0	0	0	0	1
69	3300	177.5	-525	0	0	0	0	0	0	0	1
70	3405	177.5	-525	0	0	0	0	0	0	0	1
71	4075	177.5	-525	0	0	0	0	0	0	0	1
72	4575	177.5	-525	0	0	0	0	0	0	0	1
73	5075	177.5	-525	0	0	0	0	0	0	0	1
74	5745	177.5	-525	0	0	0	0	0	0	0	1
75	5850	177.5	-525	0	0	0	0	0	0	0	1
76	6100	177.5	-525	0	0	0	0	0	0	0	1
77	0	0	0	0	0	0	0	0	0	0	0
78	0	0	0	0	0	0	0	0	0	0	0
79	0	0	0	0	0	0	0	0	0	0	0
80	0	177.5	-1025	0	0	0	0	0	0	0	1
81	250	177.5	-1025	0	0	0	0	0	0	0	1
82	355	177.5	-1025	0	0	0	0	0	0	0	1
83	1025	177.5	-1025	0	0	0	0	0	0	0	1
84	1525	177.5	-1025	0	0	0	0	0	0	0	1
85	2025	177.5	-1025	0	0	0	0	0	0	0	1
86	2695	177.5	-1025	0	0	0	0	0	0	0	1
87	2800	177.5	-1025	0	0	0	0	0	0	0	1
88	3050	177.5	-1025	0	0	0	0	0	0	0	1
89	3300	177.5	-1025	0	0	0	0	0	0	0	1
90	3405	177.5	-1025	0	0	0	0	0	0	0	1
91	4075	177.5	-1025	0	0	0	0	0	0	0	1
92	4575	177.5	-1025	0	0	0	0	0	0	0	1
93	5075	177.5	-1025	0	0	0	0	0	0	0	1
94	5745	177.5	-1025	0	0	0	0	0	0	0	1
95	5850	177.5	-1025	0	0	0	0	0	0	0	1
96	6100	177.5	-1025	0	0	0	0	0	0	0	1
97	0	0	0	0	0	0	0	0	0	0	0
98	0	0	0	0	0	0	0	0	0	0	0
99	0	0	0	0	0	0	0	0	0	0	0
100	0	177.5	-1525	0	0	0	0	0	0	0	1
101	250	177.5	-1525	0	0	0	0	0	0	0	1
102	355	177.5	-1525	0	0	0	0	0	0	0	1
103	1025	177.5	-1525	0	0	0	0	0	0	0	1
104	1525	177.5	-1525	0	0	0	0	0	0	0	1
105	2025	177.5	-1525	0	0	0	0	0	0	0	1
106	2695	177.5	-1525	0	0	0	0	0	0	0	1
107	2800	177.5	-1525	0	0	0	0	0	0	0	1
108	3050	177.5	-1525	0	0	0	0	0	0	0	1
109	3300	177.5	-1525	0	0	0	0	0	0	0	1
110	3405	177.5	-1525	0	0	0	0	0	0	0	1

111	4075	177.5	-1525	0	0	0	0	0	0	0	1
112	4575	177.5	-1525	0	0	0	0	0	0	0	1
113	5075	177.5	-1525	0	0	0	0	0	0	0	1
114	5745	177.5	-1525	0	0	0	0	0	0	0	1
115	5850	177.5	-1525	0	0	0	0	0	0	0	1
116	6100	177.5	-1525	0	0	0	0	0	0	0	1
117	0	0	0	0	0	0	0	0	0	0	0
118	0	0	0	0	0	0	0	0	0	0	0
119	0	0	0	0	0	0	0	0	0	0	0
120	0	177.5	-2025	0	0	0	0	0	0	0	1
121	250	177.5	-2025	0	0	0	0	0	0	0	1
122	355	177.5	-2025	0	0	0	0	0	0	0	1
123	1025	177.5	-2025	0	0	0	0	0	0	0	1
124	1525	177.5	-2025	0	0	0	0	0	0	0	1
125	2025	177.5	-2025	0	0	0	0	0	0	0	1
126	2695	177.5	-2025	0	0	0	0	0	0	0	1
127	2800	177.5	-2025	0	0	0	0	0	0	0	1
128	3050	177.5	-2025	0	0	0	0	0	0	0	1
129	3300	177.5	-2025	0	0	0	0	0	0	0	1
130	3405	177.5	-2025	0	0	0	0	0	0	0	1
131	4075	177.5	-2025	0	0	0	0	0	0	0	1
132	4575	177.5	-2025	0	0	0	0	0	0	0	1
133	5075	177.5	-2025	0	0	0	0	0	0	0	1
134	5745	177.5	-2025	0	0	0	0	0	0	0	1
135	5850	177.5	-2025	0	0	0	0	0	0	0	1
136	6100	177.5	-2025	0	0	0	0	0	0	0	1
137	0	0	0	0	0	0	0	0	0	0	0
138	0	0	0	0	0	0	0	0	0	0	0
139	0	0	0	0	0	0	0	0	0	0	0
140	0	177.5	-2525	0	0	0	0	0	0	0	1
141	250	177.5	-2525	0	0	0	0	0	0	0	1
142	355	177.5	-2525	0	0	0	0	0	0	0	1
143	1025	177.5	-2525	0	0	0	0	0	0	0	0
144	1525	177.5	-2525	0	0	0	0	0	0	0	0
145	2025	177.5	-2525	0	0	0	0	0	0	0	0
146	2695	177.5	-2525	0	0	0	0	0	0	0	1
147	2800	177.5	-2525	0	0	0	0	0	0	0	1
148	3050	177.5	-2525	0	0	0	0	0	0	0	1
149	3300	177.5	-2525	0	0	0	0	0	0	0	1
150	3405	177.5	-2525	0	0	0	0	0	0	0	1
151	4075	177.5	-2525	0	0	0	0	0	0	0	0
152	4575	177.5	-2525	0	0	0	0	0	0	0	0
153	5075	177.5	-2525	0	0	0	0	0	0	0	0
154	5745	177.5	-2525	0	0	0	0	0	0	0	1
155	5850	177.5	-2525	0	0	0	0	0	0	0	1
156	6100	177.5	-2525	0	0	0	0	0	0	0	1
157	0	0	0	0	0	0	0	0	0	0	0
158	0	0	0	0	0	0	0	0	0	0	0
159	0	0	0	0	0	0	0	0	0	0	0
160	0	177.5	-3025	0	0	0	0	0	0	0	1
161	250	177.5	-3025	0	0	0	0	0	0	0	1
162	355	177.5	-3025	0	0	0	0	0	0	0	1
163	1025	177.5	-3025	0	0	0	0	0	0	0	0
164	1525	177.5	-3025	0	0	0	0	0	0	0	0
165	2025	177.5	-3025	0	0	0	0	0	0	0	0
166	2695	177.5	-3025	0	0	0	0	0	0	0	1
167	2800	177.5	-3025	0	0	0	0	0	0	0	1
168	3050	177.5	-3025	0	0	0	0	0	0	0	1
169	3300	177.5	-3025	0	0	0	0	0	0	0	1
170	3405	177.5	-3025	0	0	0	0	0	0	0	1

171	4075	177.5	-3025	0	0	0	0	0	0	0	0
172	4575	177.5	-3025	0	0	0	0	0	0	0	0
173	5075	177.5	-3025	0	0	0	0	0	0	0	0
174	5745	177.5	-3025	0	0	0	0	0	0	0	1
175	5850	177.5	-3025	0	0	0	0	0	0	0	1
176	6100	177.5	-3025	0	0	0	0	0	0	0	1
177	0	0	0	0	0	0	0	0	0	0	0
178	0	0	0	0	0	0	0	0	0	0	0
179	0	0	0	0	0	0	0	0	0	0	0
180	0	177.5	-3525	0	0	0	0	0	0	0	1
181	250	177.5	-3525	0	0	0	0	0	0	0	1
182	355	177.5	-3525	0	0	0	0	0	0	0	1
183	1025	177.5	-3525	0	0	0	0	0	0	0	0
184	1525	177.5	-3525	0	0	0	0	0	0	0	0
185	2025	177.5	-3525	0	0	0	0	0	0	0	0
186	2695	177.5	-3525	0	0	0	0	0	0	0	1
187	2800	177.5	-3525	0	0	0	0	0	0	0	1
188	3050	177.5	-3525	0	0	0	0	0	0	0	1
189	3300	177.5	-3525	0	0	0	0	0	0	0	1
190	3405	177.5	-3525	0	0	0	0	0	0	0	1
191	4075	177.5	-3525	0	0	0	0	0	0	0	0
192	4575	177.5	-3525	0	0	0	0	0	0	0	0
193	5075	177.5	-3525	0	0	0	0	0	0	0	0
194	5745	177.5	-3525	0	0	0	0	0	0	0	1
195	5850	177.5	-3525	0	0	0	0	0	0	0	1
196	6100	177.5	-3525	0	0	0	0	0	0	0	1
197	0	0	0	0	0	0	0	0	0	0	0
198	0	0	0	0	0	0	0	0	0	0	0
199	0	0	0	0	0	0	0	0	0	0	0
200	0	177.5	-4025	0	0	0	0	0	0	0	1
201	250	177.5	-4025	0	0	0	0	0	0	0	1
202	355	177.5	-4025	0	0	0	0	0	0	0	1
203	1025	177.5	-4025	0	0	0	0	0	0	0	0
204	1525	177.5	-4025	0	0	0	0	0	0	0	0
205	2025	177.5	-4025	0	0	0	0	0	0	0	0
206	2695	177.5	-4025	0	0	0	0	0	0	0	1
207	2800	177.5	-4025	0	0	0	0	0	0	0	1
208	3050	177.5	-4025	0	0	0	0	0	0	0	1
209	3300	177.5	-4025	0	0	0	0	0	0	0	1
210	3405	177.5	-4025	0	0	0	0	0	0	0	1
211	4075	177.5	-4025	0	0	0	0	0	0	0	0
212	4575	177.5	-4025	0	0	0	0	0	0	0	0
213	5075	177.5	-4025	0	0	0	0	0	0	0	0
214	5745	177.5	-4025	0	0	0	0	0	0	0	1
215	5850	177.5	-4025	0	0	0	0	0	0	0	1
216	6100	177.5	-4025	0	0	0	0	0	0	0	1
217	0	0	0	0	0	0	0	0	0	0	0
218	0	0	0	0	0	0	0	0	0	0	0
219	0	0	0	0	0	0	0	0	0	0	0
220	0	177.5	-4525	0	0	0	0	0	0	0	1
221	250	177.5	-4525	0	0	0	0	0	0	0	1
222	355	177.5	-4525	0	0	0	0	0	0	0	1
223	1025	177.5	-4525	0	0	0	0	0	0	0	0
224	1525	177.5	-4525	0	0	0	0	0	0	0	0
225	2025	177.5	-4525	0	0	0	0	0	0	0	0
226	2695	177.5	-4525	0	0	0	0	0	0	0	1
227	2800	177.5	-4525	0	0	0	0	0	0	0	1
228	3050	177.5	-4525	0	0	0	0	0	0	0	1
229	3300	177.5	-4525	0	0	0	0	0	0	0	1
230	3405	177.5	-4525	0	0	0	0	0	0	0	1

231	4075	177.5	-4525	0	0	0	0	0	0	0	0
232	4575	177.5	-4525	0	0	0	0	0	0	0	0
233	5075	177.5	-4525	0	0	0	0	0	0	0	0
234	5745	177.5	-4525	0	0	0	0	0	0	0	1
235	5850	177.5	-4525	0	0	0	0	0	0	0	1
236	6100	177.5	-4525	0	0	0	0	0	0	0	1
237	0	0	0	0	0	0	0	0	0	0	0
238	0	0	0	0	0	0	0	0	0	0	0
239	0	0	0	0	0	0	0	0	0	0	0
240	0	177.5	-5000	0	0	0	0	0	0	0	1
241	250	177.5	-5000	0	0	0	0	0	0	0	1
242	355	177.5	-5000	0	0	0	0	0	0	0	1
243	1025	177.5	-5000	0	0	0	0	0	0	0	0
244	1525	177.5	-5000	0	0	0	0	0	0	0	0
245	2025	177.5	-5000	0	0	0	0	0	0	0	0
246	2695	177.5	-5000	0	0	0	0	0	0	0	1
247	2800	177.5	-5000	0	0	0	0	0	0	0	1
248	3050	177.5	-5000	0	0	0	0	0	0	0	1
249	3300	177.5	-5000	0	0	0	0	0	0	0	1
250	3405	177.5	-5000	0	0	0	0	0	0	0	1
251	4075	177.5	-5000	0	0	0	0	0	0	0	0
252	4575	177.5	-5000	0	0	0	0	0	0	0	0
253	5075	177.5	-5000	0	0	0	0	0	0	0	0
254	5745	177.5	-5000	0	0	0	0	0	0	0	1
255	5850	177.5	-5000	0	0	0	0	0	0	0	1
256	6100	177.5	-5000	0	0	0	0	0	0	0	1
257	0	0	0	0	0	0	0	0	0	0	0
258	0	0	0	0	0	0	0	0	0	0	0
259	0	0	0	0	0	0	0	0	0	0	0
260	0	177.5	-5475	0	0	0	0	0	0	0	1
261	250	177.5	-5475	0	0	0	0	0	0	0	1
262	355	177.5	-5475	0	0	0	0	0	0	0	1
263	1025	177.5	-5475	0	0	0	0	0	0	0	0
264	1525	177.5	-5475	0	0	0	0	0	0	0	0
265	2025	177.5	-5475	0	0	0	0	0	0	0	0
266	2695	177.5	-5475	0	0	0	0	0	0	0	1
267	2800	177.5	-5475	0	0	0	0	0	0	0	1
268	3050	177.5	-5475	0	0	0	0	0	0	0	1
269	3300	177.5	-5475	0	0	0	0	0	0	0	1
270	3405	177.5	-5475	0	0	0	0	0	0	0	1
271	4075	177.5	-5475	0	0	0	0	0	0	0	0
272	4575	177.5	-5475	0	0	0	0	0	0	0	0
273	5075	177.5	-5475	0	0	0	0	0	0	0	0
274	5745	177.5	-5475	0	0	0	0	0	0	0	1
275	5850	177.5	-5475	0	0	0	0	0	0	0	1
276	6100	177.5	-5475	0	0	0	0	0	0	0	1
277	0	0	0	0	0	0	0	0	0	0	0
278	0	0	0	0	0	0	0	0	0	0	0
279	0	0	0	0	0	0	0	0	0	0	0
280	0	177.5	-6100	0	1	1	1	1	1	0	1
281	250	177.5	-6100	0	0	0	0	0	0	0	1
282	355	177.5	-6100	0	0	0	0	0	0	0	1
283	1025	177.5	-6100	0	0	0	0	0	0	0	0
284	1525	177.5	-6100	0	0	0	0	0	0	0	0
285	2025	177.5	-6100	0	0	0	0	0	0	0	0
286	2695	177.5	-6100	0	0	0	0	0	0	0	1
287	2800	177.5	-6100	0	0	0	0	0	0	0	1
288	3050	177.5	-6100	0	1	0	0	0	0	0	1
289	3300	177.5	-6100	0	0	0	0	0	0	0	1
290	3405	177.5	-6100	0	0	0	0	0	0	0	1

291	4075	177.5	-6100	0	0	0	0	0	0	0	0
292	4575	177.5	-6100	0	0	0	0	0	0	0	0
293	5075	177.5	-6100	0	0	0	0	0	0	0	0
294	5745	177.5	-6100	0	0	0	0	0	0	0	1
295	5850	177.5	-6100	0	0	0	0	0	0	0	1
296	6100	177.5	-6100	0	1	1	1	1	1	0	1
297	0	0	0	0	0	0	0	0	0	0	0
298	0	0	0	0	0	0	0	0	0	0	0
299	0	0	0	0	0	0	0	0	0	0	0
300	0	80	-525	0	0	0	0	0	0	0	1
301	250	80	-525	0	0	0	0	0	0	0	1
302	355	80	-525	0	0	0	0	0	0	0	1
303	1025	80	-525	0	0	0	0	0	0	0	0
304	1525	80	-525	0	0	0	0	0	0	0	0
305	2025	80	-525	0	0	0	0	0	0	0	0
306	2695	80	-525	0	0	0	0	0	0	0	1
307	2800	80	-525	0	0	0	0	0	0	0	1
308	3050	80	-525	0	0	0	0	0	0	0	1
309	3300	80	-525	0	0	0	0	0	0	0	1
310	3405	80	-525	0	0	0	0	0	0	0	1
311	4075	80	-525	0	0	0	0	0	0	0	0
312	4575	80	-525	0	0	0	0	0	0	0	0
313	5075	80	-525	0	0	0	0	0	0	0	0
314	5745	80	-525	0	0	0	0	0	0	0	1
315	5850	80	-525	0	0	0	0	0	0	0	1
316	6100	80	-525	0	0	0	0	0	0	0	1
317	0	0	0	0	0	0	0	0	0	0	0
318	0	0	0	0	0	0	0	0	0	0	0
319	0	0	0	0	0	0	0	0	0	0	0
320	0	80	-1025	0	0	0	0	0	0	0	1
321	250	80	-1025	0	0	0	0	0	0	0	1
322	355	80	-1025	0	0	0	0	0	0	0	1
323	1025	80	-1025	0	0	0	0	0	0	0	0
324	1525	80	-1025	0	0	0	0	0	0	0	0
325	2025	80	-1025	0	0	0	0	0	0	0	0
326	2695	80	-1025	0	0	0	0	0	0	0	1
327	2800	80	-1025	0	0	0	0	0	0	0	1
328	3050	80	-1025	0	0	0	0	0	0	0	1
329	3300	80	-1025	0	0	0	0	0	0	0	1
330	3405	80	-1025	0	0	0	0	0	0	0	1
331	4075	80	-1025	0	0	0	0	0	0	0	0
332	4575	80	-1025	0	0	0	0	0	0	0	0
333	5075	80	-1025	0	0	0	0	0	0	0	0
334	5745	80	-1025	0	0	0	0	0	0	0	1
335	5850	80	-1025	0	0	0	0	0	0	0	1
336	6100	80	-1025	0	0	0	0	0	0	0	1
337	0	0	0	0	0	0	0	0	0	0	0
338	0	0	0	0	0	0	0	0	0	0	0
339	0	0	0	0	0	0	0	0	0	0	0
340	0	80	-1525	0	0	0	0	0	0	0	1
341	250	80	-1525	0	0	0	0	0	0	0	1
342	355	80	-1525	0	0	0	0	0	0	0	1
343	1025	80	-1525	0	0	0	0	0	0	0	0
344	1525	80	-1525	0	0	0	0	0	0	0	0
345	2025	80	-1525	0	0	0	0	0	0	0	0
346	2695	80	-1525	0	0	0	0	0	0	0	1
347	2800	80	-1525	0	0	0	0	0	0	0	1
348	3050	80	-1525	0	0	0	0	0	0	0	1
349	3300	80	-1525	0	0	0	0	0	0	0	1
350	3405	80	-1525	0	0	0	0	0	0	0	1

351	4075	80	-1525	0	0	0	0	0	0	0	0
352	4575	80	-1525	0	0	0	0	0	0	0	0
353	5075	80	-1525	0	0	0	0	0	0	0	0
354	5745	80	-1525	0	0	0	0	0	0	0	1
355	5850	80	-1525	0	0	0	0	0	0	0	1
356	6100	80	-1525	0	0	0	0	0	0	0	1
357	0	0	0	0	0	0	0	0	0	0	0
358	0	0	0	0	0	0	0	0	0	0	0
359	0	0	0	0	0	0	0	0	0	0	0
360	0	80	-2025	0	0	0	0	0	0	0	1
361	250	80	-2025	0	0	0	0	0	0	0	1
362	355	80	-2025	0	0	0	0	0	0	0	1
363	1025	80	-2025	0	0	0	0	0	0	0	0
364	1525	80	-2025	0	0	0	0	0	0	0	0
365	2025	80	-2025	0	0	0	0	0	0	0	0
366	2695	80	-2025	0	0	0	0	0	0	0	1
367	2800	80	-2025	0	0	0	0	0	0	0	1
368	3050	80	-2025	0	0	0	0	0	0	0	1
369	3300	80	-2025	0	0	0	0	0	0	0	1
370	3405	80	-2025	0	0	0	0	0	0	0	1
371	4075	80	-2025	0	0	0	0	0	0	0	0
372	4575	80	-2025	0	0	0	0	0	0	0	0
373	5075	80	-2025	0	0	0	0	0	0	0	0
374	5745	80	-2025	0	0	0	0	0	0	0	1
375	5850	80	-2025	0	0	0	0	0	0	0	1
376	6100	80	-2025	0	0	0	0	0	0	0	1
377	0	0	0	0	0	0	0	0	0	0	0
378	0	0	0	0	0	0	0	0	0	0	0
379	0	0	0	0	0	0	0	0	0	0	0
380	0	80	-2525	0	0	0	0	0	0	0	1
381	250	80	-2525	0	0	0	0	0	0	0	1
382	355	80	-2525	0	0	0	0	0	0	0	1
383	1025	80	-2525	0	0	0	0	0	0	0	0
384	1525	80	-2525	0	0	0	0	0	0	0	0
385	2025	80	-2525	0	0	0	0	0	0	0	0
386	2695	80	-2525	0	0	0	0	0	0	0	1
387	2800	80	-2525	0	0	0	0	0	0	0	1
388	3050	80	-2525	0	0	0	0	0	0	0	1
389	3300	80	-2525	0	0	0	0	0	0	0	1
390	3405	80	-2525	0	0	0	0	0	0	0	1
391	4075	80	-2525	0	0	0	0	0	0	0	0
392	4575	80	-2525	0	0	0	0	0	0	0	0
393	5075	80	-2525	0	0	0	0	0	0	0	0
394	5745	80	-2525	0	0	0	0	0	0	0	1
395	5850	80	-2525	0	0	0	0	0	0	0	1
396	6100	80	-2525	0	0	0	0	0	0	0	1
397	0	0	0	0	0	0	0	0	0	0	0
398	0	0	0	0	0	0	0	0	0	0	0
399	0	0	0	0	0	0	0	0	0	0	0
400	0	80	-3025	0	0	0	0	0	0	0	1
401	250	80	-3025	0	0	0	0	0	0	0	1
402	355	80	-3025	0	0	0	0	0	0	0	1
403	1025	80	-3025	0	0	0	0	0	0	0	0
404	1525	80	-3025	0	0	0	0	0	0	0	0
405	2025	80	-3025	0	0	0	0	0	0	0	0
406	2695	80	-3025	0	0	0	0	0	0	0	1
407	2800	80	-3025	0	0	0	0	0	0	0	1
408	3050	80	-3025	0	0	0	0	0	0	0	1
409	3300	80	-3025	0	0	0	0	0	0	0	1
410	3405	80	-3025	0	0	0	0	0	0	0	1

411	4075	80	-3025	0	0	0	0	0	0	0	0
412	4575	80	-3025	0	0	0	0	0	0	0	0
413	5075	80	-3025	0	0	0	0	0	0	0	0
414	5745	80	-3025	0	0	0	0	0	0	0	1
415	5850	80	-3025	0	0	0	0	0	0	0	1
416	6100	80	-3025	0	0	0	0	0	0	0	1
417	0	0	0	0	0	0	0	0	0	0	0
418	0	0	0	0	0	0	0	0	0	0	0
419	0	0	0	0	0	0	0	0	0	0	0
420	0	80	-3525	0	0	0	0	0	0	0	1
421	250	80	-3525	0	0	0	0	0	0	0	1
422	355	80	-3525	0	0	0	0	0	0	0	1
423	1025	80	-3525	0	0	0	0	0	0	0	0
424	1525	80	-3525	0	0	0	0	0	0	0	0
425	2025	80	-3525	0	0	0	0	0	0	0	0
426	2695	80	-3525	0	0	0	0	0	0	0	1
427	2800	80	-3525	0	0	0	0	0	0	0	1
428	3050	80	-3525	0	0	0	0	0	0	0	1
429	3300	80	-3525	0	0	0	0	0	0	0	1
430	3405	80	-3525	0	0	0	0	0	0	0	1
431	4075	80	-3525	0	0	0	0	0	0	0	0
432	4575	80	-3525	0	0	0	0	0	0	0	0
433	5075	80	-3525	0	0	0	0	0	0	0	0
434	5745	80	-3525	0	0	0	0	0	0	0	1
435	5850	80	-3525	0	0	0	0	0	0	0	1
436	6100	80	-3525	0	0	0	0	0	0	0	1
437	0	0	0	0	0	0	0	0	0	0	0
438	0	0	0	0	0	0	0	0	0	0	0
439	0	0	0	0	0	0	0	0	0	0	0
440	0	80	-4025	0	0	0	0	0	0	0	1
441	250	80	-4025	0	0	0	0	0	0	0	1
442	355	80	-4025	0	0	0	0	0	0	0	1
443	1025	80	-4025	0	0	0	0	0	0	0	0
444	1525	80	-4025	0	0	0	0	0	0	0	0
445	2025	80	-4025	0	0	0	0	0	0	0	0
446	2695	80	-4025	0	0	0	0	0	0	0	1
447	2800	80	-4025	0	0	0	0	0	0	0	1
448	3050	80	-4025	0	0	0	0	0	0	0	1
449	3300	80	-4025	0	0	0	0	0	0	0	1
450	3405	80	-4025	0	0	0	0	0	0	0	1
451	4075	80	-4025	0	0	0	0	0	0	0	0
452	4575	80	-4025	0	0	0	0	0	0	0	0
453	5075	80	-4025	0	0	0	0	0	0	0	0
454	5745	80	-4025	0	0	0	0	0	0	0	1
455	5850	80	-4025	0	0	0	0	0	0	0	1
456	6100	80	-4025	0	0	0	0	0	0	0	1
457	0	0	0	0	0	0	0	0	0	0	0
458	0	0	0	0	0	0	0	0	0	0	0
459	0	0	0	0	0	0	0	0	0	0	0
460	0	80	-4525	0	0	0	0	0	0	0	1
461	250	80	-4525	0	0	0	0	0	0	0	1
462	355	80	-4525	0	0	0	0	0	0	0	1
463	1025	80	-4525	0	0	0	0	0	0	0	0
464	1525	80	-4525	0	0	0	0	0	0	0	0
465	2025	80	-4525	0	0	0	0	0	0	0	0
466	2695	80	-4525	0	0	0	0	0	0	0	1
467	2800	80	-4525	0	0	0	0	0	0	0	1
468	3050	80	-4525	0	0	0	0	0	0	0	1
469	3300	80	-4525	0	0	0	0	0	0	0	1
470	3405	80	-4525	0	0	0	0	0	0	0	1

471	4075	80	-4525	0	0	0	0	0	0	0	0
472	4575	80	-4525	0	0	0	0	0	0	0	0
473	5075	80	-4525	0	0	0	0	0	0	0	0
474	5745	80	-4525	0	0	0	0	0	0	0	1
475	5850	80	-4525	0	0	0	0	0	0	0	1
476	6100	80	-4525	0	0	0	0	0	0	0	1
477	0	0	0	0	0	0	0	0	0	0	0
478	0	0	0	0	0	0	0	0	0	0	0
479	0	0	0	0	0	0	0	0	0	0	0
480	0	112.5	-5475	0	0	0	0	0	0	0	1
481	250	112.5	-5475	0	0	0	0	0	0	0	1
482	355	112.5	-5475	0	0	0	0	0	0	0	1
483	1025	112.5	-5475	0	0	0	0	0	0	0	0
484	1525	112.5	-5475	0	0	0	0	0	0	0	0
485	2025	112.5	-5475	0	0	0	0	0	0	0	0
486	2695	112.5	-5475	0	0	0	0	0	0	0	1
487	2800	112.5	-5475	0	0	0	0	0	0	0	1
488	3050	112.5	-5475	0	0	0	0	0	0	0	1
489	3300	112.5	-5475	0	0	0	0	0	0	0	1
490	3405	112.5	-5475	0	0	0	0	0	0	0	1
491	4075	112.5	-5475	0	0	0	0	0	0	0	0
492	4575	112.5	-5475	0	0	0	0	0	0	0	0
493	5075	112.5	-5475	0	0	0	0	0	0	0	0
494	5745	112.5	-5475	0	0	0	0	0	0	0	1
495	5850	112.5	-5475	0	0	0	0	0	0	0	1
496	6100	112.5	-5475	0	0	0	0	0	0	0	1
497	0	0	0	0	0	0	0	0	0	0	0
498	0	0	0	0	0	0	0	0	0	0	0
499	0	0	0	0	0	0	0	0	0	0	0
500	0	0	-250	0	0	0	0	0	0	0	1
501	0	0	-525	0	0	0	0	0	0	0	1
502	0	0	-1025	0	0	0	0	0	0	0	1
503	0	0	-1525	0	0	0	0	0	0	0	1
504	0	0	-2025	0	0	0	0	0	0	0	1
505	0	0	-2525	0	0	0	0	0	0	0	1
506	0	0	-3025	0	0	0	0	0	0	0	1
507	0	0	-3525	0	0	0	0	0	0	0	1
508	0	0	-4025	0	0	0	0	0	0	0	1
509	0	0	-4525	0	0	0	0	0	0	0	1
510	0	0	-5000	0	0	0	0	0	0	0	1
511	0	0	-5475	0	0	0	0	0	0	0	1
512	0	0	-6100	0	1	1	1	1	1	0	1
513	0	0	0	0	0	0	0	0	0	0	0
514	0	0	0	0	0	0	0	0	0	0	0
515	3050	0	-250	0	0	0	0	0	0	0	1
516	3050	0	-525	0	0	0	0	0	0	0	1
517	3050	0	-1025	0	0	0	0	0	0	0	1
518	3050	0	-1525	0	0	0	0	0	0	0	1
519	3050	0	-2025	0	0	0	0	0	0	0	1
520	3050	0	-2525	0	0	0	0	0	0	0	1
521	3050	0	-3025	0	0	0	0	0	0	0	1
522	3050	0	-3525	0	0	0	0	0	0	0	1
523	3050	0	-4025	0	0	0	0	0	0	0	1
524	3050	0	-4525	0	0	0	0	0	0	0	1
525	3050	0	-5000	0	0	0	0	0	0	0	1
526	3050	0	-5475	0	0	0	0	0	0	0	1
527	3050	0	-6100	0	1	0	0	0	0	0	1
528	0	0	0	0	0	0	0	0	0	0	0
529	0	0	0	0	0	0	0	0	0	0	0
530	6100	0	-250	0	0	0	0	0	0	0	1

531	6100	0	-525	0	0	0	0	0	0	0	1
532	6100	0	-1025	0	0	0	0	0	0	0	1
533	6100	0	-1525	0	0	0	0	0	0	0	1
534	6100	0	-2025	0	0	0	0	0	0	0	1
535	6100	0	-2525	0	0	0	0	0	0	0	1
536	6100	0	-3025	0	0	0	0	0	0	0	1
537	6100	0	-3525	0	0	0	0	0	0	0	1
538	6100	0	-4025	0	0	0	0	0	0	0	1
539	6100	0	-4525	0	0	0	0	0	0	0	1
540	6100	0	-5000	0	0	0	0	0	0	0	1
541	6100	0	-5475	0	0	0	0	0	0	0	1
542	6100	0	-6100	0	1	1	1	1	1	0	1
543	0	177.5	0	0	0	0	0	0	0	0	1
544	3050	177.5	0	0	0	0	0	0	0	0	1
545	6100	177.5	0	0	0	0	0	0	0	0	1

DRIFT A !INTERSOTREY DRIFT INPUT
3 1

ELEMENTS 1 !MEMBER GEOMETRY

1	1	2	1	0	0	+X	1
2	1	2	3	0	0	-X	1
3	1	5	4	0	0	+X	1
4	1	5	6	0	0	-X	1
5	1	8	7	0	0	+X	1
6	1	8	9	0	0	-X	1
7	2	24	25	10	11	+Z	1
8	4	25	26	11	12	+Z	1
9	4	26	27	12	13	+Z	1
10	4	27	28	13	14	+Z	1
11	4	28	29	14	15	+Z	1
12	3	29	30	15	16	+Z	1
13	3	31	32	17	18	+Z	1
14	4	32	33	18	19	+Z	1
15	4	33	34	19	20	+Z	1
16	4	34	35	20	21	+Z	1
17	4	35	36	21	22	+Z	1
18	2	36	37	22	23	+Z	1
19	12	60	61	0	0	+Z	1
20	5	61	62	82	81	0	1
21	5	62	63	83	82	0	0
22	5	63	64	84	83	0	0
23	5	64	65	85	84	0	0
24	5	65	66	86	85	0	0
25	5	66	67	87	86	0	1
26	20	67	68	0	0	+Z	1
27	20	68	69	0	0	+Z	1
28	5	69	70	90	89	0	1
29	5	70	71	91	90	0	0
30	5	71	72	92	91	0	0
31	5	72	73	93	92	0	0
32	5	73	74	94	93	0	0
33	5	74	75	95	94	0	1
34	12	75	76	0	0	+Z	1
35	12	80	81	0	0	+Z	1
36	5	81	82	102	101	0	1
37	5	82	83	103	102	0	0
38	5	83	84	104	103	0	0
39	5	84	85	105	104	0	0
40	5	85	86	106	105	0	0

41	5	86	87	107	106	0	1
42	20	87	88	0	0	+Z	1
43	20	88	89	0	0	+Z	1
44	5	89	90	110	109	0	1
45	5	90	91	111	110	0	0
46	5	91	92	112	111	0	0
47	5	92	93	113	112	0	0
48	5	93	94	114	113	0	0
49	5	94	95	115	114	0	1
50	12	95	96	0	0	+Z	1
51	12	100	101	0	0	+Z	1
52	5	101	102	122	121	0	1
53	5	102	103	123	122	0	0
54	5	103	104	124	123	0	0
55	5	104	105	125	124	0	0
56	5	105	106	126	125	0	0
57	5	106	107	127	126	0	1
58	20	107	108	0	0	+Z	1
59	20	108	109	0	0	+Z	1
60	5	109	110	130	129	0	1
61	5	110	111	131	130	0	0
62	5	111	112	132	131	0	0
63	5	112	113	133	132	0	0
64	5	113	114	134	133	0	0
65	5	114	115	135	134	0	1
66	12	115	116	0	0	+Z	1
67	12	120	121	0	0	+Z	1
68	5	121	122	142	141	0	1
69	5	122	123	143	142	0	0
70	5	123	124	144	143	0	0
71	5	124	125	145	144	0	0
72	5	125	126	146	145	0	0
73	5	126	127	147	146	0	1
74	20	127	128	0	0	+Z	1
75	20	128	129	0	0	+Z	1
76	5	129	130	150	149	0	1
77	5	130	131	151	150	0	0
78	5	131	132	152	151	0	0
79	5	132	133	153	152	0	0
80	5	133	134	154	153	0	0
81	5	134	135	155	154	0	1
82	12	135	136	0	0	+Z	1
83	12	140	141	0	0	+Z	1
84	5	141	142	162	161	0	1
85	5	142	143	163	162	0	0
86	5	143	144	164	163	0	0
87	5	144	145	165	164	0	0
88	5	145	146	166	165	0	0
89	5	146	147	167	166	0	1
90	20	147	148	0	0	+Z	1
91	20	148	149	0	0	+Z	1
92	5	149	150	170	169	0	1
93	5	150	151	171	170	0	0
94	5	151	152	172	171	0	0
95	5	152	153	173	172	0	0
96	5	153	154	174	173	0	0
97	5	154	155	175	174	0	1
98	12	155	156	0	0	+Z	1
99	12	160	161	0	0	+Z	1
100	5	161	162	182	181	0	1

101	5	162	163	183	182	0	0
102	5	163	164	184	183	0	0
103	5	164	165	185	184	0	0
104	5	165	166	186	185	0	0
105	5	166	167	187	186	0	1
106	20	167	168	0	0	+Z	1
107	20	168	169	0	0	+Z	1
108	5	169	170	190	189	0	1
109	5	170	171	191	190	0	0
110	5	171	172	192	191	0	0
111	5	172	173	193	192	0	0
112	5	173	174	194	193	0	0
113	5	174	175	195	194	0	1
114	12	175	176	0	0	+Z	1
115	12	180	181	0	0	+Z	1
116	5	181	182	202	201	0	1
117	5	182	183	203	202	0	0
118	5	183	184	204	203	0	0
119	5	184	185	205	204	0	0
120	5	185	186	206	205	0	0
121	5	186	187	207	206	0	1
122	20	187	188	0	0	+Z	1
123	20	188	189	0	0	+Z	1
124	5	189	190	210	209	0	1
125	5	190	191	211	210	0	0
126	5	191	192	212	211	0	0
127	5	192	193	213	212	0	0
128	5	193	194	214	213	0	0
129	5	194	195	215	214	0	1
130	12	195	196	0	0	+Z	1
131	12	200	201	0	0	+Z	1
132	5	201	202	222	221	0	1
133	5	202	203	223	222	0	0
134	5	203	204	224	223	0	0
135	5	204	205	225	224	0	0
136	5	205	206	226	225	0	0
137	5	206	207	227	226	0	1
138	20	207	208	0	0	+Z	1
139	20	208	209	0	0	+Z	1
140	5	209	210	230	229	0	1
141	5	210	211	231	230	0	0
142	5	211	212	232	231	0	0
143	5	212	213	233	232	0	0
144	5	213	214	234	233	0	0
145	5	214	215	235	234	0	1
146	12	215	216	0	0	+Z	1
147	5	220	221	241	240	0	1
148	5	221	222	242	241	0	1
149	5	222	223	243	242	0	0
150	5	223	224	244	243	0	0
151	5	224	225	245	244	0	0
152	5	225	226	246	245	0	0
153	5	226	227	247	246	0	1
154	5	227	228	248	247	0	1
155	5	228	229	249	248	0	1
156	5	229	230	250	249	0	1
157	5	230	231	251	250	0	0
158	5	231	232	252	251	0	0
159	5	232	233	253	252	0	0
160	5	233	234	254	253	0	0

161	5	234	235	255	254	0	1
162	5	235	236	256	255	0	1
163	5	240	241	261	260	0	1
164	5	241	242	262	261	0	1
165	5	242	243	263	262	0	0
166	5	243	244	264	263	0	0
167	5	244	245	265	264	0	0
168	5	245	246	266	265	0	0
169	5	246	247	267	266	0	1
170	5	247	248	268	267	0	1
171	5	248	249	269	268	0	1
172	5	249	250	270	269	0	1
173	5	250	251	271	270	0	0
174	5	251	252	272	271	0	0
175	5	252	253	273	272	0	0
176	5	253	254	274	273	0	0
177	5	254	255	275	274	0	1
178	5	255	256	276	275	0	1
179	5	260	261	281	280	0	1
180	5	261	262	282	281	0	1
181	5	262	263	283	282	0	0
182	5	263	264	284	283	0	0
183	5	264	265	285	284	0	0
184	5	265	266	286	285	0	0
185	5	266	267	287	286	0	1
186	5	267	268	288	287	0	1
187	5	268	269	289	288	0	1
188	5	269	270	290	289	0	1
189	5	270	271	291	290	0	0
190	5	271	272	292	291	0	0
191	5	272	273	293	292	0	0
192	5	273	274	294	293	0	0
193	5	274	275	295	294	0	1
194	5	275	276	296	295	0	1
195	13	60	61	0	0	+Z	1
196	6	61	62	301	302	+Z	1
197	6	62	63	302	303	+Z	0
198	6	63	64	303	304	+Z	0
199	6	64	65	304	305	+Z	0
200	6	65	66	305	306	+Z	0
201	6	66	67	306	307	+Z	1
202	13	67	68	0	0	+Z	1
203	13	68	69	0	0	+Z	1
204	6	69	70	309	310	+Z	1
205	6	70	71	310	311	+Z	0
206	6	71	72	311	312	+Z	0
207	6	72	73	312	313	+Z	0
208	6	73	74	313	314	+Z	0
209	6	74	75	314	315	+Z	1
210	13	75	76	0	0	+Z	1
211	13	80	81	0	0	+Z	1
212	6	81	82	321	322	+Z	1
213	6	82	83	322	323	+Z	0
214	6	83	84	323	324	+Z	0
215	6	84	85	324	325	+Z	0
216	6	85	86	325	326	+Z	0
217	6	86	87	326	327	+Z	1
218	13	87	88	0	0	+Z	1
219	13	88	89	0	0	+Z	1
220	6	89	90	329	330	+Z	1

221	6	90	91	330	331	+Z	0
222	6	91	92	331	332	+Z	0
223	6	92	93	332	333	+Z	0
224	6	93	94	333	334	+Z	0
225	6	94	95	334	335	+Z	1
226	13	95	96	0	0	+Z	1
227	13	100	101	0	0	+Z	1
228	6	101	102	341	342	+Z	1
229	6	102	103	342	343	+Z	0
230	6	103	104	343	344	+Z	0
231	6	104	105	344	345	+Z	0
232	6	105	106	345	346	+Z	0
233	6	106	107	346	347	+Z	1
234	13	107	108	0	0	+Z	1
235	13	108	109	0	0	+Z	1
236	6	109	110	349	350	+Z	1
237	6	110	111	350	351	+Z	0
238	6	111	112	351	352	+Z	0
239	6	112	113	352	353	+Z	0
240	6	113	114	353	354	+Z	0
241	6	114	115	354	355	+Z	1
242	13	115	116	0	0	+Z	1
243	13	120	121	0	0	+Z	1
244	6	121	122	361	362	+Z	1
245	6	122	123	362	363	+Z	0
246	6	123	124	363	364	+Z	0
247	6	124	125	364	365	+Z	0
248	6	125	126	365	366	+Z	0
249	6	126	127	366	367	+Z	1
250	13	127	128	0	0	+Z	1
251	13	128	129	0	0	+Z	1
252	6	129	130	369	370	+Z	1
253	6	130	131	370	371	+Z	0
254	6	131	132	371	372	+Z	0
255	6	132	133	372	373	+Z	0
256	6	133	134	373	374	+Z	0
257	6	134	135	374	375	+Z	1
258	13	135	136	0	0	+Z	1
259	13	140	141	0	0	+Z	1
260	6	141	142	381	382	+Z	1
261	6	142	143	382	383	+Z	0
262	6	143	144	383	384	+Z	0
263	6	144	145	384	385	+Z	0
264	6	145	146	385	386	+Z	0
265	6	146	147	386	387	+Z	1
266	13	147	148	0	0	+Z	1
267	13	148	149	0	0	+Z	1
268	6	149	150	389	390	+Z	1
269	6	150	151	390	391	+Z	0
270	6	151	152	391	392	+Z	0
271	6	152	153	392	393	+Z	0
272	6	153	154	393	394	+Z	0
273	6	154	155	394	395	+Z	1
274	13	155	156	0	0	+Z	1
275	13	160	161	0	0	+Z	1
276	6	161	162	401	402	+Z	1
277	6	162	163	402	403	+Z	0
278	6	163	164	403	404	+Z	0
279	6	164	165	404	405	+Z	0
280	6	165	166	405	406	+Z	0

281	6	166	167	406	407	+Z	1
282	13	167	168	0	0	+Z	1
283	13	168	169	0	0	+Z	1
284	6	169	170	409	410	+Z	1
285	6	170	171	410	411	+Z	0
286	6	171	172	411	412	+Z	0
287	6	172	173	412	413	+Z	0
288	6	173	174	413	414	+Z	0
289	6	174	175	414	415	+Z	1
290	13	175	176	0	0	+Z	1
291	13	180	181	0	0	+Z	1
292	6	181	182	421	422	+Z	1
293	6	182	183	422	423	+Z	0
294	6	183	184	423	424	+Z	0
295	6	184	185	424	425	+Z	0
296	6	185	186	425	426	+Z	0
297	6	186	187	426	427	+Z	1
298	13	187	188	0	0	+Z	1
299	13	188	189	0	0	+Z	1
300	6	189	190	429	430	+Z	1
301	6	190	191	430	431	+Z	0
302	6	191	192	431	432	+Z	0
303	6	192	193	432	433	+Z	0
304	6	193	194	433	434	+Z	0
305	6	194	195	434	435	+Z	1
306	13	195	196	0	0	+Z	1
307	13	200	201	0	0	+Z	1
308	6	201	202	441	442	+Z	1
309	6	202	203	442	443	+Z	0
310	6	203	204	443	444	+Z	0
311	6	204	205	444	445	+Z	0
312	6	205	206	445	446	+Z	0
313	6	206	207	446	447	+Z	1
314	13	207	208	0	0	+Z	1
315	13	208	209	0	0	+Z	1
316	6	209	210	449	450	+Z	1
317	6	210	211	450	451	+Z	0
318	6	211	212	451	452	+Z	0
319	6	212	213	452	453	+Z	0
320	6	213	214	453	454	+Z	0
321	6	214	215	454	455	+Z	1
322	13	215	216	0	0	+Z	1
323	13	220	221	0	0	+Z	1
324	6	221	222	461	462	+Z	1
325	6	222	223	462	463	+Z	0
326	6	223	224	463	464	+Z	0
327	6	224	225	464	465	+Z	0
328	6	225	226	465	466	+Z	0
329	6	226	227	466	467	+Z	1
330	13	227	228	0	0	+Z	1
331	13	228	229	0	0	+Z	1
332	6	229	230	469	470	+Z	1
333	6	230	231	470	471	+Z	0
334	6	231	232	471	472	+Z	0
335	6	232	233	472	473	+Z	0
336	6	233	234	473	474	+Z	0
337	6	234	235	474	475	+Z	1
338	13	235	236	0	0	+Z	1
339	7	260	261	480	481	+Z	1
340	7	261	262	481	482	+Z	1

341	7	262	263	482	483	+Z	0
342	7	263	264	483	484	+Z	0
343	7	264	265	484	485	+Z	0
344	7	265	266	485	486	+Z	0
345	7	266	267	486	487	+Z	1
346	7	267	268	487	488	+Z	1
347	7	268	269	488	489	+Z	1
348	7	269	270	489	490	+Z	1
349	7	270	271	490	491	+Z	0
350	7	271	272	491	492	+Z	0
351	7	272	273	492	493	+Z	0
352	7	273	274	493	494	+Z	0
353	7	274	275	494	495	+Z	1
354	7	275	276	495	496	+Z	1
355	8	40	60	500	501	+X	1
356	8	60	80	501	502	+X	1
357	8	80	100	502	503	+X	1
358	8	100	120	503	504	+X	1
359	8	120	140	504	505	+X	1
360	8	140	160	505	506	+X	1
361	8	160	180	506	507	+X	1
362	8	180	200	507	508	+X	1
363	8	200	220	508	509	+X	1
364	8	220	240	509	510	+X	1
365	8	240	260	510	511	+X	1
366	8	260	280	511	512	+X	1
367	9	48	68	515	516	+X	1
368	9	68	88	516	517	+X	1
369	9	88	108	517	518	+X	1
370	9	108	128	518	519	+X	1
371	9	128	148	519	520	+X	1
372	9	148	168	520	521	+X	1
373	9	168	188	521	522	+X	1
374	9	188	208	522	523	+X	1
375	9	208	228	523	524	+X	1
376	9	228	248	524	525	+X	1
377	9	248	268	525	526	+X	1
378	9	268	288	526	527	+X	1
379	8	56	76	530	531	+X	1
380	8	76	96	531	532	+X	1
381	8	96	116	532	533	+X	1
382	8	116	136	533	534	+X	1
383	8	136	156	534	535	+X	1
384	8	156	176	535	536	+X	1
385	8	176	196	536	537	+X	1
386	8	196	216	537	538	+X	1
387	8	216	236	538	539	+X	1
388	8	236	256	539	540	+X	1
389	8	256	276	540	541	+X	1
390	8	276	296	541	542	+X	1
391	10	2	24	2	10	+Z	1
392	10	30	5	16	5	+Z	1
393	10	5	31	5	17	+Z	1
394	10	37	8	23	8	+Z	1
395	11	2	40	2	500	+X	1
396	11	5	48	5	515	+X	1
397	11	8	56	8	530	+X	1
398	14	60	25	0	0	+Z	1
399	14	2	62	543	62	-Z	1
400	17	62	25	0	0	+X	1

```
401     15      62      26      0       0       +Z      1
402     15      25      63      0       0       -Z      1
403     18      63      26      0       0       +X      1
404     16      63      27      0       0       +Z      1
405     16      26      64      0       0       -Z      1
406     19      64      27      0       0       +X      1
407     16      64      28      0       0       +Z      1
408     16      27      65      0       0       -Z      1
409     18      65      28      0       0       +X      1
410     15      65      29      0       0       +Z      1
411     15      66      28      0       0       -Z      1
412     17      66      29      0       0       +X      1
413     14      66      5       66      544     +Z      1
414     14      29      68      0       0       -Z      1
415     14      68      32      0       0       +Z      1
416     14      5       70      544     70      -Z      1
417     17      70      32      0       0       +X      1
418     15      70      33      0       0       +Z      1
419     15      32      71      0       0       -Z      1
420     18      71      33      0       0       +X      1
421     16      71      34      0       0       +Z      1
422     16      33      72      0       0       -Z      1
423     19      72      34      0       0       +X      1
424     16      72      35      0       0       +Z      1
425     16      34      73      0       0       -Z      1
426     18      73      35      0       0       +X      1
427     15      73      36      0       0       +Z      1
428     15      35      74      0       0       -Z      1
429     17      74      36      0       0       +X      1
430     14      74      8       74      545     +Z      1
431     14      36      76      0       0       -Z      1

PROPS
1 FRAME                                                         !Column
2 0 0 0 0 0 0 0 0                                               !14A SECTION PARAMETERS
25400 10160 250000 10.4E+9 5.96E+9 5.96E+9 0 0 0 0 0           !14B SECION PROPERTIES
0 0 0 0                                                         !14C SECTION END PROPERTIES

2 REINFORCED                                                    !Exterior PHs
! Type  B     D   Cover  Length   weight   isteel  iconc
1       200   400   33       105        0         0       0       !control parameters
! Confined          Cover
! Ec      f'c     ft   Ec       f'c     ft
25400 -37.4 2.0 25400 -31.2 2.0                                 !concrete material
! Es         fy-   fy+  Effective length
200000  -326  326   458                                        !steel material
! A1    A2     A3     A4
301.6 301.6 301.6 301.6                                         !steel areas
! Vertical face            Horizontal face
! Ec      f'c   ft   depth  Ec    f'c   ft  depth  flexibility
25400 -10.6 0.1 100    254 -0.1 0.1 0.1     2 1 1              !diagonal concrete material
1 0 1 0.01 1 1.5 1 0                                            !confined concrete hysteresis
0.1 0 1 0.01 1 1 1 0                                            !cover concrete hysteresis
1 0 1.0 16 1.4 130 0.018 0 0 0                                  !Reinforcement hysteresis
0 0 1 0.01 1 0 0 8E-5                                           !Vertical Shear concrete hysteresis
0 0 1 0.01 1 0 0 0                                              !Horizontal Shear concrete hysteresis

3 REINFORCED                                                    !Interior PHs
! Type  B     D   Cover   Length   weight  isteel  iconc
1       200  400   33       105        0         0       0       !control parameters
```

```
! Confined           Cover
! Ec      f'c     ft    Ec       f'c     ft
25400 -37.4 2.0 25400 -31.2 2.0                                  !concrete material
! Es        fy-    fy+  Effective length
200000  -326  326    458                                         !steel material
! A1    A2     A3     A4
301.6 301.6 301.6 301.6                                          !steel areas
! Vertical face            Horizontal face
! Ec      f'c   ft   depth  Ec    f'c   ft  depth  flexibility
25400 -10.6 0.1 100    254 -0.1 0.1 0.1      2 1 1               !diagonal concrete material
1 0 1 0.01 1 1.5 1 0                                             !confined concrete hysteresis
0.1 0 1 0.01 1 1 1 0                                             !cover concrete hysteresis
1 0 1.0 16 1.4 130 0.018 0 0 0                                   !Reinforcement hysteresis
0 0 1 0.01 1 0 0 8E-5                                            !Vertical Shear concrete hysteresis
0 0 1 0.01 1 0 0 0                                               !Horizontal Shear concrete hysteresis

4 FRAME                                                          !Longitudinal Beam
1 0 0 0 0 0 0 0 0                                                !14A SECTION PARAMETERS
25400 10160 80000 1333E+6 533E+6 118E+6 0 0 0 0 0                !14B SECION PROPERTIES
0 0 0 0                                                          !14C SECTION END PROPERTIES

5 QUADRILATERAL                                                  !Shell Element
0 1 26000 0.25 45 0                                              !19A SECTION PROPERTIES

6 FRAME                                                          !Ribs
1 0 0 0 0 0 0 0 0                                                !14A SECTION PARAMETERS
27900 11200 21000 40.6E+6 12.5E+6 28.1E+6 0 0 0 0 0              !14B SECION PROPERTIES
0 0 0 0                                                          !14C SECTION END PROPERTIES

7 FRAME                                                          !End Slab
1 0 0 0 0 0 0 0 0                                                !14A SECTION PARAMETERS
26000 10400 306000 7.9E+10 354E+6 3.52E+10 0 0 0 0 0             !14B SECION PROPERTIES
0 0 0 0                                                          !14C SECTION END PROPERTIES

8 FRAME                                                          !External Transverse Beams
1 0 0 0 2 0 0 0 0                                                !14A SECTION PARAMETERS
25400 10160 89000 1333E+6 533E+6 118E+6 0 0 0 0 0                !14B SECION PROPERTIES
0 0 0 0                                                          !14C SECTION END PROPERTIES
0.02 0.02 0.02 0.02                                              !14D MEMBER BILINEAR FACTORS
1 1 1 1                                                          !14E MEMBER HINGE LENGTH
0 0 35.5E+6 -35.5E+6 0 0                                         !14I YIELD INTERACTION
0 0 0 0                                                          !14II FLEXURAL YIELD

9 FRAME                                                          !Internal Transverse Beam
1 0 0 0 2 0 0 0 0                                                !14A SECTION PARAMETERS
25400 10160 98000 1333E+6 533E+6 118E+6 0 0 0 0 0                !14B SECION PROPERTIES
0 0 0 0                                                          !14C SECTION END PROPERTIES
0.02 0.02 0.02 0.02                                              !14D MEMBER BILINEAR FACTORS
1 1 1 1                                                          !14E MEMBER HINGE LENGTH
0 0 40.5E+6 -40.5E+6 0 0                                         !14I YIELD INTERACTION
0 0 0 0                                                          !14II FLEXURAL YIELD

10 FRAME                                                         !Beam-Column Joints
1 0 0 0 0 0 0 0 0                                                !14A SECTION PARAMETERS
25400 10160 80000 2666E+6 1066E+6 236E+6 0 0 0 0 0               !14B SECION PROPERTIES
0 0 0 0                                                          !14C SECTION END PROPERTIES

11 FRAME                                                         !Transverse Beam-Column Joints
1 0 0 0 0 0 0 0 0                                                !14A SECTION PARAMETERS
25400 10160 89000 2666E+6 1066E+6 236E+6 0 0 0 0 0               !14B SECION PROPERTIES
```

```
0 0 0 0                                  !14C SECTION END PROPERTIES

12 Spring                                !External Steel interface
1 53 0 0 0 0                             !15A CONTROL PARAMETERS
129000 0 0 0 0 0 0 0 0                   !15B SECTION PROPERTIES
70000 -70000 0 0 0 0                     !15E YIELD SURFACE FORCE
0 0 0 0 0 0                              !15F YIELD SURFACE MOMENT
1 0 1.0 9.9 1.3 63 0.018 0 0 0           !Reinforcement hysteresis
0 0 0 0 0 0 0 0 0 0 0 0
0 0 0 0 0 0 0 0 0 0 0 0
0 0 0 0 0 0 0 0 0 0 0 0
0 0 0 0 0 0 0 0 0 0 0 0
0 0 0 0 0 0 0 0 0 0 0 0

13 Spring                                !Concrete interface
1 54 0 0 0 0                             !15A CONTROL PARAMETERS
2.3E+6 0 0 0 0 0 0 0 0                   !15B SECTION PROPERTIES
47300 -743000 0 0 0 0                    !15E YIELD SURFACE FORCE
0 0 0 0 0 0                              !15F YIELD SURFACE MOMENT
0.1 0 1 0.01 1 1 1 0                     !confined concrete hysteresis
0 0 0 0 0 0 0 0
0 0 0 0 0 0 0 0
0 0 0 0 0 0 0 0
0 0 0 0 0 0 0 0

14 Spring                                !Concrete Diagonal 1
1 54 0 0 0 0                             !15A CONTROL PARAMETERS
543E+3 0 0 0 0 0 0 0 0                   !15B SECTION PROPERTIES
278 -437000 0 0 0 0                      !15E YIELD SURFACE FORCE
0 0 0 0 0 0                              !15F YIELD SURFACE MOMENT
0 0 1 0.01 1 0 0 8E-5                    !confined concrete hysteresis
0 0 0 0 0 0 0 0
0 0 0 0 0 0 0 0
0 0 0 0 0 0 0 0
0 0 0 0 0 0 0 0

15 Spring                                !Concrete Diagonal 2
1 54 0 0 0 0                             !15A CONTROL PARAMETERS
568E+3 0 0 0 0 0 0 0 0                   !15B SECTION PROPERTIES
390 -613000 0 0 0 0                      !15E YIELD SURFACE FORCE
0 0 0 0 0 0                              !15F YIELD SURFACE MOMENT
0 0 1 0.01 1 0 0 8E-5                    !confined concrete hysteresis
0 0 0 0 0 0 0 0
0 0 0 0 0 0 0 0
0 0 0 0 0 0 0 0
0 0 0 0 0 0 0 0

16 Spring                                !Concrete Diagonal 3
1 54 0 0 0 0                             !15A CONTROL PARAMETERS
584E+3 0 0 0 0 0 0 0 0                   !15B SECTION PROPERTIES
342 -538000 0 0 0 0                      !15E YIELD SURFACE FORCE
0 0 0 0 0 0                              !15F YIELD SURFACE MOMENT
0 0 1 0.01 1 0 0 8E-5                    !confined concrete hysteresis
0 0 0 0 0 0 0 0
0 0 0 0 0 0 0 0
0 0 0 0 0 0 0 0
0 0 0 0 0 0 0 0

17 Spring                                !Steel tie 1
1 53 0 0 0 0                             !15A CONTROL PARAMETERS
```

```
80600 0 0 0 0 0 0 0 0                          !15B SECTION PROPERTIES
96100 -96100 0 0 0 0                           !15E YIELD SURFACE FORCE
0 0 0 0 0 0                                    !15F YIELD SURFACE MOMENT
1 0 1.0 9.9 1.3 63 0.018 0 0 0                 !Reinforcement hysteresis
0 0 0 0 0 0 0 0 0 0 0 0
0 0 0 0 0 0 0 0 0 0 0 0
0 0 0 0 0 0 0 0 0 0 0 0
0 0 0 0 0 0 0 0 0 0 0 0
0 0 0 0 0 0 0 0 0 0 0 0

18 Spring                                      !Steel tie 2
1 53 0 0 0 0                                   !15A CONTROL PARAMETERS
68400 0 0 0 0 0 0 0 0                          !15B SECTION PROPERTIES
81600 -81600 0 0 0 0                           !15E YIELD SURFACE FORCE
0 0 0 0 0 0                                    !15F YIELD SURFACE MOMENT
1 0 1.0 9.9 1.3 63 0.018 0 0 0                 !Reinforcement hysteresis
0 0 0 0 0 0 0 0 0 0 0 0
0 0 0 0 0 0 0 0 0 0 0 0
0 0 0 0 0 0 0 0 0 0 0 0
0 0 0 0 0 0 0 0 0 0 0 0
0 0 0 0 0 0 0 0 0 0 0 0

19 Spring                                      !Steel tie 3
1 53 0 0 0 0                                   !15A CONTROL PARAMETERS
58400 0 0 0 0 0 0 0 0                          !15B SECTION PROPERTIES
69700 -69700 0 0 0 0                           !15E YIELD SURFACE FORCE
0 0 0 0 0 0                                    !15F YIELD SURFACE MOMENT
1 0 1.0 9.9 1.3 63 0.018 0 0 0                 !Reinforcement hysteresis
0 0 0 0 0 0 0 0 0 0 0 0
0 0 0 0 0 0 0 0 0 0 0 0
0 0 0 0 0 0 0 0 0 0 0 0
0 0 0 0 0 0 0 0 0 0 0 0
0 0 0 0 0 0 0 0 0 0 0 0

20 Spring                                      !Center Steel interface
1 53 0 0 0 0                                   !15A CONTROL PARAMETERS
143000 0 0 0 0 0 0 0 0                         !15B SECTION PROPERTIES
70000 -70000 0 0 0 0                           !15E YIELD SURFACE FORCE
0 0 0 0 0 0                                    !15F YIELD SURFACE MOMENT
1 0 1.0 9.9 1.3 63 0.018 0 0 0                 !Reinforcement hysteresis
0 0 0 0 0 0 0 0 0 0 0 0
0 0 0 0 0 0 0 0 0 0 0 0
0 0 0 0 0 0 0 0 0 0 0 0
0 0 0 0 0 0 0 0 0 0 0 0
0 0 0 0 0 0 0 0 0 0 0 0

WEIGHTS 0

LOADS 0

EQUAKE rotation.eqf
3 1 1 1 -1 0 0 1
```

APPENDIX C. MATERIAL PROPERTIES

C.1 CONCRETE COMPRESSIVE STRENGTH

Table C-1 Summary of the concrete compressive strength

Member		Averaged Compressive stress f_c' (MPa)		
		Cylinder 1	Cylinder 2	Cylinder 3
Longitudinal beam, lower half of transverse beams, columns below the main beams, and beam-column joints	7 Days	20.6	22.2	-
	28 Days	26.5	26.5	26.7
	Start of test	28.5	32.6	32.6
	End of test	28.4	32.3	31.1
Transverse beam lap-splice and the rest of columns	7 Days	30.8	33.1	-
	28 Days	38.8	41.3	38.2
	Start of test	41.5	42.5	43.3
	End of test	52.7	50.0	47.6
Floor slab, top half of transverse beams and end slab	7 Days	22.7	25.5	-
	28 Days	32.3	30.3	29.5
	Start of test	33.4	34.6	31.1
	End of test	32.1	34.0	34.1

C.2 STRESS-STRAIN RELATIONSHIPS OF REINFORCING BARS

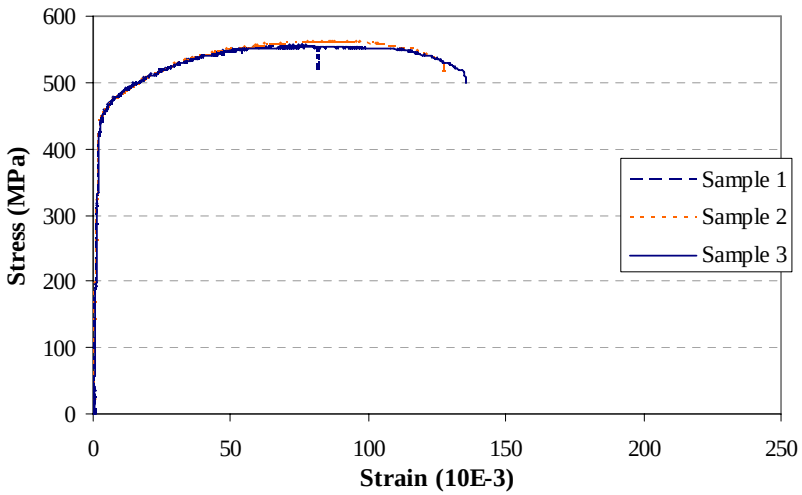

(a) *R6* reinforcing bars

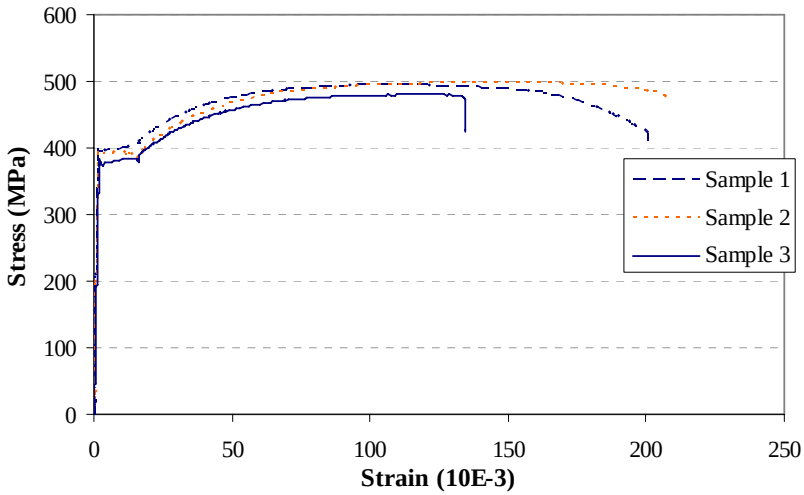

(b) *R10* reinforcing bars

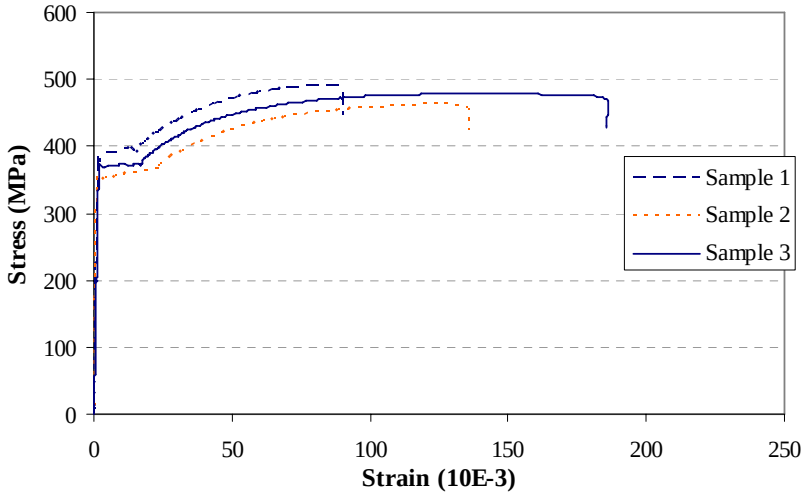

(c) *D10* reinforcing bars

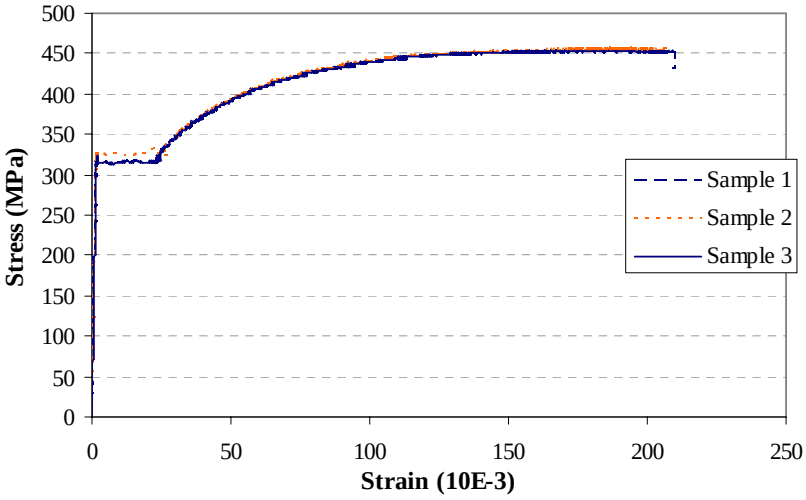

(d) *D16* reinforcing bars

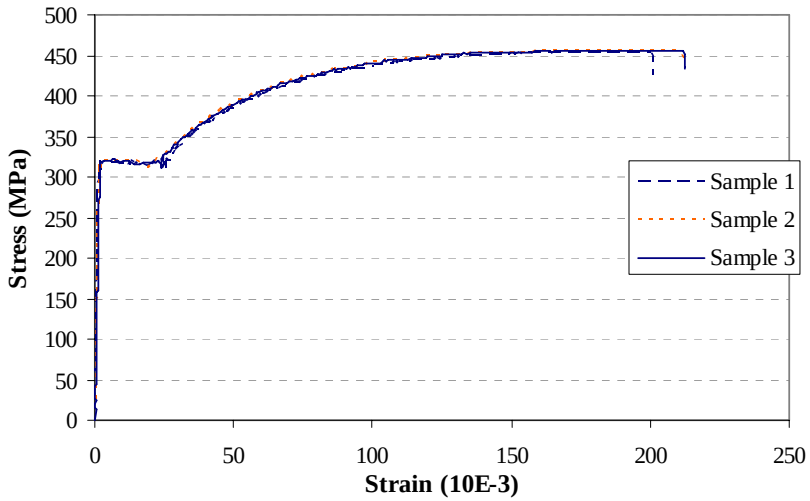

(e) *D20* reinforcing bars

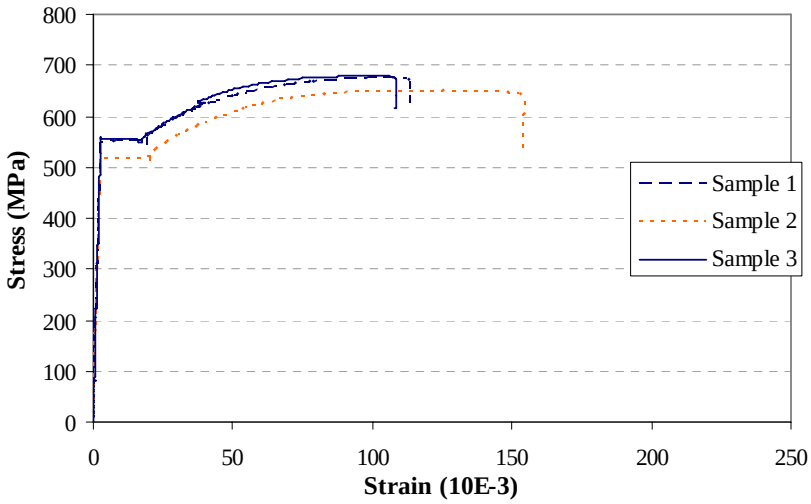

(f) *HD12* reinforcing bars

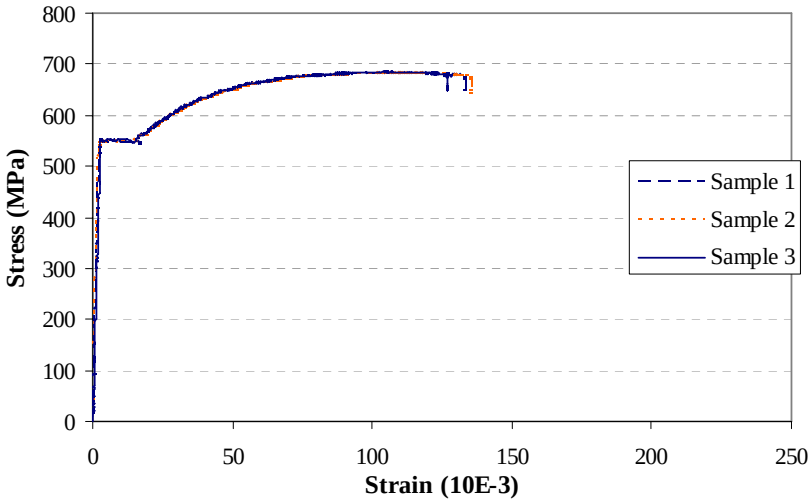

(g) *HD16* reinforcing bars

Figure C-1. Stress-strain relationships of reinforcing bars used in the sub-assemblage

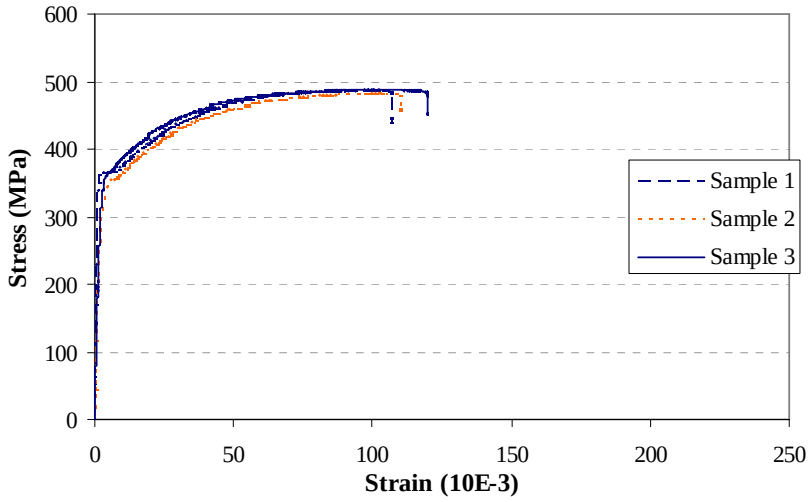

(a) Top main beam *D16* reinforcement

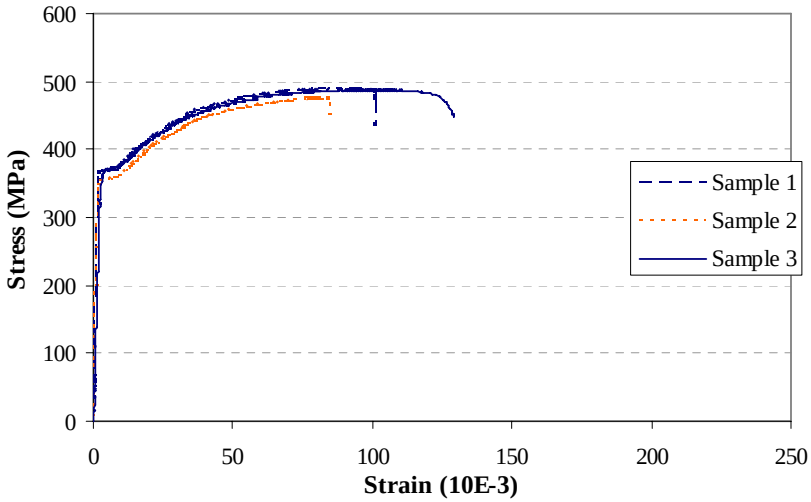

(b) Bottom main beam *D16* reinforcement

Figure C-2. Stress-strain relationships of the main beam reinforcement broken out of the sub-assemblage after the test